

Transactions of the ASME®

Journal of Turbomachinery

Published Quarterly by The American Society of Mechanical Engineers

VOLUME 114 • NUMBER 1 • JANUARY 1992

Technical Editor,
G. K. SEROVY

Associate Technical Editors
Advanced Energy Systems

M. J. MORAN
Environmental Control

H. E. HESKETH
Fuels and Combustion Technologies

D. W. PACER

Gas Turbine

S. A. MOSIER

Internal Combustion Engine

J. A. CATON

Nuclear Engineering

S. M. CHO

Power

R. W. PORTER

BOARD ON
COMMUNICATIONS
Chairman and Vice-President
M. E. FRANKE

Members-at-Large

W. BEGELL

T. F. CONRY

T. DEAR

R. L. KASTOR

J. KITTO

R. MATES

W. MORGAN

E. M. PATTON

R. E. REDER

A. VAN DER SLUYS

F. M. WHITE

B. ZIELS

President, N. H. HURT, JR.

Executive Director,

D. L. BELDEN

Treasurer, ROBERT A. BENNETT

PUBLISHING STAFF

Mng. Dir., Publ.,

CHARLES W. BEARDSLEY

Managing Editor,

CORNELIA MONAHAN

Sr. Production Editor,

VALERIE WINTERS

Production Assistant,

MARISOL ANDINO

TECHNICAL PAPERS

- 1 Turbine Preliminary Design Using Artificial Intelligence and Numerical Optimization Techniques (90-GT-148)
S. S. Tong and B. A. Gregory
- 8 Toward Improved Throughflow Capability: The Use of Three-Dimensional Viscous Flow Solvers in a Multistage Environment (90-GT-18)
W. N. Dawes
- 18 The Calculation of Three-Dimensional Viscous Flow Through Multistage Turbomachines (90-GT-19)
J. D. Denton
- 27 The Use of 3D Viscous Flow Calculations in the Design and Analysis of Industrial Centrifugal Compressors (90-GT-2)
M. V. Casey, P. Dalbert, and P. Roth
- 38 Three-Dimensional Rotational Flow in Transonic Turbomachines: Part I—Solution Obtained Using a Number of S_1 Stream Filaments of Revolution and a Central S_2 Stream Filament (90-GT-12)
Wu Chung-Hua, Wang Zhengming, and Chen Hongji
- 50 Three-Dimensional Rotational Flow in Transonic Turbomachines: Part II—Full Three-Dimensional Flow in CAS Rotor Obtained by Using a Number of S_1 and S_2 Stream Filaments (90-GT-13)
Wu Chung-Hua, Zhao Xiaolu, and Qin Lisen
- 61 Three-Dimensional Flow in an Axial Turbine: Part 1—Aerodynamic Mechanisms (90-GT-56)
D. Joslyn and R. Dring
- 71 Three-Dimensional Flow in an Axial Turbine: Part 2—Profile Attenuation (90-GT-57)
D. Joslyn and R. Dring
- 79 Assessment of Unsteady Flows in Turbines (90-GT-150)
O. P. Sharma, G. F. Pickett, and R. H. Ni
- 91 Investigation of Unsteady Flow Through a Transonic Turbine Stage: Data/Prediction Comparison for Time-Averaged and Phase-Resolved Pressure Data
M. G. Dunn, W. A. Bennett, R. A. Delaney, and K. V. Rao
- 100 Measurements of the Pressure and Velocity Distribution in Low-Speed Turbomachinery by Means of High-Frequency Pressure Transducers
S. Brodersen and D. Wulff
- 108 Influence of Periodically Unsteady Wake Flow on the Flow Separation in Blade Channels (90-GT-253)
G. H. Dibelius and E. Ahlers
- 114 On the Prediction of Unsteady Forces on Gas Turbine Blades: Part 1—Description of the Approach
T. Korakianitis
- 123 On the Prediction of Unsteady Forces on Gas Turbine Blades: Part 2—Analysis of the Results (88-GT-89 and 88-GT-90)
T. Korakianitis
- 132 The Aerodynamic and Mechanical Performance of a High-Pressure Turbine Stage in a Transient Wind Tunnel (90-GT-353)
A. G. Sheard and R. W. Ainsworth
- 141 Design of Turbomachinery Blading in Transonic Flows by the Circulation Method
T. Q. Dang
- 147 Aero-Thermal Performance of a Two-Dimensional Highly Loaded Transonic Turbine Nozzle Guide Vane: A Test Case for Inviscid and Viscous Flow Computations (90-GT-358)
T. Arts and M. Lambert de Rouvoit

(Contents Continued on p. 7)

Transactions of the ASME, Journal of Turbomachinery (ISSN 0889-504X) is published quarterly (Jan., Apr., July, Oct.) for \$125.00 per year by The American Society of Mechanical Engineers, 345 East 47th Street, New York, NY 10017. Second class postage paid at New York, NY and additional mailing offices. POSTMASTER: Send address change to Transactions of the ASME, Journal of Turbomachinery, c/o THE AMERICAN SOCIETY OF MECHANICAL ENGINEERS, 22 Law Drive, Box 2300, Fairfield, NJ 07007-2300.

CHANGES OF ADDRESS must be received at Society headquarters seven weeks before they are to be effective. Please send old label and new address.

PRICES: To members, \$36.00, annually; to nonmembers, \$125.00.

Add \$15.00 for postage to countries outside the United States and Canada.

STATEMENT from By-Laws. The Society shall not be responsible for statements or opinions advanced in papers or . . . printed in its publications (B 7.1, para. 3).

COPYRIGHT © 1992 by The American Society of Mechanical Engineers. Reprints from this publication may be made on condition that full credit be given the

TRANSACTIONS OF THE ASME—JOURNAL OF TURBOMACHINERY, and the author, and date of publication be stated.

INDEXED by Applied Mechanics Reviews and Engineering Information, Inc.

Canadian Goods & Services Tax
Registration #126148048

(Contents Continued)

- 155 **An Examination of the Contributions to Loss on a Transonic Turbine Blade in Cascade** (90-GT-264)
D. J. Mee, N. C. Baines, M. L. G. Oldfield, and T. E. Dickens
- 163 **Detailed Boundary Layer Measurements on a Transonic Turbine Cascade** (90-GT-263)
D. J. Mee, N. C. Baines, and M. L. G. Oldfield
- 173 **Secondary Flow Measurements in a Turbine Cascade With High Inlet Turbulence** (90-GT-20)
D. G. Gregory-Smith and J. G. E. Cleak
- 184 **The Influence of Blade Lean on Turbine Losses** (90-GT-55)
S. Harrison
- 191 **Endwall Losses and Flow Unsteadiness in a Turbine Blade Cascade** (90-GT-355)
L. Adjout and S. L. Dixon
- 198 **The Development of Axial Turbine Leakage Loss for Two Profiled Tip Geometries Using Linear Cascade Data** (90-GT-152)
J. P. Bindon and G. Morphis
- 204 **Prediction of Tip-Leakage Losses in Axial Turbines** (90-GT-154)
M. I. Yaras and S. A. Sjolander
- 211 **Local Heat Transfer in Turbine Disk Cavities: Part I—Rotor and Stator Cooling With Hub Injection of Coolant** (90-GT-25)
R. S. Bunker, D. E. Metzger, and S. Wittig
- 221 **Local Heat Transfer in Turbine Disk Cavities: Part II—Rotor Cooling With Radial Location Injection of Coolant** (90-GT-26)
R. S. Bunker, D. E. Metzger, and S. Wittig
- 229 **Rotating Cavity With Axial Throughflow of Cooling Air: Heat Transfer** (90-GT-16)
P. R. Farthing, C. A. Long, J. M. Owen, and J. R. Pincombe
- 237 **Rotating Cavity With Axial Throughflow of Cooling Air: Flow Structure** (90-GT-17)
P. R. Farthing, C. A. Long, J. M. Owen, and J. R. Pincombe
- 247 **Computation of Heat Transfer in Rotating Cavities Using a Two-Equation Model of Turbulence** (90-GT-135)
A. P. Morse and C. L. Ong
- 256 **A Numerical Study of the Influence of Disk Geometry on the Flow and Heat Transfer in a Rotating Cavity** (90-GT-136)
B. L. Lapworth and J. W. Chew
- 264 **Pressure Losses in Combining Subsonic Flows Through Branched Ducts** (90-GT-134)
N. I. Abou-Haider and S. L. Dixon

ANNOUNCEMENTS

- 17 **Change of address form for subscribers**
Inside Back Cover **Information for authors**

Turbine Preliminary Design Using Artificial Intelligence and Numerical Optimization Techniques

S. S. Tong

Corporate Research and Development,
General Electric Company,
Schenectady, NY 12301

B. A. Gregory

GE Aircraft Engine,
Cincinnati, OH 45215

This paper describes a new software approach to the preliminary design of aircraft engine turbines. A hybrid artificial intelligence and numerical-optimization-based design shell called Engineous was used to capture some basic turbine preliminary design knowledge, manipulate turbine design parameters, execute a turbine performance prediction program and its preprocessors, and analyze results. Engineous automatically supplements incomplete human design knowledge with symbolic and numerical search techniques when needed. This approach produced designs with higher predicted performance gains than the existing manual design process in a tenth of the turnaround time and has yielded new insights into turbine design. A comparison of turbine designs obtained by designers and by Engineous is presented here along with an overview of Engineous system architecture.

Introduction

With the development of increasingly larger and faster computers, the complexity of the problems that can be tackled using computational techniques has increased also. Over the last decade, computational tools for designing turbomachinery have gradually developed to a point where many of them are being used routinely for new product design. These tools have improved the accuracy of estimates of design performance and have reduced the need for performing experiments for design iteration. As these tools come into wider use, two important issues need to be addressed: how to prevent human intervention from becoming a bottleneck in taking full advantage of such powerful tools, and how to preserve human design expertise. With the recent rapid reduction of the price/performance ratio for engineering workstations, the market-driven pressure to reduce both design cycle time and labor force, and the advances made in certain software technologies such as artificial intelligence (AI), we now have a good opportunity to explore new approaches to turbomachinery component design problems.

In 1984, the Turbine Technology Group at GE Aircraft Engine (GEAE) became interested in "Engineering Application of AI" work being done by the GE Research and Development Center (GE-CRD). Exploratory talks were held to determine whether GE-CRD's software and GEAE's computer-aided engineering (CAE) codes were compatible tools for establishing a quick turnaround for problem-solving. We agreed that these tools were indeed compatible and proceeded to launch an aggressive program to develop a common hard-

ware platform and integrate AI into the turbine design environment.

Turbine Preliminary Design

It is commonly assumed that designing turbines should be easy. After all, turbines have been around for hundreds of years in one form or another. The fluid is in a natural state of "expansion" and turbines, unlike compressors, do not entail the additional design complexities necessary to prevent stall.

If, in fact, turbine design was ever easy, it would never be easy again after Frank Whittle, in the 1930s, suggested using the gas turbine as a means of airplane propulsion. Since that time, turbine performance has become one of the premier requirements of the gas turbine engine.

Today turbine design has been developed into an exact science (more or less). The parameters peculiar to turbine design—work distribution, vector triangles, blade loading—and all the associated losses are quickly determined by computer programs that allow for a simple determination of the shape of the turbine flow path and the number of stages required to meet the duty requirements. Even simple cooling requirements can be quickly determined from the cycle parameters. Such programs were developed many years ago but have generally grown in sophistication by an evolutionary process over the years.

Computer programs of this kind are widely used at GEAE. One such program, Turbine Design and Off Design (TDOD), has been developed into a sophisticated preliminary design tool capable of predicting the performance of a given turbine design extremely accurately (Flagg, 1967). Figure 1 illustrates this capability. The known test efficiencies for over 70 turbines (high-pressure, low-pressure, cooled, and uncooled) are plotted versus the predicted efficiency. A 45-deg line is given on the

Contributed by the International Gas Turbine Institute and presented at the 35th International Gas Turbine and Aeroengine Congress and Exposition, Brussels, Belgium, June 11-14, 1990. Manuscript received by the International Gas Turbine Institute January 16, 1990. Paper No. 90-GT-148.

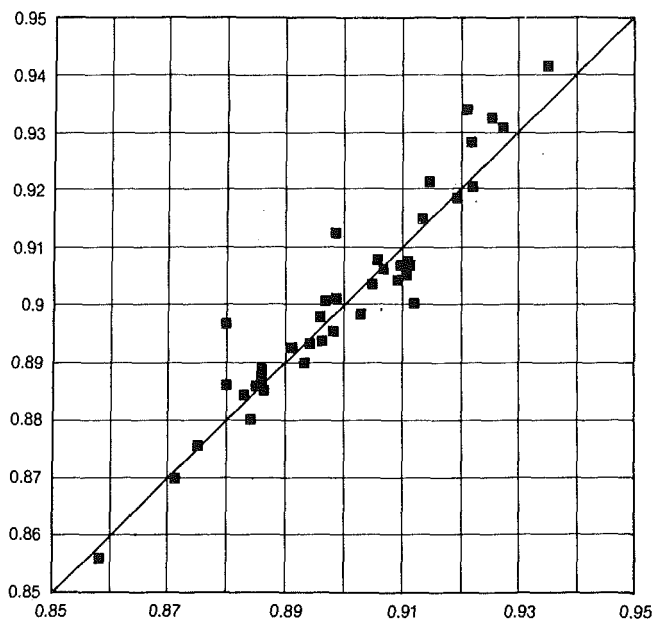


Fig. 1 Measured turbine efficiency versus turbine efficiency predicted by TDOD

figure, and it can be seen that TDOD is a competent tool for the turbine aerodynamics preliminary designer. The standard deviation is 0.1 percent.

TDOD uses a simple set of input criteria that describes the turbine flow path, the number of stages, and the stage work split. Such a tool, however, is good only for predicting the performance of a turbine as it is designed by the engineer. The designer may design a flow path that is adequate, matching all the cycle requirements of pressure, temperature, and shaft speed, but having poor performance characteristics. The designer must determine how far from optimum that particular design is and also what must be done to obtain the level of performance of that design with acceptable compromise to the cycle requirements, the performance of other components, and the mechanical design. The laborious task of fine tuning the many parameters is tedious, iterative, and expensive. What is more, the effect of changing one parameter may be of consequence to many other parameters, requiring accurate book-keeping of cause and effect.

What we have described so far is the task of a turbine designer who starts with a blank sheet of paper. More often than not, however, the designer is faced with a different task. Most gas turbine engines are developments or updated designs of current production engines. A company faced with the need to change the thrust rating of a particular engine will try to ensure that redesign is kept to a minimum in order to keep costs down. The component designer is, therefore, very often required to enhance a design with severe constraints imposed on changes (e.g., in tip diameter or length, or both). In that case, a highly iterative procedure has to be adopted so that all the performance gain can be extracted while meeting the duty requirements of the turbine.

Another major difficulty the designer is faced with is the time available to complete a design. The timetable of events for a new product to enter the marketplace is extremely long. In an attempt to shorten it, a very limited time is allocated for preliminary design that rarely allows for fine tuning.

After years of performing such design iterations, the turbine designer learns what to do at each stage of the design, which parameters can be tuned, and how dependent variables correlate. The knowledge the designer gains by long years of experience becomes a great asset to a company. It is in the business interest of a company that such knowledge should be

captured and used to set precedents for future design work and to give new and inexperienced engineers a head start in this (or indeed, any) discipline.

Engineous Shell

The needs we have described were the motivation for developing the software called Engineous. Engineous is a generic software shell that can be applied to the design of many different products. It uses state-of-the-art computer science technologies such as AI, object-oriented programming, and graphical user interface, as well as conventional computational methods such as numerical optimization and simulated annealing. Its basic approach is to separate problem-specific information from generic design functions and to organize them as knowledge bases. Engineous first draws on stored human design knowledge to emulate the design expert and rapidly produces "good" designs. After the stored human knowledge is exhausted, if time permits, Engineous automatically draws on its own set of heuristic search techniques to explore the design space. For a real-world complex problem, where required turnaround time is usually too short to exhaust all possibilities, this approach allows Engineous to produce good solutions rapidly without becoming bogged down by the existence of parameters that are irrelevant for a particular run. This hybrid, knowledge-directed and generic-searching approach distinguishes Engineous from many other design tools (Vanderplaats, 1984; Kirkpatrick et al., 1981; Tong, 1984; Rychener, 1988), which are either generalized tools incapable of taking advantage of known design features, or specialized tools that can only be applied to one problem.

There are five major functional modules in Engineous: a pre- and postprocessor for setting up and analyzing designs, a knowledge-extraction utility for installation of new applications, a collection of generic search modules to supplement incomplete knowledge, a parameter studies module to analyze the design domain, and a design knowledge base (KB). The design knowledge base contains problem-specific information that needs to be modified for each design application. The other four modules are generic and currently contain approximately 60,000 lines of Lisp code and a few hundred lines of C code for interacting with the operating systems. Depending on the application, the size of the KB varies from a few dozen lines to a few hundred.

Engineous Design Knowledge Base. The design KB can be further decomposed logically into: design parameter KB, program KB, program sequence KB, and design rules KB (see Fig. 2).

Design Parameter KB. This KB classifies each parameter as belonging to one or more of the 12 default types and attaches various properties to it. For example, Engineous attaches current value, minimum increment, default value, etc., to a "design" parameter. The "material" parameter is a symbolic type that can only take on a predefined set of symbolic values. The tip-speed, rpm, and tip-diameter parameters are coupled parameters, whose relationship is stored; any change in one parameter affects the others.

Program KB. This KB captures information on: (1) how to set up the input files, (2) how to execute an analysis code, (3) what the code's input and output parameters are, and (4) how to extract useful information from analysis output files for Engineous. The program KB also manages all pre- and postprocessing programs that need to be executed for each analysis code.

Program Sequence KB. This KB manages the execution sequence. It does not contain a hardwired procedure but rather retains only the allowable transition between programs, i.e.,

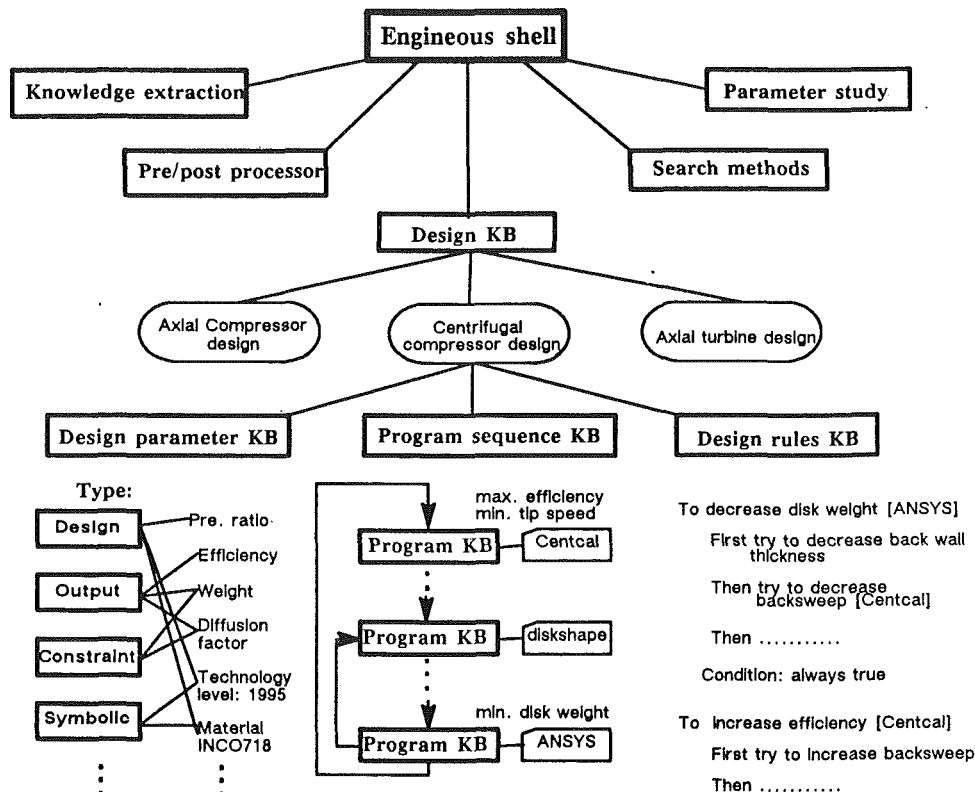


Fig. 2 Engineous system architecture (names of generic modules are in bold type in rectangular boxes; the three design modules, the design rules, design parameters, and program sequence, shown in light type, are examples from a particular application)

for each program, what programs besides itself can follow it. Which program actually runs is determined at run time depending on the parameters to be modified.

Design Rules KB. This KB captures human design knowledge in the form of logical steps a designer would go through. Engineous uses a special rule syntax developed to represent analysis-code-based iterative design knowledge. This knowledge representation is based on the observation that only a limited set of goals, premises, and actions are used during iterative design.

An Engineous design rule can be expressed in English as follows:

- Goal**—To increase X
Conditions— $Y > 3$ and Z is not at its upper limit
Then try the following actions in order:
Action 1. Separable:
 up Z by 10 percent;
 down A by 2;
 set Material to "inco718;"
 vary B , C , and D .
Action 2. Inseparable:
 set Z to 50;
 set Material to "tin125;"
 up T ;
 vary C .
Action 3. Etc.:
 This rule is weighted at 90.

where X is an output parameter that may be a part of the optimization function (e.g., turbine efficiency) or may have a lower bound (e.g., minimum flow angle), and Y and Z in the Condition part may be input or output parameters.

This rule will be fired under the following circumstances:

To increase X has become part of the current goal, the Conditions listed above are not violated, the weight of this rule is higher than other rules that can be fired, and this rule is not currently suspended because of previous repeated failures to increase X without violating other constraints. Engineous will try the actions in the order given.

The key word "separable" tells Engineous to vary one or more parameters within the action even if some others are not allowed to vary for this particular run. For Action 1, Engineous will increase Z by 10 percent of its current value if it has no upper bound, or 10 percent of the difference between its current value and its upper limit. It will subtract 2 from A and set Material to "inco718." Then it will pass B , C , and D as variable parameters to the numerical optimization module in order to maximize X . If this action does not increase X without increasing the total amount of constraint violated, Engineous will restore the values of Z , A , and Material and go to Action 2. No part of Action 2, which is an "inseparable" action, will be taken if any one of its parameters is not a design variable. If an action is successful, Engineous will repeat it until it reaches the point of diminishing returns.

See Tong (1989) for a more detailed description of the architecture of Engineous.

Engineous Search Methods. The Engineous search module combines three major technologies—expert systems, numerical optimization, and machine learning—in an "interdigitized" manner, so that they are tightly coupled and switched from one to another at various stages of a single design run. Individually, each approach has advantages and disadvantages. In combination, they complement each other in many ways.

Expert Systems. Engineous first draws on human knowledge from the design rule KB to emulate design experts. This use of an expert system yields the greatest gain with the smallest number of analyses and produces designs that engineers have

confidence in. Expert systems can also explain how and why a final design was chosen, which is important for balancing predicted performance against other factors not modeled in the analysis codes. Since the human design knowledge is often incomplete or biased, however, a pure expert system is very likely to miss better designs. Moreover, a pure expert system for complex design problems can be expensive to build and maintain. Therefore, Engineous supplements incomplete knowledge with some heuristic search techniques to emulate the human trial and error process. These techniques are invoked when human design knowledge is exhausted.

Numerical Optimization. A numerical optimization package called ADS (Vanderplaats, 1987) is invoked automatically when the expert system and trial and error process cannot make any more gains. Engineous cycles through a series of optimization plans, with each plan containing different ADS internal parameter settings. The first plan is usually run with only those parameters that, according to the knowledge base, are effective for the particular optimization goal. The advantage of numerical optimization is that it can be applied to a wide range of problems. ADS has proved to be effective for reaching a local optimum for a smooth, continuous objective function. For problems with a large number of parameters and CPU-intensive codes, however, the large number of gradient calculations required can be prohibitively expensive. ADS has difficulty handling symbolic parameters and has shown premature convergence, resulting in lower objective function value when more parameters are allowed to vary. Because of its rich set of options, it is difficult to set up ADS manually. It is also difficult for an engineer to understand why a particular solution is chosen. ADS is sensitive to the initial guess and internal parameter settings. Having Engineous cycle through a sequence of ADS runs with various ADS options has partially eliminated some of these disadvantages.

Machine Learning. The use of machine learning methodologies for function optimization was suggested by Holland (1975) and Dejong (1975), and successful demonstrations of such an approach to turbomachinery design have been shown by Tong (1986). Engineous employs a machine-learning methodology called the Genetic Algorithm (GA) (Goldberg, 1989; Grefenstette, 1987). The basic idea of GA is not to make absolute decisions as to whether a trial design should be kept or discarded, but to penalize or reward trial designs on the basis of the value of the optimization function. The process starts with a set of initial designs, called a generation, which Engineous seeds with some good designs generated by expert systems and numerical optimization. New generations of the same number of trial designs are generated first by "selection," then by "crossover," and finally by "mutation." During a selection process, designs that have a higher optimization function value have a better chance to survive and reproduce themselves, while designs with a lower value are more likely to be eliminated. Crossover exchanges a random set of parameters of some past trial designs with other designs to generate new designs. This step is constructed in such a way as to make good features tend to cross over together. A random mutation of a few trial designs takes place periodically. The mutation process is implemented by flipping bits with a binary coded representation of the design vector. After sufficient generations, clusters of good design regions with occasionally innovative answers will evolve.

Because GA is not gradient-based, it will not be trapped in a local optimum or constraint boundaries and can handle a wide range of parameter types, including symbolic parameters (e.g., material). On the other hand, GA does not explore a local optimum and requires many orders of magnitude more analysis runs to obtain useful results. GA is, however, very amenable to parallel or distributed processing.

Interdigitation. Expert systems, numerical optimization, and machine learning are tightly coupled in Engineous and work together for a single design process. Unless modified by users, the Engineous search module runs in three cycles. In the first cycle, only an expert system is used to get a good answer with a small number of runs. In the second cycle, Engineous alternates between an expert system and numerical optimization to perform local hill climbing until no further gain can be made. At this point the solution may be at a local optimum, having been trapped in a complex constraint boundary or stopped due to premature convergence. The third cycle then invokes GA for a given number of generations and, if a promising solution is found, switches back to the expert system and numerical optimization for local hill climbing. See Powell et al. (1989) for a detailed description of interdigitation of GA and expert systems.

In a real-world design process, there is seldom enough time to explore all possibilities. The sequence of Engineous cycles ranks the parameters and search methods according to their expected gain per analysis run to allow maximum gain for a given number of analyses run. A user can specify the total elapsed time, and Engineous will terminate and present the best results obtained so far. Elapsed time is better than other arbitrary "convergence" criteria. Because most optimization processes are sensitive to the initial guess and search procedure, various starting points and search procedures should be tried until time runs out.

Pre- and Postprocessor. The Engineous preprocessor provides a menu interface to the kernel to enable designers to set up different design runs using a design knowledge base already installed. For example, the choice of what to optimize, which parameters to allow to vary, and what to display for a particular run of turbine design can be made from menus. The postprocessor provides common analysis tools such as graphic and design history data base queries.

Knowledge Extraction. The knowledge extraction utilities facilitate rapid installation of new applications to Engineous. For example, input/output parameter names and types can be extracted automatically by Engineous if the analysis source code is available. To allow the running of analysis code as is without modification or recompilation, Engineous can generate source codes corresponding to the way designers prepare input files and extract relevant information from output files by following an example. Most of the problem-specific knowledge—including design rules, program sequencing information, and graphical output format—can be entered through simple menu actions. Engineous will generate the source codes and hide the internal data representations from end users.

Engineous/TDOD: Turbine Design Implementation

For turbine design with TDOD, there are approximately 110 input parameters and 20 relevant output parameters per stage. A 14-stage turbine can have as many as 1800 parameters. Although all the TDOD input and output parameters were installed in Engineous/TDOD, it should be noted that in a typical five to seven stage turbine design only approximately 100 input parameters are allowed to vary. Currently, the number of stages is not allowed to vary.

There are a few dozen design rules in this application. For example,

to increase blade exit flow angle:

- First try to decrease reaction,
- Then try to increase rpm,
- Then try to decrease loading.

This rule always applies.

The time it takes to install this application using the current

version of Engineous is estimated to be around one man-month. However, a substantially larger effort was spent to enhance Engineous to address certain problems encountered during this application.

One common problem in analysis-code-based optimization of turbomachinery components is how to manipulate flow path geometry. Since a preliminary design code like TDOD often does not model the detailed flow physics of solid surfaces, an uncontrolled optimization often leads to an unrealistic flow path design. Engineous/TDOD represents the endwall first with a small number of control points; an exponential curve-fitting routine is used to construct the flow path since most curve-fitting algorithms produce a smooth curve with a small number of control points. After a semi-optimized flow path is found, more control points can be added gradually, and the control point movement limits are gradually tightened so that fine adjustments can be made while preserving the globally smooth shape.

Another common problem is how to handle the so-called "constant-sum" parameters, where the sum of a particular set of variables must remain constant while the optimum distribution is unknown. Examples include the work distribution and the vane and blade chord length for a fixed size turbine. Any change of one variable has to be somehow coupled with changes of other variables. The results of optimization are found to be sensitive to a distribution formula, and the side effects from the parameter coupling often confuse the optimization sensitivity analysis. Currently, a simple equal distribution formula is being employed with mixed success. It is believed that an improved distribution formula will result in significant performance gains.

The flow path fitting and the chord length distribution were handled by two Fortran preprocessors attached to TDOD using the Engineous "wrapper" utility, which manages all the parameter-passing and execution of pre- and postprocessors.

Results

A multistage, low-pressure (LP) turbine was selected as a good candidate for testing the introduction of Engineous to the TDOD code. As part of an improved performance study, the turbine was required to show an increase in performance but was also required, by mechanical considerations, not to exceed its present diameter or length.

The rule KB has been constructed so that the designer may select Engineous to design for a conservative, state-of-the-art, or advanced (essentially unconstrained) approach to the optimization process. Given a set of input variables loosely defining the turbine as input, Engineous will optimize the variables to define nondimensional and dimensional turbine characteristics that meet previously specified constraints.

For the particular turbine in question, a design optimization procedure had already been started in which a designer was optimizing the turbine with a goal of 0.75 percent efficiency improvement. The Engineous design was started in tandem with that work. The resulting flow paths from each procedure are shown in Fig. 3. The designer achieved a 0.5 percent improvement in design, mainly through flow path optimization.

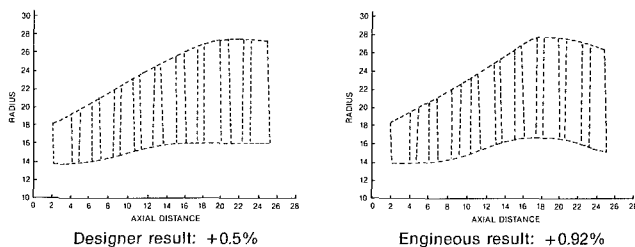


Fig. 3 Multistage LP turbines designed by a designer and by Engineous

The Engineous design achieved a 0.92 percent improvement, which came from the optimization of the flow path, stage work split, blade count, and stage reaction. The difference in turnaround time for this particular design was about 20:1 but should be stated more conservatively as 10:1 since time was needed for the preliminary work that must be performed before running Engineous. Time was also allowed for the aerodynamicist to review the results after the design process was completed. A number of other benefits also resulted from this design process:

A greater insight was gained into the tradeoff of various loss parameters. For instance, high wall slope (the rate at which the turbine diameter is increased) leads to increased losses; on the other hand, increased tip diameter increases turbine performance. These two parameters are in conflict. Yet, in the time allowed, the designer has very few options involving decisions to trade one for the other.

By designing without constraints, the turbine designer can go beyond previous experience and give direction for future work in the process of optimizing turbine designs. In this case the flow path is described in Fig. 4, where it is shown that the stage-2 outer wall flow path is used to "buy" turbine diameter by specifying a very steep wall slope (beyond what experience would suggest). Stage 3 performance, therefore, more than compensates for the loss associated with the high wall slope, giving a net gain that increases the turbine efficiency by a further 0.1 percent.

The chance of human error is minimized since the process is a closed loop. There is no transfer of data from paper to the computer; there is no misinterpretation of results; and there are no distractions.

Engineous performs the optimization of a multistage turbine design problem in a period of from 2 to 24 hours, depending on the number of stages. The actual number of submissions of the TDOD code to the CPU usually exceeds 1000, with approximately 30 percent of the iterations being successful (i.e., showing increased performance). The designer can now set up his Engineous problem before the end of the work day and the process of designing will continue overnight. The procedure allows for stopping the process, reviewing the overnight output, restarting the process to run in background, and leaving the engineer free to perform other, more skilled tasks.

Engineous/TDOD is now being used for most turbine preliminary design (PD) studies. These include turbine designs ranging from single-stage to 14-stage. High-pressure cooled turbines can also be optimized, with coolant requirements being optimized at the same time as the aerodynamics. Engineous is not limited in what is to be optimized. In other studies, weight has been the issue, with a requirement to lighten a particular design. Since Engineous is designed to optimize any input or output variable, it was possible to achieve lighter designs that did, and did not, consider turbine performance.

The power of the interdigitation is also shown with this turbine design application. Figure 5 shows, for a new single-

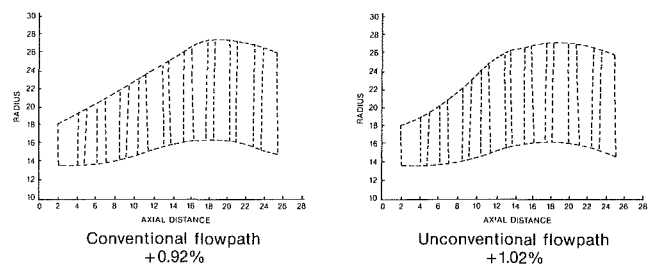


Fig. 4 Multistage LP turbines designed by Engineous with restricted and unrestricted flow path slopes

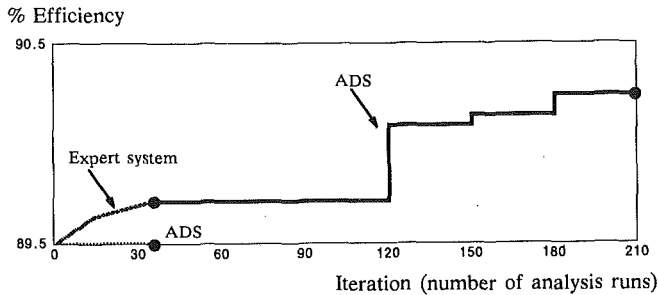


Fig. 5 Efficiency gains versus iteration for various search methods: expert system, ADS, and interdigitation of Expert system and ADS

stage turbine design, the performance gain versus iteration and search methods for the interdigitation of an expert system and numerical optimization. Although a particular ADS strategy showed little gain with that starting point, it took off and made substantial gain after the expert system achieved a better solution. Figure 6 shows the partial result of a more thorough study for a new two-stage turbine design. Over 30 ADS options with different search methods, gradient deltas, convergence criteria, and normalization were tested. The ADS work was stopped when no gain even as small as $10E-06$ could be made. It can be seen that some ADS runs did much better than the expert system in this case. The performance of ADS was found to be highly dependent on the choice of ADS parameters, whereas an expert system always produces "good" results without tuning. Full interdigitation of all three search methods outperforms each of the three search methods by an efficiency gain of as much as 1 percent, a very significant number for turbine efficiency. The final turbine was an unconventional design with some of the parameter distributions opposite to what was done traditionally. Analysis of the optimization history shows that although the use of GA resulted in only a small gain in efficiency, it does appear to have pushed the optimization process away from being trapped in constraint boundaries so that the local hill climbing process could continue. Note that without GA the partial interdigitation of expert system and ADS produced a lower-performance (0.5 percent less than that of full interdigitation) but conventional turbine.

Conclusion and Future Work

Engineous/TDOD is emerging as a standard for turbine preliminary design at GE Aircraft Engine. Through automation, Engineous explores more design options and parameter tradeoffs in a given period of time than any earlier method. It has improved design quality and reduced turnaround time.

Future extensions to this turbine design application will allow for optimization of the exhaust frame, designing a turbine from a simple set of cycle parameters, and other generalized enhancements to the postprocessing of the TDOD output data.

A major achievement of this project was convincing the engine design community that the advanced computational techniques used by Engineous—such as artificial intelligence, graphical user interface, and numerical optimization—can contribute significantly to solving real-world design problems and make their job more productive and fun. These applications have generated so much interest within GE that a more production-oriented version of Engineous, version 2.0, is currently being developed for larger-scale deployment.

Other current Engineous turbomachinery application projects include centrifugal compressor, axial compressor, detailed turbine cooling flow passage and heat transfer, and future engine conceptual design. Also, the application of Engineous to detailed design codes such as quasi three-dimensional streamline curvature routines and blade-to-blade design code is being explored.

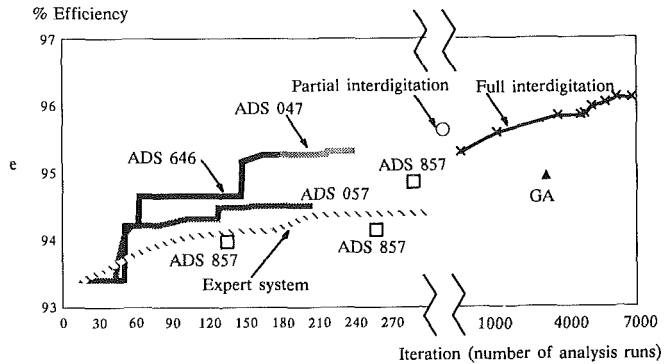


Fig. 6 Efficiency gains versus iteration for various search methods: expert system, ADS, GA, and interdigitation of all three methods; the number following ADS indicates the ADS option chosen (see Flagg, 1967): 047 Method of feasible direction, with polynomial interpolation; 057 Modified method of feasible direction, with polynomial interpolation; 646 Sequential linear programming, with method of feasible direction and Golden Section method, followed by polynomial interpolation; 857 Sequential Quadratic Programming, with modified method of feasible direction, followed by polynomial interpolation (3 solutions with different gradient delta or convergence rate)

The application described here demonstrates the powerful concept of interdigitation of search strategies. Interdigitation allows Engineous to solve a wide range of problems, from well-understood tasks where there is ample knowledge, to new design problems, from smooth to rough objective functions, from aiming for conservative design to exploring new concepts, and from problems with only real parameters to complex problems with a mixture of real, integer, and symbolic parameters.

Although using GA with other search techniques resulted in a big gain in efficiency in this application, its role is still not fully understood. Work is now in progress to analyze the interdigitation concept thoroughly in order to extract a more efficient mechanism from the GA.

Additional technological enhancement of Engineous is ongoing. The technologies currently being explored include parallel processing of analysis runs (simultaneous evaluation of multiple design scenarios), deducing design rules from design history, and developing modules that can access the nonanalytical qualities of a design such as reliability, maintainability, and life-cycle cost.

Acknowledgments

The authors would like to thank Karen Overton who managed the Engineous/TDOD application and did most of the programming work; Danny Cornett and George Geisor for installing and supporting this application; Dave Powell for the development of the interdigitation approach; and Ko-Haw Nieh for enhancing Engineous for this application. Professor Garret Vanderplaats has provided much of the ADS expertise. We would also like to thank GE for permission to publish this paper, in particular, Mr. David Cherry and Dr. Ramani Mani, who provided strong management support for this effort. This Engineous/TDOD application is funded by GE Aircraft Engine. The Engineous shell is funded and developed by the GE Research and Development Center.

References

- Dejong, K., 1975, "An Analysis of the Behavior of a Class of Genetic Adaptive Algorithms," PhD thesis, University of Michigan, Ann Arbor, MI.
- Flagg, E. E. 1967, "Analytical Procedure and Computer Program for Determining the Off-Design Performance of Axial Flow Turbines," NASA CR-710.

Goldberg, D. E., 1989, *Genetic Algorithms in Search, Optimization and Learning*, Addison-Wesley, New York.

Grefenstette, J., 1987, "Genetic Algorithms and Their Applications," *2nd International Conference on Genetic Algorithms*, Laurence Erlbaum Associates.

Holland, J., 1975, *Adaptation in Natural and Artificial Systems*, University of Michigan Press, Ann Arbor, MI.

Kirkpatrick, C., Gelatt, C., and Vecchi, M., 1981, "Optimization by Simulated Annealing," *Science*, Vol. 220 (4598), pp. 671-680.

Powell, D. J., Tong, S. S., and Skolnick, M. M., 1989, "Engineous, Domain Independent, Machine Learning for Design Optimization," *Proceedings of the Third International Conference on Genetic Algorithms*, June 4-7, George Mason University, pp. 151-159.

Russo, C., Nicklaus, D., and Tong, S., 1987, "Initial User Experience With an Artificial Intelligence Program for the Preliminary Design of Centrifugal Compressors," *ASME*, Vol. 87-GT-217, June.

Rychener, M. D., 1988, *Expert Systems for Engineering Design*, Academic Press, San Diego, CA.

Tong, S. S., 1984, "Procedures for Accurate Inviscid Flow Simulations and Profile Refinement of Turbomachinery Cascades," PhD thesis, Department of Aeronautics and Astronautics, Massachusetts Institute of Technology, p. 228.

Tong, S. S., 1986, "Coupling Artificial Intelligence and Numerical Computation for Engineering Design," presented at the AIAA 24th Aerospace Sciences Meeting, Jan. 6-9, Reno, NV.

Tong, S. S., 1989, "Coupling Symbolic Manipulation and Numerical Simulation for Complex Engineering Designs," *Mathematics and Computers in Simulation*, Vol. 31, pp. 1-12.

Vanderplaats, G. N. 1984, *Numerical Optimization Techniques for Engineering Design: With Applications*, McGraw-Hill, New York.

Vanderplaats, G., 1987, Lecture Notes on Computer Aided Optimization in Engineering Design, Union College Continuing Education course, July 27-31.

Toward Improved Throughflow Capability: The Use of Three-Dimensional Viscous Flow Solvers in a Multistage Environment

W. N. Dawes

Whittle Laboratory,
Cambridge, United Kingdom

A methodology is presented for simulating turbomachinery blade rows in a multistage environment by deploying a standard three-dimensional Navier–Stokes solver simultaneously on a number of blade rows. The principal assumptions are that the flow is steady relative to each blade row individually and that the rows can communicate via inter-row mixing planes. These mixing planes introduce circumferential averaging of flow properties but preserve quite general radial variations. Additionally, each blade can be simulated in three-dimensional or axisymmetrically (in the spirit of throughflow analysis) and a series of axisymmetric rows can be considered together with one three-dimensional row to provide, cheaply, a machine environment for that row. Two applications are presented: a transonic compressor rotor and a steam turbine nozzle guide vane simulated both isolated and as part of a stage. In both cases the behavior of the blade considered in isolation was different to when considered as part of a stage and in both cases was in much closer agreement with the experimental evidence.

Introduction

Currently, turbomachinery analysis considers two extremes. The overall machine is broadly designed using throughflow techniques (like streamline curvature), which rely heavily on a mature database (for loss and deviation for example. AGARD AR-175 (1981) describes this sort of approach in detail. The individual blade rows are examined using two-dimensional or three-dimensional Euler or Navier–Stokes solvers, nominally at an operating point similar to that supplied from the throughflow analysis, but really run as if in an isolated cascade. Suitable single-blade row solvers have been presented by many authors, see for example VKI-LS-2 (1986) and AGARD LS-140 (1985). Iterations may then be performed in an attempt to couple the two types of analysis and remove any inconsistencies (see, for example, Jennions and Stow, 1985a, 1985b).

It is increasingly clear, however, that a blade row does not necessarily perform in the same way in a machine environment as in a cascade-type setting. Quite apart from the obvious unsteadiness of the machine environment (described, for example, by Hodson, 1984), blades suffer potential interaction, must run with compatible head-flow characteristics (i.e., all rows pass the same mass flow) and may experience strong radial variation of property between rows. Examples are: A turbine nozzle guide vane with high exit swirl is prone to hub separation is tested in cascade (especially if the hub-tip ratio is low) whereas in the machine, the rotor “loads” the stator and

prevents this separation (Spurr, 1980; Williams, et al., 1986); an isolated compressor rotor stalls when its head-flow characteristic rolls over; however, in the presence of a very stable machine, the given rotor is stabilized and may even display stable positive head-flow slope operation (Longley, 1989).

The aim of this paper is to show how a standard, single blade row three-dimensional Navier–Stokes solver (Dawes, 1988) can be deployed in a machine environment to address some of these issues. The three-dimensional code is modified to handle multistage geometries by assuming steady flow relative to each individual blade row with suitable mixing planes between each row. This is clearly a simplifying assumption and not a new idea (Denton and Singh, 1979, Arts, 1985, and more recently Ni and Bogoian, 1989, have done this for the three-dimensional inviscid equations) but, as will be shown, some of the flavor of the machine environment can be captured at little extra cost. There are alternative approaches to multistage simulations, for example Giles (1988) who solves for the true nonlinear unsteady motion of a stage and Adamczyk et al. (1990) who are developing a powerful methodology based on solving a machine row by row with sophisticated averaging to represent the “missing” rows. However, both of these approaches are very expensive in computer time and probably not yet ready for the design environment. A novelty in the current approach (apart from the use of the Navier–Stokes equations) is that any of the individual blade rows can be computed fully three-dimensional or alternatively modeled axisymmetrically with blade forces and loss and deviation either correlated or processed from a previous three-dimensional solution. The axisymmetric modeling provides a particularly cost-

Contributed by the International Gas Turbine Institute and presented at the 35th International Gas Turbine and Aeroengine Congress and Exposition, Brussels, Belgium, June 11–14, 1990. Manuscript received by the International Gas Turbine Institute January 13, 1990. Paper No. 90-GT-18.

effective way to provide a "machine environment" for a blade under (three-dimensional) study.

Solutions are presented for two problems to illustrate the benefit of the methodology. First, a transonic compressor rotor is considered, both isolated and in the presence of its stator. Second, a steam turbine nozzle guide vane is simulated isolated and with its rotor. In both cases the "machine environment" is shown to be of significance.

Equations of Motion

The basic equations of motion are the fully three-dimensional Reynolds-averaged Navier-Stokes equations expressed in cylindrical coordinates in integral conservation form with the addition of a set of axisymmetric body forces. The equations are discretized on a set of six-faced control volumes, formed by a simple, structured H-mesh construction. (It is hard to imagine deploying O- or C-mesh methodology in a multistage environment.) Flow variables are stored at cell centers and values on cell faces for flux evaluation are found by simple linear interpolation conferring second-order accuracy on smoothly varying meshes. Symbolically, the code solves by time-marching the equations of motion as:

$$\frac{\Delta \text{VOL}}{\Delta t} \cdot \Delta \begin{bmatrix} \rho \\ \rho \bar{w} \\ \rho E \end{bmatrix} = \sum_{\text{CELL}} (\text{fluxes}) + [\text{sources}] + \begin{bmatrix} 0 \\ F_x \ F_\theta \ F_R \\ FE \end{bmatrix} \quad (1)$$

where \bar{w} is the relative velocity, [sources] contains terms like $\rho w_\theta^2/r$ in the radial momentum equation and the Coriolis terms

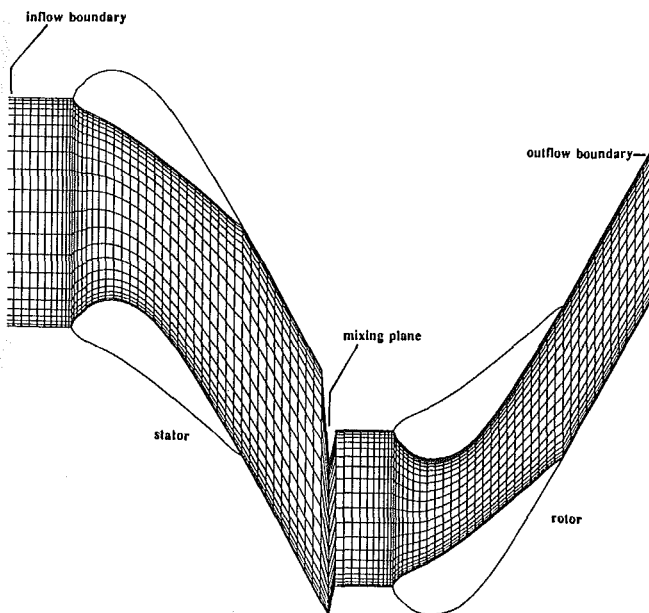


Fig. 1 Midspan blade-blade plane of a mesh for a single-stage reaction turbine

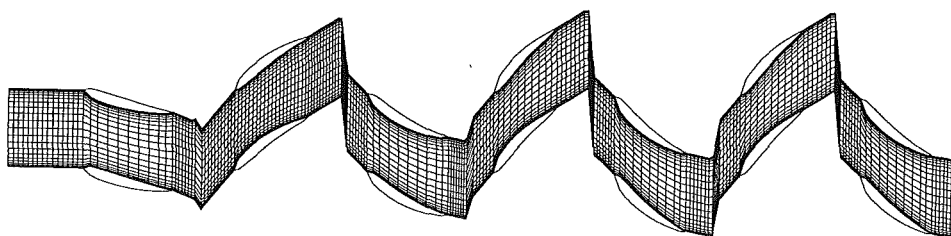


Fig. 2 Midspan blade-blade plane of a mesh for a three-stage axial compressor with inlet guide vanes

and F_x , F_θ , F_R , and FE , are axisymmetric body forces used to model the blade rows when computing axisymmetrically. Included in the (fluxes) are the shear stresses in the three momentum equations and the shear work and heat conduction terms in the energy equation. The turbulent viscous stresses are computed either from the Baldwin-Lomax (1978) mixing length model or from a single equation transport model for turbulent kinetic energy (Birch, 1987). The turbulent Prandtl number for the energy equation is assumed to be 0.9.

The basic solution algorithm has been described in detail elsewhere (for example Dawes, 1988) and consists of a two-step explicit-one-step implicit scheme derived as a preprocessed simplification of the well-known Beam-Warming algorithm but similar in implementation to a two-step Runge-Kutta method plus residual smoothing. Dawes (1988) also describes the addition of a combined second-fourth derivative artificial viscosity (switched via a pressure gradient flag), which filters out wiggles and controls shock capture and also outlines the application of multigrid convergence acceleration.

Mesh Construction for Multiple Blade Rows

A rather large data set must be built by stacking end to end standard three-dimensional single-row data sets. The code then shifts each individual data set both axially and tangentially (automatically if required) to form a consistent set of data. A simple, structured H-mesh is then constructed for all rows simultaneously (and assuming each row is to be computed in three-dimensional rather than axisymmetrically) by interpolating the input blade sections onto the desired radial set of blade-blade planes. Example meshes are shown in Fig. 1 for a single-stage reaction turbine and Fig. 2 for a three-stage axial compressor with inlet guide vanes. The evident discontinuity between rows is used to advantage by letting the last plane of cells from the upstream row and the first plane of cells from the downstream row play the role of dummy stores for the inter-row mixing calculation.

Three-Dimensional/Axisymmetric Approach

Each individual blade row can be selected to be simulated fully three dimensionally or axisymmetrically. The simulation is then subjected to the basic assumption that the flow is steady relative to each of the blade rows individually. For the three-dimensional rows, no special action is required and the axisymmetric body forces are set to zero. The axisymmetric rows require modifications to the basic code. Firstly, the blade-blade region need only be modeled by a single cell as the basic assumption in the axisymmetric model is that the circumferential flow derivatives are zero. This is accomplished quite simply in the code, and without IF statements, by writing all the circumferential DO loops as $\text{DO } i = 1, \text{NIM}(j)$ where $\text{NIM}(j)$ is IM , the three-dimensional mesh limit for the three-dimensional rows, but is 2 for the axisymmetric rows (j is the axial flag). This does waste a certain amount of memory but greatly simplifies data handling and by padding a copy of the axisymmetric flow variables right across the underlying three-dimensional mesh, simplifies also postprocessing (plotting) and restarting after a dump (whereupon an axisymmetric row can be restarted as a three-dimensional row or vice versa).

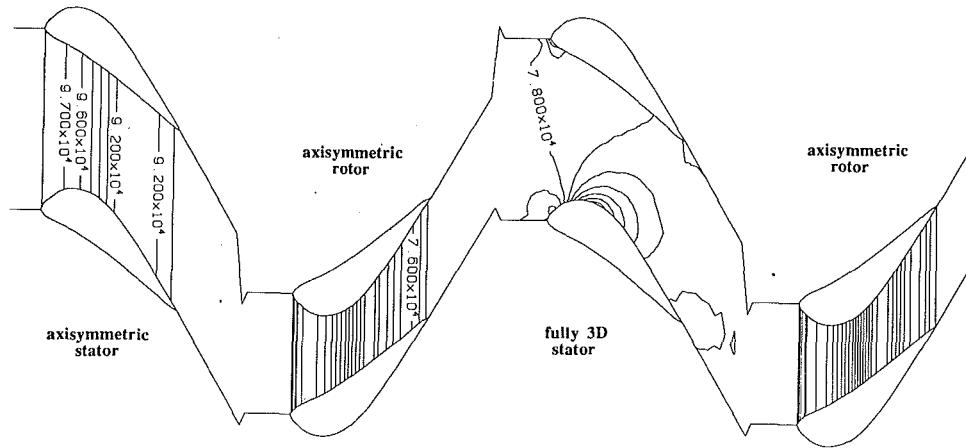


Fig. 3 Predicted static pressure variation at midspan of a two-stage reaction turbine with each row simulated axisymmetrically except for the second stator

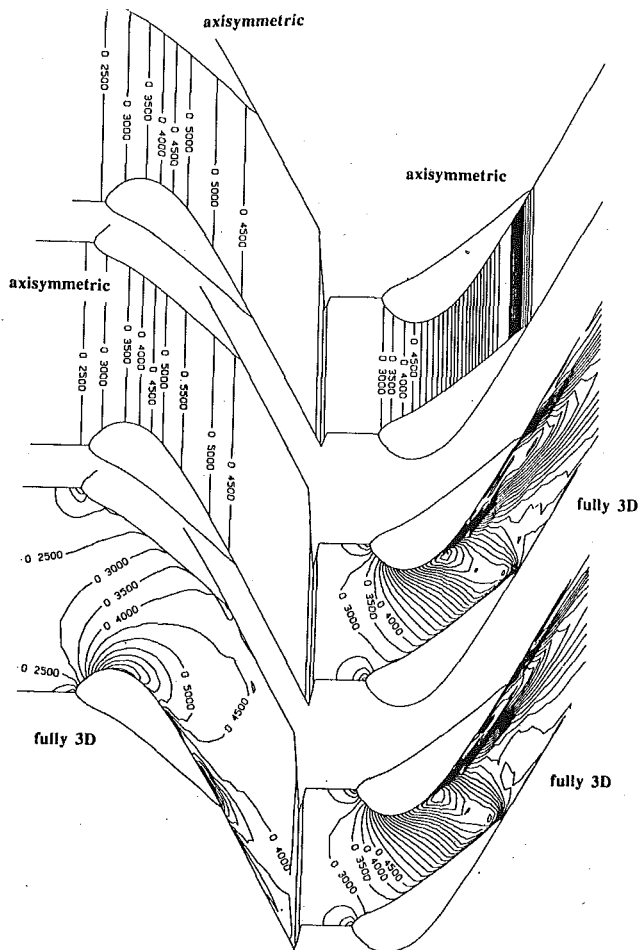


Fig. 4 A sequence of predictions for a single-stage reaction turbine

Secondly, the presence of the blades in the axisymmetric rows must be modeled. This is accomplished much as it is for standard throughflow methods (see Spurr, 1980, for a time-marching implementation). Upstream and downstream of the blade the axisymmetric body forces F_x , F_θ , and F_R (Eq. (1)) are set to zero and the swirl velocity, W_θ , solved from the θ -momentum equation. Within the blade row, the swirl velocity is deduced from the meridional velocity and a flow angle fixed by the blade camberline angle plus a deviation angle distributed linearly from blade leading edge to trailing edge. This deviation angle is either correlated (e.g., Carter) or may be processed

from a previous three-dimensional solution for that blade row. Then the effective tangential body force, $F_{\theta\text{eff}}$, is deduced from the rate of change of tangential momentum:

$$r \cdot F_{\theta\text{eff}} = \sum_{\text{CELL}} r \cdot \rho (W_\theta + \Omega r) \text{ fluxes}$$

Note that this is the force implied by constraining W_θ ; the θ -momentum equation itself does not need to be solved in the blade row. From this the implied effective blade loading is given by

$$\Delta p_{\text{eff}} = F_{\theta\text{eff}} / \text{AREA}_\theta$$

where AREA_θ is the tangential projection of the area of the cell face on the blade surface. This blade loading is distributed linearly (in the absence of a better assumption) from blade to blade and then, in conjunction with the axial and radial projections of the areas of the cell faces on the blades, gives rise to the axial and radial body forces, F_x and F_R . Of course, body forces in the momentum equations give rise to an additional term in the energy equation (here denoted FE), which is essentially the scalar product of the body forces with the three velocity components. The body forces are also modified to take blade losses into account. These losses are either correlated (e.g., Lieblein D-factor) and distributed linearly from blade leading edge to trailing edge or processed from a previous three-dimensional solution. The losses are converted to gradients of entropy and added to the body forces in the standard throughflow manner (see, for example, Jennions and Stow 1985a, 1985b). As examples of this combined three-dimensional axisymmetric approach, Fig. 3 shows a two-stage turbine for which rows one, two, and four were selected to be axisymmetric and row three (second stator) selected to be three-dimensional. Figure 4 shows a sequence of solutions for a single-stage turbine from all axisymmetric to all three-dimensional.

An axisymmetric blade row can be computed for about 5 percent of the cost of a fully three-dimensional row (1 blade-blade cell versus maybe 21). So a three-dimensional row can be studied in the presence of several axisymmetric rows (providing the machine environment) at little extra cost over the three-dimensional row alone. This is considered to be a substantial benefit of the current approach.

The Inter-row Mixing Planes

The principal assumption in the current work is that the flow is steady relative to each individual blade row. The rôle of the inter-row mixing planes is to model the communication between the rows. Any model adopted represents an approximation; nevertheless, it is possible to identify certain required

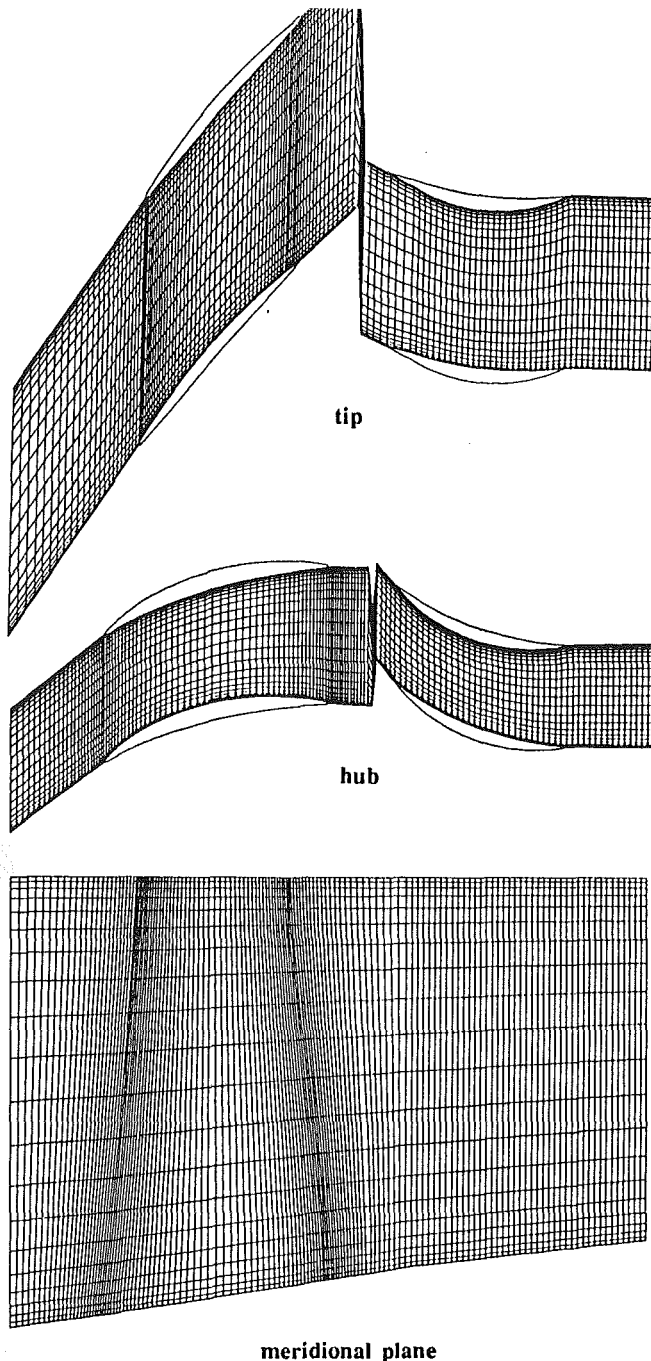
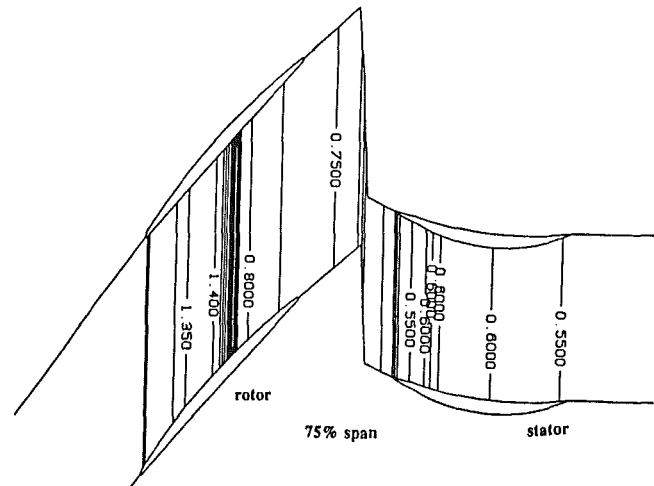
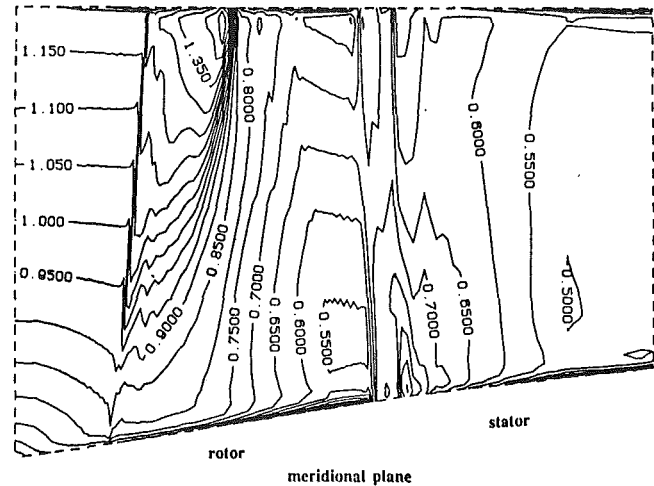


Fig. 5 the $21 \times 157 \times 21$ mesh used for the compressor rotor considered in a stage

properties of the modeling. Clearly some sort of circumferential averaging must be employed to model the relative motion of the blade rows. This averaging must, as a minimum, ensure conservation of the machine mass flow. It is important to note that although the circumferential information is smeared, the radial variation is not. So, in particular, the flow need not be in simple radial equilibrium at the mixing plane but can support meridional streamline curvature (in the mean sense). Secondly, the mixing must not introduce too much disturbance into the adjacent flows. This is rather important since blade rows in a machine are close together, of the order of fractions of axial chord apart, whereas when flow codes are run on single blade rows in a cascade type mode, the inflow and outflow boundaries are usually placed between one and two chord lengths away.

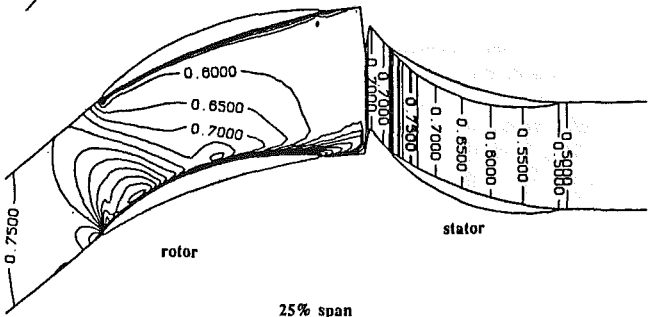
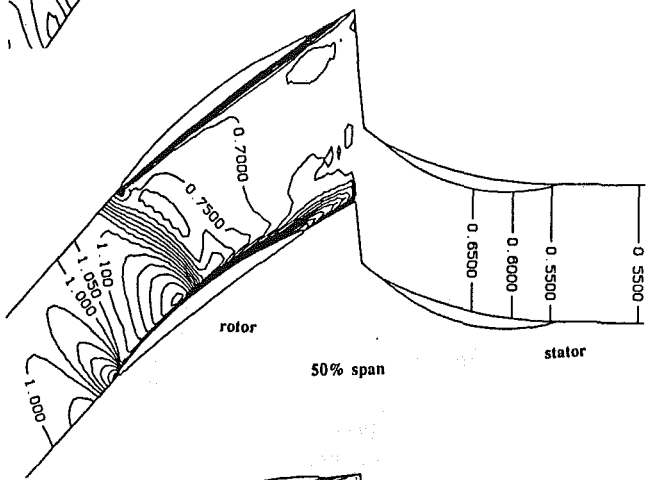
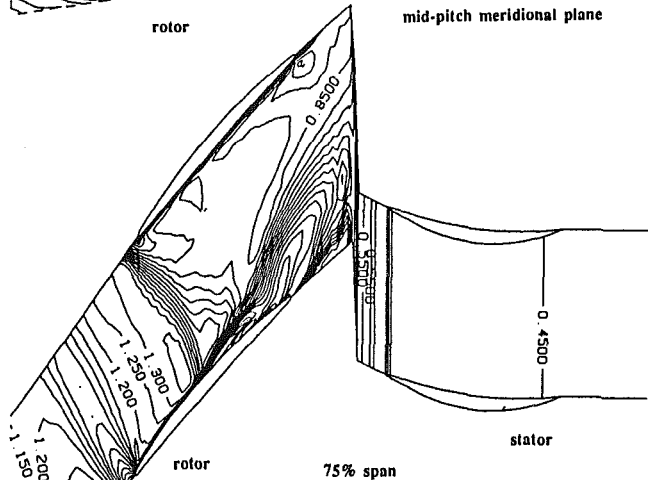
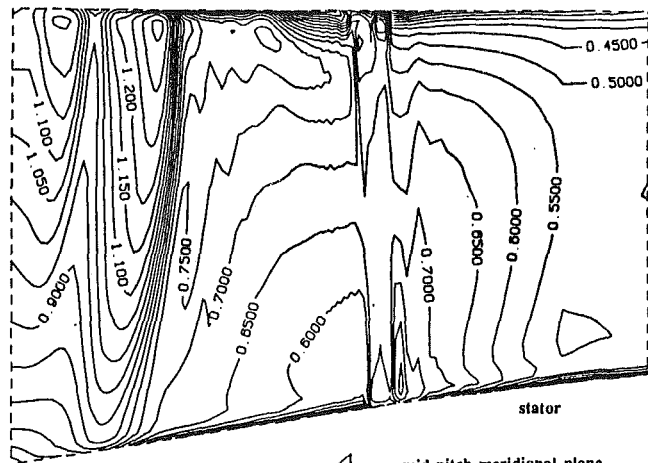


Figs. 6-7 Predicted Mach number variations for the compressor rotor simulated as part of a stage with both rotor and stator modeled axisymmetrically

The current version of the code has three options for the mixing planes. The first uses a simple area averaging of the principal flow variables ρ , ρW , and p . This ensures conservation of mass flow but will introduce a total pressure error (among others) whose magnitude will depend on the degree of non-uniformity in the flow. The second option is to model each successive blade flow more like individuals by passing mass-averaged total pressure and temperature and the flow angles downstream across the mixing plane and passing area-averaged static pressure upstream. The third option is based on an adaptation of nonreflecting boundary condition methodology (see, for example, Giles, 1988) to the mixing plane specification. The area-averaged Riemann invariants ($\Delta p \pm \rho a \Delta u$, etc.) are computed either side of the mixing plane and passed either upstream or downstream depending on the sign of the wave speeds ($u \pm a$, etc.) to update the flow variables stored in the mixing plane dummy cells. The aim of this approach is to minimize spurious reflections from the mixing planes and to permit the mixing to be carried out as close as possible to the blade rows. Simple area averaging was used for the present study.

Sample Application: Transonic Compressor Stage

To illustrate how the behavior of a given row can differ between the machine environment and when considered in isolation, we consider a transonic compressor rotor. The rotor chosen is in the first stage of a high-duty five-stage axial re-



Figs. 8-11 Predicted Mach number variations for the compressor rotor simulated as part of a stage (three-dimensional rotor; axisymmetric stator)

search compressor tested at NASA Lewis in the 1960s and reported by Kovach and Sandercock (1961). The main compressor characteristics are:

Overall total pressure rise	=	5
Design rotational speed	=	12,605 rpm
Design mass flow	=	30.6 kg/s
Tip radius (constant)	=	0.254 m
First stage total pressure rise	=	1.4
First stage hub-tip ratio	=	0.50
First stage tip relative Mach No.	=	1.4
Inlet total pressure	=	101,325 N/m ²

The first stage of the machine is modeled here and Fig. 5 shows the $21 \times 157 \times 21$ mesh used. The code runs at about 0.5 ms/point/time step on a single processor of an Alliant Fx/80. Axisymmetric blade rows cost about 5 percent of the cpu absorbed by a three-dimensional row (1 cell blade-blade as compared to 21). Typically around 1000 time steps were performed before restarting the code in a different mode and so overall computational times are not particularly frightening.

The first computation modeled both rotor and stator as axisymmetric. For design flow, a static pressure of 112,844 N/m² was imposed on the hub downstream of the stator and simple radial equilibrium employed to determine the radial variation of pressure out to the casing. This static pressure was inferred from the experimental traverse data extrapolated to the hub. Figure 6 shows the predicted Mach numbers in the meridional plane. The strong shock gives no problems as far as convergence is concerned (unlike other axisymmetric methods like streamline curvature or matrix throughflow). Figure 7 shows the predicted Mach numbers in a blade-blade plane at 75 percent span. At convergence, the axisymmetric computation passes a mass flow of 31.4 kg/s. The mass flow is too high as the correlated deviations come out too low.

Next, the all-axisymmetric solution was restarted with the rotor now specified to be fully three-dimensional (and with the same stator exit hub static pressure). The computation converges to a mass flow of around 30.55 kg/s (within 0.2 percent of the design flow). Predicted Mach number contours are shown in Fig. 8 for a meridional plane in midpitch and in Figs. 9, 10, and 11 for blade-blade planes at 75, 50 and 25 percent span, respectively. The prediction shows a typical design point flow with a just-sonic hub and an increasingly strong bow shock, just detached, outboard to the casing. By 75 percent span the shock is strong enough to separate the suction surface boundary layer and this increased blockage, averaged circumferentially, puts the tip of the stator at a positive incidence of 5-10 deg.

For the third computation the rotor was considered to be in isolation and run fully three dimensionally. The hub static pressure at exit (together with simple radial equilibrium outboard, in the absence of a better assumption) was adjusted iteratively until the rotor was passing about design flow. Predicted Mach number contours are shown in Figs. 12-15 for the midpitch meridional plane and blade-blade planes at 75, 50, and 25 percent of span. Focusing on the 75 percent blade-blade plane, Fig. 13, and comparing with the equivalent plane from the stage calculation, Fig. 9, reveals some of the differences between the "isolated" and the "stage" simulation. For the isolated rotor, the shock is slightly stronger, visibly farther upstream and interacting more strongly with the suction surface boundary layer giving rise to a bigger separation and blockage. Additionally, and more significantly, although the predicted mass flow for the isolated case is around 30.5 kg/s, it is creeping slowly but inexorably downward (at about 0.01 kg/s per 100 time steps); experience has shown that this is a clear indication of a stalling rotor. By contrast, the predicted mass flow in the stage case is holding quite steady. The feeling is, then, that the rotor is stalling when operated "isolated," but running stably when run in conjunction with a stator, i.e.,

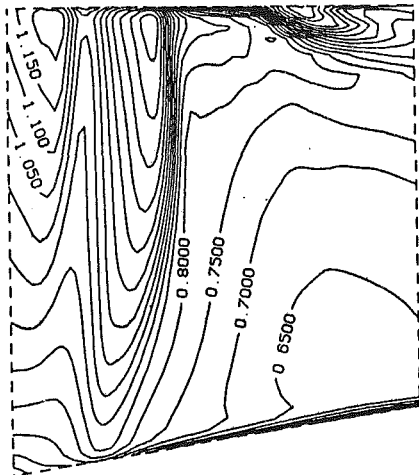
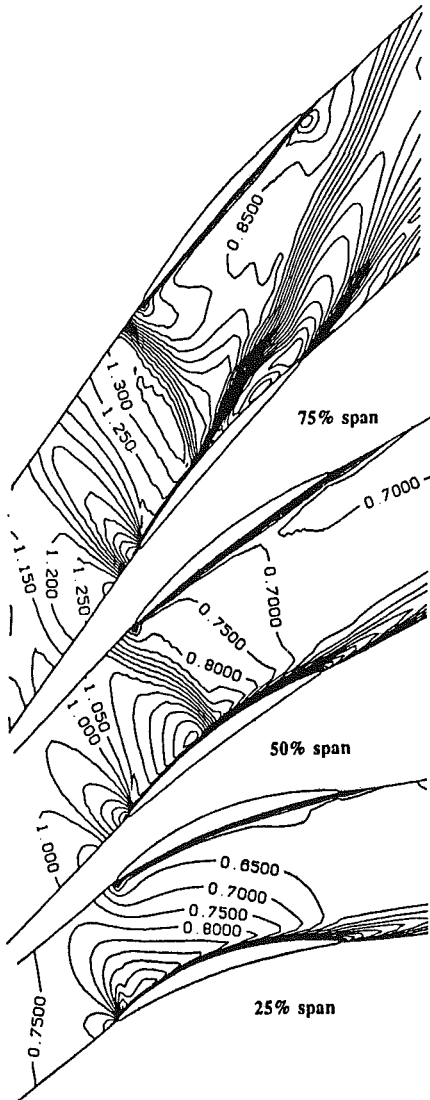


Fig. 12 Predicted Mach number contours in midpitch for the compressor rotor simulated in isolation



Figs. 13-15 Predicted Mach number contours in three blade-blade planes of the compressor rotor simulated in isolation

in a machine environment. Measurements published by Wood et al. (1987) for a similar transonic fan, tested with and without its stator, also displayed a lower stalling flow for the rotor as part of a stage compared to rotor alone.

The principle difference, as far as the rotor is concerned,

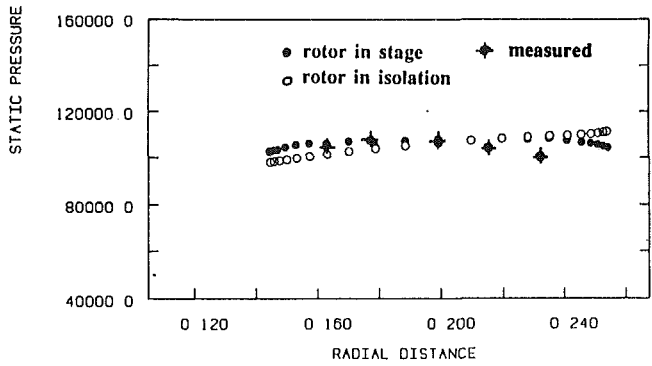


Fig. 16 Predicted and measured radial variation of static pressure downstream of the compressor rotor

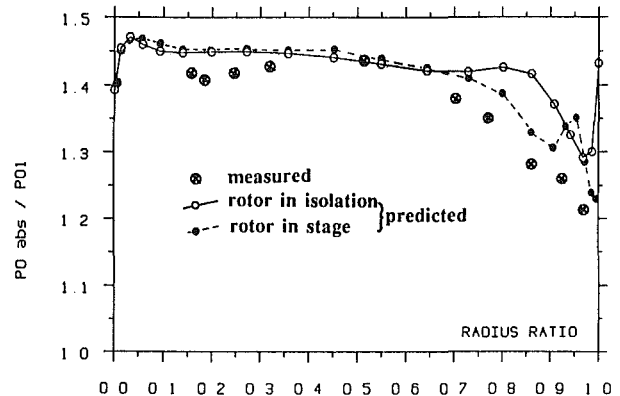


Fig. 17 Predicted and measured radial variation of circumferentially averaged total pressure ratio across the compressor rotor

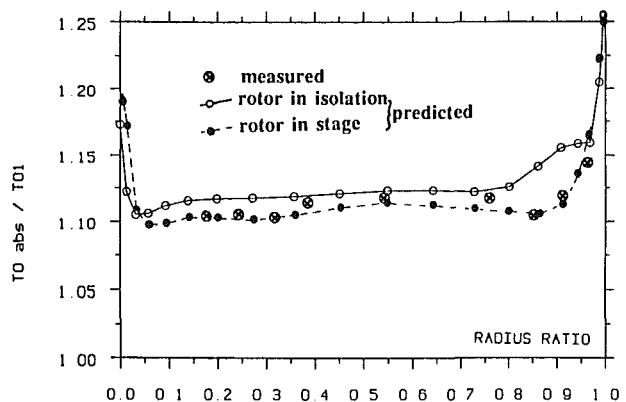


Fig. 18 Predicted and measured radial variation of circumferentially averaged total temperature ratio across the compressor rotor

between the two simulations is the radial variation of static pressure seen by the rotor at its downstream boundary. Figure 16 shows the predicted radial variation of static pressure at the mixing plane (which corresponds approximately to the experimental traverse plane) from the stage computation compared with the imposed variation from the isolated rotor case. While the mean level is not dissimilar, the pressure near the casing is lower for the stage case, explaining quite naturally the observed more stable operation of the tip sections of the rotor. The difference in static pressures is not very great but transonic rotors are particularly sensitive to their exit static pressure field. Also shown in Fig. 16 is the experimental variation of static pressure downstream of the rotor (inferred from the published Mach numbers etc.). This confirms the clear reduction of static pressure toward the casing observed for the stage calculation and in contrast to the rotor-alone computations.

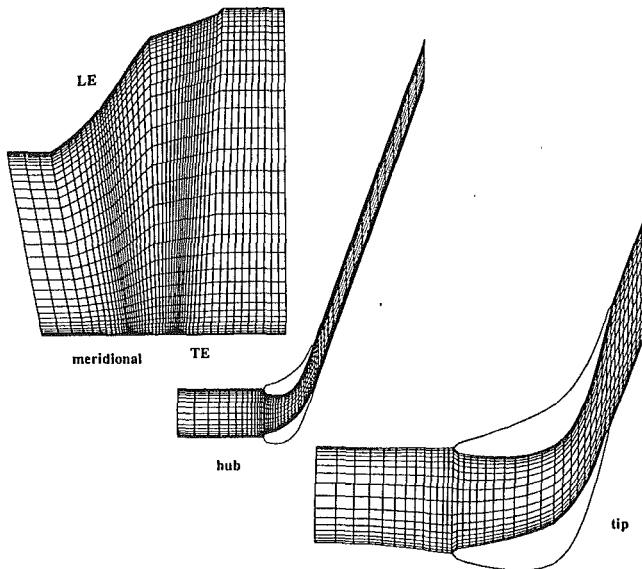


Fig. 19 The $17 \times 43 \times 33$ mesh for the guide vanes considered in isolation

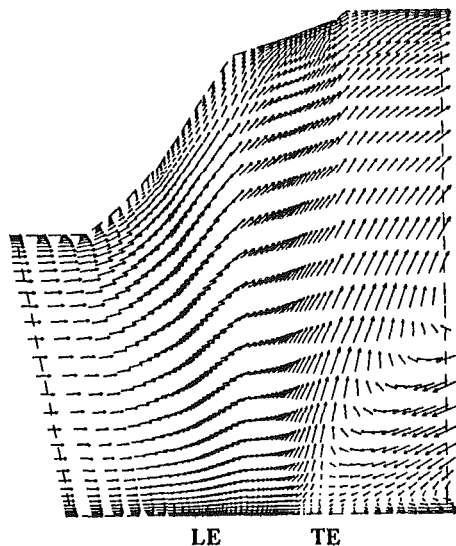


Fig. 20 Predicted velocity vectors in midpitch

Finally, Figs. 17 and 18 compare measured and predicted radial variations of circumferentially averaged total pressure ratio and total temperature ratio across the rotor. These comparisons are at the same axial location. For the inboard 60 percent of the rotor both the "isolated" and the "stage" predictions are in good agreement with measurement. Outboard of 60 percent span, the "stage" prediction is in much better agreement with measurement than the "isolated" result with the reduced effective exit static pressure seen in the stage case responsible for the fall off in total pressure and temperature ratio observed experimentally. The rotor was run without tip clearance in the current study and this may account for the discrepancy observed over the last 10 percent of the span out to the tip. Tip clearance flows are not the main thrust of this paper even though it has been shown (e.g., Dawes, 1988) that they can exert strong influence on the flow; for a many-rowed compressor it would be essential to include them. Rather, the thrust is more straightforward: The flow in individual blade rows can be strongly influenced by the imposed exit static pressure variation. (Indeed it is well known that for an isolated compressor rotor, fixing the casing static pressure plus radial equilibrium inward allows a much wider flow range to be

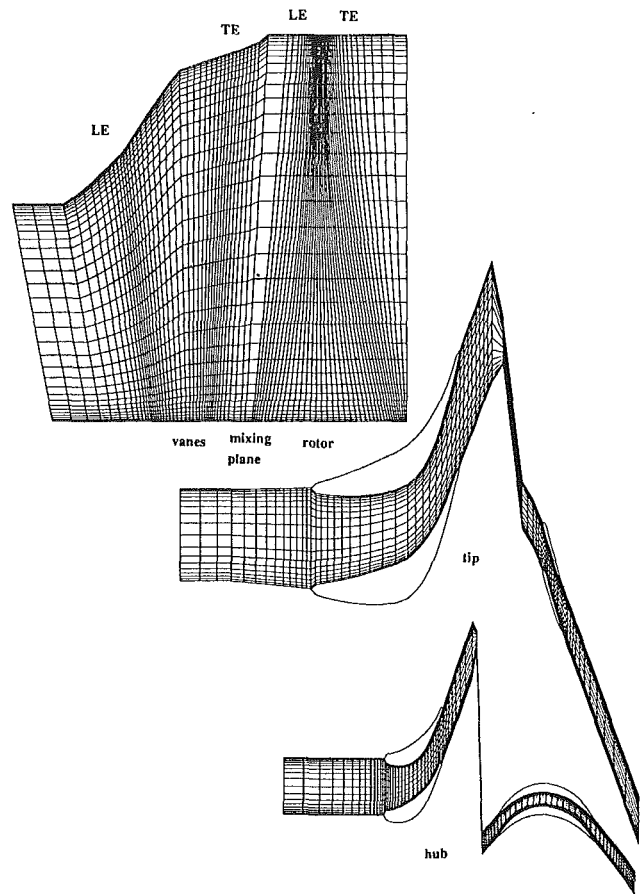


Fig. 21 The $17 \times 83 \times 33$ mesh for the guide vanes considered as part of a stage

handled compared to fixing the hub static.) The present paper simply suggests that a more systematic way of determining these boundary conditions is to consider several rows at once to give the row under study the correct flavor of the machine.

Sample Application: Low Hub-Tip Ratio Nozzle Guide Vane

A well-known experimental problem is that of testing, in a low hub-tip ratio annular cascade, turbine nozzle guide vanes with a highly swirling exit flow (Spurr, 1980; Williamson et al., 1986). The difficulty, of course, is that the swirling flow has associated with it a radially inward pressure gradient so the pressure at the hub is much lower than that at the tip. In the duct downstream of the cascade, the flow reaches some intermediate mean pressure level so that the flow near the hub may diffuse strongly. This diffusion can lead to hub separation. This is irritating experimentally and very awkward in numerical simulations (where there is a tendency for the separated zone to interact with the supposed outflow boundary leading to numerical instability). However, this is not the real issue. When the blade row is operated in a real machine there is a rotor downstream, of course, which tends to have a smaller hub pressure drop than at the tip (reaction levels increase radially outwards). The tendency for hub separation is not present to anything like the same degree. The likelihood then is that the tests on the guide vanes in isolation may be very nonrepresentative of how they will be operated in practice.

To illustrate this, computations were performed for nozzle guide vanes both in isolation and part of a stage. The vane chosen is typical of the last stage of the low-pressure cylinder of a large steam turbine and was tested (at sixth scale) in the transonic annular cascade at the CEGB's Marchwood Engineering laboratories. The basic parameters of the guide vane are

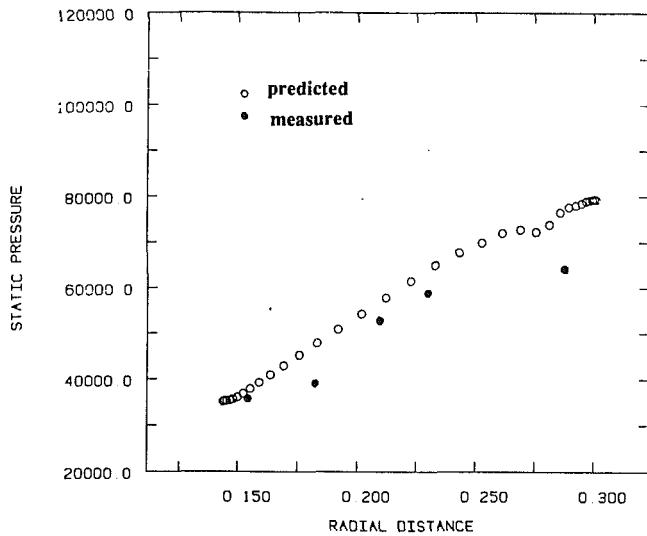


Fig. 22 Comparison of measured and predicted radial variation of static pressure downstream of the guide vanes

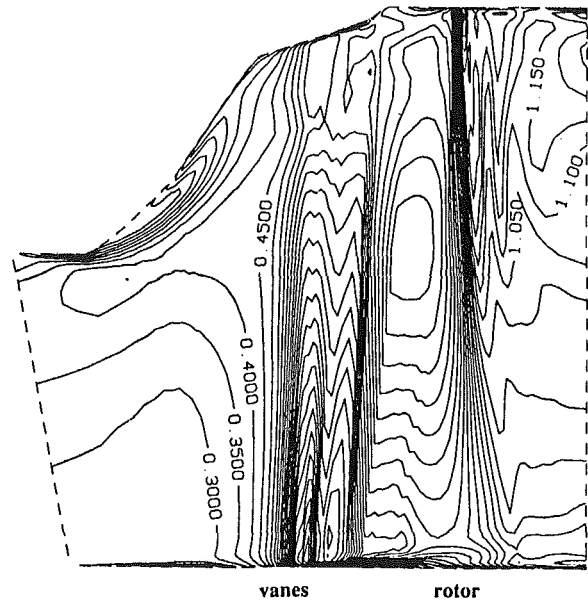


Fig. 24 Predicted Mach number contours in the midpitch plane

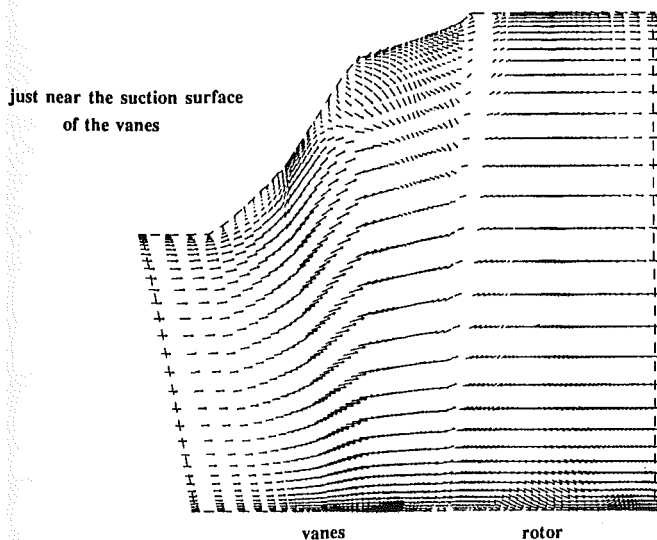
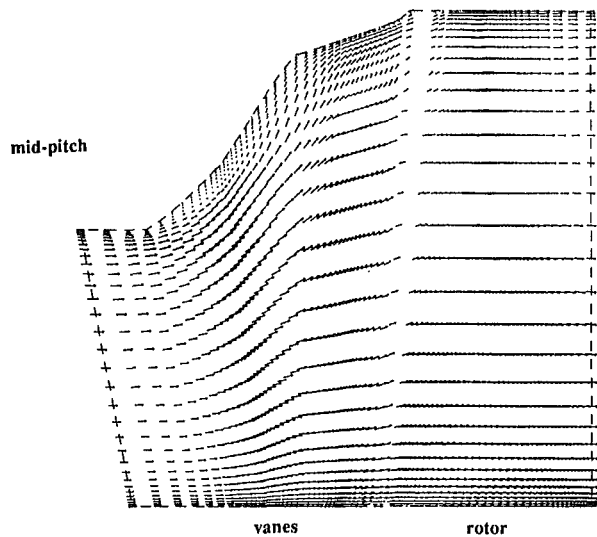


Fig. 23 Predicted velocity vectors in two meridional planes through the stage

Hub-tip ratio	=	0.48
Casing flare	=	55 deg (maximum)
Exit angle	=	70 deg (hub); 75 deg (tip)
Exit Mach number	=	1.5 (hub); 0.8 (tip)
Reynolds number	=	10^6

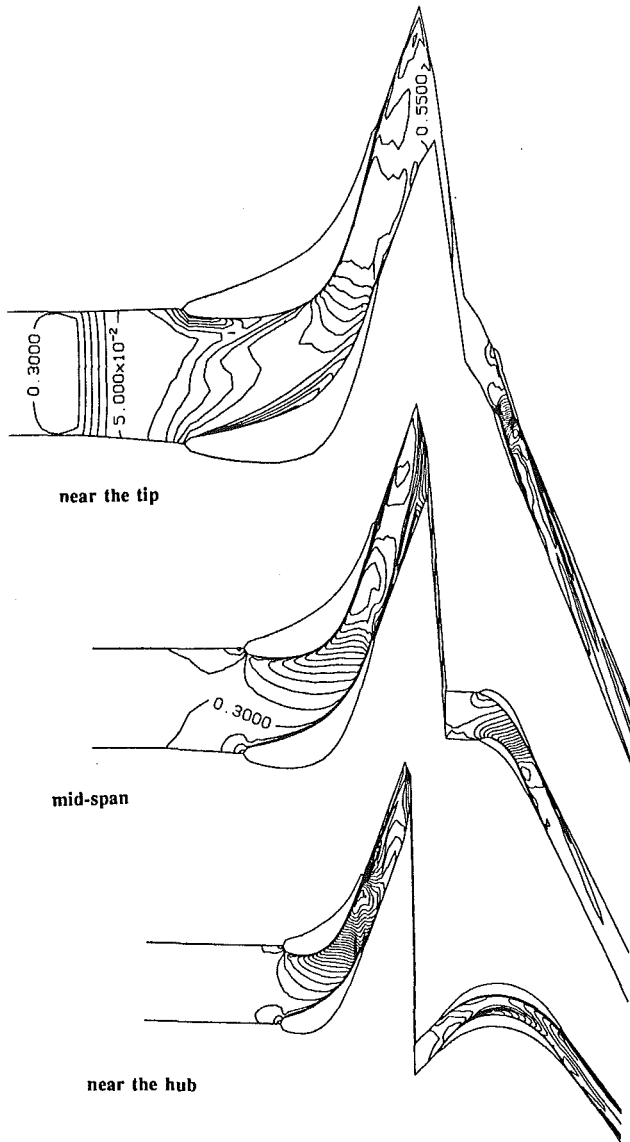
In the test (Ball et al., 1988) a perforated plate had to be installed downstream of the vanes to represent the rotor pressure drop and "to avoid severe hub separation."

Figure 19 shows the $17 \times 53 \times 33$ computation mesh used to simulate the vanes in isolation. The mesh extends about half a span both up and downstream of the blade in accordance with usual good practice. (The influence of a blade row decays exponentially with the span as its length scale.) No stable solutions could be obtained, the reason being the growth of a large hub separation, which reacts unstably with the outflow boundary condition. Figure 20 shows predicted velocity vectors in the center pitch meridional plane late into the simulation. The large separation is evident and in fact extends uniformly across the pitch.

Next the vanes were simulated as part of a stage. The $17 \times 83 \times 33$ mesh is shown in Fig. 21. The rotor is generic in origin and is simply there to provide the appropriate machine environment for the vanes. Both rotor and stator were simulated fully three dimensionally. The rotor exit static pressure boundary condition was set (by trial and error) to recover the measured hub static pressure downstream of the vanes (Fig. 22). It should be recalled that the vane exit static pressure field evolves as part of the simulation. Predicted Mach numbers and velocity vectors in the midpitch meridional plane are shown in Figs. 23 and 24. The large hub separation is now entirely absent. Mach numbers in three blade-blade planes (near-hub, mean, and near-tip) are presented in Figs. 25 to 27 to give a general picture of the operation of the stage. Finally, Fig. 28 compares measured and predicted total pressure contours downstream of the guide vanes. The level of agreement is quite satisfactory.

Concluding Discussion

A methodology has been presented for deploying three-dimensional Navier-Stokes blade-blade simulations in the context of a multistage environment. The ability to simulate blade rows axisymmetrically, if desired, means that something of the flavor of the machine environment can be provided for a par-



Figs. 25-27 Predicted Mach number contours in three blade-blade planes

ticular blade row under study with little computational overhead.

Despite the assumption of steady flow relative to each row, the blade rows do interact to first order via the combination of their mass flow-pressure drop (rise) characteristics and to second order by communication of the radial variation of properties across the mixing plane separating each blade row. The only boundary conditions required for a multistage calculation are stagnation conditions upstream of the first row and the back pressure, downstream of the last row; all the stage pressure drops (rises) and loading coefficients emerge naturally from computation. In particular this allows the radial variations of static pressure between blade rows to be predicted rather than imposed.

Two applications were presented, a transonic compressor rotor and steam turbine nozzle guide vanes, where the performance of the blade row in isolation was different from that in a machine environment. In both cases, the predicted flows with the blades as part of a stage were in closer agreement with the experimental evidence than when the blades were studied in isolation.

In the case of the compressor rotor, the rotor is more stable as part of the stage, principally because the predicted radial static pressure variation downstream of the rotor unloads the

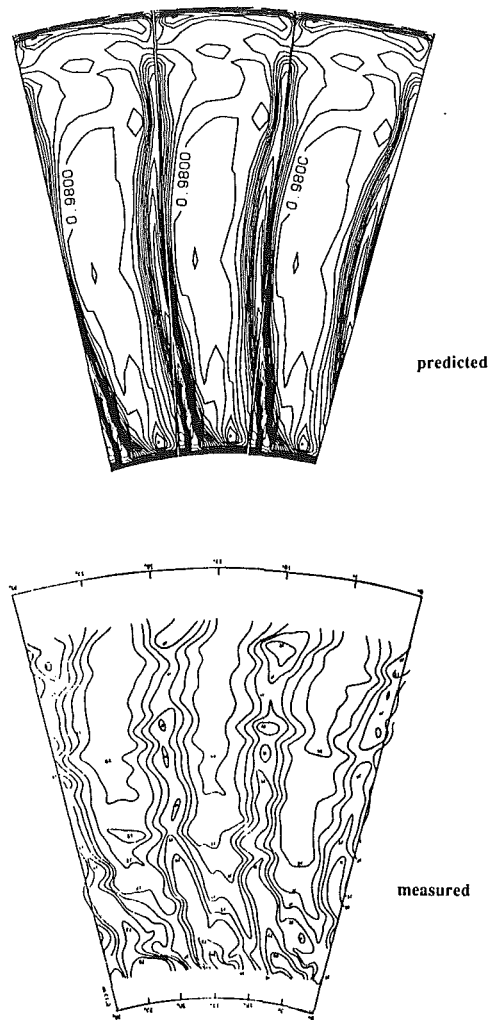


Fig. 28 Comparison of measured and predicted total pressure field downstream of the guide vanes

sensitive tip. Now of course if the radial variation of static pressure were known beforehand, then the stage simulation need not be performed, but the point is that this sort of data is not usually available (especially at the design stage) and rather than guess (using simple radial equilibrium for example) it is simply more convenient to include the machine environment. The benefit of considering blades in a machine environment is even more dramatic in the case of the turbine guide vane. Quite simply, sensible simulations cannot be performed with the vanes considered in isolation. The strong radially inward pressure gradient associated with the strongly swirling exit flow leads to strong hub diffusion to the downstream boundary and this causes, both experimentally and numerically, strong hub separation. In the presence of a rotor (or, as in the experiments, a perforated plate representing the rotor) the flow field is radically different.

References

- Adamczyk, J. J., Celestina, M. L., Beach, T. A., and Barnett, M., 1990, "Simulation of Three-Dimensional Viscous Flow Within a Multistage Turbine," *ASME JOURNAL OF TURBOMACHINERY*, Vol. 112, pp. 370-376.
- AGARD AR-175, 1981, "Through Flow Calculations in Axial Turbomachines," Propulsion and Energetics Panel Working Group 12 Report.
- AGARD LS-140, 1985, "3D Computation Techniques Applied to Internal Flows in Propulsion Systems," AGARD Lecture Series No. 140.
- Arts, T., 1985, "Calculation of the Three Dimensional, Steady, Inviscid Flow in a Transonic Axial Turbine Stage," *ASME Journal of Engineering for Gas Turbines and Power*, Vol. 107, pp. 286-292.
- Ball, G. T., Johnson, C. G., and Richards, P. H., 1988, "Aerodynamic

Measurements in the MEL Supersonic Annular Cascade," CEGB Research Report, TPRD/M/1651/RR88 (unrestricted).

Baldwin, B., and Lomax, H., 1978, "Thin Layer Approximation and Algebraic Model for Separated Turbulent Flows," AIAA Paper No. 78-257.

Birch, N. T., 1987, "Navier-Stokes Predictions of Transition, Loss and Heat Transfer in a Turbine Cascade," ASME Paper No. 87-GT-22.

Dawes, W. N., 1988, "Development of a 3D Navier-Stokes Solver for Application to All Types of Turbomachinery," ASME Paper No. 88-GT-70.

Denton, J. D., and Singh, U. K., 1979, "Time Marching Methods for Turbomachinery Calculations," in: *Application of Numerical Methods to Flow Calculations in Turbomachines*, VKI Lecture Series LS-07.

Giles, M., 1988, "Stator/Rotor Interaction in a Transonic Turbine," AIAA Paper No. 88-3093.

Hodson, H. P., 1984, "Measurements of Wake-Generated Unsteadiness in the Rotor Passages of Axial Flow Turbines," *ASME Journal of Engineering for Gas Turbines and Power*, Vol. 107, pp. 467-476.

Jennions, I. K., and Stow, P., 1985a, "A Quasi-Three-Dimensional Turbomachinery Blade Design System: Part I—Throughflow Analysis," *ASME Journal of Engineering for Gas Turbines and Power*, Vol. 107, pp. 301-307.

Jennions, I. K., and Stow, P., 1985b, "A Quasi-Three-Dimensional Turbo-

machinery Blade Design System: Part II—Computerized System," *ASME Journal of Engineering for Gas Turbines and Power*, Vol. 107, pp. 308-316.

Kovach, K., and Sandercock, D. M., 1961, "Aerodynamic Design and Performance of a Five Stage Transonic Axial Flow Compressor," *ASME Journal of Engineering for Power*, Vol. 83, pp. 303-321.

Longley, J. P., 1989, "Inlet Distortion and Compressor Stability," PhD Thesis, Cambridge University, United Kingdom.

Ni, R. R., and Bogoian, J. C., 1989, "Prediction of 3D Multistage Turbine Flowfields Using a Multiple Grid Euler Solver," AIAA Paper No. 89-0203.

Spurr, A., 1980, "A Computational and Experimental Study of Fully Three Dimensional Transonic Flow in Turbomachinery," PhD Thesis, University of Southampton, United Kingdom.

VKI LS-2, 1986, "Numerical Techniques for Viscous Flow Calculations in Turbomachinery Blading," Von Karman Institute Lecture Series No. 2

Williamson, R. G., Moustapha, S. H., and Huot, J. P., 1986, "The Effect of a Downstream Rotor on the Measured Performance of a Transonic Turbine Nozzle," *ASME JOURNAL OF TURBOMACHINERY*, Vol. 108, pp. 269-274.

Wood, J. R., Strazisar, A. J., and Simonyi, P. S., 1987, "Shock Structure Measured in a Transonic Fan Using Laser Anemometry," AGARD CP-401, *Transonic and Supersonic Phenomena in Turbomachines*.

The Calculation of Three-Dimensional Viscous Flow Through Multistage Turbomachines

J. D. Denton

Whittle Laboratory,
Cambridge, United Kingdom

The extension of a well-established three-dimensional flow calculation method to calculate the flow through multiple turbomachinery blade rows is described in this paper. To avoid calculating the unsteady flow, which is inherent in any machine containing both rotating and stationary blade rows, a mixing process is modeled at a calculating station between adjacent blade rows. The effects of this mixing on the flow within the blade rows may be minimized by using extrapolated boundary conditions at the mixing plane. Inviscid calculations are not realistic for multistage machines and so the method includes a range of options for the inclusion of viscous effects. At the simplest level such effects may be included by prescribing the spanwise variation of polytropic efficiency for each blade row. At the most sophisticated level viscous effects and machine performance can be predicted by using a thin shear layer approximation to the Navier–Stokes equations and an eddy viscosity turbulence model. For high-pressure-ratio compressors there is a strong tendency for the calculation to surge during the transient part of the flow. This is overcome by the use of a new technique, which enables the calculation to be run to a prescribed mass flow. Use of the method is illustrated by applying it to a multistage turbine of simple geometry, a two-stage low-speed experimental turbine, and two multistage axial compressors.

Introduction

Fully three-dimensional calculations for single blade rows are now well established, the most common method being time-dependent solutions of the Euler or Navier–Stokes (N–S) equations. Before applying such methods, however, the boundary conditions for the blade row must usually be established by means of a separate calculation for the whole machine. The latter will usually be performed using an axisymmetric through-flow method with empirical input to allow for viscous losses and for blade row deviations. If the exit flow predicted by the three-dimensional calculation is not compatible with the input to the throughflow calculation, e.g., different blade exit angles, then it may be necessary to repeat the whole process until compatible results are obtained from the two calculations. This can be a tedious process involving a great deal of human intervention.

To help circumvent this process, about 10 years ago, the author introduced a method of calculating the three-dimensional inviscid flow through a single-stage turbomachine, i.e., two blade rows (Denton and Singh, 1979). Since the flow through two blade rows in relative rotation is inevitably unsteady (unless they are very widely spaced) this type of calculation must involve some modeling of the real flow to remove

the effects of unsteadiness. This was achieved by circumferentially averaging the flow at an axial station approximately midway between the two rows so that the upstream row saw a circumferentially uniform downstream boundary condition and the downstream row saw a circumferentially uniform upstream flow approaching it. This averaging is not a physically realistic process unless the blade rows are widely spaced, and if performed too close to the leading or trailing edge, can lead to unrealistic predictions of the flow in those regions of the blades. However, it should be realized that this assumption of axisymmetric boundary conditions is no different in principle from that which is almost universally applied in both two dimensional, quasi-three-dimensional and full three-dimensional blade-to-blade calculations. The only difference in practice is that the condition may have to be applied closer to the blade row than would be usual in such methods.

It is also important to realize that the pitchwise averaging does not affect the spanwise variation in flow. The spanwise variation of pressure, velocity, flow angle, etc., at stations between the blade rows is obtained from the three-dimensional calculation. In particular this means that the calculation will predict the spanwise variation of stage reaction in the same way as would an axisymmetric throughflow calculation. Since the blade exit angles are automatically compatible with the blade-to-blade calculation, there is now no need to iterate between throughflow calculations and blade-to-blade calculations to obtain the flow conditions between the two blade

Contributed by the International Gas Turbine Institute and presented at the 35th International Gas Turbine and Aeroengine Congress and Exposition, Brussels, Belgium, June 11–14, 1990. Manuscript received by the International Gas Turbine Institute January 13, 1990. Paper No. 90-GT-19.

rows, and the complete flow through the stage will be predicted by a single calculation.

This single-stage three-dimensional calculation has proved especially valuable for the last stages of large steam turbines. These have very low hub-to-tip ratio, high aspect ratio, high exit Mach numbers, and large meridional pitch angles (up to 60 deg) and so the flow is highly three dimensional as well as transonic. As a result conventional throughflow calculations and coupled blade-to-blade calculations are not sufficiently accurate and the fully three-dimensional stage calculation has proved both a simpler and a more accurate tool. Examples of such calculations are given by Denton (1983) and Grant and Borthwick (1987).

Although there is no difficulty in principle in extending such three-dimensional calculations to more than a single stage, it was not thought to be worthwhile to extend the original method because of the neglect of viscous effects. An inviscid calculation through a multistage machine would inevitably give too high a mass flow for a prescribed pressure ratio and hence the velocities and flow angles could be in significant error. The result would be similar to that obtained by running a through-flow calculation without the inclusion of any losses.

Inclusion of viscous effects in three-dimensional calculations is a comparatively recent development that is still fairly expensive in terms of computer time. It is the author's opinion that in the complex turbomachine environment the accuracy of such viscous calculations is severely limited by the limitations of turbulence modeling so that at present only qualitatively accurate results can be obtained from even the most sophisticated turbulence models. In such circumstances there seems little justification for using any but the simpler turbulence models and combining them with semi-empirical corrections to enable them to predict the correct magnitude of loss. As a result mixing length eddy viscosity models are by far the most commonly used method, the Baldwin-Lomax model being especially popular. Typical of the methods available for viscous flow calculation through a single blade row is that of Dawes (1988).

In the spirit of modeling the viscous effects in the simplest possible way, the author showed how it was possible to modify a conventional Euler solver to include approximations to the viscous effects by inclusion of a body force term in the momentum equations. This force term can be calculated within a separate subroutine of the program so that the method used to estimate it is completely decoupled from the main flow solver. As originally proposed (Denton, 1986), this force term was estimated by a semi-empirical approach but it was pointed out that the model could in principle be used with any level of approximation to the full N-S equations. Over the past few years the author has developed a total of seven different subroutines for estimating the viscous force. These range in complexity from the original specification of an empirical frictional pressure loss for the blade row to a thin shear layer approximation to the full N-S equations. The most recent subroutine was developed specifically for this multistage calculation and enables the spanwise variation of polytropic efficiency for each blade row to be input to the calculation.

This approach to the inclusion of viscous effects has the advantage that different levels of approximation may be used within the same program. For example, a calculation may be

started with a very simple completely empirical model of viscous effects and after a solution has been obtained the calculation may be restarted with a more sophisticated model. The approach is especially attractive for including viscous effects in multistage calculations, where limitations on the number of grid points and the neglect of unsteady effects means that more complex methods are even less justifiable than they are for a single blade row calculation, and empirical input is likely to be essential if realistic results are to be obtained.

Three-dimensional calculations for multiple blade rows have also been developed by Adamczyk (1985), Adamczyk et al. (1990), Arts (1984), and Ni (1989). Adamczyk uses what he calls a "passage average" approach in which three-dimensional calculations are performed separately for each blade row with the effects of the other blade rows being modeled by additional force terms in the equations. Once a three-dimensional solution has been obtained for one blade row it is circumferentially averaged to obtain the force terms needed for the three-dimensional calculations in other blade rows. This approach is much more rigorous than that of the author but is inevitably more time consuming because several three-dimensional calculations have to be done for every blade row with the force terms being adjusted iteratively. Although the method makes some attempt to include unsteady effects, only the effect of unsteadiness on the time-averaged flow is captured. Viscous effects are included in the latest version of Adamczyk's method. Arts (1985) effectively couples two single blade row calculations by a common boundary condition, again effectively performing a circumferential averaging at the interface. Ni (1989) gives very few details of his method but shows results for a two-stage turbine. It is not clear whether viscous effects are included, but good agreement with experimental data is claimed and it is unlikely that this could be achieved without some modeling of viscous effects.

Calculation Method

Euler Solver. The basic Euler solver used in this method is well known and is described by Denton (1982, 1985). The method is an explicit finite volume method with spatially varied time steps and three levels of multigrid. The multigrid block sizes are not those conventionally used, with two elements per block side, but instead any number of elements can be used along the sides of each block. Usually blocks of three elements per side are found to be near optimum and so blocks of $3 \times 3 \times 3$, $9 \times 9 \times 9$, and $27 \times 27 \times 27$ elements would be used for the three levels. However, for the present application it was not considered advisable to use the third level of multigrid because the blocks are likely to extend over more than one blade row. As pointed out by the author (Denton, 1986), this level of multigrid enables high levels of grid refinement to be used without large deterioration in the rate of convergence. Typically $70 \times 28 \times 28$ mesh points will be used for a single blade row viscous calculation with the mesh spacing varied by a factor of 10-15 between points adjacent to solid surfaces and points near the center of the passage. With this number of points convergence to engineering accuracy will usually be achieved in the order of 1000 to 2000 steps.

The grid used by the method is a simple H mesh with all the variables stored at the cell corners. This may not be the

Nomenclature

F = body force, flux	T = static temperature
j = grid index in meridional flow direction	V = absolute velocity
M = mass flow rate	W = relative velocity
P = static pressure	η_p = polytropic efficiency
S = entropy	ρ = fluid density
	τ_w = wall shear stress

Subscripts

m = in streamwise direction
r = in radial direction
t = in tangential direction
x = in axial direction

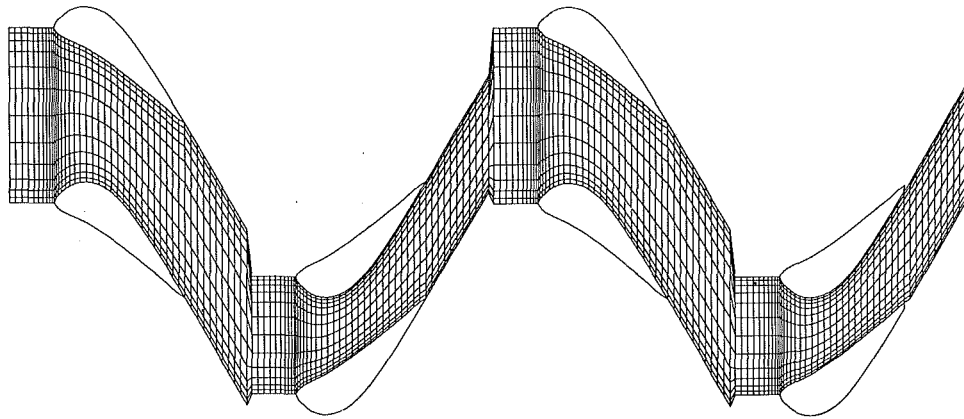


Fig. 1 Mesh for inviscid calculation on a two-stage turbine

optimal type of mesh for any one problem but the method is designed to be applicable to all types of turbomachines, ranging from axial flow to radial flow, and to include such complicating features as splitter blades, part-span shrouds, and free blade tips (i.e., propellers). Such features are easily accommodated by the H mesh but it is unlikely that any other type of mesh could be made to include many of them. The author's experience is that the errors incurred by using a highly sheared H mesh in regions such as that around a thick leading edge can be made acceptable by using sufficient mesh points. The cell corner storage of the variables is felt to be preferable to cell center storage since the formal accuracy does not decrease for rapid changes of mesh spacing. The mesh used for a calculation on a four blade row turbine is shown in Fig. 1.

Viscous Force Term. The idea behind the use of a force term in the momentum equations to model viscous effects is described by Denton (1986). The only approximation inherent in this model is the neglect of viscous effects in the energy equation, and it is shown that this is a good approximation for the adiabatic flow of fluids with Prandtl number close to unity, especially at low speeds. The viscous force acting on each finite volume must be found by summing the viscous shear stresses and normal stresses around the faces of the element. Any level of approximation to these stresses can be used and there is no inherent reason why the stresses should not be obtained from the full N-S equations. In practice it was found that remarkably realistic results could be obtained using very simple approximations to the viscous force term. That described by Denton (1986) involved an input value of skin friction coefficient and an algebraic distribution of the shear stress away from solid boundaries. It was therefore completely empirical since the effective turbulence viscosity did not depend at all upon the flow.

The method most commonly used in the latest version of the program obtains the viscous force from a thin shear layer approximation in which all normal components of viscous stress are neglected and only the shear stresses on the streamwise and bladewise faces of the cuboid shaped elements are considered; viscous stresses on the quasi-orthogonal faces (i.e., faces that are tangential to the theta direction) of the elements are neglected. In order to avoid the use of an extremely fine mesh near solid boundaries, with grid points in the laminar sublayer, it is thought preferable to use a slip model of flow on the boundaries and to calculate the shear stress on the boundary using wall functions.

The shear stress on the solid boundaries is obtained by assuming that the first grid point away from the solid surfaces (i.e., not the point lying on the surface) lies either in the laminar sublayer, or, more likely, in the logarithmic region of a turbulent boundary layer. In the latter case the well-known expression for the log law boundary layer profile

$$V^+ = 2.5 \ln Y^+ + 5.2 \quad (1a)$$

is very closely approximated by an explicit relationship between $Re_2 (= \rho V_2 y_2 / \mu)$ and $C_f (= 2\tau_w / \rho V_2^2)$. This relationship is

$$C_f = -0.001767 + \frac{0.03177}{\ln(Re_2)} + \frac{0.25614}{(\ln(Re_2))^2} \quad (1b)$$

Its use avoids the need for iteration to calculate the skin friction.

The shear stresses at points off the wall are obtained from a simple mixing length model. No attempt is made to vary the model between inner and outer regions of the boundary layer, as is done in the well-known Baldwin-Lomax and Cebeci-Smith models. Instead the turbulent viscosity is calculated in the conventional way from a mixing length, which is taken as $l = 0.41y$, where y is the perpendicular distance from the nearest wall. The mixing length calculated in this way is "cut off" by an algebraic filter at a prescribed distance from the surface. Since the calculated stresses usually decay to near zero outside the boundary layer, the precise location of this cutoff is not very important provided that it is outside the boundary layer. It is usually applied at a point 10 percent of the blade pitch from the surface as measured in the circumferential direction. The mixing length behind the trailing edge is held constant at a value which is input to the calculation. This value is usually taken as 2 percent of the blade pitch.

Having obtained the viscous shear stresses in this way, the viscous force term is obtained by summing the stresses around the bladewise and streamwise faces of every element. The viscous force acting on the elements does no work in a stationary coordinate system but does do work in a rotating system, and this work must then appear as a source term in the energy equation. However, as explained by Denton (1986), the viscous shear work and the heat conduction may be assumed almost to cancel one another and so are not included at all in the energy equation.

The Prescribed Polytopic Efficiency Model. For multi-stage calculations it was thought desirable to be able to input empirical blade row losses in a similar way to that used in some throughflow calculations. In order to do this the body force must be made to depend on the required efficiency. As shown in the appendix this can be achieved by applying a body force, F_v , per unit volume, where

$$F_v = (1 - \eta_p) \frac{dp}{dz} \text{ for a turbine} \quad (2)$$

and

$$F_v = \left(\frac{1}{\eta_p} - 1 \right) \frac{dP}{dz} \text{ for a compressor}$$

acting along the streamlines in the opposite direction to the flow. In practice, for simplicity, the streamlines are assumed to coincide with the quasi-streamlines of the grid and the magnitude of the body force acting on an element is given by

$$F_z = \text{Vol} \cdot F_v \quad (3)$$

where z is the distance along the quasi-streamline. This force must then be resolved into its three components before inclusion in the momentum equations. In the present code the value of polytropic efficiency is input as a function of spanwise position for every blade row.

This loss model will, unfortunately, not always produce a flow with exactly the prescribed value of polytropic efficiency because additional entropy increases occur due to shock waves and to numerical errors. For subsonic machines the difference between the prescribed and achieved values of polytropic efficiency will be small unless too coarse a grid, giving rise to numerical entropy production, is being used. For transonic machines, especially transonic compressors, the additional shock loss can cause significant differences between the prescribed and achieved polytropic efficiency.

The Interrow Mixing Model. The simple averaging of flow quantities at a plane between the blade rows as used previously (Denton, 1983) is equivalent to applying a mixing process between the nonuniform flow at the calculating plane upstream of the mixing plane and the mixing plane. This process conserves mass, energy, and momentum, but as with any real mixing process entropy will be created by the mixing. However, experience with inviscid flows has been that in practice the magnitude of entropy creation is negligible. The real problem with the model is that a circumferentially uniform flow may be forced to exist too close to the leading edge of the downstream blade row. This does not allow the flow to adjust circumferentially to the presence of the blade as it would in reality. As a result the leading edge loading on the blade row may be wrong and may even be physically unrealistic. The magnitude of this problem depends on the leading edge loading and thickness and on how close the leading edge is to the mixing plane. For a moderately loaded leading edge the plane can be located as close as 1/4 blade pitch upstream without apparent problems but this would not be acceptable for highly loaded leading edges. A similar problem occurs at the trailing edge of the blade row upstream of the mixing plane, but for subsonic exit flows the Kutta condition ensures zero loading at the trailing edge and so the problem is not so serious. This simple averaging process is included as an option in the present method.

A simple but effective means of relieving this problem is also included in the method. The method may be briefly described as obtaining the circumferential variation of fluxes at the mixing plane by extrapolation from the upstream and downstream planes while adjusting the level of the fluxes to satisfy overall conservation. Thus the fluxes "seen" by the blade rows are circumferentially nonuniform at the mixing plane with different circumferential variations, but the same average value, being "seen" by the upstream and downstream rows.

In more detail, the circumferential averaging process is first applied as before so that the averaged flow at the mixing plane conserves mass, momentum, and energy with the circumferential average of the nonuniform fluxes crossing the adjacent calculating stations. This process may be thought of as treating all the elements (at the same spanwise location) immediately upstream of the mixing plane as a single large element and conserving fluxes between the nonuniform flow entering its upstream face and the uniform flow leaving its downstream face, which lies on the mixing plane. However, when applying the conservation equations to the individual cells, the fluxes crossing the mixing plane are not taken to be circumferentially uniform. Instead, for the elements immediately upstream of

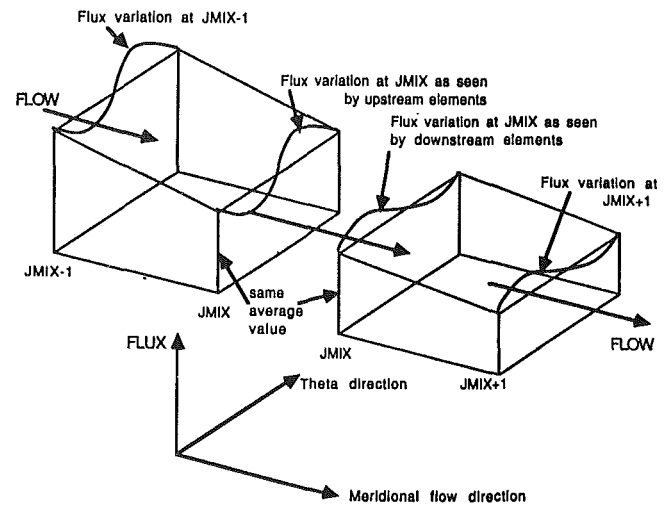


Fig. 2 Treatment of fluxes at the mixing plane

the mixing plane, the flux crossing the face on the mixing plane is obtained by multiplying the flux through the upstream face by the ratio of the circumferentially averaged flux at the mixing plane to the circumferentially averaged flux at the upstream plane, i.e.,

$$F_{j\text{mix}} = F_{j\text{mix}-1} \left(\frac{\bar{F}_{j\text{mix}}}{\bar{F}_{j\text{mix}-1}} \right) \quad (4a)$$

The idea is illustrated schematically in Fig. 2. This extrapolation of the flux variation is done at every spanwise position and is equivalent to obtaining the circumferential variation in flux from the upstream face of the element but adjusting its magnitude to satisfy overall conservation.

The same treatment is applied to the elements immediately downstream of the mixing plane. At every spanwise position the flux entering an element through the mixing plane is obtained by multiplying the flux through its downstream face by the ratio of the circumferentially averaged flux at the mixing plane to the circumferentially averaged flux at the location of the downstream face.

$$F_{j\text{mix}} = F_{j\text{mix}+1} \left(\frac{\bar{F}_{j\text{mix}}}{\bar{F}_{j\text{mix}+1}} \right) \quad (4b)$$

The treatment described is only approximate because it is effectively assumed that the derivative of the flux terms along the quasi-streamlines of the grid at the mixing plane is only due to changes in the circumferentially averaged flux. However, it does allow the flows entering and leaving the mixing plane to vary circumferentially and so is a great improvement on the previous method when the mixing plane is close to the leading or trailing edge.

Mass Flow Forcing. Traditional Euler solvers always work with boundary conditions of specified pressure ratio and allow the mass flow to be predicted by the solution. This is a well-conditioned boundary condition for most applications and is essential for choked blade rows. However, for high-pressure-ratio compressor blades, when the blade is operating near stall, the calculation may become unstable due to "numerical surge." In this the computed flow separates or generates a high loss, possibly during the transient part of the calculation; the resulting blockage reduces the mass flow, which increases the incidence on the blade, which makes the separation or loss larger, ..., etc. Thus the calculation may fail as a result of the transient induced by the initial guess rather than because of a genuinely unstable operating point. This tendency to instability becomes more pronounced as the compressor pressure ratio

increases and so it becomes almost essential to be able to ensure that each blade row is operating reasonably close to design at all times during the transient part of the calculation.

There is no known way of removing the boundary condition of prescribed pressure ratio from a time-dependent Euler or N-S method and so the alternative is to specify both mass flow and pressure ratio and to make the two compatible by generating the correct amount of loss. This is the basis of the method developed for the present code. In principle the loss is generated by a body force in the same way as the viscous terms are included; however, the details are very different.

The mass flow, $M(j)$, crossing every quasi-orthogonal plane (on which the index j is constant), is calculated, and if this differs from the prescribed mass flow, M_m , all the velocities at the plane are adjusted according to

$$\begin{aligned} \Delta &= RF * (M_m - M(j)) / M_m * (\rho V_m)_{\text{mid}} \\ \Delta(\rho V_x) &= (V_x / V_m) * \Delta \\ \Delta(\rho V_r) &= (V_r / V_m) * \Delta \\ \Delta(\rho W_t) &= (W_t / V_m) * \Delta \end{aligned} \quad (5)$$

where RF is a relaxation factor.

This adjustment makes a constant change to ρV_m at all grid points on the quasi-orthogonal surface without changing the relative flow direction. When a steady state is reached the increment in (density * velocity) produced by Eqs. (5) must be exactly canceled by an opposite change produced by the time stepping procedure. This means that the momentum fluxes are not in balance and an effective body force F_m , is acting on the elements in the direction of the relative velocity. The force can be positive or negative and its magnitude may be adjusted by changing the relaxation factor, it will produce an entropy gradient along the streamlines according to

$$F_m = T dS/dz \quad (6)$$

z being the distance along a streamline.

When this method is applied, the mass flow is very rapidly brought to a value close to the require value, M_m , and loss is produced at a rate just sufficient to make the imposed pressure ratio consistent with the imposed mass flow. Since Δ will be zero when the mass flow is equal to that specified, the flow rate obtained must always be slightly different from M_m , unless the pressure ratio and mass flow are already consistent. The small difference between the specified and calculated mass flow will be directly proportional to RF , which is in effect a scaling factor on the imposed force. In practice values of $RF = 0.25$ are found to produce negligible difference between the prescribed and the calculated mass flow.

This mass flow forcing process can be applied during the initial stages of a calculation until the initial transients have decayed and a near converged solution is obtained. This solution will have spurious loss generated by the mass flow forcing. Since this loss can be produced everywhere in the flow it may be physically unrealistic. The value of RF may then be gradually reduced, and the calculation continued, with the mass flow being allowed to find its own value as determined by the pressure ratio. This will not prevent "numerical surge" in cases where the flow is genuinely unstable, i.e., if the pressure ratio of the compressor is too high, but it will enable a much closer approach to the point of instability to be reached before the numerical instability prevents a solution from being obtained. It is doubtful whether solutions for multistage high-pressure-ratio axial compressors or for single-stage high-pressure-ratio centrifugal impellers could be obtained without this procedure.

An alternative use of the same idea is not to specify the mass flow for the machine but always to force the local mass flow toward the average value for the whole machine, as obtained by averaging the computed flow at every calculating station, i.e.,

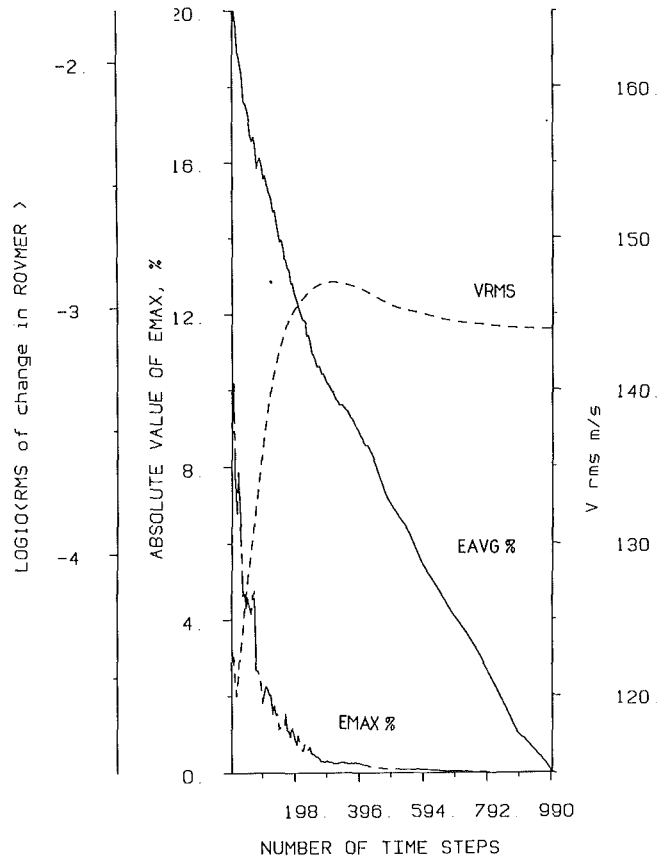


Fig. 3 Convergence of a calculation on a four-stage turbine

$$M_m = \sum_1^{JM} M(j) / JM \quad (7)$$

is used in Eq. (5). This procedure gives almost the same stabilizing effect as specifying the mass flow but it does not affect the final steady solution. In fact this use of the method often enables solutions to be obtained in significantly fewer time steps even when there is no problem with "numerical surge."

Applications of the Method

The method has been applied to several multistage turbines and compressors. There is no limit in principle to the number of blade rows that can be calculated in a single run, the limit in practice being set by the available computer power and storage. For realistic viscous solutions, a minimum of about 50 axial stations and 19 pitchwise and spanwise stations per blade row are needed, making about 18,000 points per row. Hence five blade rows would require about 90,000 mesh points and about 15 Mbytes of computer storage. A typical run time for this number of points would be 15 hours on a single processor of an Alliant FX80. If the option to specify polytropic efficiency without trying to predict detailed viscous effects is used, then the grid need only be sufficient to support an inviscid calculation and about $40 \times 13 \times 13$ grid points per blade row would be adequate. At this level the program can be run for up to four blade rows on a PC with four Mbytes of storage.

The program was initially developed for axial turbines where "numerical surge" is not a problem. Convergence for such machines was found to be surprisingly fast, as is illustrated in Fig. 3. One might expect the number of time steps required to be proportional to the number of axial calculating stations, and on this basis the convergence should be significantly slower. The reason for this faster than expected convergence is thought

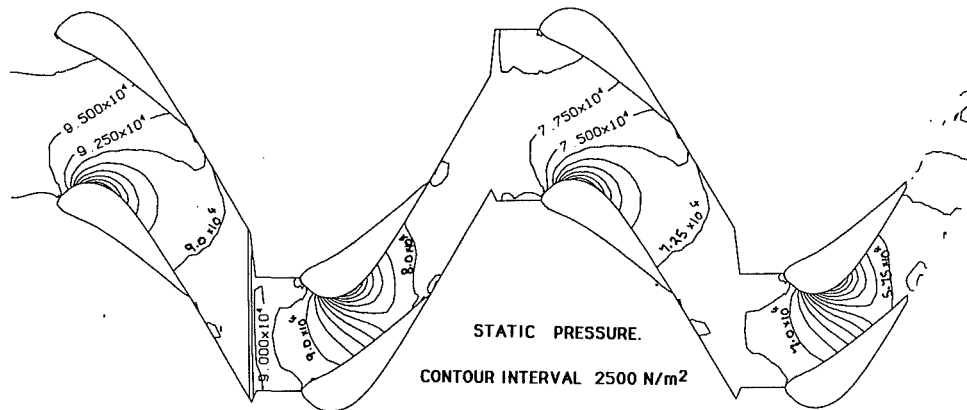


Fig. 4 Solution with wide axial spacing (0.8 x chord)

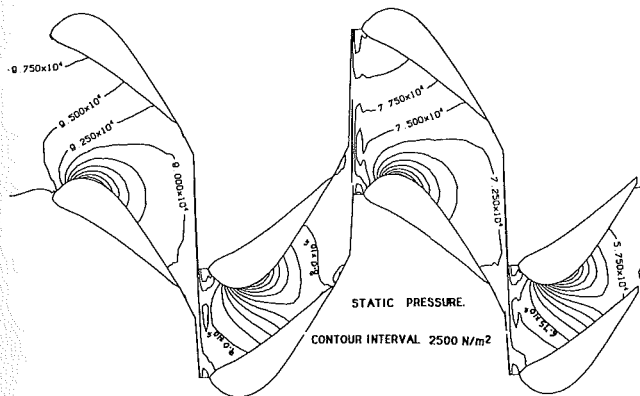


Fig. 5 Solution with reduced axial spacing (0.25 chord)

to be that for a high-pressure-ratio turbine, pressure waves are rapidly damped by the work extraction. For example a change in turbine exit pressure will produce a proportionally much smaller change in inlet pressure to the last blade row and this in turn will produce an even smaller change in the inlet pressure to the penultimate blade row, etc.

To check the effectiveness of the mixing plane treatment, calculations were performed on a two-stage axial turbine with repeating stage geometry for two different values of blade row spacing. The grid used is shown in Fig. 1. Figures 4 and 5 show the calculated static pressure contours for an interstage gap of 0.8 of the axial chord and with the gap at a more realistic level, 0.25 of the axial chord. It can be seen that there is very little difference between the two solutions except in the immediate vicinity of the mixing plane where the contouring routine is confused by the discontinuity in grid coordinates at the mixing plane. Figures 4 and 5 were obtained with a prescribed polytropic efficiency; by contrast Fig. 6 shows results for the same turbine with a finer mesh ($19 \times 180 \times 19$) and with viscous effects calculated from the thin shear layer model. The predicted polytropic efficiency in this case was 87.8 percent, which is a very reasonable value for a turbine with poor blade surface velocity distribution (the blade sections were drawn, not designed) and no tip clearance.

To check for any problems that might arise from more stages and higher pressure ratios, the same blade geometry was run with four stages and a pressure ratio of 5:1. The annulus height was increased to accommodate the increasing volume flow. No difficulties were encountered; convergence was naturally rather slower than for two stages. Nevertheless, as shown in Fig. 3, it took only about 1000 steps. Figure 7 shows the Mach number contours from this solution. The last blade row is

choked with a shock wave, which is highly smeared due to the small number of grid points per blade row.

Figure 8 shows computed velocity contours from a viscous solution at the midspan of a two-stage low-speed experimental turbine. Convergence was very slow for this case due to the low Mach numbers, peak value = 0.19. Note the very thin boundary layers associated with the mainly accelerating flow in this well designed turbine. The predicted isentropic efficiency was 88.2 percent, which is rather lower than expected for this machine; a possible explanation for this is the assumption of fully turbulent boundary layers. The experimental efficiency is not yet available.

Solutions have been obtained for a three-stage high-pressure-ratio (4.51:1) transonic compressor both using a prescribed polytropic efficiency and with calculation of viscous effects. Results cannot yet be published but experience was that the solutions were comparatively difficult to obtain because of instabilities at the mixing plane when using the improved treatment described above. The calculated efficiency was also significantly lower than the prescribed polytropic efficiency because of the neglect of shock loss.

A viscous solution for a four-stage, nine-blade row (IGV + four stages), industrial compressor with an overall pressure ratio of about 1.6 was obtained with no difficulty. Figure 9 illustrates the blade static pressure distribution at midspan for this machine. An interesting feature of this solution is the growth of the annulus wall boundary layers. A knowledge of the blockage due to these boundary layers is an important requirement for conventional throughflow calculations and its prediction is currently heavily dependent on empirical correlations. Figure 10 illustrates the computed boundary layer development through the compressor, showing the initial thin boundary layer growing to fill almost the whole annulus. No experimental data are available but it is known that a repeating velocity profile is usually obtained after a few stages, hence the results appear very plausible. Ability to predict this annulus boundary layer blockage would be an important advance in compressor design. The predicted isentropic efficiency of this machine was 82.2 percent, which is somewhat lower than might be expected for such a compressor without any tip leakage.

The method has also been used as part of the design process for a large two-stage, six-blade row, axial flow compressor with high subsonic blade surface Mach numbers. Since a conventional throughflow solution was available for this machine, it is informative to compare its predictions with those from the three-dimensional viscous calculations. To make the comparison meaningful the three-dimensional calculation was run without any attempt to model the annulus wall boundary layers. The throughflow calculation uses empirical data and correlations to predict blade row loss and deviation. Figure 11

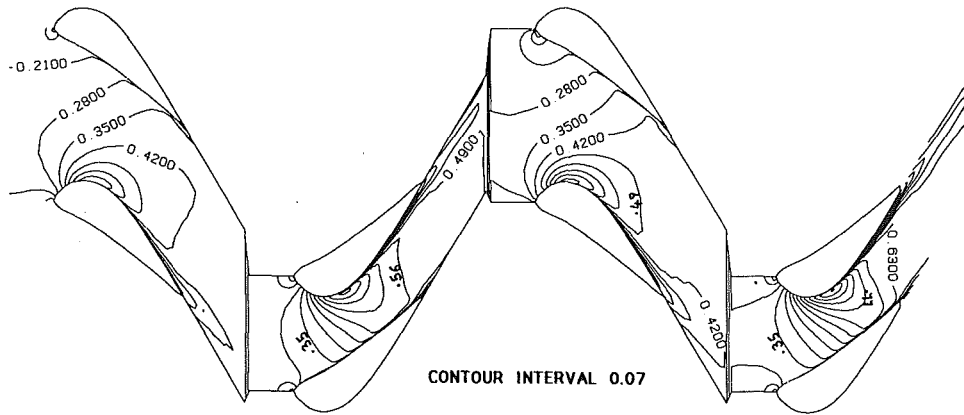


Fig. 6 Viscous solution for two-stage axial turbine Mach number contours

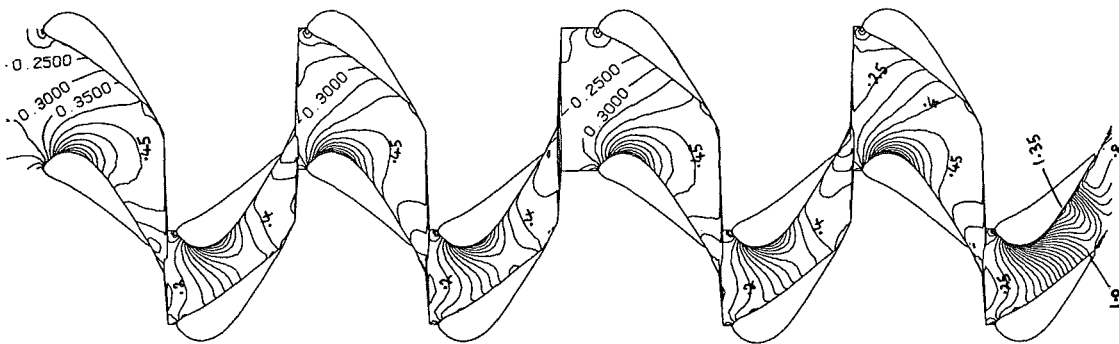


Fig. 7 Mach number contours for a four-stage turbine contour interval 0.05

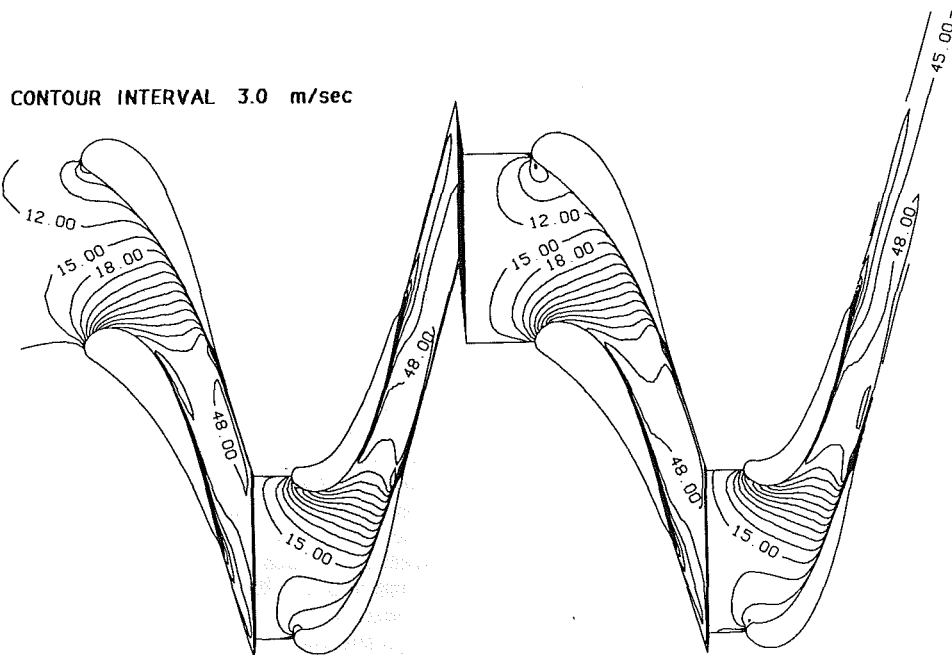


Fig. 8 Velocity contours for a low-speed two-stage turbine

compares the two predictions of relative flow angle at exit from both rotors and stators (the angles from the three-dimensional calculations are those at the mixing planes) and

shows excellent agreement between the two. Ability to predict blade row deviations without any empiricism represents a significant advance over current throughflow calculations. The

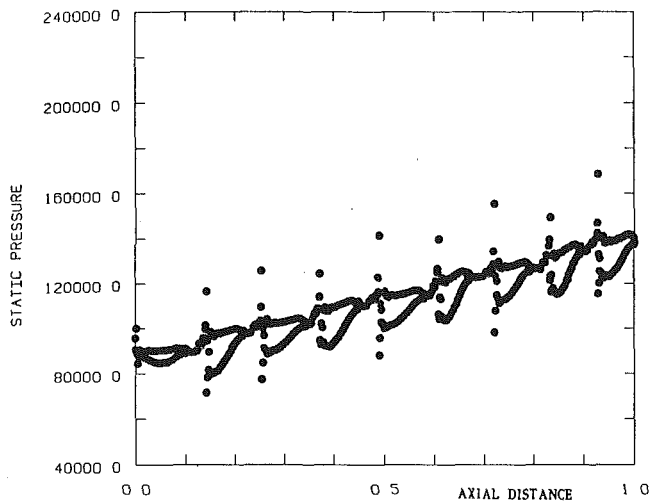


Fig. 9 Blade surface pressure distribution for a four-stage compressor with 1GV

predicted isentropic efficiency of this machine was 85.5 percent, that predicted by the throughflow calculation was 88.3 percent.

Conclusions

The method described is still at an early stage of development, but it is hoped that the results presented in this paper illustrate its potential. The main attraction of the method is its ability to reduce the amount of human intervention needed to obtain solutions for multistage turbomachines by eliminating the need to iterate between throughflow solutions and blade-to-blade solutions. At the same time it removes most of the limitations implicit in the quasi-three-dimensional approach, especially the neglect of stream surface twist and the need to assume a distribution of stream surface thickness within the blade rows.

The inclusion of viscous effects is necessarily approximate and it cannot be claimed that the method will yet provide accurate a-priori predictions of machine efficiency. However, the results quoted above, which were obtained without any empirical tuning of the method and assuming fully turbulent boundary layers, suggest that the accuracy of efficiency prediction is already comparable to that of other methods. Inclusion of tip leakage flows and losses is clearly needed before accurate modeling of the loss mechanisms can be claimed. This is very easily included in the calculation as it is already available in the single blade row version of the method. At present it is not felt that sufficient grid points can be used to give meaningful predictions of tip leakage flows in the multistage program.

In a turbine accurate prediction of viscous effects is often not essential to obtaining a good prediction of the overall flow pattern, and undesirable flow features may easily be identified using the present loss models. In a high-pressure-ratio compressor the overall flow pattern is often determined by viscous effects and semi-empirical modeling of these will be necessary for a long time to come. Hence, further comparison with experimental data and tuning of the loss models is needed before the method can be used with confidence to predict the overall flow pattern in high-pressure-ratio multistage compressors.

The status of the present method is therefore similar to that of axisymmetric throughflow calculations when, some 20 years ago, they were first developed and applied to multistage turbomachines. It is anticipated that in 10 years time methods of

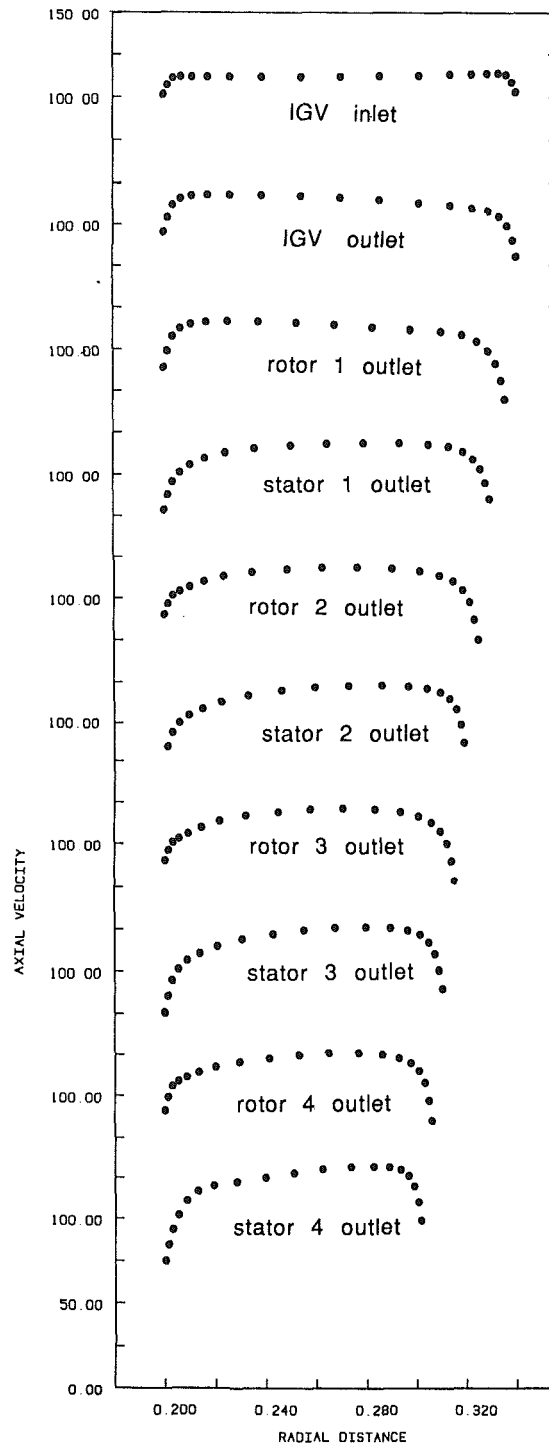


Fig. 10 Development of the axial velocity profile in a four-stage axial compressor

the present type will dominate our design procedures in the way that throughflow calculations do today.

Acknowledgments

The data for the calculation on the two-stage turbine of Fig. 8 were prepared by Dr. H. P. Hodson of the Whittle Laboratory. Those for the four-stage compressor of Figs. 9 and 10 were made available by Sulzer Escher Wyss Ltd. Preparation of data for such multistage calculations represents a considerable amount of effort and the author is grateful to all who have helped him with this task.

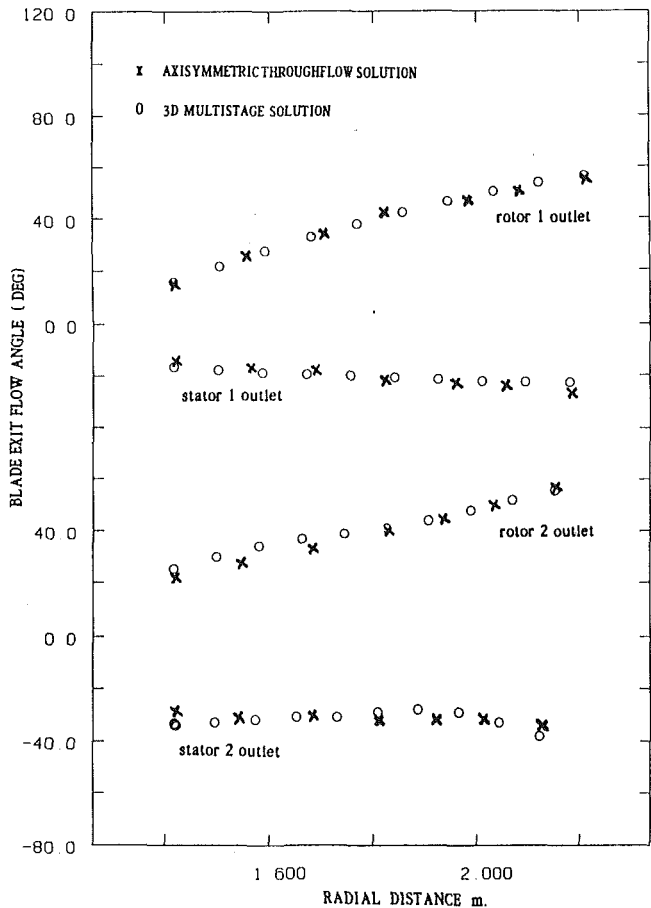


Fig. 11 Comparison of axisymmetric throughflow predictions and three-dimensional multistage predictions for the relative exit flow angles in a two-stage compressor

References

- Adamczyk, J. J., 1985, "Model Equation for Simulating Flows in Multistage Turbomachinery," ASME Paper No. 85-GT-226.
- Adamczyk, J. J., Celestina, M. L., Beach, T. A., and Barnett, M., 1990, "Simulation of Three-Dimensional Viscous Flow within a Multistage Turbine," ASME JOURNAL OF TURBOMACHINERY, Vol. 112, pp. 370-376.
- Arts, T., 1985, "Calculation of the Three-Dimensional, Steady, Inviscid Flow in a Transonic Axial Turbine Stages," ASME Journal of Engineering for Gas Turbines and Power, Vol. 107, pp. 286-292.
- Dawes, W. N., 1988, "Development of a Three-Dimensional Navier-Stokes Solver for Application to All Types of Turbomachinery," ASME Paper No. 88-GT-70.
- Denton, J. D., 1975, "A Time Marching Method for Two and Three Dimensional Blade to Blade Flow," Aero. Res. Co., R & M 3775.
- Denton, J. D., and Singh, U. K., 1974, "Time Marching Methods for Turbomachinery Flow Calculation," VKI Lecture Series, 1979-7.
- Denton, J. D., 1983, "An Improved Time-Marching Method for Turbomachinery Flow Calculation," ASME Journal of Engineering for Power, Vol. 105, pp. 514-524.

Denton, J. D., 1985a, "3D Flow Calculations on a Hypothetical Steam Turbine Last Stage," in: *Aerothermodynamics of Low Pressure Steam Turbines and Condensers*, M. J. Moore and C. H. Sieverding, eds., Hemisphere, Washington, DC.

Denton, J. D., 1985b, "Calculation of Fully Three Dimensional Flow Through Any Type of Turbomachine Blade Row," AGARD LS 140.

Denton, J. D., 1986, "The Use of a Distributed Body Force to Simulate Viscous Effects in 3D Flow Calculations," ASME Paper No. 86-GT-144.

Grant, J., and Borthwick, D., 1987, "Fully 3D Inviscid Flow Calculations for the Final Stage of a Large Low Pressure Steam Turbine," I. Mech. E. Paper No. C281/87.

Ni, R. H., 1989, "Prediction of 3D Multistage Turbine Flow Field Using a Multiple Grid Euler Solver," AIAA Paper No. 89-0203.

APPENDIX

Conversion of Polytropic Efficiency to a Body Force

For changes in state taking place with polytropic efficiency η_p , small changes in pressure and change in temperature are related by

$$\frac{dT}{T} = \left(\frac{\gamma-1}{\gamma} \right) \eta_p \frac{dP}{P} \text{ for a turbine}$$

and

$$\frac{dT}{T} = \left(\frac{\gamma-1}{\gamma} \right) \frac{1}{\eta_p} \frac{dP}{P} \text{ for a compressor}$$

From the second law

$$T dS = Cp dT - dP/\rho$$

which for a polytropic expansion gives

$$T dS = (\eta_p - 1) dP/\rho$$

where dP is negative, and for a polytropic compression gives

$$T dS = \left(\frac{1}{\eta_p} - 1 \right) dP/\rho$$

where dP is positive.

The entropy gradient along streamlines is related to the body force, F_m , per unit mass, acting along the streamline in a direction opposing the flow by

$$T dS/dz = F_m$$

where z is the distance along the streamline.

Hence

$$F_v = |dP/dz| (\eta_p - 1)$$

for a turbine and

$$F_v = |dP/dz| \left(\frac{1}{\eta_p} - 1 \right)$$

for a compressor, where $F_v (= F_m/\rho)$ is the body force per unit volume acting along the streamline in a direction opposing the flow. The force acting on a fluid element is simply obtained by multiplying F_v by the volume of the element.

The Use of 3D Viscous Flow Calculations in the Design and Analysis of Industrial Centrifugal Compressors

M. V. Casey¹

P. Dalbert

P. Roth

Thermal Turbomachinery Division,
Sulzer Escher Wyss Ltd.,
Zurich, Switzerland

The 3D viscous codes of Denton and Dawes have been used to predict the flow field and performance of a back-swept industrial centrifugal impeller without an inducer (the Eckardt impeller "B"). The calculated flow field and performance agree very well with measurements at several operating points from surge to choke. Both codes predict that the suction surface flow near the impeller inlet is on the verge of separation at the design point. Calculations with tip clearance using the Dawes code predict a thin region of backflow in the clearance jet near the casing wall. The secondary flows arising from the meridional curvature in the impeller redistribute the losses generated on the blades and give rise to a spanwise stratification of the circumferentially mass-averaged losses. The resulting spanwise entropy gradient can be included in a throughflow calculation to improve the prediction of the meridional velocity distribution at impeller exit.

Introduction

Centrifugal compressors for industrial and process gases need a very high peak efficiency and an extremely wide operating range in order to minimize the power consumption and to satisfy the variable demand of the process or plant of which they are part. In the continuing search for improved range and higher efficiency increasingly sophisticated aerodynamic computations are currently being applied in the design and analysis of the stage components.

The simplest practical technique for the aerodynamic analysis of radial impellers is the solution of the throughflow equations on a mean stream surface defined by the geometry of the blade camber surface, with modifications for the effects of incidence and slip. When combined with a linear approximation for the blade-to-blade calculation and empirical data for the losses and slip factor, such a technique can give quite accurate estimates of the flow field in most of the impeller; see, for example, Casey and Roth (1984). This approach allows the designer to examine parameters such as the leading edge incidence, the blade loading, and the suction surface diffusion, and to make appropriate design decisions. The method provides no information on the loss generation within the impeller and, therefore, does not eliminate the need to test prototypes in order to prove the design or to provide accurate performance data from surge to choke. The current generation of industrial stages has, nonetheless, been designed in this way and modern stages have generally attained efficiencies between two and six points higher than their predecessors; see Casey (1985).

¹Current address: Rolls-Royce plc., Derby DE28BJ, United Kingdom.

Contributed by the International Gas Turbine Institute and presented at the 35th International Gas Turbine and Aeroengine Congress and Exposition, Brussels, Belgium, June 11-14, 1990. Manuscript received by the International Gas Turbine Institute December 18, 1989. Paper No. 90-GT-2.

In the design of axial turbomachinery, it is now general practice to use a more complex flow analysis than this. Either blade-to-blade and throughflow calculations are iteratively coupled to determine the mean stream surface and the stream-tube height variation through the stage, or a fully 3D inviscid method is used. In the case of radial impellers neither of these approaches is considered to be worthwhile since they have few substantial advantages over the simple technique outlined above other than the elimination of the empirical slip factor. This is due to the fact that the velocity distributions and pressure gradients are largely determined by the curvature and the swirl of the flow and in a radial impeller these can be calculated quite accurately by the simple analysis. Radial impellers usually have blades of low span in flow channels with strong meridional curvature. This means that the effect of meridional streamline curvature is more or less fixed by the hub and shroud contours. The spacing between the blades is small compared to their length so that the mean relative flow angle within the impeller is quite accurately given by the blade camber angle, and the approximation of linear blade-to-blade velocity gradients is quite reasonable.

The important deviations between the simple model and the real flow in the impeller arise as a result of the neglect of viscous effects, tip leakage flows, and secondary flows, as shown by Eckardt (1976) and Johnson and Moore (1980). If further gains in component efficiencies are to be attained in the next generation of radial stages then improved computational models of the complex turbulent impeller flow field and the sources of loss are required.

During the last few years several computer codes for solving the 3D viscous flow equations for turbomachinery geometries have been published and applied in the development of aeroen-

gine turbomachinery components. This paper describes work carried out to test the applicability of two well-known codes, the Denton LOSS3D code (Denton, 1986, 1988) and the Dawes BTOB3D code (Dawes, 1988), to the design and analysis of industrial compressor impellers.

Objectives and Scope

The study was initiated to investigate the ability of the Dawes and Denton codes to predict the performance and the flow field of typical backswept industrial compressors. Considerable research material has already been published on the use of these and similar codes in the calculation of radial impellers with a relatively long axial length, an axial-flow inducer-type inlet and a low degree of backsweep (e.g., Moore et al., 1984; Krain and Hoffman, 1989). This paper describes experience gained with 3D viscous codes in the calculation of an impeller geometry typical of those found in multistage industrial compressors (and, to some extent, in pumps) with a relatively short axial length, with the blade inlet swept back into the bend from the axial to the radial direction and with a high degree of backsweep (40 deg).

The main emphasis of this work is an assessment of these codes from the user's point of view. The types of question considered are:

- Can these codes be used to predict the performance of a typical industrial impeller at the design point and can they predict the characteristic curves from surge to choke?
- Do the predicted flow fields agree with the measured flow fields at design and off-design conditions?
- Do the secondary flows in industrial-type impellers with swept-back inlets differ from more conventional impellers with axial inducer-type inlets?
- Can the knowledge gained from the 3D viscous calculations be used to improve standard throughflow design procedures and to improve impeller designs?

The measured flow field and performance of a typical industrial impeller at a number of operating points are presented and compared with the predictions of the codes. The results are used to suggest an empirical modification to the simple throughflow model that improves the predictions of the impeller outlet velocity profile of these simple methods.

Test Case: Eckardt "B" Impeller

Few test geometries are available where detailed measurements of the flow field of centrifugal impellers have been made. The most widely known cases are Eckardt's impellers "0" and

"A", which were measured in the mid-1970s in an industrial sponsored research program of the German research organization FVV (Forschungsvereinigung Verbrennungskraftmaschinen) at the DLR (Deutsche Luft- und Raumfahrt), formerly DFVLR (Deutsche Forschungs- und Versuchsanstalt fuer Luft- und Raumfahrt). The "0" and "A" impellers have already been used extensively for code validation. The Eckardt "B" impeller is less well known than the "0" and "A" impellers since details of the measurements have not been published in the literature and can only be found in the internal FVV and DFVLR reports produced by Eckardt et al. (1977a, 1977b, 1978). Some information on the performance and the geometry of the Eckardt "B" impeller has already been published in the work of Japikse (1987) where he compares the predictions of single-zone and two-zone modeling with performance data sets on the three impellers.

The performance measurements on all three impellers made by the DFVLR used laser two-focus velocimetry, pneumatic probes, and high response pressure transducers. The high quality and accuracy of the Eckardt measurement data on the "0" and "A" impellers are commented on by both Japikse (1987) and by Hah et al. (1988). The measurements on the "B" impeller were carried out by the same research team using the same instrumentation. Owing to time limitations toward the end of the research project this impeller was not studied in quite as much detail as the other two wheels.

The "B" impeller was designed in 1975 by Sulzer Brothers. It had a similar geometry to shrouded impellers used in multistage industrial compressors (Jenny, 1976). In order to carry out the laser two-focus and performance measurements in the same test rig as the "0" and "A" impellers, it was necessary to use an unshrouded impeller with the same casing wall geometry, the same blade number, and the same outlet width as the other two impellers. This compromised the impeller design to some extent, but the use of a different hub contour (see Fig. 1) and more backsweep than the other impellers enabled a wheel to be designed that was aerodynamically similar to typical medium flow coefficient wheels in use in multistage industrial compressors at the time.

The aerodynamic design calculations were carried out with a computer program following Traupel (1977). This is similar to a single-pass streamline curvature throughflow method in which the curvature of the meridional streamlines is determined directly from the hub and casing geometry and is not updated by subsequent iteration. The downstream calculating planes have no upstream influence and this means that the design method was inevitably limited in its ability to predict incidence and loading at the leading edge.

The blade camber line was selected to be a ruled surface in

Nomenclature

b = blade span	N = rotational speed (rpm)	T = total temperature
b_2 = impeller outlet width	p = static pressure	U = impeller blade speed
C_m = meridional velocity	p^* = total pressure	W = relative velocity
C_u = circumferential velocity	p_4^*/p_1^* = total pressure ratio at flange	y = pitchwise coordinate
D_2 = impeller diameter	p_{out}/p_1^* = static-to-total pressure ratio	Z = number of blades
d = blade thickness	$Ro = Wr/Ur_c$ = Rossby number	z = axial and spanwise coordinate
H = total enthalpy	r = radius	β_1, β_2 = blade inlet and outlet angles
I = pitchwise index	r_c = radius of curvature	
j = tip clearance	s = entropy	Subscripts
J = streamwise index	t = blade pitch	out = outlet of calculating grid
K = spanwise index	TE = trailing edge	1 = impeller inlet
LE = leading edge		2 = impeller outlet
m = mass flow rate		4 = outlet flange

Note: All blade angles are measured relative to the tangential direction

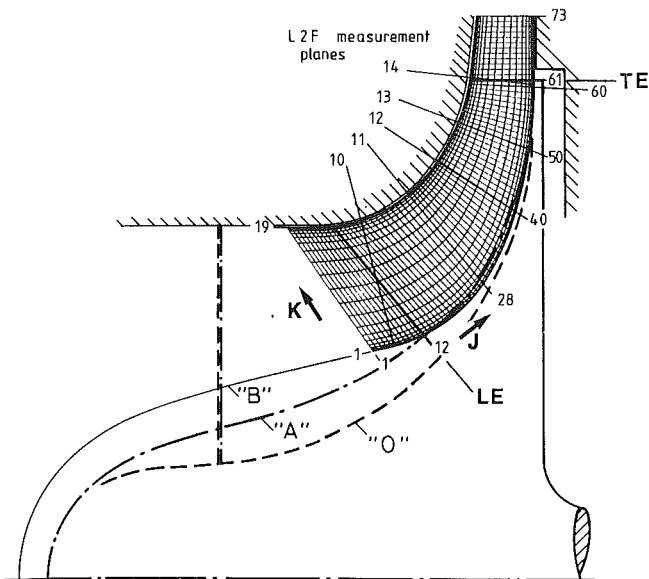


Fig. 1(a) Eckardt impeller "B" showing the computational grid in the meridional plane with streamwise index J and spanwise index K and a comparison with the impellers "O" and "A"

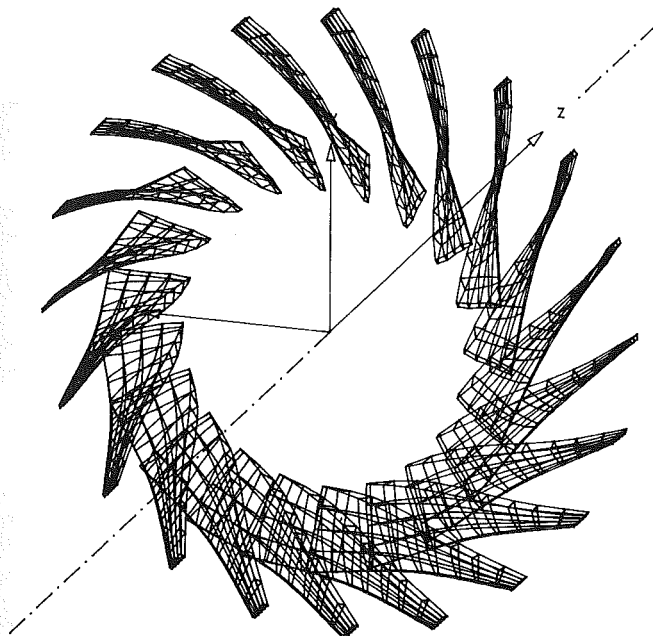


Fig. 1(b) Perspective view of blades of impeller "B" plotted with a reduced computational grid

which the straight-line generators of the surface were oriented such that they passed through the axis of the wheel or, in other words, the generating lines had no lean in the circumferential direction. This is fairly typical of industrial impellers with shrouds as it leads to reduced bending stresses in the blades. Although the blade generators are not leaning in the circumferential direction, they are leaning in the meridional plane to give rise to a strongly swept-back leading edge and, as a result, the blades have no radial-standing elements. The blades of an open impeller with this type of geometry tend to deflect outward as the rotational speed is increased. The impeller blade tip contour was modified during the measurements to allow for this deflection by machining a larger stationary tip clearance at the inlet than at the outlet.

Table 1 Geometry of the Eckardt "B" impeller

Impeller diameter	$D_2 = 400$ mm
Impeller outlet width	$b_2 = 26$ mm
Blade thickness	$d = 2$ mm (tip)-7 mm (hub)
Tip clearance	$j \approx 0.75$ mm (at 14,000 rpm)
Number of blades	$Z = 20$
Blade outlet angle	$\beta_2 = 50$ deg
Blade inlet angle	$\beta_1 = 30$ deg (tip)-45 deg (hub)

The main geometric details of the "B" impeller are given in Table 1.

The impeller was manufactured from steel by forging the blades and welding them onto the hub disk. This resulted in some small discrepancies between the blade thickness intended and that actually obtained from the workshop. The geometry used in the calculations presented here is based on the measured mean blade thickness of the impeller as manufactured.

The impeller "B" is shown in Figs. 1(a) and 1(b). The impeller is relatively short, the blades being roughly two-thirds as long as the "O" and "A" impellers in the meridional plane. The inlet to the impeller is swept back in the meridional plane from the casing to the hub and lies in the bend from the axial to the radial direction. There is no inducer in the axial part of the flow channel. This is typical of industrial impellers for use in multistage compressors where rotor dynamic considerations mean that a relatively thick shaft is required. The impeller outlet angle of 50 deg (a backsweep of 40 deg) is also typical of industrial impellers that need a wide operating range. The measured characteristic curve of the impeller with a vaneless diffuser is shown in Fig. 2(a), where it can be seen that the large degree of backsweep means that the peak efficiency of the stage occurs at a flow volume about 30 percent greater than that at the peak pressure rise. The inlet angle of the blades was selected to achieve a low incidence on the hub and shroud streamtubes, within the limitations of the design method. This, combined with the large backsweep, led to relatively straight blades, as shown in Fig. 1(b).

Brief Description of Codes Used

The two CFD codes used in this work were both developed at the Whittle Laboratory of Cambridge University, United Kingdom. Both codes can be used to solve the 3D viscous flow field through an arbitrary turbomachine blade row. They do, however, use different numerical schemes, boundary conditions, and turbulence models. Both codes use an H-grid in which the blade-to-blade grid lines lie purely in the circumferential direction, and both require exactly similar geometrical input data to generate the computational mesh. Both codes also use multigrid methods to speed convergence. Full details of the theory of the methods are given in the papers by the authors of the codes and only a very brief description is given below.

The Denton LOSS3D code is based on Denton's highly developed finite-volume time-marching Euler codes and simulates viscous effects by the introduction of a distributed body force (Denton, 1986). The magnitude and distribution of this force are determined by a simple turbulence model. The surface shear stress is calculated by assuming that grid points one element away from solid surfaces lie within the log-law region of the turbulent boundary layer and distribution of the shear stress is performed by a simple eddy viscosity model (Denton, 1988).

The Dawes BTOB3D code solves the time-dependent Reynolds-averaged Navier-Stokes equations in finite volume form with a mixed explicit/implicit method (Dawes, 1988). Turbulence modeling is via mixing-length closure and the widely used Baldwin-Lomax model. The Dawes code can also be used to calculate turbomachinery blading with tip clearance, al-

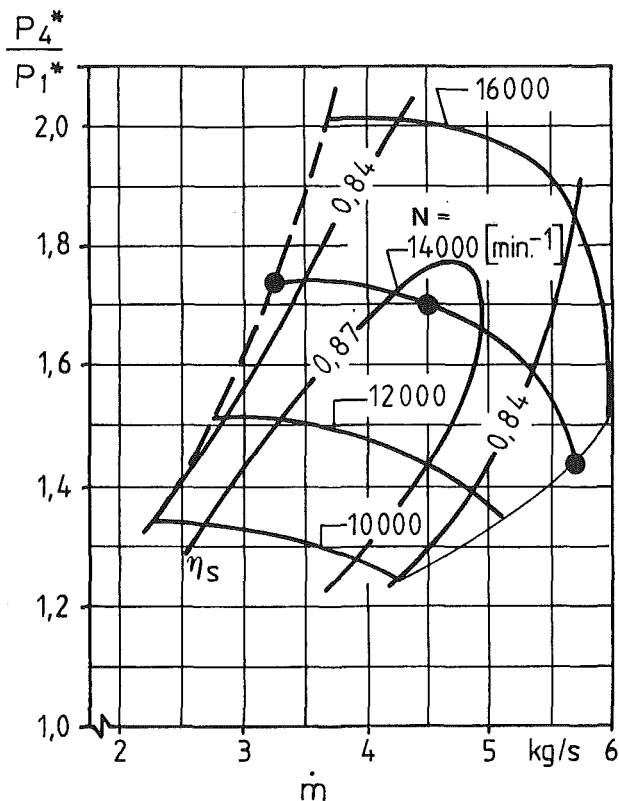


Fig. 2(a) Performance map of the Eckardt impeller "B" (see Eckardt et al., 1978)

though many of the calculations reported here were carried out without tip clearance in order to make a direct comparison with the Denton LOSS3D code possible.

The codes automatically apply appropriate boundary conditions on the solid walls and the periodicity condition upstream and downstream of the blade row. The Denton code assumes that the casing and hub walls within the blade region rotate with the blades, as in a shrouded impeller with a stationary inlet and a stationary diffuser. The Dawes code assumes that the casing wall is stationary, as in an unshrouded wheel, but that the whole of the hub rotates, including those parts that are upstream and downstream of the blade row. The spanwise distributions of total temperature, total pressure, and absolute flow angle were specified at the inflow boundary ($J = 1$); see Fig. 1(a). The static pressure on the hub side of the flow channel is specified at the outflow boundary ($r/r_2 = 1.1265$ and $J = 73$; see Fig. 1a). No details of the inlet boundary layer or inlet turbulence levels were specified as input to either code.

Computational Mesh and Calculation Times

The same $19 \times 73 \times 19$ computational mesh with 26,353 nodes was used for all of the calculations reported here. The grid was set up with advice from the authors of the codes, and used grid-stretching in the pitchwise and spanwise directions and some concentration of streamwise grid lines near the leading edge. The grid was selected so that the internal measurement planes (planes 11, 12, and 13) of the laser two-focus anemometer corresponded to spanwise grid lines ($J = 28, 40,$ and 50); see Fig. 1(a). Calculations with tip clearance using the Dawes code were carried out on the same grid, whereby the three spanwise grid lines near the casing ($K = 17, 18,$ and 19) were taken to be within the tip gap ($j/b_2 = 2.8$ percent).

Both codes were implemented on a Micro VAX 3600 computer. Acceptable convergence was generally attained after 1500 time steps, and this required approximately 23 hours cpu

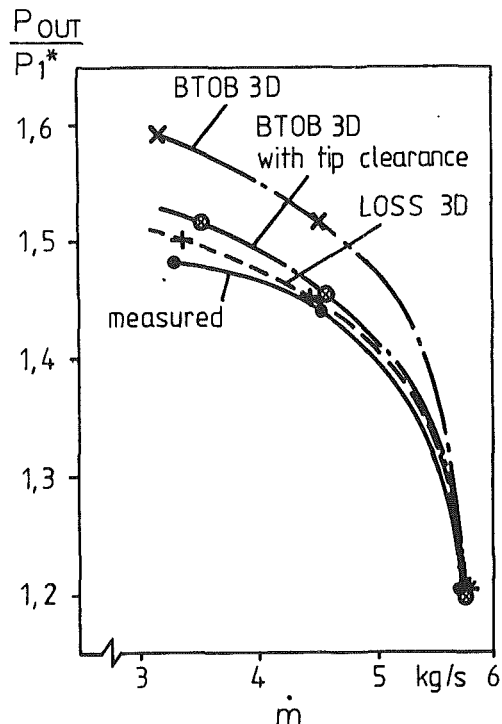


Fig. 2(b) Measured (Eckardt et al., 1977b) and calculated exit static pressure ratio as function of the mass flow at 14,000 rpm

time for the Dawes code and about 7 hours cpu time for the Denton code. The difference in cpu time required by the programs has meant that most experience has been gained with the Denton code.

As the main emphasis of this work has been to demonstrate the application of CFD codes in a design environment, the effects of grid size on the solutions have not been investigated. The grid used is the finest grid that is compatible with the need to achieve a converged solution with the Denton code overnight. Both Dawes and Denton have separately investigated and published results showing the effect of grid size on the predictions of their codes.

Prediction of Characteristic Curves

The characteristics curves were calculated by specifying a series of downstream static pressures on the hub-side diffuser wall. The exit static pressure initially chosen was taken from the measured value of the diffuser wall pressure corresponding to the measurement point (mass flow) being calculated. Although the measured static pressure was used the numerical computation did not converge on the measured mass flow because the calculated losses were less than those in the real stage. The exit static pressure was then adjusted (increased) until the correct mass flow was attained (to within 1.0 percent). Different exit static pressures were needed for each of the codes to achieve the required mass flow. This procedure is rather inconvenient given that both computer programs require a large amount of computational time, and represents a serious disadvantage of the codes for routine applications in the design of radial stages.

The operating points on the steep part of the characteristic toward the choking line of the impeller converged directly to the correct mass flow with the specified exit pressure from the measurements. The peak efficiency point required only two or three attempts with different exit pressures. Considerably more effort was needed to obtain results for a mass flow close to the surge point. With the Denton program the surge point could be calculated by using the mass-flow forcing capability of the program. This generates artificial losses in the impeller

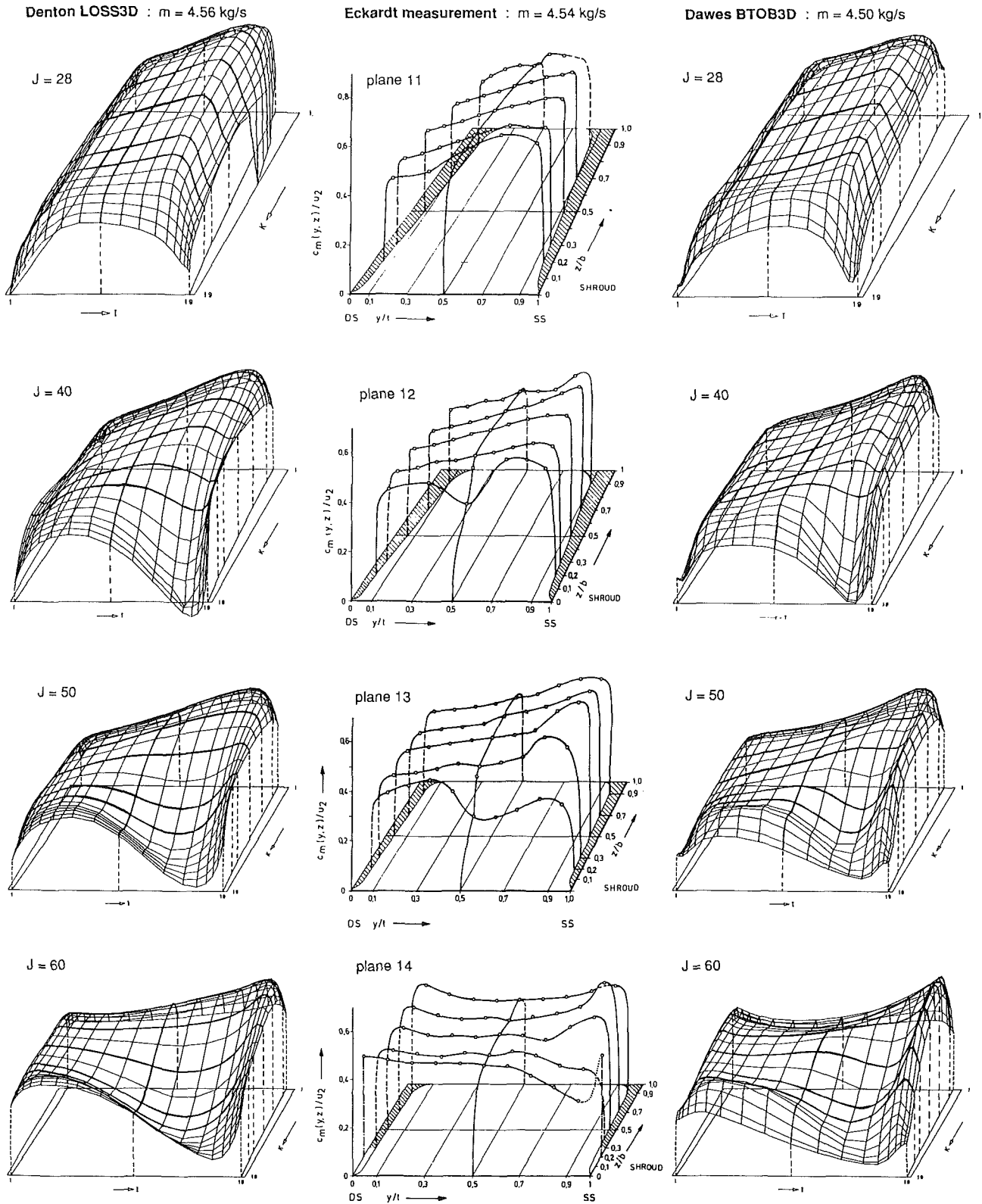


Fig. 3 Measured and calculated meridional velocity profiles at the four different measurement planes within the impeller at the design point (pitchwise index l and spanwise index K)

such that a specified mass flow can be obtained for a given exit pressure. Once a converged solution had been obtained at the correct mass flow and exit pressure, the mass-flow forcing was switched off, the smoothing factors increased slightly, and the run restarted with slightly increased exit pressure. With the Dawes program, the only way to approach the surge point was to step along the characteristic with very small increments of

exit static pressure. In both cases the calculation of operating points close to the surge point required a great deal of calculating time and a lot of patience.

The results are presented as characteristics of the static-to-total pressure ratio versus the mass flow rate (Fig. 2b). Both codes tend to overestimate the measured pressure rise of the impeller slightly. The BTOB3D calculations with no tip clear-

ance give, as can be expected, the lowest losses and highest pressure ratio. The agreement between the test data and calculations of both codes is extremely good considering the large difference in turbulence models of the two codes, the fact that the inlet boundary layer thickness and inlet turbulence levels are not specified, and the different boundary conditions imposed at the casing. In view of these differences it would be unwise to draw any conclusions as to the quality of the turbulence models used on the basis of these comparisons. Nevertheless, the good agreement between the methods would seem to indicate that in radial impeller performance predictions the exact nature of the turbulence model used may not be so important, provided that the most important effects such as boundary layer blockage and secondary flows are properly taken into account.

Prediction of Impeller Flow Field

Figure 3 presents a comparison between the predicted distribution of the meridional velocity component at the peak efficiency point and the measured distributions. The first column presents the results from the Denton LOSS3D code, the second contains the measured distributions, and the third shows the Dawes BTOB3D results without tip clearance. The rows from top to bottom give the development of the flow at the different laser two-focus measurement planes from inlet to outlet. The numerical codes are in remarkably good agreement with each other and also show good agreement with the measured trends. The use of different boundary conditions at the casing wall does not seem to cause any substantial differences in the predictions of the meridional flow field by the two methods.

The most interesting feature of the impeller flow field is the collapse of the meridional velocity in the shroud/suction-side corner of the flow channel quite early in the impeller. Unfortunately, no measurement data are available close enough to the shroud to establish the exact flow mechanism by which this occurs. Both codes clearly demonstrate that the flow is on the verge of separation on the blade suction surface in a region where the streamwise pressure gradient is high.

The Denton LOSS3D code predicts that flow separation occurs quite early in the stage. A small region of backflow can be seen near the hub on the suction surface at streamwise calculation plane 28, measurement plane 11. In this region the meridional velocity could not be measured as the flow was unsteady, as is indicated by the dotted line in the central diagram in the top row of Fig. 3. Both codes predict a large distortion in meridional velocity profile at the shroud that grows steadily through the impeller and is maintained to the outlet plane. The magnitude of the resulting wake at the impeller outlet is well predicted. The calculated position of the wake is slightly closer to the suction surface than its measured position, which can be attributed to the neglect of the tip clearance in these calculations.

Figure 4 provides a more detailed examination at three operating points of the meridional velocity distribution at measurement plane 11 just downstream of the leading edge close to where the separation begins. The laser measurements of the impeller at the surge point identified a region of high turbulence near the shroud, which was attributed to a flow separation and is denoted "Abloseblase" ("separation bubble"). Both codes predict a deterioration in the meridional velocity profile as the surge point is approached, and without tip clearance both codes predict a small backflow along the suction surface shroud corner of the blade at the surge point. Calculations with the Dawes BTOB3D code including tip clearance show extensive backflow across the whole pitch at the blade tip. The low-momentum fluid is closer to the pressure side of the flow channel when tip clearance is included in the calculations.

Some more details of the flow separation and secondary flows predicted by the codes are given in Figs. 5 and 6. Figure

5 shows the calculated meridional velocity vectors on three meridional planes located close to the suction surface, at midpitch, and close to the pressure surface, respectively. Figure 6 shows the relative velocity vectors in the near-casing blade-to-blade ($K = 18$). The results are presented for the LOSS3D code and the BTOB3D code with and without tip clearance at the peak efficiency point.

Figure 5 shows that there is little spanwise movement close to the blade surfaces at the inlet of the impeller. Farther downstream there are strong secondary flows in the spanwise direction toward the casing on both the suction and the pressure surfaces of the blades. At midpitch there is a slight trend for the main flow to move toward the hub to compensate for the shift in mass flow toward the shroud within the boundary layers on the blades. The secondary flows that arise from the meridional flow curvature in the Eckardt "B" impeller are rather stronger than those arising in the Eckardt "O" and "A" impellers as can be expected from the high curvature. The Rossby number for the "O" and "A" impellers is $Ro \approx 1$ and that for the "B" wheel is $Ro \approx 2$. The detailed motion of the secondary flows in the impeller corresponds to that expected from the simple model of Johnson (1978), and is similar to but stronger than that reported by Krain and Hoffman (1989), Moore et al. (1984) and others. Johnson and Moore (1980) noted that the axial-to-radial bend dominates the secondary flows in an impeller with an axial inducer. In this industrial radial impeller without an inducer, the principal flow curvature is also due to the axial-to-radial bend and gives rise to a very strong motion of the boundary layer fluid to the inside of the bend. The secondary flow pattern is remarkably similar to that expected for a viscous flow in a pipe bend.

Figures 5 and 6 show only small differences between the Denton and Dawes calculations without tip clearance. The Dawes calculation with tip clearance predicts a very different flow field in the tip region, with a thin layer of reverse flow near to the casing wall. Reverse flows similar to this have been reported by Chen et al. (1989) using a colored dye injection method. It can be seen that the momentum of the tip leakage jet shifts the fluid with low forward velocity (the wake) toward the pressure side of the flow channel.

Figure 7 shows a plot of the secondary flow velocities at midspan across the blade pitch at several meridional stations. The velocities have been taken from the results of the Dawes BTOB3D code without tip clearance at the design point and similar trends were found in the other calculations. For convenience, the secondary flow velocities have been taken to be the velocities normal to the pitchwise grid surface. The plot shows the clear trend of spanwise velocities toward the casing within the boundary layers on both the pressure and the suction surfaces and the compensating movement of the flow in the middle of the channel toward the hub. Figure 7 also shows that there is a variation in spanwise velocity across the pitch outside of the boundary layers close to the impeller inlet, which decreases toward the impeller outlet. This is caused by an axial component of vorticity, which in turn induces a twist in the blade-to-blade stream surfaces and is unrelated to secondary flow in the boundary layers. It arises because the inlet flow is irrotational in the absolute system and the relative flow then has an axial component of vorticity as a result of the impeller rotation.

Implications for Impeller Design

In view of the simplicity of the turbulence models used in each of the codes, the different boundary conditions on the shroud, and the neglect of the tip clearance in some of the calculations, the very good agreement with the measurements is remarkable. The codes provide considerably more information than the measurements with respect to spanwise flows. The laser measurements were unable to penetrate the blade

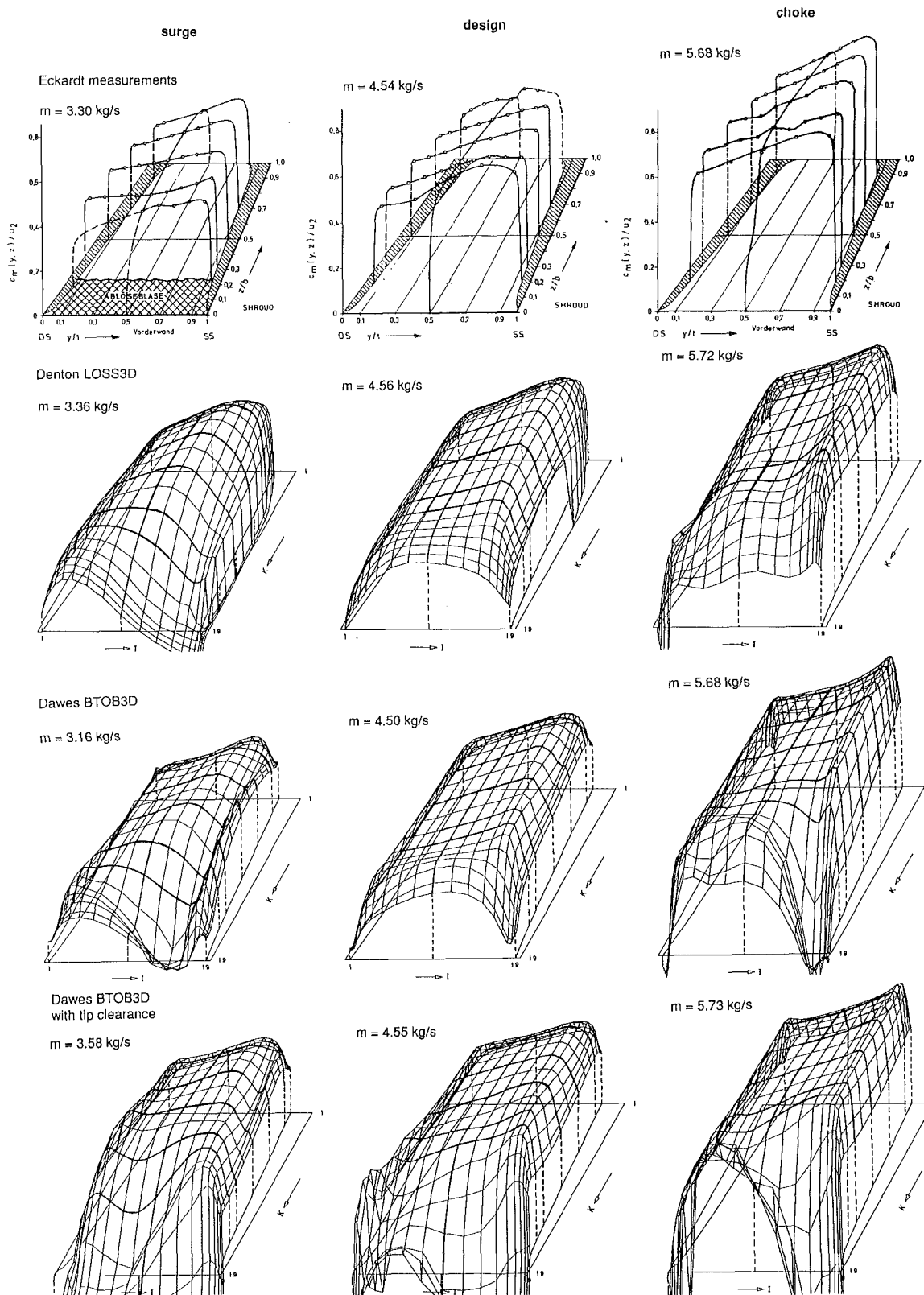


Fig. 4 Measured and calculated meridional velocity profiles near to the impeller inlet (measurement plane 11 and streamwise index $J = 28$) at three different operating points

surface boundary layers, and, in any case, were unable to provide any information on the velocity components in the planes of the laser measurement traverses.

Modern 3D viscous codes are clearly capable of providing the designer with enormous detail of the flow field in a radial impeller, including some data that are currently not very

straightforward to measure (spanwise flows, backflows, and separation), and there can be no doubt that they will become a standard tool for the impeller designer in the future. A large amount of time is, however, required not only for the calculations but also for the preprocessing and postprocessing of the large quantities of numerical data involved.

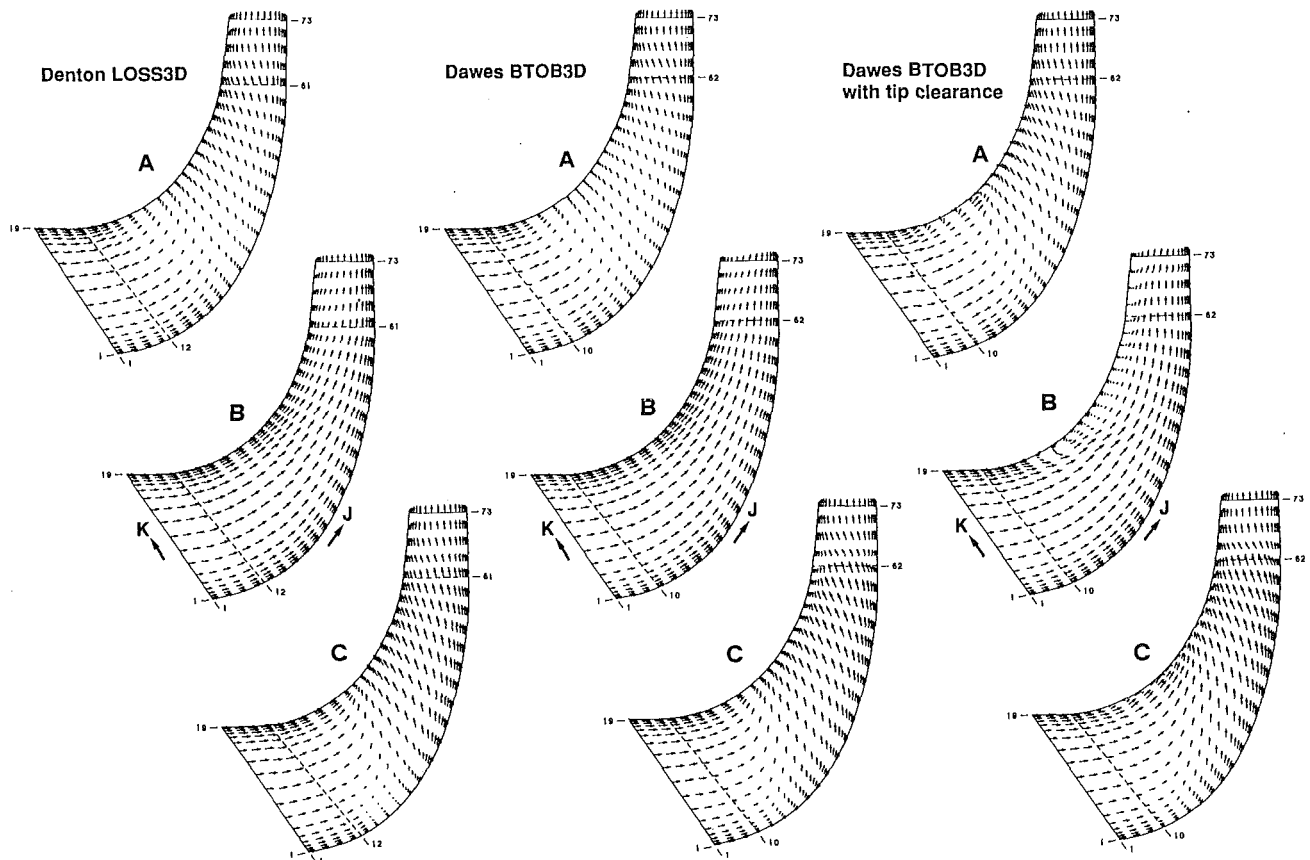


Fig. 5 Calculated meridional velocity vectors at the design points: A = near the blade pressure side ($l = 2$), B = at midpitch ($l = 10$), C = near the blade suction side ($l = 18$)

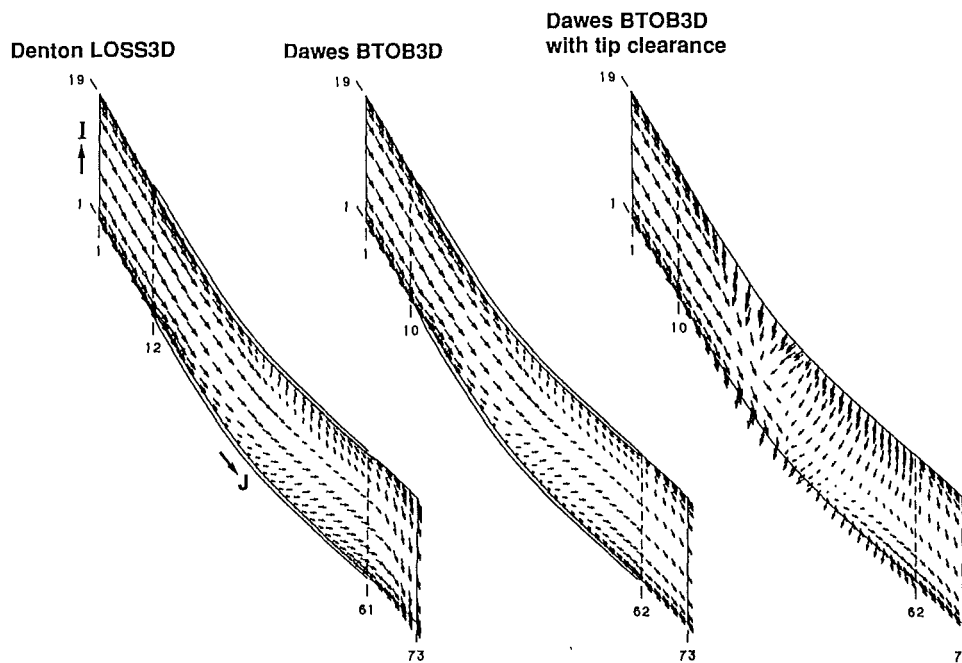


Fig. 6 Calculated relative velocity vectors at the design point near shroud ($K = 18$)

The preprocessing of the impeller geometry for calculations with 3D viscous codes can be a tedious and time-consuming problem, and is greatly simplified when a numerical method for the definition of the geometry of the impellers is available.

For design applications with the Denton and Dawes codes the geometry definition method of Casey (1983) has been adapted to prepare the coordinate data automatically for the input files, and without this level of automation it would not be possible

to use the codes in a practical design system. The similarity of the grids used by both codes has allowed the development of a single postprocessor to analyze the results and to produce the necessary graphic output with plots of Mach number contours, velocity vectors, flow angles, mass-averaged mean values, and temperature-entropy diagrams of the impeller compression path, etc.

Typically it is just possible with the help of the pre- and post processors to use these 3D viscous codes to compute and analyze the results of a single geometric configuration at a single operating point in a working day. Two-dimensional meridional throughflow calculations allow many more geometries and operating points to be analyzed in the same time span and for this reason will continue to retain their importance in the design of radial wheels, even when the speed and size of computers increase. In the future, a throughflow method will probably still be used to filter out poor designs on the basis of incidence, blade loading distribution, and suction surface diffusion, prior to the use of a fully 3D viscous calculation for performance estimates. It is therefore of interest to consider the implications of the results of the 3D viscous calculations for the improvement of conventional throughflow calculation methods for radial wheels.

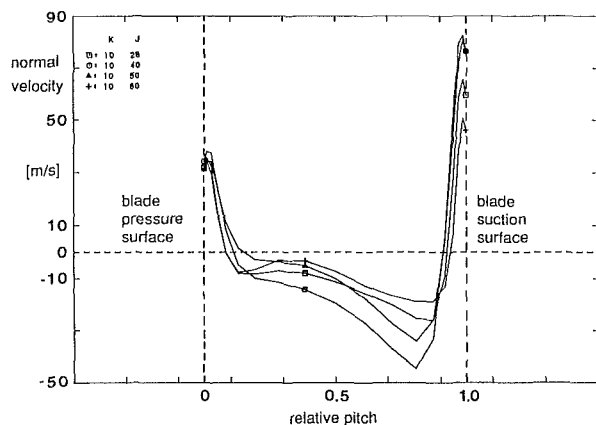


Fig. 7 Pitchwise variation of velocity normal to the blade-to-blade plane at midspan ($K = 10$): Dawes BTOB3D calculation with $m = 4.50$ kg/s

Improvement of Throughflow Models

The two main limitations of simple throughflow methods are that they are: (a) unable to provide any information about the loss generation and flow separation within the stage, and (b) unable to account for the nonaxisymmetric nature of the secondary flows. The results of the 3D calculations presented here have been used to modify the throughflow method of Casey and Roth (1984) to take better account of the effect of the secondary flows on the distribution of losses in the wheel.

The spanwise velocity gradient at the impeller outlet in a throughflow calculation is calculated from a velocity gradient equation of the form (Casey and Roth, 1984):

$$C_m \{ dC_m/db \} = dH/db - T \{ ds/db \} - (1/2r^2) \{ d(r^2 C_u^2)/db \} + C_m^2/r_c$$

In a typical throughflow calculation of a radial impeller, the first three terms of the right-hand side of the equation are zero at the impeller outlet; the stagnation enthalpy (H), entropy (s) and swirl (rC_u) in the flow are calculated on the mean streamline from the specified empirical losses and slip factor and are then taken to be constant across the span so that gradients with respect to the spanwise direction (b) are zero. The last term, the meridional streamline curvature term, thus determines the gradient of meridional velocity across the impeller outlet. The highest meridional velocity at impeller outlet is predicted to be close to the casing, although flow measurements and 3D viscous flow calculations invariably show that the highest circumferentially averaged meridional velocity occurs close to the hub.

The calculations carried out with the 3D viscous codes show that for this impeller the main contribution to the meridional velocity gradient at the impeller outlet is made by the loss gradient term (second term) in this equation. The enthalpy gradient and swirl gradient terms (first and third terms) of the velocity gradient equation may, as a first approximation, be neglected in comparison with the entropy gradient term. The mass-averaged loss distribution at the peak efficiency point predicted by the codes is shown in Fig. 8. The losses are fairly uniformly generated across the span and are redistributed by the high secondary flow velocities shown in Fig. 7.

This leads to a strong spanwise stratification in the circumferentially mass-averaged losses at the impeller outlet. The different boundary conditions at the casing, the neglect of tip

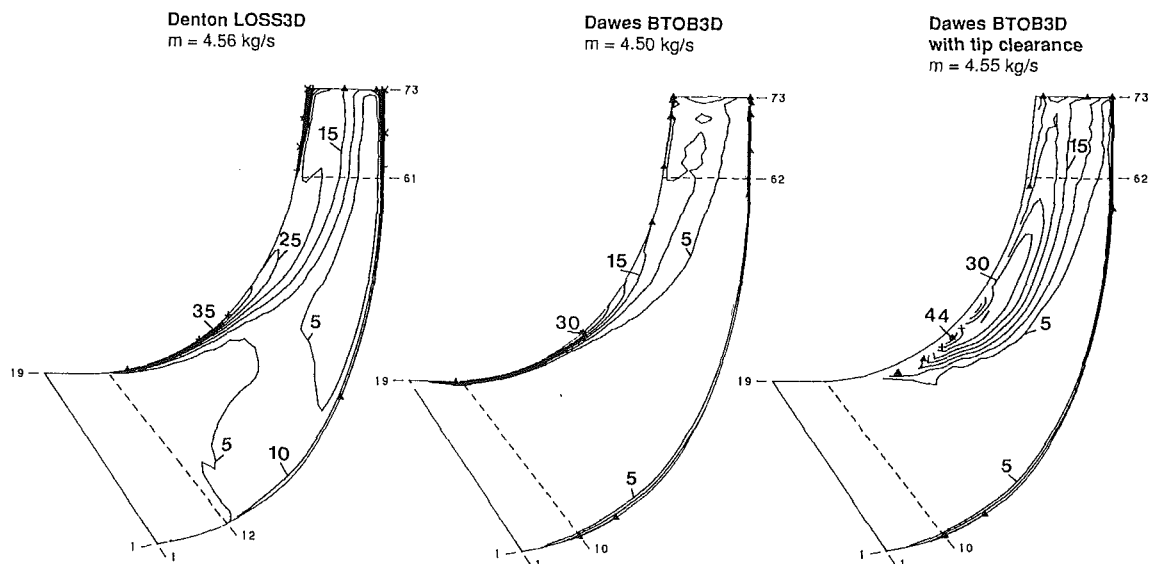


Fig. 8 Circumferentially mass-averaged distributions of entropy (J/kgK) at the peak efficiency point (spacing 5 J/kgK)

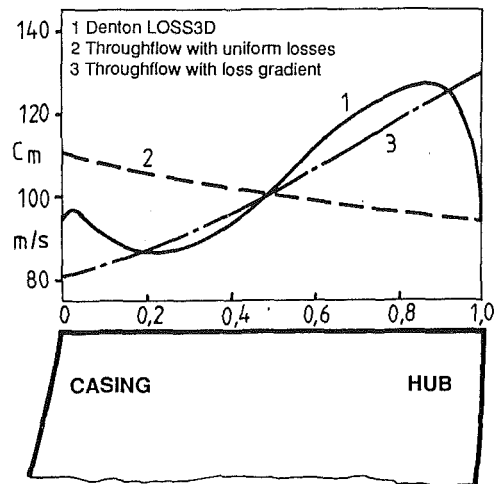


Fig. 9 Circumferentially mass-averaged meridional velocity at impeller exit at the peak efficiency point

clearance in some of the calculations, and the different losses predicted by the codes give somewhat different loss distributions within the impeller. All three calculations predict a strong loss gradient at impeller outlet from the casing to the hub.

An obvious method of including this loss stratification in a simple throughflow code is to distribute the losses across the impeller span in such a way that higher losses occur in the shroud stream-tube. Such a distribution of losses automatically leads to a reduced meridional flow on the shroud, and in view of the high empiricism needed to specify the losses, slip factor, and blockage, it is not considered worthwhile to take the blockage effect of the boundary layers into account separately. An approach similar to this was proposed by Jansen (1970). However, at that time it was believed that an entropy gradient at the impeller outlet was probably caused by the high losses from the leakage flows through the tip clearance gap and the high velocities and large wetted surface on the stream-tube adjacent to the shroud.

Figure 9 shows a prediction of the meridional flow field at the outlet of the Eckardt "B" impeller calculated with the throughflow method of Casey and Roth (1984) with and without the modifications suggested above. The simple expedient of a distributed loss across the span leads to results for the meridional velocity distribution that are in much closer agreement with the 3D flow calculations. The stratification of the losses at impeller outlet were specified on the basis of the results in Fig. 8, and it is hoped that experience with other impellers will lead to a more general method to determine this in the future.

It is interesting to note that in recent work on the improvement of throughflow methods for multistage axial compressor flows, the main trend is toward an inclusion of the effect of spanwise mixing on the distributions of losses and momentum. The mixing is postulated as being caused either by secondary flows (Adkins and Smith, 1981) or by turbulent diffusion processes (Gallimore, 1986), and in both theories any effect of the meridional streamline curvature on the spanwise flow is considered to be negligible. In a radial impeller with high meridional curvature the secondary flows do not give rise to a mixing of the losses across the span, but rather act in such a way that the losses become stratified. The calculations with the 3D viscous codes presented here show that it is necessary to include spanwise stratification of the losses, and not spanwise mixing, in order to improve the prediction of throughflow methods for radial wheels.

Conclusions

The main conclusions of this paper are:

- The Denton LOSS3D code and the Dawes BTOB3D code both provide good agreement with measured flow fields of the Eckardt "B" impeller over a wide range of operating points from near surge to choke. Despite the large differences in the numerical methods, the casing boundary conditions, and the turbulence models used, both codes predict similar flow fields. The Denton code requires less than a third of the computational time than the Dawes code.
- Both codes identified a region on the verge of separation in the impeller inlet on the suction surface. The flow separation was strongest and in best agreement with the measurements in the flow calculations with the Dawes BTOB3D code taking into account the tip clearance.
- The codes tend to underestimate slightly the loss generation in the impeller, and good predictions of efficiency are not yet possible.
- The calculation of operating points near the surge is hindered by the flat pressure rise versus mass flow characteristic of the impeller. Mass flow rates near surge can only be calculated if the calculations are repeatedly restarted from a converged solution with steadily increasing pressure ratio. This approach is extremely time consuming.
- The codes provide considerable insight into the development of the strong secondary flows in the impeller, which lead to a wakelike distortion in the meridional velocities at impeller outlet at the suction-side shroud corner. Calculations with tip clearance show that the wake moves toward the center of the shroud under the influence of the clearance jet.
- The secondary flow pattern in this industrial impeller is mainly influenced by the pressure gradient across the span caused by the very high meridional curvature. The secondary flows are much stronger than those in the Eckardt "0" and "A" impellers with an axial inducer.
- The secondary flows along the blade surfaces cause the high loss regions of the flow in the blade boundary layers to migrate toward the casing. The losses are generated fairly uniformly across the span and redistributed by the secondary flows. This leads to a spanwise stratification in the circumferentially mass-averaged losses.
- The outlet velocity profile predicted by simple throughflow calculations can be improved if this spanwise stratification of the losses is taken into account.

Acknowledgments

The authors are indebted to Dr. J. D. Denton and Dr. W. N. Dawes of the Whittle laboratory at Cambridge University, England, for their advice and help in the implementation and use of the codes described in this work. Thanks are also due to Dr. D. Eckardt for the measurements on this impeller, to Dr. E. Rikli for his insight and organizing talent in arranging a suitable computer for these calculations, and to Prof. J. Moore, Dr. J. D. Denton, and Dr. Y. N. Chen for their very useful discussion of the results.

The authors also wish to thank the Thermal Turbomachinery Division of Sulzer Escher Wyss Ltd. for permission to publish this paper.

References

- Adkins, G. G., and Smith, L. H., 1988, "Spanwise Mixing in Axial-Flow Turbomachines," *ASME Journal of Engineering for Power*, Vol. 103, pp. 97-110.
- Casey, M. V., 1983, "A Computational Geometry for the Blades and Internal Flow Channels of Centrifugal Compressors," *ASME Journal of Engineering for Power*, Vol. 105, pp. 288-295.
- Casey, M. V., and Roth, P., 1984, "A Streamline Curvature Throughflow Method for Radial Turbocompressors," in: *Computational Methods in Turbomachinery*, IMechE Publication 1984-3, London, Paper No. C57/84.

- Casey, M. V., 1985, "The Aerodynamic Development of High-Performance Radial Compressor Stages for Industrial Turbocompressors," *Thermische Strömungsmaschinen '85*, VDI Bericht No. 572.1, pp. 167-181.
- Chen, Y. N., Haupt, U., and Rautenberg, M., 1989, "The Vortex-Filament Nature of Reverse Flow on the Verge of Rotating Stall," *ASME JOURNAL OF TURBOMACHINERY*, Vol. 111, pp. 450-461.
- Dawes, W. N., 1988, "Development of a 3D Navier-Stokes Solver for Application to all Types of Turbomachinery," ASME Paper No. 88-GT-70.
- Denton, J. D., 1986, "The Use of a Distributed Body Force to Simulate Viscous Effects in 3D Flow Calculations," ASME Paper No. 86-GT-144.
- Denton, J. D., 1988, Private Communication.
- Eckardt, D., 1976, "Detailed Flow Investigations Within a High-Speed Centrifugal Compressor Impeller," *ASME Journal of Fluids Engineering*, Vol. 98, pp. 390-402.
- Eckardt, D., Trueltzsch, K. J., and Weimann, W., 1977a, "Untersuchung der Laufradstroemung in hochbelasteten Radialverdichterstufen Rad B, $\beta = 50^\circ$," FVV Radialverdichter Vorhaben No. 182, Heft 243, FVV Frankfurt.
- Eckardt, D., Trueltzsch, K. J., and Weimann, W., 1977b, "Vergleichende Stroemungsuntersuchungen an drei Radialverdichter- Laufraedern mit konventionellen Messverfahren," FVV Radialverdichter Vorhaben No. 182, Heft 237, FVV Frankfurt.
- Eckardt, D., Trueltzsch, K. J., and Weimann, W., 1978, "L2F-Messungen der Laufradstroemung und instationaere Druckverlaeufoe des Radialverdichter-Laufrades $\beta = 50^\circ$," Bericht I 352-78/2, DFVLR Cologne.
- Gallimore, S. J., 1986, "Spanwise Mixing in Multistage Axial Flow Compressors: Part 2—Throughflow Calculations Including Mixing," *ASME JOURNAL OF TURBOMACHINERY*, Vol. 108, pp. 10-16.
- Jenny, R., 1976, "Auslegung des Laufrades B mit rueckwaerts gekruemmten Schaufeln fuer das FVV-Forschungsvorhaben Radialverdichter," Sulzer Thermal Turbomachinery Department, Internal Study TK 76/03.
- Jansen, W., 1970, "A Method for Calculating the Flow in a Centrifugal Impeller When Entropy Gradients are Present," Paper 12, *Internal Aerodynamics (Turbomachinery)*, IMechE, London, pp. 133-146.
- Japikse, D., 1987, "A Critical Evaluation of Three Centrifugal Compressors With Pedigree Data Sets: Part 5—Studies in Component Performance," *ASME JOURNAL OF TURBOMACHINERY*, Vol. 109, pp. 1-9.
- Johnson, M. W., 1978, "Secondary Flow in Rotating Bends," *ASME Journal of Engineering for Power*, Vol. 100, pp. 553-560.
- Johnson, M. W., and Moore, J., 1980, "The Development of Wake Flow in a Centrifugal Impeller," *ASME Journal of Engineering for Power*, Vol. 102, pp. 382-390.
- Krain, H., and Hoffman, W., 1989, "Verification of an Impeller Design by Laser Measurements and 3D-Viscous Flow Calculations," ASME Paper No. 89-GT-159.
- Moore, J., Moore, J. G., and Timmis, P. H., 1984, "Performance Evaluation of Centrifugal Compressor Impellers Using Three-Dimensional Viscous Flow Calculations," *ASME Journal of Engineering for Gas Turbines and Power*, Vol. 106, pp. 475-481.
- Traupel, W., 1977, *Thermische Turbomaschinen*, Vol. 1, 3rd ed., Springer-Verlag, Berlin, pp. 365-374.

Three-Dimensional Rotational Flow in Transonic Turbomachines: Part I—Solution Obtained Using a Number of S_1 Stream Filaments of Revolution and a Central S_2 Stream Filament

Wu Chung-Hua

Wang Zhengming

Chen Hongji

Chinese Academy of Sciences,
Beijing, People's Republic of China

The general theory of three-dimensional flow in subsonic and supersonic turbomachines (Wu, 1952a) is extended to the three-dimensional rotational flow in transonic turbomachines. In Part I of this paper, an approximation that the S_1 stream filaments are filaments of revolution is made. Then, the three-dimensional solution is obtained by an iterative solution between a number of S_1 stream filaments and a single S_2 stream filament. A recently developed relatively simple and quick method of solving the transonic S_1 flow is utilized. The complete procedure is illustrated with the solution of the three-dimensional flow in the DFVLR rotor operating at the design point. The solution is presented in detail, special emphasis being placed on the fulfillment of the convergence requirement. The character of the three-dimensional field obtained is examined with the three-dimensional structure of the passage shock, the relative Mach number contours on a number of S_1 surfaces, S_2 surfaces, and cross surfaces, and the variations of the thickness of S_1 and S_2 filaments. Comparison between the calculated three-dimensional field with the DFVLR measured data shows that the character of the flow field and the streamwise variation of the flow variables in the middle of the flow channel are in good agreement. It is recommended that the method presented herein can be used for three-dimensional design of transonic turbomachines.

Introduction

A general theory of steady three-dimensional flow of a non-viscous gas in subsonic and supersonic turbomachines having arbitrary hub and casing shapes and a finite number of blades was presented by Wu in 1952. The solution of the direct and inverse problem is obtained by investigating an appropriate combination of flows on relative streamsurfaces whose intersections with a Z plane either inside or outside the blade row form a circular arc or a radial line. Thus, the solution of the three-dimensional flow is greatly simplified mathematically into a number of solutions of two-dimensional flow. Based on this theory quasi three-dimensional solutions in subsonic compressors and turbines have been reported by a number of authors, for example, Bosman and El-Sharawi (1977), Biniaris (1975), Goulas (1980), Prince et al. (1984), and Jennions and Stowe (1985); full three-dimensional solutions in subsonic centrifugal and axial-flow compressors by Krimerman and Adler

(1978); and quasi-three-dimensional solution for transonic compressors by McDonald et al. (1980), Sarathy (1982), and Broichhausen and Gallus (1982).

At the Institute of Engineering Thermophysics, Chinese Academy of Sciences, this general theory has been refined (Wu, 1965) and applied to solving a number of typical design and analysis problems. Computing codes based on body-fitting general curvilinear coordinates (Wu, 1976) have been programmed for subsonic flow on S_1 and S_2 surface, and a computing system has also been constructed to carry out the iterative three-dimensional solution (Wu, 1985). Recently, efforts have been made at IET¹ to extend this theory to transonic turbomachines. First, relatively simple and quick methods of solving the transonic flow on S_1 and S_2 surfaces were developed. Then, the computing codes were put together to carry out the iterative three-dimensional solution. In Part I of the paper, development for the case in which the S_1 surfaces are assumed to be surfaces of revolution is presented. Part II of the paper presents the development for the general case, in which no such assumption is made.

¹Contributed by the International Gas Turbine Institute and presented at the 35th International Gas Turbine and Aeroengine Congress and Exposition, Brussels, Belgium, June 11-14, 1990. Manuscript received by the International Gas Turbine Institute January 8, 1990. Paper No. 90-GT-12.

Basic Considerations

Basic Aerothermodynamic Relations. The basic aero-thermodynamic equations for the relative flow of a real gas passing through a turbomachine blade row rotating at a constant angular speed were given by Wu (1952a, 1965) in an invariant vector form as follows:

Conservation of mass

$$\frac{\partial \rho}{\partial t} + \nabla \cdot (\rho \mathbf{W}) = 0 \quad (1)$$

Second law of motion.

$$\frac{\partial \mathbf{W}}{\partial t} - \mathbf{W} \times [\nabla \times \mathbf{V}] = -\nabla I + T \nabla S + \frac{1}{\rho} \nabla \cdot \Pi' \quad (2)$$

First law of thermodynamics:

$$\frac{dI}{dt} = \frac{1}{\rho} \frac{\partial p}{\partial t} + \left[\dot{q} + \frac{1}{\rho} \nabla \cdot (\Pi' \cdot \mathbf{W}) \right] \quad (3)$$

Second law of thermodynamics:

$$T \frac{ds}{dt} > \dot{q} \quad (4)$$

In this formulation, the entropy s and the new thermodynamic property I are considered as the two independent thermodynamic properties. I was found in early turbomachine flow calculation and analysis by Wu (1951, 1952b) to play the same role in the flow relative to a rotating blade row as the stagnation enthalpy in the flow relative to a stationary blade row. It is defined by the following equations:

$$i = h - \frac{U^2}{2} \quad (5)$$

$$I = i + \frac{\mathbf{W}^2}{2} \quad (6)$$

It is appropriate to call i and I , respectively, rothalpy and stagnation rothalpy (Wu, 1953b). This choice simplifies calculation greatly. In steady adiabatic inviscid calculations, I is an invariant along a streamline, and is uniform over the whole flow field when it is uniform at the inlet. In adiabatic inviscid flow, the entropy s is also an invariant along a streamline, but in transonic flow, it has a steep increase across a shock.

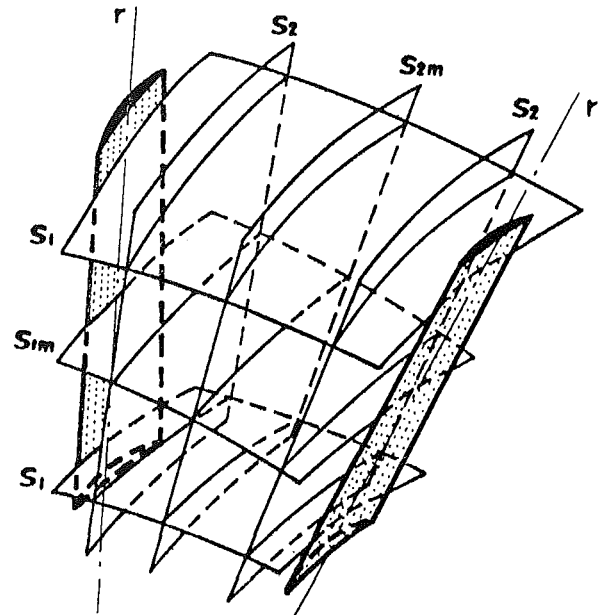


Fig. 1 Relative stream surfaces S_1 and S_2

Steady Flow on S_1 and S_2 Families of Relative Streamsurfaces. An approach was suggested by Wu (1952a) to investigate the three-dimensional rotational flow in a turbomachine by iterative calculation of the flows on two families of relative streamsurfaces S_1 and S_2 (Fig. 1).

In the S_1 family, the streamsurfaces at the casing and hub are usually considered to follow the shape of the bounding wall, which is surface of revolution. Recent theoretical consideration (Cai, 1983) shows that if, during the design process, the derivative of $(V_{\theta r})$ normal to the wall is chosen to be equal to the product of radius and meridional component of the absolute vorticity, i.e.,

$$\frac{\partial(V_{\theta r})}{\partial n} = r(\nabla \times \mathbf{V})_t \quad (7)$$

the flow surface is a surface of revolution.

The deviations of S_1 streamsurfaces from the surface of

Nomenclature

e_i = base vector of x^i coordinate system
 e^i = reciprocal base vector of x^i coordinate system
 g = Jacobian of matrix g_{ij}
 g_{ij} = covariant metric tensor of x^i coordinate system
 g^{ij} = contravariant metric tensor of x^i coordinate system
 H = absolute stagnation enthalpy per unit mass = $h + v^2/2$
 h = enthalpy per unit mass of fluid
 i = rothalpy per unit mass = $h - u^2/2$
 I = relative stagnation rothalpy per unit mass of gas = $i + W^2/2$
 l, ϕ = orthogonal coordinates on surface of revolution

\mathbf{n} = unit vector normal to the stream surface
 \dot{q} = heat transfer to unit mass of gas per unit time
 r, ϕ, z = cylindrical coordinates
 R = gas constant
 s = entropy per unit mass of gas
 T = absolute temperature of gas
 t = time
 \mathbf{U} = blade velocity at radius r
 \mathbf{V} = absolute velocity of gas
 $V_{\theta r}$ = angular momentum of gas about axis of rotation
 \mathbf{W} = relative velocity of gas
 w^i = contravariant component of relative velocity of gas
 w_i = covariant component of relative velocity of gas
 W^i = physical component of \mathbf{W} tangent to x^i

x^i = nonorthogonal curvilinear coordinates
 α = relaxation factor
 β = angle between \mathbf{W} and its meridional component
 θ_{ij} = angle included by the coordinate lines x^i and x^j
 ν = coefficient of artificial viscosity
 Π' = viscous force tensor
 $\bar{\rho}$ = artificial density
 $\sigma = \tan^{-1}(dr/dz)$
 τ = normal, circumferential, or radial thickness of stream filament
 ψ = stream function
 Ω = axial-velocity density ratio
 ω = angular speed of blade
 $\frac{\partial}{\partial x^i}$ = derivative of a flow variable on the stream surface with respect to the coordinate x^i

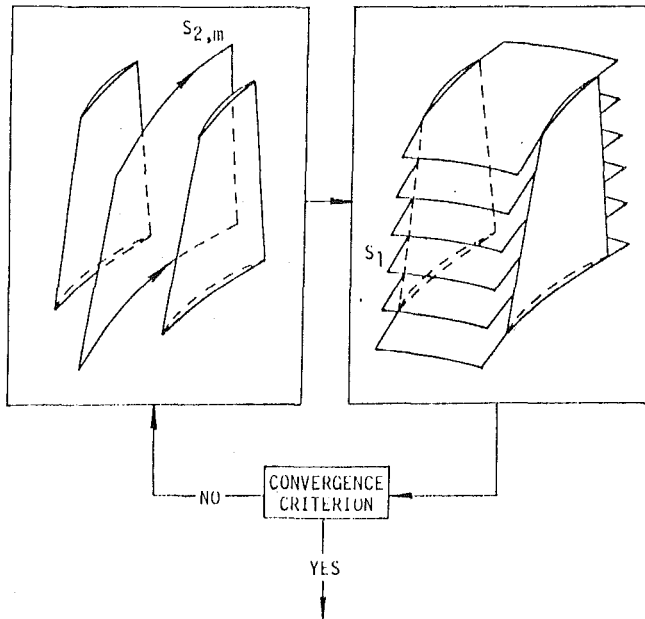


Fig. 2 S_1 - $S_{2,m}$ iteration

revolution obtained in the three-dimensional flow calculations, for, respectively, subsonic axial-flow compressor and turbine (Wang et al., 1983; Zhao et al., 1985), as indicated by the local value of $\Delta r/r$, is less than, respectively, 1 and 3 percent. It may be expected that, at least for the axial-flow type of turbomachine, the deviation of S_1 streamsurface from surface of revolution is small even for transonic flow, and the assumption that all S_1 surfaces are surfaces of revolution may yield results of acceptable accuracy.

Approximate Three-Dimensional Calculations. The approximation that the S_1 stream surfaces are surfaces of revolution greatly simplifies the three-dimensional calculation. The three-dimensional flow field can then be obtained by solving the flow along a number of S_1 stream surfaces, which are formed by revolving a number of streamlines obtained on an S_2 surface located in the middle of the blade passage. The shape of this S_2 surface only approximately resembles the blade camber surface or the midchannel surface, and has to be determined through the iterative solution between this single S_2 surface and a number of S_1 surfaces (Fig. 2). This iterative solution of three-dimensional flow may be called the simplified three-dimensional solution, approximate three-dimensional solution, or quasi-three-dimensional solution.

In this formulation of the three-dimensional solution, the role played by the S_2 surface in the iterative solution is not self-apparent and also the difference between this quasi-three-dimensional solution and other quasi-three-dimensional solutions obtained by other authors, in which either an axially symmetric meridional flow or a circumferentially averaged hub-to-tip flow is employed instead of the $S_{2,m}$ flow. This problem can be cleared up by the following consideration (see Fig. 3).

The complete three-dimensional flow passage formed by two adjacent blades is divided into, say, $(m - 1)/2$ S_1 stream filaments formed by $[(m - 1)/2 + 1]$ S_1 streamsurfaces. For instance, the solution of the flow on a thin S_1 stream surface number 2, with the variation of the normal distance between surfaces number 1 and number 3 taken into account, is equivalent to the solution of the flow along the thin stream filament, which is bounded by the surfaces numbered 1 and 3, when the distance between surfaces 1 and 3 is sufficiently small. Thus, the summation of the solutions of the flows on all S_1 surfaces 2, 4, 6, ..., $(m - 1)$ is equivalent to the solution of the flow

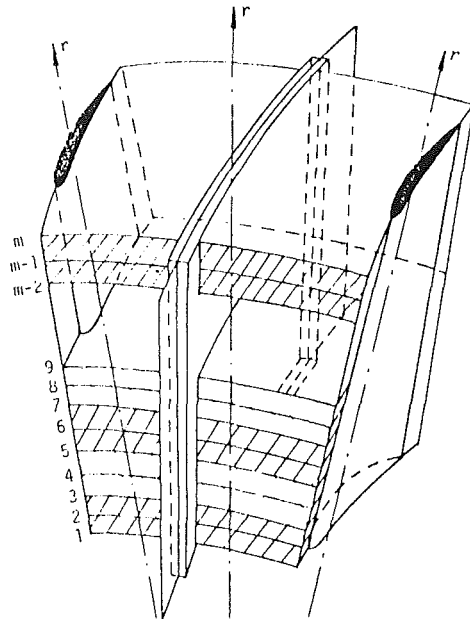


Fig. 3 $(m - 1)/2$ stream filaments formed by $(m - 1)/2 + 1$ stream surfaces

along all the filaments extending over the whole flow passage. The solution of $S_{2,m}$ flow is for providing the radii of the surfaces of revolution and the normal distance between them, τ . As long as the variable $\tau = f(x^i)$ is taken into account in the solution of the S_1 surface flow, different methods of quasi-three-dimensional solution are different only in the difference in the geometry of the S_1 stream filaments (or S_1 stream surfaces) determined by an $S_{2,m}$ solution, an axisymmetric meridional solution, or a circumferentially averaged solution. The advantage of using the $S_{2,m}$ solution is that, being the solution of the flow along a physically existing $S_{2,m}$ surface, it represents the throughflow in the flow passage, and that the quasi-three-dimensional solution obtained in this way can be readily extended to a full three-dimensional solution, for which the same computing code programmed for calculating the $S_{2,m}$ flow can be used for calculating several other S_2 flows.

Governing Equations. When the fluid motion on an S_1 or S_2 streamsurface is followed, i.e., the variables considered are those on the stream surface, the continuity equation is (Wu and Brown, 1951a; Wu, 1952b)

$$\nabla \cdot (\tau \rho \mathbf{W}) = 0 \quad (1a)$$

Physically, τ is the normal thickness of the thin S_1 or S_2 stream filament, the central surface of which is the S_1 or S_2 surface under consideration. In the calculation of S_1 or S_2 flow, only the variation of the dimensionless value of the filament thickness (say, relative to its inlet value) is involved, so, theoretically, the filament can be as thin as desired.

In cascade tests, when there is no separation of flow from the blade surface, measurement of the pressure distribution around the blade surface usually agrees very well with that obtained by adiabatic inviscid calculation. Hence, S_1 calculations are usually based on the adiabatic inviscid condition, and Eqs. (2) to (4) are simplified to the following equations (Wu, 1952a):

$$\mathbf{W} \times (\nabla \times \mathbf{V}) = \nabla I - T \nabla s \quad (2a)$$

$$\frac{dI}{dt} = 0 \quad (3a)$$

and

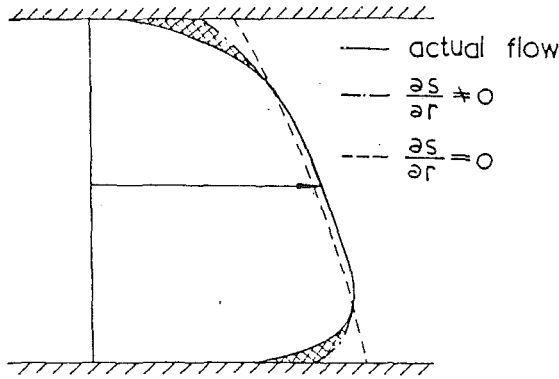


Fig. 4 Velocity variation considering and neglecting entropy gradient

$$\frac{ds}{dt} \geq 0 \quad (4a)$$

For S_2 flow, the viscous terms in Eqs. (2) and (3) can be considered to be negligible over the central region outside the hub and casing wall boundary layers, but the boundary layers along the hub and casing wall greatly affect the radial variation of velocity (Fig. 4). This effect on gas flow cannot be neglected in the design or analysis calculation of turbomachines. An approximate engineering method suggested by Wu et al. (1950), which has been widely used in engineering calculations, is to neglect the viscous stresses in the equation of motion, Eq. (2), but to consider the entropy increase in the flowing gas estimated by the polytropic efficiency (Wu, 1950), or rotor efficiency and stator stagnation pressure loss (Members of C&T Div., 1956). (To account for the effect that the calculated velocity in the wall boundary region is higher than the actual velocity, a corresponding mass flow coefficient K_g slightly greater than one should be used in the calculation.)

Method of Solution for Transonic Flow Along S_1 Filament of Revolution

Recently, several relatively simple and quick methods of solution for transonic flow along S_1 stream filaments have been developed and can be used in the S_1/S_2 iterative solution of three-dimensional flow in transonic turbomachines. Among them, the one based on stream function governing equations (Zhao, 1984; Wang, 1985a; Hua and Wu, 1986), and the one based on separate region calculation with shock fitting (C. Wu et al., 1984; W. Wu et al., 1985) can be used, respectively, for general purpose and more accurate calculation.

Use of General Curvilinear Coordinates and Corresponding Nonorthogonal Velocity Components. To calculate the flow on a given S_1 surface of revolution, it is most convenient to take nonorthogonal curvilinear coordinates x^1 and x^2 on the S_1 surface and x^3 normal to it (see Fig. 5). Then the continuity equation (1a) and the equation of motion (2a) become, respectively (Wu, 1976)

$$\frac{\partial(\tau\rho W^1 \sqrt{a_{22}} \sin \theta_{12})}{\partial x^1} + \frac{\partial(\tau\rho W^2 \sqrt{a_{11}} \sin \theta_{12})}{\partial x^2} = 0 \quad (1b)$$

and

$$\begin{aligned} & \frac{\partial}{\partial x^2} [(W^1 + W^2 \cos \theta_{12}) \sqrt{a_{11}}] - \frac{\partial}{\partial x^1} [(W^1 \cos \theta_{12} + W^2) \sqrt{a_{22}}] \\ & = -2\tau \sqrt{a_{11} a_{22}} \omega \sin \sigma \sin \theta_{12} + \frac{\sqrt{a_{11}}}{W^1} \left(\frac{\partial I}{\partial x^2} - T \frac{\partial S}{\partial x^2} \right) \end{aligned} \quad (2b)$$

In the preceding equations a_{11} , a_{22} , a_{12} , and $\cos \theta_{12}$ can be obtained by numerical differentiation from given geometric data with respect to the orthogonal cylindrical coordinates l and φ as follows:

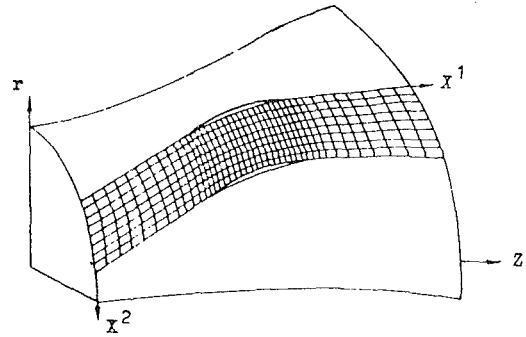


Fig. 5 Nonorthogonal curvilinear coordinates on S_1 surface of revolution

$$a_{11} = \frac{\partial l}{\partial x^1} \frac{\partial l}{\partial x^1} + r^2 \frac{\partial \varphi}{\partial x^1} \frac{\partial \varphi}{\partial x^1} \quad (8)$$

$$a_{22} = \frac{\partial l}{\partial x^2} \frac{\partial l}{\partial x^2} + r^2 \frac{\partial \varphi}{\partial x^2} \frac{\partial \varphi}{\partial x^2} \quad (9)$$

$$a_{12} = \frac{\partial l}{\partial x^1} \frac{\partial l}{\partial x^2} + r^2 \frac{\partial \varphi}{\partial x^1} \frac{\partial \varphi}{\partial x^2} \quad (10)$$

$$\cos \theta_{12} = \frac{a_{12}}{\sqrt{a_{11}} \sqrt{a_{22}}} \quad (11)$$

Transonic Stream Function Principal Equation Solved by the Use of Artificial Compressibility. Equation (1b) is the necessary and sufficient condition that there exists a function ψ , with

$$\frac{\partial \psi}{\partial x^1} = -\tau \rho W^2 \sqrt{a_{11}} \sin \theta_{12} \quad (12a)$$

$$\frac{\partial \psi}{\partial x^2} = \tau \rho W^1 \sqrt{a_{22}} \sin \theta_{12} \quad (12b)$$

Substituting Eq. (12) into Eq. (2b) results in the following conservation form of the stream-function principal equation:

$$\begin{aligned} & \frac{\partial}{\partial x^2} \left(A_1 \frac{1}{\rho} \frac{\partial \Psi}{\partial x^2} - A_2 \frac{1}{\rho} \frac{\partial \Psi}{\partial x^1} \right) - \frac{\partial}{\partial x^1} \left(A_2 \frac{1}{\rho} \frac{\partial \Psi}{\partial x^2} - A_3 \frac{1}{\rho} \frac{\partial \Psi}{\partial x^1} \right) \\ & = \frac{\sqrt{a_{11}}}{W^1} \left(\frac{\partial I}{\partial x^2} - T \frac{\partial S}{\partial x^2} \right) - 2\sqrt{a_{11}} \sqrt{a_{22}} \omega \sin \sigma \sin \theta_{12} \end{aligned} \quad (13)$$

where

$$\begin{aligned} A_1 &= \sqrt{a_{11}} / (\sqrt{a_{22}} \sin \theta_{12} \tau) \quad A_2 = \cos \theta_{12} / (\sin \theta_{12} \tau) \\ A_3 &= \sqrt{a_{22}} / (\sqrt{a_{11}} \sin \theta_{12} \tau) \end{aligned}$$

It is to be noticed that whereas the dynamic Eqs. (2a) and (2b) are equations governing the flow on the S_1 stream surface, the principal Eq. (13) is an equation governing the flow along an S_1 stream filament, since it contains the variable τ (or τ/τ_i) in the equation as a result of combining Eqs. (12a) and (12b) with Eq. (2) to form the principal Eq. (13). Thus, calculation of flow on an S_1 stream surface becomes calculation of flow along an S_1 stream filament.

In the solution, the variation of entropy is taken into account in the density calculation as follows:

$$\rho = \rho_i \cdot \left(\frac{I + \frac{1}{2} \omega^2 r^2 - \frac{1}{2} (W)^2}{H_i} \right)^{\frac{1}{k-1}} e^{\frac{S-S_i}{R}} \quad (14)$$

in which $W = [(W^1)^2 + (W^2)^2 + 2W^1 W^2 \cos \theta_{12}]^{1/2}$. The entropy increase across a shock is calculated by the usual formula.

The principal Eq. (13) is a mixed-type equation. It can be solved by modifying the density so as to introduce numerical

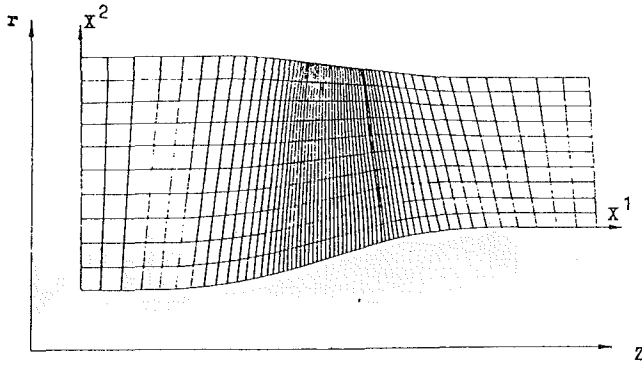


Fig. 6 Nonorthogonal curvilinear coordinates on meridional plane employed in S_2 calculation

dissipation necessary in the supersonic region (Hafez et al., 1979). The modified density is chosen in the present investigation as follows:

When $W^2 > 0$

$$\tilde{\rho}_{j,k} = \rho_{j,k} - \nu_{j,k} \left[\left(\frac{W^1}{W} \right) (\rho_{j,k} - \rho_{j-1,k}) + \left(\frac{W^2}{W} \right) (\rho_{j,k} - \rho_{j,k-1}) (\sqrt{a_{11}}/\sqrt{a_{22}})_{j,k} \right] \quad (15a)$$

When $W^2 < 0$

$$\tilde{\rho}_{j,k} = \rho_{j,k} - \nu_{j,k} \left[\left(\frac{W^1}{W} \right) (\rho_{j,k} - \rho_{j-1,k}) - \left(\frac{W^2}{W} \right) (\rho_{j,k} - \rho_{j,k+1}) (\sqrt{a_{11}}/\sqrt{a_{22}})_{j,k} \right] \quad (15b)$$

where

$$\nu_{j,k} = C \cdot \text{MAX}[0, 1 - 1/M_{j,k}^2]$$

Method of Solution for Transonic Flow Along S_2 Stream Filament

Whereas the shape of the S_1 surface is given both in the design problem and analysis problem, i.e., the flow is always solved for a given geometry, the S_2 surface flow is mostly encountered in an inverse or design problem, i.e., the solution of $S_{2,m}$ flow (including the shape of the $S_{2,m}$ surface) is obtained for a certain specified variation of a flow variable (Wu, 1950, 1952b). The one variable commonly used is $V_{\theta r}$ (Wu, 1951, 1952a, 1953). Thus, it is convenient to take the nonorthogonal curvilinear coordinates x^1 and x^2 on the meridional plane (Fig. 6) and x^3 to be the angular coordinate of the cylindrical coordinate system.

To emphasize the fact that all dependent variables are those on the S_2 surface, whereas the independent variables are on the meridional plane, a bold partial derivative sign is used to denote the partial derivative following motion on the S_2 surface. They are related to the ordinary derivative on the meridional plane by

$$\frac{\partial}{\partial x^1} = \frac{\partial}{\partial x^1} + \frac{\partial}{\partial \varphi} \frac{\partial \varphi}{\partial x^1} = \frac{\partial}{\partial x^1} + \frac{N_1}{N_{\varphi} r \sqrt{a_{11}}} \frac{\partial}{\partial \varphi} \quad (16a)$$

$$\frac{\partial}{\partial x^2} = \frac{\partial}{\partial x^2} + \frac{\partial}{\partial \varphi} \frac{\partial \varphi}{\partial x^2} = \frac{\partial}{\partial x^2} - \frac{N_3}{N_{\varphi} r \sqrt{a_{22}}} \frac{\partial}{\partial \varphi} \quad (16b)$$

The relation between the two partial derivatives is shown in Fig. 7.

Utilizing this derivative and relations of nonorthogonal velocity components, the following governing equations are obtained (Wu, 1976):

Continuity

$$\frac{\partial}{\partial x^1} (\tau \rho W^1 \sqrt{a_{22}} \sin \theta_{12}) + \frac{\partial}{\partial x^2} (\tau \rho W^2 \sqrt{a_{11}} \sin \theta_{12}) = 0 \quad (17)$$

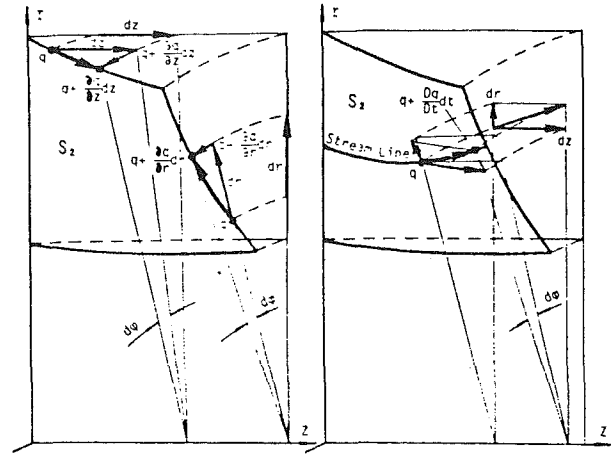


Fig. 7 Partial derivative and total derivative following motion on S_2

where τ is the circumferential thickness of the S_2 stream filament.

Dynamic equation

$$\frac{W^2}{\sqrt{a_{22}}} \left\{ \frac{\partial}{\partial x^1} \left[(W^1 \cos \theta_{12} + W^2) \sqrt{a_{22}} \right] - \frac{\partial}{\partial x^2} [(W^1 + W^2 \cos \theta_{12}) \sqrt{a_{11}}] \right\} + \frac{W_{\varphi}}{r} \frac{\partial (V_{\theta r})}{\partial x^1} - \frac{\partial I}{\partial x^1} + T \frac{\partial s}{\partial x^1} = -f_1 \quad (18a)$$

$$\frac{\partial}{\partial x^2} [(W^1 + W^2 \cos \theta_{12}) \sqrt{a_{11}}] - \frac{\partial}{\partial x^1} [(W^1 \cos \theta_{12} + W^2) \sqrt{a_{22}}] = \frac{\sqrt{a_{11}}}{W^1} \left[-\frac{W_{\varphi}}{r} \frac{\partial (V_{\theta r})}{\partial x^2} + \frac{\partial I}{\partial x^2} - T \frac{\partial s}{\partial x^2} - f_2 \right] \quad (18b)$$

$$\frac{d(V_{\theta r})}{dt} = \frac{W^1}{\sqrt{a_{11}}} \frac{\partial (V_{\theta r})}{\partial x^1} + \frac{W^2}{\sqrt{a_{22}}} \frac{\partial (V_{\theta r})}{\partial x^2} = f_{\varphi} = F_{\varphi} r \quad (18c)$$

where f_i is the covariant component of the same force vector derived in the general theory by Wu (1952b):

$$\mathbf{F} = - \left(\frac{1}{n_{\varphi}} \frac{1}{\rho} \frac{\partial p}{\partial \varphi} \right) \mathbf{n} = - \frac{1}{N_{\varphi} r \rho} \frac{\partial p}{\partial \varphi} \mathbf{n} = f_i \mathbf{e}^i = F_i \mathbf{u}^i \quad (19)$$

Stream Function Principal Equation. From Eq. (17) there exists a function ψ with

$$\frac{\partial \psi}{\partial x^2} = \tau \rho W^1 \sqrt{a_{22}} \sin \theta_{12} \quad (20a)$$

$$\frac{\partial \psi}{\partial x^1} = -\tau \rho W^2 \sqrt{a_{11}} \sin \theta_{12} \quad (20b)$$

Substituting Eqs. (20a) and (20b) into Eq. (18b) results in

$$\frac{1}{a_{11}} \frac{\partial^2 \psi}{\partial (x^1)^2} - 2 \frac{\cos \theta_{12}}{\sqrt{a_{11} a_{22}}} \frac{\partial^2 \psi}{\partial x^1 \partial x^2} + \frac{1}{a_{22}} \frac{\partial^2 \psi}{\partial (x^2)^2} + \frac{J}{\sqrt{a_{11}}} \frac{\partial \psi}{\partial x^1} + \frac{K}{\sqrt{a_{11}}} \frac{\partial \psi}{\partial x^2} = M \quad (21)$$

where

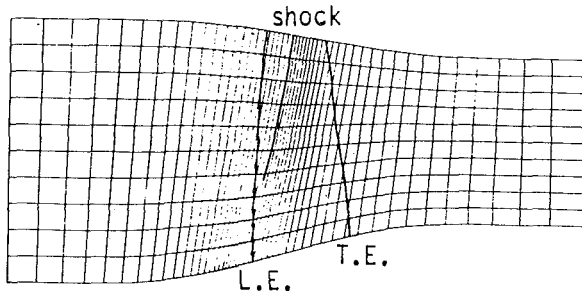


Fig. 8 Grid employed in the S_2 calculation embedding a shock discontinuity

$$J = -\frac{\partial \ln(\sqrt{a_{11}/a_{22}} \tau \sin \theta_{12})}{\sqrt{a_{11}} \partial x^1} + \frac{\cos \theta_{12}}{\sqrt{a_{22}}} \frac{\partial \ln \tau}{\partial x^2} + \frac{1}{\sin \theta_{12} \sqrt{a_{22}}} \frac{\partial \theta_{12}}{\partial x^2}$$

$$K = -\frac{\partial \ln(\sqrt{a_{22}/a_{11}} \tau \sin \theta_{12})}{\sqrt{a_{22}} \partial x^2} + \frac{\cos \theta_{12}}{\sqrt{a_{11}}} \frac{\partial \ln \tau}{\partial x^1} + \frac{1}{\sin \theta_{12} \sqrt{a_{11}}} \frac{\partial \theta_{12}}{\partial x^1}$$

$$M = \left(\frac{1}{\sqrt{a_{11}}} \frac{\partial \ln \rho}{\partial x^1} - \frac{\cos \theta_{12}}{\sqrt{a_{22}}} \frac{\partial \ln \rho}{\partial x^2} \right) \frac{1}{\sqrt{a_{11}}} \frac{\partial \psi}{\partial x^1} + \left(\frac{1}{\sqrt{a_{22}}} \frac{\partial \ln \rho}{\partial x^2} - \frac{\cos \theta_{12}}{\sqrt{a_{11}}} \frac{\partial \ln \rho}{\partial x^1} \right) \frac{1}{\sqrt{a_{22}}} \frac{\partial \psi}{\partial x^2} + \frac{\tau \sin \theta_{12}}{\sqrt{a_{11} a_{22}}} \rho C$$

$$C = \frac{\sqrt{a_{11}}}{W^1} \left[-\frac{W_\phi}{r} \frac{\partial (V_\theta r)}{\partial x^2} + \frac{\partial I}{\partial x^2} - T \frac{\partial s}{\partial x^2} - f_2 \right]$$

It was first shown by Wu (1952a) and later more thoroughly analyzed by Chen and Wu (1985) that in the design problem of S_2 surface flow when the angular momentum $V_\theta r$ is prescribed by the designer, the stream-function principal Eq. (21) remains elliptic as long as the meridional component of the velocity is less than the speed of sound. This provides a sound mathematical basis for solving the difficult transonic S_2 flow problem in a simple manner, when the meridional velocity component is subsonic. However, it is important to notice that the streamwise variation of the angular momentum in transonic turbomachines is quite different from that in the subsonic turbomachine, especially in the shock region. When the prescribed value of $V_\theta r$ and τ have abrupt changes in the shock region, the Mach number contours obtained in the calculation show clearly a shock line quite similar to the one constructed from the measured data (Chen and Wu, 1988). Furthermore, when the subsonic code is slightly modified by adding another computation station besides the original one at the shock line (Fig. 8) to store values of the flow variables just upstream and downstream of the shock, and by putting in $V_\theta r$ and τ values, which have appropriate abrupt changes across the shock line, the flow field on the S_2 surface obtained shows a shock discontinuity (Chen and Wu, 1988).

Inverse or Design Problem of S_2 Flow. In the inverse solution of S_2 flow, the f_2 component of F needed in the solution of the principal Eq. (21) is to be calculated from the condition of integrability by the following equation

$$\frac{f_2}{f_\phi} = \left(\frac{f_2}{f_\phi} \right)_0 + \int_{(x^1)_0}^{x^1} \frac{\partial}{\partial x^2} \left(\frac{f_1}{f_\phi} \right) dx^1 \quad (22)$$

in which f_1 and f_ϕ are to be calculated from Eqs. (18a) and (18c).

After the flow variables are obtained from the solution, the angular coordinate of the $S_{2,m}$ surface can be obtained by the following equation:

$$\phi = \phi_0 + \int_0^l \frac{W_\phi}{r \sqrt{(W^1)^2 + (W^2)^2 + 2W^1 W^2 \cos \theta_{12}}} dl \quad (23)$$

Thus in the inverse problem, the coordinate of the S_2 surface is determined at the end of the solution.

In the direct or analysis problem, the shape of the S_2 surface and the corresponding variation of τ or τ/τ_i are given. A set of nonorthogonal curvilinear coordinates may be chosen on the S_2 surface and a conservation form of the stream function principal equation can be obtained (Zhao, 1986) to calculate the transonic flow on S_2 . This differential equation is always hyperbolic when the relative velocity is supersonic, no matter whether the meridional velocity is supersonic or not.

To take advantage of the fact that the governing differential equation is elliptic when the meridional velocity is subsonic, the principal Eq. (21) can be used for the direct problem in the following manner:

From the orthogonality relation between \mathbf{W} and \mathbf{n} ,

$$W_\phi = - \left(\frac{N_1}{N_\phi} W^1 + \frac{N_2}{N_\phi} W^2 \right) \sin \theta_{12} \quad (24)$$

then

$$V_\theta r = (\omega r + W_\phi) r \quad (25)$$

and W_ϕ or $V_\theta r$ is calculated from the values of W^1 and W^2 obtained in the present cycle and used as input value for the next cycle. Except for this additional step, calculation for the direct problem proceeds just like that in the inverse problem.

It may be noticed that in the three-dimensional solution, the vorticity component in the direction normal to the S_1 surface is taken into account in the solution of the principal Eq. (13). Also, in the solution of $S_{2,m}$ surfaces, all three vorticity components are taken into account in Eqs. (18a)–(18c). In the case where f_2 is small and is neglected, only the vorticity components tangent, respectively, to x^1 and x^2 coordinate lines are taken into account in the principal Eq. (21).

Convergence of Iterative Three-Dimensional Solution

The key issue for the success of the present method of solving the three-dimensional transonic flow by iterative calculation between an $S_{2,m}$ surface calculation and a number of S_1 surface calculations is the convergence problem. In the case of high subsonic flow through a compressor stator (Zhu and Wu, 1983), it was found that when the entropy values of the two surfaces at the same intersecting point are kept the same, a convergent solution with

$$|(r_{S_2}^{(n)} - r_{S_2}^{(n-1)})/r_{S_2}^{(n-1)}| < 0.3 \text{ percent}$$

$$|(\tau_{S_2}^{(n)} - \tau_{S_2}^{(n-1)})/\tau_{S_2}^{(n-1)}| < 0.8 \text{ percent}$$

$$|(M_{S_2} - M_{S_1})/M_{S_1}| < 2 \text{ percent}$$

was obtained after only four cycles of iteration. For transonic flow it is expected that the convergence of solution would be more difficult to obtain than that in subsonic flow due to the presence of the passage shock. However, it is believed that, in the present method, the fact that the shock discontinuity is determined in the S_1 solution, and that the abrupt changes in entropy and $V_\theta r$ across the shock obtained in the S_1 solution are taken as the input values to the $S_{2,m}$ solution, will be of help in achieving convergence of the three-dimensional iterative solution.

In the example cited above, the criteria $|\Delta r/r|_{\max}$ and $|\Delta \tau/\tau|_{\max}$ are used to judge the convergence, whereas $|(M_{S_1} - M_{S_2})/M_{S_1}|_{\max}$ is used to judge the consistency. Between convergence and consistency, the former is the more essential. If convergence is not achieved, good consistency is impossible. On the other hand, even in the case of a high degree of convergence, there may be an irreducible inconsistency of the Mach number. It is believed that consistency of entropy and mass

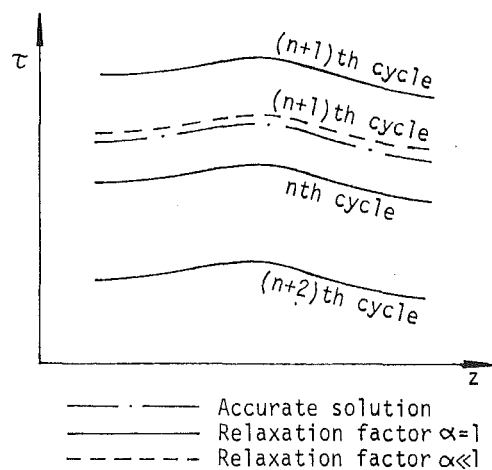


Fig. 9 Sketch of local fluctuation of S_1 stream filament thickness during iteration and the effect of relaxation factor

flow coefficient in the S_1 and S_2 calculations is especially important for the consistency between the S_1 and S_2 solutions.

The use of a proper value of relaxation factor is very important for convergence. During the calculation for flow in a transonic rotor, the thickness value of the S_1 stream filament near the casing fluctuated and diverged when relaxation factor was not used (see Fig. 9). This kind of divergence is something like that in the iterative calculation of the following algebraic equation:

$$x^{(n)} = f(x^{(n-1)})$$

when $f'(x) < -1$. Hence, in order to obtain and speed up convergence, a small relaxation factor was used.

In the numerical example to be presented in the following section, the same grid pattern in the x^1 direction is employed for both S_1 and S_2 calculations, and the entropy and mass flow coefficients are kept consistent in both S_1 and S_2 calculations. It is found that the use of a relaxation factor of relatively small value is very efficacious to obtain quick convergence. The consistency is at the same time relatively good. In the case of high subsonic flow through a compressor rotor, the relative change in S_1 filament thickness is reduced to below 2 percent and the relative differences between S_1 and S_2 Mach number and flow angle are reduced to, respectively, 0.9 percent and 0.3 deg. In the case of transonic flow in a compressor rotor, the tip Mach number of which is 1.37, the relative change in S_1 filament thickness is reduced to below 1 percent and the relative difference between S_1 and S_2 Mach number at the same grid point is below 4 percent. These values of inconsistency are probably due to the fact that artificial density is employed in S_1 but not in S_2 calculations and that the conservation form of the principal equation is employed in S_1 but not in S_2 calculations.

Steps for Approximate Iterative Solution of Three-Dimensional Transonic Flow

Design Problem. The methods of solving transonic flows on S_1 and S_2 surfaces described in the preceding sections can be combined to form a relatively simple method of turbomachine blade design based on three-dimensional rotational flow. The absolute motion can be either irrotational or rotational at the blade inlet. In the present paper, the approximation is made that all S_1 surfaces are surfaces of revolution.

1 Given Data: The flow path in the meridional plane is usually determined by the simplified-radial-equilibrium calculation. (A method of obtaining the passage shape for a desirable pressure or velocity distribution on the hub and casing walls is also available (Zhu et al., 1989).) Also given are the

design mass flow, the mass flow coefficient, the design rotative blade speed, and the radial distribution of the stagnation pressure and temperature at the blade inlet and outlet. These data include a radial variation of stagnation pressure loss through stator blades or isentropic efficiency of the rotors. They should be checked and modified at the end of the design process with some boundary layer calculation and loss evaluation, and in some cases by testing.

In the first cycle of calculation, the variations of $V_{\theta r}$ and relative stream filament thickness of $S_{2,m}$, τ/τ_i , are empirically assumed. In later cycles, they are taken from S_1 calculation results. Their final values obtained at the end of the design process correspond to the blade shape determined in the blade design calculation. Their differences from the starting values are not important. On the other hand, if the flow field obtained at the end of the design process has something undesirable, it may be improved by starting with some other $V_{\theta r}$ distribution or/and with some reductions in the blade exit stagnation pressure and temperature.

2 With these given data, the stream function field of $S_{2,m}$ is obtained by solving Eq. (21). Then, \mathbf{W} components, T , p , ρ , streamline distribution, and S_2 surface coordinate ϕ are calculated.

3 A number of the meridional projections of the streamlines obtained in the $S_{2,m}$ are revolved about the machine axis to form a number of S_1 surfaces of revolution and the distance between them determines the τ variation. The flow angle obtained at the outlet station is one boundary condition for the following S_1 calculation.

4 Either an inverse method is used to obtain the blade shape, such as the mean-streamline method (Wu and Brown, 1951b), or a standard blade profile is chosen on a conical surface, which approximates the S_1 surface of revolution in the blade region.

5 Solutions of transonic flows on a number of S_1 surfaces by Eq. (13) give the complete flow field for the whole flow channel. Except for the radius and filament thickness, all flow variables vary in the circumferential direction. The velocity distribution around the blade can be quite effectively improved by the method given by Wang (1985b).

6 For rotor blades, the centers of gravity of the blade sections are stacked on a line, which deviates slightly from a radial line for strength consideration. For stator blades, the stacking point and stacking line can be arbitrarily chosen.

7 The variations of $V_{\theta r}$ obtained along the mid-streamlines on S_1 are used for the next cycle of $S_{2,m}$ calculation. So are the position of the shock line, the abrupt changes of entropy, and other flow variables across the shock.

Steps (2)–(7) are repeated for the next cycle, and so forth, until convergence is obtained.

It is believed that the procedure described above provides a practical three-dimensional blade design method. Past experiences in radial equilibrium calculations, cascade test results, two-dimensional blade design techniques, single and multistage test results can be very well utilized in this design system. A direct three-dimensional solution method cannot yield three-dimensional blade design as effectively as this method. The computation time of the former is also much longer than that of the latter.

Direct Problem. In the approximate iterative three-dimensional solution of the direct problem, it may be desirable to start the computation on a number of S_1 surfaces, and to follow it with computation on the $S_{2,m}$ surface. To take advantage of the elliptic solution of the $S_{2,m}$ principal equation when the meridional velocity is subsonic, $V_{\theta r}$ obtained in the S_1 solution is used as input to the $S_{2,m}$ calculation.

Illustrative Example and Discussion

In order to assess the convergence behavior and the accuracy

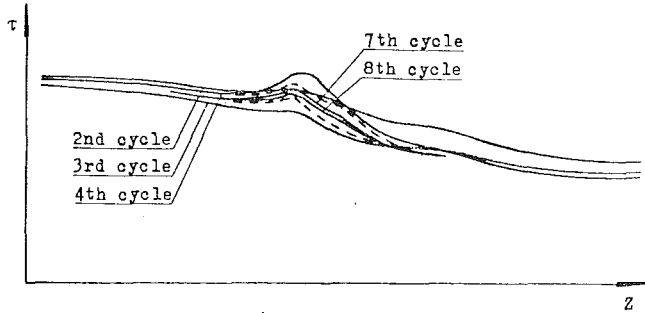


Fig. 10 Schematic drawing of variation process of tip S_1 filament thickness

of the approximate (quasi-) three-dimensional design or analysis method presented herein, the method is applied to computing the flow field in the DFVLR rotor operating at the design point, for which a measured flow field is available for comparison. The design stagnation pressure ratio is 1.51 and the inlet relative Mach number at the blade tip is about 1.37. The $V_{\theta r}$ distribution at the outlet at design point is determined from experimental data and is used as the fixed boundary value of the direct problem.

For $S_{2,m}$, a grid system of 61 stations along x^1 and 11 stations along x^2 are chosen on the meridional plane (Fig. 6). Seven S_1 surfaces are used in the calculation. They are located at, respectively, 0, 10, 30, 50, 70, 90, and 100 percent of the blade height at the inlet station. The grid system chosen on the S_1 surface also has 61 stations along the x^1 coordinate and 15 stations along the x^2 coordinate. In order to see how high a convergence level can be obtained for this moderately high transonic flow, nine cycles of calculation were carried out and the convergence level obtained (relative change of flow variable less than 1 percent) is as good as that previously obtained for subsonic flow. The significant advantage of the transonic three-dimensional calculating method is that the computation can be carried out at low cost in a reasonable time period or on a modern personal computer, which is readily available to a design engineer. For instance, the computing time for the transonic S_1 and S_2 solution is about 8 min each on an IBM PS-II machine. Thus, the total time required is about 300 min on such machines. Therefore, this relatively inexpensive approximate three-dimensional code is quite suitable for design investigations and tradeoff studies. The final choice may then be checked and refined by a full three-dimensional analysis code or even by a viscous code, which is now beginning to be available. This means that the proposed method is also practical for transonic turbomachines.

Variation of the Flow Variables During the Convergence Process. During the first few cycles of calculation there was a general tendency toward convergence. But in the region near the casing the values of S_1 filament thickness soon began to fluctuate. Also its magnitude tends to increase (see Fig. 10). A small relaxation factor less than 1 was used to make the process convergent. It was noticed in the seventh cycle, a small τ_1 input to S_1 calculation (the lower solid line in Fig. 10) yields a large value of output from the S_2 calculation (the upper dashed line in Fig. 10) and vice versa in the eighth cycle. The solution is seen to lie between the two. The middle value was taken as the input to the ninth cycle and the output obtained is less than 1 percent from the final value.

The abrupt change in the streamlines across the shock is indicated in Fig. 11.

The streamwise variation of τ for the seven S_1 surfaces assumed in the first cycle and obtained in the ninth cycle are

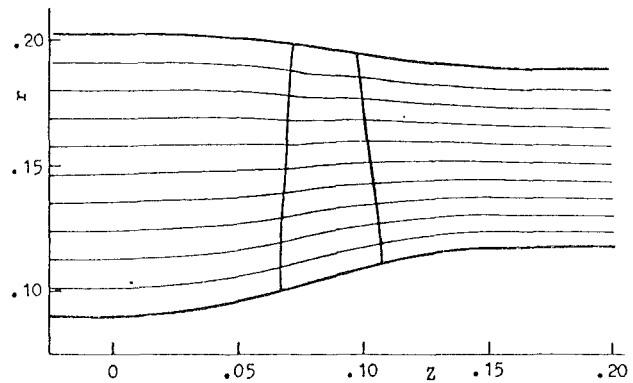


Fig. 11 S_2 output stream lines of ninth cycle

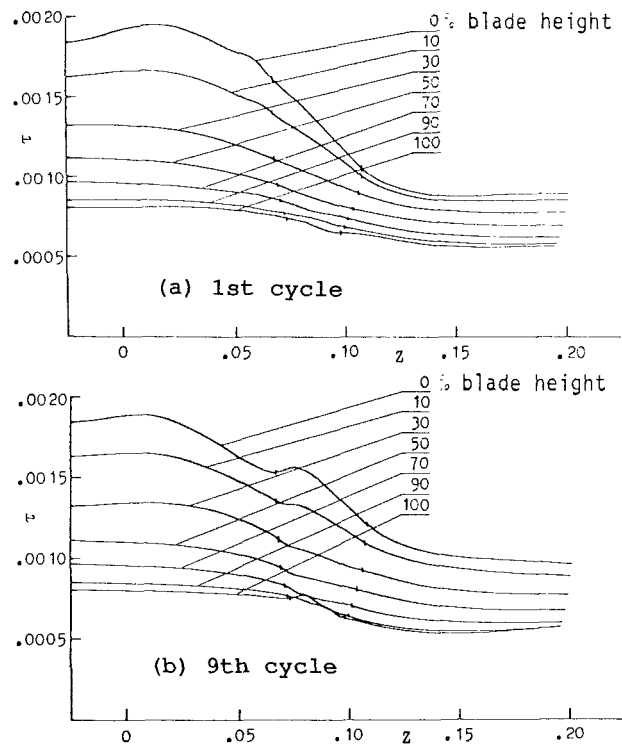


Fig. 12 S_1 filament thickness

shown, respectively, in Fig. 12(a) and 12(b), and the values of r and τ , respectively, of the streamline at 70 and 100 percent blade height in the seventh, eighth, and ninth cycles of calculation are listed, respectively, in Tables 1 and 2.

The converging process of $V_{\theta r}$ is similar to that of τ of S_1 . The variation of $V_{\theta r}$, relative to its value at the exit, along the seven streamlines in the ninth cycle of calculation (Fig. 13(b)) is compared to that in the first cycle of calculation.

On the other hand, the change in the stream filament thickness of $S_{2,m}$ is relatively simple. The streamwise value on the seven streamlines used as input value to the ninth cycle are shown in Fig. 14(b) and are compared to those assumed in the first cycle (Fig. 14(a)). The abrupt change in τ (and $V_{\theta r}$, streamline) is clearly seen in Fig. 14(b) (and 13(b), 11).

Figure 15(a) shows the Mach number variation along the mean streamlines obtained on the seven S_1 surfaces in the ninth cycle, whereas Fig. 15(b) shows those along the streamlines on the $S_{2,m}$ surface obtained in the ninth cycle. They are very close, the maximum difference between the two being less than 4 percent. This is the same value previously obtained in the iteration for a subsonic rotor. This means that in the present

Table 1 The values of thickness of the S_1 stream filament at the blade tip in the last three cycles

Station No.	L.E.	21	22	23	24	25	26	27	28	29	30
Seventh cycle	0.754	0.756	0.760	0.767	0.771	0.775	0.769	0.759	0.747	0.735	0.723
Eighth cycle	0.756	0.758	0.763	0.771	0.777	0.782	0.775	0.766	0.756	0.744	0.733
Ninth cycle	0.755	0.757	0.761	0.769	0.774	0.779	0.772	0.763	0.751	0.739	0.728
Station No.	31	32	33	34	35	36	37	38	39	T.E.	
Seventh cycle	0.712	0.704	0.696	0.688	0.676	0.663	0.654	0.644	0.638	0.629	
Eighth cycle	0.723	0.716	0.709	0.701	0.687	0.673	0.662	0.651	0.643	0.633	
Ninth cycle	0.717	0.710	0.703	0.694	0.681	0.668	0.658	0.647	0.641	0.631	

Table 2 The values of radius of the S_1 streamsurface of revolution at 70 percent blade height in the last cycles

Station No.	L.E.	21	22	23	24	25	26	27	28	29	30
Seventh cycle	.16815	.16807	.16800	.16796	.16799	.16807	.16814	.16818	.16817	.16814	.16811
Eighth cycle	.16816	.16809	.16802	.16799	.16803	.16813	.16823	.16825	.16825	.16821	.16818
Ninth cycle	.16816	.16808	.16801	.16798	.16801	.16810	.16818	.16822	.16821	.16818	.16815
Station No.	31	32	33	34	35	36	37	38	39	T.E.	
Seventh cycle	.16810	.16810	.16812	.16815	.16818	.16819	.16820	.16820	.16819	.16818	
Eighth cycle	.16817	.16817	.16820	.16823	.16826	.16828	.16829	.16830	.16829	.16828	
Ninth cycle	.16813	.16814	.16816	.16819	.16822	.16824	.16825	.16825	.16824	.16823	

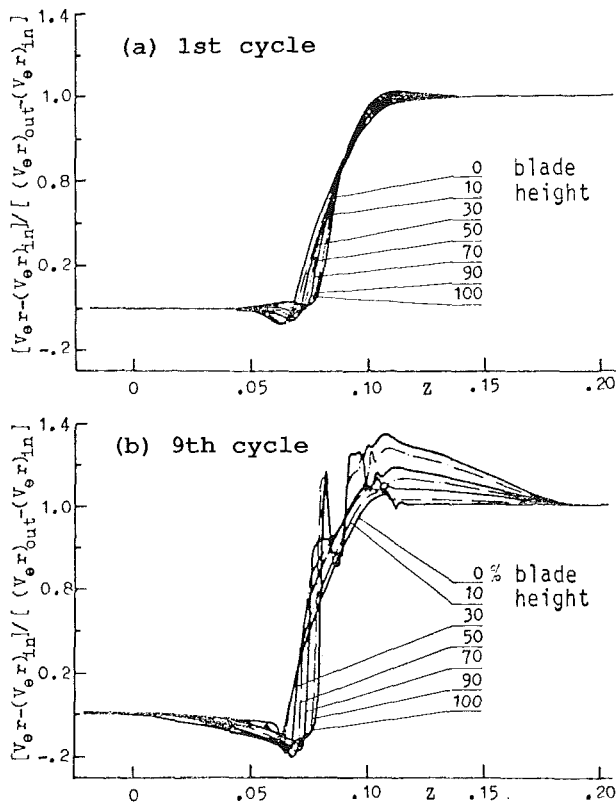


Fig. 13 S_2 input $V_{\theta r}$

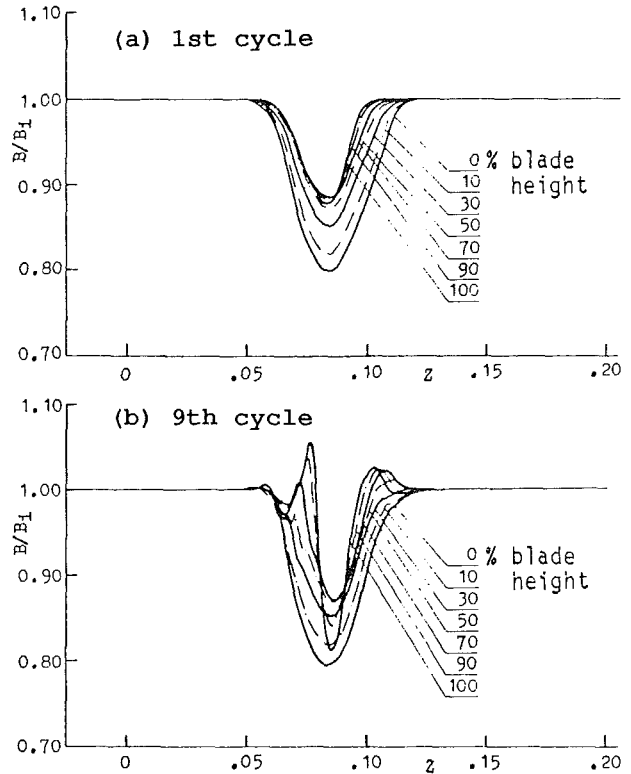


Fig. 14 S_2 input filament thickness

solution of moderately high transonic flow, the convergence and consistency levels obtained are as good as those in the subsonic case.

Three-Dimensional Flow Field. In the approximate three-dimensional solution presented herein, the three-dimensional flow field is obtained on the seven S_1 filaments of revolution extending over the whole blade passage (the $S_{2,m}$ calculation is used mainly for obtaining the geometry of the S_1 filaments). The constant Mach number contours on these S_1 surfaces can be readily obtained from the calculation. However, in order

that comparison with test data can be made, the contours on S_1 surfaces at 18, 45, 68, and 89 percent span are obtained through interpolation and are shown in Figs. 16(a-d). They show clearly the strong effect of the passage shock. The solution of S_1 surface flow can also be used to obtain the radial variation of flow variables at a number of stations along the flow direction. Two of them, the relative Mach number and flow angle β , are shown in Fig. 17.

In order to see more clearly the effect of the three-dimensional passage shock on the three-dimensional flow field, the three-dimensional passage shock is constructed in scale and is shown in Fig. 18. At the tip Mach number of 1.37 and a hub-

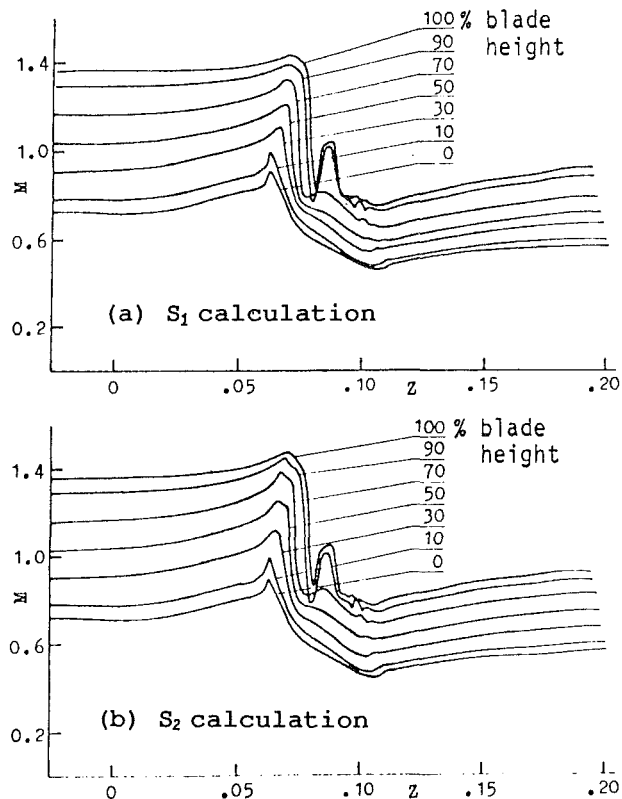


Fig. 15 Output Mach number on stream lines of ninth cycle

tip ratio of 0.5, the passage shock is seen to extend from the casing almost all the way inward to the hub.

Although only the flow variation on the central S_2 surface is directly available in the iterative three-dimensional solution, those on the other S_2 surfaces can be constructed by the data on the corresponding streamlines on different S_1 surfaces. Constant Mach number contours on the suction and pressure surfaces are obtained in this way and are shown together with that on the central S_2 surface in Fig. 19. A second passage shock is seen on the suction surface and the central S_2 surface, extending only a short distance inward from the casing. From data on these S_2 surfaces, streamwise variations of flow variables on certain streamlines can be readily obtained. For instance, the variation of flow angle along three streamlines on the $S_{2,m}$ surface at 18, 68, and 89 percent blade height (at inlet) are shown in Fig. 20. The variation of flow variables can also be shown on surfaces, formed by x^2 and x^3 coordinates. The variations of M , β , and p on these surfaces are particularly useful for observing the influence of the passage shock and the magnitude of vorticity or secondary flow. Mach number contours on three such surfaces are shown in Fig. 21. On the 10 percent C surface, the intersection of the shock surface and this surface is seen to extend from casing all the way inward to a point, which is very near the hub. At the 90 percent C surface, the flow is almost entirely subsonic.

Comparison Between the Computed Flow Field and DFVLR Measured Data. The approximate three-dimensional transonic solution obtained by the present method is compared with available DFVLR measured data in Figs. 16, 17, and 20.

The character of the flow field obtained by the present method is seen to be in good agreement with that constructed from DFVLR measured data. In the region near 18 percent span, there appears a supersonic zone near the leading edge of the suction surface. In the middle of the span, there appears

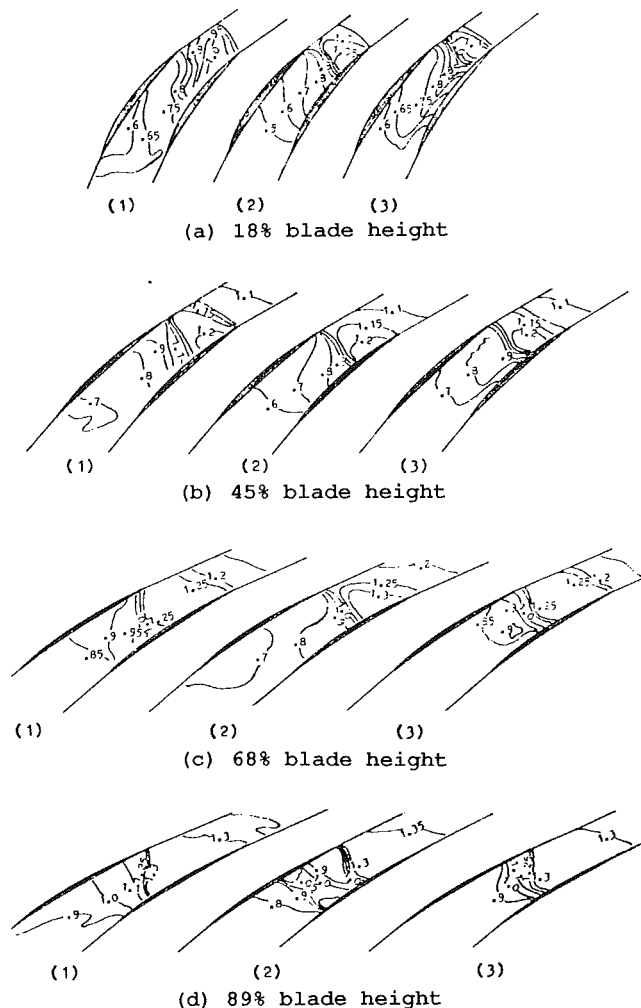


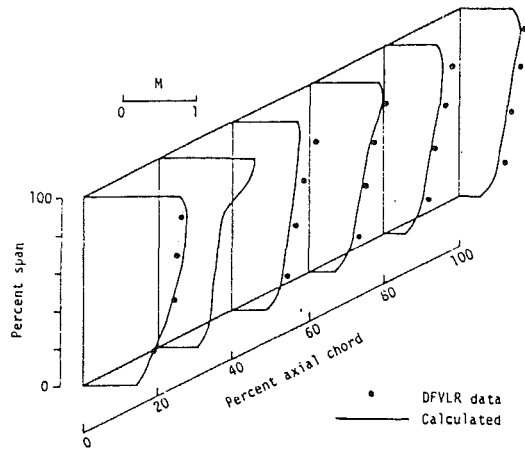
Fig. 16 Mach number contours on S_1 surface: (1) DFVLR measured data; (2) calculated by present method; (3) calculation by McDonald et al. (1980)

a bow wave a short distance in front of the leading edge, and the wave extending to the flow passage to form a passage shock. At about two-thirds of the span, the shock appears to be nearly attached to the leading edge. In the blade tip region, there is a second shock downstream of the bow wave/passage shock and the shock is nearly normal to the suction surface. The position of the passage shock obtained in the calculation is seen to be slightly in front of the measured position. This difference is seen to be inherent in the solution of transonic flow by the use of the stream function/artificial density method (Zhao, 1984; Wang, 1985a; Hua and Wu, 1986). Also, the computed shock is more nearly normal to the suction surface, whereas in the measured data, the passage shock is more inclined to the suction surface.

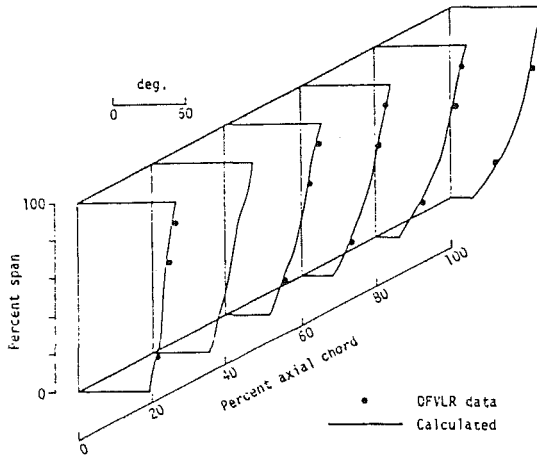
The result calculated by a different method (McDonald et al., 1980) is included in Fig. 16 for comparison. The character of flow is similar, but there is some difference in the magnitude between the two calculated results.

In Fig. 17, values of M and β interpolated from DFVLR measured data are shown. Their radial variations are seen to be quite similar to those obtained in the present calculation. The agreement in the magnitude between the two is seen to be slightly better in the values of β .

The values of relative flow angle β along 18, 68, and 89 percent span streamlines on the $S_{2,m}$ surface taken from measured data are shown in Fig. 20. The calculated results are seen to be in quite good agreement with the experimental data.



(a) Mach number



(b) flow angle

Fig. 17 Radial variation at a number of station

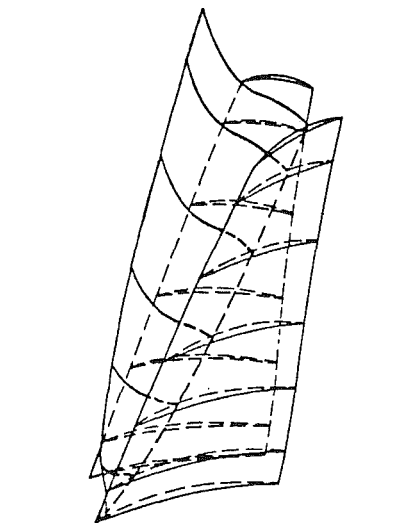


Fig. 18 Three-dimensional passage shock

Conclusion

Wu's general theory of three-dimensional flow in subsonic and supersonic turbomachines based on the iterative solution of relative S_1 and S_2 stream-filament flow has been developed

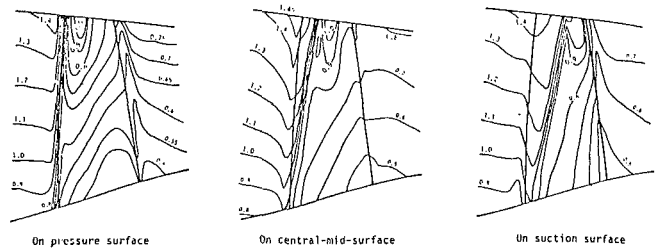


Fig. 19 Constant Mach number contours on three S_2 surfaces

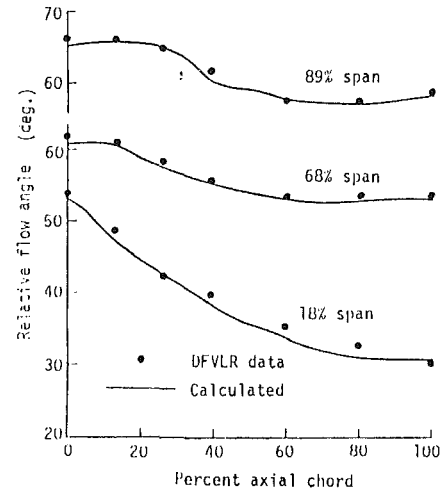


Fig. 20 Variation of flow angle along three stream lines on the $S_{2,m}$ surface

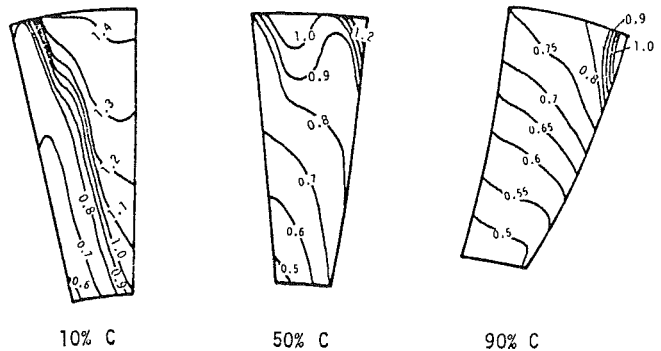


Fig. 21 Constant Mach number contours on three spanwise surfaces formed by (x^2, x^3) coordinates

to calculate the three-dimensional rotational flow in transonic turbomachines. Recently developed relatively simple and fast computer programs for solving the transonic flow in S_1 and S_2 stream filaments are utilized.

Test computation of this system to the DFVLR rotor operating at the design point (tip Mach number 1.37) shows that the convergence behavior of the solution was quite satisfactory. Good convergence (maximum relative change of flow variables is less than 1 percent) was obtained. Also the consistency is less than 4 percent.

The three-dimensional flow field obtained shows that the character of the flow field is in good agreement with the available DFVLR measurement, but the passage shock obtained in the solution lies a short distance upstream of the measured position, and the shape of the shock surface calculated is more normal to the suction surface of the blade than the measured one. The flow field calculated in the midpart of the flow channel is in good agreement with the measured data.

It is recommended that the computing system presented can be very conveniently used for three-dimensional design of transonic turbomachines.

Acknowledgments

The authors wish to thank Dr. H. B. Weyer of DFVLR for the details of blade geometry and the L2F data.

References

- Bosman, C., and El-sharawi, M. A. I., 1977, "Quasi-Three-Dimensional Numerical Solution of Flow in Turbomachines," *ASME Journal of Fluids Engineering*, Vol. 99, pp. 132-140.
- Bianiaris, S., 1975, "The Calculation of the Quasi-Three-Dimensional Flow in the Axial Gas Turbine," *ASME Journal of Engineering for Power*, Vol. 97, pp. 283-294.
- Broichhausen, K. D., and Gallus, H. E., 1981, "The Complete Three-Dimensional Experimental Analysis of the Flow Through Supersonic Compressor Stages," Paper No. AIAA-81-0067.
- Cai, Ruixian, 1983, "Constraint on Design Parameters and Twist of S_1 Surface in Turbomachines," *Scientia Sinica*, Series A, Apr.
- Chen Hongji and Wu Chung Hua, 1985, "Solution of Inverse Problem of Transonic Flow on S_2 Surface Using an Elliptic Algorithm," *Proceedings of 7th ISABE*, pp. 465-473.
- Chen Hongji and Wu Chung-Hua, 1988, "Shock Embedding Discontinuous Solution of Elliptic Equation for Inverse Problem of Transonic S_2 Flow," *ASME JOURNAL OF TURBOMACHINERY*, Vol. 110, pp. 347-353.
- Goulas, A., 1980, "Flow in Centrifugal Compressor Impeller," AGARD Conference Proceedings No. 282.
- Hafez, M., South, J., and Marman, E., 1979, "Artificial Compressibility Methods for Numerical Solution of Transonic Potential Equations," *AIAA J.*, Vol. 17, pp. 838-844.
- Hua Yaonan and Wu Wenquan, 1986, "Numerical Solution of Transonic Stream Function Equation on S_1 Stream Surface in Cascade," *ASME Paper No. 86-GT-110*.
- Jennions, I. K., and Stow, P., 1985, "A Quasi-Three-Dimensional Turbomachinery Blade Design System," *ASME Journal of Engineering for Gas Turbines and Power*, Vol. 107, pp. 301-316.
- Krimerman, Y., and Adler, D., 1978, "The Complete Three-Dimensional Calculation Compressible Flow Field in Turbo Impellers," *Journal Mechanical Engineering Science*, Vol. 20, No. 3, pp. 149-158.
- McDonald, P. M., et al., 1980, "A Comparison Between Measured and Computed Flow Field in a Transonic Compressor Rotor," *ASME Journal of Engineering for Power*, Vol. 102, No. 4, pp. 883-891.
- Members of C&T Div., 1956, "Aerodynamic Design of Axial-Flow Compressors," NACA RM E56803A.
- Prince, T. C., et al., 1984, "Three Dimensional Computation of an Impeller Flow," *ASME Journal of Engineering for Gas Turbines and Power*, Vol. 106, pp. 523-529.
- Sarathy, K. P., 1982, "Computation of Three-Dimensional Flow Fields Through Rotating Blade Rows and Comparison With Experiment," *Journal of Engineering for Power*, Vol. 104, p. 395.
- Wang, Qing-hua, Wu Wen-quan, Zhu Gen-xing, Li Wei-hong, and Wu Chung-Hua, 1983, "Solution of Three-Dimensional Compressible Flow in an Axial-Flow Compressor Stator by the Use of S_1 and S_2 Relative Surface," *Journal of Engineering Thermophysics*, Vol. 4 [in Chinese].
- Wang Zhengming, 1985a, "Solution of Transonic S_1 Surface Flow by Successfully Reversing the Direction of Integration of the Stream Function Equation," *ASME Journal of Engineering for Power*, Vol. 107, Apr.
- Wang Zhengming, 1985b, "Inverse Design Calculations for Transonic Cascade," *ASME Paper No. 85-GT-6*.
- Wu Chung-Hua and Wolfenstein, L., 1950, "Application of Radial-Equilibrium-Condition to Axial-Flow Compressor and Turbine Design," NACA TR 955.
- Wu Chung-Hua, 1951, "A General Through-Flow Theory of Fluid Flow With Subsonic or Supersonic Velocity in Turbomachines Having Arbitrary Hub and Casing Shapes," NACA TN 2302.
- Wu Chung-Hua and Brown, C. A., 1951a, "Method of Analysis for Compressible Flow Past Arbitrary Turbomachine Blade on General Surface of Revolution," NACA TN 2407.
- Wu, Chung-Hua and Brown, C. A., 1951b, "A Method of Designing Turbomachine Blades With a Desirable Thickness Distribution for Compressible Flow Along an Arbitrary Stream Filament of Revolution," NACA TN2455.
- Wu Chung-Hua, 1952a, "A General Theory of Three-Dimensional Flow in Subsonic and Supersonic Turbomachines of Axial and Mixed-Flow Types," *ASME Paper No. 50-A-79; Trans. ASME*, Vol. 74, NACA TN 2604.
- Wu Chung-Hua, 1952b, "Matrix and Relaxation Solution That Determine Subsonic Through-Flow in an Axial-Flow Gas Turbine," NACA TN 2750.
- Wu Chung-Hua, 1953a, "Subsonic Flow of Air Through a Single Stage and a Seven Stage Compressor," NACA TN 2961.
- Wu Chung-Hua, 1953b, Discussion to "A Practical Solution of a Three-Dimensional Flow Problem of Axial-Flow Turbomachinery," *Trans. ASME*, Vol. 75, pp. 802-803.
- Wu Chung-Hua, 1965, "Fundamental Aerothermodynamic Equations for Stationary and Moving Coordinate Systems: Action of Viscous Forces and Physical Significance of Viscous Terms," *Journal of Mechanical Engineering*, Vol. 13, No. 4 [in Chinese]; *Engineering Thermophysics in China*, Vol. 1, No. 1, 1980, Rumford Pub. Co., USA.
- Wu Chung-Hua, 1976, "Three-Dimensional Turbomachines Flow Equations Expressed With Respect to Nonorthogonal Curvilinear Coordinates and Methods of Solution," *Proceedings of the 3rd International Symposium on Air-Breathing Engines*, pp. 233-252.
- Wu Chung-Hua and Zhu Genxing, 1983, "Determination of the Appropriate Upstream and Downstream Combinations in Rotating Cascade Experiment and Calculation of Arbitrary S_1 Stream Surface for an Embedded Blade Row," *Journal of Engineering Thermophysics*, Vol. 4, No. 1 [in Chinese].
- Wu C. H., Wu, W., Hua, Y., and Wang, B., 1984, "Transonic Cascade Flow With Given Shock Shape Solved by Separate Subsonic and Supersonic Computations," *Computational Methods in Turbomachinery*, IMechE, Paper No. C19/84, pp. 133-140.
- Wu Chung-Hua, 1985, "Contribution of Basic Research in the Gas Dynamics of Turbomachinery in the Institute of Engineering Thermophysics," Chinese Academy of Sciences, *Proceedings of Seventh International Symposium on Air Breathing Engines*, Supplement, pp. 1-24, Beijing, China.
- Wu Chung-Hua, Wang Jian-an, Fang Zong-yi, and Wang Qing-huan, 1985, "L2F Velocity Measurement and Calculation of Three-Dimensional Flow in an Axial Compressor Rotor," presented at the 7th ISABE, Beijing.
- Wu Wenquan, Wu Chunghua, and Yu Dabang, 1985, "Transonic Cascade Flow Solved by Separate Supersonic and Subsonic Computation With Shock Fitting," *ASME Journal of Engineering for Gas Turbines and Power*, Vol. 107, Apr.
- Zhao Xiaolu, 1984, "Solution of Transonic Flow Along S_1 Stream Surface Employing Nonorthogonal Curvilinear Coordinates and Corresponding Non-orthogonal Velocity Components," *Journal of Engineering Thermophysics* [in Chinese], Aug.; C84/84, *Computational Methods in Turbomachinery*, IMechE.
- Zhao Xiaolu, Sun Chunlin, and Wu Chunghua, 1985, "A Simple Method for Solving Three-Dimensional Inverse Problems of Turbomachine Flow and the Annular Constraint Condition," *ASME Journal of Engineering for Gas Turbines and Power*, Vol. 107, pp. 293-300.
- Zhao Xiaolu, 1986, "Stream Function Solution of Transonic Flow Along S_2 Stream surface of Axial Turbomachines," *ASME Journal of Engineering for Gas Turbines and Power*, Vol. 108, pp. 138-143.
- Zhu, G. X., and Wu, C. H., 1983, "Three-Dimensional Subsonic Flow Through a Stator by Use of a Central S_2 Stream Surface and Several S_1 Surfaces of Revolution," *Journal of Engineering Thermophysics*, Vol. 4, No. 2 [in Chinese].
- Zhu Genxing, Ge Manchu, and Lou Yiping, 1989, "The Inverse and Hybrid Problems Research of Axial, Mixed and Centrifugal Turbomachine Along S_2 Surface With the Velocities Distribution Given for the Hub and Casing of Meridional Section," *Journal of Engineering Thermophysics*, Vol. 10, No. 3 [in Chinese].

Three-Dimensional Rotational Flow in Transonic Turbomachines: Part II—Full Three-Dimensional Flow in CAS Rotor Obtained by Using a Number of S_1 and S_2 Stream Filaments

Wu Chung-Hua

Zhao Xiaolu

Qin Lisen

Chinese Academy of Sciences,
Beijing, People's Republic of China

The general theory for three-dimensional flow in subsonic and supersonic turbomachines has recently been extended to transonic turbomachines. In this paper, which is Part II of the study, quasi- and full three-dimensional solutions of the transonic flow in the CAS rotor are presented. The solutions are obtained by iterative calculation between a number of S_1 stream filaments and, respectively, a central $S_{2,m}$ stream filament and a number of S_2 stream filaments. Relatively simple methods developed recently for solving the transonic flow along S_1 and S_2 stream filaments are used in the calculation. The three-dimensional flow fields in the CAS rotor obtained by the present method are presented in detail with special emphasis on the converging process for the configuration of the S_1 and S_2 stream filaments. The three-dimensional flow fields obtained in the quasi- and full three-dimensional solutions are quite similar, but the former gives a lower peak Mach number and a smaller circumferential variation in Mach number than the latter. A comparison between the theoretical solution and the Laser-2-Focus measurement shows that the character of the transonic flow including the three-dimensional shock structure is in good agreement, but the measured velocity is slightly higher than the calculated one over most of the flow field.

Introduction

A general theory for steady three-dimensional flow of a nonviscous gas in subsonic and supersonic turbomachines having arbitrary hub and casing shapes was presented by Wu in the early 1950s (Wu, 1952). By investigating an appropriate combination of flow on relative streamsurfaces, the solution of the three-dimensional flow is greatly simplified into a number of solutions of two-dimensional flow. Since then, a number of quasi-three-dimensional design and analysis solutions have been obtained by iterative calculation between a number of S_1 surfaces of revolution and a single S_2 surface (see Part I of the present paper: Wu et al., 1992). Relatively few full three-dimensional solutions have been obtained by iterative calculation between a number of general S_1 and a number of general S_2 surfaces. They are the solution obtained by Krimerman and Adler (1978) for a subsonic centrifugal impeller, the solution obtained by Zhu and Wu (1983) and Wang et al. (1985) for,

respectively, a subsonic axial stator and rotor, and by Teipel and Wiedermann (1987) for a transonic centrifugal compressor diffuser. Although ultra-high-speed, large-storage computers are becoming available at large research institutions and large design offices, the calculation of full three-dimensional flow fields by a direct solution of the dynamic equations on the basis of the time-marching technique is still a very time-consuming process and very expensive. During the past few years efforts have been made at the Institute of Engineering Thermophysics, CAS, to develop relatively simple and quick methods for solving the transonic flow on S_1 and S_2 surfaces. These new methods are incorporated to carry out the iterative solution of the three-dimensional transonic flow in turbomachinery. This computing system can be put into operation on a microcomputer. (For instance, on a super-microcomputer, one calculation of an S_1 or S_2 transonic flow needs about one minute.) In Part II of the present paper, this computing system is presented and applied to solving the three-dimensional transonic flow in the CAS compressor rotor. The calculated result is compared with L2F measurements.

Contributed by the International Gas Turbine Institute and presented at the 35th International Gas Turbine and Aeroengine Congress and Exposition, Brussels, Belgium, June 11-14, 1990. Manuscript received by the International Gas Turbine Institute January 8, 1990. Paper No. 90-GT-13.

Three-Dimensional Flow in Turbomachines Obtained by Iterative Calculation Between S_1 and S_2 Streamsurfaces

Governing Equations. The calculation of the steady adiabatic, inviscid flow on S_1 and S_2 streamsurfaces is based on the following basic invariant vector form of aero-thermodynamic equations (Wu, 1952, 1965):

Continuity

$$\nabla \cdot (\rho \mathbf{W}) = 0 \quad (1)$$

Newton's Second Law of Motion

$$\mathbf{W} \times (\nabla \times \mathbf{V}) = \nabla I - T \nabla s \quad (2)$$

First Law of Thermodynamics

$$dI/dt = 0 \quad (3)$$

Second Law of Thermodynamics

$$ds/dt \geq 0 \quad (4)$$

In the preceding equations, I and s are considered as the two independent thermodynamic properties defining the thermodynamic state of the gas. The density in Eq. (1) is related to I , s , and W by

$$\rho = \rho_i \cdot \left(\frac{I + \frac{1}{2} \omega^2 r^2 - \frac{1}{2} (W)^2}{H_i} \right)^{\frac{1}{K-1}} e^{\frac{s_i - s}{R}} \quad (5)$$

Transonic Flow Along S_1 Stream Filament. In general, the S_1 surface may be twisted and have abrupt changes in shape in the shock region. The method given by Zhao (1984) for solving transonic flow on an S_1 streamsurface of revolution is extended to that on an arbitrarily twisted S_1 surface by Zhao and Qin (1987). In a three-dimensional calculation, the shape of this general S_1 surface is obtained by joining the corresponding streamlines on a number of S_2 surfaces.

For the flow calculation on a general S_1 streamsurface, x^1 and x^2 coordinates were chosen on the S_1 surface and x^3 on the radial direction (Fig. 1). Then,

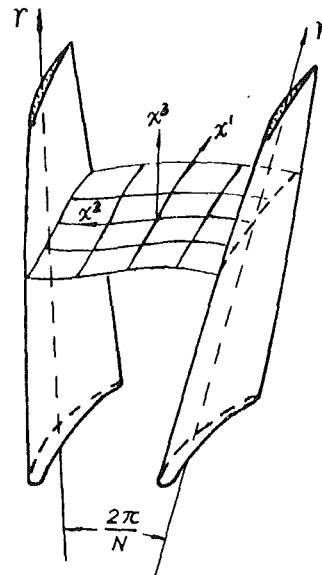


Fig. 1 General S_1 streamsurface

$$\mathbf{e}_1 = \frac{\partial \mathbf{r}}{\partial x^1} \mathbf{r} + \frac{\partial \mathbf{z}}{\partial x^1} \mathbf{z} + r \frac{\partial \varphi}{\partial x^1} \boldsymbol{\varphi}$$

$$\mathbf{e}_2 = \frac{\partial \mathbf{r}}{\partial x^2} \mathbf{r} + \frac{\partial \mathbf{z}}{\partial x^2} \mathbf{z} + r \frac{\partial \varphi}{\partial x^2} \boldsymbol{\varphi}$$

$$\mathbf{e}_3 = \frac{\partial \mathbf{r}}{\partial \psi} \mathbf{r} \quad (6)$$

where

$$\frac{\partial \mathbf{r}}{\partial \psi} = \boldsymbol{\tau}_r.$$

The continuity equation and the principal stream function equation in conservative form are, respectively,

$$\frac{\partial}{\partial x^1} (\rho \tau \sqrt{a_{22}} \sin \theta_{12} W^1) + \frac{\partial}{\partial x^2} (\rho \tau \sqrt{a_{11}} \sin \theta_{12} W^2) = 0 \quad (7)$$

Nomenclature

a_{ij} = covariant metric tensor of x^i coordinate system

\mathbf{e}_i = base vector of x^i coordinate system

\mathbf{e}^i = reciprocal base vector of x^i coordinate system

g = Jacobian of matrix g_{ij}

g_{ij} = covariant metric tensor of x^i coordinate system

g^{ij} = contravariant metric tensor of x^i coordinate system

H = absolute stagnation enthalpy per unit mass of gas = $h + v^2/2$

h = enthalpy per unit mass of gas

i = rothalpy per unit mass of gas = $h - u^2/2$

I = relative stagnation rothalpy per unit mass of gas = $i + W^2/2$

l, φ = orthogonal coordinates on surface of revolution

\mathbf{n} = unit vector normal to the stream surface

p = pressure

q = heat transfer to unit mass of gas per unit time

r, φ, z = cylindrical coordinates

R = gas constant

s = entropy per unit mass of gas

T = absolute temperature of gas

t = time or blade thickness

\mathbf{U} = blade velocity at radius r

\mathbf{V} = absolute velocity of gas

$V_{\theta r}$ = angular momentum of gas about axis of rotation

\mathbf{W} = relative velocity of gas

w^i = contravariant component of relative velocity of gas

w_i = covariant component of relative velocity of gas

W^i = physical component of \mathbf{W} tangent to x^i

x^i = general curvilinear coordinates

α = relaxation factor

β = angle between \mathbf{W} and its meridional component

η_s = isentropic efficiency

θ_{ij} = angle included by the coordinate lines x^i and x^j

μ = coefficient of artificial viscosity

$\tilde{\rho}$ = artificial density

$\sigma = \tan^{-1} dr/dz$

τ = thickness of stream filament

ψ = stream function

ω = angular speed of blade

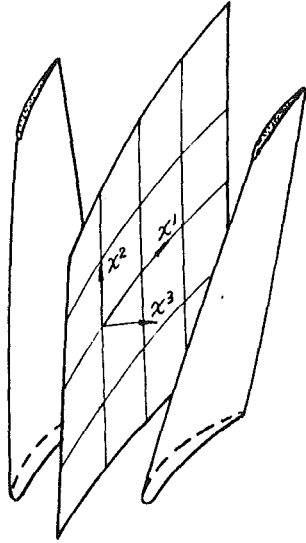


Fig. 2 Surface coordinate system for S_2

and

$$\frac{\partial}{\partial x^2} \left(A_1 \frac{1}{\rho} \frac{\partial \Psi}{\partial x^2} - A_2 \frac{1}{\rho} \frac{\partial \Psi}{\partial x^1} \right) - \frac{\partial}{\partial x^1} \left(A_2 \frac{1}{\rho} \frac{\partial \Psi}{\partial x^2} - A_3 \frac{1}{\rho} \frac{\partial \Psi}{\partial x^1} \right) = A_4 \quad (8)$$

where

$$A_1 = \sqrt{a_{11}} / (\sqrt{a_{22}} \sin \theta_{12} r) \quad A_2 = \cos \theta_{12} / (\sin \theta_{12} r)$$

$$A_3 = \sqrt{a_{22}} / (\sqrt{a_{11}} \sin \theta_{21} r)$$

$$A_4 = \frac{\sqrt{a_{11}}}{W^1} \left(\frac{\partial I}{\partial x^2} - T \frac{\partial s}{\partial x^2} \right) - 2 \sqrt{D(z, \varphi) / D(x^1, x^2)} \omega \cos(\mathbf{n}, \mathbf{r})$$

These equations are only slightly different from those derived for solving the transonic flow on an S_1 streamsurface of revolution (Zhao, 1984).

In order to stabilize the solution of the mixed-type partial differential equation, artificial compressibility (Hafez et al., 1979) is introduced to the density term by

$$\tilde{\rho} = \rho - \mu \rho_s \Delta s \quad (9)$$

with

$$\mu = \max \left[0, c \left(1 - \frac{1}{M^2} \right) \right]$$

Discretizing Eq. (8) leads to the following matrix equation:

$$[M][\psi] = [P] \quad (10)$$

where the coefficient matrix $\{M\}$ is a function of $\tilde{\rho}$. In order that the coefficient matrix $\{M\}$ is not to be decomposed in every cycle of iteration, Eq. (10) is transformed into (see Zhao, 1984, for details)

$$[M'][\Delta\psi]^{(n+1)} = \tilde{\rho}[R]^{(n)} \quad (11)$$

so that the decomposition of $\{M\}$ has to be done only once in the first cycle. The subsequent solutions are obtained with relatively quick forward and backward substitutions. Equation (8) is rewritten in the following form for calculating W :

$$\frac{\partial}{\partial x^2} (\sqrt{a_{11}} W^1) = \frac{\partial}{\partial x^1} \left(A_2 \frac{1}{\tilde{\rho}} \frac{\partial \Psi}{\partial x^2} - A_3 \frac{1}{\tilde{\rho}} \frac{\partial \Psi}{\partial x^1} \right) + \frac{\partial}{\partial x^2} \left(A_2 \frac{1}{\tilde{\rho}} \frac{\partial \Psi}{\partial x^1} \right) + A_4 \quad (12)$$

The terms on the right-hand side are updated consistently with

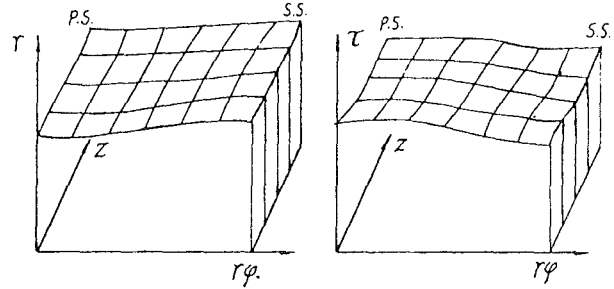


Fig. 3 Variation of r and τ for a general S_1 surface

the calculation of ψ . This integration procedure is needed only across the sonic line, but it may be used everywhere. It proceeds from an assumed value of W on an initial curve. The distribution of ρ and W along the curve is obtained from the Σ - ϕ plot given by Wu (1952), as in the case of subsonic flow. Then W is updated by

$$W^2 / W^1 = -(\sqrt{a_{11}} \partial \Psi / \partial x^1) / (\sqrt{a_{22}} \partial \Psi / \partial x^2) \quad (13)$$

Knowing W^1 and W^2 , W and ρ are determined, respectively, by the following equation:

$$W = [(W^1)^2 + (W^2)^2 + 2W^1W^2 \cos \theta_{12}]^{1/2} \quad (14)$$

and Eq. (5).

The midchannel streamline can be conveniently chosen to be the initial line. A sketch of the radius and τ of an S_1 surface near the blade tip is given in Fig. 3.

Transonic Flow Along S_2 Stream Filament. For a three-dimensional design problem, a desirable distribution of the angular momentum $V_\theta r$, rather than the shape of S_{2m} is usually prescribed. It is then convenient to choose the x^1 and x^2 coordinates on the meridional plane. The solution of the flow on the S_{2m} surface as well as the shape of the S_{2m} surface are obtained by the use of the special partial derivatives following the motion on the surface. (See Fig. 7 of Part I (Wu et al., 1992).)

After the first cycle of calculation, the shape of the S_2 surface and the circumferential filament thickness τ_ϕ are defined by the streamlines obtained during the S_1 calculation. The S_2 calculation is then a direct calculation. But it is possible to treat the direct problem as an inverse problem by taking the $V_\theta r$ obtained in the S_1 calculation as the input value to the S_2 calculation. However, when the meridional velocity component is supersonic, the principal stream function equation becomes hyperbolic even though $V_\theta r$ is prescribed.

In the solution of the S_2 direct problem, the S_2 surface is given. It is convenient to choose x^1 and x^2 coordinates on the S_2 surface and x^3 coordinate perpendicular to it (Fig. 2). The tensor elements of the coordinate system are determined as follows: Let $dx^3 = 1$, then $\sqrt{g_{33}} = \tau_n$ and the governing equation of the transonic flow along the S_2 filament is

$$\frac{\partial}{\partial x^2} \left(C_1 \frac{1}{\rho} \frac{\partial \Psi}{\partial x^2} - C_2 \frac{1}{\rho} \frac{\partial \Psi}{\partial x^1} \right) - \frac{\partial}{\partial x^1} \left(C_2 \frac{1}{\rho} \frac{\partial \Psi}{\partial x^2} - C_3 \frac{1}{\rho} \frac{\partial \Psi}{\partial x^1} \right) = C_4 \quad (15)$$

where

$$C_1 = \sqrt{g_{11}} / (\sqrt{g_{22}} \sin \theta_{21} \tau_n)$$

$$C_3 = \sqrt{g_{22}} / (\sqrt{g_{11}} \sin \theta_{21} \tau_n)$$

$$C_2 = \cos \theta_{21} / (\sin \theta_{21} \tau_n)$$

$$C_4 = 2\sqrt{g_{11}} \sqrt{g_{22}} \omega^3 \sin \theta_{12} + \frac{\sqrt{g_{11}}}{W^1} \left(\frac{\partial I}{\partial x^2} - T \frac{\partial s}{\partial x^2} \right)$$

It is seen that Eq. (15) contains only two unknowns ψ and ρ , and is, therefore, simpler than the one, which contains the unknown $V_{\theta r}$ term on the right-hand side of the equation when the equation is expressed with respect to a meridional coordinate system. To solve this equation, the traditional ρ - ψ iteration procedure is applied. The convergence rate of iteration seems to be faster than the ρ - ψ - $V_{\theta r}$ iterative process. Again the artificial compressibility method is used to solve the mixed-type partial differential equation for the S_2 transonic flow.

Equation (15) is also written as a velocity gradient equation

$$\frac{\partial}{\partial x^2} (\sqrt{a_{11}} W^2) = \frac{\partial}{\partial x^1} \left(C_2 \frac{1}{\rho} \frac{\partial \Psi}{\partial x^2} - C_3 \frac{1}{\rho} \frac{\partial \Psi}{\partial x^1} \right) + \frac{\partial}{\partial x^2} \left(C_2 \frac{1}{\rho} \frac{\partial \Psi}{\partial x^1} \right) + C_4 \quad (16)$$

Then the variation of W from hub to tip is determined by integrating this equation. Since in most transonic fans and compressors, the flow is subsonic along the hub, the initial curve is conveniently chosen there. W^1 , W^2 , W_ϕ , W , and ρ are calculated in the same way as in transonic S_1 flow and Eq. (5).

Steps for Full Three-Dimensional Solution

Direct Problem. For axial turbomachinery, it is desirable to start computation on S_1 surfaces (assumed to be surfaces of revolution) and followed by computation on S_2 surfaces. The geometry of the S_2 surface is obtained from the solution of the flow on S_1 surfaces. In the second cycle, the geometry of the S_1 surfaces is obtained from the solution of the flow on S_2 surfaces. This process is carried on until convergence is reached.

In radial and mixed-flow types of turbomachinery the S_2 surface is strongly guided by the blades and the three-dimensional computation may be started on the S_2 surface.

Inverse Problem. If the three-dimensional shape of the blade is specified by the designer, the calculation is just like that in a direct problem. The designer may modify the blade shape according to the solution he obtained, but this is rather time-consuming. A more practical way of three-dimensional design is to prescribe some desirable variation of a key flow variable, such as the angular momentum $V_{\theta r}$ on the S_{2m} surface. After the solution on the S_{2m} is obtained, a standard blade section can be selected on a conical surface, which approximates the S_1 surface over the blade region. Alternatively, the blade section may be designed on the S_1 surface by some theoretical inverse method. The blade sections are then stacked with due regard to stresses. The three-dimensional blade thus constructed can be checked by a full three-dimensional direct-problem calculation if desired. It is believed that a quasi-three-dimensional blade design is adequate for most situations and that a quasi-three-dimensional design followed by a full three-dimensional solution of the direct problem for the more demanding situation is the practical way of blade design based on three-dimensional flow.

In the full three-dimensional calculation, the boundary condition used for each step of calculation is the same as in the quasi-three-dimensional calculation, except for the periodicity condition on the S_1 surface. The S_1 surfaces, especially those located in the midspan region, are generally twisted. Downstream of the blade there is a trailing vortex, which cannot be taken into account in the present calculation. Just downstream of the trailing edge, the Dirichlet boundary condition is used, i.e., the values of stream function ψ on the two boundary lines (stagnation streamlines) are directly given in the calculation. It is found that the twist of the S_1 surfaces diminishes quickly downstream of the blade. Only a short distance away from the blade, the S_1 surface becomes the surface of revolution and the usual periodicity condition can be applied again.

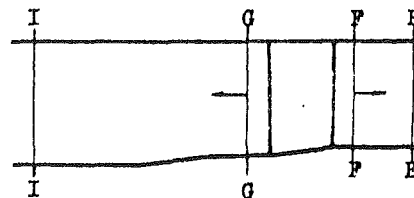


Fig. 4 Far upstream and far downstream boundary conditions

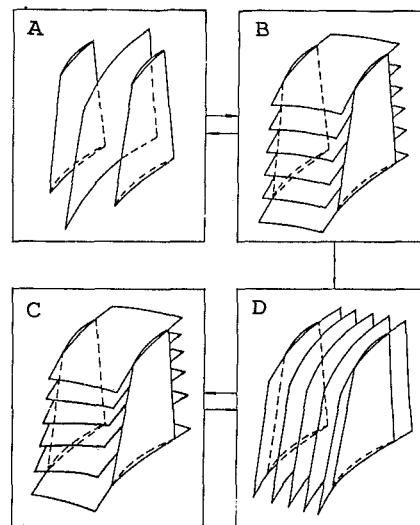


Fig. 5 Flow chart of three-dimensional solution

The far upstream and far downstream boundary condition required in an S_1 calculation is not readily available when there are blade rows upstream and downstream. For a quasi-three-dimensional solution, the far upstream and downstream condition has been obtained in the following manner: Starting from the station immediately ahead of (G-G) and behind (F-F) the blade row (Fig. 4) and using the flow condition at these stations, the S_2 calculation is performed, first in the direction upstream of the inlet station I-I and then downstream of the outlet station E-E. Any blade row in the flow passage is ignored. The flow conditions obtained at I-I and E-E are then used as the boundary conditions to carry out calculations for S_1 flow, passing through the blade passage. In this way the flow conditions at stations GG and FF determined in the original S_{2m} calculation are preserved in the following S_1 calculation. This method can also be used for the full three-dimensional calculation.

A Compact Three-Dimensional Computing System. A compact three-dimensional computing system has been constructed by incorporating into the system the following two codes: (1) a transonic S_1 code with x^1 and x^2 coordinates placed on the general S_1 surface, (2) an S_2 code with x^1 and x^2 coordinates placed on the meridional surface and with $V_{\theta r}$ considered as the given value for the S_2 surface. These two codes together can perform the four functions necessary to carry out full three-dimensional solutions as shown in Fig. 5. Each of the four functions can be combined in different ways to carry out different kinds of solutions. For instance, a quasi-three-dimensional blade design calculation needs iteration only between A and B. If the design is to be followed by a full three-dimensional calculation of the blade, iteration between C and D will be performed. For the three-dimensional solution of a direct problem of axial machines, A and B or A, B, C, D may be used. For radial and mixed-flow machines, the calculation may proceed in the order of B-A-B-... or B-C-B-C-.... In the computer system, both S_1 and S_2 codes can handle the subsonic

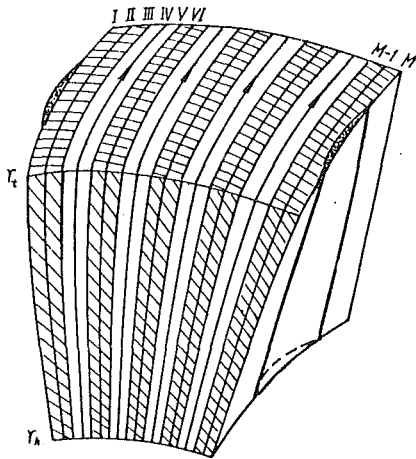


Fig. 6 S_2 stream surfaces and S_2 stream filaments

and transonic (as long as the meridional velocity is subsonic) flow, and the S_1 code can handle the general S_1 surface as well as the special case of S_1 surface of revolution.

The quasi-three-dimensional solution, which is obtained by iterative calculation between a number of S_1 surfaces of revolution and a single $S_{2,m}$ surface, can be considered as the solution obtained for the flow along a number of S_1 stream filaments of revolution, which extend from hub to casing. Now, the full three-dimensional solution, which is obtained by iterative calculation between a number of S_1 surfaces and a number of S_2 surfaces, can be considered as the solution obtained for the flow along a number of general S_1 stream filaments, which extend from hub to casing, as well as the solution obtained for the flow along a number of S_2 stream filaments, which extend from blade to blade (Fig. 6).

Three-Dimensional Flow In the CAS Transonic Rotor and Comparison With L2F Measurements

CAS Transonic Rotor Experimental Investigation. For basic investigation of a transonic compressor, a single-stage research compressor was designed and manufactured in cooperation with Shenyang Aeroengine Company. The compressor was designed for a stagnation pressure ratio of 1.5 and an isentropic efficiency of 0.85. The rotor tip speed is 400 m/s at the design point. The inlet hub-to-tip ratio is 0.4 and the corrected mass flow per unit frontal area is 188 kg/m²·s. The average inlet Mach number is 0.616. The aerodynamic design of the compressor is basically the same as that described herein for the quasi-three-dimensional design. The design requirements are prescribed on the $S_{2,m}$ surface, and the blade sections are designed on S_1 surfaces of revolution. The theoretical method of calculating transonic flow on an S_1 surface was not available at that time and the shock model given by Miller et al. (1961) was employed. The overall performances of the stage measured at Shenyang Aeroengine Company and at the Institute of Engineering Thermophysics, CAS, agree with each other. Both the measured pressure ratio and isentropic efficiency at the design point exceed the design value. The theoretical calculation was compared with the Laser-2-Focus measurement made at IET. For overall performance, L2F measurements were only made at the inlet and outlet stations. At the inlet station data were taken only at one circumferential position, whereas at the outlet station data were taken at 16 circumferential positions. Detailed L2F measurements were first made for the peak efficiency point at 70 percent design speed. The equivalent mass flow is 144.8 kg/m²·s, the stagnation pressure ratio is 1.21, and the isentropic efficiency is 93.2 percent. The flow speed and the flow angle were recorded at 8 axial stations, 6 to 14 radial positions, and 10 to 16

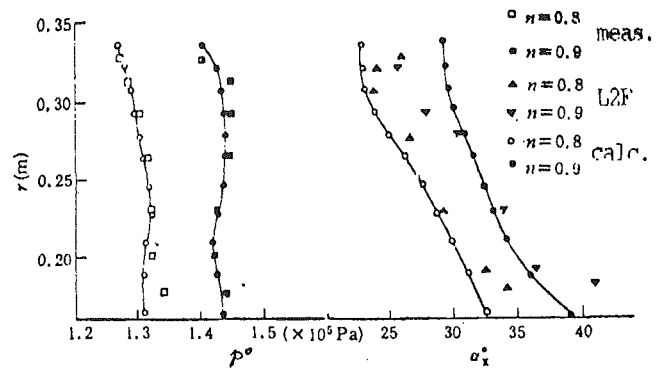


Fig. 7 Radial distributions of p^0 and α at outlet

circumferential positions. All the measuring points are on the S_1 or the S_2 stream surfaces obtained in the design calculation. At 80 and 90 percent design speed, supersonic flow appears in the rotor passage. The relative Mach numbers at the rotor tip are, respectively, 1.08 and 1.18. The operating point is near the maximum efficiency point. The equivalent mass flow per unit frontal area, pressure ratio, and efficiency obtained by torque measurement are, respectively, 164 and 172 kg/m²·s, 1.275 and 1.427, 0.93 and 0.92.

Quasi-Three Dimensional Solution for Transonic Flow in CAS Rotor.

The quasi-three-dimensional solutions of transonic rotor are obtained for 80 and 90 percent design speed. The stagnation pressure and the absolute flow angle, which were measured respectively by Setra capacitance transistor and L2F velocimeter, are taken as the outlet boundary conditions. The other main input data are: flow path (in meridional plane); blade geometry (coordinates given on S_1 surface or on manufacturing templates); inlet pressure and temperature, rotor speed, mass flow, and mass flow coefficient.

The first step is solution of the flow angle on a $S_{2,m}$ surface about midway between two adjacent blades. A computer code with given absolute outlet flow angle and rotor efficiency is used for this purpose. The isentropic efficiency of the rotor is determined by the torque measurement, and the radial distribution of rotor efficiency is calculated with the stagnation pressure and temperature measurements. With the absolute velocity and flow angle measured by an L2F velocimeter, the angular momentum $V_{\theta}r$ is calculated. In the procedure of calculation, the outlet flow angle α and radial distribution of efficiency η_s are updated successively, until $V_{\theta}r$ converged and the calculated pressure p^0 is in agreement with the experiment. This process usually takes three to five cycles. The set of values of radial distribution of p^0 , α , $V_{\theta}r$ at the outlet station and the rotor efficiency η_s are to be used for three-dimensional calculation of the internal flow field and is to be compared with the L2F measured internal flow field. Figure 7 shows the calculated values as compared to the measured values at the outlet station. From this solution of $S_{2,m}$, the geometry of the eleven S_1 surfaces of revolution and the variation of the S_1 stream filaments are obtained. The coordinates of the corresponding blade surface are calculated by interpolation. After the solutions of the flow on eleven S_1 surfaces are obtained, a new $S_{2,m}$ surface together with the corresponding variations of stream filament thickness and $V_{\theta}r$ on the surface are obtained. In both cases, six iterations are required to reach a convergence level of 5 percent.

The converging process in the 90 percent design speed case is illustrated with the variations of the thickness of the S_1 filament No. 10 in Fig. 8. The angular momentum $V_{\theta}r$ along streamline No. 2 and No. 10 on the $S_{2,m}$ surface during iteration are shown in Fig. 9. In Fig. 10, the relative Mach numbers

along the streamlines obtained on intersection of S_1 and $S_{2,m}$ surfaces are shown. The closeness between the two values shows the degree of consistency as well as convergence reached in the solution.

Table 1 gives the geometry and major flow parameters on six S_1 stream filaments obtained in the solution.

In the table, values of r_0 , $r_{0.5}$, r_1 , and τ/τ_0 show clearly the quasi-three-dimensional nature of the S_1 streamsurfaces. The flow on the S_1 surface, although mathematically two-dimensional, cannot be obtained by calculating flow on a two-dimensional plane or on a cylindrical surface.

The circumferential variations of relative Mach number at six axial stations and on five S_1 surfaces are shown in Fig. 11. The streamwise variation of the angular momentum $V_{\theta}r$ and

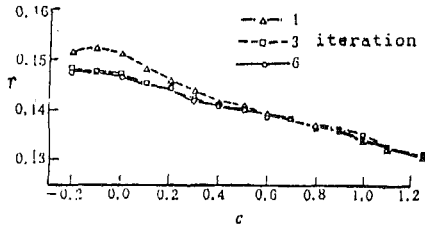


Fig. 8 Variation of τ of S_1 filament No. 10

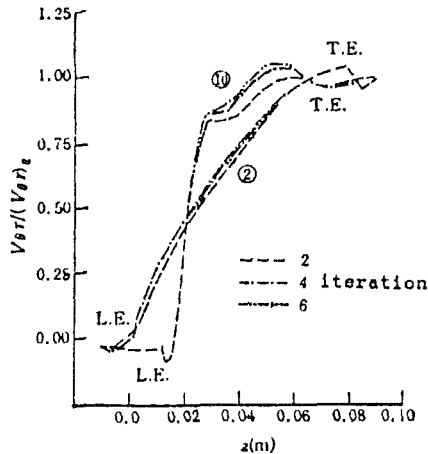


Fig. 9 Variation of $V_{\theta}r$ on S_{2m}

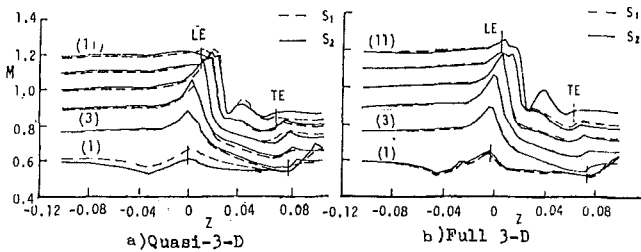


Fig. 10 Relative Mach number along intersecting streamline obtained on S_1 and on S_{2m}

the S_2 filament thickness at the mean streamline on six S_1 streamsurfaces are shown respectively in Figs. 12 and 13. On the S_1 surface near the hub, the flow is subsonic and these curves resemble those previously obtained in subsonic compressor. But for the S_1 surface located in the region where a passage shock exists, the curves are greatly affected by the shock.

Full Three-Dimensional Solution for Transonic Flow in CAS Rotor. A full three-dimensional solution can be made by going into the multi- S_2 calculation immediately after the completion of the multi- S_1 calculation in the first cycle of iteration (A-B-C in Fig. 5). But in the present calculation multi- S_2 calculation is carried out after the completion of the quasi-three-dimensional solution (A-B-A-B in Fig. 5). It is found that the iterative calculation between six (in the first four cycles) to eleven (in the last two cycles) S_1 surfaces and seven S_2 surfaces (Fig. 14) reaches an acceptable level of convergence and consistency after six cycles of iteration. There are 52 (21 in the blade region) and 11 stations, respectively, along x^1 and x^2 coordinates on each S_1 surface, and 52 and 11 stations, respectively, along x^1 and x^2 coordinates on each S_2 surface. The solution of the flow on the seven S_2 surfaces employed in the iterative calculation is based on the "inverse type" solution, i.e., $V_{\theta}r$ obtained in the S_1 solution is taken as the input value to the S_2 surface flow. The S_2 surface adjacent to the blade surface is placed at a short distance from it, and the mass flow between them is 5 percent of the total flow. The S_1 computer code and the S_2 computer code are connected through two interpolation codes so that $V_{\theta}r$ distribution and S_2 filament thickness obtained in the solution of flow on S_1 surfaces are interpolated for input values to different S_2 surfaces. Similarly, the geometry of the S_1 surfaces and the filament thickness τ obtained in the solution of flow on S_2 surfaces are interpolated for input values to the S_1 surfaces.

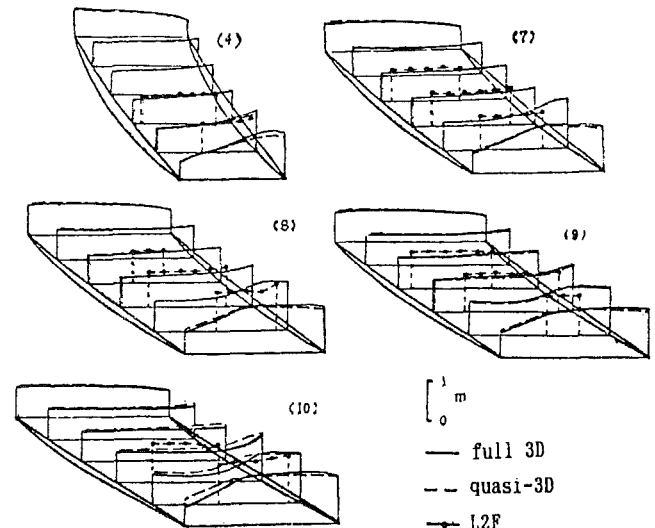


Fig. 11 Circumferential variations of Mach number

Table 1 Major parameters on six S_1 stream filaments of revolution

S	M	β_1 deg	β_2 deg	Coordinate r, m			τ/τ_0			$\tau_{1.0}$ τ_0	σ deg
				$\bar{c}=0$	$\bar{c}=.5$	$\bar{c}=1$	$\bar{c}=0$	$\bar{c}=.5$	$\bar{c}=1$		
11	1.180	-66.2	-56.2	.3426	.3390	.3354	1.000	1.014	.943	.943	-7.98
9	1.089	-64.2	-51.2	.3133	.3102	.3078	1.092	1.021	.979	.896	-5.49
7	.993	-61.3	-45.7	.2807	.2801	.2788	1.234	1.121	1.071	.868	-1.73
5	.883	-57.4	-38.5	.2434	.2460	.2465	1.404	1.305	1.206	.859	2.61
3	.758	-51.2	-27.6	.1986	.2055	.2096	1.730	1.589	1.433	.929	8.62
1	.609	-38.7	3.8	.1370	.1499	.1628	2.638	2.461	1.929	.731	18.41

$\tau_0 = .001410$

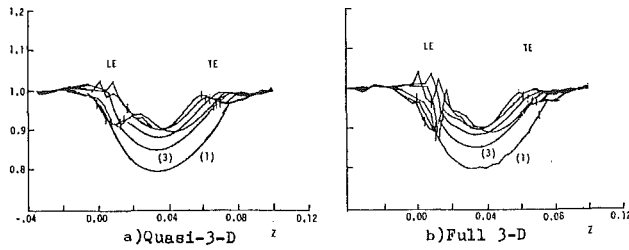


Fig. 12 Variation of S_2 filament thickness along mean streamlines on six S_1 surfaces

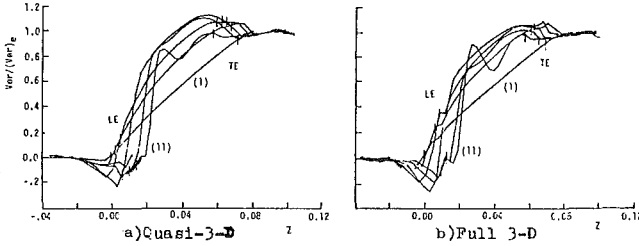


Fig. 13 Variation of V_{θ}/r along mean streamlines on six S_1 surfaces

It is found during calculation that the twist of the S_1 surface in the radial direction is relatively large at the blade leading edge and relatively small at the blade trailing edge (Fig. 15). For instance, the radii of S_1 surface No. 5 at the blade leading edge are, respectively, 0.2429 m at the pressure surface and 0.2465 m at the suction surface, a difference of 0.0036 m, or 1.48 percent. But at the trailing edge, they are, respectively, 0.2469 m and 0.2479 m, only a difference of 0.001 m, or 0.4 percent. The flow angle at the outlet station is given by the solution of S_2 surface flow.

Similar to the quasi-three-dimensional solution, the entropy increases across the rotor at different radii are calculated according to the rotor efficiency at these radii. The variation of entropy increases along the x^1 direction are obtained by considering that (1) there is no entropy increase in the flow up to shock line, (2) entropy increases abruptly across the shock, and (3) from there on it increases linearly to the outlet value. In order to be consistent, the value of entropy used in the S_1 calculation is the same as in the S_2 calculation at the same grid point. Because of lack of data on how entropy varies from blade to blade, the circumferential variation of entropy is considered neither on the S_1 surface, nor on the different S_2 surfaces.

Converging Process. Since the main difference between a quasi-three-dimensional solution and a full three-dimensional solution is whether the radius of the S_1 surface is or is not circumferentially constant, the convergence in the geometry of the S_1 surface is an indication of the convergence of the full three-dimensional solution. Table 2 lists the changes in the radii of four S_1 surfaces during iteration. The corresponding changes in S_1 filament are listed in Table 3.

Geometry of S_1 and S_2 Stream Filaments. Data in Tables 4 and 5 and Fig. 15 show that the radius of the S_1 surface increases in the circumferential direction at the blade leading edge, and the difference decreases toward the blade trailing edge. On the other hand, the filament thickness at the leading edge is larger near the pressure surface at large radius and larger near the suction surface at small radius. The difference decreases toward the trailing edge. The complicated configuration of the S_1 stream filament is a combined result of the flow vorticity and the passage shock. In subsonic flow, the relative circumferential difference in the radius is found to be about 0.2 percent, but in transonic flow the maximum value

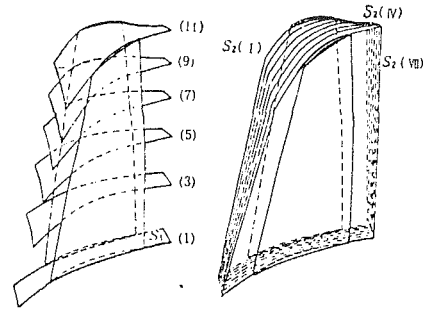


Fig. 14 Six general S_1 and seven general S_2 stream surfaces

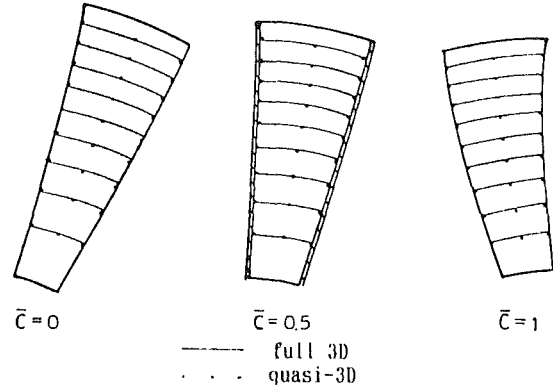


Fig. 15 Intersection of S_1 stream surfaces with three spanwise surfaces

is about 1.3 percent, an order of magnitude higher. The geometry of the S_1 stream filaments is given in Table 6.

Three-Dimensional Flow Field. The three-dimensional geometry of the S_1 stream filaments is the crux of the flow in the transonic rotor, because this geometry and the blade section lying in the filament determine the flow along these filaments, and consequently the flow over the whole channel. The flows determined on these S_1 filaments are shown in Fig. 16 in terms of constant Mach number contours. They are drawn for flow fields including four stations upstream and three stations downstream of the blade. The major geometry and inlet and outlet flow conditions are listed in Table 7, in which a and b denote the two corners at the upstream station, e and f at midpoint of chord length, c and d at the downstream station. r_c/r_a , τ_c/τ_a and r_d/r_b , τ_d/τ_b denote contraction in r and filament thickness τ , respectively, on the two sides. The inlet Mach number varies from 0.6 at the hub to 1.25 at the tip. The supersonic region begins to appear on surface 3. On surface 7 a bow wave appears and extends to the suction surface as a passage shock. On the tip surface 11, the passage shock hits the suction surface at about 50 percent chord point.

Similarly, the three-dimensional geometry of the S_2 stream filaments and the meridional wall shape determine the flow along these filaments, and consequently the flow over the whole channel. Figure 17 shows the constant Mach number contours on the S_2 filaments. It may be noticed that, whereas in the quasi-three-dimensional solution only flow on one S_2 surface (the S_{2m} surface), which took part in the iteration, is directly obtained in the solution, in full three-dimensional solution the flow on all S_2 surfaces, which took part in the iteration, are directly obtained in the solution. It is seen that the circumferentially uniform flow at the inlet station becomes nonuniform near the blade leading edge, where tip Mach number varies from 1.18 on S_2 (I) to 1.21 on S_2 (VII). It becomes uniform again at three stations downstream of the blade. From the pressure surface of one blade toward the suction surface of the adjacent blade, the intersection line of the shock and the surface becomes longer and moves downstream. The flow condition on S_2 (I) and (VII) should be particularly useful in

Table 2 Changes in radius of general S_1 surfaces during iteration

Sta.	Cycle	$S_2(I)$			$S_2(IV)$			$S_2(VII)$		
		21	31	41	21	31	41	21	31	41
9	1	.3111	.3102	.3083	.3125	.3102	.3077	.3127	.3098	.3070
	5	.3118	.3101	.3081	.3131	.3108	.3082	.3137	.3108	.3080
	6	.3118	.3101	.2781	.3131	.3108	.3082	.3137	.3108	.3080
7	1	.2784	.2796	.2793	.2807	.2806	.2792	.2814	.2802	.2792
	5	.2791	.2794	.2790	.2811	.2804	.2794	.2823	.2806	.2793
	6	.2791	.2794	.2790	.2811	.2805	.2794	.2823	.2806	.2794
5	1	.2425	.2453	.2473	.2451	.2476	.2481	.2471	.2483	.2490
	5	.2430	.2453	.2469	.2445	.2468	.2476	.2466	.2475	.2480
	6	.2429	.2453	.2469	.2445	.2467	.2476	.2465	.2474	.2479

Table 3 Changes in filament thickness of general S_1 surfaces (τ/τ_0)

Sta.	Cycle	$S_2(I)$			$S_2(IV)$			$S_2(VII)$		
		21	31	41	21	31	41	21	31	41
9	1	1.143	1.054	.986	1.096	1.035	.987	1.087	1.050	.987
	5	1.126	1.054	.986	1.084	1.039	.977	1.061	1.037	.955
	6	1.126	1.052	.985	1.084	1.037	.977	1.062	1.036	.955
7	1	1.189	1.131	1.063	1.174	1.087	1.033	1.127	1.059	.989
	5	1.201	1.136	1.075	1.199	1.120	1.062	1.166	1.103	1.034
	6	1.202	1.138	1.075	1.200	1.121	1.062	1.167	1.104	1.035
5	1	1.388	1.328	1.229	1.388	1.294	1.201	1.373	1.277	1.160
	5	1.366	1.298	1.213	1.401	1.295	1.204	1.374	1.279	1.158
	6	1.367	1.299	1.213	1.402	1.296	1.204	1.375	1.279	1.159

$\tau_0 = 0.001410$

Table 4 Coordinate r of S_1 streamsurfaces

Sta.	$S_1(7)$					$S_1(4)$				
	$S_2(I)$	$S_2(II)$	$S_2(III)$	$S_2(IV)$	$S_2(V)$	$S_2(I)$	$S_2(II)$	$S_2(III)$	$S_2(IV)$	$S_2(V)$
17	.2792	.2802	.2806	.2811	.2815	.2201	.2205	.2214	.2222	.2229
21	.2792	.2800	.2811	.2820	.2825	.2229	.2230	.2239	.2248	.2259
25	.2792	.2800	.2806	.2812	.2819	.2243	.2248	.2256	.2263	.2268
33	.2795	.2802	.2803	.2804	.2802	.2271	.2278	.2284	.2287	.2290
41	.2789	.2793	.2793	.2793	.2794	.2294	.2299	.2301	.2303	.2307
45	.2784	.2785	.2785	.2785	.2787	.2304	.2305	.2306	.2305	.2308

Table 5 Thickness of S_1 stream filaments (τ/τ_0)

Sta.	$S_1(11)$ (Filament of revolution)					$S_1(7)$ (General filament)				
	$S_2(I)$	$S_2(II)$	$S_2(III)$	$S_2(IV)$	$S_2(V)$	$S_2(I)$	$S_2(II)$	$S_2(III)$	$S_2(IV)$	$S_2(V)$
16	1.026	1.017	1.008	1.001	.995	1.251	1.262	1.253	1.246	1.239
21	1.054	1.043	1.021	1.007	.996	1.202	1.209	1.200	1.187	1.167
31	1.028	.986	.970	.957	.957	1.138	1.130	1.121	1.114	1.104
41	.954	.946	.954	.957	.968	1.075	1.067	1.062	1.058	1.052
46	.929	.928	.929	.929	.928	1.042	1.039	1.038	1.037	1.035
Sta.	$S_1(4)$ (General filament)					$S_1(1)$ (Filament of revolution)				
	$S_2(I)$	$S_2(II)$	$S_2(III)$	$S_2(IV)$	$S_2(V)$	$S_2(I)$	$S_2(II)$	$S_2(III)$	$S_2(IV)$	$S_2(V)$
16	1.643	1.653	1.653	1.652	1.647	3.497	3.488	3.542	3.592	3.695
21	1.502	1.533	1.546	1.557	1.543	2.876	2.872	2.955	3.053	3.172
31	1.418	1.431	1.430	1.429	1.121	2.613	2.603	2.662	2.709	2.738
41	1.317	1.316	1.316	1.306	1.297	1.962	2.055	2.099	2.133	2.191
46	1.255	1.256	1.255	1.254	1.251	1.692	1.703	1.711	1.720	1.741

$\tau_0 = 0.001410$

the investigation of boundary layer flow along the blade surfaces.

Using data obtained on these two families of stream surfaces, a three-dimensional view of the shock can easily be constructed (Fig. 18). The passage shock is seen to extend from the casing part way (about two-thirds) down to the hub. The shock is nearly normal to the suction surface and more inclined at lower radius.

Using data obtained on the S_1 and S_2 surfaces, constant Mach number contours can also be constructed on a number of a third family of surfaces, which are formed by the x^2 and x^3 coordinates, nearly normal to S_1 and S_2 surfaces at stations 1 (L.E.), 5, 9, 11, and 21 (T.E.) (Fig. 19). It is seen that in

the streamwise direction the shock intersection line becomes shorter and the circumferential gradient in Mach number becomes smaller. Between stations 11 and 21, there appears a reverse circumferential Mach number gradient in the lower part of the passage. Consequently, there is also a reverse circumferential gradient in pressure, which will affect the boundary layer along the hub wall.

Constant σ contours are obtained on five such surfaces and are shown in Fig. 20. At station $J=0$ (one station upstream of the blade), there is a significant difference circumferentially in the upper half of the flow channel. At the pressure surface side σ is +2 deg, whereas on the suction surface side, σ is -2 to -6 deg. This difference in σ means that the air is moving

Table 6 Geometry of S_2 stream filaments

	Sta.	r, m				φ, rad				τ/τ_0			
		$S_2(I)$	$S_2(III)$	$S_2(V)$	$S_2(VII)$	$S_2(I)$	$S_2(III)$	$S_2(V)$	$S_2(VII)$	$S_2(I)$	$S_2(III)$	$S_2(V)$	$S_2(VII)$
$S_1(9)$	16	.3132	.3125	.3130	.3131					1.006	1.004	1.003	1.009
	21	.3118	.3124	.3135	.3137	.224	.146	.089	.012	1.078	.975	.995	1.032
	31	.3101	.3106	.3110	.3108	.080	.020	-.043	-.111	.879	.922	.889	.910
	41	.3081	.3083	.3081	.3080	.018	-.058	-.129	-.198	1.022	.955	.996	.998
	46	.3065	.3066	.3066	.3066	-.115	-.066	-.260	-.333	1.000	1.000	1.000	1.000
$S_1(7)$	16	.2784	.2789	.2798	.2802					1.001	1.001	.999	1.000
	21	.2791	.2800	.2820	.2823	.224	.155	.088	.012	1.259	.959	1.005	1.016
	31	.2794	.2801	.2807	.2806	.075	.011	-.053	-.120	.955	.922	.890	.870
	41	.2790	.2795	.2794	.2794	-.020	-.095	-.160	-.236	.998	.983	.999	1.062
	46	.2784	.2786	.2787	.2787	-.021	-.282	-.354	-.427	1.000	1.000	1.001	1.000
$S_1(5)$	16	.2400	.2404	.2416	.2422					1.000	1.001	.999	.999
	21	.2429	.2434	.2455	.2465	.255	.154	.085	.011	1.324	.990	.960	1.054
	31	.2453	.2461	.2472	.2474	.074	.010	-.056	-.124	.962	.913	.864	.824
	41	.2469	.2474	.2477	.2479	-.035	-.108	-.180	-.252	.946	.964	1.004	1.145
	46	.2475	.2477	.2478	.2479	-.265	-.338	-.410	-.483	1.000	1.001	1.001	1.000
$S_1(3)$	16	.1933	.1934	.1946	.1935					.999	.998	.996	.999
	21	.1993	.1991	.2009	.2021	.225	.154	.083	.010	1.293	.980	.904	.957
	31	.2050	.2054	.2066	.2071	.072	.006	-.059	-.127	.958	.890	.828	.775
	41	.2097	.2102	.2108	.2113	-.042	-.114	-.187	-.259	.948	.960	.996	1.160
	46	.2119	.2121	.2123	.2125	-.305	-.377	-.450	-.522	1.000	.999	.999	.999

Table 7 Major parameters on six S_1 stream filaments

S_1	M	β_1 deg	β_2 deg	Coordinate r, m			τ/τ_0			γ_c/γ_a	τ_c/τ_a
				a	e	c	a	e	c		
				b	f	d	b	f	d		
11	1.182	-66.2	-56.3	.3426	.3394	.3335	.1446	.1449	.1299	.973	.898
				.3426	.3394	.3335	.1390	.1394	.1289	.973	.927
9	1.093	-64.1	-51.3	.3123	.3103	.3069	.1589	.1483	.1361	.983	.857
				.3134	.3108	.3071	.1534	.1461	.1353	.980	.882
7	.994	-61.3	-45.8	.2788	.2794	.2784	.1771	.1604	.1497	.999	.845
				.2808	.2806	.2788	.1728	.1557	.1480	.993	.866
5	.885	-57.4	-38.5	.2406	.2453	.2467	.2065	.1831	.1681	1.025	.814
				.2432	.2474	.2475	.2047	.1804	.1657	1.081	.809
3	.358	-51.3	-27.5	.1943	.2050	.2106	.2692	.2236	.1965	1.084	.747
				.1966	.2071	.2118	.2670	.2282	.1957	1.077	.773
1	.606	-38.8	3.8	.1254	.1486	.1674	.4840	.3648	.2373	1.335	.490
				.1254	.1486	.1674	.5171	.3681	.2594	1.335	.493

outward on the left and moving inward on the right. At station 2, the air on the upper left is now moving inward with -8 to -10 deg. Thus, there is a twist of S_1 surface between station 0 and 2. It is nearly uniform circumferentially at station 6. At station 10, there appears a sharp change in the flow direction of 2 deg over most part of the channel. At station 21, the value of σ is again nearly uniform in the circumferential direction.

The streamwise variations of filament thickness and angular momentum $V_{\theta}r$ of S_2 stream filaments (I), (IV), and (VII) are shown, respectively, in Figs. 21 and 22. As for the filament thickness τ , the variation in the subsonic hub region is similar to that of $(p-t)/p$, except that there is a high peak value at the leading edge on the S_2 (I). In the supersonic upper region, the variations on S_2 (I) and S_2 (VII) are quite different from $(P-t)/p$. On S_2 (IV), there is still some resemblance, but it has two peaks around the leading edge, indicating the effects of bow wave and passage shock.

The variation in $V_{\theta}r$ is somewhat similar. In the hub region it is only slightly modified from the usual shape in subsonic flow. But in the upper part, there is quite a peak at leading edge near the pressure surface and an overshoot at the trailing edge near the suction surface. In the tip region, there is either a two-step rise or fluctuation in the $V_{\theta}r$ variation.

Difference Between Quasi-Three-Dimensional and Full Three-Dimensional Solutions. The difference between quasi-three-dimensional and full three-dimensional solutions is entirely due to the difference in the geometry of the S_1 stream

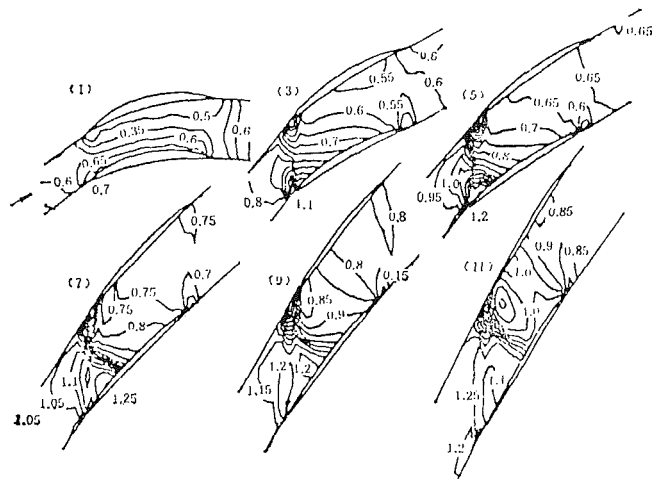


Fig. 16 Mach number contours on six S_1 surfaces

filament. Tables 1 and 7 show the major difference between the S_1 stream filaments involved in the two calculations.

First, there is some difference in the geometry of the S_{2m} in the radial coordinate and in the contraction of the filament thickness. Figure 13 shows the difference in the streamwise variation of the S_{2m} filament thickness.

It is seen that rather complicated variation in the full three-

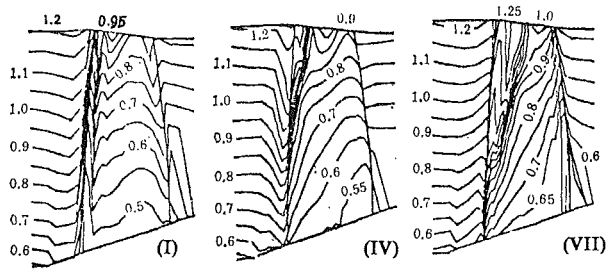


Fig. 17 Mach number contours on three S_2 surfaces

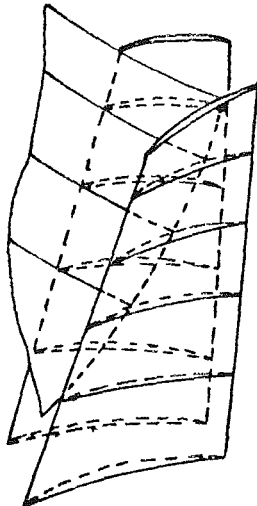


Fig. 18 Three-dimensional shock

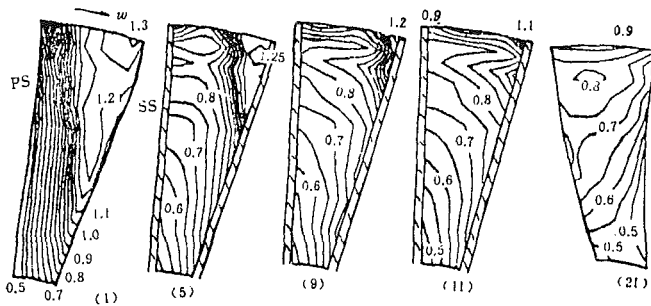


Fig. 19 Mach number contours on five spanwise surfaces

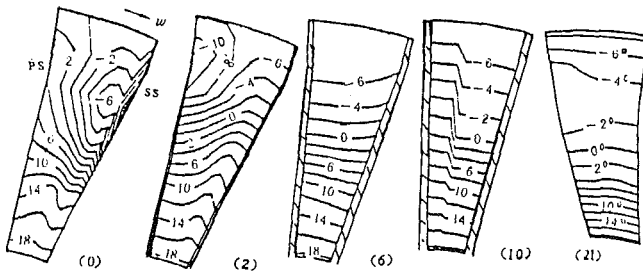


Fig. 20 Constant σ contours on five spanwise surfaces

dimensional flow is much simplified in the quasi-three-dimensional flow. The streamwise variations of this important flow variable $V_{\theta r}$ on the S_{2m} surface are compared in Fig. 12. It shows that there is a higher overshoot in the quasi-three-dimensional solution. The streamwise variations of Mach number along the intersecting streamline of the S_1 and S_{2m} surfaces obtained in the solution on the two surfaces are compared in Fig. 10. The full three-dimensional solution is seen to have reached a higher level of consistency and convergence than the quasi-three-dimensional solution. The former is seen, in general, to give a slightly higher peak Mach number than the

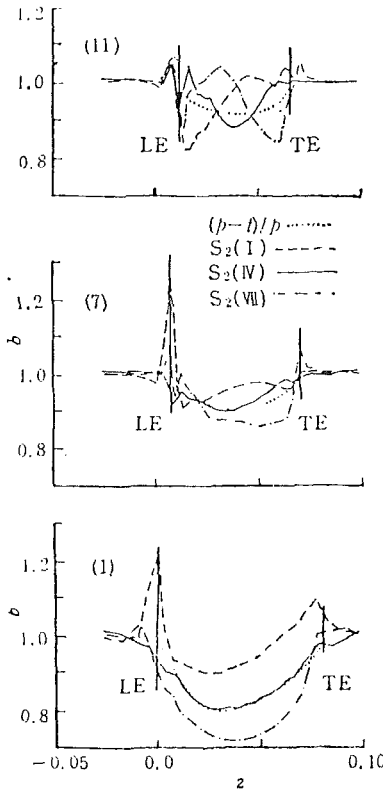


Fig. 21 Chordwise variations of S_2 filament thickness

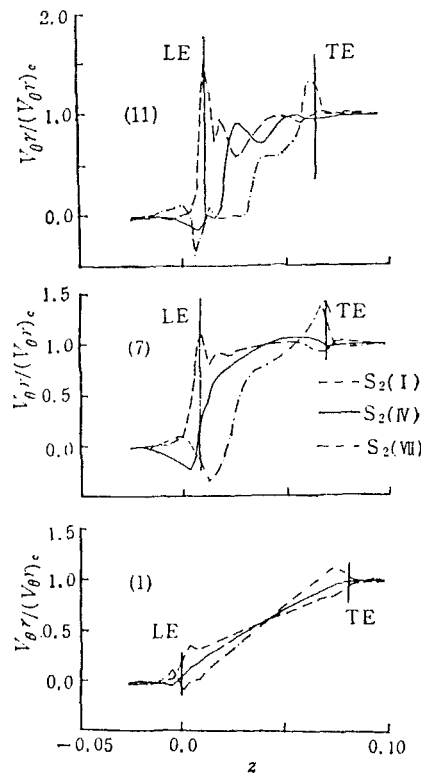
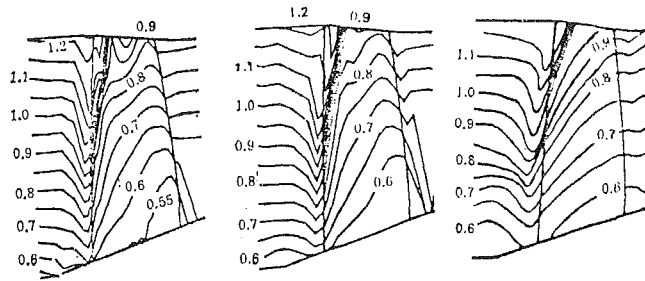


Fig. 22 Chordwise variation of $V_{\theta r}$ on S_2 surfaces

latter. This difference is also noticeable in the comparison of the constant Mach number contour maps on the S_{2m} surface shown in Fig. 23.

Circumferential variations of Mach number at six stations on five S_1 surfaces obtained in quasi-three-dimensional and full three-dimensional solution are compared in Fig. 11. In addition to the factors influencing the solution mentioned



(a) full 3D (b) quasi-3D (c) L2F

Fig. 23 Comparison of Mach number contours on S_{2m}

above, the circumferential variation in the S_1 geometry in the full three-dimensional solution also influences the result. It can be seen from Tables 4, 5, and 7, that for S_1 surfaces above S_1 (7), the filament thickness and its contraction on the side near the pressure surface are significantly different from those on the side near the suction surface. The combined effect on the velocity distribution is that, on S_1 surfaces above S_1 (7), the Mach number of the full three-dimensional solution is higher in the region from midchannel to suction surface and lower in the region from midchannel to pressure surface, than that of the quasi-three-dimensional solution.

Comparison With L2F Measurement. Efforts were made at IET to obtain internal flow on S_1 surfaces 4, 7, 8, 9, 10 by the use of a Laser-2-Focus velocimeter developed by DFVLR. The measured values are shown in Fig. 11. In general, the measured values are a little higher than the calculated, but at the second station on these surfaces, the measured values near the suction surface are lower than the calculated values. Constant Mach number contours constructed from the L2F measured data are shown in Fig. 23. The trend is similar, but again the measured Mach number is a little higher than the calculated values.

Conclusion

The general theory of three-dimensional flow in subsonic and supersonic turbomachinery based on the iteration between S_1 and S_2 streamsurfaces has been successfully extended to transonic turbomachinery. In this extension, recently developed, relatively simple and quick methods for solving transonic flow on S_1 and S_2 streamsurfaces are utilized. For the CAS transonic rotor, full three-dimensional solution is obtained after six cycles of iteration by using the quasi-three-dimensional solution as the starting value. The full three-dimensional solution obtained has a higher level of consistency and convergence than the quasi-three-dimensional solution. The difference between the full and quasi-three-dimensional solution is: The former gives a higher peak Mach number than the latter. The difference is mainly due to the circumferential variation of the S_1 filament thickness. A comparison between the theoretical solution and the L2F measurement shows that the character of the transonic flow including the three-dimensional shock structure is in good agreement, and the measured velocity is a little higher than the calculated one over most of the flow region, except at the 20 percent chord station in the upper half region near the suction surface, where the measured velocity is a little lower.

A practical three-dimensional computer-aided design and analysis (3D-CADA) system has been constructed by the use of the general S_1 code and general S_2 code presented herein. The recommended procedure of 3D-CADA is as follows:

(1) Prescribe the throughflow design requirements on the S_{2m} surface and obtain the S_{2m} solution. (2) Design the blade section on a number of general S_1 stream filaments. (3) Stack

the blade sections. (4) Obtain the full three-dimensional solution for the blade just designed. (5) Modify step 1 or step 2 and repeat (3) and (4) until the results obtained meet the design requirements.

It is believed that knowing the configuration of the three-dimensional geometry of the S_1 stream filaments, which are obtained in the solution of the present method and in which the blade section is going to operate, better design of the blade sections and, consequently, better design of the whole blade can be realized. Another advantage of the present method is that the computer storage is small and the amount of CPU time is also small so that all the computations can be performed on a microcomputer.

References

- Academia Sinica and Shenyang Aeroengine Company, 1976, "Theory, Methods and Application of Three-Dimensional Flow Design of Transonic Axial Flow Compressor," Research Report; *Journal of Engineering Thermophysics*, Vol. 1, No. 1, 1980, pp. 44-54.
- Hafez, M. M., South, J. C., and Murman, E. M., 1979, "Artificial Compressibility Methods for Numerical Solution of Transonic Full Potential Equation," *AIAA J.*, Vol. 17, pp. 838-844.
- Krimerman, Y., and Adler, D., 1978, "The Complete Three-Dimensional Calculation Compressible Flow Field in Turboimpellers," *Journal of Mechanical Engineering Science*, Vol. 20, No. 3, pp. 149-158.
- Miller, G. R., Lewis, G. W., Jr., and Hartman, M. J., 1961, "Shock Losses in Transonic Compressor Blade Row," *ASME Journal of Engineering for Power*, Vol. 83, pp. 235-242.
- Teipel, L., and Wiedermann, A., 1987, "Three-Dimensional Flow-Field Calculation of High-Loaded Centrifugal Compressor Diffusion," *ASME JOURNAL OF TURBOMACHINERY*, Vol. 109, pp. 20-26.
- Wang Qinghuan, Zhu Gengxing, and Wu Chung-Hua, 1985, "Quasi-Three-Dimensional and Full Three-Dimensional Rotational Flow Calculations in Turbomachines," *ASME Journal of Engineering for Gas Turbines and Power*, Vol. 107, pp. 277-285.
- Wang Zhengming, 1984, "Solution of Transonic S_1 Surface Flow by Successfully Reversing the Direction of Integration of the Stream Function Equation," *Journal of Engineering Thermophysics* [in Chinese]; *ASME Journal of Engineering for Gas Turbines and Power*, Vol. 107, 1985, pp. 317-322.
- Wang Qing-huan, Zhu Gen-xing, and Wu Chung-Hua, 1985, "Quasi-Three-Dimensional and Full Three-Dimensional Rotational Flow Calculations in Turbomachines," *ASME Journal of Engineering for Gas Turbines and Power*, Vol. 107, pp. 293-300.
- Wu Chung-Hua, 1952, "A General Theory of Three-Dimensional Flow in Subsonic and Supersonic Turbomachines of Axial, and Mixed-Flow Types," *Trans. ASME*, Vol. 74, pp. 1363-1380; NACA TN 2604.
- Wu Chung-Hua, 1976, "Three-Dimensional Turbomachines Flow Equations Expressed With Respect to Nonorthogonal Curvilinear Coordinates and Methods of Solution," *Proceedings of the 3rd International Symposium on Air-Breathing Engines*, pp. 233-252; *Engineering Thermophysics in China*, Vol. 1, No. 2, 1980, Rumford Pub. Co., USA.
- Wu Chung-Hua, 1980, "Fundamental Aerothermodynamic Equations for Stationary and Moving Coordinate Systems: Action of Viscous Forces and Physical Significance of Viscous Terms," *Journal of Mechanical Engineering*, 1965, Vol. 13, No. 4, Dec. [in Chinese]; *Engineering Thermophysics in China*, 1980, Vol. 1, No. 1, Rumford Pub. Co., USA.
- Wu Chung-Hua, and Zhu Gengxing, 1983, "Determination of the Appropriate Upstream and Downstream Conditions in Rotating Cascade Experiment and Calculation of Arbitrary S_1 Stream Surface for an Embedded Blade Row," *Journal of Engineering Thermophysics*, Vol. 4, No. 1 [in Chinese].
- Wu Chung-Hua, Wang Jianan, Fang Zongyi, and Wang Qinghuan, 1985, "1.2F Velocity Measurement and Calculation of Three-Dimensional Flow in an Axial Compressor Rotor," presented at the 7th ISABE, Beijing.
- Wu Chung-Hua, Wang Zhengming, and Chen Hongji, 1992, "Three-Dimensional Rotational Flow in Transonic Turbomachines: Part I—Solution Obtained Using a Number of S_1 Stream Filaments of Revolution and a Central S_2 Stream Filament," *ASME JOURNAL OF TURBOMACHINERY*, Vol. 114, this issue.
- Zhao X., 1984, "Solution of Transonic Flow Along S_1 Stream Surface Employing Non-orthogonal Curvilinear Coordinates and Corresponding Non-orthogonal Velocity Components," *Journal of Engineering Thermophysics*, Vol. 5 [in Chinese]; C84/84, *Computational Methods in Turbomachinery*, I. Mech. E.
- Zhao Xiaolu and Qin Lisen, 1987, "Stream Function Solution of Transonic Flow Along an Arbitrary Twisted S_1 Stream Surface," *Journal of Engineering Thermophysics*, Vol. 8, No. 4 [in Chinese].
- Zhao Xiaolu, 1986, "Stream Function Solution of Transonic Flow Along S_2 Stream Surface of Axial Turbomachines," *ASME Journal of Engineering for Gas Turbines and Power*, Vol. 108, pp. 138-143.
- Zhu, G. X., and Wu Chung-Hua, 1983, "Three-Dimensional Subsonic Flow Through a Stator by Use of a Central S_2 Stream Surface and Several S_1 Surfaces of Revolution," *Journal of Engineering Thermophysics*, Vol. 4, No. 2 [in Chinese].

Three-Dimensional Flow in an Axial Turbine: Part 1— Aerodynamic Mechanisms

D. Joslyn

R. Dring

United Technologies Research Center,
East Hartford, CT 06108

This paper presents an exhaustive experimental documentation of the three-dimensional nature of the flow in a one-and-one-half stage axial turbine. The intent was to examine the flow within, and downstream of, both the stator and rotor airfoil rows so as to delineate the dominant physical mechanisms. Part 1 of this paper presents the aerodynamic results including: (1) airflow and endwall surface flow visualization, (2) full-span airfoil pressure distributions, and (3) radial-circumferential distributions of the total and static pressures, and of the yaw and pitch angles in the flow. Part 2 of the paper presents results describing the mixing, or attenuation, of a simulated spanwise inlet temperature profile as it passed through the turbine. Although the flow in each airfoil row possessed a degree of three-dimensionality, that in the rotor was the strongest.

Introduction

Turbines have been evolving in a direction that necessitates both an improved understanding of and an improved ability to predict the three-dimensional nature of the flows they produce. This evolution is being driven by a trend toward lower aspect ratio as well as by a trend toward airfoils with highly three-dimensional geometry (e.g., lean, bow, and sweep). In addition, computational tools are developing at a rate so as to accelerate this evolution.

The three-dimensionality of the flow in an axial turbine can be produced by a wide variety of mechanisms. These mechanisms are present when the airfoil geometry is essentially two-dimensional and they can become even more important when the airfoils are three dimensional. While the intent of introducing three-dimensionality in the geometry is often to reduce the three-dimensionality of the flow and to improve performance, this cannot be fully achieved without an understanding of the flow mechanisms. These mechanisms include, but are not limited to, the following: (1) the leading edge horseshoe vortex, (2) secondary flow and the passage vortex, (3) airfoil and endwall boundary layers, (4) the relative eddy, (5) unshrouded rotor tip leakage, (6) airfoil wakes, and (7) wake-airfoil interaction.

In summary, the intent of the aerodynamic portion of this effort was to document the three-dimensional flow in a one and one half stage turbine, i.e., the radial transport. This documentation includes surface flow visualization, airfoil pressure distributions, and aerodynamic traverse data downstream of each airfoil row (total and static pressures, flow speed, yaw, and pitch). In Part 2 of this paper (Joslyn and Dring, 1992),

the redistribution of an inlet temperature profile was simulated by measuring the redistribution of an inlet trace gas profile. The trace gas concentration (simulating adiabatic recovery temperature) was documented locally on the airfoil and end wall surfaces as well as with traverse measurements in the flow downstream of each airfoil row.

Since the beginning of this program there has been a dramatic advancement in the computational state of the art. The first evidence of this was seen in the work by Rai (1987) in which he calculated the flow through the entire first stage of the present turbine. His calculation was three dimensional, compressible, viscous, and in a time accurate manner it captured the unsteadiness due to stator-rotor interaction. Recently Adamczyk et al. (1990) have demonstrated a three-dimensional viscous prediction of the flow through this stage based on an "average passage" approach. The data acquired in this program give a basis with which to assess these new computational codes and on which designers can begin to estimate the distribution of the adiabatic recovery temperature in the flow as well as on the airfoil and end wall surfaces.

Description of the Experiment

Large-Scale Rotating Rig (LSRR). The Large-Scale Rotating Rig (LSRR) was designed for carrying out detailed experimental investigations of the flow within turbine and compressor airfoil rows. Primary considerations were to provide a facility that would: (1) be of sufficient size to permit a high degree of resolution of three-dimensional flows, (2) possess a high degree of flexibility in regard to the configurations that could be tested, and (3) enable measurements to be made directly in the rotating frame of reference.

The facility is of the open circuit type. Flow enters through a 12-ft-diameter inlet. A 6-in.-thick section of honeycomb is mounted at the inlet face to remove any crossflow effects. The

Contributed by the International Gas Turbine Institute and presented at the 35th International Gas Turbine and Aeroengine Congress and Exposition, Brussels, Belgium, June 11-14, 1990. Manuscript received by the International Gas Turbine Institute January 9, 1990. Paper No. 90-GT-56.

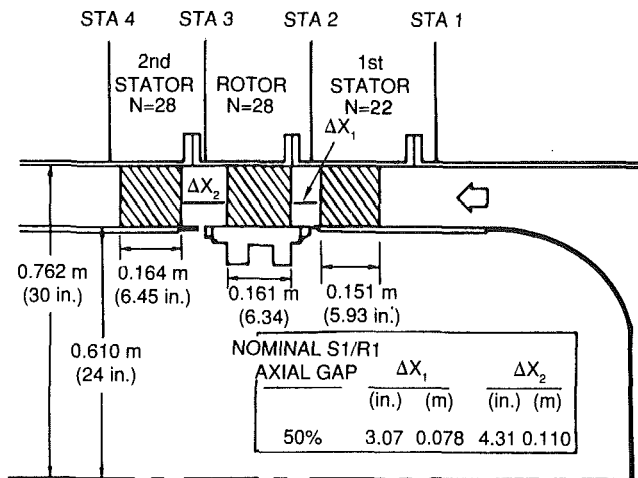


Fig. 1 United Technologies Research Center large-scale rotating rig

inlet smoothly contracts the cross section down to a 5-ft diameter. The flow then passes through three fine mesh screens.

The test section consists of a series of constant diameter casings enclosing the first-stage stator and rotor, and the second stator of the turbine model (Fig. 1). The turbine has a hub/tip ratio of 0.8 and all three airfoils have aspect ratios close to unity. The axial gaps between the rows can be varied greatly. In a previous study of rotor-stator interaction (Dring et al., 1981) the gap between the first-stage stator and rotor was set at both 15 and 65 percent. In the present program the 50 percent gap configuration was used. This was done to enable traverse data to be taken at Plane 2 (which is 17 percent behind the first stator) and at Plane 3 (which is 36 percent behind the rotor). The percentages here are in terms of airfoil axial chord. Traverse data were also taken at Plane 4, which is 14 percent behind the second stator. Inlet traverse documentation was done at Plane 1, which is 97 percent upstream of the first stator leading edge.

Downstream of the test section the flow passes through an annular diffuser into a centrifugal blower and is discharged from the rig. A vortex valve at the blower inlet controls the flow rate. The blower can provide a pressure rise of up to 21 in. of water. This enables axial velocities in the turbine test section of up to 80 feet per second to be set. The rotor is driven or braked by a hydraulic pump and motor system, which is capable of shaft speeds up to 890 rpm.

Aerodynamic Instrumentation. Aerodynamic instrumentation is available in the LSSR for making steady-state meas-

urements of aerodynamic flow parameters including total pressure, static pressure, flow velocity, flow direction, and temperature. These capabilities exist in both the stationary and rotating frames of reference. The stationary frame probe traverse mechanism can be positioned at selected axial planes. This traverse mechanism can drive a probe radially and circumferentially, and rotate it in yaw. A separate traverse mechanism for the rotating frame of reference is mounted inside the hub. This traverse can also drive a probe radially, circumferentially, and in yaw. A dedicated, on-line, automatic data acquisition and control system is used to monitor and control the experiment. This system calibrates all transducers (in both the rotating and stationary frames), monitors the turbine flow coefficient (C_x/U_m), controls probe position, and acquires, reduces, prints, and plots the data.

The aerodynamic instrumentation in the LSSR that was used in this program consisted of (1) airfoil static pressure taps at 22 locations around each airfoil perimeter and at seven spanwise locations (3, 12.5, 25, 50, 75, 87/5, and 98 percent span), (2) hub and tip endwall static pressure taps at 31 circumferential locations upstream and downstream of each airflow row, and (3) radial/circumferential five-hole probe (United Sensors USC-F-152) measuring total pressure, static pressure, flow velocity, and direction at the exit of each airfoil row. The traverse data were acquired at Planes 1, 2, 3, and 4 located respectively at 97 percent axial chord upstream of the first stator, 17 percent axial chord downstream of the first stator, 36 percent axial chord downstream of the rotor, and 14 percent axial chord downstream of the second stator.

Data Presentation Format. All of the data were reduced to dimensionless parameters. The aerodynamic pressure data were reduced to pressure coefficients based on the turbine inlet total pressure (PTOA) and a dynamic pressure (Q_{U_m}) based on the midspan wheel speed (U_m). The velocities were non-dimensionalized with the midspan wheel speed. Flow angles were measured from the axial direction. "Circumferentially averaged" flow angles were based on average velocity components rather than on average angles.

Test Conditions. Because the flow in the LSSR is essentially incompressible ($M < 0.2$) there is only one parameter that controls the velocity triangles, the flow coefficient, C_x/U_m . All of the data were acquired at the nominal design flow coefficient of 0.78. This was done by setting the shaft speed to 410 rpm and the axial velocity at the model inlet (Plane 1) to 75 ft/sec. At these conditions, the Reynolds numbers (based on axial chord and midspan exit flow speed) for the first stator, rotor, and second stator were 6.4×10^5 , 5.8×10^5 , and 5.9×10^5 , respectively. The nominal inlet turbulence level was 0.5 percent.

Nomenclature

B_x = airfoil axial chord	Q_U = dynamic pressure based on U	β = relative flow direction (from axial)
C = absolute flow speed	Q_{U_m} = dynamic pressure based on U_m	ρ = density
C_t = absolute tangential flow speed	U = rotor wheel speed	τ = airfoil pitch
(C_x/U_m) = flow coefficient	U_m = rotor wheel speed at midspan	Superscripts
CP = pressure coefficient = $(PTOA - P)/Q_{U_m}$	W = relative flow speed	-a, AA = circumferential area average
M = Mach number	W_t = relative tangential flow speed	-m, MA = circumferential mass average
PS = static pressure	x = axial distance	Subscripts
PTABS = absolute total pressure	y = tangential distance	t = tangential
PTOA = turbine inlet absolute total pressure	α = absolute flow direction (from axial)	x = axial
PTREL = relative total pressure		
PTROT = rotary total pressure = $PTREL - Q_U$		

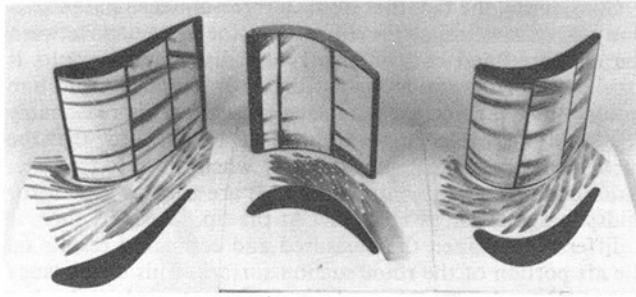


Fig. 2(a) Experimental surface flow visualization, stator suction surfaces, and rotor pressure surface

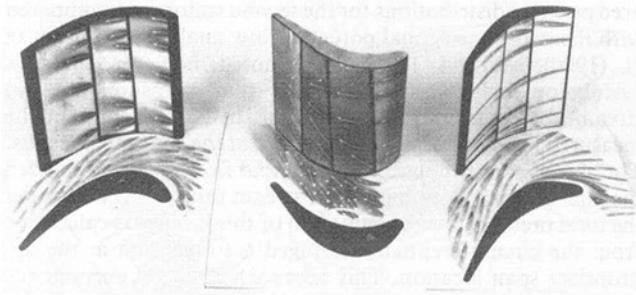


Fig. 2(b) Experimental surface flow visualization, stator pressure surface, and rotor suction surface

At the turbine inlet (Plane 1) the hub and tip boundary layer displacement thicknesses were 0.9 and 1.5 percent span, respectively. The hub and tip momentum thicknesses were 0.7 and 1.1 percent span, respectively.

Aerodynamics Results

Surface Streamlines. The experimental results were obtained by bonding Ozalid paper to the airfoil and end wall surfaces and then flowing a small amount of gaseous ammonia back through the surface static pressure taps. The ammonia reacted with the paper, leaving permanent blue streaks. In some cases the ammonia was introduced through a fine hypodermic tube in the flow.

The flow visualization on the suction surfaces of the first and second stators and on the pressure surface of the rotor is shown in Fig. 2(a). The hub end wall flow visualization is also shown. This photograph was constructed by making a model of the turbine and bonding the exposed Ozalid paper to it. In a similar manner, the flow visualization on the pressure surfaces of the first and second stators and on the suction surface of the rotor is shown in Fig. 2(b). Where possible, for the sake of clarity, arrows have added to the streaks on the Ozalid paper.

The measured results indicate a midspan region on the first stator that is very nearly two dimensional on both the suction and pressure surfaces. The hub and tip secondary flow are apparent near the end walls on the airfoil suction surface. The secondary flow at the tip appears to have the greater spanwise extent of the two. The hub end wall results show the overturning due to the secondary flow. Horseshoe vortices at the hub and tip leading edges are evident near the end walls on the forward portion of the airfoil pressure surface as well as on the end walls themselves. The tip end wall flow visualization (Joslyn and Dring, 1989) is similar to that on the hub.

The dominant feature on the rotor pressure surface is the radial flow toward the tip due to the relative eddy. This is an inviscid mechanism due to the relative vorticity in the rotating frame of the reference. Its effect is strongest on the forward portion of the pressure surface because the surface flow speed

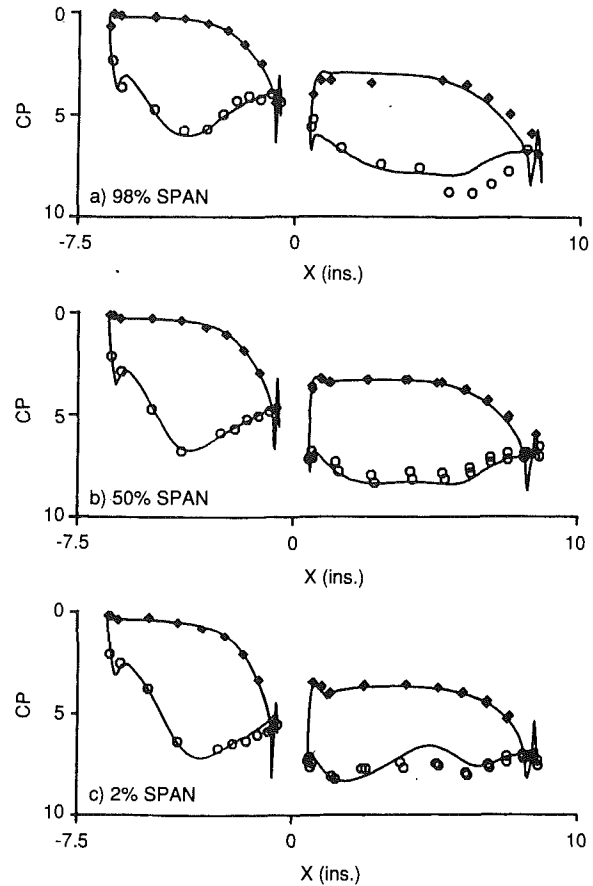


Fig. 3 First stator and rotor full-span pressure distributions

is lowest there (Dring and Joslyn, 1983). The surface streamlines turn away from the radial direction as the flow accelerates toward the trailing edge. The hub end wall flow shows overturning due to secondary flow.

The surface flow on the second stator is similar to that on the first stator. This is true in spite of the fact that this stator is geometrically far more similar to the rotor. The midspan region on both the suction and pressure surfaces is relatively two dimensional. The region influenced by the tip secondary flow is much larger than that influenced by the hub secondary flow. This aspect of the similarity is due to the fact that both stators had a large absolute exit swirl and hence a strong radial static pressure gradient. This gradient tends to drive low total pressure fluid, such as that in the secondary flow vortices, radially inward toward the hub. The absence of the radial flow on the pressure surface is due to the stator being in the stationary frame of reference and hence having no relative eddy (as in the rotor). The flow on the hub end wall shows clear evidence of overturning due to secondary flow, and also the presence of a leading edge horseshoe vortex. The tip end wall flow visualization for the first and second stators (Joslyn and Dring, 1989) is similar in character to the hub flow visualization.

Airfoil Pressure Distribution. Static pressures measured on the first-stage stator and rotor are shown in Fig. 3 for the 2, 50, and 98 percent span locations. The curves are the time-averaged computed results by Rai (1987) and the symbols are the measured results. This comparison was made in spite of the fact that the rotor aspect ratio in the computation was low (by the factor of 11/14) and in spite of the fact that the tip clearance in the computation was too small (0.4 percent versus 1.0 percent span). The results by Madavan et al. (1989), however, showed that the impact of the rotor aspect ratio on the

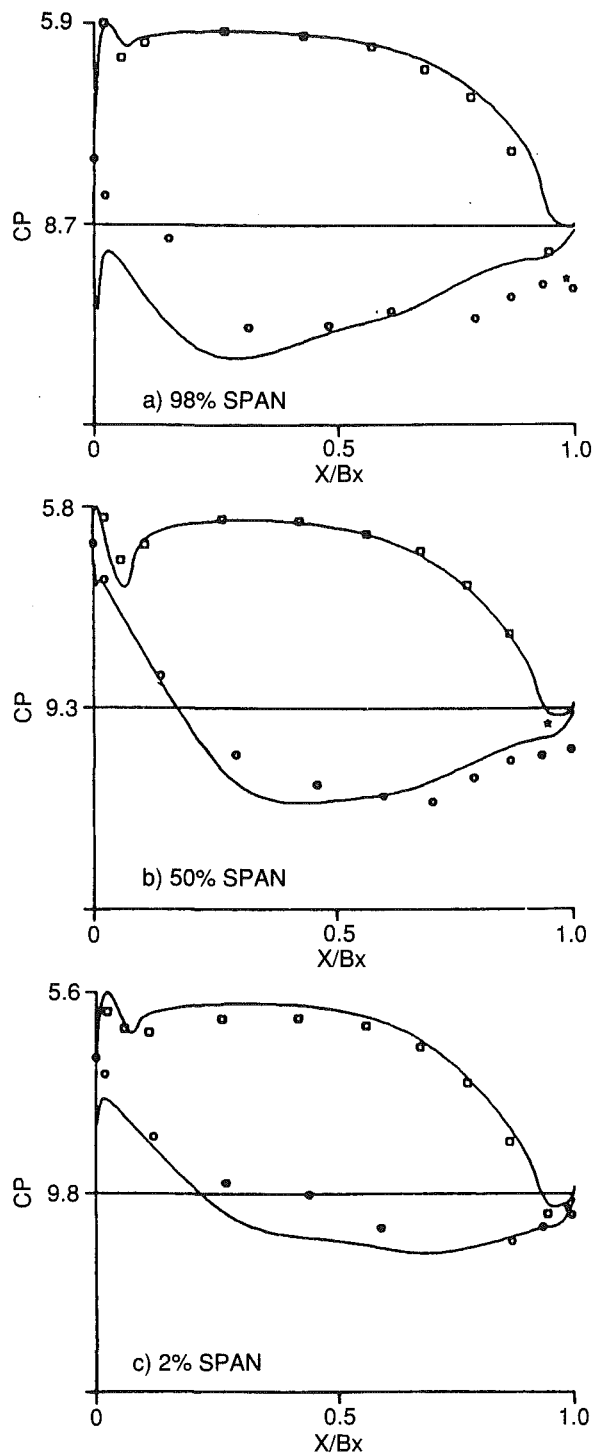


Fig. 4 Second-stator full-span pressure distributions

rotor pressure distributions was relatively small. The same cannot necessarily be said for the effect of rotor tip clearance, especially at the 98 percent span location. This question remains to be answered (Rai, 1989).

The measured rotor pressure distribution data are shown as pairs of symbols at the 2 and 50 percent span locations. These two symbols represent the range of the measurements that have been taken on the rotor during the various experiments that have been conducted between 1977 and 1988. A similar comparison for the first stator showed that the range of measurements for this airfoil was within the size of the symbols.

Considering the fact that this is a three-dimensional prediction of the flow through the entire stage, the agreement between the measured and computed pressure distribution results is excellent. For the stator the agreement is excellent from hub to tip. For the rotor the agreement at the hub is reasonably good and the results of Madavan et al. (1989) show that the suction surface agreement gets better when the correct aspect ratio (and a finer computational grid) are used. At the rotor midspan agreement is excellent. At the tip, however, there is a difference between the measured and computed results on the aft portion of the rotor suction surface. This discrepancy may well be due to the small tip clearance used in the Rai (1987) calculation.

Since the calculations by Rai (1987) and Madavan et al. (1989) included only the first-stage stator and rotor, the measured pressure distributions for the second stator were compared with the two-dimensional potential flow analysis by Caspar et al. (1980) in Fig. 4. It should be noted, however, that this calculation included the effects of total pressure loss and streamtube contraction. The symbols in Fig. 4 represent the measured results and the curves represent the computed results. The aerodynamic input to the potential flow analysis included the inlet and exit flow angles, the stream tube contraction, and the total pressure loss (or gain). All of this input was calculated from the circumferentially averaged traverse data at the appropriate span location. This approach does not account for the fact that there was significant radial transport upstream of, within, and downstream of the airfoil.

The agreement between the measured and computed results for the second stator (Fig. 4) is reasonably good, especially on the pressure surface. The measured and computed results on the suction surface show the same trend of the minimum pressure moving forward from the hub (2 percent span) to the tip (98 percent span). The suction surface results at the tip suggest that the second stator was operating with a less positive incidence than that calculated from the rotor exit traverse data. The rotor exit traverse data showed some very strong gradients in absolute flow angle due to the rotor tip leakage in this region (Fig. 13). Thus there was a strong likelihood that the actual stator incidence was significantly different from that used in the calculation.

In general the agreement between the computed and measured airfoil pressure distributions was good, but it appears that radial mixing can have a significant impact on the effective incidence an airfoil responds to. The surface streamlines as well as the airfoil pressure distributions indicate that all three rows of airfoils are free of any significant boundary layer separation even though there are regions of strong adverse pressure gradient on the suction surface of each airfoil.

Traverse Results. Five-hole probe traverse measurements of total pressure, static pressure, flow velocity, and direction were made downstream of each airfoil. To demonstrate periodicity, the measurements were taken over two first stator pitches. The traverse results are presented in contour plots, secondary flow vector plots, and in spanwise distribution of circumferential averages. An increment of 0.1 was used for all of the contour plots (Figs. 5a, 6a, and 7a). In the plots of the secondary flow velocity vectors, the length of the arrows was proportional to the secondary flow speed. The secondary flow vectors represent the total velocity vector viewed from a particular direction. This viewing direction was on a cylindrical surface and in the yaw direction corresponding to the averaged flow angle at midspan.

For the spanwise distribution plots, two circumferential averages were used depending on the specific quantity being averaged. The two averages were the area average and the mass average. They are defined as follows:

Area average of a quantity F :

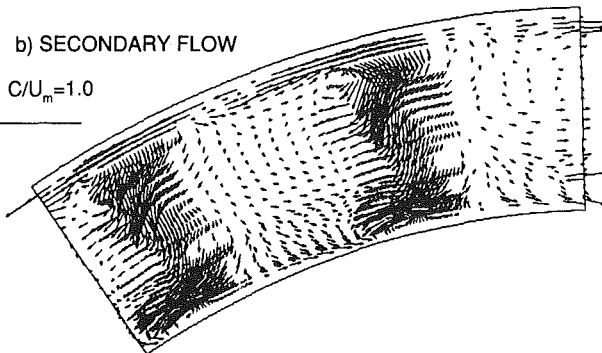
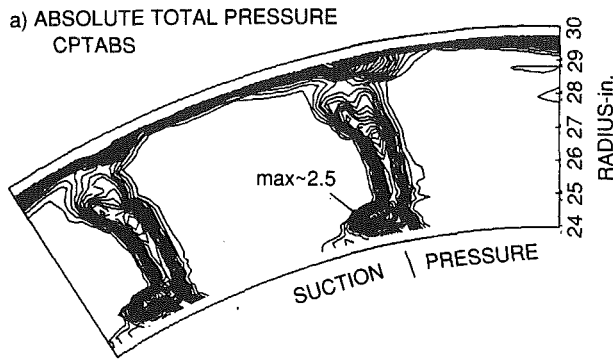


Fig. 5 First stator exit traverse, plane 2; absolute, measured 17 percent aft

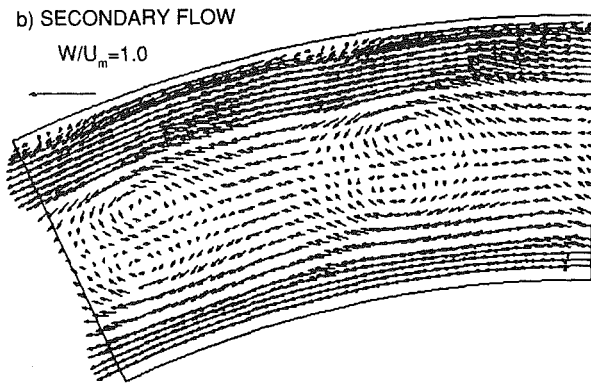
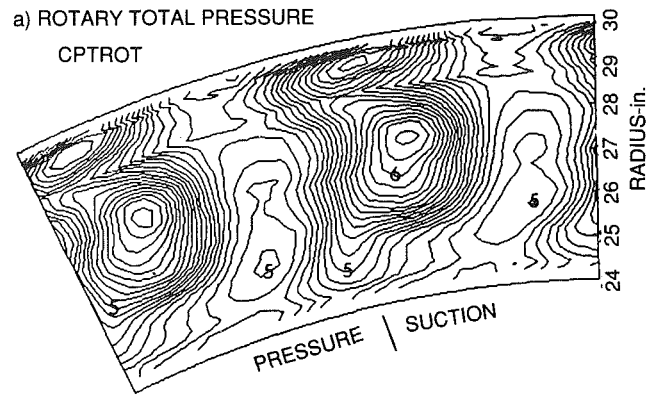


Fig. 6 Rotor exit results, plane 3; relative, measured 36 percent aft

$$\bar{F}^a = FAA = \frac{\int_0^\tau F \cdot dy}{\int_0^\tau dy} \quad (1)$$

Mass average of a quantity F :

$$\bar{F}^m = FMA = \frac{\int_0^\tau F \cdot \rho C_x dy}{\int_0^\tau \rho C_x dy} \quad (2)$$

The choice of which average was used was based on through-flow analysis considerations (Dring and Oates, 1990a, 1990b). The absolute and rotary total pressures were mass averaged, while the static pressure and axial velocity were area averaged. Absolute and relative flow angles were also calculated based on the way they would be used in a throughflow calculation, i.e., as the arctangent of the ratio of the area-averaged tangential and axial velocity components (CTAA or WTAA and CXAA). The absolute and relative flow angles were calculated as follows:

$$\alpha = \arctan(CTAA/CXAA) \quad (3)$$

$$\beta = \arctan(WTAA/CXAA) \quad (4)$$

Total pressure coefficient contours at Plane 2 in the flow downstream of the first stator are shown in Fig. 5(a). The measured results show the migration toward the hub of the low total pressure hub and tip secondary flow regions. The total pressure regions have a maximum local loss of about 1.5 for the tip secondary flow (near 65 percent span) and 2.5 for the hub secondary flow (near 13 percent span). The results indicate a thicker end wall boundary layer at the tip than at the hub. This is due in part to the thicker inlet (Plane 1) boundary layer at the tip.

The measured secondary flow vectors downstream of the

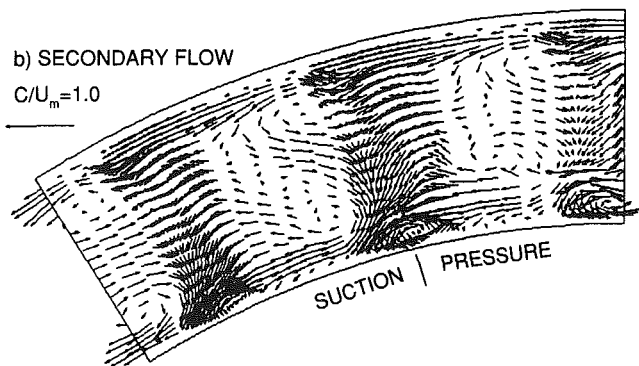
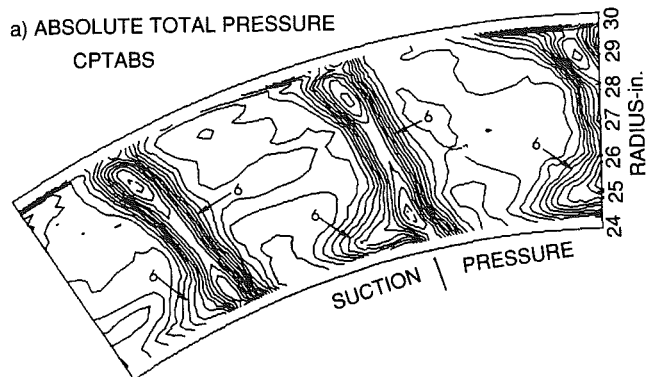


Fig. 7 Second-stator exit results, plane 4; absolute, measured 14 percent aft

first stator are shown in Fig. 5(b). It corresponds to looking upstream at the velocity vectors from the direction of the averaged yaw angle at midspan. Each vector represents a measurement location. It can be seen that the data density was

highest in the airfoil wakes and near the end walls. The results in Fig. 5(b) show the radial transport toward the hub in the stator wake due to the strong radial static pressure gradient at this plane (Fig. 11). This is the mechanism that moves the tip secondary flow away from the tip end wall and toward the hub (Fig. 5a). It is also the mechanism that drives the hub secondary flow down toward the hub end wall. The vortical motion in the hub and tip secondary flow can also be seen in the velocity vectors (Fig. 5b).

The flow aft of the rotor is shown in terms of contours of rotary total pressure coefficient in Fig. 6(a). The numbers shown are values of CPTROT. The traverse data acquired over two rotor pitches at Plane 3. Since there were 22 first-stator airfoils and 28 rotor airfoils, the circumferential width of the figure is smaller by a factor of (11/14) relative to that shown for the first stator. There is a large low total pressure region downstream of the rotor centered at about 60 percent span. This is due to the secondary flows occurring as the hub and tip end wall flows impact the rotor suction surface and move toward the midspan region (Fig. 6b). It is interesting to note that the hub and tip secondary flows have merged into a single low total pressure region. This region is located very close to the center of the tip secondary flow vortex (Fig. 6b).

Similar results from a plane cascade experiment were reported by Moore and Ransmayr (1984) and by Moore and Adhye (1985). Their cascade experiment was carried out using an airfoil section that was nominally identical to the present rotor midspan section. Their cascade aspect ratio was 1.00, which is also very close to that of the present rotor (1.06). Their results showed that the low total pressure regions due to the hub and tip secondary flows moved away from the end walls toward midspan. At a plane located 40 percent aft of the airfoil trailing edge they essentially merged into a single low total pressure region (Moore and Adhye, 1985, Figs. 8 and 10). This is consistent with the present results, which were taken 36 percent aft of the rotor trailing edge. The present results are also very similar to those presented by Madavan et al. (1989) in their Fig. 20(b). Keep in mind that this similarity was achieved in spite of the difference in rotor tip clearance. The effect of the rotor tip leakage flow in the measurements could be seen by the regions of low rotary total pressure between 80 percent span and the tip.

The secondary flow velocity vectors in the flow aft of the rotor are shown in Fig. 6(b). This plot was generated in the same way as Fig. 5(b) for the flow aft of the first stator. The viewing angle is the average relative yaw angle at midspan. Two distinct counterrotating vortices are evident in the flow downstream of each rotor airfoil passage. These are the hub and tip secondary flow vortices. Their origins on the hub and tip end walls of the rotor passage can be seen in the rotor flow visualization (Fig. 2b). As mentioned above, the region of low rotary total pressure (Fig. 6a) was centered over the tip secondary flow vortex at about 60 percent span.

The second-stage stator aerodynamic traverse results were acquired at Plane 4. Since there were 22 first stators and 28 second stators there was no practical way of quantifying the "average" passage (short of taking traverse data behind 14 adjacent second-stator passages). The difficulty here can be seen in the absolute total pressure coefficient contours shown in Fig. 7(a). These were taken over two first-stator pitches (or 2.545 second-stator pitches). The effects of the first stator can be seen most clearly in the nonperiodic nature of the relatively weak gradients in the flow between the second stator wakes. The wakes themselves, however, are surprisingly periodic. The numbers shown in the contour plot are values of CPTABS.

In spite of the fact that the second-stator geometry was far more similar to the rotor than to the first stator, the second-stator wake was far more similar to that of the first stator (compare Fig. 7a with Figs. 5a and 6a). The main reason for this is that the flow aft of both stators had a much larger

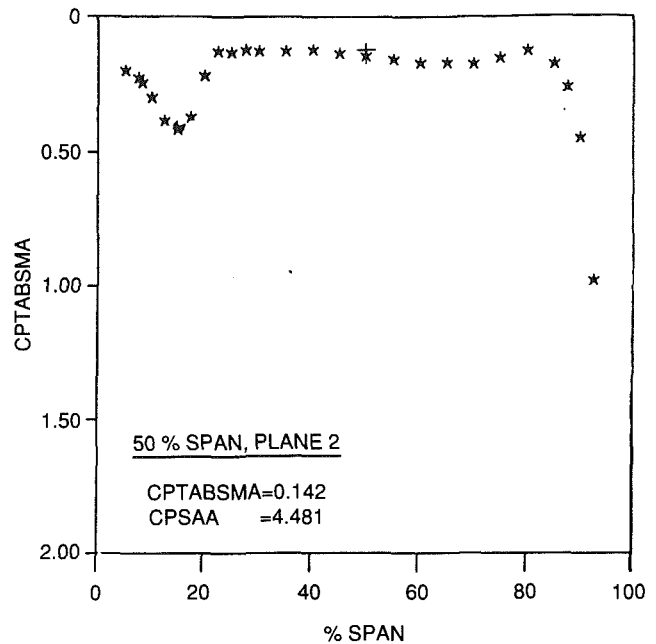


Fig. 8 First stator exit results, plane 2; absolute, measured 17 percent aft, absolute total pressure, circumferential mass average

absolute swirl, and hence a much stronger radial static pressure gradient than the flow aft of the rotor (Fig. 11). This gradient drives low total pressure fluid toward the hub. In the absence of this gradient, low total pressure fluid tends to accumulate near midspan. This is true both for the rotor (Fig. 6a) and for a similar plane cascade (Moore and Ransmayr, 1984; Moore and Adhye, 1985), both of which had aspect ratios near unity.

As can be seen in Fig. 7b, there is a very strong secondary flow present 14 percent aft of the second stator. As with the first stator, there is strong flow from tip to hub in the wakes due to the radial static pressure gradient. Close to the hub (≈ 10 percent span) in each wake there is a strong vortical motion that could be a result of the hub secondary flow. There are also relatively weak vortical motions of opposite sign in the regions between the wakes, around 30 and 74 percent span. These weaker vortices varied in radial and circumferential location from passage to passage and might be a vestige of the rotor hub and tip secondary flow.

The spanwise distribution of the circumferentially mass-averaged absolute total pressure obtained downstream of the first stator is presented in Fig. 8. Since the absolute total pressure at the stator inlet is at a CPTABS of zero, Fig. 8 is a direct measure of the total pressure loss ($\Delta PT/QUM$) at midspan for the first stator wakes shown in Fig. 8 is 0.14. A boundary layer analysis (Edwards et al., 1981; Carter et al., 1982) using the turbulent mixing model by Cebeci and Smith (1974) was carried out based on the computed stator pressure distribution (Fig. 3b) and on the wake-mixing analysis of Stewart (1959). This analysis gave a total pressure loss of 0.12 (versus 0.14). The fact that the measured value is higher may be a result of several things. It can be seen in the surface flow patterns (Fig. 2) and in the total pressure contour plot (Fig. 5a) that the stator tip secondary flow has penetrated inward to the midspan region. This can also be seen in the secondary flow vector plot for this plane (Fig. 5b). The gradient in stator loss from hub to tip can also be seen in Fig. 8. It is interesting to note that the measured loss between 23 and 40 percent span, where the flow on the airfoil is nearly two dimensional, agrees closely with the value of 0.12 predicted at midspan.

It was known from heat transfer measurements made on this stator (Blair et al., 1989a) that for low turbulence (0.5

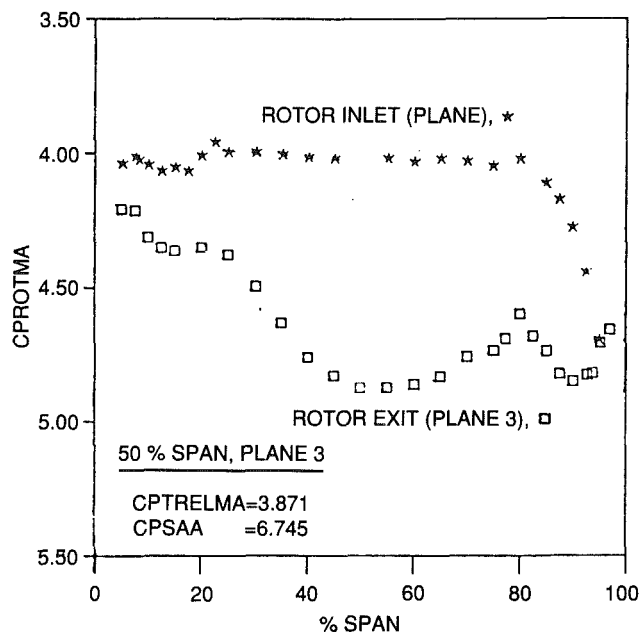


Fig. 9 Rotor inlet and exit rotary total pressure

percent) inlet conditions, the stator boundary layer was laminar up to the minimum pressure, where a rapid transition to turbulent flow occurred. A boundary layer analysis simulating this situation was carried out using the code by Edwards et al. (1981) and Carter et al. (1982), and the transitional mixing model by McDonald and Kreskovsky (1974). A free-stream turbulence of 10 percent was needed for the prediction to match the transitional behavior of the measured heat transfer data (Blair et al., 1989b, see Fig. 9a). This approach predicted a loss that was 30 percent smaller than the fully turbulent prediction (0.083 versus 0.12). This suggests that there is no location in the wake of this stator where the flow (or the loss) is purely two dimensional.

The rotary total pressure was calculated from measurements made in the absolute frame at Plane 2 and in the relative frame at Plane 3 and then circumferentially mass averaged. The spanwise distributions of these results are presented in Fig. 9. In the rotating frame of reference, rotary total pressure is the kinematic equivalent of absolute total pressure in the stationary frame of reference. Just as a gradient in absolute total pressure is required to generate a secondary flow in the stationary frame of reference, a gradient in rotary (not relative) total pressure is required to generate a secondary flow in the rotating frame of reference (Hawthorne, 1974). Strong gradients in rotary total pressure at Plane 2 (rotor inlet) were limited to the endwall regions. It could thus be anticipated that there would be little or no gradient-driven secondary flow due to the "relatively eddy" is not gradient driven. It is driven by the axial component of vorticity due to the rotating frame of reference (Dring and Joslyn, 1983). It is the relative eddy that gives rise to the radial flow toward the tip on the rotor pressure surface (Fig. 2a). At the rotor exit (Plane 3) low total pressure regions due to the hub and tip secondary flows and the rotor tip leakage can be seen around 50 and 90 percent span, respectively. The lifting of the secondary flows away from the hub results in a relatively high total pressure in the region. An indication of the loss in rotary total pressure across the rotor can be seen as the difference between the inlet and exit rotary total pressure profiles. A large loss exists across the entire rotor span, varying from about 0.4 at 15 percent span to 0.9 near midspan.

The spanwise distribution of the circumferentially mass-averaged absolute total pressure obtained upstream and downstream of the second stator is presented in Fig. 10. In an effort

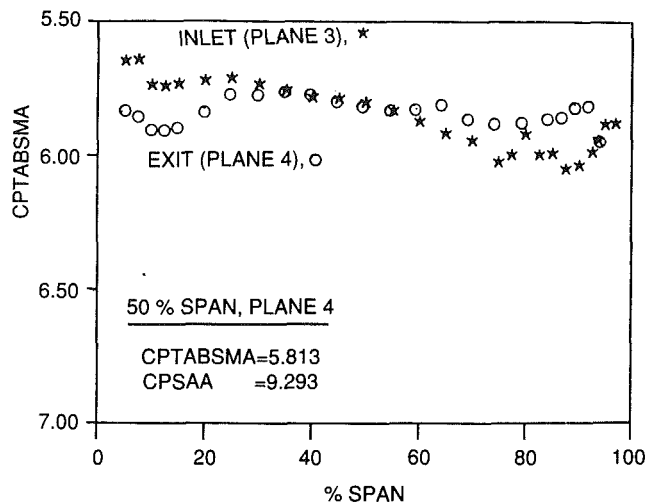


Fig. 10 Second stator inlet and exit absolute total pressure

to deal with the issue of defining an "average" passage, the results were averaged both over two first-stator passages and over two second-stator passages. The differences between the two were generally smaller than the symbol size. Only near the end walls did the differences approach 0.1. Accordingly, all of the data presented here were averaged over two second-stator pitches. The main point to be seen in the second stator inlet distribution is that aside from a slight negative gradient there are no strong gradients in the midspan region and hence the secondary flow in the second stator should be dominated by the end wall secondary flows.

The total pressure loss across the second stator is indicated by the difference between the inlet and exit total pressure profiles. There is a total pressure "loss" region near the hub and a "gain" region near the tip. The maximum changes in CPTABS are on the order of 0.2. This observation of a local "gain" in total pressure indicates that significant radial transport of the high and low total pressure fluid occurred between the stator inlet and exit (Planes 3 and 4). This is reinforced by observations concerning the inlet flow angle for the second stator at 98 percent span.

Under- and overturning patterns aft of the second stator can also be clearly seen in the spanwise distribution of the absolute exit flow angle (Fig. 12). The overturning near the hub reached a maximum at about 10 percent span and that near the tip reached a maximum at about 90 percent span. The overturning due to secondary flow was evident between these maxima and the end walls where the flow tended toward tangential (90 deg). The second-stator exit absolute flow angle distribution displays trends that are similar to those of the first stator except in the tip region between 70 to 95 percent span. Here the second-stator distribution is nearly the mirror image of that of the first stator. The trend observed in this region aft of the second stator may very well be due to the rotor tip leakage vortex centered at 90 percent span at Plane 3 (Fig. 6). This vortex would tend to enhance overturning in the region between its center and the tip endwall (Sharma et al., 1988). Underturning would be enhanced in the region between the rotor tip leakage vortex and midspan.

The spanwise distributions of circumferentially area-averaged static pressure aft of the three airfoils are shown in Fig. 11. Note that the radial pressure gradients for both the first and second stators are greater than that for the rotor. Since the absolute swirl aft of the first and second stators was large (approximately 68 deg) compared to the rotor exit absolute swirl (approximately 35 deg), it is not surprising to see much stronger static pressure gradients aft of the stators. These strong gradients aft of the stators tend to drive low total pressure

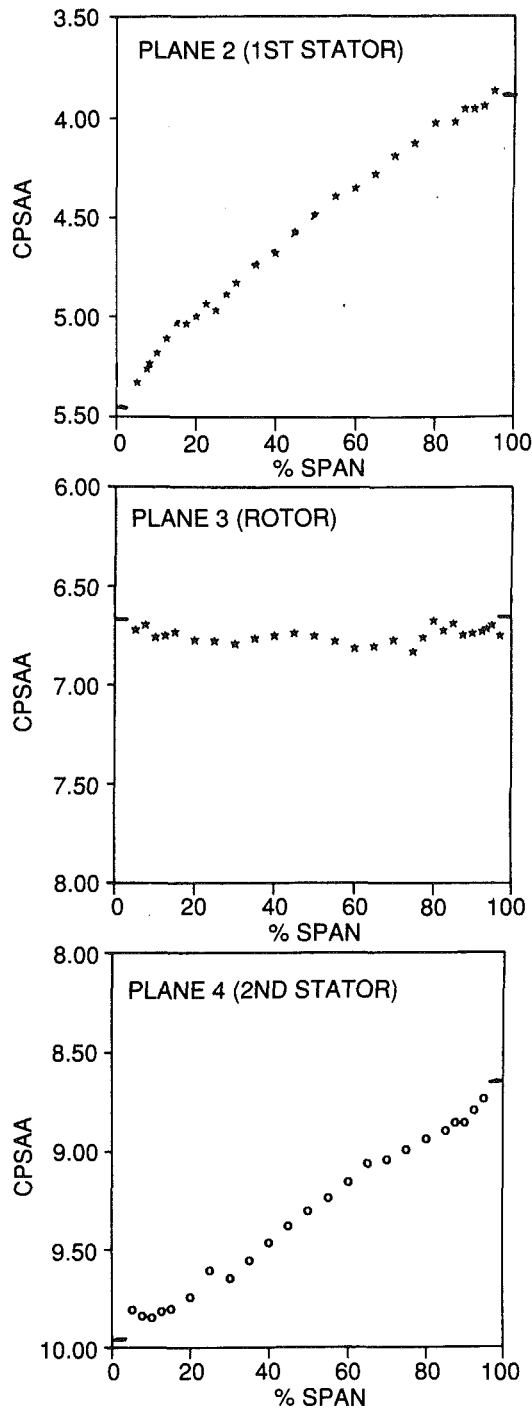


Fig. 11 Static pressure, circumferential area average at airfoil exit

fluid, such as that in the secondary flow vortices and in the wakes, inward toward the hub, e.g., Figs. 5(a) and 7(a). Also shown, as the horizontal bars, in Fig. 11, are the circumferentially area-averaged static pressures measured on the hub and tip endwalls. The traverse results generally extrapolate to these values.

The spanwise distribution of the measured yaw angles aft of the three airfoils are shown in Fig. 12. These angles are based on the area-averaged velocity components, as required by throughflow theory (Dring and Oates, 1990a, 1990b). The first and second-stator absolute exit flow angle (α) distributions are calculated from absolute frame traverse measurements. The rotor exit relative flow angle (β) distribution is calculated from the relative frame traverse measurements. Aft of the first stator

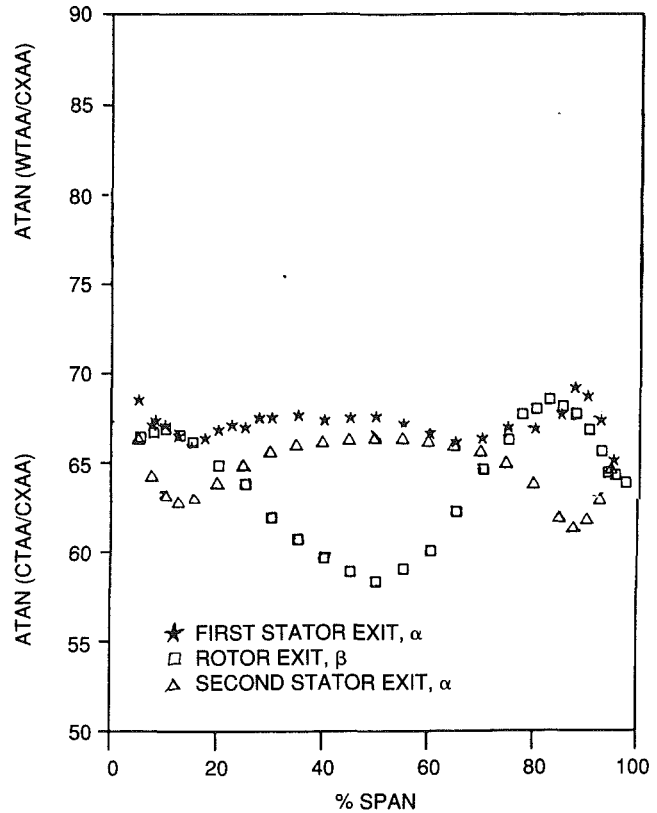


Fig. 12 Exit flow angles

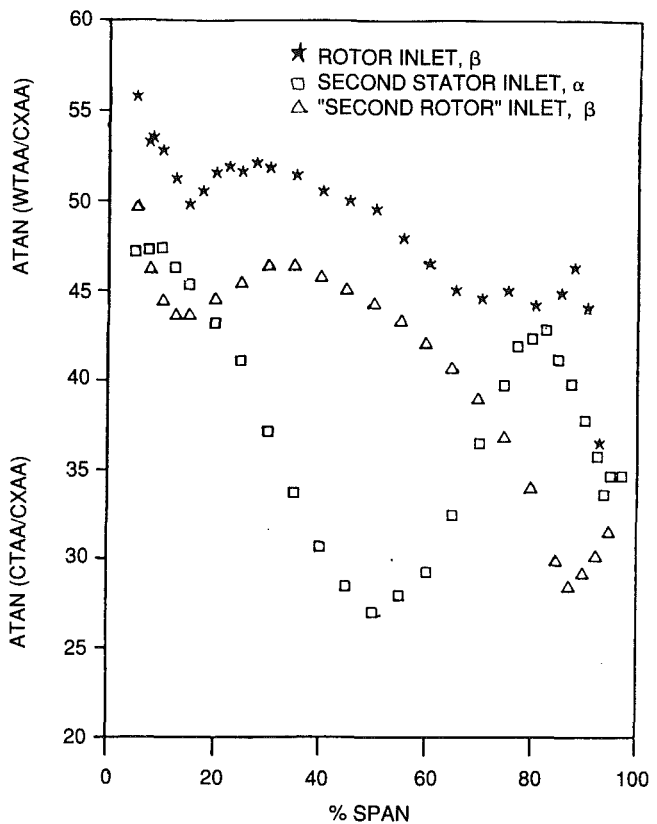


Fig. 13 Inlet flow angles

near the hub end wall the results indicate the expected trend toward overturning. The experimental flow visualization results also showed this trend toward overturning on the hub end wall (Fig. 2). The measured flow angles near the tip,

however, indicate a trend toward overturning (toward axial). This difference may be a result of a problem with the instrumentation (due to wall interference effects). There is also the possibility that the entire trend toward overturning occurred between 95 percent span and the tip end wall.

The issue of under- and overturning aft of the rotor is illustrated in the spanwise distribution of the rotor relative exit flow angle. This plot of flow angle, Fig. 12, very closely resembles the plot of rotor exit axial velocity, Fig. 14, when it is inverted. Regions of high angle (overturning) correspond to regions of low axial velocity and vice versa. It is also interesting to note that the region with the highest loss (Fig. 9) nearly coincides with the overturning (high axial velocity) region aft of the rotor.

The spanwise distributions of the inlet yaw angles for the rotor and second stator are shown in Fig. 13. Also shown is the inlet angle for a "second-stage rotor." The inlet flow angle for the first stator is zero and is not shown in Fig. 13. The same observations made for the exit flow angles (Fig. 12) are true also for the inlet flow angles. The main difference is that the variations in inlet angle are much larger due to the addition of wheel speed to the respective absolute or relative velocity vector.

The circumferentially area-averaged axial velocity component aft of the three airfoils is plotted as a function of span in Fig. 14. Aft of the first stator the overturning due to the hub and tip secondary flow results in higher than average axial velocity away from the walls. Close to the walls, overturning and the reduced total pressure result in a decrease in axial velocity. The effect is greater at the tip. Aft of the rotor, the overturning between the hub and tip secondary flow vortices caused a higher axial velocity in this region (near midspan). Conversely, the overturning regions above and below the two secondary flow vortices have caused a lower axial velocity in these regions (near 10 and 80 percent span). The higher axial velocity due to the overturning caused by the tip leakage can be seen near the tip. Aft of the second stator, the overturning observed in the secondary flows near the hub and tip end walls has caused higher than average axial velocity in these regions. The overturning due to the secondary flow causes the axial velocity to begin to decrease very close to the end walls.

All of the data shown are presented in greater detail by Joslyn and Dring (1989).

Conclusions

This concludes the presentation of the aerodynamic results. The intent in acquiring all this aerodynamic data was that it would provide: (1) a good basis of the assessment of computational methods, and (2) an explanation for the profile attenuation data that will be discussed in the second part of this paper. The main conclusions from the aerodynamic portion of this study are:

1 Surface flow visualization indicated that hub and tip secondary flows were the main cause of three dimensionality and radial transport in the stators. Traverse results aft of the stators showed that radial transport in the wakes was also a strong contributor.

2 Surface flow visualization indicated that hub and tip secondary flows, as well as the relative eddy and tip leakage, were the main causes of three-dimensionality for the rotor. Traverse results aft of the rotor showed that radial transport in the wakes was relatively weak due to the low level of absolute swirl.

3 The pressure distributions on the first stator were only weakly influenced by the three-dimensionality of the flow.

4 The pressure distributions on the rotor were strongly influenced by the three-dimensionality of the flow, at the hub due to secondary flow and at the tip due to leakage flow through the clearance gap.

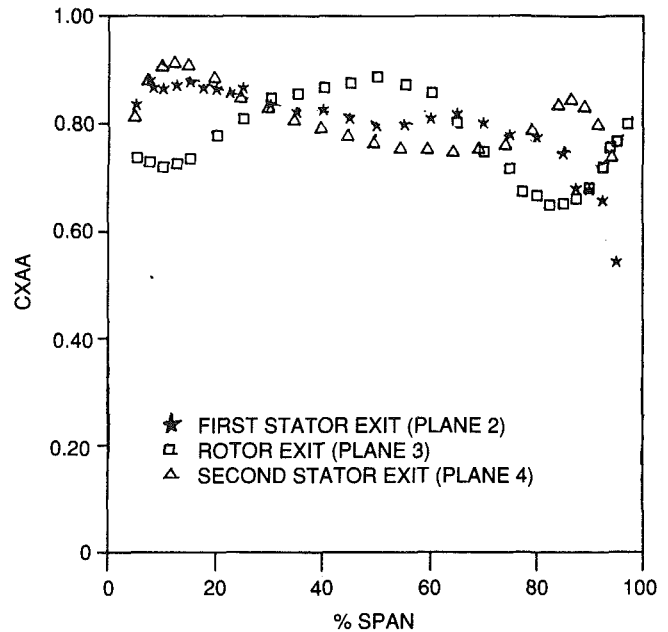


Fig. 14 Axial velocity ($C_x U_m$), circumferential area average at airfoil exit

5 The second-stator pressure distribution appears to have been significantly affected by radial mixing immediately upstream of the airfoil. This mixing appears to have altered its incidence.

6 In spite of the fact that the high loss fluid aft of the rotor was swept up into a single region around midspan (as in a nonrotating cascade), the hub and tip secondary flow vortices were still clearly present.

7 Although the second-stator airfoil is similar to the rotor airfoil, its wake is similar to that of the first stator because of its high absolute exit swirl.

8 The three-dimensionality of the flow over the second stator is complicated by the presence of the upstream rotor (and possibly by the upstream stator).

Acknowledgments

The authors owe a debt of gratitude to a number of talented, patient, and committed people for the success of this program. Bill Tierney breathed life back into a traverse system that had been dormant and he kept it working faithfully. Ray Valliere acquired most of the data and on numerous occasions he demonstrated his formidable trouble-shooting skills. Finally, Lisa Vaughn and Diane Rodimon spent many long weeks reducing the data and generating the figures in this paper. We are privileged to have each one of these people as a co-worker. This experimental program was carried out under Air Force funding under the direction of Dr. James Wilson, Dr. James McMichael, and Captain Henry Helin, AFOSR Contract No. F49620-86-C-0020.

References

- Adamczyk, J. J., Celestina, M. L., Beach, T. A., and Barnett, M., 1990, "Simulation of Three-Dimensional Viscous Flow Within a Multistage Turbine," *ASME JOURNAL OF TURBOMACHINERY*, Vol. 112, pp. 370-376.
- Adkins, G. G., Jr., and Smith, L. H., Jr., 1982, "Spanwise Mixing in Axial Flow Turbomachines," *ASME Journal of Engineering for Power*, Vol. 104, pp. 97-110.
- Blair, M. F., Dring, R. P., and Joslyn, H. D., 1989a, "The Effects of Tur-

bulence and Stator/Rotor Interactions on Turbine Heat Transfer: Part I—Design Operation Conditions,” *ASME JOURNAL OF TURBOMACHINERY*, Vol. 111, pp. 87–96.

Blair, M. F., Dring, R. P., and Joslyn, H. D., 1989b, “The Effects of Turbulence and Stator/Rotor Interactions on Turbine Heat Transfer: Part II—Effects of Reynolds Number and Incidence,” *ASME JOURNAL OF TURBOMACHINERY*, Vol. 111, pp. 97–103.

Carter, J. E., Edwards, D. E., and Werle, M. J., 1982, “Coordinate Transformation for Laminar and Turbulent Boundary Layers,” *AIAA Journal*, Vol. 20, pp. 282–284.

Caspar, J. R., Hobbs, D. E., and Davis, R. L., 1980, “Calculation of Two-Dimensional Potential Cascade Flow Using Finite Area Methods,” *AIAA Journal*, Vol. 18, pp. 103–109.

Cebeci, T., and Smith, A. M. O., 1974, *Analysis of Turbulent Boundary Layers*, Academic Press, New York.

Dring, R. P., and Joslyn, H. D., 1983, “The Relative Eddy in Axial Turbine Rotor Passages,” *ASME Paper No. 83-GT-22*.

Dring, R. P., Joslyn, H. D., Hardin, L. W., and Wagner, J. H., 1981, “Turbine Rotor–Stator Interaction,” *ASME Journal of Engineering for Power*, Vol. 106, pp. 729–742.

Dring, R. P., and Oates, G. C., 1990a, “Throughflow Theory for Nonaxisymmetric Turbomachinery Flow: Part I—Formulation,” *ASME JOURNAL OF TURBOMACHINERY*, Vol. 112, pp. 320–327.

Dring, R. P., and Oates, G. C., 1990b, “Throughflow Theory for Nonaxisymmetric Turbomachinery Flow: Part II—Assessment,” *ASME JOURNAL OF TURBOMACHINERY*, Vol. 112, pp. 328–337.

Edwards, D. E., Carter, J. E., and Werle, M. J., 1981, “Analysis of the Boundary Layer Equations Including a Coordinate Transformation—The ABLE Code,” United Technologies Research Center Report number UTRC-81-30.

Gallimore, S. J., and Cumpsty, N. A., 1986, “Spanwise Mixing in Multistage Axial Flow Compressors: Part I—Experimental Investigation,” *ASME JOURNAL OF TURBOMACHINERY*, Vol. 108, pp. 2–9.

Gallimore, S. J., 1986, “Spanwise Mixing in Multistage Axial Flow Compressors Part 2—Throughflow Calculations Including Mixing,” *ASME JOURNAL OF TURBOMACHINERY*, Vol. 108, pp. 10–16.

Harthorne, W. R., 1974, “Secondary Vorticity in Stratified Compressible Fluids in Rotating Systems,” CUED/A-Turbo/TR63, University of Cambridge, United Kingdom.

Joslyn, H. D., and Dring, R. P., 1989, “Three Dimensional Flow and Temperature Profile Attenuation in an Axial Turbine,” Final Report, AFOSR, Contract F49620-86-C-0020, Mar. 15.

Joslyn, H. D., and Dring, R. P., 1992, “Three-Dimensional Flow in an Axial Turbine: Part 2—Profile Attenuation,” *ASME JOURNAL OF TURBOMACHINERY*, Vol. 114, this issue.

Madavan, N. K., Rai, M. M., and Gavali, S., 1989, “Grid Refinement Studies of Turbine Rotor–Stator Interaction,” *AIAA Paper No. AIAA-89-0325*.

McDonald, H., and Kreskovsky, J. P., 1974, “Effect of Free-Stream Turbulence on the Turbulent Boundary Layer,” *International Journal of Heat and Mass Transfer*, Vol. 17, pp. 705–716.

Moore, J., and Ransmayr, A., 1984, “Flow in a Turbine Cascade, Part I: Losses and Leading Edges Effects,” *ASME Journal of Engineering for Gas Turbines and Power*, Vol. 106, pp. 400–408.

Moore, J., and Adhye, R. Y., 1985, “Secondary Flows and Losses Downstream of a Turbine Cascade,” *ASME Journal of Engineering for Gas Turbines and Power*, Vol. 107, pp. 961–968.

Rai, M. M., 1987, “Unsteady Three-Dimensional Navier-Stokes Simulations of Turbine Rotor–Stator Interaction Including Tip Effects,” *AIAA Paper No. AIAA 87-2058*.

Rai, M. M., 1989, Private Communication Regarding a Turbine Stage Calculation at NASA/Ames With the Same Rotor Aspect Ratio and Tip Clearance as in the Experiment, Jan. 12.

Sharma, O. P., Renaud, E., Butler, T. L., Milsaps, K., Dring, R. P., Joslyn, H. D., 1988, “Rotor–Stator Interaction in Multi-stage Axial-Flow Turbines,” *AIAA Paper No. AIAA-88-3013*.

Stabe, R. G., Whitney, W. J., and Moffitt, T. P., 1984, “Performance of a High Work Low Aspect Ratio Turbine Tested With a Realistic Inlet Radial Temperature Profile,” *AIAA Paper No. AIAA-84-1161*.

Stewart, W. L., 1959, “Analysis of Two-Dimensional Flow Loss Characteristics Downstream of Turbomachine Blade Rows in Terms of Basic Boundary Layer Characteristics,” *NACA-TN-3515*, July.

Three-Dimensional Flow in an Axial Turbine: Part 2—Profile Attenuation

D. Joslyn

R. Dring

United Technologies Research Center,
East Hartford, CT 06108

This paper presents an exhaustive experimental documentation of the three-dimensional nature of the flow in a one-and-one-half stage axial turbine. The intent was to examine the flow within, and downstream of, both the stator and rotor airfoil rows so as to delineate the dominant physical mechanisms. Part 1 of this paper presented the aerodynamic results. Part 2 presents documentation of the mixing, or attenuation, of a simulated spanwise inlet temperature profile as it passed through the turbine, including: (1) the simulated combustor exit-turbine inlet temperature profile, (2) surface measurements on the airfoils and endwalls of the three airfoil rows, and (3) radial-circumferential distributions downstream of each airfoil. Although all three rows contributed to profile attenuation, the impact of the rotor was strongest.

Introduction

The thermal analysis of a turbine airfoil is based on the delicate balancing of aerodynamics and thermodynamics. The external aerodynamics dictates the nature of the inviscid velocity distribution on the airfoil surface. The surface boundary layer dictates the heat load that the airfoil internal cooling scheme must absorb. This heat load is influenced by at least two additional factors, the introduction of film cooling, and the potentially nonuniform distribution of adiabatic recovery temperature in the free-stream flow. The internal cooling scheme of the airfoil must be locally tailored to absorb the highly nonuniform heat load and to produce an airfoil surface temperature distribution that is acceptable both in terms of the temperature levels and their gradients. Most of these aspects of heat transfer technology have been the focus of intense research over the years (Suo, 1978).

There is, however, a variety of turbine heat transfer mechanisms that have received very little attention for the simple reason that they are difficult to simulate experimentally. These are the mechanisms related to the actual turbine environment. They are related to the fact that the adiabatic recovery temperature of the combustor-generated flow entering the turbine is highly nonuniform, both circumferentially and radially. While the presence of these mechanisms has been acknowledged by the industry for many years, there is no definitive body of information currently available to quantify their impact.

The designer's goal is to devise an airfoil cooling scheme that produces not only the desired averaged temperature, but also an acceptably uniform temperature, i.e., controlling the

temperature gradients. Airfoils rarely burn out "on the average." They burn out locally. This necessitates designing a cooling scheme not for the average heat load, but for the local heat load. Since the adiabatic recovery temperature of the flow is the driving potential for the heat load, and since the adiabatic recovery temperature in the flow entering the turbine is highly nonuniform, it would be of value to be able to predict the attenuation (mixing) of the temperature profile through the turbine and the distribution of the recovery temperature on the airfoil and end wall surfaces.

A study of the effect of an inlet temperature profile on turbine performance was carried out by Stabe et al. (1984). They studied a single-stage gas generator turbine with an axisymmetric inlet temperature profile. Their results indicated that turbine aerodynamic performance was very insensitive to the inlet temperature profile. It should be pointed out, however, that the magnitude of the temperature profile they used was weak when compared to those commonly occurring in engines.

Temperature profile attenuation occurs because of radial transport. If the flow remained on stream surfaces, as assumed in strip theory, existing prediction methods would be sufficient. It is an unavoidable fact, however, that there are always strong radial transport mechanisms in turbines. These can be divided into two broad categories: deterministic and diffusive.

At the outset of this study it was anticipated that the deterministic mechanisms would be dominant in a turbine. An analysis by Adkins and Smith (1982) based on these mechanisms had been successful in predicting many aspects of spanwise mixing in a number of axial compressors. Since that time, however, something of a controversy has arisen over the relative contributions of the deterministic and diffusive mechanisms. The works of Gallimore and Cumpsty (1986) and Gallimore (1986) pointed out that a model based on diffusive mechanisms could also predict many aspects of spanwise mix-

Contributed by the International Gas Turbine Institute and presented at the 35th International Gas Turbine and Aeroengine Congress and Exposition, Brussels, Belgium, June 11-14, 1990. Manuscript received by the International Gas Turbine Institute January 9, 1990. Paper No. 90-GT-57.

ing in axial compressors. Most recently Wisler et al. (1987) have demonstrated that there are regions of the flow in an axial compressor where one or the other mechanism dominates. All of this previous work has been in axial compressors. The flow in axial turbines is, to put it mildly, very different. Turbines have strong flow accelerations and much higher flow turning. The secondary flows in turbines are also much stronger. In the present experiment the turbulence at the turbine inlet is small relative to the turbulence exiting a combustor. The inlet turbulence was 0.5 percent, while estimates of the turbulence in combustor exit flows are in the vicinity of 10 percent. This issue of the relative importance of the deterministic and diffusive mechanisms would, to a degree, be answered by an experiment with a high turbine inlet turbulence. However, this was beyond the scope of the present study.

Trace Gas Simulation

The primary objective of this study was to determine the degree to which an axisymmetric inlet temperature profile was attenuated, or mixed out, by the three-dimensional aerodynamic mechanisms present in a turbine. This was accomplished by documenting the aerodynamic flow field in the turbine (Part 1, Joslyn and Dring, 1992) and by measuring a simulated temperature profile as it was convected through the turbine.

Outside of the work extraction process (which is not modeled by the simulation), the temperature field does not play a major role in the three-dimensional nature of the flow in a turbine. Munk and Prim (1974) demonstrated that temperature gradients do not affect the streamline pattern of a flow. Their analysis, however, was restricted to flows in the absolute frame of reference. An extension of these concepts to the rotating frame of reference was demonstrated by Hawthorne (1974). He showed that secondary vorticity in the rotating frame of reference could be generated by gradients in the rotary total pressure as well as by gradients in the rotary total temperature (or density). For constant density flow in the rotating frame, the rotary total pressure is the kinematic equivalent of total pressure in the absolute frame in that a gradient in rotary total pressure is required to generate secondary vorticity. As pointed out by Hawthorne (1974) in the discussion of his Eq. (54), the effects of the rotary total pressure and temperature gradients will generally reinforce each other. However, it can also be seen in Hawthorne's Eq. (54) that the pressure gradient term should generally dominate the temperature gradient term. The conclusion here was that, in spite of the fact that the work extraction process and density gradients were not being modeled in the present experiment, the trace gas technique would give a reasonable simulation of the attenuation of an inlet temperature profile.

The application of the mass transfer analogy to obtain heat transfer information, i.e., temperature field redistributions, has been well documented in the past by Eckert and Goldstein (1976), Pederson et al. (1977), and Dring et al. (1980). The main assumption in this analogy is that throughout the flow field the turbulent Prandtl number (which governs heat transfer) and the turbulent Schmidt number (which governs mass transfer) vary in such a manner that their ratio, the turbulent Lewis number, is close to unity at all points. This assumption has been shown to be accurate for turbulent wakes and jets by Reynolds (1976). Although there are basic differences in the flow, it was expected that the analogy would be even better in the present turbine flow field due to the large-scale viscous

and inviscid radial flow mechanisms present. In Part 1 (Joslyn and Dring, 1992) it was demonstrated that these include the horseshoe and secondary flow vortices, as well as the relative eddy and the radial transport in the stator wakes.

The simulation was carried out using a distribution of a trace gas to simulate the total temperature field, that is, the radial temperature profile at the turbine inlet was simulated with a radial (nominally axisymmetric) profile of trace gas concentration. Carbon dioxide was chosen as the trace gas. Its molecular weight (44) is somewhat greater than that of air (29) but it has the advantages that it is neither toxic nor combustible. Other experimenters have used ethylene as a trace gas because its molecular weight (28) is closer to that of air. The safety hazard of using large quantities of a combustible gas precluded its application in the present experiment. The effects of the molecular weight of the trace gas are essentially eliminated as a result of the very low concentration levels used in the experiment. The maximum concentration was typically 1500 ppm (1000 to 1200 ppm above ambient), or 0.15 percent.

The mass transfer analogy was chosen to study turbine inlet temperature profile attenuation since for the present application a mass transfer process could be set up with greater accuracy in the boundary conditions. This included a well-defined axisymmetric inlet trace gas profile and "adiabatic" surfaces throughout the turbine model. In addition, a mass transfer process could be studied more accurately and more economically than the corresponding thermal process. The trace gas technique was applied to the problem of turbine temperature profile attenuation in a "proof-of-principles" experiment by Joslyn and Dring (1988). This paper demonstrated both the techniques necessary to generate the desired inlet profile and the measurement technique and its application in both the absolute and rotating frames of reference.

Description of the Experiment

Trace Gas Instrumentation. The UTRC Large-Scale Rotating Rig (LSRR) and turbine model used in this study are described in Part 1 of this paper (Joslyn and Dring, 1992). In addition to its aerodynamic measurement system, the LSRR has an independent system to measure trace gas concentrations. Concentrations were determined by drawing a gas sample through a conventional static pressure tap, a rotating rake mounted on the rotor hub, or a traverse probe in the flow. The static pressure taps were located both on the airfoils and on the end walls. The 19-element rake was mounted on the rotor hub and in line with the rotor leading edge plane. The traverse probe was installed in the planes used for the aerodynamic measurements (Part 1). Measurements were made in both the stationary and rotating frames of reference and the measurement sites for trace gas sampling were the same as those for the aerodynamic testing.

Gas samples were drawn from the sampling site (tap, rake, or probe) and fed into a gas analyzer. Since carbon dioxide was used as the trace gas, a Beckman Non-Dispersive infrared (NDIR) analyzer (Model 865) was used to measure the concentrations. The output of the NDIR was acquired, recorded, printed, and plotted by its own dedicated minicomputer. This computer also calibrated the NDIR using a series of calibration gases. The accuracy of the NDIR was 5 ppm. Ambient concentration varied between 300 and 500 ppm. The inlet concentration profile varied from ambient near the end walls to 1000 to 1500 ppm above ambient at its maximum. This trace

Nomenclature

B_x = airfoil axial chord
 C = trace gas concentration

CP = pressure coefficient = $(PTOA - P)/Q_{U_m}$

F = dimensionless concentration, Eq. (1)
 x = axial distance

gas measurement technique has been demonstrated previously in the LSRR turbine model in studies of the redistribution of (1) an axisymmetric inlet radial profile (Joslyn and Dring, 1988), and (2) a simulated combustor-generated hot streak (Butler et al., 1986).

The trace gas concentration data was reduced to a dimensionless coefficient based on the maximum and minimum (ambient) concentrations at the turbine inlet, Plane 1.

$$F = (C - C_{\min}) / (C_{\max} - C_{\min}) \quad (1)$$

where C_{\max} and C_{\min} are at Plane 1 and where $C_{\min} \approx C_{\text{amb}}$. Thus, throughout the turbine the concentration parameter varied between 0.0 and 1.0. The nominal C_{\max} at the inlet was based on the average of a number of radial surveys at the turbine inlet plane. Since the concentration in the incoming flow was not precisely axisymmetric, there are small regions in the flow where the local concentration parameter slightly exceeded 1.0. All circumferential averages of the concentration parameter presented are area averages (versus mass averages).

Inlet Trace Gas Profile. The inlet trace gas profile was generated with an array of five concentric injector rings located in a plane 63 in. (1.58 m) upstream of the first-stator leading edge. The turbine center body ended 24 in. (0.61 m) upstream of the first-stator leading edge and hence the flow velocity around the injector rings was very low (Part 1, Fig. 1). The rings were located far enough upstream of the first stator (approximately 13 chords) that their wakes were completely mixed out at the inlet traverse plane (Plane 1). The 3:1 flow area contraction between the rings and Plane 1 (due to the 0.8 hub/tip ratio) also contributed to the absence of the injector ring wakes.

The injector rings were fabricated from stainless steel tubes 0.5 in. in diameter. This was large enough that the static pressure in the rings was constant circumferentially. Around the circumference of each ring 144 miniature brass nozzle inserts, 0.020 in. in diameter, were uniformly distributed. Trace gas (carbon dioxide) was injected into the flow simultaneously through all five rings. By independently controlling the flow to each ring, the radial trace gas concentration profile at Plane 1 could be tailored to simulate any number of combustor exit (turbine inlet) temperature profiles. The profile used in this program was lowest at the hub and tip (i.e., ambient concentration, ≈ 400 ppm) and had its maximum near 60 percent span (typically 1200 ppm above ambient). This type of profile is typical of a wide range of engine applications (Taylor and Sabla, 1988).

The major difficulty in this approach was in achieving an acceptable degree of axisymmetry in the inlet trace gas profile (at Plane 1). This problem was aggravated by small differences in the size of the 720 holes in the injector rings and by minuscule distortions in the flow over the rings. The problem was further complicated by the fact that while a large number of inlet surveys would be needed to document the inlet concentration distribution exhaustively, practicality limited the program to a relatively small number. In this program surveys in Plane 1 were carried out at four circumferential locations 90 deg apart.

Trace Gas Results

Inlet Profile. The inlet trace gas profile was generated by adjusting the CO_2 flow rate to each of the five injector rings upstream of the test section. It was documented at Plane 1, 97 percent axial chord upstream of the stator leading edge. This inlet documentation was carried out by making radial traverses from hub to tip endwalls at four circumferential locations. After considerable adjustment the results presented in Fig. 1 were obtained. The range of concentrations at each radial location is indicative of the degree of trace gas profile axisymmetry achieved in the inlet flow. The nonaxisymmetry

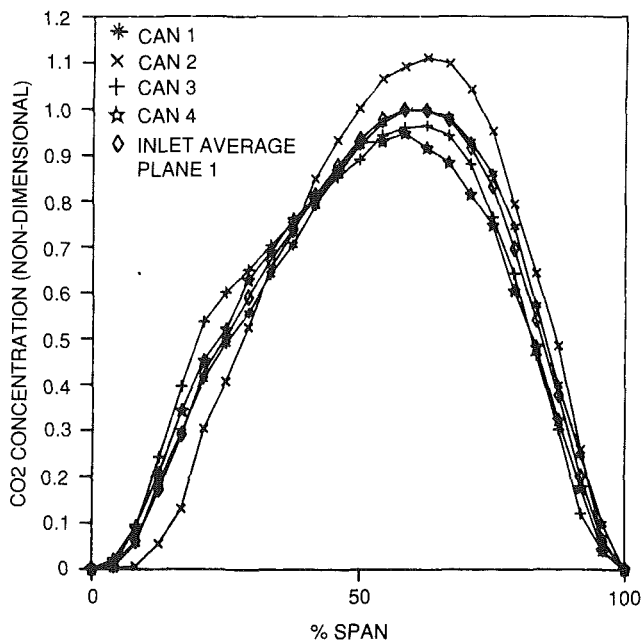


Fig. 1 Inlet, plane 1, trace gas concentration profiles

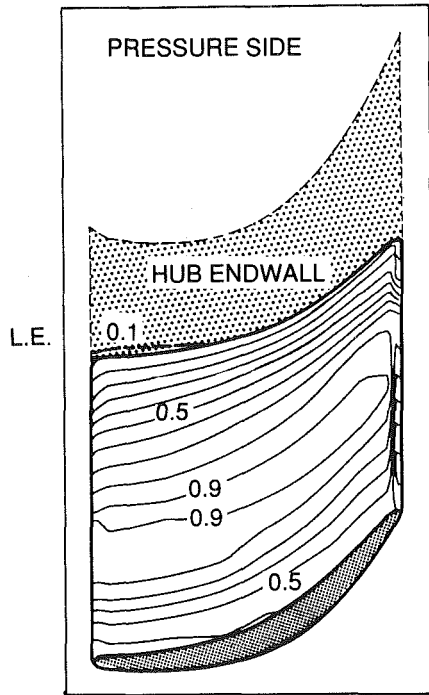
in the inlet trace gas concentration parameter was approximately 0.1. As mentioned above, the measurement uncertainty in the NDIR readings (both here and in the data presented below) was much less than this. The average of the four inlet profile measurements is also shown. The average inlet trace gas profile served as a basis of comparison for the data measured at the various locations through the turbine. The dimensionless concentration parameter was based on this profile, 0.0 representing the minimum and 1.0 the maximum. The location of the maximum at 60 percent span corresponded to typical engine turbine inlet temperature profiles (Taylor and Sabla, 1988).

The radial area average of the inlet trace gas profile at Plane 1 was 0.57. Since the flow velocity at this plane was axial and uniform (except for the hub and tip boundary layers) this average corresponded closely to the concentration that the flow in the turbine will approach as it becomes increasingly mixed out. The results of the trace gas measurements will be discussed on a row-by-row basis across the turbine.

First Stator. The trace gas measurements made on the surface of the first-stage stator and on the hub endwall are presented in Fig. 2. These results were based on measurements made at seven span locations and at 22 locations around the perimeter of the airfoil and at 30 locations on the hub. The concentrations were rendered in terms of contours to indicate the variation of the dimensionless concentration parameter between 0.0 and 1.0. Generally speaking, the distributions of the high and low concentration fluid on the airfoil surfaces are what one might have expected based on the surface flow visualization (Part 1, Fig. 2).

There is a high concentration region around midspan extending from the leading to the trailing edge of the airfoil. It is nearly uniform in spanwise extent on the pressure surface but on the suction surface there is a spanwise contraction due to the hub and tip secondary flows. The tip secondary flow was seen to be the more influential of the two due to the general tip-to-hub transport of the low-momentum fluid. The hub end wall concentration is relatively uniform and at a very low level. This was also true for the tip end wall (not shown).

Concentration measurements made at the seven span locations on the stator leading edge are compared with the average inlet profile in Fig. 3. The only major change is an increase in concentration at the stator tip and a much smaller increase



TIP

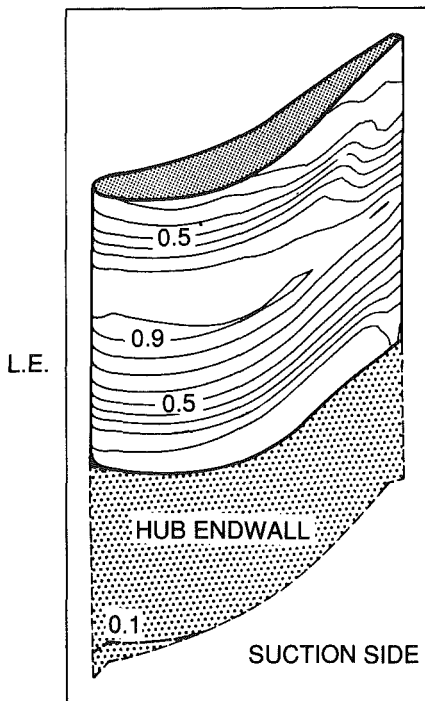


Fig. 2 First-stator surface trace gas concentration

at the hub. These increases may have been due to the leading edge horseshoe vortex bringing higher concentration fluid toward the end walls. Recall that the tip inlet boundary layer is roughly 50 percent thicker than that at the hub (Part 1). The increases may also have been due partially to the nonaxisymmetry of the inlet concentration. The increase at the tip, however, is too large to attribute to nonaxisymmetry. The horseshoe vortex, therefore, could be an important mechanism for transporting hot core-flow fluid to the end walls.

The traverse data at Plane 1, 17 percent axial chord aft of the first stator, is shown in Fig. 4. As with the aerodynamic measurements, data were acquired over two first-stator pitches.

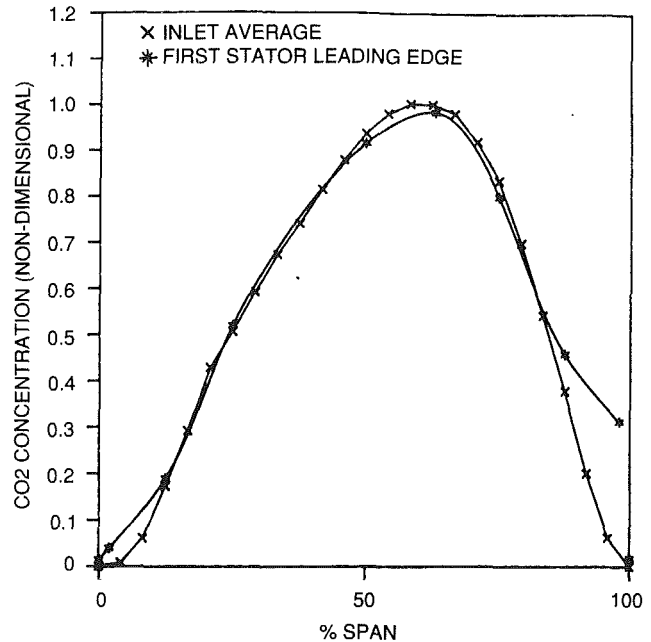


Fig. 3 First-stator leading edge trace gas concentration profile

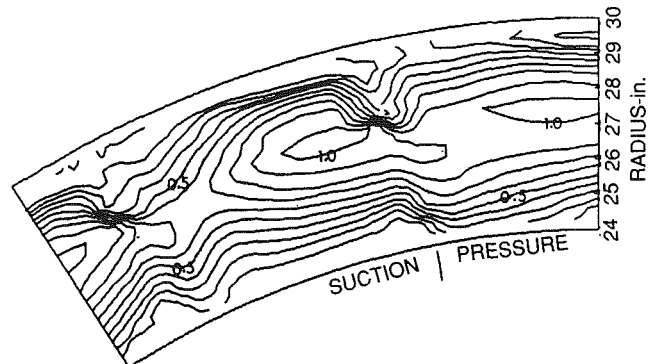


Fig. 4 First stator exit, plane 2, trace gas contours, $\Delta F=0.1$

The degree of periodicity in these results was consistent with an inlet nonaxisymmetry of approximately 0.1. The dominant feature in these contours was the radial transport toward the hub that occurred in the stator wakes. This could be seen by comparing these concentration data with the stator exit total pressure data and with the stator exit secondary flow data in Part 1 (Figs. 5a and 5b, respectively). The strong flow toward the hub in the stator wake carried the high and low-concentration fluid with it. There is also evidence that the secondary flow is driving low-concentration fluid up the stator suction surface near the hub. Between the wakes the contours remained relatively axisymmetric. The main driver for temperature profile attenuation here is the radial transport due to the secondary flow and due to the radial pressure gradient in the airfoil wake.

Rotor. The trace gas measurements made on the surface of the rotor and on the hub endwall are presented in Fig. 5. These results are based on measurements made at seven span locations and at 22 locations around the perimeter of the airfoil and at 28 locations on the hub endwall. The concentrations have been rendered in terms of contours to indicate the variation of the dimensionless concentration parameter between 0.0 and 1.0. Overall, the distributions of the high and low-concentration fluid on the airfoil surfaces are what one might have expected based on the surface flow visualization (Part 1, Figs. 2a and 2b). The three-dimensional flow mechanisms are much stronger on the rotor than on the first stator. This can

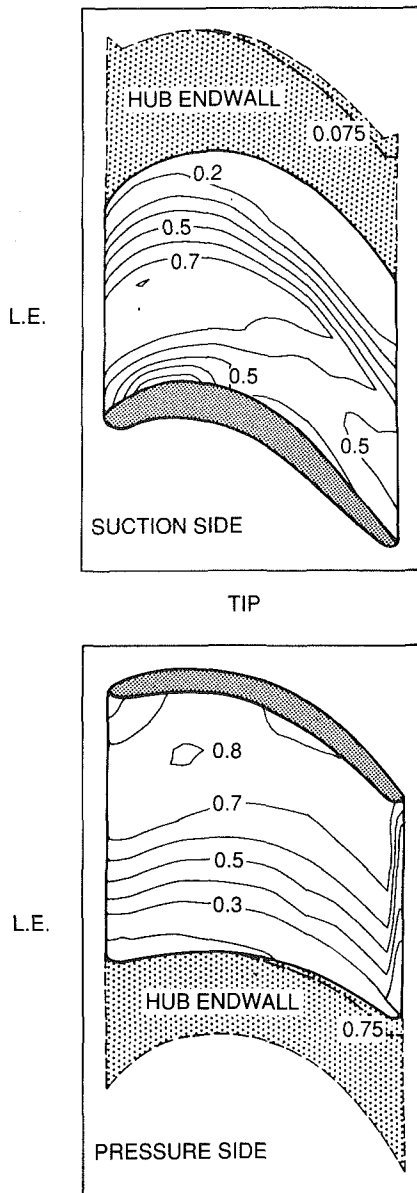


Fig. 5 Rotor surface trace gas concentration

be seen on both the suction and pressure surfaces. The suction surface is strongly influenced by the hub and tip secondary flows. They prevent the high-concentration fluid from reaching the trailing edge by driving the lower concentration fluid from the end walls out onto the rotor suction surface. The relatively high concentration region at the tip (along the aft portion of the suction surface) is due to the leakage flow through the rotor tip clearance.

Strong radial transport is present on the pressure surface due to the "relative eddy" (Dring and Joslyn, 1983). This inviscid mechanism is strictly associated with the rotating frame of reference. Its primary effect is to transport the high-concentration fluid that enters the rotor passage near midspan outward toward the tip along the pressure surface. This is the source of the relatively high concentration tip leakage fluid on the suction surface near the tip. This fluid has been transported radially out toward the tip along the pressure surface. It is then convected through the rotor tip clearance gap by the strong pressure gradient there. The conclusion is that the temperature of the flow leaking over a rotor tip is not the relatively cool fluid that enters the rotor passage near the tip but rather the

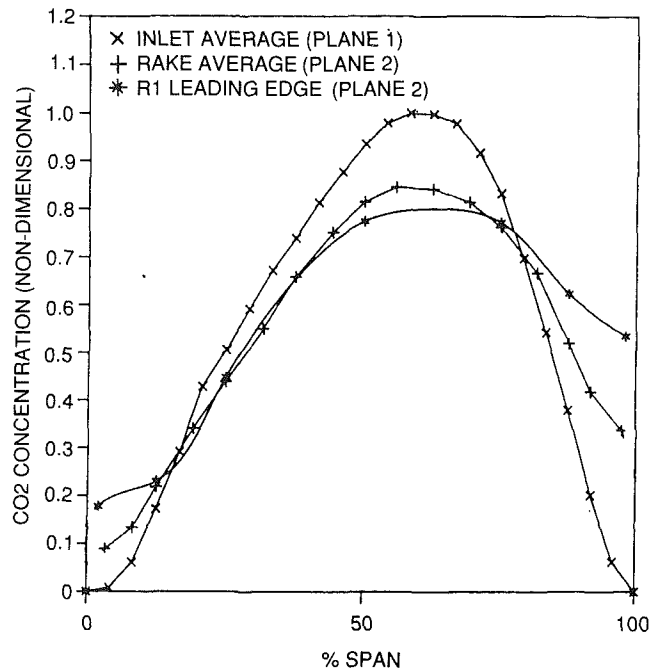


Fig. 6 Comparison of the rotor rake and the rotor leading edge profiles

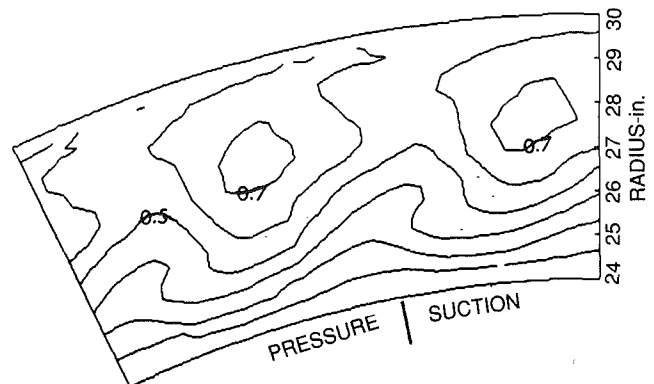


Fig. 7 Rotor exit relative, plane 3; relative, trace gas contours, $\Delta F = 0.1$

much hotter fluid that enters the passage near midspan. This is one of the reasons why rotor tip durability has frequently been a problem throughout the industry. As on the first-stator hub, the concentration distribution on the rotor hub was very uniform and at a relatively low level.

The concentration profiles from the leading edge measurements made at the seven spanwise locations on the rotor airfoil are compared with the rotor leading edge rake (mounted on the rotor hub) data and with the turbine inlet profile in Fig. 6. Relative to the inlet profile, these results show a further reduction of the maximum concentration and an increase near the end walls. The mechanisms contributing to this include the radial flow in the first stator wake and in its secondary flow, and also horseshoe vortices at the rotor hub leading edge.

The traverse data taken in the rotating frame of reference at Plane 3, 36 percent aft of the rotor, are presented in Fig. 7. These results were acquired over two rotor pitches. All nonaxisymmetry at the rotor inlet was averaged out by the rotor motion. Accordingly, the profile redistribution at this plane is due to the rotor secondary flow. The maximum concentration has been reduced from about 0.85 at the rotor leading edge rake (Fig. 6) to about 0.7 at this traverse plane. There is a high degree of periodicity in the results due to the rotor

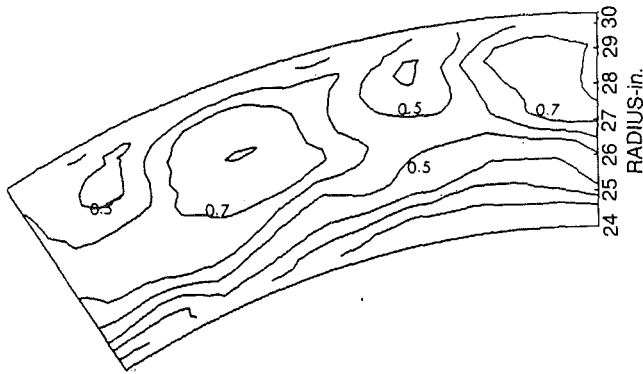


Fig. 8 Rotor exit absolute, plane 3; absolute, trace gas contours, $\Delta F = 0.1$

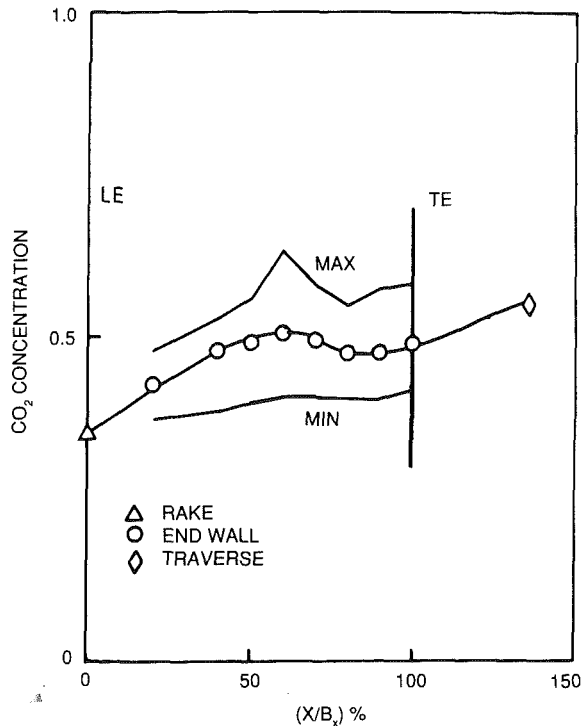


Fig. 9 Rotor shroud trace gas concentration

averaging out the inlet nonaxisymmetries. The fact that these contours were driven by secondary flow can be seen by overlaying Fig. 7 and the rotor exit secondary flow vectors shown in Part 1, Fig. 6(b).

The traverse data taken in the absolute frame of reference at Plane 3, 36 percent aft of the rotor, are presented in Fig. 8. These results were acquired over two first-stage stator pitches. It is evident from the periodic variations in these results that the distortions introduced by the first stator are being convected through the rotor. Unlike the rotating frame results, these results contain the influence of the nonaxisymmetries in the turbine inlet concentration. It is noteworthy that these distortions persist through the first stage. This suggests that it might be possible to reduce the second-stator heat load by setting the second-stator airfoil count equal to that of the first stator and by locating the airfoils in the relatively cool parts of the flow. It is interesting to note that the maximum concentration in both the rotating and stationary frame traverses is somewhat above 0.7. This indicates that the temporal and spatial variations in both frames of reference are of the same magnitude ($\text{max} - \text{min} \approx 0.2$).

Upon comparing the rotor inlet rake results (Fig. 6) with the rotor exit traverse results in the tip region, a large increase in trace gas concentration from the rotor inlet to the rotor exit

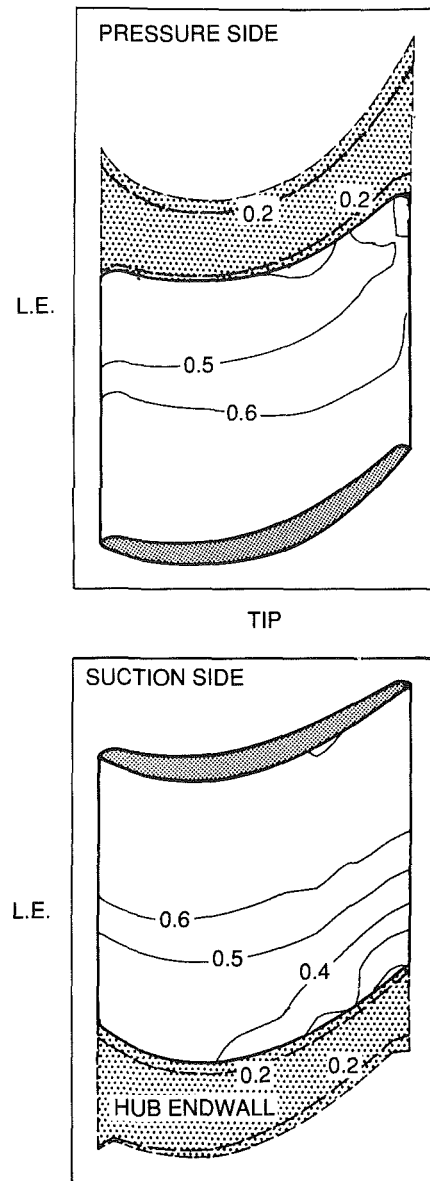


Fig. 10 Second-stator surface trace gas concentration

was observed. The rotor inlet rake indicated a concentration near the tip of about 0.35. The rotor exit traverses in both the absolute and rotating frames indicated a tip concentration of about 0.55. These results, along with data acquired on the stationary rotor shroud between the rotor leading and trailing edges, are shown in Fig. 9. A general increase in the concentration at the tip can be seen from the rotor leading edge to the rotor exit traverse plane (36 percent aft). This increase is due to the transport toward the tip of high concentration fluid from the midspan region. This transport is due to the relative eddy, rotor tip leakage, and the rotor tip secondary flow vortex.

The shroud results plotted in Fig. 9 between the rotor leading and trailing edges are the averages of seven measurements distributed over one first stator pitch at each axial location. The "Max" and "Min" lines represent the envelope of these results. The width of this band is due partially to the nonaxisymmetry of the concentration in the inlet flow and partially to the nonaxisymmetries generated by the first stator.

Second Stator. The trace gas measurements made on the surface of the second-stage stator and on the hub endwall are presented in Fig. 10. These results were based on measurements

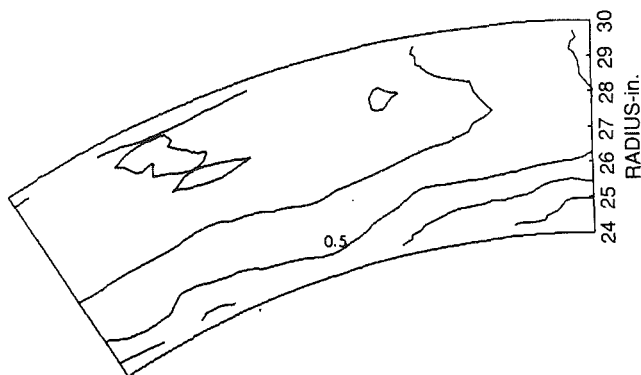


Fig. 11 Second-stator exit, plane 4, trace gas contours, $\Delta F = 0.1$

made at seven span locations and at 22 locations around the perimeter of the airfoil and at 30 locations on the hub endwall. The concentrations were rendered in terms of contours to indicate the variation of the dimensionless concentration parameter between 0.0 and 1.0. The distributions of the high and low-concentration fluid on the airfoil surfaces are what one might have expected based on the surface flow visualization (Part 1, Fig. 2). The fact that the mixing across the rotor is strong is evident by the reduced number of the contours on the second stator. The concentration profile has been driven to approach the average concentration of 0.57.

As on the first stator, the distribution on the second-stator pressure surface is relatively uniform from the leading edge to the trailing edge. Both the suction and pressure surfaces no longer have distributions that are symmetric about midspan (as on the first stator) but rather they have an almost linear gradient from lower concentrations at the hub to higher concentrations at the tip. This is a result of the radial redistribution through the rotor passage due to the relative eddy (rotation of the Bernoulli surfaces). As on the first stator and rotor hubs, the concentration distribution on the second stator hub is very uniform and at a relatively low level. The same is true for the tip end wall (not shown).

The conclusion reached here is that the radial redistribution occurring in the rotor can transport the higher concentration fluid out toward the second stator tip. This suggests that the high heat load conditions on second stators will be nearer the tip, rather than at midspan. Parenthetically, the relative eddy is an inviscid mechanism (Dring and Joslyn, 1983). It should be predicted relatively accurately by the three-dimensional Euler calculations that are becoming increasingly common in the industry.

The results of the traverse data taken at Plane 4, 14 percent axial chord aft of the second stator, are presented in Fig. 11. The most striking feature here is that the concentration distribution is nearly axisymmetric and that the hub-to-tip gradient is very weak. These data were acquired over two first-stator pitches; however, because of the axisymmetry, it didn't matter much whether they were averaged across the pitch of the first or second stator. Circumferentially averaged second-stator exit traverse data indicated there was continued mixing toward a uniform profile.

A summary of the concentration profile attenuation process across the three rows of turbine airfoils is given in Fig. 12. Four profiles are presented: (1) the average inlet profile, (2) the rotating rotor leading edge rake profile, (3) the circumferential average of the rotor exit traverse data acquired in the rotating frame of reference, and (4) the circumferential average of the second stator exit traverse data. The most noticeable change across the first stator (between Planes 1 and 2) is the reduction in the maximum (from 1.0 to 0.85). There is also transport of high-concentration fluid onto the end walls, the most noticeable occurring at the tip. The reduction in the maximum and the increase at the end walls is due to a com-

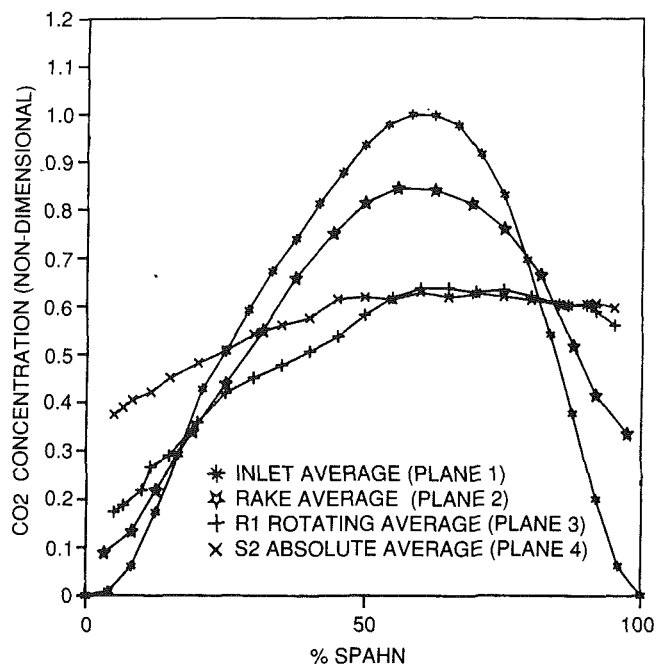


Fig. 12 Comparison of concentration profiles at planes 1, 2, 3, and 4

ination of the leading edge horseshoe vortex and the passage secondary flow at the hub and tip. Radial flow in the wake toward the hub also contributes to the increase in the hub end wall region. Across the rotor there is a further reduction (from 0.85 to 0.65) in the maximum concentration. Although high-concentration fluid is transported onto both endwalls by passage second flows, the relative eddy and the tip leakage vortex combine to produce a significant increase in concentration in the tip endwall region. Between 60 percent span to the tip endwall, the concentration is nearly constant and is significantly greater than that in the tip endwall region at the stage inlet. The results at the second-stator exit indicate changes have occurred mainly near the hub and there is continued mixing toward a uniform concentration distribution.

The salient features of the trace gas concentration data shown are (1) the reduction in the profile maximum, (2) the increase in the hub and tip minima, and (3) the strong impact of the rotor in the profile attenuation process. Another important (and expected) feature of these results is that both from above and from below the local concentration is approaching the inlet area-averaged value of 0.57.

All the data shown here are presented in greater detail by Joslyn and Dring (1989).

Conclusions

The trace gas technique gave an excellent simulation of temperature insofar as the profile attenuation process was concerned. Adiabatic boundary conditions were observed exactly and measurements on the airfoil and in the flow were made with very high accuracy. The main conclusions from the profile attenuation portion of this study are:

- 1 The major sources of radial mixing due to the first stator were the radial flow in its wake due to the radial static pressure and the end wall secondary flows. Radial mixing continued to occur in the axial gap between the first stator and the rotor.

- 2 Radial mixing in the rotor was dominated by the hub and tip secondary flows, the relative eddy, and the tip leakage flow.

- 3 The circumferential variations in trace gas concentration in the flow entering the second stator suggest that it might be possible to reduce the second-stator heat load by setting the second-stator airfoil count equal to that of the first stator and by locating the airfoils in the relatively cool parts of the flow.

4 The effect of the relative eddy in the rotor passage was preferentially to drive high-concentration (hot) fluid toward the tip and this results in higher heat loads at the second stator tip.

5 The radial mixing in the flow over the rotor caused an increase in the trace gas concentration along the stationary rotor tip shroud.

6 The concentration gradients in the flow aft of the second stator were very weak.

7 The profile attenuation process was nearly complete aft of the second stator and although all three airfoils played powerful roles, for this configuration the rotor was the strongest.

Acknowledgments

The authors owe a debt of gratitude to a number of talented, patient, and committed people for the success of this program. Bill Tierney breathed life back into a traverse system that had been dormant and he kept it working faithfully. Ray Valliere acquired most of the data and on numerous occasions he demonstrated his formidable trouble-shooting skills. Finally, Lisa Vaughn and Diane Rodimon spent many long weeks reducing the data and generating the figures in this paper. We are privileged to have each of these people as a co-worker. This experimental program was carried out under Air Force funding under the direction of Dr. James Wilson, Dr. James McMichael, and Captain Henry Helin, AFOSR Contract No. F49620-86-C-0020.

References

Adkins, G. G., Jr., and Smith, L. H., Jr., 1982, "Spanwise Mixing in Axial-Flow Turbomachines," *ASME Journal of Engineering for Power*, Vol. 104, pp. 97-110.

Butler, T. P., Sharma, O. P., Joslyn, H. D., and Dring, R. P., 1986, "Redistribution of an Inlet Temperature Distortion in an Axial Flow Turbine Stage," AIAA Paper No. AIAA-86-1468; *Journal of Propulsion and Power*, Vol. 5, Jan-Feb. 1989, pp. 64-71.

Dring, R. P., Blair, M. F., and Joslyn, H. D., 1980, "Experimental Investigation of Film Cooling on a Turbine Rotor Blade," *ASME Journal of Engineering for Power*, Vol. 102, pp. 81-87.

Dring, R. P., and Joslyn, H. D., 1983, "The Relative Eddy in Axial Turbine Rotor Passages," ASME Paper No. 83-GT-22.

Eckert, E. R. G., and Goldstein, R. J., 1976, *Measurement Methods in Heat Transfer*, 2nd ed., Hemisphere Publishing Corp., Washington, DC.

Gallimore, S. J., and Cumpsty, N. A., 1986, "Spanwise Mixing in Multistage Axial Flow Compressors: Part 1—Experimental Investigation," *ASME JOURNAL OF TURBOMACHINERY*, Vol. 108, pp. 2-9.

Gallimore, S. J., 1986, "Spanwise Mixing in Multistage Axial Flow Compressors: Part 2—Throughflow Calculations Including Mixing," *ASME JOURNAL OF TURBOMACHINERY*, Vol. 108, pp. 10-16.

Harthorne, W. R., 1974, "Secondary Vorticity in Stratified Compressible Fluids in Rotating Systems," CUED/A-Turbo-TR63, University of Cambridge, United Kingdom.

Joslyn, H.D., and Dring, R. P., 1988, "A Trace Gas Technique to Study Mixing in a Turbine Stage," *ASME JOURNAL OF TURBOMACHINERY*, Vol. 110, pp. 38-43.

Joslyn, H. D., and Dring, R. P., 1989, "Three Dimensional Flow and Temperature Profile Attenuation in an Axial Turbine," Final Report, AFOSR, Contract F49620-86-C-0020, Mar. 15 (R89-957334-1).

Joslyn, H.D., and Dring, R. P., 1992, "Three-Dimensional Flow in an Axial Turbine: Part 1—Aerodynamic Mechanisms," *ASME JOURNAL OF TURBOMACHINERY*, Vol. 114, this issue.

Munk, M., and Prim, R. C., 1947, "On the Multiplicity of Steady Gas Flows Having the Same Streamline Pattern," *Proceedings of the National Academy of Sciences*, U.S., Vol. 33.

Pederson, D. R., Eckert, E. R. G., and Goldstein, R. J., 1977, "Film Cooling With Large Density Differences Between the Mainstream and the Secondary Fluid Measured by the Heat-Mass Transfer Analogy," *ASME Journal of Heat Transfer*, Vol. 99, pp. 620-627.

Reynolds, A. J., 1976, "The Variation of Turbulent Prandtl and Schmidt Numbers in Wakes and Jets," *International Journal of Heat and Mass Transfer*, Vol. 19, pp. 757-764.

Stabe, R. G., Whitney, W. J. and Moffitt, T. P., 1984, "Performance of a High Work Low Aspect Ratio Turbine Tested With a Realistic Inlet Radial Temperature Profile," AIAA Paper No. AIAA 84-1161.

Suo, M., 1978, "The Aerothermodynamics of Aircraft Gas Turbine Engines," AFAPL-TR-78-52, G. C. Oates, ed., Chap. 19, "Turbine Cooling."

Taylor, J. R., and Sabla, P. E., 1988, "Combustion Systems Design," University of Tennessee Space Institute Short Course in Aeropropulsion, Apr.

Wisler, D. C., Bauer, R. C., and Okiishi, T. H., 1987, "Secondary Flow, Turbulent Diffusion, and Mixing in Axial-Flow Compressors," *ASME JOURNAL OF TURBOMACHINERY*, Vol. 109, pp. 455-482.

O. P. Sharma

G. F. Pickett

R. H. Ni

Pratt & Whitney,
East Hartford, CT 06108

Assessment of Unsteady Flows in Turbines

The impacts of unsteady flow research activities on flow simulation methods used in the turbine design process are assessed. Results from experimental investigations that identify the impact of periodic unsteadiness on the time-averaged flows in turbines and results from numerical simulations obtained by using three-dimensional unsteady Computational Fluid Dynamics (CFD) codes indicate that some of the unsteady flow features can be fairly accurately predicted. Flow parameters that can be modeled with existing steady CFD codes are distinguished from those that require unsteady codes.

Introduction

Real flows in turbines are highly unsteady and three dimensional due to relative movements of adjacent airfoil rows and circumferential as well as spanwise gradients in total pressure and temperature induced by upstream airfoil rows, burners, and inlet systems. Designs of turbines are, however, based on Computational Fluid Dynamics (CFD) codes that rely on numerical solutions of three-dimensional steady flow equations through turbine airfoil rows. Unsteady effects in these codes are implicitly accounted for through the use of empirical correlations and "experience factors." Due to the unavailability of appropriate data bases, the numerical values for these "experience factors" do not reflect the real physics. Application of current design procedures, outside the regime from which the experience factors were deduced, can result in extensive development costs.

A significant level of research activity has recently been directed toward quantifying the impact of unsteadiness on turbine performance and heat loads in order to develop more physics-based prediction systems for multistage turbines. Factors that have contributed to the rise in research activity in the turbine field include:

- Short duration test facilities (Dunn, 1980; Epstein et al., 1984).
- Instrumentation, data acquisition, and data reduction systems (Williams, 1988; Anand and Lakshminarayana, 1978; Sharma et al., 1985).
- Large storage and high-speed computers.
- Improved solution algorithms for unsteady inviscid and viscous flow equations (Erdos et al., 1977; Rai, 1987; Ni et al., 1989).
- Computer graphics and animation techniques that permit real time visualization of the experimental and computed results (Sharma et al., 1985; Rai, 1987; Ni et al., 1989).

The overall objective of this paper is to assess the impact

of these research activities on flow simulation methods used in the turbine design process. In particular, flow parameters that can be modeled with existing steady CFD codes are distinguished from those that require unsteady CFD codes.

CFD Codes and Experimental Data Used in Existing Turbine Design Procedures

Significant advances in the simulation capabilities of steady flow through turbines have been made over the past fifteen years due to the development of three-dimensional CFD codes (Denton, 1975; Ni, 1982; Rhie, 1986; Hah, 1984). Turbine design engineers have utilized these CFD codes to improve the performance of turbines through three-dimensional stacking of airfoils and recontouring of flow paths (Huber et al., 1985; Hourmouziadis and Hubner, 1985). It may be pointed out here that the main contributions to the enhancement in turbine performance have been realized through redistribution of flow, which can be achieved primarily by using Euler codes. Optimization of airfoil rows by using Navier-Stokes codes, through minimization of losses, has not yet been fully exploited in the design process due to the unavailability of faster and larger storage computers and to the limitation of accurate turbulence models.

The fundamental physics of the flow-through turbine airfoil rows was identified from detailed experiments conducted in a turbine cascade with different magnitudes of incoming boundary layer thicknesses (total pressure profiles, Langston et al., 1977; Barber and Langston, 1979; Graziani et al., 1980). Results from these experiments, shown in Fig. 1, clearly demonstrate that airfoil loadings and exit angle distributions are highly dependent on the incoming total pressure profiles to the cascade (Fig. 1a), and that the net losses for the cascade are not affected by the inlet profiles (Fig. 1b).

These results indicate that three-dimensional Navier-Stokes codes with wall functions or three-dimensional Euler codes with relatively simple loss models are sufficient to define the flow through turbine airfoil rows provided incoming boundary conditions (total pressure and angle profiles) are appropriately defined. There is, however, a need to calibrate the wall functions and surface shear models in these codes by using cascade

Contributed by the International Gas Turbine Institute and presented at the 35th International Gas Turbine and Aeroengine Congress and Exposition, Brussels, Belgium, June 11-14, 1990. Manuscript received by the International Gas Turbine Institute January 26, 1990. Paper No. 90-GT-150.

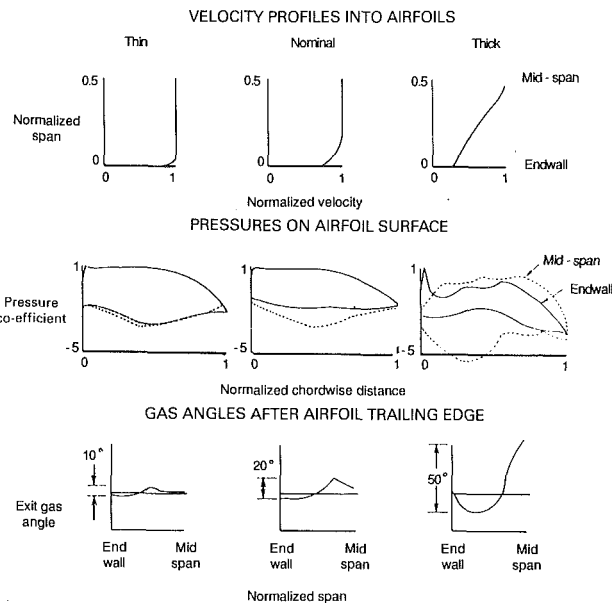


Fig. 1(a) Spanwise distributions of airfoil loadings and gap-averaged exit gas angles strongly influenced by incoming total pressure (velocity) profiles in cascades (Langston et al., 1977; Graziani et al., 1980; Barber and Langston, 1979)

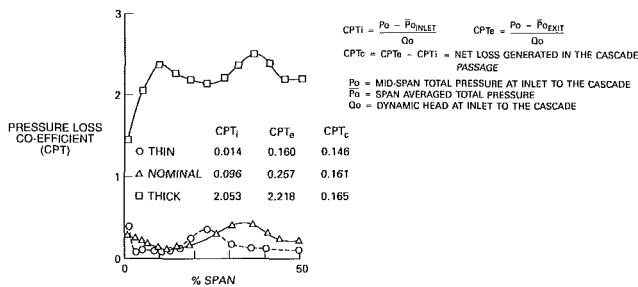


Fig. 1(b) Net losses generated in the cascade passage unaffected by the inlet velocity profile (Langston et al., 1977; Graziani et al., 1980; Barber and Langston, 1979)

and turbine rig data to ensure that the models are applicable over a range of airfoil designs.

To provide realistic estimates of inflow boundary conditions for each airfoil row in a multistage turbine environment, a three-dimensional steady multistage code was developed (Ni and Bogdan, 1989). This code is based on the numerical solution of three-dimensional Euler equations. The evolution of losses in this code is modeled by using surface drag forces similar to the one discussed by Denton (1986). Schematics of flow calculations through a two-stage turbine by using this multistage code are shown in Fig. 2. Flow simulations using this code are conducted by specifying boundary conditions at inlet (total pressure, flow angles, and total temperature) to the first stator and at exit (static pressure) to the second rotor. The flow conditions upstream of the last three airfoil rows are computed during the calculation process and are averaged in the circumferential direction to provide steady, axisymmetric upstream boundary conditions to the subsequent airfoil rows. This procedure has been demonstrated to yield accurate estimates of airfoil loadings and flow distribution as shown in the example of Fig. 2.

Application of the above procedure in the design process has yielded significant improvements in the turbine performance. The improvement in performance for the example shown in Fig. 3 (Huber et al., 1985) was primarily achieved by leaning and bowing of airfoils to achieve desirable loading distributions.

Three-dimensional, steady flow calculation methods such as that discussed above are routinely and interactively used by turbine designers to increase the performance of multistage turbines.

Two approaches can be undertaken to advance the state of the art of the turbine design process further:

(i) improve loss and heat load prediction capabilities of the steady three-dimensional codes.

(ii) account for unsteady effects that are not adequately modeled in the current steady CFD codes.

The first approach requires development of CFD codes that have very low numerical losses and development of reliable turbulence models that will permit accurate predictions of transitional, separated, and turbulent flow regimes. Advancement in the development of turbulence models that will predict the growth of boundary layers on turbine airfoils by using physics-based concepts is anticipated to be achieved by analysis of numerical data currently being generated at the Center for Turbulence Research (1987) through the full simulation of Navier-Stokes equations. In addition to development of CFD codes, adaptive grid techniques that can capture the domain of loss generation in a cost-effective manner are needed (Dannenhofer and Baron, 1985). Physics-based models are unlikely to be available to the turbine designers in the next decade. In the meantime, designers have to contend with available empirical turbulence models and computational grids.

The second approach requires identification and modeling of unsteady flow mechanisms that are currently unaccounted for in the design process. These unsteady flow mechanisms in turbines, obtained from basic experimental and numerical investigations, are discussed in the following sections.

Unsteady Flow Effects in Turbines—Experimental Data

With the exception of first stators, flows in all turbine airfoils are highly unsteady because they periodically encounter flow distortions generated by upstream airfoil rows and combustors. These periodic distortions contain both large-scale organized flow structures (streamwise vortices) and randomly moving small-scale flow structures (wakes and temperature streaks). The induced unsteady flows are dependent on the scale of upstream distortions. The effects of wakes and temperature streaks and those induced by streamwise vortices are discussed below.

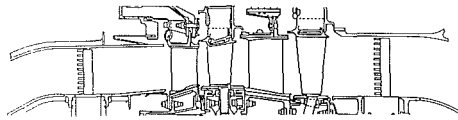
Effects of Upstream Wakes and Temperature Streaks. The circumferential variations in the velocity field downstream of the first stators for turbines are normally generated by the drag on the airfoil and endwall surfaces, which causes a reduction in velocity and increases in the turbulence levels in the low velocity regions. In some flow situations, especially for airfoil rows downstream of a combustor, high-velocity jets exist due to large circumferential gradients in temperatures. The effects of these upstream velocity variations can be simply illustrated through the use of velocity triangles, as shown in Fig. 4 (Kerbrock and Mikolajczak, 1970; Greitzer and Tan, 1987). This figure shows that the low-velocity fluid has a normal velocity component toward the suction side of the downstream airfoil indicating that the high-turbulence, low-velocity fluid from the upstream airfoil wake will migrate toward the suction side of the airfoil. In a similar manner, high-velocity (high-temperature) fluid will migrate toward the pressure side of the downstream airfoil. This preferential migration of fluid particles has three effects:

(i) Alterations in the boundary layer characteristics of the airfoil through its effect on the transition process.

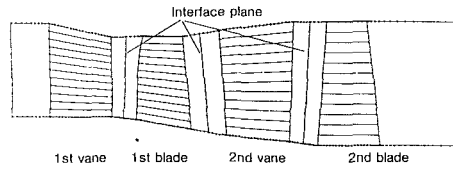
(ii) Variation in the secondary flow generation for downstream passages.

(iii) Redistribution of stagnation enthalpy.

ELEVATION VIEW OF A TWO-STAGE HIGH PRESSURE TURBINE RIG.



COMPUTATIONAL BOUNDARIES FOR THE MULTI-STAGE FLOW SIMULATION.



COMPUTATIONAL MESH USED FOR THE TWO-STAGE TURBINE FLOW SIMULATION.

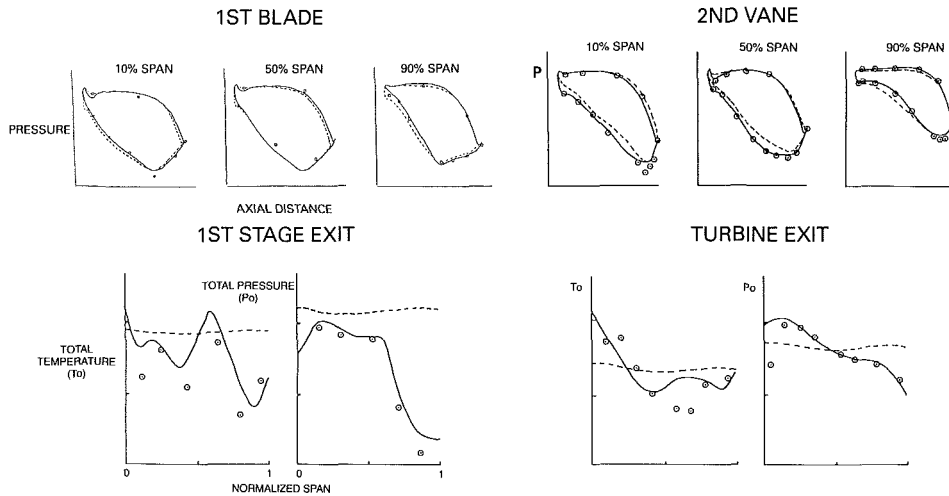
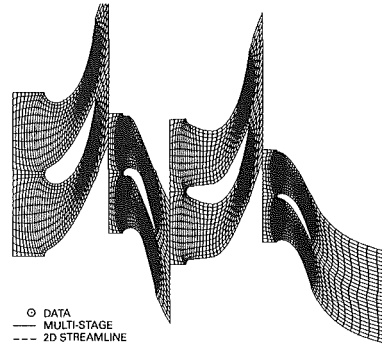


Fig. 2 Three-dimensional steady multistage Euler code of Ni and Bogoiian (1989) provides accurate estimates of airfoil loadings and total pressure as well as total temperature profiles in multistage turbines

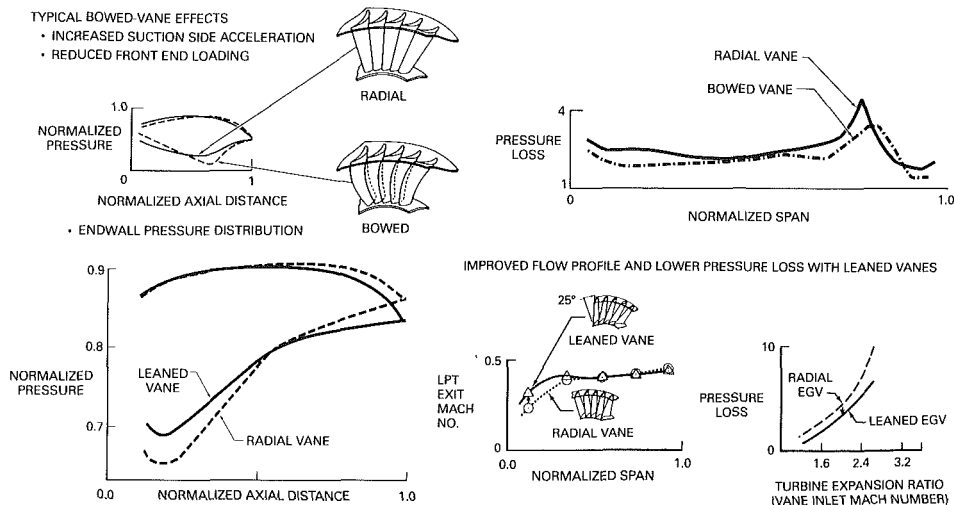


Fig. 3 Bowed and leaned vanes designed by Huber et al. (1985) to improve loading distributions in endwall regions by using three-dimensional Euler codes yielded improved performance over the baseline radial designs

Effect of Upstream Wakes on Losses and Heat Loads. Detailed experimental investigations have been conducted to identify the influence of upstream periodic wakes on boundary layer characteristics (Doorly et al., 1985; Hodson, 1985; Blair et al., 1989a, 1989b; Sharma et al., 1988; Scholz, 1977; Mayle and Dullenkopf, 1990). The characteristics of boundary layers on airfoil suction sides, affected by periodic movement of the upstream wakes, were clearly illustrated by Doorly et al. (1985). Time-resolved heat transfer data were obtained in a stationary cascade at a low and a high background turbulence level with and without an upstream rotating rod that simulated wakes from upstream airfoils. These data, plotted in Fig. 5a, indicate that upstream wakes have relatively little effect on turbulent boundary layers and significant effects on laminar boundary layers. This figure shows that time-averaged heat transfer and losses for turbine airfoils, which normally have large regions laminar flow in a steady flow environment, are expected to increase in an unsteady environment.

The time-averaged effect of upstream wakes on the boundary layer thickness and heat transfer coefficient for the suction sides of two separate rotor airfoils (Hodson, 1985; Blair et al., 1989a, 1989b) are shown in Fig. 5(b), which also shows the data obtained for those airfoils in steady cascade configurations and calculated values from a boundary layer code. The steady cascade data are shown to yield good agreement with transitional calculations. The time-averaged data, however, lie between the transitional and fully turbulent calculations. Figure 5(b) indicates that the nature of transition is influenced by the periodic variation of turbulence imposed by wakes from upstream airfoil rows. In addition, losses and heat loads in an unsteady environment are larger than those measured in steady cascade configurations. For typical turbine airfoils, losses induced by unsteady effects may be on the order of 25 to 100 percent of the losses for those airfoils in a steady flow environment (Sharma et al., 1988; Scholz, 1977).

Effect of Upstream Wakes on Secondary Flows. In addition to affecting the characteristics of airfoil boundary layers,

wakes from upstream airfoil rows also affect the generation of secondary flows as discussed below (Sharma et al., 1985, 1988; Hebert and Tiederman, 1990).

Unsteady experimental data for a rotor passage, obtained by using high-response probes in a large scale rotating rig, are shown in Fig. 6 (Sharma et al., 1985). Figure 6 shows three instantaneous contour plots of relative total pressure coefficient upstream and downstream of the rotor passage, and large variations in the exit flow structures for the three different inlet conditions. The exit flow field (Fig. 6a) shows three distinct vortices due to the hub and tip secondary flows and the tip leakage effects. Without the tip leakage vortex, the flow field shown in Fig. 6(a) is similar to the one expected for this airfoil in a steady cascade environment. The tip leakage vortex for the rotor shows least variation (Figs. 6a, b, and c) indicating that the leakage phenomenon is not influenced by upstream

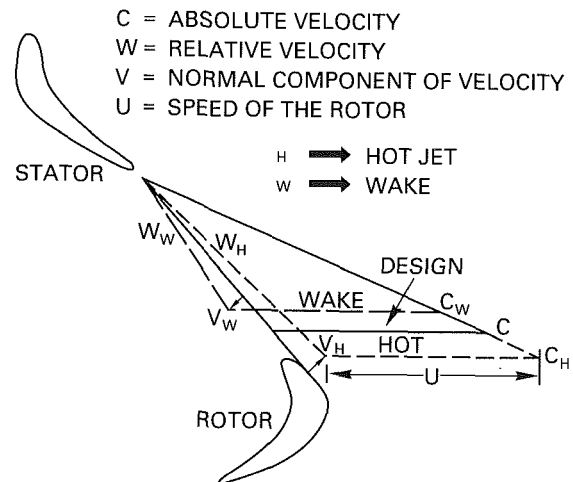


Fig. 4 Wakes and hot jets from upstream stators induce preferential flow migration toward the suction and pressure sides of the downstream rotors (Kerrebrock and Mikolajczak, 1970)

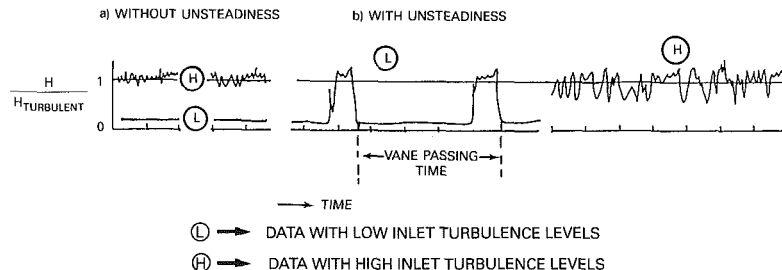


Fig. 5(a) Measured time-resolved heat transfer on a turbine airfoil suction side (Doorly et al., 1985) at two background turbulence levels in an unsteady environment shows a larger effect on a laminar boundary layer and little effect on a turbulent boundary layer

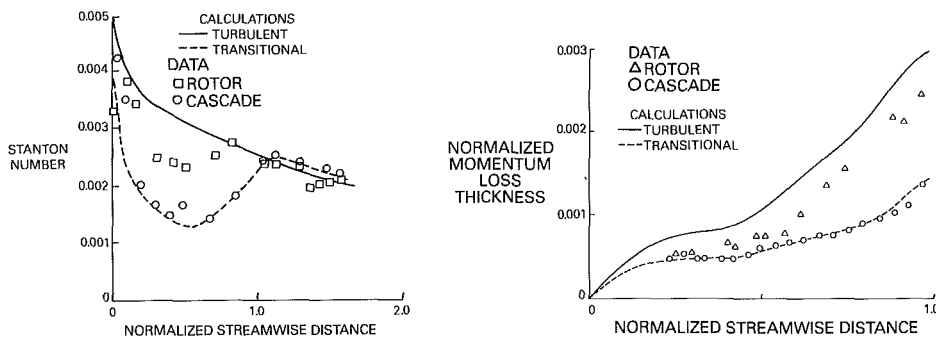


Fig. 5(b) Measured streamwise distribution of time-averaged Stanton number of Blair et al. (1989a, 1989b) and Sharma et al. (1988) and boundary layer thickness of Hodson (1985) show larger values in an unsteady environment than in a steady cascade configuration

$$\text{CPTR} = \frac{\text{RELATIVE TOTAL PRESSURE} - \text{REFERENCE PRESSURE}}{\text{DYNAMIC HEAD BASED ON WHEEL SPEED AT MID-SPAN}}$$

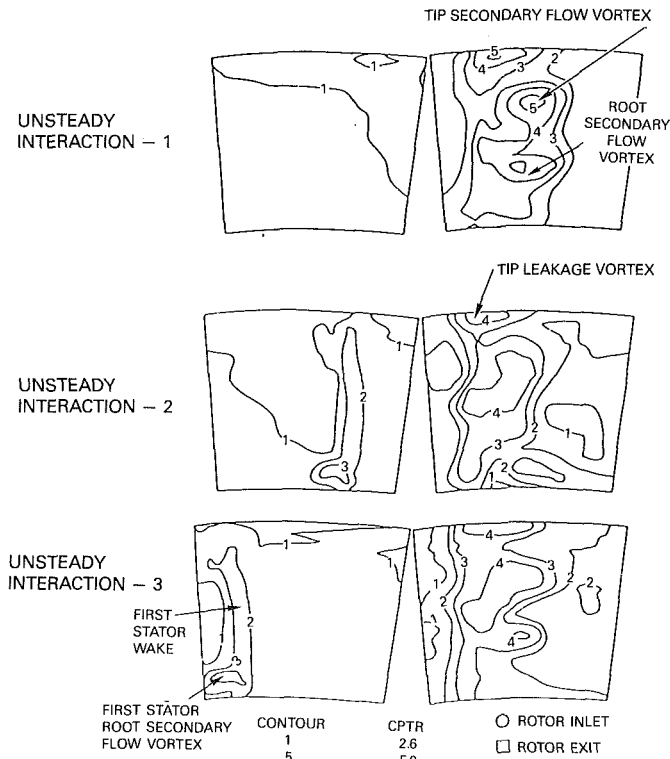


Fig. 6 Secondary flow structures downstream of a rotor (Sharma et al., 1988) obtained from unsteady measurements show large variation in their size, indicating effects of upstream stator wakes

circumferential distortions. The hub secondary flow vortex shows the largest variation transforming from a distinct structure in Fig. 6(a) to a diffused structure in Fig. 6(b), and becoming almost nonexistent in Fig. 6(c). This indicates that the secondary flow generation mechanisms, especially at the hub, are strongly influenced by the upstream circumferential distortions such as wakes. The overall variation in the size of the tip secondary flow vortex is smaller than that of the hub vortex but larger than the leakage vortex.

The periodic variation in the size and strength of the secondary flow vortices observed in this experimental investigation shows almost 40 percent variation in the secondary flow losses for the rotor passage (Sharma et al., 1988).

Effects of Upstream Temperature Streaks on Segregation of Hot and Cold Air in Turbine Rotors. Results from an experimental investigation, conducted to quantify the influence of burner-induced hot streaks on segregation of hot and cold air in turbine rotors, are discussed. In this investigation, experimental data were acquired in the UTRC Large-Scale Rotating Rig (LSRR) by introducing temperature streaks upstream of the first stator (Fig. 7a). Two types of temperature profile were generated upstream of the first stator, these being:

(i) Hot streak with a circular cross section to yield a temperature profile both in the radial and the circumferential direction; some of the results from this investigation were reported by Butler et al. (1986).

(ii) Hot streak with a rectangular cross section to yield a radially uniform profile that had temperature gradients mainly in the circumferential direction.

The hot air in these experiments was seeded with carbon dioxide (CO₂) to facilitate measurements of its migration in the turbine by using a gas sampling technique (Butler et al., 1986). The temperature patterns at the exit of the first stator

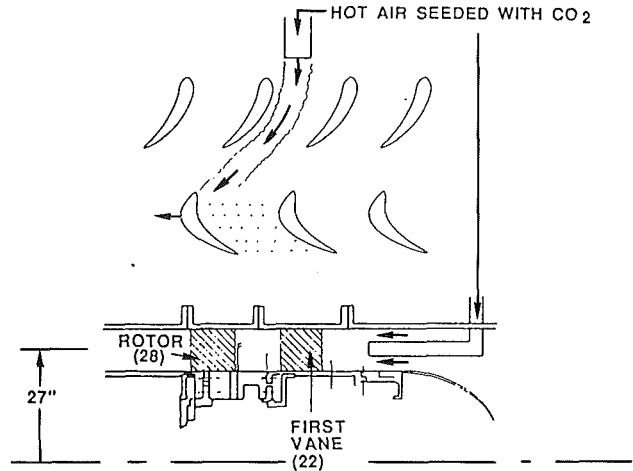


Fig. 7(a) Schematics of the experimental apparatus used to simulate the redistribution of hot streak in the turbine rotor (Butler et al., 1986)

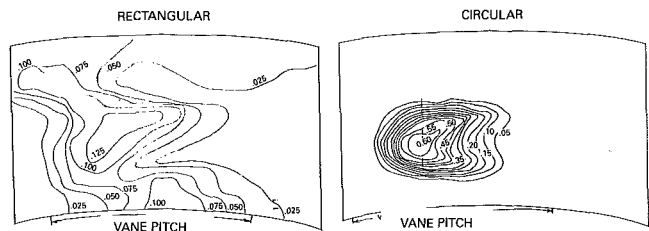


Fig. 7(b) Contour plots of normalized CO₂ concentration downstream of the first stator in the UTRC LSRR obtained with circular and rectangular hot streaks; high values imply high temperatures

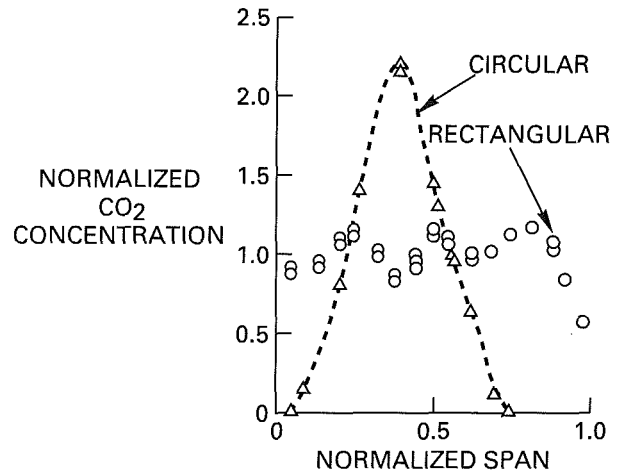


Fig. 7(c) Spanwise distribution of normalized CO₂ concentration profiles (indicators of temperatures) measured in the rotor frame for the circular and rectangular hot streaks

for these tests are given in Fig. 7(b), which indicates relatively small mixing in the first stator. As expected, this result is compatible with the Munk and Prim (1947) principle. Spanwise distributions of axisymmetric CO₂ concentration profiles at the inlet to the rotor, measured by using a rotating probe for these two tests, are given in Fig. 7(c). The circular streak generated a parabolic concentration (temperature) profile whereas the rectangular streak generated a radially uniform profile.

Measured concentrations of CO₂ on the rotor airfoil surfaces, for the rectangular hot streak, are shown in Fig. 8, which indicates higher levels of CO₂ concentration on the rotor airfoil pressure side than on the suction side. Similar results were obtained with the circular hot streak as discussed by Butler et al. (1986). These results demonstrate that pressure sides of

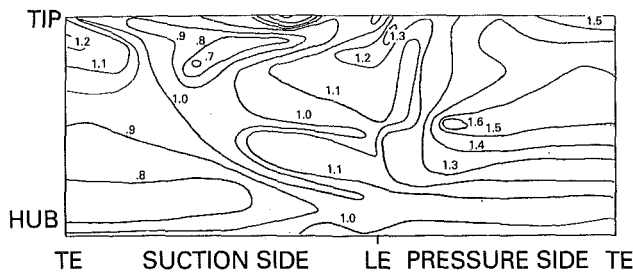


Fig. 8 Larger time-averaged CO₂ concentration (temperatures) measured on the pressure side of the rotor airfoil relative to the suction side indicate segregation of hot and cold air

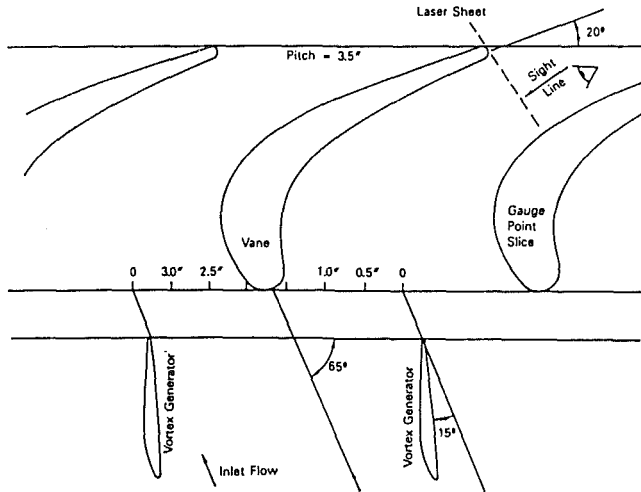


Fig. 9 Cascade and inlet airfoil geometry used to investigate migration of inlet streamwise vortices in the cascade passage (LaFleur et al., 1988)

rotor airfoils operate at substantially higher temperatures than the suction sides when the incoming flow has a circumferentially nonuniform temperature profile.

Interpretation of the data obtained from an actual engine environment indicates that the pressure sides of the first rotor airfoils in a high-pressure turbine can operate anywhere between 100°–700°F hotter than the suction sides. Large amounts of cooling air are required to accommodate these temperature levels, resulting in reduced efficiency of the cycle and increased specific fuel consumption of the engine.

Effects of Upstream Streamwise Vortices. Secondary flows are generated in turbine airfoil rows due to incoming endwall boundary layer profiles and large turnings in the airfoil passages. These secondary flows leave the airfoil rows as organized streamwise vortices (Langston et al., 1977; Barber and Langston, 1979; Graziani et al., 1980; Marchal and Sieverding, 1977; Moore and Adhye, 1985). Few investigations have been published in the literature directed toward understanding the interaction of these upstream vortices on the flow characteristics of the downstream airfoil rows. Results from two experimental investigations are discussed here to demonstrate that incoming streamwise vortices have a major influence on the secondary flow and viscous flow behavior of the downstream airfoil rows.

In the first investigation, which was a joint University of Connecticut/Pratt & Whitney program (LaFleur et al., 1988), secondary flow vortices were generated upstream of a turbine cascade in a water tunnel by suspending a cascade of low turning airfoils at the inlet (Fig. 9). Flow visualization data were obtained by utilizing dyes and laser lighting techniques and at various axial planes in the downstream cascade by using sheets of laser lights. Data were also acquired by indexing the upstream cascade to identify the effects of incoming vortices when they entered near the pressure and suction sides of the

downstream cascade airfoil. A photograph of the incoming vortices is shown in Fig. 10(a). The direction of rotation of these vortices is opposite to that of the passage vortices for the downstream cascade. These incoming vortices simulate the quasi-steady effect of the secondary flow vortices generated by upstream airfoil rows in a multistage turbine.

Photographs of the flow patterns obtained at the gage plane of the downstream cascade are shown in Figs. 10(b) and (c). Figure 10(b) shows flow patterns at the gage plane for the test condition when these vortices were introduced near the airfoil suction side of the downstream cascade. A stable flow phenomenon is observed and the incoming vortices are found to be “hugging” the airfoil suction side. A diffused and elongated flow structure is observed for the secondary flow vortex generated in the downstream cascade at this test condition.

Interesting flow phenomena were observed when the incoming vortices were introduced near the pressure side of the downstream cascade. An unsteady flow pattern was observed in the downstream cascade for this test condition. Photographs of the flow pattern at the downstream cascade gage plane for this test condition are shown in Fig. 10(c). This figure shows that the incoming vortices periodically collapse and reform for this test condition. These data indicate that at specific rotor–stator interaction locations, secondary flows of the upstream airfoil will be substantially modified by the boundary condition imposed by the downstream airfoil. In addition, it can be seen that the incoming secondary flow vortices will preferentially migrate toward the suction side of the downstream airfoil. Review of data from this test also indicates that the size and strength of the secondary flow for the downstream cascade are lower than those obtained for this cascade in the absence of upstream vortices.

In the second investigation detailed aerodynamic and heat transfer data were acquired for the second stator in the UTRC Large-Scale Rotating Rig (Blair, 1989a, 1989b). The airfoil cross section and gas triangles for this second stator are similar to the one for the upstream rotor where detailed aerodynamic and heat transfer data are available to provide direct comparisons between the two airfoils. The rotor is mainly influenced by the wakes from the first stator (which has relatively small secondary flows) whereas the second stator is largely affected by the secondary flow generated in the upstream rotor.

Spanwise distribution of the gap-averaged exit gas angle data from the second stator (Sharma et al., 1988) is compared to the data obtained for the rotor in Fig. 11(a). The data for the rotor show overturning in the endwall regions and underturning in the midspan regions showing characteristics of classical secondary flows expected for an airfoil row. The data for the second stator, however, show underturning in the endwall regions and overturning in the midspan region, indicating that this flow is strongly influenced by the incoming secondary vortices from the upstream rotor.

Measured midspan heat transfer data from the second stator are compared to the data obtained for the rotor in Fig. 11(b), which also shows the calculated heat transfer coefficient by using a boundary layer code run in a turbulent mode. Although the loading distributions at the midspan of the two airfoils are very similar, significantly higher levels of heat transfer coefficients are measured for the second stator than for the rotor. In addition, the heat transfer coefficient distribution for the second stator shows almost a constant value for the latter 75 percent of the airfoil surface, which is much higher than that from turbulent calculations. This result indicates that the heat load for this airfoil is affected by the incoming secondary flow vortices.

A plot of the unsteady data (Fig. 12) downstream of the second stator indicates that at certain rotor second stator interaction locations, secondary flow vortices from the upstream rotor convect through the second stator almost unaffected. These vortices induce flow impingement at the midspan of the

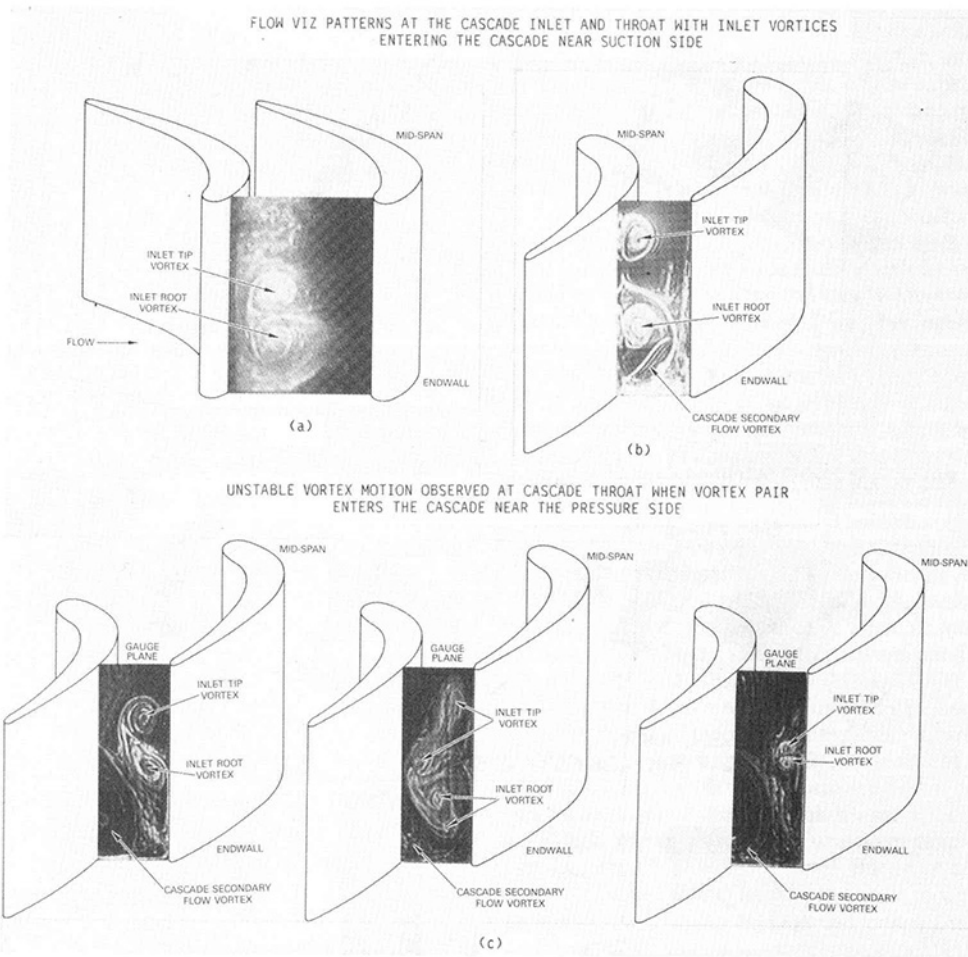


Fig. 10 Flow visualization patterns at the cascade inlet (a) and at the gage plane (b, c); flow patterns at the gage plane obtained by introducing the incoming vortices near the suction (b) and the pressure (c) side of the cascade (LaFleur et al., 1988)

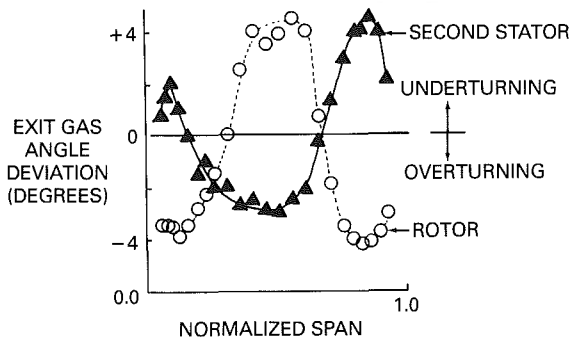


Fig. 11(a) Measured spanwise distribution of gap-averaged exit gas angles downstream of the second stator show opposite characteristics of the secondary flow to the rotor (Sharma et al., 1988)

suction side of the second stator, causing increased levels of heat transfer coefficients and a tendency of the flow to overturn. In addition, these vortices induce flow toward the pressure sides in the endwall regions, causing underturning of the flow as observed in Fig. 11(b).

It is apparent from the above discussion that incoming streamwise vortices may have a potent effect on both heat loads and flow distribution for downstream row airfoils.

Unsteady Flow Effects in Turbines: Semi-empirical Models and Numerical Simulations

Progress in predicting unsteady flow effects in turbines has recently been made due to the formulation of semi-empirical

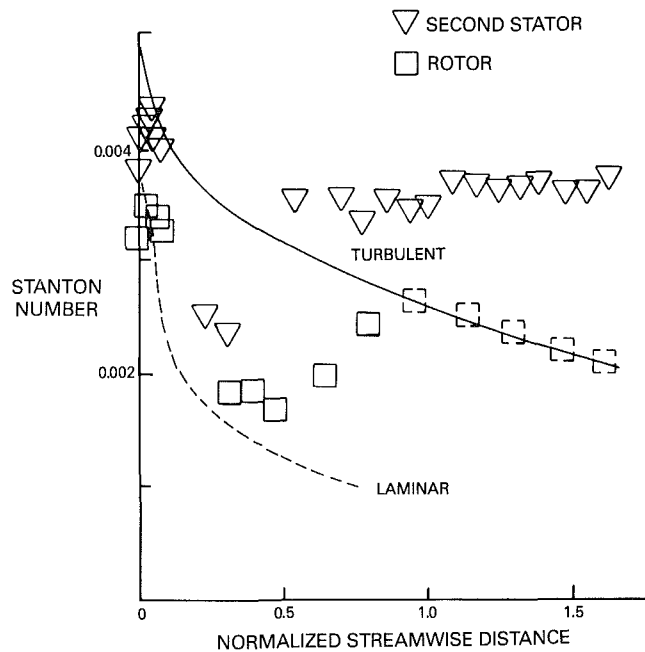


Fig. 11(b) Higher levels of heat loads measured on the second stator suction side than on the rotor, although both have similar geometries and loadings (Blair et al., 1989a, 1989b; Sharma et al., 1988)

models and the development of unsteady CFD codes that permit simulation of periodic unsteady flows through multistage

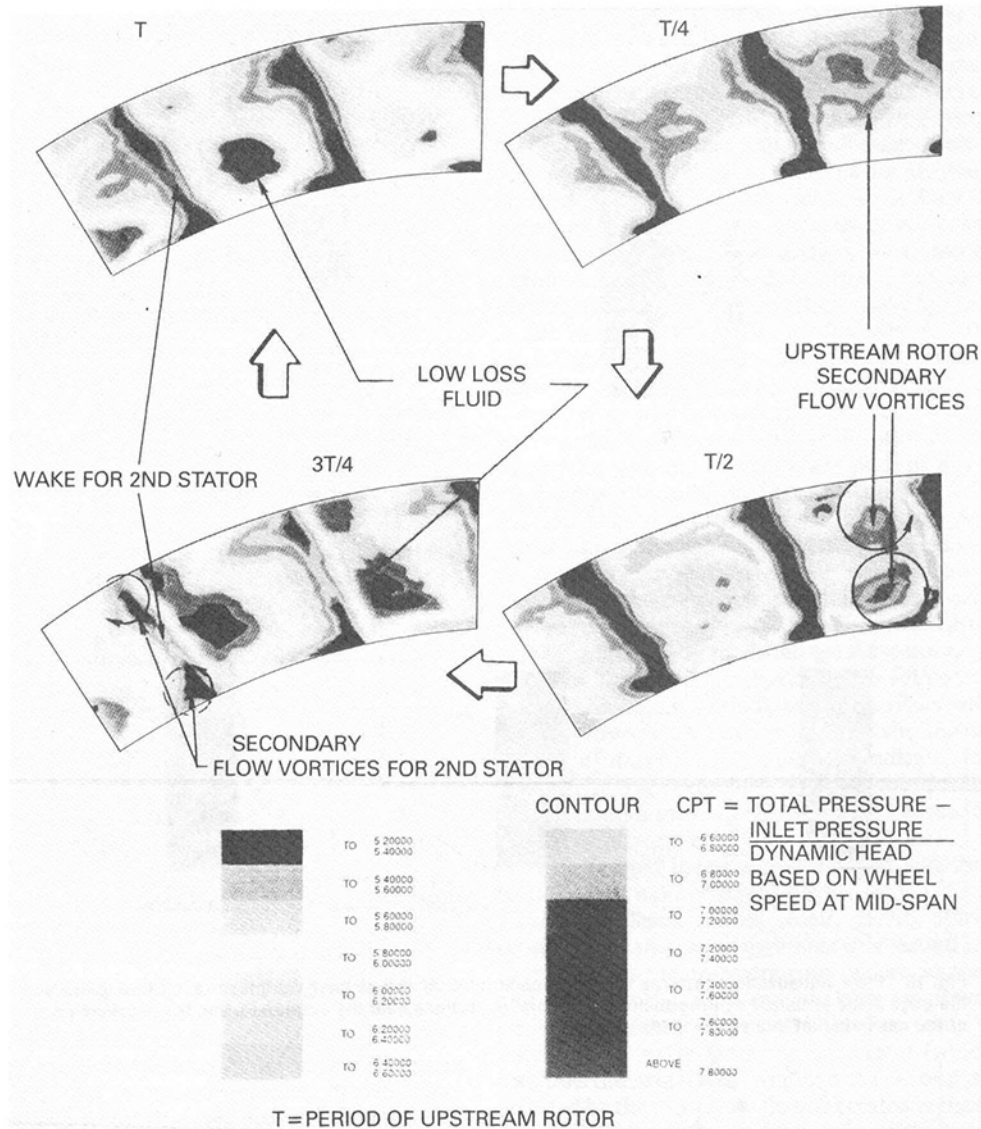


Fig. 12 Unsteady total pressure loss contours measured downstream of the second stator indicate that upstream rotor secondary flow vortices periodically persist through the second stator passage (Sharma et al., 1988)

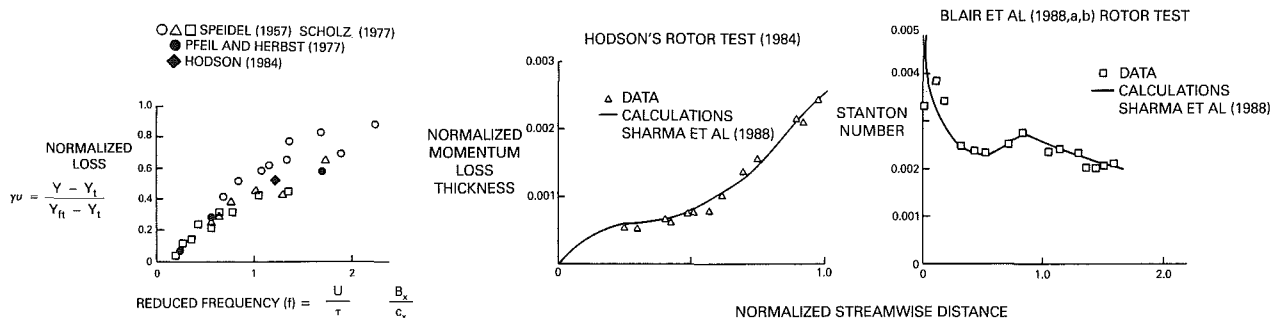


Fig. 13(a) Additional time-averaged loss (γu) generated due to unsteadiness induced by upstream wakes can be related to reduced frequency (f) (Sharma et al., 1988); (b), (c) Sharma et al. (1988) model yields good estimates of time-averaged momentum loss thickness and Stanton numbers from data acquired in an unsteady flow environment

turbines. The semi-empirical models have primarily been formulated to account for the time-averaged effect of upstream wakes on the characteristics of boundary layers for downstream row airfoils. The unsteady CFD codes provide a vehicle through which effects of upstream row wakes and burner-induced temperature streaks on the secondary flow and tem-

perature patterns on the surfaces of the downstream rotors can be investigated.

Semi-empirical Models for Wake-Boundary Layer Interaction. One of the earliest attempts to account for the effects of upstream wakes on the performance (profile losses) for

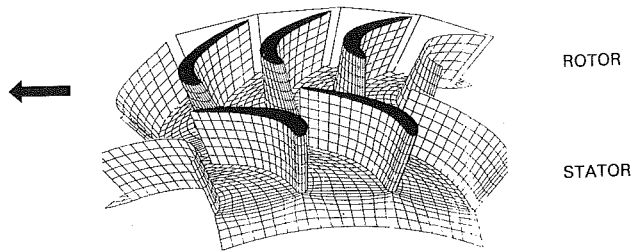


Fig. 14(a) Computational mesh of Ni et al. (1989) for the UTRC Large-Scale Rotating Rig

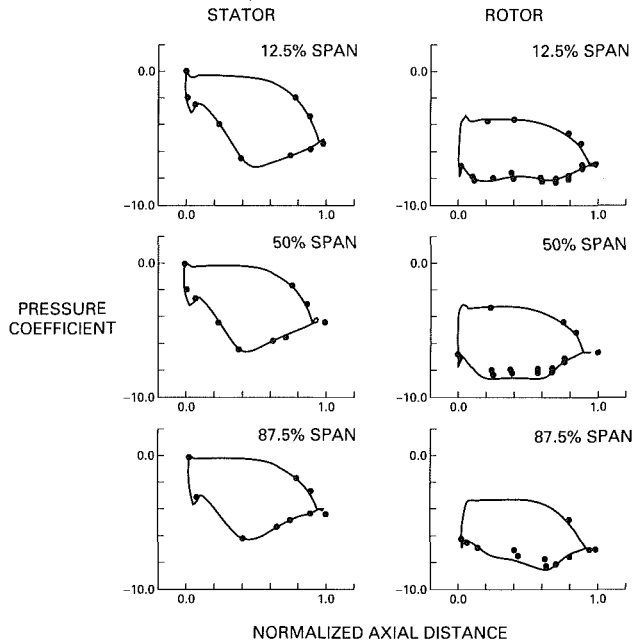


Fig. 14(b) Predicted time-averaged pressure distributions from the three-dimensional unsteady Euler code of Ni et al., showing good agreement with measured data for the LSRR first stage. Both steady and unsteady multistage codes yield similar results for loadings.

downstream airfoils is due to Speidel (1957). In this summary of Speidel's results, Scholz (1977) showed that change in profile losses for airfoils in an unsteady environment can be related to a reduced frequency. Figure 13 reproduced from Sharma et al. (1988), which includes data by Speidel (1957), Hodson (1985), and Pfeil and Herbst (1977), shows that normalized increase in profile loss (γu) for turbine cascades in an unsteady environment is a function of a reduced frequency (f).

In Fig. 13, Y represents the profile loss, subscripts t and ft refer to the transitional and the fully turbulent conditions of the airfoil boundary layers, and the overbar indicates the time-averaged condition. The reduced frequency f can be viewed as a ratio of the flow change period to the flow interaction period. The flow change period is taken as u (relative speed of upstream airflow row) divided by τ (pitch of the airfoils in the upstream row). The flow interaction period is approximated by Cx (average axial velocity in the downstream passage) divided by Bx (axial chord of the downstream airfoil).

A correlation deduced from Fig. 13 yields a reasonable method for estimating profile losses for airfoils in a multirow environment. This correlation can also be used to enhance the intermittency factor on airfoil suction surfaces, as described by Sharma et al. (1988), to provide detailed predictions of the development of time-averaged boundary layers affected by the wake induced unsteadiness. Application of this model yields good agreement with data acquired in rotors by Hodson (1985) and Blair et al. (1989a, 1989b) as shown in Figs. 13(b) and 13(c).

Hodson (1989) has proposed modifications to the above

model through the use of an alternative expression for the flow interaction period and theoretical arguments indicating that Y_{ft} represents the transitional loss at high incoming turbulence levels. Mayle and Dullenkopf (1990) have proposed a modified expression for boundary layer intermittency factor in an unsteady flow environment. Both of these models yield a smaller effect of unsteadiness on the airfoil boundary layer than predicted by the model used in Figs. 13(b) and 13(c).

All of the above models, however, predict increases in both losses and heat loads for downstream airfoils in an unsteady flow environment, provided these airfoils are known to have attached boundary layers for steady incoming flows. In situations such as low Reynolds number operating conditions, where airfoils have extended regions of separated laminar flows (Binder et al., 1989), interaction from upstream wakes can result in lower losses in an unsteady environment relative to the steady flow operating condition. All of the above discussed models should be able to predict this behavior; the evaluation of this aspect of these models is yet to be verified.

Unsteady Flow Effects in Turbines: Numerical Simulations. Improved insight into the effects of upstream wakes and temperature streaks on the flow development in a turbine environment can be gained through the analysis of numerical results obtained from unsteady flow simulations through a turbine stage. These simulations were conducted by using a three-dimensional unsteady multistage Euler code with a ratio of 3 stator to 4 rotor airfoils (instead of 22 stator and 28 rotor airfoils) in order to contain computer requirements (Ni et al., 1989; Ni and Takahashi, 1989). Two sets of simulations were conducted, one with a uniform upstream total temperature profile to simulate the flow conditions of Sharma et al. (1985, 1988) and the other with an upstream temperature streak to simulate the flow conditions of Butler et al. (1986). A wall shear stress model was used in this code to simulate the viscous flow effects. The tip leakage flow was not modeled in the calculation.

The computational mesh used in these simulations is shown in Fig. 14(a). A total of 70,000 grid points were used in the axial, radial, and tangential direction to simulate the flow field. The time-accurate solver and the interpolation method at the interface were used to obtain the unsteady periodic solution in time. Convergence was obtained at about 20,000 time steps or six rotor cycles (rotor moving past one stator airfoil pitch), requiring about 10 CPU hours on a CRAY XMP computer for each simulation. Calculated time-averaged loadings on the stator and the rotor airfoils from both simulations are compared to the experimental data in Fig. 14(b) at three spanwise locations. The experimental data are shown to be in good agreement with the predictions. It should also be pointed out that these predictions are almost identical to the predictions obtained by the steady multistage code of Ni and Bogoyan (1989), indicating that unsteadiness has relatively little effect on time-averaged loadings on airfoil surfaces in a multistage turbine operating at subsonic flow conditions.

Lewis et al. (1987) showed that time-averaged loads on the stator and the rotor of a transonic turbine obtained using unsteady code were smaller than those predicted for those airfoils by using a steady code. No experimental data were presented by these authors to indicate which of the two predictions was more accurate.

Effect of Upstream Wakes on Rotor Secondary Flows. The effects of upstream wakes on the secondary flow generation on the downstream rotor can be deduced by reviewing the unsteady total pressure contours downstream of the rotor from the simulation conducted with a uniform upstream total temperature profile. Contour plots of the computed instantaneous relative total pressure coefficients downstream of the rotor, together with the 3-stator-4-rotor configuration, are shown in Fig. 15(a), which indicates a strong effect of unsteadiness on

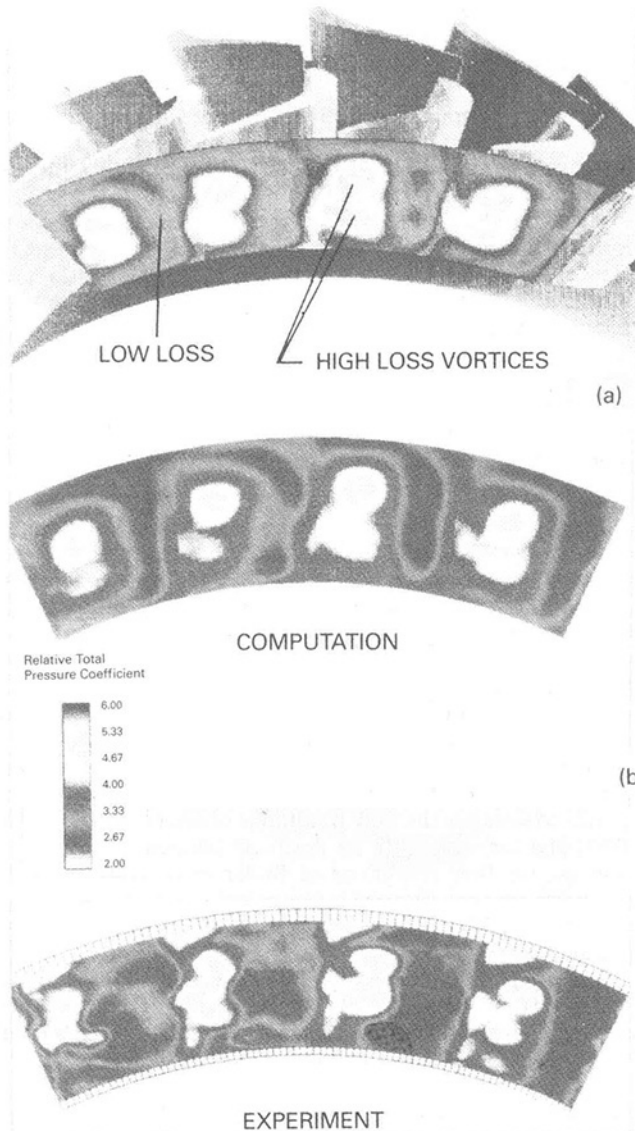


Fig. 15 Relative total pressure loss at exit of rotor: (a) location of data plane; (b) periodic disappearance of root secondary flow vortex is in agreement with experimental data

the rotor flow field. Organized flow structures seen in this figure indicate the existence of different secondary flow vortices in each rotor airfoil passage. The secondary flow vortices in the tip region are similar in all four rotor passages, which indicate that circumferential distortions generated by the upstream stator have relatively little effect on the flow in the tip region. Significant passage-to-passage variations in the flow structures are observed in the root region. In particular, there are substantial reductions in the strength of the root secondary flow vortex as the rotor moves past the stator airfoils. This periodic disappearance of the root secondary flow vortex is in excellent agreement with experimental data discussed previously and is shown in Fig. 15(b). The comparison indicates that the unsteady flow simulation using an Euler code successfully predicts the unsteady and distorted flow features observed in the experimental data with primitive modeling of viscous effects.

Results from this numerical study clearly demonstrate that Euler codes can be used to obtain first-order effects of flow unsteadiness in turbines.

Effect of Upstream Temperature Streaks on the Rotor Flow Field. The flow simulation with the hot streak was conducted by utilizing 1 hot-streak, 3 stator, and 4 rotor airfoil passages



Fig. 16 Snapshot in time of three-dimensional unsteady Euler simulation of hot streak in LSRR stage turbine. The hot streak convects through the stator passage with no distortion and then interacts with the passing rotor.

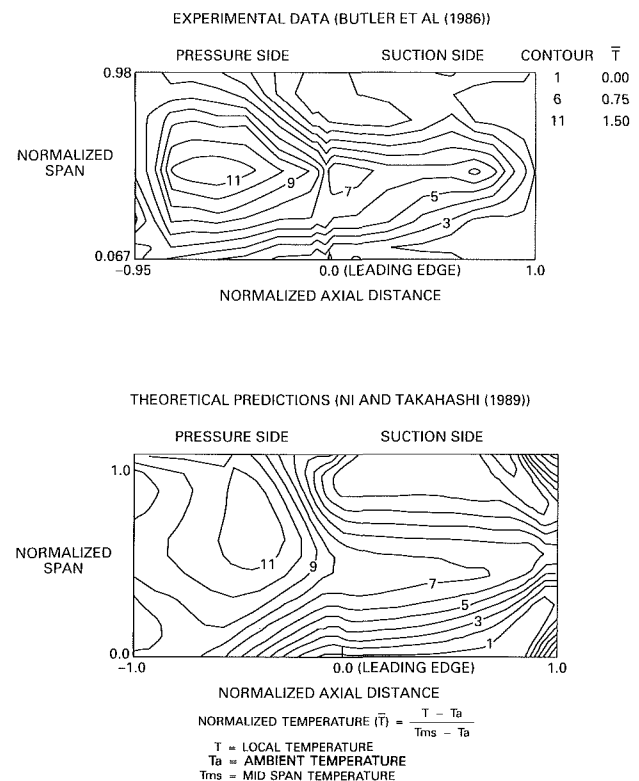


Fig. 17 Time-averaged normalized temperatures (\bar{T}) predicted by three-dimensional unsteady Euler code yield good agreement with temperature patterns measured on the two surfaces of the rotor airfoil

(instead of 1 hot-streak, 22 stator, and 28 rotor airfoil passages for the experiment of Butler et al., 1986). An instantaneous picture of the hot streak in the turbine stage from this simulation is shown in Fig. 16. The hot streak is shown to convect through the stator passage with little distortion and then interacts with the passing rotor where it tends to linger on the rotor airfoil pressure side.

The time-averaged results from this simulation are compared to the experimental data of Butler et al. (1986) and are shown in Fig. 17. The temperature patterns on both sides of the airfoil are fairly well predicted by the unsteady simulation. The simulation and the data both indicate that the pressure sides of the rotor airfoil operate at a higher temperature than the suction sides.

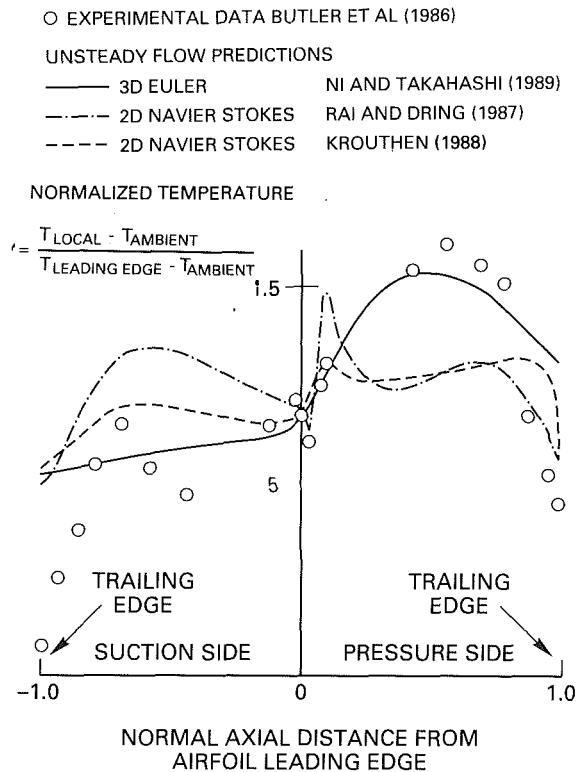


Fig. 18 Higher time-averaged temperatures predicted on the pressure sides for the rotor airfoil, by using two-dimensional unsteady Navier-Stokes and three-dimensional unsteady Euler codes, than on the suction side. Experimental data and calculations by Ni and Takahashi (1989) and Krouthen (1988) conducted at flow coefficient of 0.68; calculations by Rai and Dring (1987) at flow coefficient of 0.78.

Normalized temperatures at the midspan of the rotor airfoil from the circular hot-streak experiments are compared to theoretical predictions in Fig. 18. Three sets of theoretical predictions are shown in this figure. The solid line in Fig. 18 represents predictions obtained from the three-dimensional unsteady multistage Euler code, the chained and the dotted lines are predictions obtained by using two-dimensional unsteady Navier-Stokes codes from Rai and Dring (1986) and Krouthen (1988), respectively. All three prediction methods yield qualitative agreement with the data, showing peak temperature levels on the rotor airfoil pressure side. In the initial three quarters of the airfoil, three-dimensional, rotational, unsteady aspects of the flow play a dominant role in the temperature segregation phenomena as indicated by excellent agreement between experimental data and theoretical predictions obtained by the three-dimensional unsteady Euler code. The flow in the last quarter of the airfoil is largely influenced by the unsteady viscous flow mechanisms as illustrated in Fig. 18 where the predicted temperature distributions by the two-dimensional unsteady Navier-Stokes codes show similarities with the experimental data. It should be reiterated here that two-dimensional, steady simulations for this experiment will show the same temperature levels on the two sides of the airfoil, indicating that an account of unsteadiness is essential to show segregation of the hot and cold air in rotor passages.

Implication of Results

Results from unsteady numerical simulations, discussed in the previous section, indicate that time-averaged loadings on airfoil surfaces (and endwalls) are not influenced by unsteadiness even in the presence of temperature streaks. This indicates that currently used CFD codes that compute steady three-dimensional flows through multistage turbines provide ade-

quate information about this aspect of the flow field in the design process.

Results from both experimental data and numerical simulations clearly indicate that the pressure sides of turbine airfoils operate at higher temperatures than the suction sides in the presence of circumferentially nonuniform temperature profiles. Steady CFD codes, currently used in the design process, do not predict this phenomenon. There is, therefore, a need either to develop models that would predict this phenomenon in the steady codes as discussed by Adamczyk et al. (1990), or to incorporate the use of unsteady CFD codes in the design process. However, significant computer speed and storage enhancement will be needed before these unsteady codes can be routinely used in the design process.

Results of the experimental data indicate that the spanwise distributions of exit gas angles from an airfoil row, with incoming strong streamwise vortices, are significantly different from those expected for that airfoil row in the absence of upstream vortices. These results imply that the design of the downstream rotor, conducted without accounting for the flow field generated by the upstream rotor, may result in poor performance. Procedures, therefore, need to be developed that can account for the incoming streamwise vortices on the flow distributions of the airfoil passages. Some progress in this area has been reported by Adamczyk et al. (1990). Although unsteady flow simulation was not conducted for this test case, it is expected that such a simulation will predict the experimental behavior. The unsteady flow simulation codes are expected to make important contributions in the development of low aspect ratio multistage turbines. For high aspect ratio turbines, however, the currently used steady CFD codes are adequate since such turbines have fairly small amounts of secondary flows.

Procedures to estimate losses and heat loads in multistage turbines are the weakest link in the design process due to the unavailability of reliable turbulence models. Results of the experimental data, however, indicate that if the flow is turbulent on airfoil surfaces, and the incoming streamwise vortices are weak, then unsteadiness has no further detrimental effect and the current design procedures are adequate. For airfoil rows operating with strong incoming streamwise vortices, however, enhancements in heat loads (and losses) can be expected. In addition, turbine airfoils designed to have large regions of laminar flow on airfoil surfaces are expected to have substantial increases in the losses and heat loads in an unsteady environment. Some progress in the modeling of the effects of periodic unsteadiness on the loss and heat loads is reported by Sharma et al. (1988), Mayle and Dullenkopf (1990), and Hodson (1989). There is clearly a need for continued development of unsteady Navier-Stokes codes (Rai, 1987) to predict the magnitude of losses and heat loads in an unsteady environment in multistage turbines. Significant reduction in their execution time (1000 hours currently to about 1 hour) are, however, needed before these codes can be routinely utilized in the turbine design process.

Conclusions

The following conclusions are drawn from the discussions presented in this paper:

- Three-dimensional steady multistage flow prediction codes provide accurate estimates of loadings for airfoil rows even in the presence of periodic unsteadiness and temperature distortions.
- Turbine inlet circumferential temperature distortions result in hotter pressure sides and colder suction sides for rotor airfoils. This phenomenon is not adequately predicted by the three-dimensional steady multistage codes that are currently used in turbine design procedure. The three-dimensional, unsteady, multistage codes, however, predict this phenomenon accurately, indicating that these codes should be utilized in the design process.

- Incoming streamwise vortices have a large impact on the unsteady flow distribution and time-averaged heat loads for downstream airfoil rows and effects of these flow structures should be accounted for in the design of low aspect ratio turbines.
- Further development of unsteady Navier-Stokes codes is required to provide accurate estimates of heat loads and losses in realistic turbine environments.

Acknowledgments

The authors wish to thank Pratt & Whitney management for their permission to publish this paper. The authors are also grateful to Mr. L. R. Anderson and Dr. A. M. Pfeffer for their encouragement and support during this research project.

References

- Adamczyk, J. J., Celestina, M. L., Beach, T. A., and Barnett, M., 1990, "Simulation of Three-Dimensional Viscous Flow Within a Multistage Turbine," *ASME JOURNAL OF TURBOMACHINERY*, Vol. 112, pp. 370-376.
- Anand, A. K., and Lakshminarayana, B., 1978, "An Experimental Study of Three-Dimensional Turbulent Boundary Layer and Turbulence Characteristics Inside a Turbomachinery Rotor Passage," *ASME Journal of Engineering for Power*, Vol. 100, pp. 676-690.
- Barber, T. J., and Langston, L. S., 1979, "Three-Dimensional Modeling of Cascade Flows," AIAA Paper No. 79-0047.
- Binder, A., Schroeder, Th., and Hourmouziadis, J., 1989, "Turbulence Measurements in a Multistage Low-Pressure Turbine," *ASME JOURNAL OF TURBOMACHINERY*, Vol. 111, pp. 153-161.
- Blair, M. F., Dring, R. P., and Joslyn, H. D., 1989a, "The Effects of Turbulence and Stator Rotor Interactions on Turbine Heat Transfer: Part I—Design Operating Conditions," *ASME JOURNAL OF TURBOMACHINERY*, Vol. 111, pp. 87-96.
- Blair, M. F., Dring, R. P., and Joslyn, H. D., 1989, "The Effects of Turbulence and Stator Rotor Interactions on Turbine Heat Transfer: Part II—The Effects of Reynolds Number and Incidence," *ASME JOURNAL OF TURBOMACHINERY*, Vol. 111, pp. 97-103.
- Butler, T. L., Sharma, O. P., Joslyn, H. D., and Dring, R. P., 1986, "Redistribution of an Inlet Temperature Distortion in an Axial Flow Turbine Stage," AIAA Paper No. 86-1468.
- Center for Turbulence Research, 1987, "Studying Turbulence Using Numerical Simulation Databases," Proceedings of the 1987 Summer Program, Report CTR-587, Stanford University, CA.
- Dannenheffer, J. R., and Baron, J. R., 1985, "Grid Adaption for the 2-D Euler Equations," AIAA Paper No. 85-0484.
- Denton, J. D., 1975, "A Time Marching Method for Two and Three Dimensional Blade to Blade Flows," A.R.C., R&M 3775.
- Denton, J. D., 1986, "The Use of a Distributed Body Force to Simulate Viscous Flows in 3-D Flow Calculations," ASME Paper No. 86-GT-144.
- Doorly, D. J., Oldfield, M. L. G., and Scrivener, C. T. J., 1985, "Wake-Passing in a Turbine Rotor Cascade," AGARD CP-390, Paper No. 7, Bergen, Norway.
- Dunn, M. G., 1980, "Measurement of Heat Flux and Pressure in a Turbine Stage," AFAPL-TR-81-2055.
- Epstein, A. H., Guenette, G. R., and Norton, R. J. G., 1984, "The MIT Blowdown Turbine Facility," ASME Paper No. 84-GT-116.
- Erdos, J. I., Alzner, F., and McNally, W., 1977, "Numerical Solution of Periodic Transonic Flow Through a Fan Stage," *AIAA Journal*, Vol. 15, pp. 1559-1568.
- Graziani, R. A., Blair, M. F., Taylor, J. R., and Mayle, R. E., 1980, "An Experimental Study of Endwall and Airfoil Surface Heat Transfer in a Large Scale Turbulent Blade Cascade," *ASME Journal of Engineering for Power*, Vol. 102, pp. 257-267.
- Greitzer, E. M., and Tan, C. S., 1987, "Unsteady Flow in Turbomachinery: Basic Phenomena and Practical Aspects," Updated Version of the Special Lecture Given at the International Gas Turbine Congress, Tokyo.
- Hah, C., 1984, "A Navier-Stokes Analysis of Three-Dimensional Turbulent Flows Inside Turbine Blade Rows at Design and Off-Design Conditions," *ASME Journal of Engineering for Gas Turbines and Power*, Vol. 106, pp. 421-429.
- Hebert, G. J., and Tiederman, W. G., 1990, "Comparison of Steady and Unsteady Secondary Flows in a Turbine Stator Cascade," *ASME JOURNAL OF TURBOMACHINERY*, Vol. 112, pp. 625-632.
- Hodson, H. P., 1985, "Measurements of Wake-Generated Unsteadiness in the Rotor Passages of Axial Flow Turbines," *ASME Journal of Engineering for Gas Turbines and Power*, Vol. 107, pp. 467-476.
- Hodson, H. P., 1989, "The Prediction of Unsteady Transition and Profile Loss," submitted to *JOURNAL OF TURBOMACHINERY*; Private Communication.
- Hourmouziadis, J., and Hubner, J. N., 1985, "3-D Design of Turbine Airfoils," ASME Paper No. 85-GT-188.
- Huber, F. W., Rowey, R. J., and Ni, R.-H., 1985, "Application of 3D Flow Computation to Gas Turbine Aerodynamic Design," Paper No. AIAA-85-1216.
- Kerrebrock, J. L., and Mikolajczak, A. A., 1970, "Intra Stator Transport of Rotor Wakes and Its Effect on Compressor Performance," *ASME Journal of Engineering for Power*, Vol. 92, pp. 359-370.
- Krouthen, B., 1988, "Numerical Investigation of Hot Streaks in Turbines," CFDL TR-88-9, MIT, Cambridge, MA.
- LaFleur, R. S., Langston, L. S., and Sharma, O. P., 1988, "Flow Visualization Investigation Through a Turbine Cascade With Incoming Streamwise Vortices," Unpublished Report, University of Connecticut, Storrs.
- Lakshminarayana, B., 1975, "Effects of Inlet Temperature Gradients on Turbomachinery Performance," *ASME Journal of Engineering for Power*, Vol. 97, pp. 64-74.
- Langston, L. S., Nice, M. L., and Hooper, R. M., 1977, "Three-Dimensional Flow Within a Turbine Cascade Passage," *ASME Journal of Engineering for Power*, Vol. 99, pp. 21-28.
- Lewis, J. P., Delaney, R. A., and Hall, E. J., 1987, "Numerical Prediction of Turbine Vane-Blade Interaction," AIAA Paper 87-2149.
- Marchal, P., and Sieverding, C. M., 1977, "Secondary Flows Within a Turbomachinery Blading," *Secondary Flow in Turbomachines*, AGARD-CP-214.
- Mayle, R. E., and Dullenkopf, K., 1990, "A Theory for Wake-Induced Transition," *ASME JOURNAL OF TURBOMACHINERY*, Vol. 112, pp. 188-195.
- Moore, J., and Adhye, R. Y., 1985, "Secondary Flows and Losses Downstream of a Turbine Cascade," *ASME Journal of Engineering for Gas Turbines and Power*, Vol. 107, pp. 961-968.
- Munk, M., and Prim, R. C., 1947, "On the Multiplicity of Steady Gas Flows Having the Same Streamline Pattern," *Proceedings of the National Academy of Sciences, U.S.*, Vol. 33.
- Ni, R.-H., 1982, "A Multiple-Grid Scheme for Solving the Euler Equations," *AIAA Journal*, Vol. 20, pp. 1565-1571.
- Ni, R. H., and Bogoian, J. C., 1989, "Prediction of 3-D Multistage Turbine Flow Field Using a Multiple-Grid Euler Solver," AIAA Paper No. 89-0203.
- Ni, R. H., and Takahashi, R., 1989, "Hot Streak Migration in a Turbine—An Unsteady Flow Simulation," NASA MSFC CFD Workshop.
- Ni, R., Sharma, O., Takahashi, R., and Bogoian, J., 1989, "3D Unsteady Flow Simulation Through a Turbine Stage," presented in the 1989 Australian Aeronautical Conference: Research and Technology—The Next Decade, Melbourne, Australia.
- Pfeil, H., and Herbst, R., 1979, "Transition Procedure for Instationary Boundary Layers," ASME Paper No. 79-GT-128.
- Rai, M. M., and Dring, R. P., 1986, "Navier-Stokes Analysis of Redistribution of Inlet Temperature Profile in a Turbine," Paper No. AIAA-87-2146.
- Rai, M. M., 1987, "Unsteady Three-Dimensional Simulations of Turbine Rotor-Stator Interactions," AIAA Paper No. 87-2058.
- Rhie, C. M., 1986, "A Pressure Based Navier-Stokes Solver Using the Multi-Grid Method," AIAA Paper No. 86-0207.
- Scholz, N., 1977, "Aerodynamics of Cascades," AGARD-AG-220.
- Schultz, D. L., Jones, T. V., Oldfield, M. L. G., and Daniels, L. C., 1977, "A New Transient Facility for the Measurement of Heat Transfer Rates," Conference Proceedings No. 220, *High Temperature Problems in Gas Turbine Engines*, pp. 33-1 to 33-27.
- Sharma, O. P., Butler, T. L., Joslyn, H. D., and Dring, R. P., 1985, "Three-Dimensional Unsteady Flow in an Axial Flow Turbine," *Journal of Propulsion and Power*, Vol. 1, No. 1.
- Sharma, O. P., Renaud, E., Butler, T. L., Milsaps, K., Dring, R. P., and Joslyn, H. D., 1988, "Rotor-Stator Interaction in Multistage Axial Turbines," AIAA Paper No. 88-3013.
- Speidel, L., 1957, "Beeinflussung der Laminaren Crezschicht durch Periodische Storungen der Zust Romung," *Flugwiss 5*, Vol. 9.
- Williams, M. C., 1988, "Inter and Intrablade Row Laser Velocimetry Studies of Gas Turbine Compressor Flows," *ASME JOURNAL OF TURBOMACHINERY*, Vol. 110, pp. 369-376.

M. G. Dunn
Calspan Corp.,
Buffalo, NY 14225

W. A. Bennett

R. A. Delaney

K. V. Rao

Allison Gas Turbine Division,
General Motors Corporation,
Indianapolis, IN 46206-0420

Investigation of Unsteady Flow Through a Transonic Turbine Stage: Data/Prediction Comparison for Time-Averaged and Phase-Resolved Pressure Data

This paper presents time-averaged and phase-resolved measurements of the surface pressure data for the vane and blade of a transonic single-stage research turbine. The data are compared and contrasted with predictions from an unsteady Euler/Navier-Stokes code. The data were taken in a shock-tunnel facility in which the flow was generated with a short-duration source of heated and pressurized air. Surface-mounted high-response pressure transducers were used to obtain the pressure measurements. The turbine was operating at the design flow function, the design stage pressure ratio, and 100 percent corrected speed. A matrix of data was obtained at two vane exit conditions and two vane/rotor axial spacings.

Introduction

Turbomachinery flow fields are inherently unsteady for many reasons, which include turbulence generated in the combustor and disturbances generated when rotating blades transit nozzle guide vane wakes and exit passages. Years of experience has illustrated that these flows can be considered to be quasi-steady and satisfactory flow field predictions can be performed. In order to compare predictions with experimental data, the data are generally time averaged (Dunn et al., 1984; Dunn and Chupp, 1987; Rae et al., 1988; Sharma et al., 1987; Taulbee et al., 1989). However, the state of the art in instrumentation and flow computations has progressed to the point where relevant unsteady calculations can be performed and unsteady flow field measurements needed for comparison with these predictions can be obtained. Rao and Delaney (1990) have summarized many of the papers that have treated the prediction of the unsteady flow environment. A few others that are particularly relevant to this paper will be noted here. The early work of Kemp and Sears (1953, 1955) was the catalyst for much of the research that followed. Subsequently, Giesing (1968), Parker (1969), and Kerrebrock and Mikolajczak (1970) made contributions to the understanding of these problems. More recently, Fleeter et al. (1978, 1979), Dring et al. (1980, 1982), and Dring and Joslyn (1981) have used large-scale rotating axial compressor and turbine stages, respectively, to obtain experimental data on the nature of the unsteady flow field. Also, Hodson (1984, 1985a, 1985b) has used several

different facilities to study wake-generated unsteadiness in vane exit passages and to perform measurements of boundary-layer transition and flow separation.

A high-pressure turbine, designed by Allison Gas Turbine Division, was constructed solely for the purpose of the analysis/measurement program described in this paper. This stage was installed in a shock-tunnel facility and time-averaged and phase-resolved pressure measurements were obtained on both the vane and the blade. The stage was constructed so that two vane positions could be investigated: (1) closed position for which the vane exit flow was transonic ($M = 1.1$) and (2) open position for which the vane exit flow was high subsonic ($M = 0.9$). Further, the stage was constructed so that the vane-blade spacing could be easily changed, allowing for repetition of vane and blade measurements at different rotor-stator spacings under nearly identical inlet conditions. Measurements are described for two different spacings with the vane in the closed position and for one spacing with the vane in the open position. Time-averaged and phase-resolved surface-pressure data were obtained for each of these configurations. The influence of vane-blade spacing on the stage heat-flux distributions has previously been investigated by Dring et al. (1983), Dunn and Hause (1982), Blair et al. (1989a, 1989b), and Dunn and Chupp (1989). The measurements reported in those papers were performed for a significantly different turbine than the one used here (this turbine stage operated in the transonic range) in that the investigations of Dring and Joslyn (1983) and Blair et al. (1989a, 1989b) were conducted using the UTRC low-speed rotating rig (1.5-m diameter), the investigations of Dunn and Hause (1982) were performed using the Garrett TFE731-2 HP turbine stage, and the investigations of Dunn and Chupp (1989)

Contributed by the International Gas Turbine Institute for publication in the JOURNAL OF TURBOMACHINERY. Manuscript received at ASME Headquarters May 1991.

were performed using the Teledyne 702 HP turbine stage. The stage characteristics of the three turbines just noted are given in the respective papers.

The purpose of this paper is to report the results of a combined computational and experimental program. This paper briefly describes the experimental apparatus and the experimental technique and compares the time-averaged and phase-resolved surface pressure data for the vane and the blade with the predicted results from the method of Rao and Delaney (1990).

Experimental Apparatus

The experimental apparatus used here consists of the shock-tunnel facility, the turbine stage, the model to house the stage, and the instrumentation installed along the model flow path and on the vanes and blades. Brief descriptions of each of these components are given in the following paragraphs.

Shock-Tunnel Facility. The wheel diameter of the turbine was 0.53 m (21 in.), which required a facility¹ that could accommodate the physical size and weight-flow requirements of a large turbine. The facility used here was designed to accommodate large turbines, those with wheel diameters as large as 1 m (≈ 39 in.). The facility utilizes a 0.46-m (18.5-in.) i.d. helium/air-driven shock tube with a 12.2-m (40-ft) long driver tube, an 18.3-m (60-ft) long driven tube, a primary nozzle, and a 2.75-m (9-ft) diameter by 10.4-m (34-ft) long dump tank. The driver tube is sufficiently long that the wave system reflected from the end of the driver tube does not terminate the test time prematurely. This facility has a long running time for a shock-tunnel facility, being on the order of 35 to 40 ms.

Turbine Stage. The turbine stage used in this work was designed and constructed by Allison Gas Turbine Division specifically for the purposes of the research program described here. The stage consists of 30 vanes and 45 blades. Other stage geometry parameters are given in Table 1. The vane setting angle is variable and can be in either the fully open or fully closed position. The total-to-total stage pressure ratio for the closed position is 3.44 versus 2.36 for the open position and the turbine weight flow for the closed position is 10.20 kg/s versus 12.52 kg/s for the open position. The corrected speed for this turbine in the closed vane position is about 11,400 rpm and in the open vane position is about 11,000 rpm. Blade row velocity diagram information and stage inlet conditions for the two vane setting angles are presented in Table 2. The inlet

¹A detailed description of the facility and its operation is beyond the scope of this paper. For a complete description of the tunnel construction, operation, and calibration the reader is referred to Final Report WRDC-TR-89-2027, "Operating Point Verification Data for a Large Shock Tunnel Test Facility."

turbulence intensity value of 5 percent given in Table 2 is an estimated value based on previous measurements performed in the facility. The length scale and the spectrum of the turbulence are not known.

Model to House Turbine Stage and Flow Path Measurements. Several previous publications (Dunn and Hause, 1982; Dunn et al., 1986; Dunn and Chupp, 1987) have illustrated the concept of the model used to house the Garrett 731-2 turbine, the Garrett low aspect ratio turbine (LART), and the Teledyne 702 turbine. Details given in those papers describe how the model housing the turbine stage is located in the expanding flow portion of the shock-tunnel facility. It is important here to describe some details of the model used to house the Allison turbine stage. Figure 1 is a sketch of the model illustrating a large-diameter inlet duct in which the Mach number is on the order of 0.05, followed by a rapid contraction in which the flow is accelerated to the vane inlet. The vane axial position relative to the rotor is easily changed by moving the spacers and saddle shown in Fig. 1. The flow channel downstream of the rotor exit is a constant area annulus up to the exit nozzle at the rear of the model. The function of this exit nozzle is to set the pressure and temperature ratio across the turbine stage.

Figure 2 is a sketch of the internal model geometry in the immediate vicinity of the stage. The numbers along the flow path (1, 2, 3A, 3B, etc.) refer to locations for which static pressure measurements were taken using flush diaphragm piezoelectric pressure transducers. Positions 1 and 2 at the vane leading edge refer to the vane leading-edge locations for the two vane-blade spacings. The rotor always remains in the same axial position, whereas the vane location is changed by moving the spacers. Upstream of the vane, the Mach number is so low that the total pressure is nearly equal to the static pressure measured at stations 1 and 2. The flow is isentropic at this point so that the total temperature is equal to the temperature behind the reflected shock. Rakes of total-pressure and total-temperature probes were used downstream of the rotor exit to

Table 1 VBI turbine stage geometry

Parameter	Stator	Rotor
Number of airfoils	30	45
Chord, m	0.066	0.046
Spacing, m	0.050	0.033
Chord/spacing	1.32	1.39
Mean radius, m	0.241	0.239
Aspect ratio	0.72	1.10
Leading edge radius, m	0.0045	0.0022
Trailing edge radius, m	0.00075	0.00075
Hub/tip radius, m	0.82	0.81
Tip radius, m	0.265	0.265
Trailing edge blockage, percent	7.94	8.94

Table 2 VBI turbine stage aerodynamics

Parameter	Closed vane setting		Open vane setting	
	Stator	Rotor	Stator	Rotor
Rotor speed, rpm	--	11,400	--	11,000
Stage equivalent work, J/kg	--	7.82×10^4	--	5.75×10^4
Stage expansion ratio (total-to-static)	--	4.06	--	2.43
Inlet relative Mach number	0.164	0.483	0.197	0.406
Exit relative Mach number	1.121	1.054	0.918	0.880
Inlet relative flow angle, deg	0.0	-49.18	0.0	-41.51
Exit relative flow angle, deg	-72.66	62.22	-69.55	62.49
Inlet total temperature, K	522	522	522	522
Inlet total pressure, kPa	303.4	--	303.4	--
Corrected flow, kg/s	10.20	--	12.52	--
Inlet Reynolds number	8×10^5	--	8×10^5	--
Inlet turbulence intensity, percent	5.0	--	5.0	--
Reduced frequency	7.8	8.5	8.0	8.5
Vane setting angle, deg	-61.0	--	-57.0	--
Vane-blade spacing, m (percent C_x)	0.015 (40)		0.015 (38)	
	0.025 (66)		0.025 (64)	

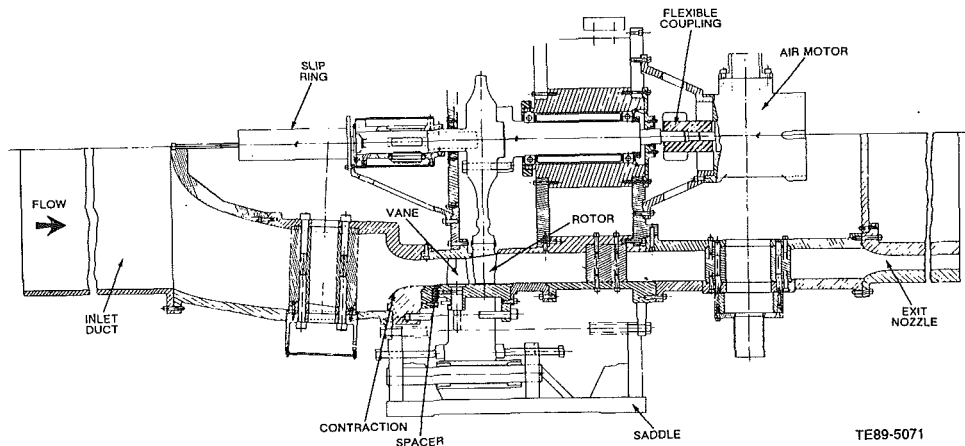


Fig. 1 Sketch of model housing turbine stage

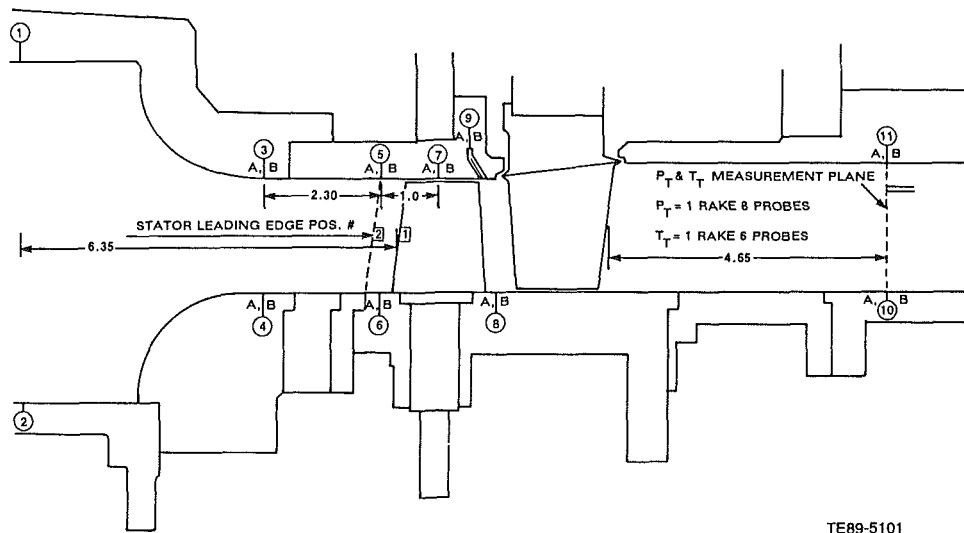


Fig. 2 Sketch of engine pressure instrumentation locations

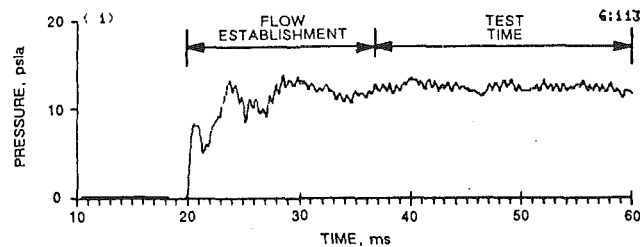
measure profiles of these parameters across the channel. Figs. 3(a) and 3(b) present typical total pressure histories and Figs. 3(c) and 3(d) present typical total temperature histories measured downstream of the rotor.

Stage Instrumentation. One of the essential elements that contributed to the success of this experiment is the miniature pressure transducers that were installed on the vanes and blades. The transducers, which were mounted flush with the surface, were Kulite units with an active area of 6.25×10^{-4} m (0.025 in.) by 6.25×10^{-4} m (0.025 in.), and a thickness of about 3.25×10^{-4} m (0.0139 in.). A very thin layer of silastic material is placed over these transducers to provide a thermal barrier (this is an effective technique for short-duration measurements) and thus significantly reduce temperature sensitivity. This material is applied under a microscope in an effort to preserve the proper surface contour of the component. Similar transducers were previously used on a rotating turbine blade and typical results were described by Dunn et al. (1989). The installed frequency response of these units is in excess of 100 kHz. Twenty of these units were installed on both the vanes and blades. The instrumentation was concentrated on the mid-span portion of the vane and the blade. The vane was sufficiently large that ten transducers could be put on a single vane. However, because the blade was smaller, not more than four or five were installed on any one blade so as not to disrupt the surface contour. The locations of these transducers are shown on a single vane and blade in Fig. 4.

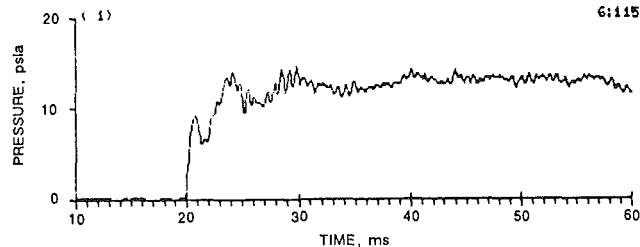
Each of the pressure transducers is calibrated after installation in the blades (and vanes) but before the turbine assembly (model) is placed in the facility receiver tank. The calibration is done at five or six points over the range of anticipated pressure. A straight line is then fit to these data to obtain the slope of the gage response in psi/mv. Periodically throughout the test series, the receiver tank is pressurized and the slope of the gage response is checked against the initial calibration. These periodic checks produce results to within 1 to 1.5 percent of the initial slope. During the discussion of results, it will be illustrated that the baseline pressure corresponds to a condition for which the rotor is at design speed and the receiver tank pressure is known (3 torr). The onset of flow at the turbine stage will be evident as will the steady-state pressure level. This pressure is converted to engineering units by multiplying the delta voltage by the gage response slope.

Discussion of Results

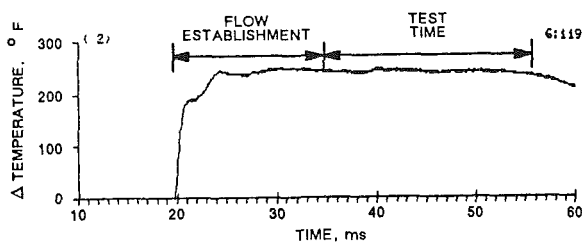
Both time-averaged and phase-resolved surface-pressure data were obtained on the vane and the blade for the various stage configurations described earlier. Because of the space limitations of this paper, only a small portion of the data that were collected can be presented. All of the results are given in the final report by Delaney et al. (1990). It was noted earlier that several authors have performed measurements of unsteady pressure loading on turbine blades but these measurements were performed in a different environment than described here.



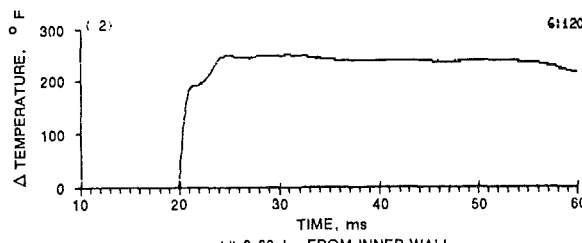
(a) 0.76-in. FROM INNER WALL



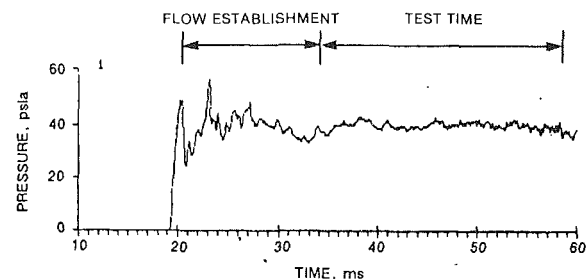
(b) 1.24-in. FROM INNER WALL



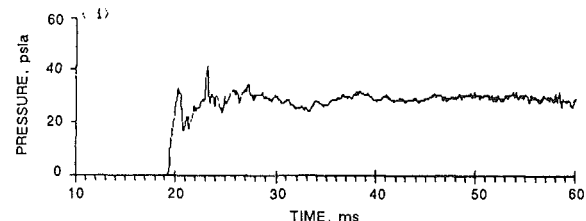
(c) 0.62-in. FROM INNER WALL



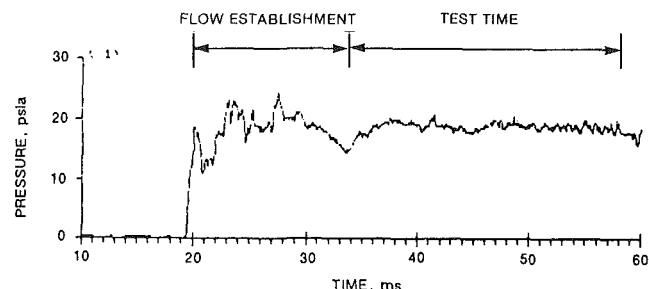
(d) 0.82-in. FROM INNER WALL



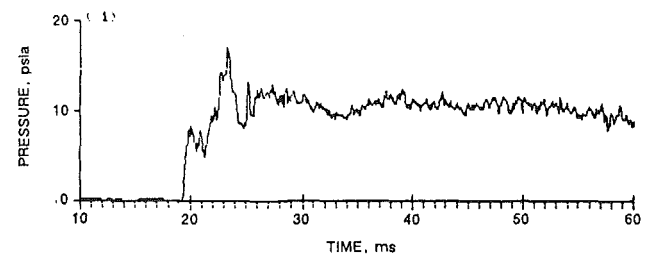
(a) VANE PRESSURE SURFACE, $S/S_T = 25.3\%$



(b) VANE PRESSURE SURFACE, $S/S_T = 73.6\%$



(c) BLADE PRESSURE SURFACE, $S/S_T = 11\%$



(d) BLADE SUCTION SURFACE, $S/S_T = 49.6\%$

Fig. 3 Typical total pressure and total temperature histories just downstream of rotor

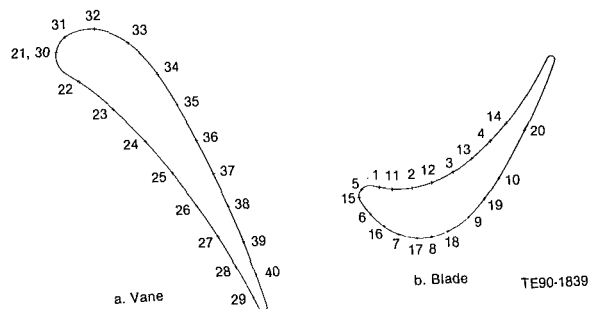


Fig. 4 Pressure transducer locations on vane and blade

All of the interactive computations were performed on an axisymmetry blade-to-blade stream surface with the radius and stream tube variation defined by Allison's turbine aerodynamic design system. Stage inflow and outflow boundary condition data were also obtained from this design system.

The interactive Euler and Navier-Stokes computations were performed on overlapping O-type grids for the vane and blade rows. The solutions for each row were coupled by interpolating

Fig. 5 Typical surface pressure measurements on vane and blade

inflow boundary data for the vane solution from the blade solution. Nonreflective inflow and outflow boundary conditions based on the method of characteristics were imposed at the stage inflow and outflow boundaries. A phase-lagged boundary treatment, which allows for unequal numbers of airfoils in each blade row, was enforced on the spatially periodic grid boundaries. Unsteady interactive solutions were started from steady solutions for each isolated blade row. The unsteady solutions were assumed to be converged when the root-mean-square of the pressure differences between solutions one blade passing period apart approached zero. Typically, converged quasi-steady unsteady solutions were obtained after one full revolution of the rotor.

Time Histories of Vane and Blade Surface Pressure. Time histories of the vane and blade surface-pressure data obtained with the vane in the closed position and for a rotor-stator spacing of 0.015 m (0.602 in.) are shown in Fig. 5. With the vane in the closed position the exit Mach number is supersonic ($M = 1.1$), which results in a vane trailing edge shock system that produces substantial unsteadiness on the downstream ro-

tor. Figures 5(a) and 5(b) show the surface-pressure history at 25.3 and 73.6 percent wetted distance on the vane pressure surface. Figure 5(c) shows the surface-pressure history at 11.1 percent wetted distance on the blade pressure surface and Fig. 5(d) shows the pressure history at 49.6 percent wetted distance on the blade suction surface. The flow establishment time is noted on these figures as is the test time. During the test time, the mean pressure is shown to be relatively constant.

The data shown were obtained with the rotor turning at 11,400 rpm. Figures 5(c) and 5(d) demonstrate the level of activity of the data during the useful test time. This activity is not random, but rather is due to the unsteady pressure signal that results when the blade passes by one vane passage. Later in this paper, fast Fourier transforms of the phase-resolved pressure data will be presented to illustrate this point. The surface pressure data were both time averaged and phase resolved. The phase-resolved results were then ensemble averaged. The results of those efforts are given below.

Time-Averaged Pressure Distributions on Vane and Blade. Figures 6 and 7 present the time-averaged surface-pressure distributions for the vane and blade with the vane in the closed position and the rotor-stator spacing equal to 0.015 m (0.602 in.). In both these figures, the bars through the symbols represent one standard deviation. Also shown in Figs. 6 and 7 are unsteady Euler and Navier-Stokes predictions. The experimental data shown in Fig. 6 have been adjusted upward by 2.8 percent (for comparison purposes) to match the Euler prediction at 25 percent wetted distance on the pressure surface. About 1.0 percent of this 2.8 percent adjustment can be attributed to total pressure losses in the contraction. It was noted earlier in this paper that the reproducibility of the slope of the pressure gage response was on the order of 1 to 1.5 percent, which would account for a large portion of the remaining 1.8 percent. In general, the predictions follow the trend of the data. On the vane pressure surface, the two predictions are essentially in agreement; however, both fail to predict the pressure decrease in the vicinity of 75 percent wetted distance. (There appears to be no physical explanation from steady isolated airfoil row testing experience for the measured decrease in pressure, which was repeatable from run to run in the experiments.) However, from the stagnation region to 60 percent wetted distance, both predictions follow the data. On the vane suction surface, the predictions are in agreement until about 40 percent wetted distance and both agree with the data from the stagnation region up to about 10 percent wetted distance. Neither prediction matches the pressure level at 20 and 40 percent, but both predictions closely match the pressure level from 50 percent wetted distance on to the trailing edge. The differences in the predictions from 40 to 60 percent wetted distance are related to the differences in viscous and inviscid treatment of the trailing edge flow. The trailing edge flow has a strong influence on the predicted flow conditions on the uncovered suction surface, particularly near the throat at approximately 50 percent wetted distance. The significant differences shown between the suction surface predictions and the data at 20 and 40 percent wetted distance are not currently understood.

Figure 7 presents a comparison between the blade data and the results of the Euler and Navier-Stokes predictions. On both surfaces, the predictions are relatively close to each other with the Navier-Stokes prediction falling slightly lower. The agreement on the pressure surface between the data and the predictions is reasonable. On the suction surface the predictions are above the data and neither solution predicts the oscillatory behavior of the data between 18 and 33 percent wetted distance.

The influence of rotor-stator spacing on the surface-pressure distribution was investigated by keeping the vane at the closed setting and increasing the spacing from 0.015 m (0.062 in.) to

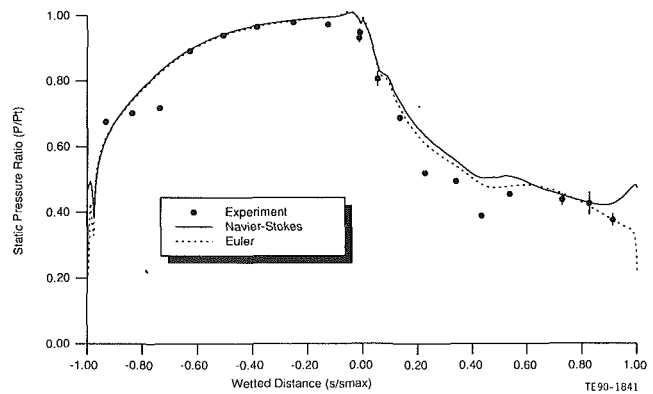


Fig. 6 Predicted and measured time-averaged pressure distributions on the vane; closed vane setting, spacing = 0.6 in.

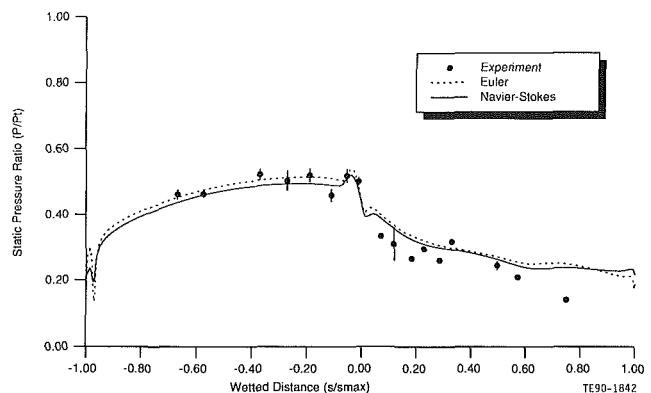


Fig. 7 Predicted and measured time-averaged pressure distributions on the blade; closed vane setting, spacing = 0.6 in.

0.0254 m (1.0 in.). On the initial run at the wide spacing, several of the pressure transducers near the trailing edge of the vane were destroyed. The measurements proceeded using the remaining instrumentation.

In general, Figs. 6 and 7 do not show significant differences between the Euler and Navier-Stokes predictions. Therefore, in the results to follow only the Euler predictions will be given. In the interest of economy, Navier-Stokes computations were not made for rig configurations with wide vane-blade spacing.

Figures 8 and 9 present comparisons between the data and the Euler prediction for the vane and blade, respectively, with the vane at the closed setting and the spacing equal to 0.0254 m. The comparisons shown on Figs. 8 and 9 are similar to those shown on Figs. 6 and 7 for the 0.015-m spacing. The level of agreement between the data and the predictions is about the same as that for the close spacing. It is clear by comparing Figs. 6 and 8 and Figs. 7 and 9, respectively, that the influence of rotor-stator spacing (over the range covered) is negligible.

To investigate the influence of vane exit conditions on the interactive flow field, the vane setting was changed from the closed setting to the open setting while maintaining the rotor-stator spacing at 0.0254 m (1.0 in.) and the measurements were repeated. The vane exit Mach number in this case was subsonic ($M = 0.9$) whereas a supersonic ($M = 1.1$) condition existed for the closed setting. The most obvious effect of the interactive flow field was a reduction in the unsteady activity on the blade as a result of the absence of a vane trailing edge shock system.

Figures 10 and 11 present a comparison of the vane and blade experimental data with the Euler code predictions for the configuration with the vane at the open setting and the rotor-stator spacing equal to 0.0254 m (1.0 in.). The level of agreement between the data and the predictions shown in Fig. 10 is similar to that previously shown in Fig. 8 for the closed setting with the greatest discrepancy occurring near the suction

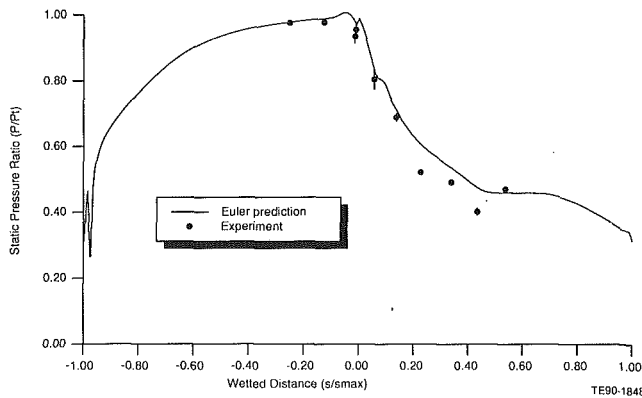


Fig. 8 Predicted and measured time-averaged pressure distributions on the vane; closed vane setting, spacing = 1.0 in.

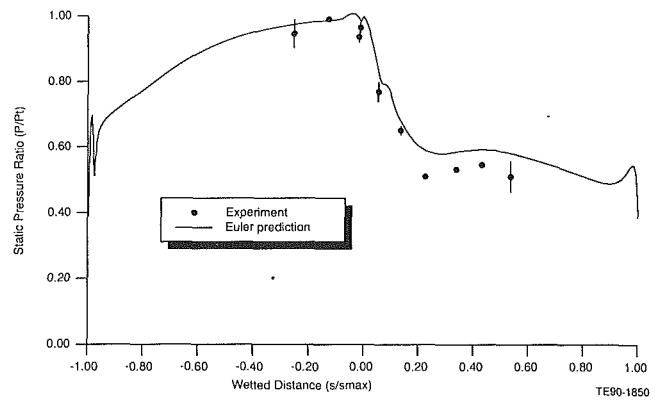


Fig. 10 Predicted and measured time-averaged pressure distributions on the vane; open vane setting, spacing = 1.0 in.

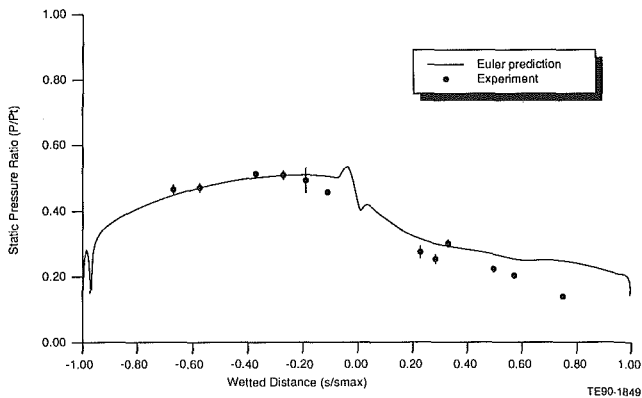


Fig. 9 Predicted and measurement time-averaged pressure distributions on the blade; closed vane setting, spacing = 1.0 in.

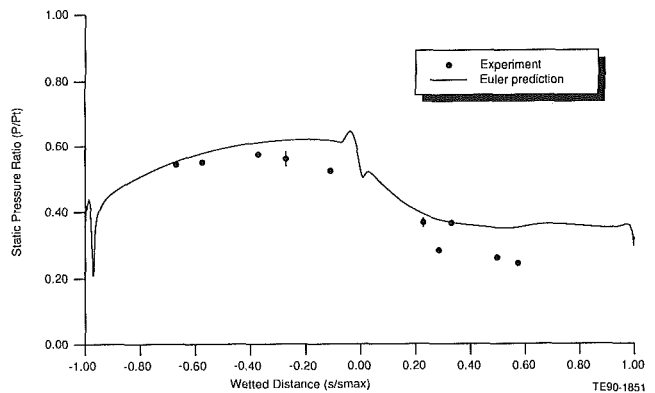


Fig. 11 Predicted and measured time-averaged pressure distributions on the blade; open vane setting, spacing = 1.0 in.

surface throat. The comparison for the blade presented in Fig. 11 illustrates a reasonable agreement in trend over most of the pressure surface, but the prediction is consistently above the data.

Comparison of the vane data in Figs. 8 and 10 for the closed and open vane settings, respectively, illustrates that the pressure level on the aft portion of the vane suction surface is lower for the closed vane setting due to the lower exit pressure. This effect is seen beyond 45 percent wetted distance on the vane suction surface. The pressure surface was essentially uninfluenced by the vane setting. Figures 9 and 11 suggest that the pressure loading over the entire blade surface was influenced by resetting the vane. Consistent with the reduced relative Mach number into the blade, the pressure for the open setting was consistently greater than that measured with the vane at the closed setting.

Magnitude of Unsteady Pressure Loading on Blade. Comparisons between the maximum predicted and measured unsteady airfoil surface pressure loadings on the vane and blade for the closed vane setting and rotor-stator spacing of 0.015 m (0.602 in.) are presented in Figs. 12 and 13. Both the Euler and the Navier-Stokes (N-S) predictions are included. The magnitude of the unsteady fluctuations predicted by the N-S code is consistently smaller than that predicted by the Euler code due to the presence of boundary layers and wakes. As illustrated in Fig. 12, the vane unsteady pressure fluctuations were predicted to occur on the suction surface from about 40 percent wetted distance on to the trailing edge. Since the vane is choked for this setting, no unsteadiness propagates upstream of the vane throat, as shown in Fig. 12. Downstream of the throat on the vane suction surface, both predictions and measurements show significant unsteadiness. With the exception of the unsteady data at 53 and 82 percent

wetted distance, the experimental results fall within the N-S predicted envelope. Although not all of the data fall within the predicted envelope, they are reasonably close. Both predictions agree reasonably well, except near the suction surface throat location, where the differences in trailing edge modeling between the Euler and Navier-Stokes computations have a significant impact.

Figure 13 presents the predicted blade unsteady pressure envelopes from the Euler and the N-S codes and compares the results with the measurements. Again, the N-S envelope is smaller than the Euler envelope. However, in this case, the Euler prediction agrees more favorably with the data. From both the predictions and measurements, the effect of the vane trailing edge shock striking the rotor is very evident from the strong unsteadiness from 10 percent wetted distance on the pressure surface to 30 percent wetted distance on the suction surface. These results show a more rapid reduction in unsteadiness on the suction surface than on the pressure surface. A particularly interesting result is that the unsteadiness persists at a higher level on the pressure surface than the suction surface.

Figure 14 presents a comparison between the predicted blade surface unsteady pressure envelope from the Euler solution and the measurements for the closed vane setting and the wide rotor-stator spacing. Again, reasonably good agreement is shown between the prediction and the data with the best agreement on the blade pressure surface. Comparison of these results with those presented in Fig. 13 for the close spacing shows the effect of spacing on the blade surface unsteadiness. As expected, these results show a reduction in the unsteady envelope with increased rotor-stator spacing.

Phase-Resolved Unsteady Pressures on Blade and Vane. A

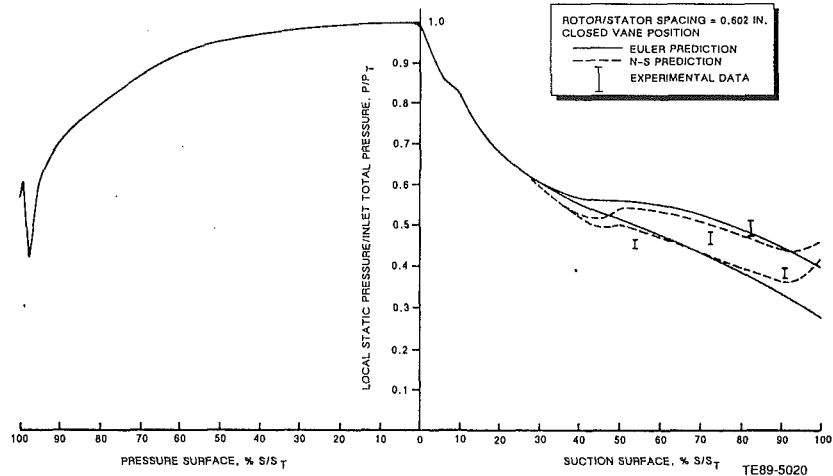


Fig. 12 Comparison between predicted and measured pressure excursions for vane; closed vane setting, spacing = 0.6 in.

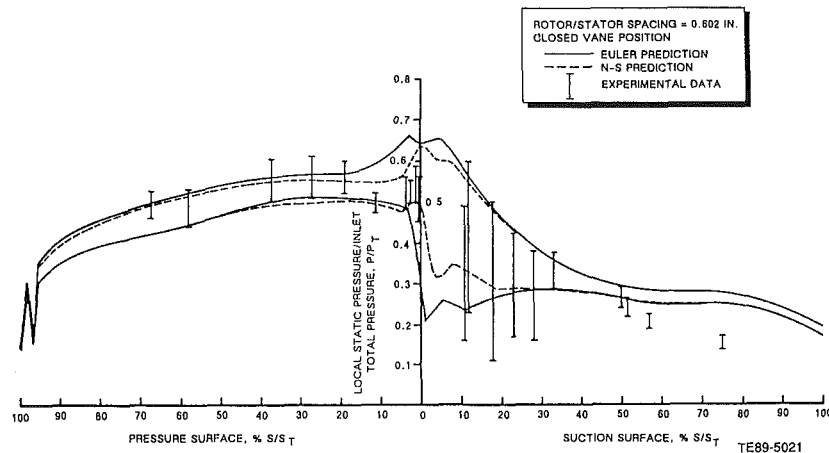


Fig. 13 Comparison between predicted and measured pressure excursions for blade; closed vane setting, spacing = 0.6 in.

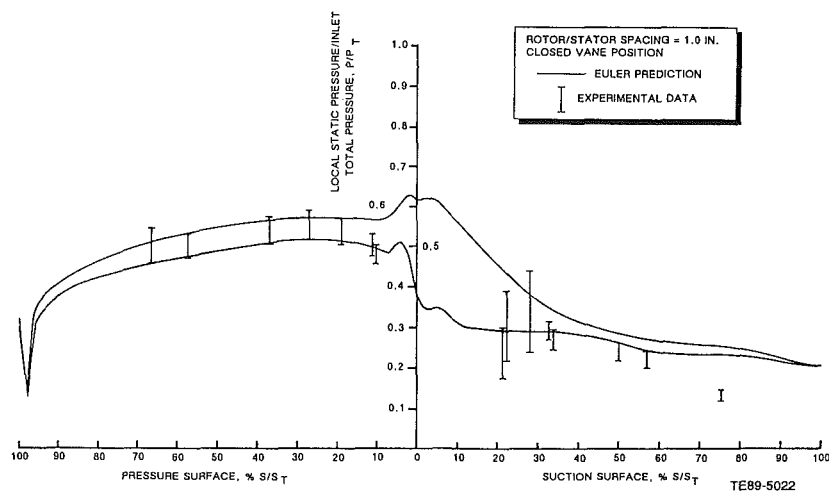


Fig. 14 Comparison between predicted and measured pressure excursions for blade; closed vane setting, spacing = 1.0 in.

shaft encoder that provided 720 pulses, 360 pulses, and 1 pulse per revolution was used to locate an instrumented blade relative to a particular vane trailing edge. Since this turbine has 30 vanes, each vane passage is 12 deg in duration. The 720 pulses per revolution signal from the encoder was used to trigger the data recording system as described by Dunn et al. (1989) and Dunn (1990) so that the blade data were sampled every one-

half degree. The local static pressure was then normalized by the inlet total pressure for a given run and the data were ensemble averaged over one to two rotor revolutions. Phase-resolved data were recorded for all Kulite transducers shown in Fig. 4. A Fourier analysis of these pressure data was performed using FFT techniques. Typical results of this analysis will be shown below.

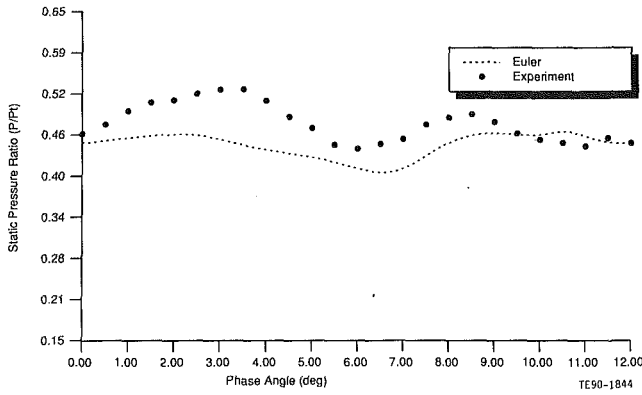


Fig. 15(a) Phase-resolved pressure history at 57.4 percent wetted distance on blade pressure surface (Kulite No. 4); closed vane setting, spacing = 0.6 in.

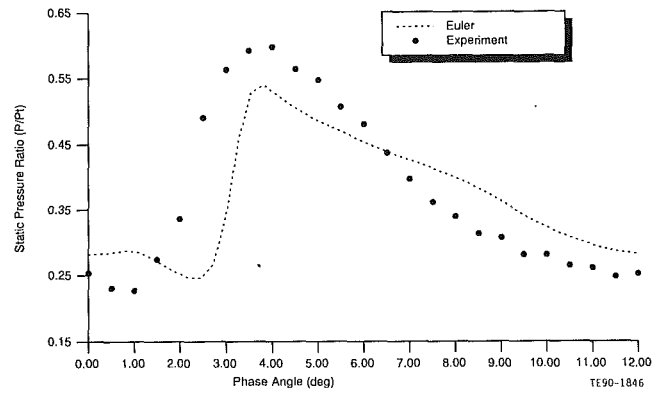


Fig. 17(a) Phase-resolved pressure history at 11.8 percent wetted distance on blade suction surface (Kulite No. 16); closed vane setting, spacing = 0.6 in.

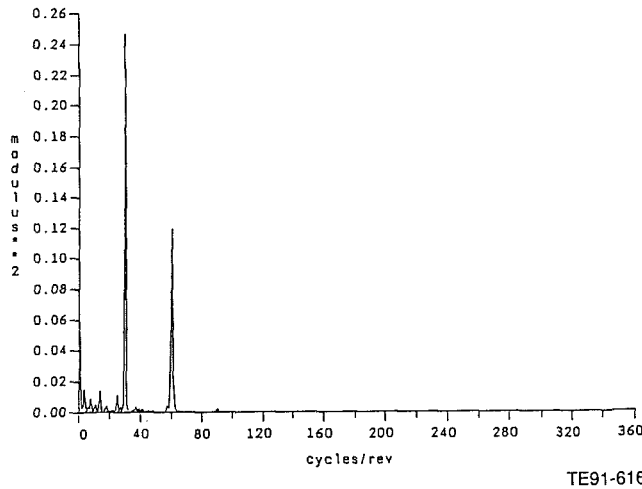


Fig. 15(b) FFT of phase-resolved pressure history at 57.4 percent wetted distance on blade suction surface (Kulite No. 4); closed vane setting, spacing = 0.6 in.

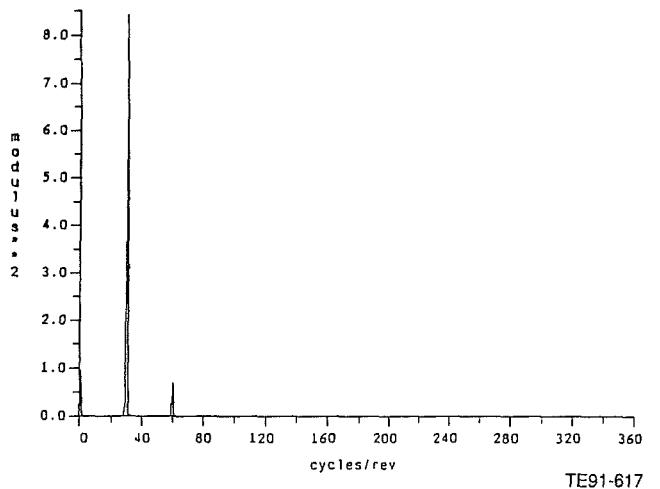


Fig. 17(b) FFT of phase-resolved pressure history at 11.8 percent wetted distance on blade suction surface (Kulite No. 16); closed vane setting, spacing = 0.6 in.

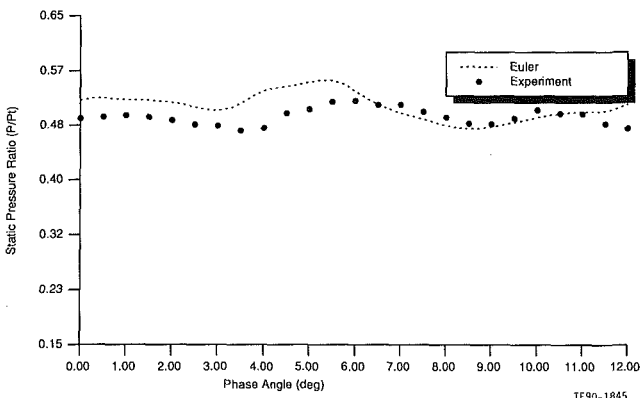


Fig. 16 Phase-resolved pressure history at 11.2 percent wetted distance on blade pressure surface (Kulite No. 11); closed vane setting, spacing = 0.6 in.

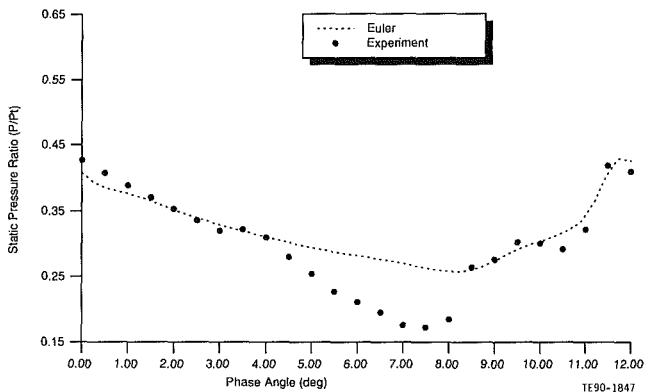


Fig. 18 Phase-resolved pressure history at 22.8 percent wetted distance on blade suction surface (Kulite No. 17); closed vane setting, spacing = 0.6 in.

Blade surface phase-resolved pressure data are compared with Euler predictions at blade Kulite locations 4, 11, 16, and 17 (see Fig. 4) in Figs. 15(a), 16, 17(a), and 18, respectively. Overall, the agreement is reasonable, particularly with regard to phase. At all locations, the unsteady pressure amplitudes are slightly underpredicted. As shown previously in Fig. 13, the strong effect of the vane trailing edge shock on the blade pressure distribution is clearly evident in Figs. 17 and 18 at Kulite locations 16 and 17 on the suction surface near the

leading edge. The pressure surface, on the other hand, is not influenced by the shock as indicated by the lower pressure fluctuations shown in Figs. 15 and 16. On the basis of the agreement achieved between these inviscid Euler predictions and the data, it is suggested that the effect of the vane trailing edge shock on the blade unsteady pressures dominates any effect of the vane wakes.

Figures 15(b) and 17(b) are the results of the Fourier analysis that was performed on the phase-resolved pressure data noted

in the first paragraph of this section. Both of these figures clearly illustrate the dominant signal occurring at 30 cycles/revolution, which corresponds to the number of vanes. Also appearing on the figures is the second harmonic at 60 cycles/revolution. The third harmonic occurring at 90 cycles/revolution can be seen on the FFT result shown in Fig. 15(b).

Conclusions

Time-averaged and phase-resolved surface pressure measurements for the vane and the blade of a transonic turbine stage have been measured and compared with the predictions from Euler and Navier–Stokes analyses. The experimentally determined time-averaged surface pressure distributions are shown to be in reasonable agreement with the predictions for both the vane and the blade.

The phase-resolved pressure data for the blade have also been compared with the prediction at several locations. The agreement between the experimental data and the prediction is reasonably good. For the transonic vane exit condition, high-amplitude unsteadiness occurs near the blade leading edge and is the result of the vane trailing edge shock striking the rotor.

Acknowledgments

The work reported herein was supported in part by Allison Gas Turbine Division and in part by the U.S. Air Force Wright Research and Development Center under Contract No. F33615-83-C-2339 with Allison Gas Turbine Division. The experimental work was performed by Calspan Corporation under subcontract with Allison. The authors would like to express their thanks to Allison, Calspan, and the U.S. Air Force for permission to publish this paper. The authors would also like to acknowledge the support of Air Force personnel W. H. Troha, J. H. Friddell, and R. E. Gray.

References

- Blair, M. F., Dring, R. P., and Joslyn, H. H., 1989a, "The Effects of Turbulence and Stator/Rotor Interactions on Turbine Heat Transfer: Part I—Design Operating Conditions," *ASME JOURNAL OF TURBOMACHINERY*, Vol. 111, pp. 87–96.
- Blair, M. F., Dring, R. P., and Joslyn, H. D., 1989b, "The Effects of Turbulence and Stator/Rotor Interactions on Turbine Heat Transfer: Part II—Effects of Reynolds Number and Incidence," *ASME JOURNAL OF TURBOMACHINERY*, Vol. 111, pp. 97–103.
- Delaney, R. A., Helton, D. J., Bennett, W. A., Dunn, M. G., Rao, K. V., and Kwon Okey, 1990 "Turbine Vane-Blade Interaction," Final Report, WRDC-TR-89-2154, Vol. 1.
- Dring, R. P., Blair, M. F., and Joslyn, H. D., 1980, "An Experimental Investigation of Film Cooling on a Turbine Rotor Blade," *ASME JOURNAL OF ENGINEERING FOR POWER*, Vol. 102, pp. 81–87.
- Dring, R. P., and Joslyn, H. D., 1981, "Measurement of Turbine Rotor Blade Flows," *ASME JOURNAL OF ENGINEERING FOR POWER*, Vol. 103, pp. 400–405.
- Dring, R. P., Joslyn, H. D., Hardin, L. W., and Wagner, J. H., 1982, "Turbine Rotor-Stator Interaction," *ASME JOURNAL OF ENGINEERING FOR POWER*, Vol. 104, pp. 729–742.
- Dring, R. P., and Joslyn, H. D., 1983, "Relative Eddy in Axial Rotor Passages," *ASME Paper No. 83-GT-22*.
- Dunn, M. G., and Hause, A., 1982, "Measurement of Heat Flux and Pressure in a Turbine Stage," *ASME JOURNAL OF ENGINEERING FOR POWER*, Vol. 104, pp. 215–223.
- Dunn, M. G., Rae, W. J., and Holt, J. L., 1984, "Measurement and Analyses of Heat Flux Data in a Turbine Stage—Discussion of Results and Comparison With Predictions," *ASME JOURNAL OF ENGINEERING FOR GAS TURBINES AND POWER*, Vol. 106, pp. 234–240.
- Dunn, M. G., Martin, H. L., and Stanek, M. J., 1986, "Heat-Flux and Pressure Measurements and Comparison With Prediction for a Low Aspect Ratio Turbine Stage," *ASME JOURNAL OF TURBOMACHINERY*, Vol. 108, pp. 108–115.
- Dunn, M. G., and Chupp, R. E., 1987, "Time-Averaged Heat-Flux Distributions and Comparison With Prediction for the Teledyne 702 hp Turbine Stage," *ASME JOURNAL OF TURBOMACHINERY*, Vol. 110, pp. 51–56.
- Dunn, M. G., and Chupp, R. E., 1989, "Influence of Vane/Blade Spacing and Injection on Stage Heat Flux Distributions," *AIAA J. of Propulsion and Power*, Vol. 5, pp. 212–200.
- Dunn, M. G., Seymour, P. J., Woodward, S. H., George, W. K., and Chupp, R. E., 1989, "Phase-Resolved Heat-Flux Measurements on the Blade of a Full-Scale Rotating Turbine," *ASME JOURNAL OF TURBOMACHINERY*, Vol. 111, pp. 1–18.
- Dunn, M. G., 1990, "Phase and Time-Resolved Measurements of Unsteady Heat Transfer and Pressure in a Full-Stage Rotating Turbine," *ASME JOURNAL OF TURBOMACHINERY*, Vol. 112, pp. 531–538.
- Fleeter, S., Jay, R. L., and Bennett, W. A., 1978, "Rotor Wake Generated Unsteady Aerodynamic Response of a Compressor Stator," *ASME JOURNAL OF ENGINEERING FOR POWER*, Vol. 100, pp. 664–675.
- Fleeter, S., Jay, R. L., and Bennett, W. A., 1979, "Wake Induced Time-Variant Aerodynamics Including Rotor-Stator Axial Spacing Effects," *AIAA Paper 79-0152*.
- Giesing, J. P., 1968, "Nonlinear Interaction of Two Lifting Bodies in Arbitrary Unsteady Motion," *ASME JOURNAL OF BASIC ENGINEERING*, Vol. 90, pp. 287–294.
- Hodson, H. P., 1984, "Boundary Layer and Loss Measurements on the Rotor of an Axial-Flow Turbine," *ASME JOURNAL OF ENGINEERING FOR GAS TURBINES AND POWER*, Vol. 106, pp. 391–399.
- Hodson, H. P., 1985a, "Measurements of Wake-Generated Unsteadiness in the Rotor Passages of Axial Flow Turbines," *ASME JOURNAL OF ENGINEERING FOR GAS TURBINES AND POWER*, Vol. 107, pp. 467–476.
- Hodson, H. P., 1985b, "Boundary-Layer Transition and Separation Near the Leading Edge of a High-Speed Turbine Blade," *ASME JOURNAL OF ENGINEERING FOR GAS TURBINES AND POWER*, Vol. 107, pp. 127–134.
- Kemp, N. H., and Sears, W. R., 1953, "Aerodynamic Interference Between Moving Blade Rows," *J. Aero. Sci.*, Vol. 20, pp. 585–597.
- Kemp, N. H., and Sears, W. R., 1955, "The Unsteady Forces Due to Viscous Wakes in Turbomachine," *J. Aero. Sci.*, Vol. 22, pp. 478–483.
- Kerrebrock, J. L., and Mikolajczak, A. A., 1970, "Intra-stator Transport of Rotor Wakes and Its Effect on Compressor Performance," *ASME JOURNAL OF ENGINEERING FOR POWER*, Vol. 92, pp. 359–368.
- Parker, R., 1969, "Relation Between Blade Row Spacings and Potential Flow Interaction Effects in Turbomechanics," *Proceedings of the Institute of Mechanical Engineering*, Vol. 184, Pt. 3G, No. 11, pp. 1–8.
- Rae, W. J., Taulbee, D. B., Civinskis, K. C., and Dunn, M. G., 1988, "Turbine-Stage Heat Transfer: Comparison of Short-Duration Measurements With State-of-the-Art Predictions," *AIAA J. of Propulsion and Power*, Vol. 4, No. 6, pp. 541–548.
- Rao, K. V., and Delaney, R. A., 1990, "Investigation of Unsteady Flow Through a Transonic Turbine Stage, Part I—Analysis," *AIAA Paper No. 90-2408*.
- Sharma, O. P., Nguyen, P., Ni, R. H., Rhie, C. M., White, J. A., and Finke, A. K., 1987, "Aerodynamics and Heat Transfer Analysis of a Low Aspect Ratio Turbine," *AIAA Paper No. 87-1916*.
- Taulbee, D. B., Tran, L., and Dunn, M. G., 1989, "Stagnation Point and Surface Heat Transfer for a Turbine Stage: Prediction and Comparison With Data," *ASME JOURNAL OF TURBOMACHINERY*, Vol. 111, pp. 28–35.

Measurements of the Pressure and Velocity Distribution in Low-Speed Turbomachinery by Means of High-Frequency Pressure Transducers

S. Brodersen¹

D. Wulff

Pfleiderer—Institut für
Strömungsmaschinen,
Technische Universität Braunschweig,
3300 Braunschweig,
Federal Republic of Germany

The flow in a low-speed, single-stage compressor with a very high blade loading has been measured using a two-probe arrangement. The measuring technique and data reduction procedure described have been especially adjusted for application in low-speed turbomachinery. Those machines show only small pressure fluctuations in the flow downstream of the rotor, for which specific requirements concerning the measuring technique have been taken into account. The probes used contain unsteady pressure transducers and simulate an unsteady multisensor pressure probe. This technique proves to be suitable for applications in low-speed turbomachinery. The measurements are based on phase-locked ensemble averages of multiple samples, where the data are acquired using a simple and convenient experimental setup. This allows the velocity and pressure distribution of the flow to be determined in rotor coordinates. The results show the flow field and the loss distribution of an aerodynamically highly loaded rotor at design flow rate.

1 Introduction

The present study was stimulated by earlier investigations concerning the performance of very highly loaded axial-flow stages (Schroeder, 1982; Schiller, 1984; Brodersen, 1987). In these investigations it was found that the blade loading of single stages can be chosen higher than two-dimensional boundary data, without damaging the overall performance. The blade loading is expressed by the diffusion number D (see Lieblein, 1965, and Table 1); the two-dimensional value for beginning separation of the profile suction side boundary layer is $D = 0.6$. For estimating the performance of the test rotors, conventional measurements were carried out using a five-hole conical probe, which was sufficient for the aim of the experiments. However, in order to obtain a better understanding of the flow mechanism, especially in the very highly loaded hub region, the application of any high-response probe (hot-wire or laser-velocimetry techniques) is necessary. Because the loss distribution is also of interest, the use of unsteady pressure transducers is required here. In turbomachines with low pressure rise, unsteady pressure measurements are difficult to carry out due to the relatively low velocities compared to high-speed turbomachinery. This results in a low fluctuating part of the measuring signal. Additionally, the lowest nominal pressure range of commercially available high-frequency miniature pressure

transducers is 35 kPa, which is ten times higher than the dynamic pressure behind the typical rotor in this investigation. With the chosen transducer it is possible to measure the pressure fluctuations as well as the steady part, i.e., the static pressure. For the design of the pressure probes used in this investigation the following requirements have been imposed: (i) The head of the miniature pressure transducers should not be enclosed in order to offer the full frequency response of the pure transducer; (ii) the transducers should be applied in such a way that they offer the highest sensitivity to changes in velocity and flow angle; (iii) the probe dimensions should be as small as possible to have only a small influence on the rotor flow and to give the potential for localized measurements in flow gradients; (iv) it should be possible to carry out three-dimensional measurements.

The literature reports some examples of the application of miniature pressure transducers on fluid-flow measurements. The applications include flow-angle insensitive Pitot tubes (Bammert and Rautenberg, 1973; Kerrebrock et al., 1974; Gerich, 1974; Eckardt, 1975; Gallus et al., 1976, 1980; Castorph and Lahm, 1980; Larguier, 1981; Zierke and Okiishi, 1982; Joslyn et al., 1983; Madhavan and Wright, 1985), cylindrical probes (Das and Jiang, 1984; Fiala, 1986), spherical probes (Matsunaga et al., 1978; Kerrebrock et al., 1980), and wedge probes (Heneka, 1983; Bubeck and Wachter, 1987). Shreeve et al. (1978) and Shreeve and Neuhoff (1984) published a measuring technique where a three-dimensional high-frequency pressure probe is simulated by use of two separate impact

¹ Present address: KSB Aktiengesellschaft, 6710 Frankenthal, Federal Republic of Germany.

Contributed by the International Gas Turbine Institute for publication in the *JOURNAL OF TURBOMACHINERY*. Manuscript received by the International Gas Turbine Institute December 1988.

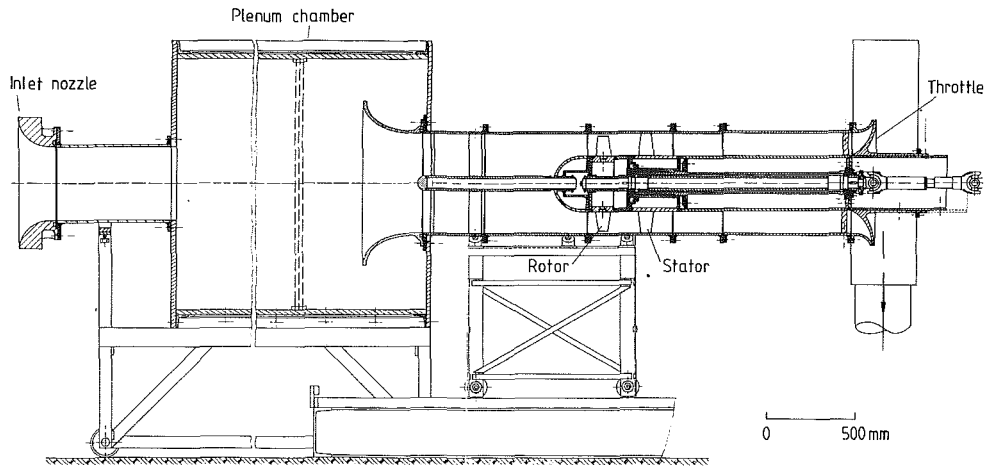


Fig. 1 Test rig

probes (dual probe digital sampling technique). High-frequency Pitot tubes only allow the determination of fluctuations in total pressure whereas the other probe types and measuring techniques mentioned above allow the determination of a two-dimensional or three-dimensional flow field downstream of the rotor. The latter also include information about the pressure and loss distribution in the measuring plane.

In the present study, the measuring technique of Shreeve et al. (1978) and Shreeve and Neuhoﬀ (1984) was adopted and modified to the features of low-speed turbomachines. Best of all it fulfills the abovementioned requirements. One major advantage of this technique can be seen in the way in which the miniature transducers are used. In order to achieve the smallest possible probe size the transducer geometry itself is used as the probe head geometry. Only about one third of the transducer's length is inserted into a mounting on the shaft. Thus, one can make use of the full frequency response of the bare transducer. Two separate probes of this kind are arranged to simulate a conventional three-dimensional pneumatic flow probe. This arrangement provides the smallest possible probe geometries, in particular when compared to probes that incorporate several transducers. The measuring technique also allows the determination of the periodic three-dimensional velocity and pressure field in rotor coordinates.

2 Test Setup and Measuring Technique

The test rig used for these experiments is shown in Fig. 1. It consists of an inlet nozzle, plenum chamber with screens, second nozzle, test compressor, and throttle. After passing the throttle, the flow enters a suction fan. This is necessary for adjusting the pressure losses, which are mainly caused by the deflection in the plenum chamber. The single stage has a constant-speed rotor (4500 rpm) of free vortex design. Table 1

Table 1 Design data of the test rotor

Flow coefficient ϕ_D	0.45	$\phi = c_1/u_{o.d.}$							
Pressure rise coefficient ψ_D	0.60	$\psi = \frac{2 \Delta p_{s3-1}}{\rho u_{o.d.}^2}$							
Outer diameter	400 mm								
Blade height	90 mm								
Chord length	60 mm								
Number of blades	16								
Hub-tip ratio	0.55								
Rotational speed	75/s								
Axial distance rotor-stator	120 mm								
Design diffusion numbers:	$D = \left[1 - \frac{w_2}{w_1} \right] + \frac{1}{2} \frac{\Delta w_t}{w_1}$								
h (%)	5	15	30	40	50	60	70	85	95
D (-)	0.706	0.702	0.675	0.651	0.625	0.600	0.575	0.551	0.548

summarizes the main geometric and design parameters of the tested rotor. Figure 2 contains a schematic sketch of the test section and the arrangement of the probes. This arrangement consists basically of two probes, A and B, which are positioned on the same radius and are located 45 deg apart. The peripheral distance of the probes corresponds to an even number of angular positions at which measurements are taken (0.9 deg each, in rotor coordinates). Thus, it is ensured that successive meas-

Nomenclature

C_{ij}, D_{ij} = calibration coefficients
 $c_{1,2,3}$ = absolute velocity, m/s
 c_p = pressure coefficient
 D = diffusion factor
 h = percentage of blade height
 d_{r-s} = axial distance rotor-stator
 p = pressure, Pa
 q = dynamic pressure, Pa
 U_0 = output voltage of transducers, V
 u = circumferential velocity, m/s

$w_{1,2,3}$ = relative velocity, m/s
 α = absolute flow angle, deg
 γ = pitch angle, deg
 δ, ϵ = calibration coefficients
 ζ_L = loss coefficient (total pressure loss/inlet dynamic pressure)
 σ = blade solidity
 ϕ = flow coefficient
 ψ = pressure rise coefficient

Subscripts

A, B = probe A, probe B
 D = design
 $geom$ = geometric
 m = meridian
 max = maximum value
 $o.d.$ = outer diameter
 ref = reference
 s = static
 t = tangential

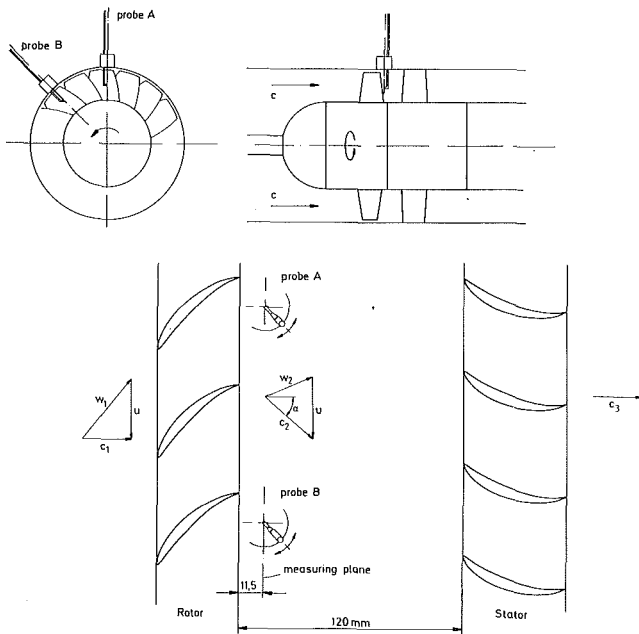


Fig. 2 Experimental setup and arrangement of probes in the test section

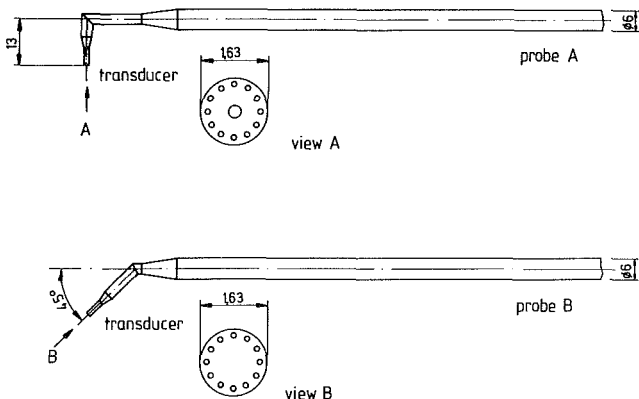


Fig. 3 Used probe types A and B

Measurements can be taken with the separate probes at the same position relative to one blade. As Table 1 shows, the axial distance between rotor and stator at midspan is 120 mm, or two times the blade chord length. Since both probes A and B are located close to the rotor, this distance is sufficiently large so that the stator position relative to the probes does not affect the pressure readings. This was proved by reading the probe pressures after adjusting the stator row in different circumferential positions. The probes are eccentrically mounted in plugs with the probe tips on the axis of rotation, i.e., the axis of the plug. Both probes A and B (Fig. 3) incorporate Kulite XCS-062-5d transducers, which are inserted into the probe body up to one third of their length. The head of probe B is inclined by 45 deg relative to the shaft axis, which results in a high sensitivity to changes in the flow angle. If the separated probes were assembled as a single probe, it would look like a conventional multisensor steady flow probe. In the two-probe arrangement, the lateral sensors of the multisensor probe, which enable one to read the flow angle by balancing the pressures, are simulated by turning probe A about its axis.

The scheme of the data acquisition system is illustrated in Fig. 4. The signals from the pressure transducers pass through a d-c amplifier and (via simultaneous sample and hold and a 12 bit analog-to-digital converter) are initially stored in a 512 kbyte digital data memory. The data of the digital memory

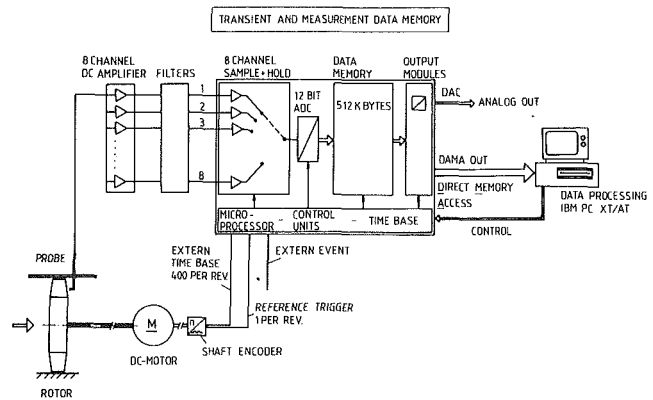


Fig. 4 Scheme of the data acquisition system

are then transferred to the disk of the PC. The data recording is triggered by shaft encoder pulses, which are used in the data memory as an external time base. For the measurements presented here, 400 pulses per revolution were used, corresponding to an interval of 0.9 deg in rotor coordinates or to 25 samples per blade passage. The use of an additional reference pulse ensures a clear relation between recorded data and the rotor position. Since the probes A and B are located 45 deg apart (which is equivalent to 50 pulses from the shaft encoder) the simultaneously recorded data of both probes are shifted by 50 counts, relative to one rotor blade. At the data reduction the data strings of both probes are then reshifted. This procedure leads to sets of data that are taken at different positions in machine coordinates but at the same geometric position in rotor coordinates. The blade passing frequency of the rotor investigated as given by the number of blades and rotational speed is approximately 1.2 kHz. The data sampling rate is 30 kHz, allowing the detection of frequencies up to 15 kHz, which was considered to be sufficient. The frequency range for the transducers as tested by the manufacturer is up to 20 kHz.

For measuring the flow field behind the rotor, probes A and B are first traversed to the same radial position. Then both probes are adjusted at identical positions relative to the average flow angle (see Fig. 2; eight positions in intervals of 20 deg). At each angular position the unsteady probe pressures are recorded over approximately 40 rotor rotations. This procedure is repeated for every radius chosen. The average flow angle has either been taken from the rotor design calculation or from measurements with a conventional probe. Before and after each test run the transducer's characteristics were checked for offset and slope, and were stored together with the probe data. Since the temperature rise produced by the rotor is only about 3 K and the transducers used did not show a change in sensitivity with temperature (which is described in the next section), this enables an easy evaluation of the probe data.

At the data reduction the stored probe data are first phase lock averaged over 30 rotor rotations. Preliminary tests indicated that this number of rotations for averaging the data was sufficient for the tests presented here. A higher number did not significantly change the results. For each probe this procedure leads to eight average pressure curves over 400 angular positions on one radius. An example is shown in Fig. 5 where the data of probes A and B are already reshifted as mentioned above. For one angular position in the flow field, data from Fig. 5 are taken and plotted over the probe angle in Fig. 6. Fourth-order polynomials are fitted to the probe data where the maximum of the polynomials projected at the abscissa correspond to the local flow angles. In Fig. 7 results from Fig. 5 are shown that are recorded from one probe over two blade passages and are presented in the same way as in Fig. 6. The reference pressure p_{ref} is either the atmospheric pressure or another, known constant pressure on the reverse

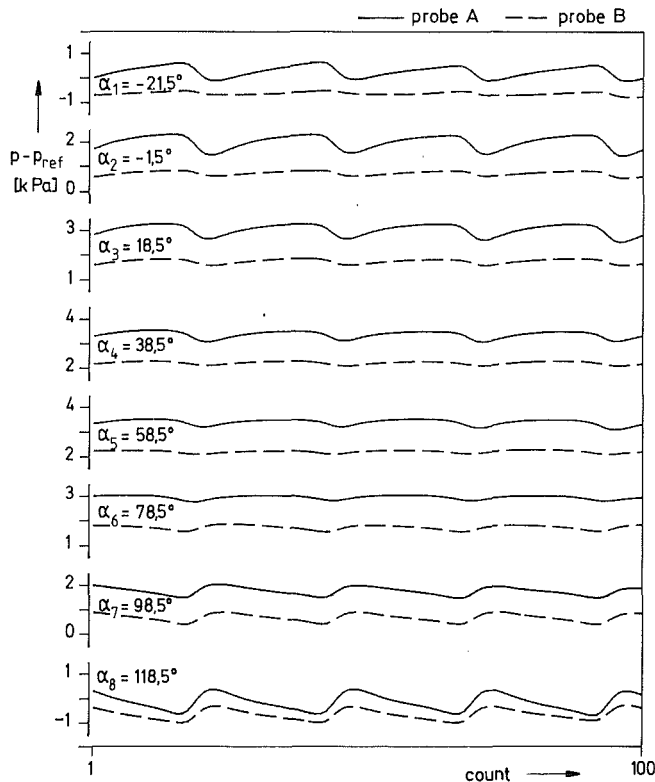


Fig. 5 Ensemble average pressures measured at eight probe angle settings over four blade passages

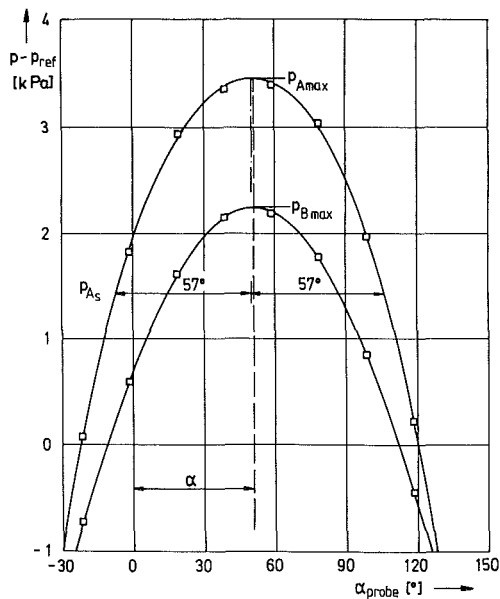


Fig. 6 Average pressure readings from probe A and B over probe angle (chosen from Fig. 5 for a single point in the flow field)

of the transducer, whereby p_{ref} was brought up through the hollow probe shaft. An adjustment of the reference pressure is necessary in cases where the dynamic head is on the same level as the pressure loss on the flow through the test rig. Thus it is ensured that the transducers always operate in the positive pressure range.

3 Data Reduction and Probe Feature

In order to obtain the local velocities and loss coefficients from the measured pressures, the probes were calibrated like a common multisensor pneumatic flow probe. The probe cal-

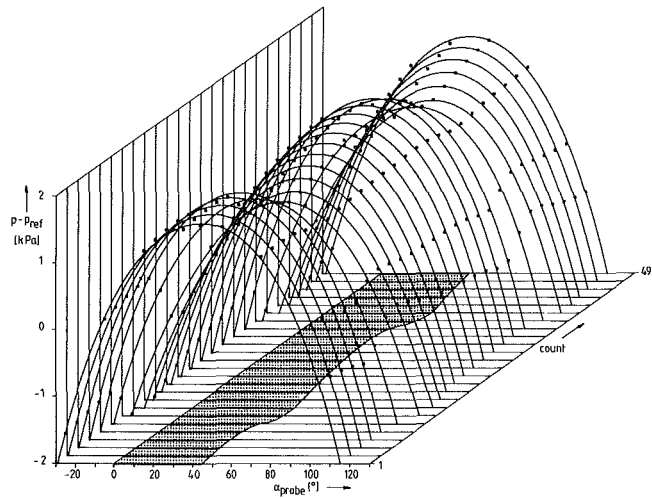


Fig. 7 Ensemble average pressures (probe A) of eight probe angle settings fitted by a fourth-order polynomial

ibration was carried out in a uniform, steady free jet of 250 mm diameter produced by a calibrated wind tunnel. During the probe calibration the reference pressure tubes of the transducers were connected to the ambient pressure. Before the calibration, every transducer used was checked to ensure there was no change in sensitivity with temperature. At several dynamic pressures, i.e., free jet velocities, the probe voltages were measured depending on the flow angle α and pitch angle γ (probe A and B have been calibrated separately). Results are shown in Figs. 8 and 9. Within the range $\alpha = \pm 15$ deg, probe A is quite insensitive to changes in flow direction; at high flow angles the pressure measured at the probe tip drops. At $\alpha_s = 57.0$ deg, the probe pressure is equal to the static pressure. This value for α_s largely depends on the probe tip geometry, as a large number of preliminary tests with various probe tip geometries showed. As a result of these tests, the value $\alpha_s = 57.0$ deg was achieved by rounding the otherwise sharp cylindrical edge at the transducer tip. Additionally, within certain limits, there is a slight dependency of α_s as on the pitch angle. As mentioned before, the geometric angle of probe B, $\gamma_{geom} = 45$ deg, was chosen to maximize the sensitivity to changes in pitch angle. The calibration results of probe B (Fig. 9) reflect this aim. In general, the probe tips should be as symmetric as possible in order to obtain symmetric pressure curves over the flow angle. The preliminary tests with different tip geometries showed that the probes, i.e., the pressure transducers, are very sensitive to manufacturing tolerances concerning the tip geometry and the precision of the hole arrangement in the protection screens.

For use of the calibration data, the probe outputs from Figs. 8 and 9 are approximated by fourth-order polynomials. By use of these polynomials maximum probe pressures p_{Amax} and p_{Bmax} as well as the static pressure (p_{As} at α_s , which is nearly identical with the reference pressure during the calibration) can be calculated. For probe B the maximum values of the polynomials are identical with the maximum pressures measured, whereas these values differ in the case of probe A. As can be seen in Fig. 8, the calibration curves of probe A exhibit flat-topped characteristics in the range $\alpha = \pm 15$ deg, caused by the flow around the probe tip and by the arrangement of the holes in the protection screen. Therefore, an additional evaluation of the calibration data is needed for probe A, which accounts for the difference between the pressures calculated with the polynomials and the real stagnation pressure. For this purpose, the pressure coefficient c_{pAmax} is used:

$$c_{pAmax} = f(\gamma) = \frac{p_{Amax} - p_s}{q} \quad (1)$$

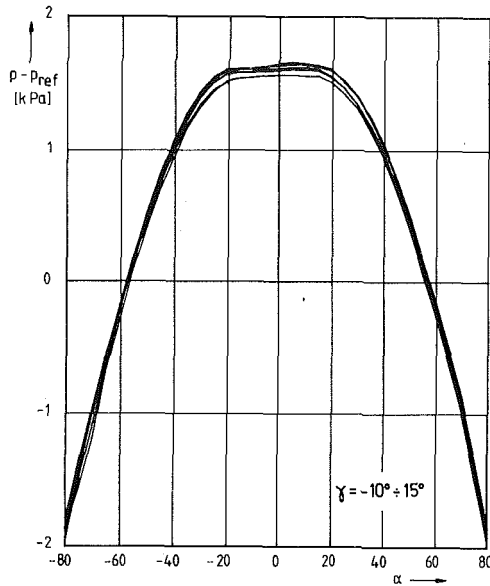


Fig. 8 Calibration data of probe A at dynamic pressure $q = 2$ kPa and six pitch angles γ

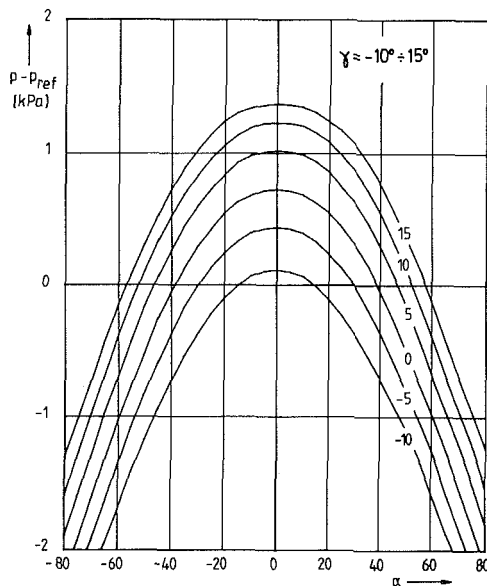


Fig. 9 Calibration data of probe B at dynamic pressure $q = 2$ kPa and six pitch angles γ

which reflects the influence of pitch angle γ on $p_{A \max}$. For different probe tip geometries, an extension of Eq. (1) could be necessary ($c_{p_{A \max}} = f(\gamma, q)$). In order to check how far the use of a polynomial approximation and its maximum value is meaningful to determine the probe pressures, several sets of probe pressures were taken. Each of them consisted of eight values measured at intervals of 20 deg during the calibration (corresponding to the procedure during the machine measurements; compare with Fig. 6). For all sets the average value of the chosen angles were different from zero, which results in an asymmetric distribution of the data $p(\alpha)$ around the flow angle. The offset between the real flow angle (zero at calibration) and the average angle of the data sets corresponded to the changes in absolute flow direction as found to be typical in the investigated rotor flow. With these data the maximum of their polynomials, i.e., $p_{A \max}$ and $p_{B \max}$, were calculated and compared with each other. This check resulted in an average deviation for $p_{A \max}$ and $p_{B \max}$ of about 0.4 percent, which is considered to be small enough.

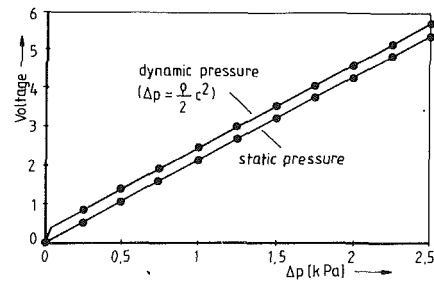


Fig. 10 Influence of transducer cooling on transducer characteristics

For the evaluation of the probe pressures measured in the rotor downstream polynomials versus the flow angle were again fitted to the data. An example is shown in Fig. 6. As mentioned before, the reference pressure here is different from the one applied during the calibration. The complete three-dimensional evaluation of the probe data was carried out with the pressures $p_{A \max}$, $p_{A s}$, and $p_{B \max}$ using the calibrating data of the probe A/probe B arrangement, which are described by the following equations:

$$\gamma = f(q, \epsilon) = \sum_{i=1}^m \left(\sum_{j=1}^n C_{ij} q^{(j-1)} \right) \epsilon^{(i-1)} \quad (2)$$

and

$$q = f(\delta, \gamma) = \sum_{i=1}^m \left(\sum_{j=1}^n D_{ij} \gamma^{(j-1)} \right) \delta^{(i-1)} \quad (3)$$

with the coefficients

$$\epsilon = \frac{p_{A \max} - p_{B \max}}{p_{A \max} - p_{A s}} \quad (4)$$

and

$$\delta = p_{A \max} - p_{A s} \quad (5)$$

By calculating the maximum of the polynomial of probe B, the local flow angle α is determined (probe B enables a better determination of the existing flow angle than probe A). However, depending on the probe (transducer) tip geometry again, an additional influence $\alpha = f(\gamma, q)$ may need to be taken into account. Using the above relations, velocities and pressures in the rotor downstream are calculated from the measured probe pressures: (i) In the first step the dynamic pressure, q , is assumed to be $p_{A \max} - p_{A s}$ from the probe A curve, with the static pressure $p_{A s}$ read at $\alpha = \pm 57$ deg. The real static pressure is nearly equivalent to $p_{A s}$, but in detail also depends on pitch angle, γ ; (ii) next, the pitch angle, γ , is obtained from the probe pressures, using Eqs. (2)–(5); (iii) since Eqs. (2) and (3) are nonlinear an iteration is necessary for obtaining q and γ ; (iv) the static pressure is determined with γ , using the calibrated pressure coefficient $c_{p_{A \max}}$ in Eq. (1). Following this procedure only a few iteration steps are necessary for the reduction of the measured probe pressures.

A peculiarity of the use of transducers as probe tips is that the pressure-sensitive diaphragm, which in still air is heated by the supply of the transducer bridge circuit, is cooled by the air flow. A light wind is sufficient to alter the heat transfer characteristics from free convection to forced cooling. This causes an imbalance in the Wheatstone Bridge, which the temperature compensation module naturally cannot compensate. That this effect is a constant value is shown in Fig. 10, where the amplified probe output voltage is drawn over the pressure difference at the transducer. The lower curve shows the probe output at a static pressure difference, whereas the upper curve shows the output at an equivalent dynamic pressure, which is offset due to the cooling effect. At this point, it should be noted again that the influence of the stagnation temperature

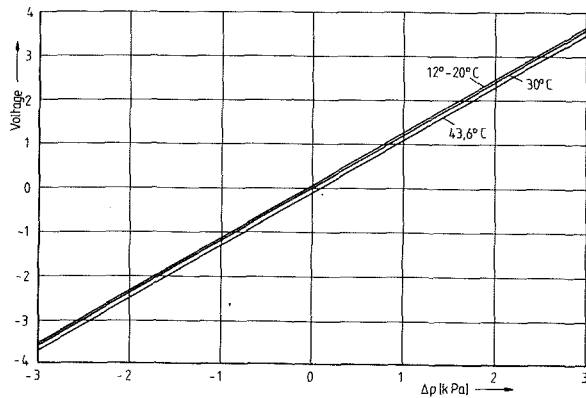


Fig. 11 Influence of temperature on transducer characteristics

is negligible at low flow velocities, as typical for low-speed turbomachinery. This allows a simple correction for the cooling effect during the on-line calibration of the transducers, which is carried out before and after the machine measurements. Figure 11 shows typical characteristics of a pressure transducer used in these experiments as a function of the environmental temperature. The characteristics are offset with increasing temperature, but without any change in linearity and slope. The good linearity around the zero point cannot always be expected but makes the application reported here much easier.

4 Test Results

The results discussed here were taken from investigations on an aerodynamically highly loaded axial-flow stage at design flow. As stated in the introduction, the blade loading is expressed by the diffusion number, D , with the two-dimensional boundary value for starting separation $D = 0.6$. The design data of the investigated rotor are shown in Table 1. The design diffusion factors show significantly higher values above this boundary, especially in the hub region. However, the stage characteristics in Fig. 12 still exhibit a range of stable operation toward lower flow rate. The experiments by Schroeder (1982), Schiller (1984), and Brodersen (1987) who investigated several highly loaded rotors (including the one of Table 1) revealed that, under certain circumstances, loading rates as high as shown in Table 1 might be acceptable (in order to minimize the machine size of single-stage machines). The loss coefficients of the rotor investigated, which were taken using a conventional five-hole probe, are shown in Fig. 13 for the machine running at design flow and lower flow rates. It can be clearly seen that the high hub loading causes high losses in the hub region. These are nearly on the same level as the losses in the tip region where in addition to the wall influence, the tip clearance also has an effect. However, for all flow rates the loss distributions exhibit a distinct peak at some distance from the hub. Very close to the hub the losses are again lower. This behavior is particularly interesting since the curves do not change the character at low flow rates, although even at design flow a much larger portion of the blade span is highly loaded. The loss peak only moves a little radially outward. In the investigations mentioned above, this qualitative loss distribution was determined also for other rotors depending on the aerodynamic blade loading. An explanation for this behavior is the occurrence of the so-called corner stall, which is well described by Lakshminarayana et al. (1986). The aim of the experiments reported here is to measure the local pressure loss distribution downstream of the rotor at design flow in order to detect the location and extent of the high loss region.

The velocity vectors at the extremely highly loaded hub region are shown for three blade passages in Fig. 14. It can be seen that the wakes are clear and occupy a large portion of

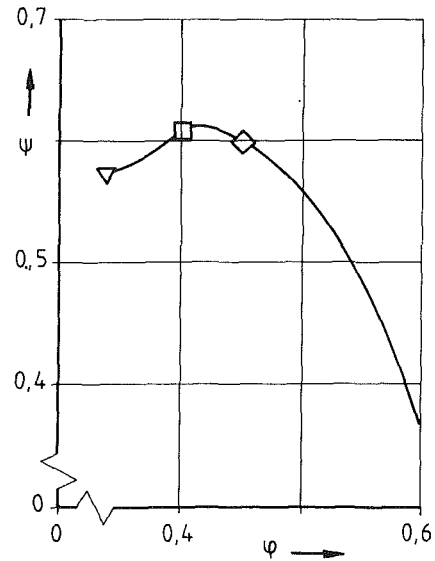


Fig. 12 Characteristics of investigated stage

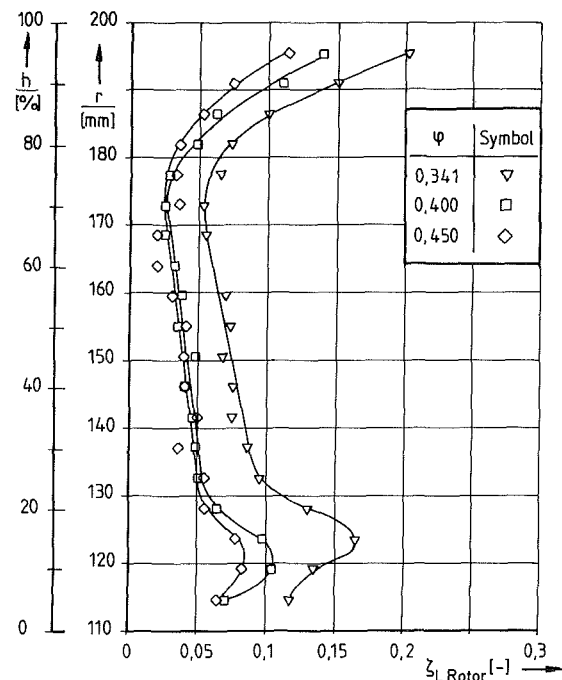


Fig. 13 Spanwise loss distribution of investigated rotor at design flow and two lower flow rates (see Fig. 12)

the blade-to-blade spacing. The distribution of the radial flow component in the rotating frame is shown in Fig. 15 for the flow behind two blade passages. Because the measurements were done in a plane perpendicular to the machine axis and because the rotor blades are twisted, only the blade trailing edge at the hub is axially projected into this figure in order to indicate the blade position. The plot shows a strong relative radial flow in the wake region, which was expected for the high loading condition. From this, it could further be expected that the transport of low-energy flow in the thick suction side boundary layer and subsequently the radial flow in the following wake would result in higher losses also at midspan (such secondary radial flow at the suction side trailing edge is well described by Dring et al., 1982). Beneath the outward flow, other secondary flows as a secondary vortex in the hub region can be detected. It can be assumed that a vortex developed in the hub wall/blade suction side area is the mechanism that

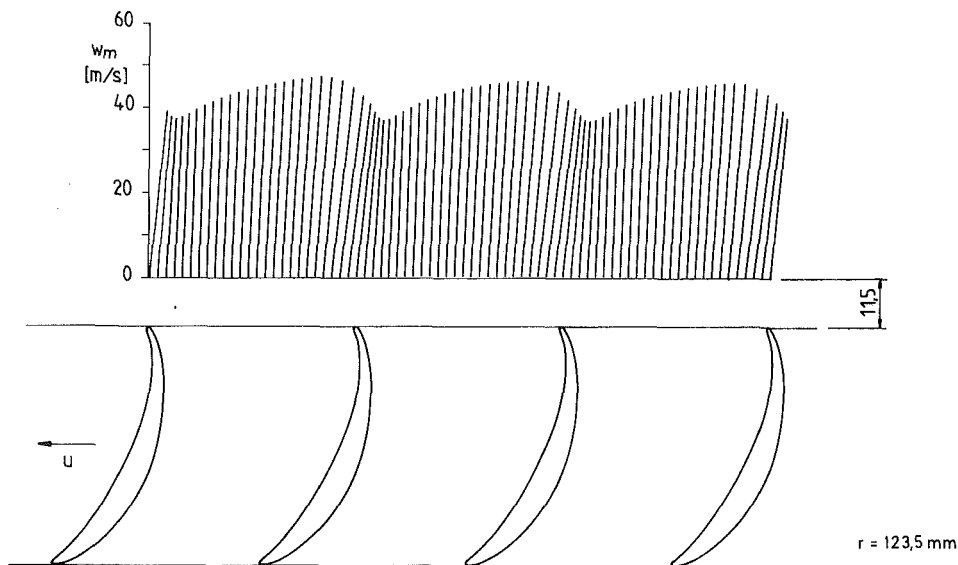


Fig. 14 Relative velocity downstream of the rotor at 15 percent of blade height

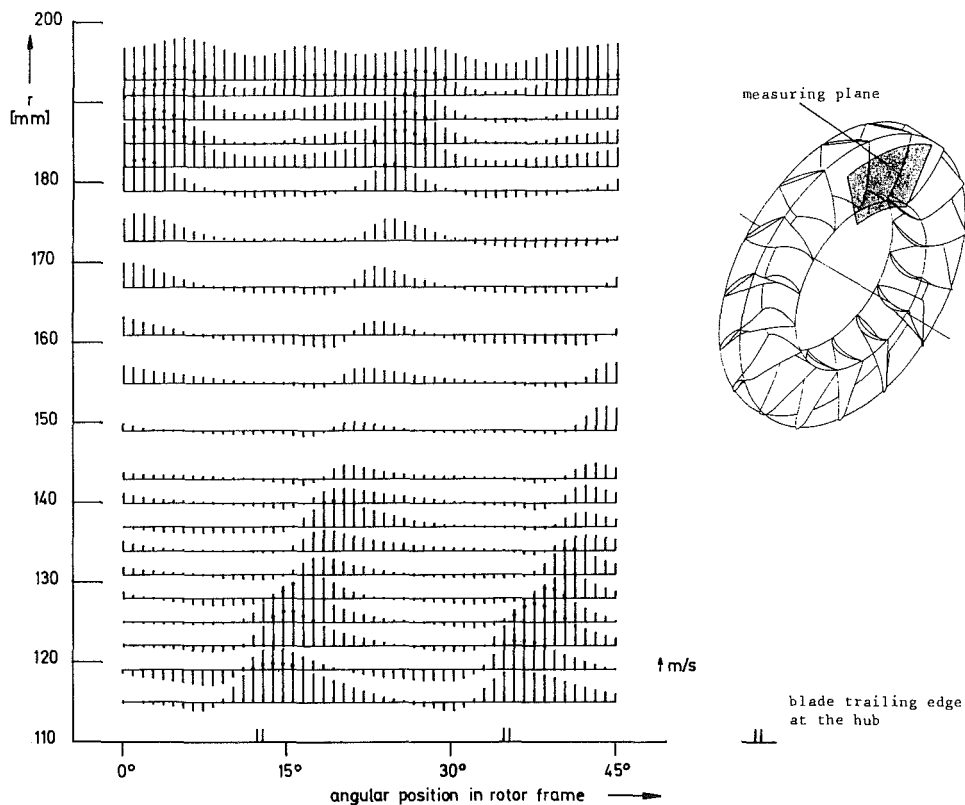


Fig. 15 Relative radial components over two blade passages

confines the high loss peak to the hub. The additional strong transport of low-energy flow radially outward could be considered as one reason why an extremely high loading of the hub region is possible without damaging the stage overall performance. The loss distribution over two blade passages in Fig. 16 clearly shows that single, confined loss peaks are present for each blade passage (as in Fig. 15, the axial projection of the blade trailing edge is indicated at the hub). Furthermore at midspan and higher radii, where the flow follows coaxial streamlines, the comparison with the results from Fig. 13 (solid line in Fig. 16) shows good agreement for the measured loss coefficients. However, very close to the tip clearance and in

the hub region, the values from probes A/B and from the conventional probe differ. Although the conventional probe was located approximately 10 mm farther downstream and therefore secondary, radial flows have to be taken into consideration (as shown in Fig. 15), this difference indicates the disadvantage of using steady pressure probes in fluctuating flows. At further increased loads, i.e., at lower flow rates, Fig. 13 shows that the region of high losses grows and moves a little radially outward. At these flow rates similar results, like the one shown in Fig. 16 for design flow, have been obtained (not shown here). Summarizing the results of the probe A/B measurements, it has been shown that an extremely high load-

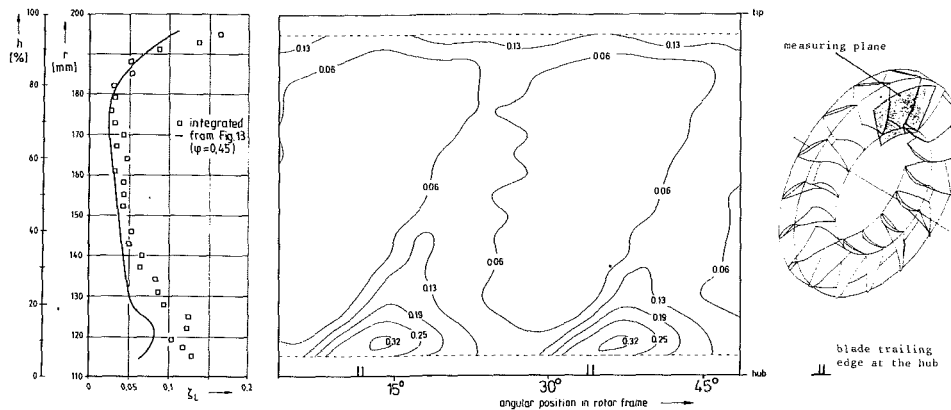


Fig. 16 Distribution of loss coefficients measured by means of probe A and B

ing of the hub region leads to a strong relative radial flow and a confined region of very high losses, where the latter is probably produced by secondary vortices. These mechanisms are considered to be typical for very high loading rates.

5 Summary

The results presented here were drawn from an investigation of the flow field downstream of a highly loaded axial flow stage, where the measurements were carried out at design flow rate. In order to obtain the local velocity and pressure distribution in rotor coordinates, a measuring technique was applied that is a modified version of a method developed by others for experiments in high-speed turbomachinery. This method simulates an unsteady multisensor pressure probe by the use of two separated high-frequency miniature pressure transducers. It uses the smallest possible probe tip geometries. It is shown that this measuring technique is also suitable for use in low-speed turbomachines with typically small pressure fluctuations in the rotor downstream. This was one major aim of the investigation. The modifications permit simplifications in the data reduction and some geometric changes of probe details. In addition, the experimental setup is simple and convenient. A comparison of the measuring data with conventional measurements showed good agreement. The measured velocity and pressure distributions show strong relative flows, whereby the loss distribution exhibits a confined pressure loss peak in the hub region.

References

Bammert, K., and Rautenberg, M., 1973, "Messung zeitlich veränderlicher Strömungsvorgänge im Radialverdichter," *VDI-Berichte 193*, p. 187.
 Brodersen, S., 1987, "Experimentelle Untersuchungen an hochbelasteten Axialventilatoren mit kleinem Nabenverhältnis," Dissertation TU Braunschweig, Federal Republic of Germany.
 Bubeck, H., and Wachter, J., 1987, "Development and Application of a High Frequency Wedge Probe," ASME Paper No. 87-GT-216.
 Castorph, D., and Lahm, G., 1980, "Untersuchung zur Nachlaufströmung einer Axialturbinenstufe," *VDI-Berichte 361*, p. 11.
 Das, D. K., and Jiang, H. K., 1984, "An Experimental Study of Rotating Stall in a Multistage Axial-Flow Compressor," *ASME Journal of Engineering for Gas Turbines and Power*, Vol. 106, pp. 542-551.
 Dring, R. P., Joslyn, H. D., and Hardin, L. W., 1982, "An Investigation of Axial Compressor Rotor Aerodynamics," *ASME Journal of Engineering for Power*, Vol. 97, p. 337.

Fiala, A., 1986, "Instationäre Druckmessungen in einem umlaufenden Radialrad," *Mitteilungen des Instituts für Dampf- und Gasturbinen*, No. 13, TU Wien, Austria.
 Gallus, H. E., Kummel, W., and Wallmann, Th., 1976, "Messungen zur Wechselwirkung von Laufrad- und Leitrad-Beschaufelungen in einer Axialverdichterstufe," *VDI-Berichte 264*, p. 103.
 Gallus, H. E., Lambertz, J., and Wallmann, Th., 1980, "Blade-Row Interaction in an Axial-Flow Subsonic Compressor Stage," *ASME Journal of Engineering for Power*, Vol. 102, p. 169.
 Gerich, R., 1974, "Untersuchungen über die instationäre Strömung in einer schnellläufigen Francis-Modell-Turbine mit besonderer Berücksichtigung des Teillastverhaltens," *Dissertation TU München*, Federal Republic of Germany.
 Heneka, A., 1983, "Entwicklung und Erprobung einer Keilsonde für instationäre dreidimensionale Strömungsmessungen in Turbomaschinen," *Dissertation Universität Stuttgart*, Federal Republic of Germany.
 Joslyn, H. D., Dring, R. P., and Sharma, O. P., 1983, "Unsteady Three-Dimensional Turbine Aerodynamics," *ASME Journal of Engineering for Power*, Vol. 105, p. 322.
 Kerrebrock, J. L., et al., 1974, "The MIT Blowdown Compressor Facility," *ASME Journal of Engineering for Power*, Vol. 96, p. 394.
 Kerrebrock, J. L., Epstein, A. H., and Thompkins, W. T., Jr., 1980, "A Miniature High Frequency Sphere Probe," in: B. Lakshminarayana and X. X. Runstadler, eds., *Measurement Methods in Rotating Components of Turbomachinery*, p. 91.
 Lakshminarayana, B., Sitaram, N., and Zhang, J., 1986, "End-Wall and Profile Losses in a Low-Speed Axial Flow Compressor Rotor," *ASME Journal of Engineering for Gas Turbines and Power*, Vol. 108, pp. 22-31.
 Larguier, R., 1981, "Experimental Analysis Methods for Unsteady Flows in Turbomachines," *ASME Journal of Engineering for Power*, Vol. 103, p. 415.
 Lieblein, S., 1965, "Experimental Flow in Two-Dimensional Cascades," in: *Aerodynamic Design of Axial-Flow Compressors*, NACA SP-36, Chap. IV, Washington, DC.
 Madhavan, S., and Wright, T., 1985, "Rotating Stall Caused by Pressure Surface Flow Separation on Centrifugal Fan Blades," *ASME Journal of Engineering for Gas Turbines and Power*, Vol. 107, p. 775.
 Matsunaga, S., Ishibashi, H., and Nishi, M., 1978, "Accurate Measurement of Nonsteady Three-Dimensional Incompressible Flow by Means of a Combined Five-Hole Probe," in: *Nonsteady Fluid Dynamics*, ASME, pp. 65-72.
 Schiller, F., 1984, "Theoretische und experimentelle Untersuchungen zur Bestimmung der Belastungsgrenze bei hochbelasteten Axialventilatoren," *Dissertation TU Braunschweig*, Federal Republic of Germany.
 Schroder, C., 1982, "Experimentelle Untersuchungen zur Auslegung hochbelasteter Axialventilatoren," *Dissertation TU Braunschweig*, Federal Republic of Germany.
 Shreeve, R. P., et al., 1978, "Determination of Transonic Compressor Flow Field by Synchronized Sampling of Stationary Fast Response Transducers," in: *Nonsteady Fluid Dynamics*, ASME, pp. 91-101.
 Shreeve, R. P., and Neuhoff, F., 1984, "Measurements of the Flow From a High-Speed Compressor Rotor Using a Dual Probe Digital Sampling (DPDS) Technique," *ASME Journal of Engineering for Gas Turbines and Power*, Vol. 106, pp. 366-375.
 Zierke, W. C., and Okishi, T. H., 1982, "Measurement and Analysis of Total-Pressure Unsteadiness Data From an Axial-Flow Compressor Stage," *ASME Journal of Engineering for Power*, Vol. 104, p. 479.

Influence of Periodically Unsteady Wake Flow on the Flow Separation in Blade Channels

G. H. Dibelius

E. Ahlers

Institute of Steam and Gas Turbines,
RWTH Aachen,
D-5100 Aachen, Federal Republic of
Germany

The influence of periodically unsteady perturbations on the turbulent flow along the suction side of turbine blades is investigated in a test rig. The blade suction side is represented by a flat plate 550 mm in length. The pressure profile typically encountered in a turbine blade channel is generated by a curved wall opposite to the flat plate. The angle of the divergent part of the test channel and hence the pressure can be increased to induce flow separation on the flat plate. For simulation of the wakes from the upstream blade row, the incoming flow is periodically disturbed by a wake generator consisting of five flat profiles arranged in front and parallel to the plate rotating with adjustable speed and phase angle. An LDV with high spatial resolution is used to measure averaged and fluctuating components of the velocity inside the boundary layer flow down to a distance of $y = 0.05$ mm from the plate surface, determining the boundary layer parameters as well as the wall shear stress. By Fourier analysis of the measured time-related velocity distributions, the stochastic and periodic parts of the overall turbulence are identified. With a periodic wake flow the separation is shifted downstream as compared to the steady flow situation. This is due to the energization of the boundary layer flow associated with the conversion of periodic in stochastic parts of the turbulence. Conclusions resulting from the experimental findings for the theoretical understanding of the flow turbine cascades are discussed in particular with respect to turbulence modeling.

Introduction

Gas turbine bladings are designed for high aerodynamic loads. Thus, there is a danger of flow separation on the suction side of the profiles. Flow separation is influenced by the turbulent unsteady flow conditions and the pressure gradients in the turbomachine. Calculation procedures used so far for the aerodynamic layout of turbine bladings do not consider the flow structure adequately. Therefore, more experimental data are needed for improving the calculation procedures, in particular with respect to turbulence modeling of the stochastic as well as the periodic and nonisotropic velocity fluctuations in turbomachinery.

The development of airfoil-type boundary layers with unsteady flow conditions has been investigated by many authors. A compilation of experimental work is given by Carr (1981). In most of the experiments the blade suction side is represented by a flat plate. Pressure gradients are generated by curved walls opposite the flat plate. Detailed information about the flow structure in a pressure-induced detachment zone under steady and unsteady flow conditions with an oscillating average velocity is given by Simpson et al. (1981, 1983). In a turbomachine, the flow perturbations from an upstream blade row move in the circumferential direction with only small changes

of average velocity. Thus, Doorly and his group (1988) simulate with their heat exchange experiments a moving blade row by a rotating disk with cylindrical bars mounted in the radial direction. Schulz et al. (1990) use a rotor with cylindrical rods for their studies of the three-dimensional flow field in the endwall region of an annular compressor cascade. Pfeil et al. (1983) use a rotating cylinder cascade for their investigations on the laminar-turbulent transition of periodically disturbed boundary layers. The influence of periodically unsteady wakes on the flow separation in blade channels has not been investigated systematically until now. Therefore, at the Institute of Steam and Gas Turbines experimental work on this subject is under way by simulating the cascade flow in a special test rig.

Test Apparatus

The measurements were made in a low-speed open-circuit wind tunnel. A sketch of the test section is shown in Fig. 1. The blade suction side is represented by a flat plate of $L = 550$ mm length. For ensuring defined starting conditions for the boundary layer flow on the flat plate, the flow near the wall is removed before the leading edge of the test plate. Laminar-turbulent transition is enforced by a trip edge at a streamwise location of $x/L = 0.05$. The pressure profile typically encountered in a turbine blade channel is generated by a curved wall opposite to the flat plate and is measured at 21 streamwise positions on the plate surface. The angle of the divergent part

Contributed by the International Gas Turbine Institute and presented at the 35th International Gas Turbine and Aeroengine Congress and Exposition, Brussels, Belgium, June 11-14, 1990. Manuscript received by the International Gas Turbine Institute January 15, 1990. Paper No. 90-GT-253.

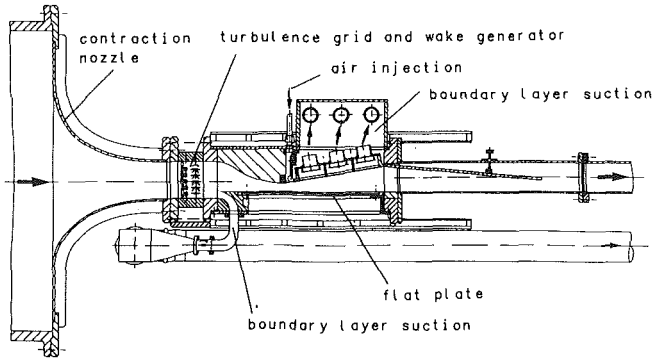


Fig. 1 Test section

of the test channel can be increased up to $\alpha_D = 10$ deg inducing flow separation on the flat plate. The oncoming boundary layer is partially removed by a highly two-dimensional suction system. To permit flow measurements with laser-Doppler-velocimetry (LDV), both side walls and a part of the flat plate are made of glass. The inviscid core flow at the entrance of the test section was found to be uniform and two dimensional.

In turbomachines the oncoming flow to a blade row is influenced by the wake flow of bladings located upstream. The ones from far upstream are equalized by mixing processes and cause an increase of stochastic turbulence in the flow. The wakes of the blade row rotating directly upstream super-impose periodic fluctuations of the local velocity and the flow angle. In order to simulate these conditions, a turbulence grid and a wake generator are installed in the entry cross section of the test rig upstream of the flat plate.

The turbulence grid consisting of cylindrical bars perpendicular to each other raises the turbulence level of the flow up to 6.5 percent.

Different methods are given in the literature for simulating the periodically unsteady wake flow of a blade row. The best results were obtained with test facilities where the flow unsteadiness was generated by rotating cylindrical bars (e.g., Doorly, 1988; Schulz et al., 1990; Pfeil et al., 1983).

However, avoiding interaction of up and downward moving spokes is difficult and requires much space. Therefore, a new type of wake generator consisting of five flat profiles rotating with adjustable speed was designed and built. Each profile causes a large wake with increased turbulence level in the upright position of highest drag (Fig. 2). Adjacent profiles coupled by a gear box are positioned with an angular deviation $\Delta\varphi$ to each other in order to keep the channel blockage constant while rotating. The wake shape is the same as encountered in turbomachines (Fig. 3). By turning the generator, the wake

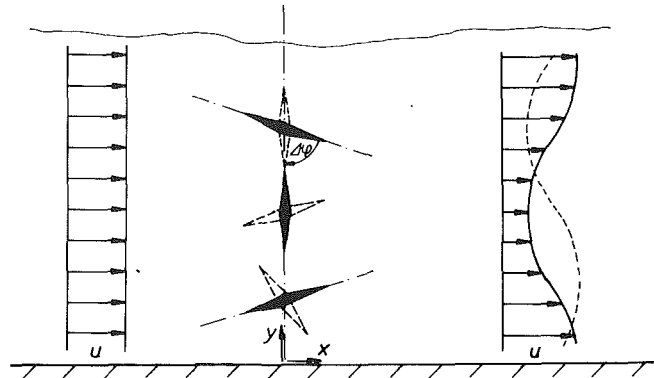


Fig. 2 Principle of the wake generator

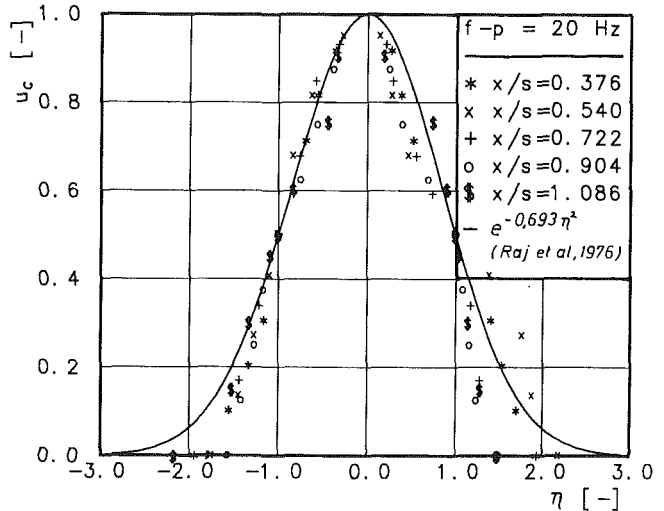


Fig. 3 Velocity distribution in the wake

changes its position (Fig. 4) and is transported downstream with the mean flow. In this way periodic flow perturbations up to frequencies of $f_p = 60$ Hz can be achieved. The angular position is determined by an angle decoder synchronized with the velocity measurements.

Figure 5 visualizes the decay of periodic flow perturbations with increasing axial distance from the wake generator. The results are compared to experimental data of other authors (e.g., Raj and Lakshminarayana, 1976; Reynolds and Lakshminarayana, 1979) and our own measurements in a test turbine. The axial distance in Fig. 5 is scaled with the blade chord length for the cascade measurements. In analogy, the distance from the wake generator is set in relation to the length L of

Nomenclature

c_f = skin friction coefficient = $\tau_w / (\rho/2 \cdot u_\delta^2)$
 c_p = pressure coefficient = $(p - p_1) / (\rho_1/2 \cdot u_1^2)$
 f = frequency
 H_{12} = shape factor = δ^*/Θ
 L = length of the flat plate
 p = pressure
 Re = Reynolds number
 s = blade chord length
 u = streamwise velocity component
 u_c = dimensionless velocity in the wake = $u_{\max} - u / u_{\max} - u_{\min}$

v = velocity component normal to the flat plate
 x = streamwise direction
 y = vertical direction
 α = angle
 $\Delta\varphi$ = deviation angle of the wake generator profiles
 δ = boundary layer thickness
 δ^* = boundary layer displacement thickness
 η = dimensionless coordinate in the velocity wake
 Θ = boundary layer momentum thickness
 ρ = density
 τ = shear stress

Subscripts

1 = entry cross section
 D = diffusor
 L = flat plate length
min = minimum
max = maximum
 p = periodic
 δ = boundary layer thickness
 Θ = boundary layer momentum thickness

Superscripts

(-) = time-averaged
(~) = periodical fluctuation
(') = stochastic fluctuation

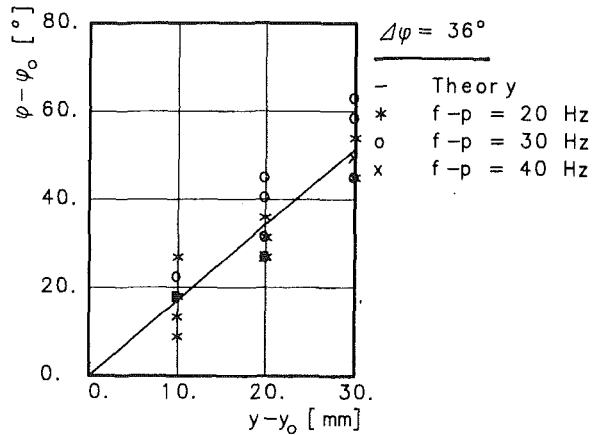


Fig. 4 Movement of the wake normal to the mean flow direction

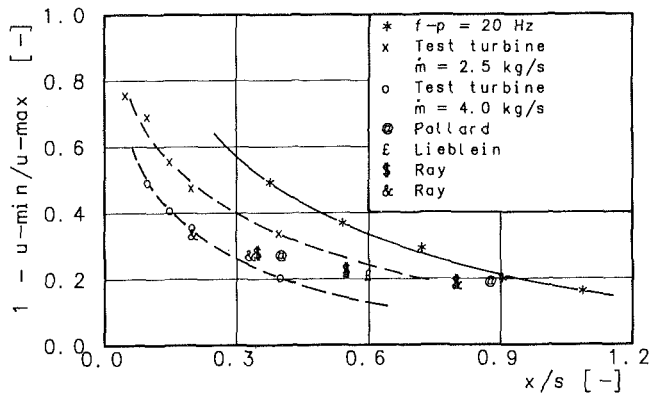


Fig. 5 Development of the velocity wake with increasing axial distance

the flat plate. The test results prove the ability of the wake generator to simulate the unsteady wake flow of a moving blade row.

Laser-Doppler-Velocimeter and Signal Processing

A one-velocity-component directionally sensitive fringe-type LDV system has been used to measure the streamwise velocity component u in the test rig. The optical setup of the LDV was modified at the Institute of Steam and Gas Turbines in order to allow velocity measurements in the boundary layer flow with high signal quality and spatial resolution. The system has been described in more detail by Minten (1988). The optical setup is shown schematically in Fig. 6. The sending and receiving optical systems are arranged perpendicular to each other. Thus, the received scattered light signal is not distorted by reflected portions of the incident laser light. In addition, a slot orifice in the receiving optical path reducing the measuring volume size to 0.1 mm in the vertical direction accounts for a high level of spatial resolution. Minten (1988) has shown that averaged and fluctuating components of the velocity inside the boundary layer can be measured as close to the plate surface as $y=0.05$ mm. Thus, the boundary layer parameters as well as the wall shear stress can be determined from the measured velocity profiles. The Doppler signals are evaluated by a counter-type LDV processor and transferred to a personal computer by a self-designed interface enabling cycle-resolved measurements with unsteady flow conditions as well as the accurate determination of the time between two measuring events. By Fourier analysis of the averaged time-related velocity distributions, the stochastic and periodic parts of the overall turbulence are identified.

The interpretation of LDV measurements in a highly turbulent flow has to make up for the velocity bias. By measuring

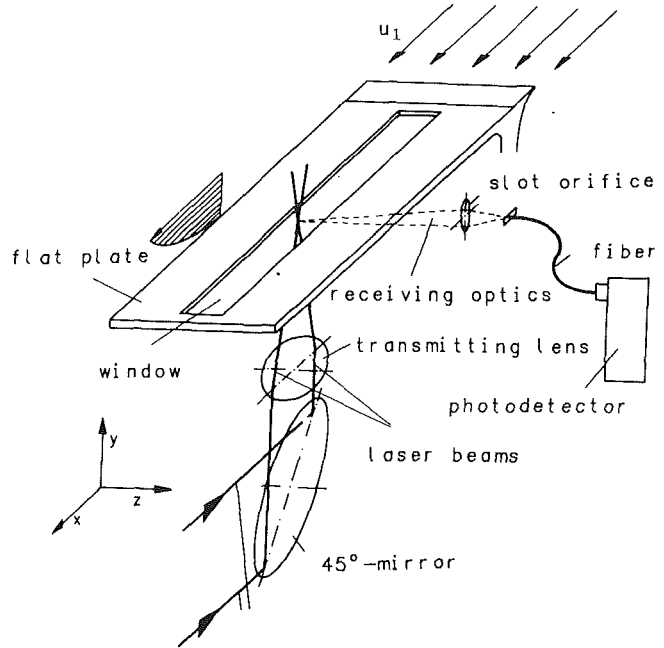


Fig. 6 LDV setup for boundary layer measurements

time intervals between two signal bursts, correct averages of mean velocity and velocity fluctuations can be achieved by numerical integration of the time-related velocity distribution. This method, described in detail by Minten (1988), has been used for the present investigation.

Before entering the wind tunnel plenum chamber, the test flow was seeded with monodisperse di-2-ethylhexyl-sebacate (DES) droplets with a particle size of about $1 \mu\text{m}$. Thus, data rates up to 2000 1/s in the core flow and 100 1/s in the near wall region were obtained.

The accuracy of the measurements presented depends essentially on the ability of the scattering particles to follow the flow fluctuations. Errors in signal processing and evaluation were estimated to be less than 0.5 percent. Errors due to velocity gradients in the flow are not significant for any data presented here because of the small measuring volume size. Therefore, the overall error of the presented results is less than 2 percent.

Results

In order to determine the influence of the unsteadiness on the flow detachment, velocity profiles were measured at different streamwise positions with steady and unsteady flow conditions at a diffuser angle of $\alpha_D = 10$ deg. The average flow velocity at the flat plate leading edge determined by measurement of the mass flow was $u_1 = 10$ m/s. The Reynolds number based on the length of the flat plate (equivalent to the chord of the blade) is $Re_L = 3.7 \times 10^5$. For reaching a Strouhal number similar to that in a gas turbine, a wake frequency of $f_p = 20$ Hz was chosen for the investigations with unsteady flow conditions.

The pressure profiles on the flat plate given in terms of

$$c_p = \frac{p - p_1}{\frac{\rho_1 \cdot u_1^2}{2}}$$

are shown in Fig. 7. For steady flow conditions the pressure in the diffuser increases strongly in the first part and only slightly in the second part. Under unsteady flow conditions the pressure recovery in the diffuser is more uniform, resulting from unseparated flow.

Tripping the boundary layer in a highly accelerating flow,

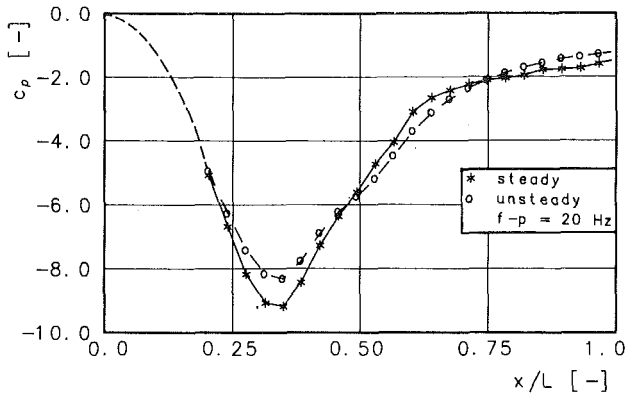


Fig. 7 Pressure along the flat plate

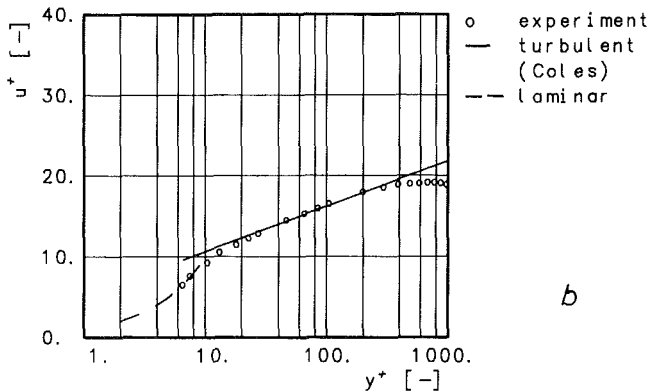
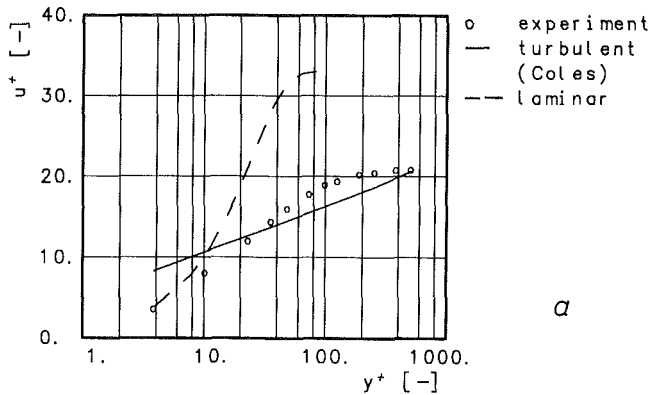


Fig. 8 Velocity distribution in the boundary layer at a streamwise location of $x/L = 0.349$; (a) steady flow; (b) unsteady flow

one has to take into account the possibility of relaminarization of the boundary layer. For the measuring results presented here, the trip edge led to a fully turbulent boundary layer over the whole length of the flat plate. This is shown in Fig. 8, where the boundary layer profiles at the minimum channel cross section are compared with the logarithmic law of the wall for both steady and unsteady flow conditions.

The mean velocity distributions measured in the boundary layer along the plate with LDV are shown in Figs. 9 and 10 at different streamwise locations. The development of the velocity distributions up to flow separation is typical for flows with an adverse pressure gradient. Under steady flow conditions the flow separation occurs at $x/L = 0.75$ (Fig. 9). At this position the velocity gradient at the wall and thus the wall shear stress τ_w are zero. Downstream of that location a backflow region is built up in the vicinity of the wall growing to 8 percent of the channel width at $x/L = 0.931$.

For the unsteady flow no separation can be found from the

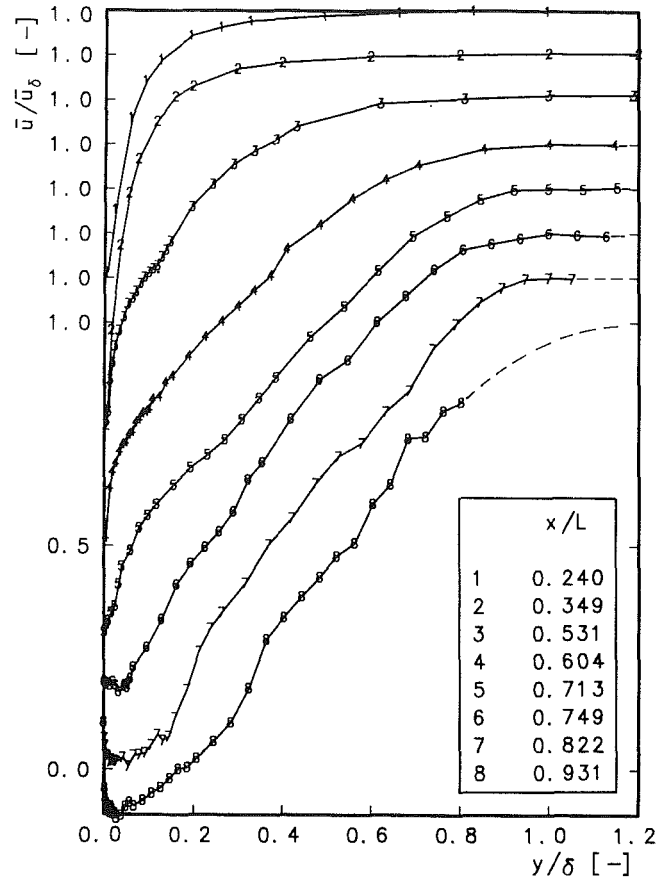


Fig. 9 Mean velocity distribution in the boundary layer for steady flow

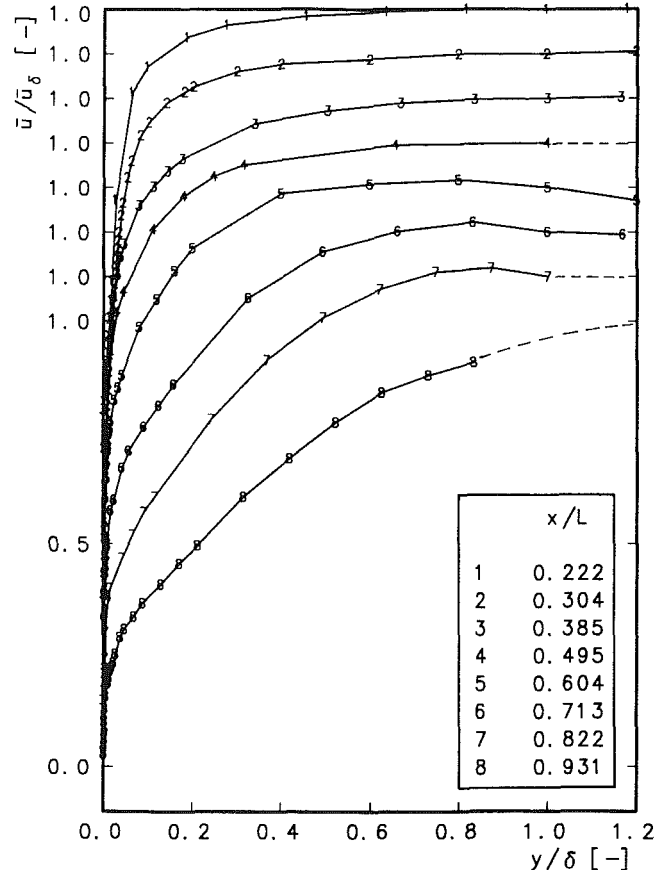


Fig. 10 Mean velocity distribution in the boundary layer for unsteady flow

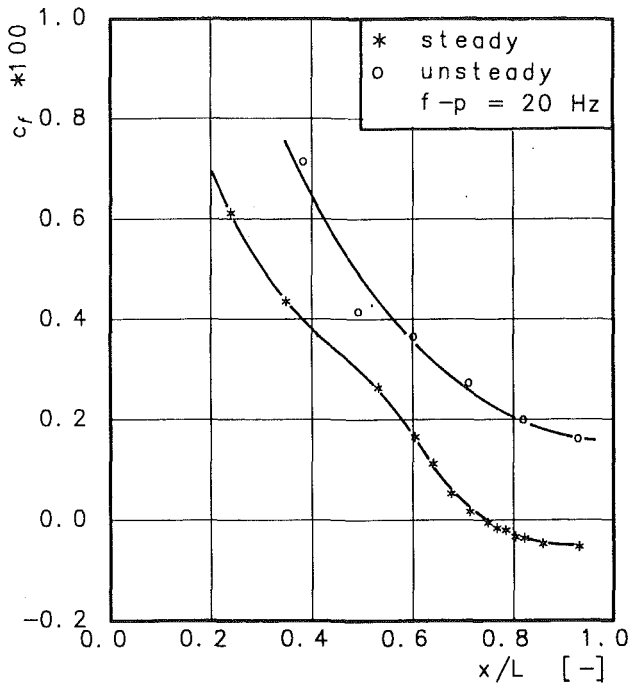


Fig. 11 Wall shear stress along the flat plate

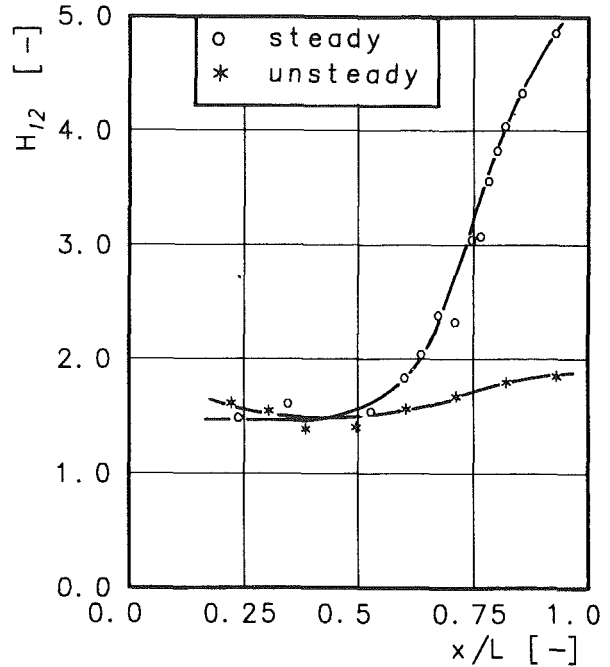


Fig. 13 Shape factor H_{12} along the flat plate

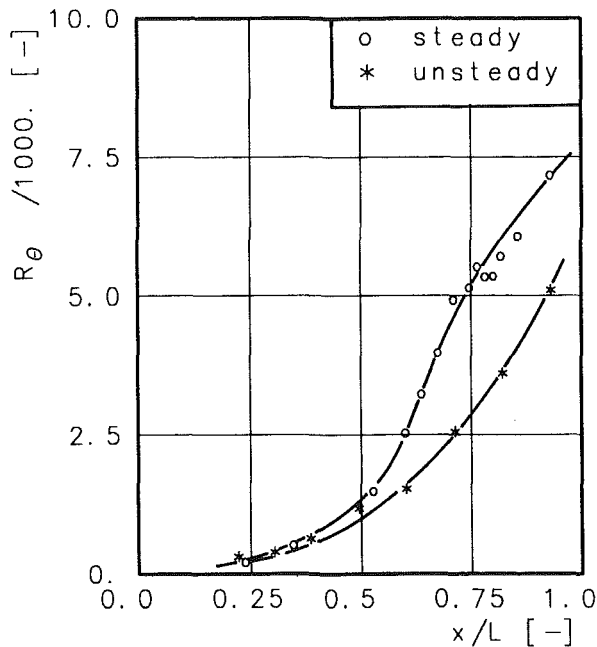


Fig. 12 Momentum thickness Reynolds number along the flat plate

velocity profiles at any streamwise location in the test rig. This fact becomes obvious also in Figs. 11-13, where the wall shear stress in terms of

$$c_f = \frac{\tau_w}{\frac{\rho}{2} \cdot u_0^2}$$

the momentum thickness Reynolds number Re_θ and the shape factor H_{12} are shown over the plate length. The onset of flow separation could only be identified by analyzing the fraction of time the flow was in the upstream direction.

The development of the boundary layer in the diffuser of the test section is influenced by the different pressure distributions for the same geometric setup under steady and un-

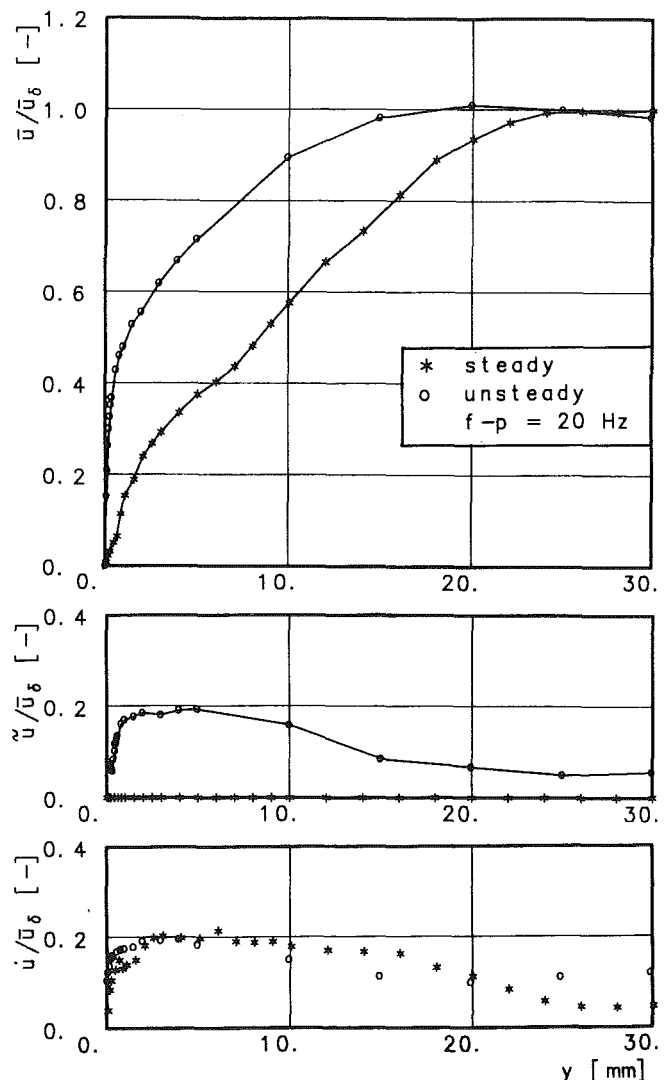


Fig. 14 Velocity distribution in the boundary layer at a streamwise location $x/L = 0.713$

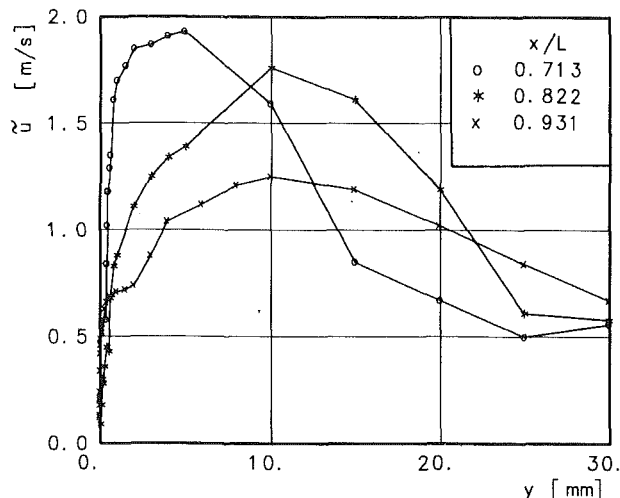


Fig. 15 Distribution of periodic velocity fluctuations in the boundary layer downstream of $x/L = 0.713$

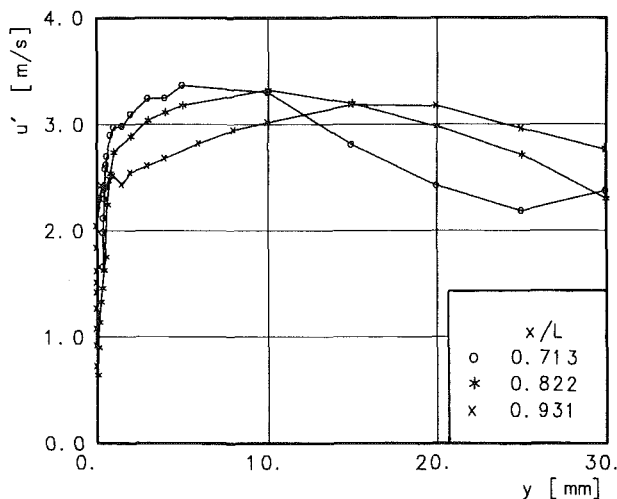


Fig. 16 Distribution of stochastic velocity fluctuations in the boundary layer downstream of $x/L = 0.713$

steady flow conditions (Fig. 7). The more uniform pressure shape in the case of unsteady flow is the result of periodic flow perturbations and causes a downshift of the separation zone. Otherwise the difference between the pressure distributions is small and such a significant effect on flow detachment as shown in Figs. 9–13 is unlikely. Another explanation for the displacement of separation zone can be derived from Fig. 14. The distributions of the mean velocity u , the stochastic turbulence u' , and the periodic fluctuations \bar{u} are compared for both steady and unsteady flow conditions at a streamwise location of $x/L = 0.713$, the periodic and stochastic parts of the overall turbulence being determined by Fourier analysis from the cycle resolved measurements (see the section “Laser-Doppler-Velocimeter and signal processing”). At this position upstream of the detachment zone the periodic perturbations have introduced much more kinetic energy into the boundary layer com-

pared to the steady flow case. However, the stochastic turbulence levels differ much less. The crosswise slope of the stochastic turbulence seems to make an energy transfer into the boundary layer more likely for the unsteady case. In addition, periodic fluctuations are still present in the boundary layer at this location. Farther down, they decay and are shifted more toward the core flow (Fig. 15). Correspondingly the maximum of the stochastic turbulence distribution is also moving farther into the core flow (Fig. 16). Due to this conversion process the boundary layer is energized and flow detachment is shifted to a location downstream of the last measuring position.

Conclusions

The periodically unsteady wake flow in a turbomachine causes a significant downshift of the separation zone on the blade suction side and thus has a stabilizing effect on the blade channel flow.

The downshift is linked to the energization of the boundary layer flow by turbulent mixing processes. The increased energy transport between the core flow and the boundary layer is associated with the conversion of periodic into stochastic parts of the velocity fluctuations.

The statistical turbulence models used so far for blade flow calculations in turbomachinery do not describe the local flow structure with periodic velocity fluctuations being converted into stochastic turbulence. Improved results are expected from modeling the Reynolds shear stresses and thus the energy exchange in the flow.

Results presented in this paper are based only on the measurements of the u component of velocity. To confirm the assumptions derived from these measurements and to create a solid data base for the proposed turbulence model, additional measurements of the v component in the flow should be realized.

References

- Carr, L. W., 1981, “A Compilation of Unsteady Turbulent Boundary Layer Data,” AGARD-AG 265.
- Doorly, D. J., 1988, “Modeling the Unsteady Flow in a Turbine Rotor Passage,” *ASME JOURNAL OF TURBOMACHINERY*, Vol. 110, pp. 27–37.
- Minten, G., 1988, “Die Anwendung des Laser-Doppler-Anemometers zur Bestimmung der Wandschubspannung und des Geschwindigkeitsfeldes in ablösenden Grenzschichten,” Dissertation, RWTH Aachen, FRG.
- Pfeil, H., Herbst, R., and Schröder, T., 1983, “Investigation of the Laminar-Turbulent-Transition of Boundary Layers Disturbed by Wakes,” *ASME Journal of Engineering for Power*, Vol. 105, pp. 130–137.
- Raj, R., and Lakshminarayana, B., 1976, “Three-Dimensional Characteristics of Turbulent Wakes Behind Rotors of Axial Turbomachinery,” *ASME Journal of Engineering for Power*, Vol. 98, pp. 218–227.
- Reynolds, B., Lakshminarayana, B., and Ravindarath, A., 1979, “Characteristics of the Near Wake of a Compressor of a Fan Rotor Blade,” *AIAA Journal*, Vol. 17, No. 9.
- Schulz, H. D., Gallus, H. E., and Lakshminarayana, B., 1990, “Three-Dimensional Separated Flow Field in the Endwall Region of an Annular Compressor Cascade in the Presence of Rotor-Stator Interaction: Part I—Quasi-Steady Flow Field and Comparison With Steady State Data; Part II—Unsteady Flow and Pressure Field,” *ASME JOURNAL OF TURBOMACHINERY*, Vol. 112, pp. 669–690.
- Simpson, R. L., et al., 1981, 1983, “The Structure of a Separating Turbulent Boundary Layer, Part 1: Mean Flow and Reynolds Stresses,” *J. Fluid Mech.*, Vol. 113; “Part 2: Higher Order Turbulence Results,” *J. Fluid Mech.*, Vol. 113; “Part 4: Effects of Periodic Free Stream Unsteadiness,” *J. Fluid Mech.*, Vol. 115; “Part 5: Frequency Effects on Periodic Unsteady Free-Stream Flows,” *J. Fluid Mech.*, Vol. 115.

On the Prediction of Unsteady Forces on Gas Turbine Blades: Part 1—Description of the Approach

T. Korakianitis

Assistant Professor of Mechanical
Engineering,
Washington University,
St. Louis, MO 63130

This article investigates the generation of unsteady forces on turbine blades due to potential-flow interaction and viscous-wake interaction from upstream blade rows. A computer program is used to calculate the unsteady forces on the rotor blades. Results are obtained by modeling the effects of the stator viscous wake and the stator potential-flow field on the rotor flow field. The results for one steady and one unsteady flow case are compared with known analytical and experimental data. The amplitudes for the two types of interaction are based on an analysis of available viscous wake data, on measurements of the potential-flow disturbance downstream of typical turbine stators, and on a parametric study of the effects of the amplitudes on the results of the unsteady forces generated on a typical turbine rotor cascade.

Introduction

Given a two-dimensional stator and rotor velocity diagram, one can proceed to design the shape of the two-dimensional cascade of the rotor with pitch S_{rb} and of the stator with pitch S_{sb} . There still remains the choice of the number of rotor blades to stator blades, which is equal to the stator-to-rotor-pitch ratio R . The effect of R on the stage geometry is shown in Fig. 1, where the geometry of the downstream rotor is kept constant, the nondimensional geometry of the upstream stator is identical, but R is varied by changing the value of S_{sb} . After the value of R is chosen, designers need an initial estimate of the forced response of the cascades.

Vibration problems are reduced to equations of the form:

$$[m] \frac{d^2\{X\}}{dt^2} + [C] \frac{d\{X\}}{dt} + [K]\{X\} = \{F(t)\} \quad (1)$$

The natural frequencies of the structure can be obtained by solving these equations with $\{F(t)\} = 0$. However, to solve for the forced response, displacements, and vibratory stresses, one must input a forcing function $\{F(t)\} \neq 0$. Similar arguments can be used for the energy approach (finite element methods). Thus designers need an initial estimate of the blade forces $F(t)$ during the preliminary stages of design, before the shape of the cascades has been decided upon. The need for a practical method to predict the unsteady forces on turbine blades in the early stages of design will remain, even when computer programs that can evaluate the unsteady-compressible-viscous-flow equations become widely available.

Background

A recent research program provided a design method for the prediction of the unsteady forces ($\{F(t)\}$) in Eq. (1) before any time was invested in designing the blade shapes in detail (Korakianitis, 1987). The disturbances on the downstream rotor flow field from the upstream stator viscous-wake and potential-flow interactions were modeled and a computer program was used to predict the flow field around the rotor cascades. The viscous wake is a result of the boundary layers of the stator cascades and is a velocity defect that extends downstream

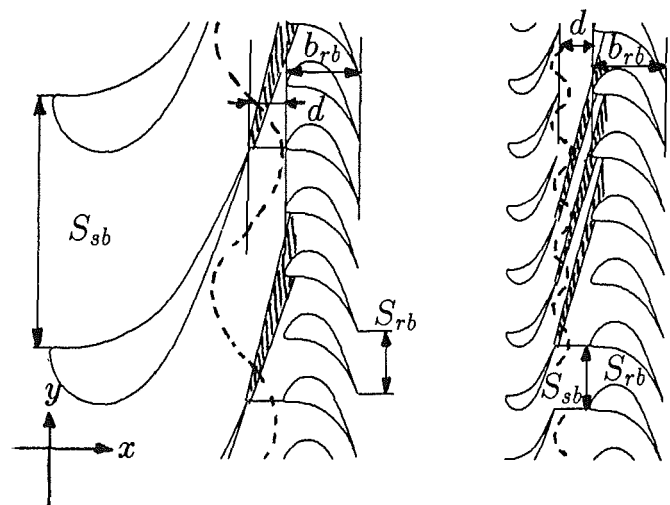


Fig. 1 The effect of R on the stage geometry; velocity diagrams and downstream rotors (flow from left to right) are identical: on the left $R = S_{sb}/S_{rb} = 4.0$; on the right $R = S_{sb}/S_{rb} = 1.0$

Contributed by the International Gas Turbine Institute for publication in the JOURNAL OF TURBOMACHINERY. Manuscript received at ASME Headquarters December 1990.

from the stator trailing edge (illustrated in the hatched regions of Fig. 1). The potential-flow field is a time-dependent pressure variation that exists in the spaces (blade passages and in the axial gap) around the two moving cascades, which affects the local flow conditions both upstream and downstream. The effect of the stator potential-flow field on the rotor potential-flow field is illustrated in Fig. 1 as a dashed line in the region of the stator trailing edges. As shown in Fig. 1 the value of R affects the size of the wake with respect to the rotor, and it also affects the frequency and decay rate of the potential-flow effect.

This article presents the models for the rotor-inlet boundary, compares computations with results of analytical and experimental data, and investigates the effect of the amplitudes of the disturbances based on experimental and computational data. The effects of R and the stator-to-rotor axial gap d are investigated in Part 2 (Korakianitis, 1992).

Computer Program

In recent years many algorithms have been implemented in solving the unsteady compressible inviscid equations for steady flow (time-marching to convergence), and a few in solving the unsteady compressible viscous and inviscid equations. For this study a program that could model the unsteady flow was required. Such programs have been developed by Erdos and Alzner (1977), Krammer (1982), Koya and Kotake (1985), Rai (1985), Fourmaux (1986), and Giles (1987). In addition Scott and Hankey (1986) modified the program developed by Shang (1983); and Mitchell (1980) and Hodson (1983, 1985a) modified Denton's (1975) program to solve for unsteady flows.

Giles' (1987) computer program UNSFLO (which models the two-dimensional, unsteady, compressible, inviscid flow around rotor blades) was used to compute the flow field and the forces for ranges of R and α_N . This program was chosen because it can handle arbitrary values of R with reasonable CPU and storage requirements due to a novel "tilting" of the time domain. In the computational field the problem was simplified by considering the rotor blade in the rotor-relative frame. The wake and the potential-flow interaction were modeled at the computational rotor-inlet boundary moving at the relative speed.

The accuracy of the computations was ensured by comparing the results of calculations using UNSFLO with the results of four steady and unsteady-flow cases of known theoretical or experimental output (originally published in more detail in Korakianitis, 1987, 1988, and Giles, 1987). Two of those cases are outlined here.

For steady flows we include a comparison of computed results with the closed-form analytic solution for the incompressible potential flow past Gostelow's (1984) compressor cascade. The theoretical solution was obtained by a conformal-transformation method. The numerical solution used a 400×100 grid extending 0.75 axial chords upstream of the leading edge and 0.50 axial chords downstream of the trailing edge. The flow conditions were $M_i = 0.200$, $M_o = 0.135$, $\alpha_i = 53.5$ deg, and $\alpha_o = 30.0$ deg. Figure 2 shows the calculated and theoretical incompressible pressure-rise coefficient. The two solutions are in excellent agreement.

For unsteady flows we include a comparison of computed results with the experimental data obtained with laser two-

Nomenclature

A = amplitude of a harmonic (Eq. (18))	ST = sawtooth function (Eq. (4))	θ = phase of a harmonic (Eq. (18))
B = amplitude of potential variation (Eq. (7))	T_z = moment (in the z direction) (Eq. (17))	ξ = parameter for the x decay of Φ (Eqs. (7), (9))
b = axial chord	t = time	ρ = relative total density at rotor inlet
C = damping matrix (Eq. (1))	u = velocity component in the x direction	Φ = velocity potential defined by Eq. (6)
C_L = tangential loading (lift) coefficient	V = velocity	ω = rotor passing frequency (Eq. (16))
c = rotor-inlet total sonic velocity (Eq. (17))	V_{ip} = velocity perturbation due to potential, fraction of c (Eq. (14))	$\tilde{\omega}$ = reduced frequency parameter (Eq. (16))
D = wake amplitude, fraction of c_N (Eq. (2))	v = velocity component in the y direction	
d = stator-rotor axial gap (fraction of b_{rb})	W = characteristic width of the wake, expressed as fraction of S_{sb} (Eq. (2))	
F = dimensional force (Eq. (17))	$\{X\}$ = displacement vector (Eq. (1))	Subscripts
F' = nondimensional force (Eq. (17))	(x, y, z) = Cartesian coordinates (in subscripts also)	$n \in \{0, 1, 2, \dots\}$ = order of a harmonic
$j \equiv \sqrt{-1}$ (Eq. (18))	α = flow angle	i, o = cascade inlet, outlet, respectively
K = stiffness matrix (Eq. (1))	$\Delta\epsilon, \epsilon$ = angles locating the potential (Eqs. (14), (15))	ip = property for potential-flow model
M = Mach number	δ = perturbation operator (on u and v)	iw = flow property in the wake
m = mass matrix (Eq. (1))	ζ = parameter for the y period of Φ (Eqs. (7), (10))	N = stator exit (nozzle)
\Re = real part of an expression (in Eq. (18))	η = parameter for the wake location (Eq. (3))	nd = nondimensional (Eq. (19))
$R \equiv S_{sb}/S_{rb}$ = stator-to-rotor-pitch ratio		np = parameter, equal to 1 or 10 (Eq. (19))
S = pitch of a cascade		p = pressure side
		rb = rotor blade row
		s = suction side
		sb = stator blade row
		ss = steady flow

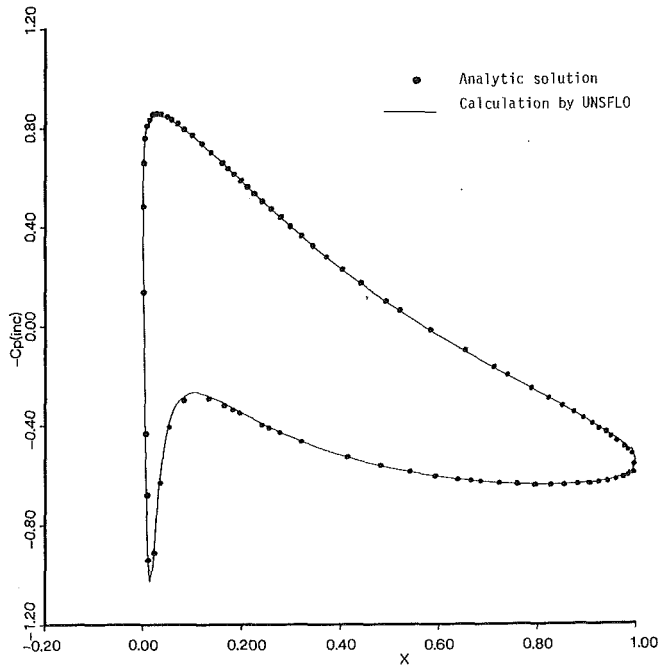


Fig. 2 Theoretical and calculated pressure-rise coefficient for Gostelow's compressor cascade

focus velocimeter measurements in a rotor cascade operating behind a stator at the DLR (Cologne, Federal Republic of Germany). The data have been analyzed in a series of experimental studies by Binder and Romey (1983), Binder et al. (1985, 1987), and Binder (1985). Here comparisons are shown for the midspan section, where the axial distance between the stator and the rotor is 79.6 percent of the stator axial chord. This axial distance is large enough for the potential-flow interaction effects to be negligible, so that the unsteadiness of the flow is mainly due to the velocity wakes. For the calculated results shown the computations were performed on a 125×25 grid per rotor passage. The relative flow conditions were: $\alpha_i = 46.7$ deg, $M_i = 0.434$, $\alpha_o = -62.0$ deg, and $M_o = 0.635$; and the stator-to-rotor-pitch ratio R is 1.55. The velocity wake was described (in the stator frame) by a sinusoidal velocity-defect function of amplitude 6.5 percent. The sinusoidal wake model and the amplitude were chosen as the best simple model that fit the experimental data. The measured velocity variation at the inlet is not exactly sinusoidal, but for comparison purposes the sinusoidal model was a reasonable match to the data and it was considered sufficiently accurate (see axial locations P1 and P2 in part (b) of Fig. 3).

Figure 3 shows the computed results in the form of entropy contours superimposed on unsteady flow vectors. The unsteady flow vectors at each point are defined as the local instantaneous-flow vector minus the local average-flow vector. The entropy contours identify the stator wakes as they enter the passage, are chopped and sheared by the rotor blades. The centerlines of the wakes are marked by thicker dashed lines. The blades of the figures have been labeled by numbers to facilitate the discussion. The entropy contours show one stator wake touching the leading edge of blade 0. This same wake is shown to be sheared over the leading edge of blade 0 and acting in the passage between blades 0 and 1. The previous stator wake enters the passage between blades -2 and -1. This wake has been chopped by blade -1 and is also acting in the passage between blades -1 and 0. The centerlines of the wakes are between two counterrotating vortices. These are features common to all stator-wake/rotor interactions and they are explained in Part 2 (Korakianitis, 1992). The computed wake patterns shown in Fig. 3 are in good agreement with the ex-

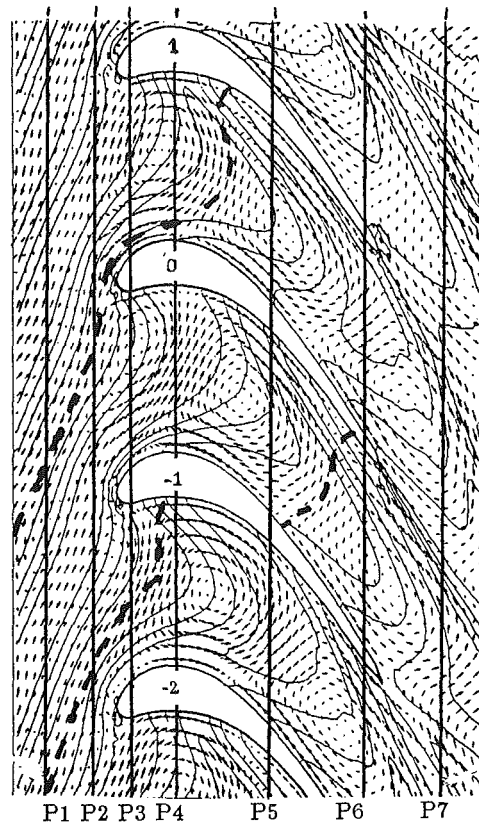


Fig. 3(a) Computed entropy contours and unsteady flow vectors (with marked axial positions P1-P7)

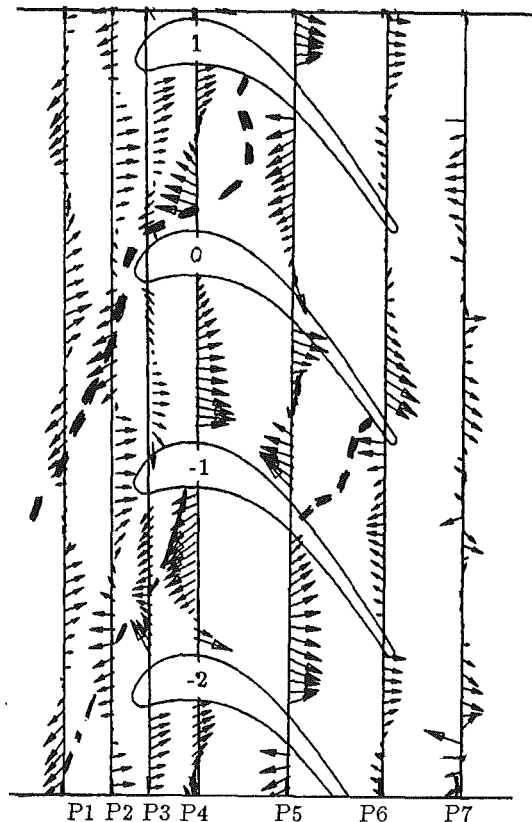


Fig. 3(b) Experimental unsteady flow vectors for seven axial locations, P1-P7

Fig. 3 Computed and experimental results for the DLR (ex DFVLR) rotor cascade

perimentally obtained instantaneous patterns of turbulent intensity (shown in Fig. 15 of Binder et al., 1985), and the instantaneous patterns of fluctuation energy (shown in Fig. 8 of Binder, 1985). Figure 3 also shows measured unsteady flow vectors at seven axial locations for tangential positions that correspond approximately to the same passages (between blades - 1, 0, and 1). The measured unsteady flow vectors shown in Fig. 3 have been multiplied by a constant and are shown larger than the computed ones for clarity. The measured and calculated unsteady flow vectors show recirculating flow patterns that are in similar locations for most of the passage. The agreement is not very good in regions near the trailing edge of the rotor cascade. This is because the measured wake is close enough but not exactly a sinusoidal velocity defect, and the differences between the actual wake and the model are amplified by the turning and shearing of the wake flow in the passage. Despite this small discrepancy, which is caused by the shortcomings of the sinusoidal wake model of the computed results, the agreement between the measured data and the computed results is very good; and it could be improved by refining the wake model of the computation.

Experimental Data on Wakes

Two numbers identify the velocity disturbances: the maximum amplitude of the velocity defect D , expressed as a fraction of the undisturbed velocity; and the "width" W of the velocity defect (see Eq. (2)). For stators the velocity defect refers to absolute velocities and for rotors it refers to relative velocities. Since most velocity wakes observed in experimental data have velocity distributions that resemble (they never actually match) Gaussian distributions, the width of the velocity defect is characterized by the corresponding characteristic width of the Gaussian distribution that would best fit the velocity data. In the following this width is expressed as a fraction of the pitch of the blade cascade that generates the wake. In most cases the pressure side of the velocity wake is narrower than the suction side, especially for small axial distances downstream of the cascade that generates the wake. The reason for this is that the boundary layer of the pressure side is thinner than the boundary layer of the suction side. For most cascades with suction-side flow that does not separate, the difference between the two characteristic widths is less than 5 percent (of the pitch of the cascade that generates the wake). In some cases, however, the boundary layer on the suction side may separate in regions of adverse pressure gradient. If the separated boundary layer does not reattach before the trailing edge then the boundary layer is relatively thick, and as a result the characteristic width of the suction side is considerably larger than the characteristic width of the pressure side. Because of the above, two "characteristic widths" are used: the suction-side characteristic width, and the pressure-side characteristic width. Both the amplitudes of the wakes and the characteristic widths of the wakes are functions of the axial distance downstream from the trailing edge at which the measurements are taken. In the following this distance is expressed as a fraction of the axial chord of the blade that generates the wake.

Figure 4 shows a complication of such data found in the literature. Such data for isolated airfoils have been obtained by Silverstein et al. (1939) and Ramaprian (1984). Compressor or fan data have been obtained by Wisler and Mossey (1972), Kiock (1973), Evans (1973, 1975), Raj and Lakshminarayana (1976), Hirsch and Kool (1977), Lakshminarayana and Davino (1979), Ravindranath and Lakshminarayana (1980, 1981), Gallus et al. (1980), Dring et al. (1980, 1982a), Ispas et al. (1980), Zierke and Okiishi (1981), Hobbs et al. (1982), Gallus and Hoenen (1983), and Pfeil and Sieber (1986). Turbine data have been obtained by Dring and his co-workers (1982b), Hodson (1983, 1985a, 1985b), Chen (1985), Moore and Adhye (1985),

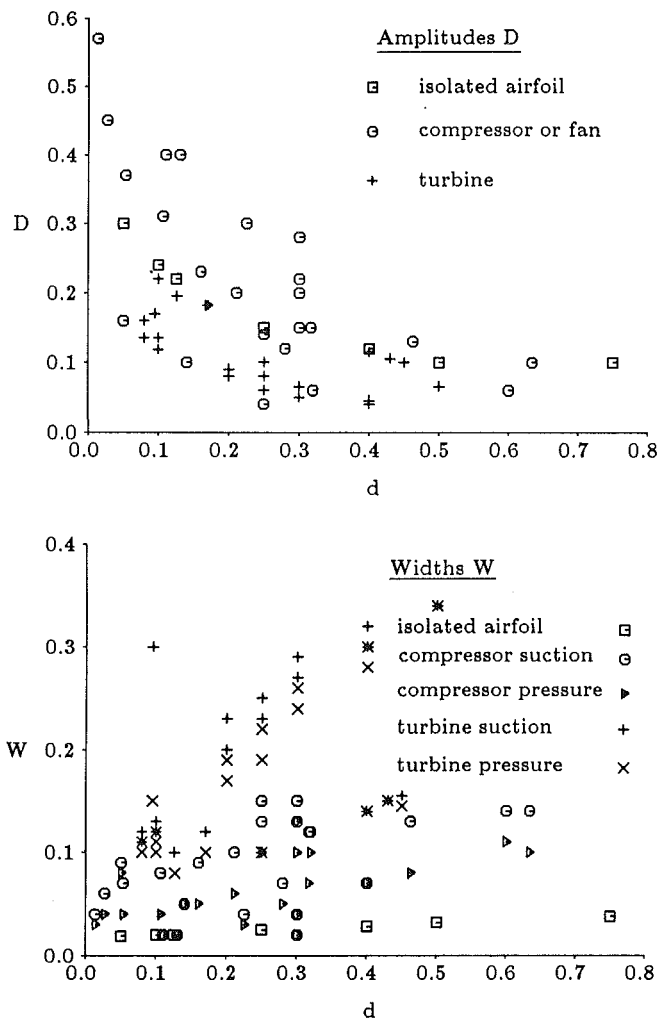


Fig. 4 Amplitudes D and widths W versus d

Hubensteiner (1986), Binder and Romey (1983), Binder et al. (1985, 1987), Binder (1985) (these are the data that were used for the unsteady-flow test case included above), and Wittig et al. (1987).

In the above we have presented representative experimental data that indicate the structure of the interaction downstream of turbomachinery cascades. There are data available for compressor rotor and compressor stator cascades, fewer data on isolated airfoils, and even fewer or turbine cascades. The main difference between compressor and turbine data is that compressor wakes are relatively thinner than turbine wakes. Experimental evidence to that effect can be found in the compressor wakes of Wagner et al. (1979), Gallus and Hoenen (1983), Okiishi et al. (1985), and Tweedt and Okiishi (1985).

Viscous-Wake-Interaction Model

The resulting interaction at the stator-outlet/rotor-inlet boundary depends on axial and radial pressure gradients, on varying outlet angle across the span, and on compressibility effects. If the objective was to investigate the unsteady forces on rotor blades arising from the interaction with a known stator or with a series of stators of known geometry, then one could try to identify the best interaction model for the stator-outlet/rotor-inlet boundary. This could be done by reviewing the above data and performing additional relevant calculations. For stators of known geometry, techniques such as those published by Kool and Hirsch (1982) could be used to predict the

amplitude and decay rate of the velocity wake, based on the pressure gradients across the trailing edge and along the span of the cascade generating the wake. However, for the purposes of this work we do not have a specific stator, or a set of stators in mind. We want the results to be general and, as far as the stator geometry is concerned, to depend only on the nozzle angle and on the stator-to-rotor-pitch ratio. Identifying a wake and its decay rate for each case is impractical. It is therefore more appropriate to choose the wake characteristics and to conduct a study of the effect of variation of the amplitude of the interaction.

It is possible to express the velocity distribution of the wake by the summation of a Fourier series of sinusoidal wakes. This method has been employed previously by Krishnappa (1972) to evaluate fan-noise generation. However, the addition of Fourier series to model the wake assumes a linear problem. The Euler equations are nonlinear equations, and therefore the unsteady-force results that would be obtained from such a linearized analysis would be unreliable.

The wake model we used in this study assumes that in the stator frame the flow vectors in the wake are parallel to the undisturbed flow (a velocity deficit with no angle variation or turbulence), that the static pressure is constant across the wake, that the total enthalpy is constant across the wake, and that the velocity defect is an asymmetric Gaussian distribution. The above are modeled by:

$$\begin{aligned} u_{iw,s} &= c_N \left[1 - D \cdot \exp\left(-\frac{ST(\eta)^2}{W_s^2}\right) \right] \cos(\alpha_N) \\ u_{iw,p} &= c_N \left[1 - D \cdot \exp\left(-\frac{ST(\eta)^2}{W_p^2}\right) \right] \cos(\alpha_N) \\ v_{iw,s} &= c_N \left[1 - D \cdot \exp\left(-\frac{ST(\eta)^2}{W_s^2}\right) \right] \sin(\alpha_N) \\ v_{iw,p} &= c_N \left[1 - D \cdot \exp\left(-\frac{ST(\eta)^2}{W_p^2}\right) \right] \sin(\alpha_N) \end{aligned} \quad (2)$$

The parameter η is defined by:

$$\eta = \frac{y - \tan(\alpha_N)x}{S_{sb}} \quad (3)$$

so that the periodic sawtooth function ST with period of one stator pitch S_{sb} , which is used to define the wake, can be expressed as a function of η for any value of passage number n by:

$$ST(\eta) = \eta - n, \quad n - \frac{1}{2} < \eta < n + \frac{1}{2} \quad (4)$$

In the calculations the velocity wake was modeled as an asymmetric Gaussian distribution with amplitude $D=0.10$, pressure-side characteristic width $W_p=0.13$, and suction side characteristic width $W_s=0.18$. This wake was used for axial gap of 30 percent of the rotor axial chord. The remaining question is what is the appropriate decay rate for this wake. In previous calculations Mitchell (1980) and Hodson (1983, 1985a) tried to match numerical (artificial) viscosity with the experimentally measured viscosity. This method is acceptable when one cascade at one set of conditions is under investigation, but in general each cascade will exhibit its own decay characteristics. Numerical tests of the effect of numerical viscosity indicated that the resulting unsteady forces were not significantly affected by the resulting different strength and decay rate of the wakes (Korakianitis, 1987).

Potential-Flow-Interaction Model

The model for the potential-flow disturbance was developed by observing the experimentally measured and computed static pressure fields of various turbine-blade cascades. The static pressure fields of most of these cascades indicate that across the line of the trailing edges of the cascades there is a variation of static pressure with maxima at (or very near) the trailing edges and minima at (or very near) the middle of the passage. The exact location and shape of the pressure variation depends on the geometric shape of the passage (and thus on the geometric shape of the cascade). The pressure variation is nearly sinusoidal and the amplitude of the pressure disturbance decays very fast with distance downstream. Measured cascade data such as those shown in Fig. 6 of Sonoda (1985) and Fig. 4 of Yamamoto and Yanagi (1985) exhibit the same trends.

The static pressure variation across the trailing edges is affected by secondary flows and it varies across the span. This three-dimensional variation of the static pressure (and thus the three-dimensional variation of the potential-flow interaction) can be seen in the data on highly loaded turbine cascades obtained by Moustapha et al. (1985) by comparing Figs. 8 and 9 and Figs. 10 and 11 of that reference. It can also be seen by observing the static pressure contours along the span downstream of the trailing edge of the turbine nozzle cascade investigated by Boletis and Sieverding (1984) (shown in Fig. 7 of that reference) and by Sieverding et al. (1984) (shown in Fig. 6 of that reference). The latter also shows the rapid decay of the potential-flow interaction: Significant static pressure variation is shown in the passage 11 percent of the axial chord aft of the trailing edge; very small static pressure variation is shown 31 percent of the axial chord aft of the trailing edge; and almost not noticeable static pressure variation is shown 68 percent of the axial chord aft of the trailing edge. Clearly secondary flows affect the exact location of the pressure minimum, as well as the magnitude of the static pressure variation.

The potential-flow model is derived as an isentropic, irrotational perturbation to uniform flow (see page 198 of the text by Liepmann and Roshko, 1957):

$$(1 - M_x^2) \frac{\partial^2 \Phi}{\partial x^2} - 2M_x M_y \frac{\partial^2 \Phi}{\partial x \partial y} + (1 - M_y^2) \frac{\partial^2 \Phi}{\partial y^2} = 0 \quad (5)$$

The velocity potential is defined by:

$$\frac{\partial \Phi}{\partial x} \equiv u \quad \frac{\partial \Phi}{\partial y} \equiv v \quad (6)$$

For subsonic flows in the passages of interest to this study one expects that the potential-flow interaction is periodic in the y direction and that it decays exponentially in the x direction. Thus the general solution of Eq. (5) is of the form:

$$\Phi(x, y) = B \cdot \exp(j\zeta y + \xi x) \quad (7)$$

Substituting Eq. (7) into Eq. (5) one obtains:

$$(1 - M_x^2)\xi^2 - 2jM_x M_y \zeta \xi - (1 - M_y^2)\zeta^2 = 0 \quad (8)$$

Solving the above equation for ξ gives:

$$\xi = \frac{jM_x M_y \pm \sqrt{1 - M_x^2}}{1 - M_x^2} \zeta \quad (9)$$

where M is given by $M = \sqrt{M_x^2 + M_y^2}$.

The behavior of this solution depends on whether the steady flow in the stator frame is subsonic or supersonic. In this work we concentrate on subsonic solutions. If the flow is subsonic ξ has both a real and an imaginary part. For subsonic flows the real part of the solution for ξ must be negative, since we know that the potential-flow-interaction effects must decay downstream. Thus we choose the negative root in the equation for ξ . The imaginary part of the solution for ξ combines with the other imaginary part of the exponential in Eq. 7 to govern

the periodicity. For Eq. 7 to satisfy the periodicity condition ζ must be an integer multiple of $2\pi/S_{sb}$, where S_{sb} is the stator pitch. The most important mode in this periodic solution is the fundamental mode, which is characterized by:

$$\zeta = 2\pi/S_{sb} \quad (10)$$

Substituting these values for ζ and ξ in Eq. (7) yields the following expression for the potential:

$$\Phi(x, y) = B \cdot \exp \left[-\frac{2\pi}{S_{sb}} \frac{\sqrt{1-M^2}}{1-M_x^2} x \right] \cdot \exp \left[j \frac{2\pi}{S_{sb}} (y - \tan(\alpha_{ip})x) \right] \quad (11)$$

where

$$\tan(\alpha_{ip}) = -\frac{M_x M_y}{1-M_x^2} \quad (12)$$

In the above the subscript ip denotes potential values at the inlet boundary and the angle α_{ip} is the angle of the line that the local pressure maxima and minima due to the potential-flow interaction propagate downstream from the stator trailing edges.

The local perturbation velocities are obtained by substituting the above solution for $\Phi(x, y)$ into Eq. (6):

$$\begin{aligned} \delta v &= j \frac{2\pi}{S_{sb}} \cdot \Phi(x, y) \\ \delta u &= - \left[j \tan(\alpha_{ip}) + \frac{\sqrt{1-M^2}}{1-M_x^2} \right] \frac{2\pi}{S_{sb}} \cdot \Phi(x, y) \\ &= \left[-\tan(\alpha_{ip}) + j \frac{\sqrt{1-M^2}}{1-M_x^2} \right] \cdot \delta v \end{aligned} \quad (13)$$

B does not have a simple physical representation. It is more convenient to re-evaluate the above expressions for δu and δv as functions of the maximum perturbation in v at the inlet boundary, which is denoted by V_{ip} . Then the velocity perturbations are a function of the axial distance from the inlet boundary ($x-x_{inl}$), where x_{inl} denotes the axial location of the computational inlet boundary. Based on Eq. (11) the solution for δv and δu can be written as:

$$\delta v = -V_{ip} \cdot \exp \left[-\frac{2\pi}{S_{sb}} \frac{\sqrt{1-M^2}}{1-M_x^2} (x-x_{inl}) \right] \cdot \sin[2\pi(\epsilon + \Delta\epsilon)] \quad (14)$$

$$\begin{aligned} \delta u &= -\tan(\alpha_{ip})\delta v - \frac{\sqrt{1-M^2}}{1-M_x^2} V_{ip} \\ &\cdot \exp \left[-\frac{2\pi}{S_{sb}} \frac{\sqrt{1-M^2}}{1-M_x^2} (x-x_{inl}) \right] \cdot \cos[2\pi(\epsilon + \Delta\epsilon)] \end{aligned}$$

where ϵ at any location is given by

$$\epsilon = \frac{y - \tan(\alpha_{ip})x}{S_{sb}} \quad (15)$$

In the above $\Delta\epsilon$ is a phase-shifting constant, which is used to ensure that the maximum amplitude in the pressure disturbance due to the potential-flow field of the stator coincides with the centerlines of the velocity wakes at the (x, y) locations that model the stator trailing edges.

The amplitude of V_{ip} was chosen by investigating the pressure and velocity fluctuations at the line of the trailing edges of numerous typical subsonic turbine-stator cascades and across other lines a little downstream (5 and 10 percent of the axial

chord) and parallel to the line of the trailing edges. These measurements indicated that across the line of the trailing edges the pressure fluctuations were typically between 4 and 4.5 percent of the average pressure. The corresponding values of V_{ip} for various values of V_{rb} were between 4.52 and 5.31 percent of c_N .

The combined disturbance of the potential-flow interaction and the wake interaction at the inlet boundary is found by adding the values of the two disturbances at the inlet boundary.

Effects of the Disturbance Amplitudes

Results were obtained for $1 \leq R \leq 4$ and for three different α_N for each one of thirteen rotor cascades, and for axial gaps $d=0.30$. The three values of α_N were chosen so as to result in rotor speeds between 380 and 580 m/s, while ensuring that the stator exit Mach number did not exceed 0.96. The results have been reported by Korakianitis (1987) and some trends are analyzed by Korakianitis (1992). Some results are shown here for one of the cascades, which has $\alpha_i=40$ deg, $\alpha_o=-72$ deg, $M_i=0.2318$, $M_o=0.80$, $C_L=0.80$, $S_{rb}=0.9534 b_{rb}$, and stagger angle of -44 deg. The steady-flow performance of the sample cascade is shown in Fig. 5.

The interblade phase angle and the reduced frequency (inversely proportional to R) are parameters that are frequently

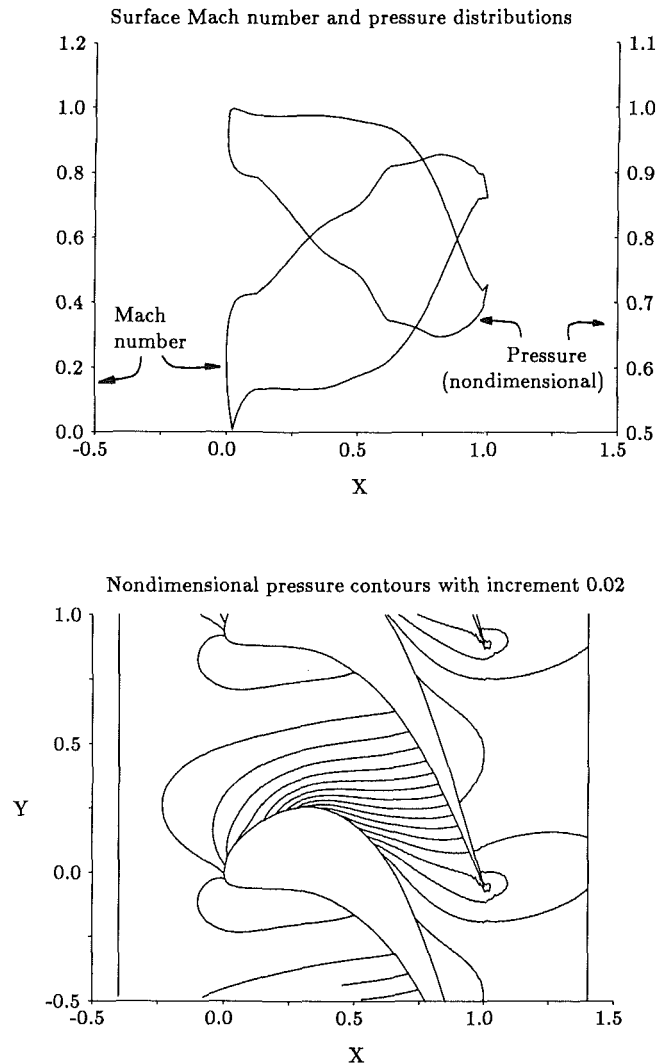


Fig. 5 Steady-flow performance of a typical rotor cascade. For this sample cascade $\alpha_i=40$ deg; $\alpha_o=-72$ deg; $M_i=0.234$; and $M_o=0.800$.

used in the discussion of unsteady flow effects in turbomachines. These parameters cannot be used effectively for the discussion of both the wake interaction and the potential-flow interaction. There are two reasons for this: The two effects propagate into the rotor flow field at different phases; and the decay rates of the potential-flow interaction and of the wake interaction do not vary uniformly with any of those parameters. (A more detailed discussion is given by Korakianitis 1987.) In this article we chose to present the results in the form of amplitudes and phases of the harmonics of the unsteady forces spatially analyzed over S_{sb} as a function of R and α_N . To obtain the corresponding reduced frequency parameters one can use:

$$\tilde{\omega} \equiv \frac{\omega \cdot b_{rb}}{c_x} = \frac{2\pi V_{rb}}{R S_{rb}} \cdot \frac{b_{rb}}{c_x} \quad (16)$$

The dimensional forces (such as F_x in the x direction) are related to the nondimensional forces (F'_x) by:

$$F'_x \equiv \frac{F_x/z}{\rho b_{rb} c^2} \quad (17)$$

(The moment T'_z is divided by b_{rb}^2 .) The steady-flow (constant) forces for the sample cascade of Fig. 5 were: $F'_{x,ss} = 0.2052$; $F'_{y,ss} = 0.1424$; and the moment $T'_{z,ss} = 0.1334$.

The amplitudes of the unsteady forces were obtained from:

$$F'_x(y) = \Re \left\{ \sum_{n=0}^{\infty} A_{x,n} \cdot \exp(j\theta_{x,n}) \cdot \exp\left(\frac{j2\pi ny}{S_{sb}}\right) \right\} \quad (18)$$

The origin (zero) of the period of the unsteadiness in each case corresponds to the y location in which a stator velocity wake touches the leading edge of a rotor blade. The end of the period is characterized by the velocity wake from the next stator blade touching the leading edge of the same rotor blade. The average unsteady forces and moment are in most cases between 90 and 100 percent of the steady force, and in the results the amplitude of the average forces and moment ($n=0$) have been divided by 10 to show the figures within a reasonable scale. The nondimensionalized amplitudes (e.g., $A_{nd,x,n}$), of the Fourier harmonics of the nondimensionalized forces shown in the results are related to the nondimensional amplitudes ($A_{x,n}$) by:

$$A_{nd,x,n} = \frac{A_{x,n}}{np \cdot F'_{x,ss}} \quad (19)$$

where $np=10$ for $n=0$ (fundamental harmonic), and $np=1$ for $n=1, 2, \dots$

The results exhibited similar trends for all cascades and for the forces in the axial (x), tangential (y), and for the moment in the z direction, and they have been detailed by Korakianitis (1987). Here we present results for $R=2.0$ and for the medium α_N for the forces in the x direction for the sample cascade.

Results of $A_{nd,x,n}$ for the isolated viscous-wake interaction (with $V_{ip}=0$) for this sample cascade are shown in Fig. 6. These indicate that as D increases and with $W_p=0.13$ and $W_s=0.18$, $A_{nd,x,0}$ is between 90 and 100 percent (the latter for zero disturbance) of the corresponding forces and moment in steady-flow conditions. This is because the forces are generated by the rate of change of momentum through the cascade and the wake interaction results in a small loss of momentum. $A_{nd,x,1}$ increases slightly from the origin (no disturbance results in steady forces and moment) to surprisingly low amplitudes for $D=0.30$ (which is a very strong wake; see Fig. 4). $A_{nd,x,2}$ is very small and it increases with increasing D . The phases of the disturbances (not shown here because they do not contribute to the discussion) are constant, indicating similar flow patterns through the rotor passages.

Results of $A_{nd,x,n}$ for the isolated potential-flow interaction (with $D=0$) for this sample cascade are shown in Fig. 7. These indicate that as V_{ip} increases $A_{nd,x,0}$ remains constant at 100 percent of the corresponding forces and moment in steady-

Table 1 Additional information on the sample cascade and a legend for reading the figures

α_N	78.24°
V_{rb} in m/s	520
$n=0$	□
$n=1$	⊙
$n=2$	△

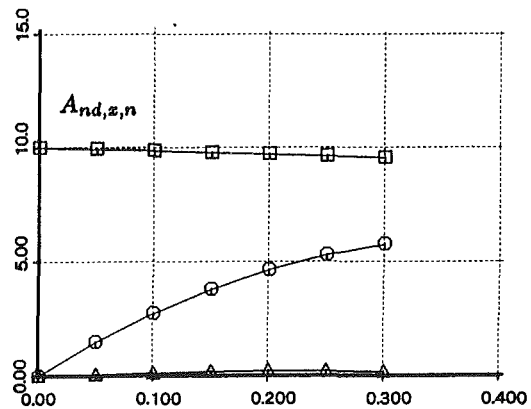


Fig. 6 Nondimensionalized amplitudes $A_{nd,x,n}$ of the harmonics of $F'_x(y)$ over S_{sb} for $R=2.00$ and for the isolated viscous-wake interaction as a function of D (the abscissa) with $W_p=0.13$ and $W_s=0.18$. Table 1 includes a legend for the figure.

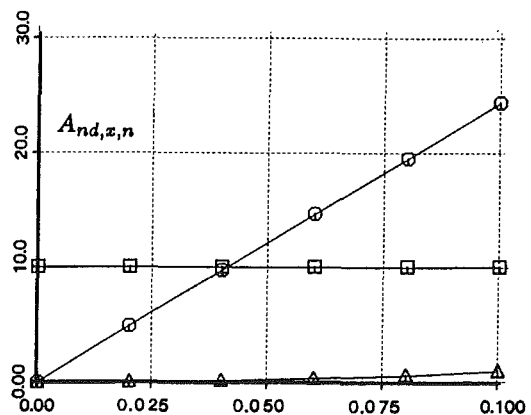


Fig. 7 Nondimensionalized amplitudes $A_{nd,x,n}$ of the harmonics of $F'_x(y)$ over S_{sb} for $R=2.00$ and for the isolated potential-flow interaction as a function of V_{ip} (the abscissa). Table 1 includes a legend for the figure.

flow conditions. This is because the forces are generated by the rate of change of momentum through the cascade and the potential-flow interaction does not result in any loss of momentum. $A_{nd,x,1}$ increases considerably and linearly with the amplitude of V_{ip} from the origin (no disturbance results in steady forces and moment) to surprisingly high amplitudes for $V_{ip}=0.10$. This is because it would require a fairly large pressure variation for the potential-flow interaction to generate a velocity disturbance of this amplitude. The second-harmonic amplitude of the unsteady forces and moment are very small, and they increase with increasing V_{ip} . The phases of the disturbances (not shown here because they do not contribute to the discussion) are constant, indicating similar flow patterns through the rotor passages.

The above suggest that large variations in the amplitude of the wake do not change the amplitudes of the harmonics of the unsteady forces and moment significantly. To prove this statement we ran a set of tests for three different values of α_N for two different cascades while maintaining $V_{ip}=0.05$ for $1.0 < R < 4.0$ and for different values of D . The results of these

tests (which are not shown here because they do not contribute to the discussion) proved that the amplitudes of the harmonics of the unsteady forces and moments do not change significantly with the amplitude of the wake defect.

Although in theory one needs all the terms of the sum in Eq. (18) (to infinity), in practice the third and higher harmonics of the forces and moments were negligible. By observing the results of Figs. 6 and 7 (and by considering the analysis of the results discussed by Korakianitis, 1992) one concludes that for $R \geq 1.5$ the isolated potential-flow interaction results in unsteady forces with harmonic amplitudes that are higher than those for the isolated viscous-wake interaction.

Conclusions

The unsteady forces on two-dimensional gas turbine rotors due to potential-flow interaction and viscous-wake interaction from upstream blade rows were computed using a two-dimensional, compressible, inviscid rotor/stator-disturbance interaction program. The results of computations were compared with analytical and experimental data. The viscous wake and the potential-flow interaction from the upstream stator were modeled at the rotor-inlet boundary. A parametric study of the amplitudes of the disturbances shows that the results are not very sensitive to changes in the amplitude of the viscous wake, while they are sensitive to changes in the amplitude of the potential-flow interaction. For stator-to-rotor-pitch ratio $R = 2.0$ we conclude the following: The effect of the wake on the momentum deficit (performance) is about 5 percent, and the first harmonic of the spatially (or temporally) analyzed unsteady load is about 6 percent of the steady-flow load; the first harmonic of the spatially (or temporally) analyzed unsteady load due to the potential-flow interaction is about 12 percent of the steady-flow load; and the higher harmonics are negligible for both the wake and the potential-flow interaction.

Acknowledgments

The author thanks Professors David Gordon Wilson, A. D. Carmichael, Michael B. Giles, and Anthony T. Patera of MIT, and Mr. Dennis C. Evans of GE (Lynn, Massachusetts) for their advice, support, encouragement, and constructive suggestions. The material presented in this paper was part of a larger research program funded by GE.

References

- Binder, A., and Romey, R., 1983, "Secondary Flow Effects and Mixing of the Wake Behind a Turbine Stator," *ASME Journal of Engineering for Power*, Vol. 105, pp. 40-46.
- Binder, A., Förster, W., Kruse, H., and Rogge, H., 1985, "An Experimental Investigation Into the Effects of Wake on the Unsteady Turbine Rotor Flow," *ASME Journal of Engineering for Gas Turbines and Power*, Vol. 107, pp. 458-466.
- Binder, A., 1985, "Turbulence Production Due to Secondary Vortex Cutting in a Turbine Rotor," *ASME Journal of Engineering for Gas Turbines and Power*, Vol. 107, pp. 1039-1046.
- Binder, A., Förster, W., Mach, K., and Rogge, H., 1987, "Unsteady Flow Interaction Caused by Stator Secondary Vortices in a Turbine Rotor," *ASME JOURNAL OF TURBOMACHINERY*, Vol. 109, pp. 251-257.
- Boletis, E., and Sieverding, C. H., 1984, "Experimental Study of the Flow Field Behind an Annular Turbine Nozzle Guide Vane With and Without Downstream Rotor," *ASME Paper No. 84-GT-15*.
- Chen, S., 1985, "Application of the Rotating Water Table to Nozzle Wake Excitation in Low Pressure Turbines," *ASME Paper No. 85-IGT-45*.
- Denton, J. D., 1975, "A Time Marching Method for Two and Three Dimensional Blade to Blade Flow," *British ARC, R & M 3775*.
- Dring, R. P., Joslyn, H. D., and Hardin, L. W., 1980, "Experimental Investigation of Compressor Rotor Wakes," *United Technologies Research Center, East Hartford, CT 06108, AFAPL-TR-79-2107, Jan.*
- Dring, R. P., Joslyn, H. D., and Hardin, L. W., 1982a, "An Investigation of Axial Compressor Rotor Aerodynamics," *ASME Journal of Engineering for Power*, Vol. 104, pp. 84-96.
- Dring, R. P., Joslyn, H. D., Hardin, L. W., and Wagner, J. H., 1982b,

- "Turbine Rotor-Stator Interaction," *ASME Journal of Engineering for Power*, Vol. 104, pp. 729-742.
- Erdoes, J. I., and Alzner, E., 1977, "Computation of Unsteady Transonic Flows Through Rotating and Stationary Cascades," *NASA-CR-2900*.
- Evans, R. L., 1973, "Turbulent Boundary Layers on Axial Flow Compressor Blades," PhD thesis, University of Cambridge, United Kingdom.
- Evans, R. L., 1975, "Turbulence and Unsteadiness Measurements Downstream of a Moving Blade Row," *ASME Journal of Engineering for Power*, Vol. 97, pp. 131-139.
- Fourmaux, A., 1986, "Unsteady Flow Calculation in Cascades," *ASME Paper No. 86-GT-178*.
- Gallus, H. E., Lambert, J., and Wallmann, T., 1980, "Blade-Row Interaction in Axial-Flow Subsonic Compressor Stage," *ASME Journal of Engineering for Power*, Vol. 102, pp. 169-177.
- Gallus, H. E., and Hoenen, H., 1983, "Measurement of 3-D Unsteady Flow Downstream of Rotor and Stator Blades in Axial-Flow Compressors," *ASME Paper No. 83-Tokyo-IGTC-68*.
- Giles, M. B., 1988, "Calculation of Unsteady Wake/Rotor Interactions," *AIAA Journal of Propulsion and Power*, Vol. 4, No. 4.
- Gostelow, J. P., 1984, *Cascade Aerodynamics*, Pergamon Press, New York.
- Hirsch, C., and Kool, P., 1977, "Measurement of the Three Dimensional Flow Field Behind an Axial Compressor Stage," *ASME Journal of Engineering for Power*, Vol. 99, pp. 168-180.
- Hobbs, D. E., Wagner, J. H., Dannenhoffer, J. F., and Dring, R. P., 1982, "Experimental Investigation of Compressor Cascade Wakes," *ASME Paper No. 82-GT-299*.
- Hodson, H. P., 1983, "Unsteady Boundary-Layers on Axial-Flow Turbine Rotor Blades," PhD thesis, University of Cambridge, United Kingdom.
- Hodson, H. P., 1985a, "An Inviscid Blade-to-Blade Prediction of a Wake-Generated Unsteady Flow," *ASME Journal of Engineering for Gas Turbines and Power*, Vol. 107, pp. 337-344.
- Hodson, H. P., 1985b, "Measurements of Wake-Generated Unsteadiness in the Rotor Passages of Axial Flow Turbines," *ASME Journal of Engineering for Gas Turbines and Power*, Vol. 107, pp. 467-476.
- Hubensteiner, M., 1986, "Einfluss der Schaufelprofilform auf die instationären Schaufelkräfte eines mittleren Turbinengitters (Influence of the Blade-Profile on the Unsteady Blade-Forces of a Middle Turbine Stage)," *VDI Berichte*, pp. 209-232.
- Ispas, I., Grollius, H., and Gallus, H. E., 1980, "Über den Einfluss von Nachlaufdübeln auf die instationäre Druckverteilung an den nachfolgenden Schaufelreihen in Axialverdichtern und Axialturbinen," *Sonderdruck aus VDI-Berichte*, No. 361, pp. 33-43.
- Kiock, R., 1973, "Turbulence Downstream of Stationary and Rotating Cascades," *ASME Paper No. 73-GT-80*.
- Kool, P., and Hirsch, C., 1982, "A Prediction Scheme for the Decay of a Turbomachine Blade Wake," *ASME Paper No. 82-GT-273*.
- Korakianitis, T., 1987, "A Design Method for the Prediction of Unsteady Forces on Subsonic, Axial Gas-Turbine Blades," Doctoral thesis (Sc.D.) in Mechanical Engineering, Massachusetts Institute of Technology, Cambridge, MA.
- Korakianitis, T., 1988, "On the Prediction of Unsteady Forces on Gas-Turbine Blades: Part 1—Typical Results and Potential-Flow-Interaction Effects," *ASME Paper No. 88-GT-89*.
- Korakianitis, T., 1992, "On the Prediction of Unsteady Forces on Gas Turbine Blades: Part 2—Analysis of the Results," *ASME JOURNAL OF TURBOMACHINERY*, Vol. 114, pp. 123-131.
- Koya, M., and Kotake, S., 1985, "Numerical Analysis of Fully Three-Dimensional Periodic Flows Through a Turbine Stage," *ASME Journal of Engineering for Gas Turbines and Power*, Vol. 107, pp. 945-952.
- Krammer, P., 1982, "Computation of Unsteady Blade Forces in Turbomachines by Means of Potential Flow Theory and by Simulating Viscous Wakes," *ASME Paper No. 82-GT-198*.
- Krishnappa, G., 1972, "Blade Interaction Noise From Lift Fans," *The Journal of the Acoustical Society of America*, Vol. 51, pp. 1464-1470.
- Lakshminarayana, B., and Davino, R., 1979, "Mean Velocity and Decay Characteristics of the Guidevane and Stator Blade Wake of an Axial Flow Compressor," *ASME Paper No. 79-GT-9*.
- Liepmann, H. W., and Roshko, A., 1957, *Elements of Gasdynamics*, Wiley, New York.
- Mitchell, N. A., 1980, "A Time Marching Method for Unsteady Two-Dimensional Flow in a Blade Passage," *International Journal of Heat and Fluid Flow*, Vol. 2, pp. 205-220.
- Moore, J., and Adhye, R. Y., 1985, "Secondary Flows and Losses Downstream of a Turbine Cascade," *ASME Journal of Engineering for Gas Turbines and Power*, Vol. 107, pp. 961-968.
- Moustapha, S. H., Paron, G. J., and Wade, J. H. T., 1985, "Secondary Flow in Cascades of Highly Loaded Turbine Blades," *ASME Journal of Engineering for Gas Turbines and Power*, Vol. 107, pp. 1031-1038.
- Okiishi, T. H., Hathaway, M. D., and Hansen, J. L., 1985, "A Note on Blade Wake Interaction Influence on Compressor Stator Row Aerodynamic Performance," *ASME Journal of Engineering for Gas Turbines and Power*, Vol. 107, pp. 549-551.
- Pfeil, H., and Sieber, J., 1986, "Velocity Distribution and Decay Characteristics of Wakes Behind a Compressor Rotor-Blade," *ASME Paper No. 86-GT-115*.
- Rai, M. M., 1985, "Navier-Stokes Simulations of Rotor-Stator Interaction Using Patched and Overlaid Grids," *AIAA Paper No. 85-1519*.

- Raj, R., and Lakshminarayana, B., 1976, "Three Dimensional Characteristics of Turbulent Wakes Behind Rotors of Axial Flow Turbomachinery," *ASME Journal of Engineering for Power*, Vol. 98, pp. 218-228.
- Ramaprian, B. R., 1984, "Study of Large-Scale Mixing in Developing Wakes Behind Streamlined Bodies," NASA-CR-173478.
- Ravindranath, A., and Lakshminarayana, B., 1980, "Mean Velocity and Decay Characteristics of the Near-and-Far-Wake of a Compressor Rotor Blade of Moderate Loading," *ASME Journal of Engineering for Power*, Vol. 102, pp. 535-548.
- Ravindranath, A., and Lakshminarayana, B., 1981, "Rotor Wake Mixing Effects Downstream of a Compressor Rotor," ASME Paper No. 81-GT-98.
- Scott, J. N., and Hankey, W. L., 1986, "Navier-Stokes Solutions of Unsteady Flow in a Compressor Rotor," *ASME JOURNAL OF TURBOMACHINERY*, Vol. 108, pp. 170-179.
- Shang, J. S., 1983, "Numerical Simulation of Wing Fuselage Aerodynamic Interaction," AIAA Paper No. 83-0225.
- Sieverding, C. H., Van Hove, W., and Boletis, E., 1984, "Experimental Study of the Three-Dimensional Flow Field in an Annular Turbine Nozzle Guidevane," *ASME Journal of Engineering for Gas Turbines and Power*, Vol. 106, pp. 437-448.
- Silverstein, A., Katzoff, S., and Bullivant, W. K., 1939, "Downwash and Wake Behind Plain and Flapped Airfoils," NACA Report 651.
- Sonoda, T., 1985, "Experimental Investigation on a Spatial Development of Streamwise Vortices in a Turbine Inlet Guide Vane Cascade," ASME Paper No. 85-GT-20.
- Tweedt, D. L., and Okiishi, T. H., 1985, "An Experimental Investigation of Stator/Rotor Interaction Influence on Multistage Compressor Rotor Flow," AIAA Paper No. 85-0009.
- Wagner, J. H., Okiishi, T. H., and Holbrook, G. J., 1979, "Periodically Unsteady Flow in an Imbedded Stage of a Multistage, Axial-Flow Turbomachine," *ASME Journal of Engineering for Power*, Vol. 101, pp. 42-51.
- Wisler, D. C., and Mossey, P. W., 1972, "Gas Velocity Measurements Within a Compressor Rotor Passage Using the Laser Doppler Velocimeter," ASME Paper No. 72-WA/GT-2.
- Wittig, S., Dullenkopf, K., Schulz, A., and Hestermann, R., 1987, "Laser-Doppler Studies of the Wake-Effected Flow Field in a Turbine Cascade," *ASME JOURNAL OF TURBOMACHINERY*, Vol. 109, pp. 170-176.
- Yamamoto, A., and Yanagi, R., 1985, "Production and Development of Secondary Flows and Losses Within a Three Dimensional Turbine," ASME Paper No. 85-GT-217.
- Zierke, W. C., and Okiishi, T. H., 1981, "Measurement and Analysis of Total-Pressure Unsteadiness Data From an Axial-Flow Compressor Stage," ASME Paper No. 81-Gr/GT-2.

On the Prediction of Unsteady Forces on Gas Turbine Blades: Part 2—Analysis of the Results

T. Korakianitis

Assistant Professor of Mechanical Engineering,
Washington University,
St. Louis, MO 63130

This article investigates the generation of unsteady forces on turbine blades due to potential-flow interaction and viscous-wake interaction from upstream blade rows. A computer program is used to calculate the unsteady forces on the rotor blades. Results for typical stator-to-rotor-pitch ratios and stator outlet-flow angles show that the first spatial harmonic of the unsteady force may decrease for higher stator-to-rotor-pitch ratios, while the higher spatial harmonics increase. This (apparently counterintuitive) trend for the first harmonic, and other blade row interaction issues, are explained by considering the mechanisms by which the viscous wakes and the potential-flow interaction affect the flow field. The interaction mechanism is shown to vary with the stator-to-rotor-pitch ratio and with the outlet flow angle of the stator. It is also shown that varying the axial gap between rotor and stator can minimize the magnitude of the unsteady part of the forces generated by the combined effects of the two interactions.

Introduction

The desire for more efficient, lighter, cheaper engines leads designers to consider combinations of fewer stages per engine (higher loading per stage), fewer blades per stage (larger tangential loading), and closer axial spacing between blade rows. The increased blade loading makes good aero-dynamic performance harder to obtain. The closer spacing between blade rows means that the excitations have less space to diffuse, so that the vibratory stresses that build up in modern blades are higher than those of older designs. The requirement for cheaper and lighter engines also means larger and fewer stator blades in a given stage. This increases the stator-to-rotor-pitch ratio R . The effect of increasing R is shown in Fig. 1, where the geometry of the downstream rotor is kept constant, the non-dimensional geometry of the upstream stator is identical, but R is varied by changing the value of S_{sb} . In addition a multitude of transient phenomena are at work around a blade. Depending on the flow conditions, the unsteady flow may generate forces on the blade that were not foreseen by steady-flow blade-design methods or quasi-steady approximations. Thus new designs are forced into regions of the design matrix where there is little (if any) previous experience.

Until recently the problem of turbine-blade vibration remained practically unsolved, despite various theoretical formulations of the problem. Dring and Heiser (1985) wrote: "It is interesting to note that no methods now exist to predict the magnitude of the aerodynamically induced vibratory stresses. Most designers simply assume that they will not exceed the

values they have previously experienced because there is no other choice ...".

Vibration problems are reduced to sets of equations of the form:

$$[m] \frac{d^2\{X\}}{dt^2} + [C] \frac{d\{X\}}{dt} + [K]\{X\} = \{F(t)\} \quad (1)$$

Designers need an initial estimate of the blade forces $F(t)$ ($\neq 0$) from the preliminary stages of design, before the shape of the cascades has been decided upon. The need for a method to predict the unsteady forces on turbine blades in the early stages of design will remain, even when computer programs

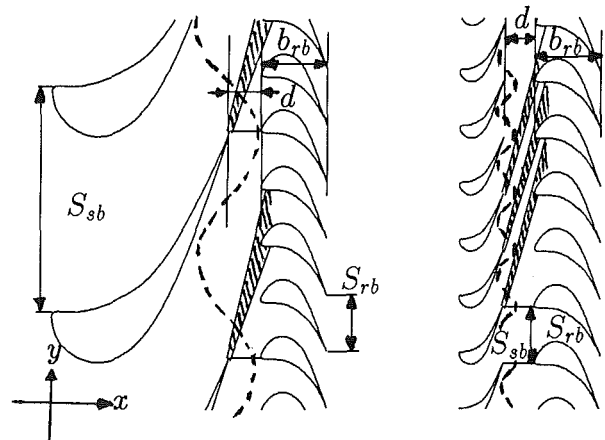


Fig. 1 The effect of R on the stage geometry. The velocity diagrams and the downstream rotors (flow from left to right) are identical. On the left, $R = S_{sb}/S_{rb} = 4.0$; on the right, $R = S_{sb}/S_{rb} = 1.0$.

Contributed by the International Gas Turbine Institute and based on two papers presented at the 33rd International Gas Turbine Conference and Exhibition, Amsterdam, The Netherlands, June 5-9, 1988. Manuscript received at ASME Headquarters December 1990. Paper Nos. 88-GT-89 and 88-GT-90.

that can evaluate the unsteady-compressible-viscous-flow equations for stator-rotor configurations become widely available.

Background

For the purposes of preliminary design it would be sufficient to study these unsteady forces on representative blades, since for slightly different blades the forces would be slightly different, but of the same order of magnitude and nature. A recent research program provided a design method for the prediction of the unsteady forces ($\{F(t)\}$ in Eq. (1)) before any time was invested in designing the blade shapes in detail (Korakianitis, 1987). The inputs to this method are: the stator and rotor velocity diagrams; the tangential spacing between blades; and the stator-to-rotor-pitch ratio R of the stage. The output is an estimate of the forces and moments acting on the two-dimensional rotor segment as a function of the relative location of rotor to stator, which can be converted to a function of time $F(t)$.

A two-dimensional parametric blade-design method was developed (Korakianitis, 1989), and thirteen representative turbine blades were designed. In these designs the location of the suction and pressure surfaces is used to control the performance of the cascade. The relative $M_o = 0.80$, $50 \text{ deg} \geq \alpha_i \geq 30 \text{ deg}$, $-50 \text{ deg} \geq \alpha_o \geq -75 \text{ deg}$ and $1.20 \geq C_L \geq 0.80$. The full geometry of these blades is available (from Korakianitis, 1987). For two-dimensional velocity diagrams of constant axial velocity one can evaluate the rotor velocity V_{rb} (and hence the stator and rotor velocity diagram) given α_N , α_i , α_o , and M_o .

Giles' (1988) computer program UNSFLO (which models the two-dimensional, unsteady, compressible, inviscid flow around rotor blades) was used to compute the flow field and the forces for ranges of R and α_N . In the computational field the problem was simplified by considering the rotor blade in the rotor-relative frame. The wake and the potential-flow interaction were modeled at the computational rotor-inlet boundary moving at the relative speed. A review of experimental data (see Korakianitis, 1987, 1992) revealed that the rate of diffusion of the velocity wakes is low and they can be felt a few chords downstream of the trailing edge at which they are generated. For subsonic cases the potential-flow interaction diffuses much faster than the velocity wakes (within about half a chord downstream of the plane in which they are created). For $d = 0.30$ the wake was modeled as an asymmetric Gaussian-distribution velocity defect of amplitude 10 percent of c_N , pressure-side characteristic width 13 percent and suction-side characteristic width 18 percent of S_{sb} . The potential-flow

interaction was modeled as a sinusoidal variation of the potential, which resulted in a 4.52 to 5.31 percent variation in the tangential component of velocity near the stator trailing edge. (In part 1 (Korakianitis, 1992) we studied the effect of the magnitude of the potential-flow disturbance; in this article we used 5 percent to obtain the results shown below.) Details of these models and the reasoning for the choice of the amplitudes of the perturbations were published by Korakianitis (1987, 1992).

The purpose of this paper is to explain the trends in the magnitude of the unsteady forces by investigating the influence of the wake and of the potential-flow interaction for various values of R .

Typical Results

Results were obtained for $1 \leq R \leq 4$ and for three different α_N for each one of the thirteen rotor cascades, and for axial gaps $d = 0.30$. The three values of α_N were chosen so as to result in rotor speeds between 380 and 580 m/s, while ensuring that the stator exit Mach number did not exceed 0.96. The full set of results has been given by Korakianitis (1987). The discussion here is facilitated by showing results for the cascade shown in Fig. 2. This cascade had $\alpha_i = 40 \text{ deg}$; $\alpha_o = -72 \text{ deg}$; $M_i = 0.2318$; $M_o = 0.80$; $C_L = 0.80$; $S_{rb} = 0.9534 \cdot b_{rb}$; and stagger angle -44 deg . Additional information for the high, medium, and nozzle angle for that cascade, and a legend for reading the results from the figures, are included in Table 1.

As explained in Part 1 (Korakianitis, 1992) we chose to present the results in the form of amplitudes and phases of the harmonics of the unsteady forces spatially analyzed over S_{sb} as a function of R and α_N , because the conventional parameters (the interblade phase angle and the reduced frequency parameter, which is inversely proportional to R) cannot be used effectively for the discussion of both the wake interaction and the potential-flow interaction. To obtain the corresponding reduced frequency parameters one can use:

$$\tilde{\omega} \equiv \frac{\omega \cdot b_{rb}}{c_x} = \frac{2\pi V_{rb}}{RS_{rb}} \cdot \frac{b_{rb}}{c_x} \quad (2)$$

The dimensional forces (such as F_x in the x direction) are related to the nondimensional forces (F'_x) by:

$$F'_x \equiv \frac{F_x/z}{\rho b_{rb} c^2} \quad (3)$$

(the moment T'_z is divided by b_{rb}^2). The steady-flow (constant) forces for the sample cascade of Fig. 2 were: $F'_{x,ss} = 0.2052$; $F'_{y,ss} = 0.1424$; and the moment $T'_{z,ss} = 0.1334$.

Nomenclature

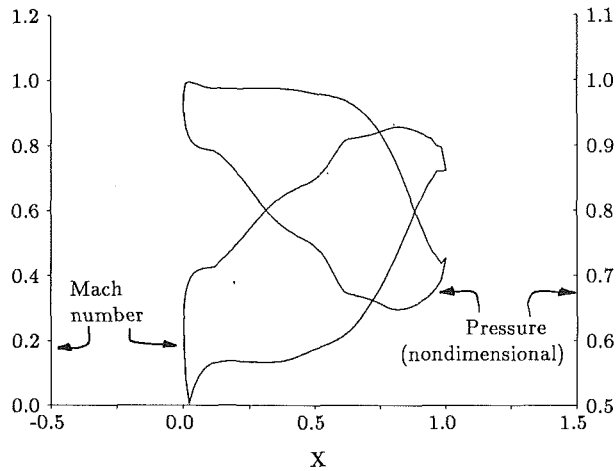
A = amplitude of a harmonic (Eq. (4))
 b = axial chord
 C = damping matrix (Eq. (1))
 C_L = tangential loading (lift) coefficient
 c = rotor-inlet total sonic velocity (Eq. (3))
 d = stator-rotor axial gap (fraction of b_{rb})
 F = dimensional force (Eq. (3))
 F' = nondimensional force (Eq. (3))
 $j \equiv \sqrt{-1}$ (Eq. (4))
 K = stiffness matrix (Eq. (1))
 M = Mach number
 m = mass matrix (Eq. (1))
 \Re = real part of an expression (in Eq. (4))
 $R \equiv S_{sb}/S_{rb}$ = stator-to-rotor-pitch ratio
 S = pitch of a cascade
 T_z = moment (in the z direction) (Eq. (3))
 t = time

V = velocity
 $\{X\}$ = displacement vector (Eq. (1))
 (x, y, z) = Cartesian coordinates (in subscripts also)
 α = flow angle
 θ = phase of a harmonic (Eq. (4))
 ρ = relative total density at rotor inlet
 ω = rotor passing frequency (Eq. (2))
 $\tilde{\omega}$ = reduced frequency parameter (Eq. (2))

Subscripts

$n \in \{0, 1, 2, \dots\}$ = order of a harmonic
 i, o = cascade inlet, outlet, respectively
 N = stator-exit (nozzle)
 nd = nondimensional (Eq. (5))
 np = parameter, equal to 1 or 10 (Eq. (5))
 rb = rotor blade row
 sb = stator blade row
 ss = steady flow

Surface Mach number and pressure distributions



Nondimensional pressure contours with increment 0.02

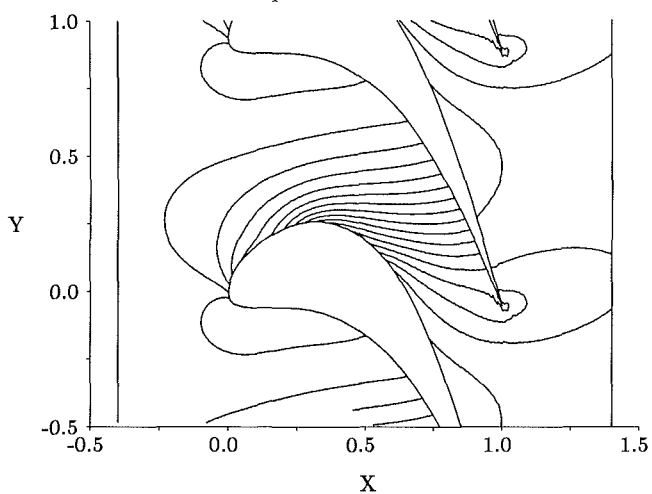


Fig. 2 Steady-flow performance of a typical rotor cascade. For this sample cascade $\alpha_i = 40$ deg; $\alpha_o = -72$ deg; $M_i = 0.234$; and $M_o = 0.800$.

The amplitudes of the unsteady forces were obtained from:

$$F'_x(y) = \Re \left\{ \sum_{n=0}^{\infty} A_{x,n} \cdot \exp(j\theta_{x,n}) \cdot \exp\left(\frac{j2\pi ny}{S_{sb}}\right) \right\} \quad (4)$$

The origin (zero) of the period of the unsteadiness in each case corresponds to the y location in which a stator velocity wake touches the leading edge of a rotor blade. The end of the period is characterized by the velocity wake from the next stator blade touching the leading edge of the same rotor blade. The average unsteady forces and moment are in most cases between 90 and 100 percent of the steady force, and in the results the amplitude of the average forces and moment ($n = 0$) have been divided by 10 to show the figures within a reasonable scale. The nondimensionalized amplitudes (e.g., $A_{nd,x,n}$), of the Fourier harmonics of the nondimensionalized forces shown in the results are related to the nondimensional amplitudes ($A_{x,n}$) by:

$$A_{nd,x,n} = \frac{A_{x,n}}{np \cdot F'_{x,ss}} \quad (5)$$

where $np = 10$ for $n = 0$ (fundamental harmonic), and $np = 1$ for $n = 1, 2, \dots$

The results exhibited similar trends for all cascades and for the forces in the axial (x), tangential (y), and for the moment in the z direction. To facilitate the discussion here we present results for the forces in the x direction for one of the cascades.

Table 1 Additional information on the sample cascade and a legend for reading the figures

	high	medium	low
α_N	79.24°	78.24°	75.58°
V_{rb} in m/s	580	520	400
line	—	- - -	- · - · -
$n = 0$	□	+	↑
$n = 1$	⊙	×	⊗
$n = 2$	△	◇	⊠

Typical results of $A_{nd,x,n}$ and $\theta_{x,n}$ for the combined viscous-wake and potential-flow interaction for this sample cascade are shown on the left side (part (a)) of Fig. 3. The figures are explained below. Within each figure of results and for each harmonic amplitude or phase, three lines are shown. The solid line corresponds to the high α_N , the dashed line corresponds to the medium α_N , and the dashed-and-dotted line corresponds to the low α_N . The average-harmonic amplitudes ($n = 0$) coincide for all cases examined here, so that the fundamental-harmonic amplitudes for the high, medium, and low α_N are not distinguishable from each other in the figures.

Although in theory one needs all the terms of the sum in Eq. (4) (to infinity), in practice the third and higher harmonics of the forces and moments were less than 0.3 percent of the force in steady flow for all the (subsonic) cases examined. Therefore only the first two harmonics are considered in the discussion of the results.

For all the blades $A_{nd,x,0}$, $A_{nd,y,0}$, and $A_{nd,z,0}$ are between 90 and 100 percent of the steady-flow forces and moment. This is because the wake interaction is a velocity defect, which results in a small loss of momentum at the rotor-inlet boundary (the potential-flow interaction does not result in a loss of momentum). In most cases the first-harmonic amplitudes of the unsteady forces and moment gradually increase as R increases from unity, and then they drop for higher values of R . This decrease in the amplitudes of the first harmonics occurs for lower values of R for the lower α_N in almost all the cases. The value of R at which the amplitudes of the first harmonics start to decrease are lower for the blades in which the α_N values are lower. The second-harmonic amplitudes of the unsteady forces and moment are one order of magnitude smaller than the amplitudes of the first harmonics, and they typically increase monotonically with increasing values of R . One would expect that as R increases the magnitude of the first harmonic would increase monotonically, as the relative importance of the unsteadiness increases. But this is not the case in all the results. This contradicts the expectations of quasi-steady approximations (which would predict a monotonic increase in the unsteady part of the forces and moment with increasing R). These results are due to the combined interaction of two effects: the velocity-wake interaction, and the potential-flow interaction. The two interactions affect the forces on the blades in a different way. In practice neither of the two effects can be eliminated from real turbomachinery flows in normal operating conditions. To explain the results it is advantageous to investigate the effects of each type of interaction isolated from the other.

Viscous-Wake-Interaction Effects

The results of a series of computational tests on the cascade of Fig. 2 in which the only disturbance was the wake, defined as above, are shown in the middle (part (b)) of Fig. 3. As R increases the first harmonic amplitude of the unsteady force increases to a maximum and then drops. This drop occurs for larger values of R for the higher stator-outlet angles. The first-harmonic amplitudes of the unsteady forces for the wake interaction are much smaller than the first-harmonic amplitudes

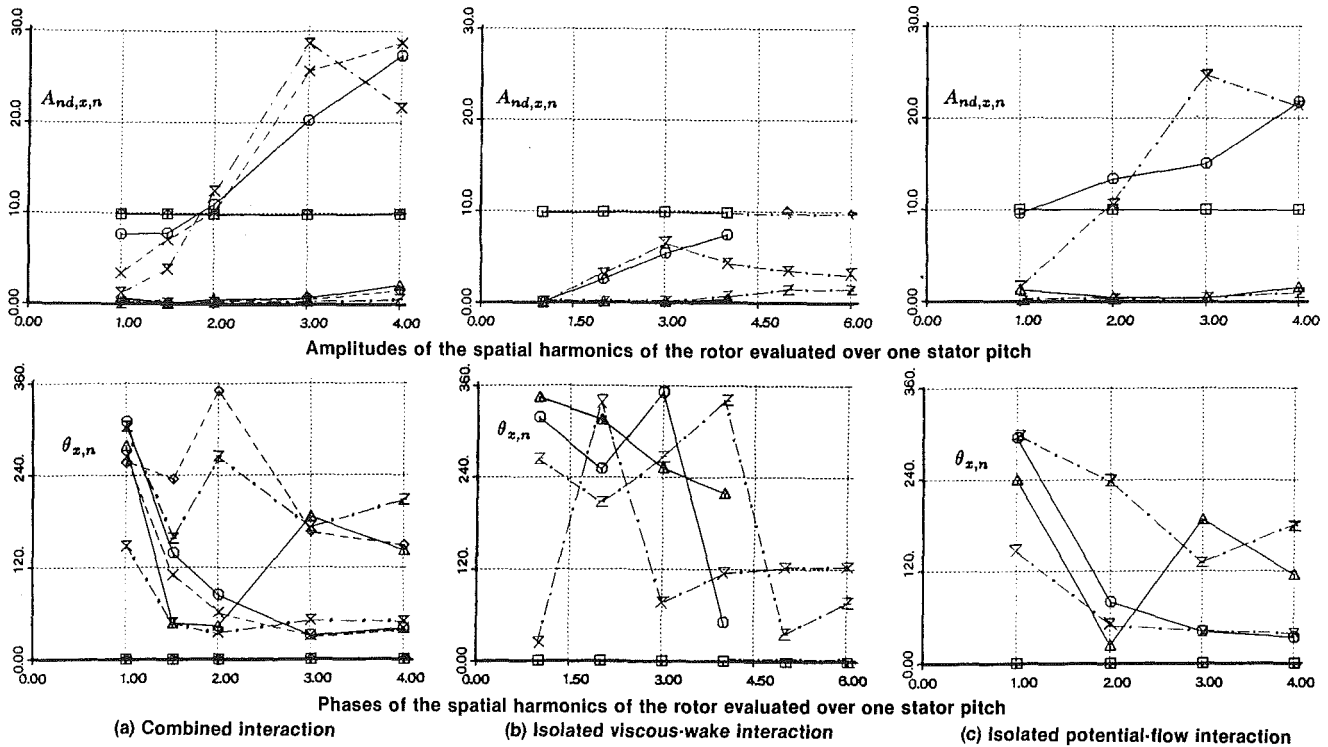


Fig. 3 Amplitudes and phases of the harmonics of $F_x'(y)$ as a function of R (the abscissae) and α_N . Table 1 includes a legend for the figure.

of the unsteady forces for the combined interaction, especially for large values of R . This indicates that for large values of R the potential-flow interaction plays a significant role in the generation of the unsteadiness.

The best way to show the propagation of the wake through the passages is to show the propagation of entropy contours through the passages. This is shown in Fig. 4, which shows entropy contours superimposed on unsteady-flow vectors (defined as instantaneous-flow vector minus steady-flow vector). Figure 5 shows the entropy contours and the corresponding unsteady pressure contours (defined as instantaneous pressure minus steady-flow pressure shown in Fig. 2). Similar plots for higher α_N show the same trends except that the wake of the low stator-outlet angle will be out of the rotor passages at an earlier point in the stator frame (or at an earlier part of the period) than the wake of the high α_N .

In the region of the leading edge the stagnation point decelerates the flow, while in the middle of the passage the velocities are much higher. This variation of flow velocity in the entrance to the rotor passage causes the wake to bend slightly around the leading edge of blade 0. When this blade has moved a little farther upstream it will cut the wake into two segments. The upstream portion of the wake will remain attached to the stator trailing edge, while the downstream portion of the wake will act in the passage between blades 0 and 1. This portion of the wake will propagate in the passage downstream. The wake from the previous stator has already been cut and the downstream portion of it is shown in Figs. 4 and 5 acting in the passage between blades -1 and 0. Since $R = 2.0$ the flow in the passage between blades -1 and 0 is identical to the flow in the passage between blades 1 and 2.

The flow patterns observed upstream and downstream of the wake centerlines are recirculating-flow patterns, which have been observed in the experimental data obtained by Adachi and Murakami (1979), Binder and Romey (1983), Binder et al. (1985), Binder (1985) (recirculating-flow patterns are not shown in these references, but were deduced from the original data, which we purchased, and are shown in Fig. 3 of Part 1 (Korakianitis, 1992)), Hodson (1983, 1984) and others. These recirculating-flow patterns can be explained by refining the

earlier wake-interaction models of Meyer (1958), Lefcort (1965), and Smith (1966). The above do not explain the rotation of the wake centerlines in the rotor passages. The recirculating-flow patterns are explained by a lower-momentum-fluid "jet" that transports lower-momentum fluid from the wake region near the pressure surface to the wake region near the suction surface. When the wake fluid approaches the suction surface it curves to produce recirculating-flow patterns, which are shown as two counterrotating vortices in the unsteady-flow-vector plots. These vortices flank the wake centerline. One vortex is upstream of the wake centerline and the other vortex is downstream of the wake centerline. Since the initial vorticity of the flow must be conserved, the two vortices flanking each wake segment in the rotor passages are of equal and opposite sign. The upstream unsteady-flow-vector vortex is directed into the plane of the flow (defined negative) and the downstream unsteady-flow-vector vortex is directed out of the plane of the flow (defined positive).

This relative motion of wake fluid from the pressure side of the passage to the suction side causes a thinning of the wake near the pressure side and a thickening of the wake near the suction side. The ends of the wake, which are attached to the two sides of the passage, propagate downstream at the local flow velocities, which are approximately equal to the local flow velocities in steady flow. Since the local flow velocities on the suction side are higher than the local flow velocities on the pressure side of the passage, the portion of the wake that is attached to the suction surface propagates downstream faster than the portion of the wake attached to the pressure surface. This results in a counterclockwise turning of the wake centerline in the passage. Near the trailing edges of the cascade there is a region of diffusion on the suction surface of the blades, which decelerates the passage- and the wake-velocity distribution across the line of the trailing edges.

These "jets" result in an instantaneous pressure minimum on the pressure surface (due to suction from the generation of the "jet") and an instantaneous pressure maximum on the suction surface (due to impingement of the "jet"). The temporal variation of these instantaneous pressure maxima and minima, which act in addition to the local pressure in steady

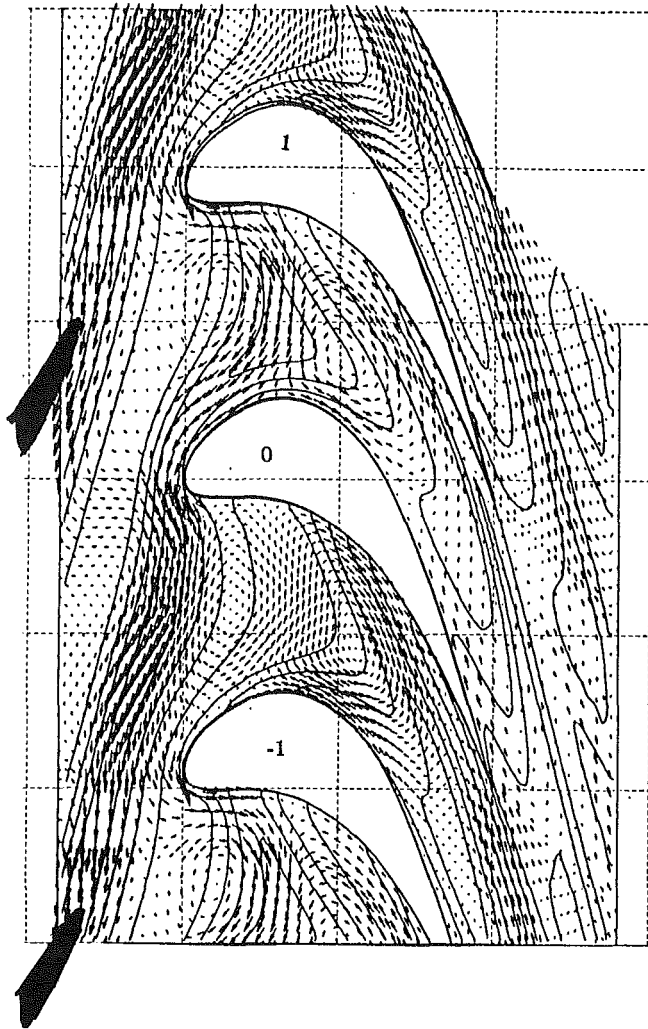


Fig. 4 Entropy contours (increment 0.40) and unsteady flow vectors for $R = 2.0$, for low α_N and for isolated wake interaction

flow, generate the unsteady forces on the blade. Better explanations of the wake propagation have been published recently (Korakianitis, 1991). The magnitudes of the harmonic amplitudes of the unsteady forces depend on the variations of these unsteady pressures from the average pressure on the rotor blades (hence the definition of the unsteady pressure contours). The phases of the harmonic amplitudes of the unsteady forces depend on the nozzle angle that generated the wake, because the nozzle angle determines the angle with which the wake enters the rotor passages.

As R increases, the width of the wake increases proportionately, and it occupies a larger portion of the rotor passage. Alternatively, as R increases, fewer and wider viscous wakes act per rotor-blade passage. This explains the general trend to higher first-harmonic amplitudes for the unsteady forces and moment as R increases. Extending this argument one would expect the amplitude of the first harmonic to increase monotonically and perhaps level off at some high value of R . This does not explain the drop in the amplitude of the first harmonic for high values of R . The reason for this drop is that the mechanism for the generation of the unsteady forces due to the wake interaction changes when the wake becomes wide enough, or when α_N becomes low enough. Then the downstream unsteady-flow-vector vortex of the wake (the positive one) exits from the rotor passage while the upstream unsteady-flow-vector vortex (the negative one) is still in the process of forming. The effect of this is shown in Fig. 6, which shows the location of the velocity wakes for $R = 6.0$ for the low α_N

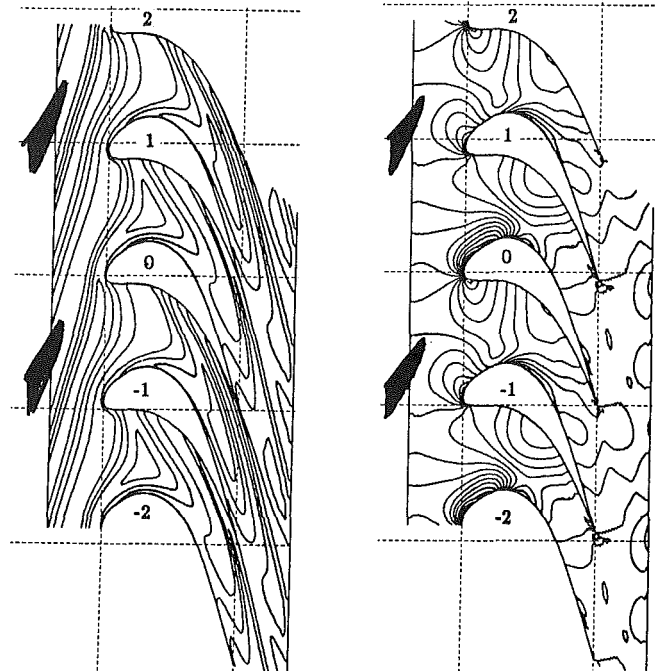


Fig. 5 Entropy contours (left, increment 0.40) and unsteady pressure contours (right, increment 0.002) for $R = 2.0$, for low α_N for isolated wake interaction

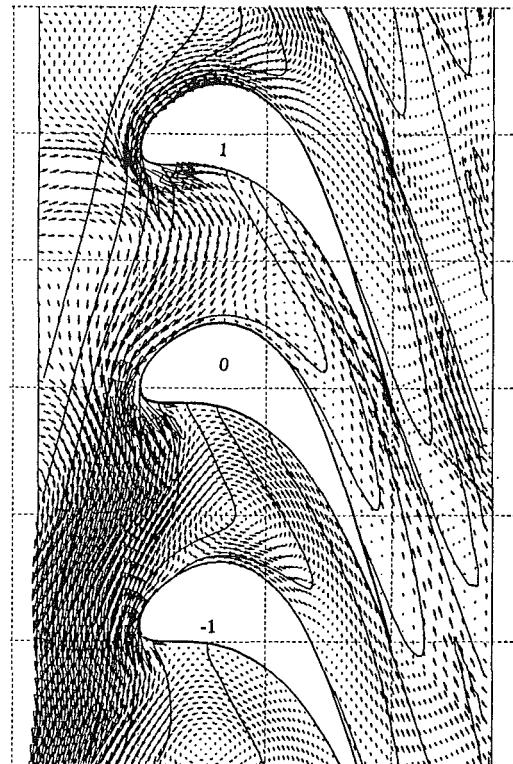


Fig. 6 Entropy contours (increment 0.40) and unsteady flow vectors for $R = 6.0$, for low α_N and for isolated wake interaction

case as entropy contours superimposed on unsteady flow vectors. Figure 7 shows the entropy contours and the corresponding unsteady pressure contours, which indicate that the wake affects the passages between blades 2, 3, 4, and 5 very little. Unsteady flow vectors are therefore shown for the passages between blades -1 , 0, and 1 only. The wake in this case is so wide with respect to the rotors that a portion of the wake flow has curved into the passage between blades -2 and -1 and it has already formed the downstream (positive) unsteady-flow-

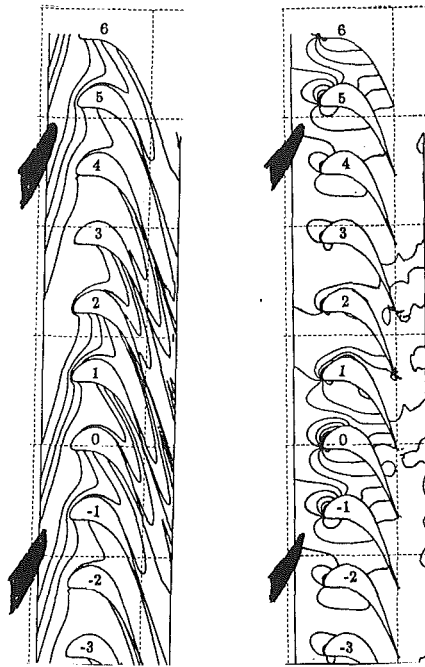


Fig. 7 Entropy contours (left, increment 0.40) and unsteady pressure contours (right, increment 0.004) for $R = 6.0$, for low α_N and for isolated wake interaction

vector vortex. In fact this action has almost started in the passage between blades -3 and 2 . In the passage between blades 1 and 2 the downstream (positive) unsteady-flow-vector vortex has already propagated downstream of the rotor cascade and its "jet" effect produces suction on the suction surface of blade 2 . In the same passage (between blades 1 and 2) the upstream (negative) unsteady-flow-vector vortex has just about formed and its "jet" effect produces pressure on the suction surface of blade 2 . These effects reduce the amplitude of the first harmonic of the unsteady forces.

For smaller values of R the downstream (positive) vortices act in a similar fashion, but this effect near the trailing edges is minimized for two reasons. The first reason is that for smaller values of R there usually is more than one wake per passage. The other wakes act to produce the "jets" in the middle of the passages, which minimize the effect of the vortex near the trailing edge acting to reduce the unsteady forces. The second reason is that for smaller values of R the unsteady force associated with each individual vortex (or "jet") is smaller than the unsteady force associated with each individual vortex for larger values of R . Thus when the downstream vortex exits the trailing edge region it actually acts in a way contrary to the way the unsteady-flow-vector vortices acted in the middle of the passage, where they always produced unsteady-pressure maxima on the suction side and unsteady-pressure minima on the pressure side. Therefore when the combination of the value of R and α_N is such as to result in one or less wake acting per rotor passage, then the first-harmonic amplitude of the unsteady forces due to the isolated wake interaction will be smaller than that for smaller values of R . The above effects become more dominant as R increases and as α_N decreases.

For relatively small values of R the variation of the unsteady forces along the full stator period is almost a sinusoidal function, because a number of wakes act on the passages to produce consecutive local maxima and minima in the unsteady pressures (see Fig. 5). As R increases the variation of the unsteady forces along the full stator period is less of a sinusoidal function, because fewer and wider wakes act per rotor passage. When R is large enough for one wake to act on some (but not all) of the rotor passages of one period, the effect of the wider wake is a reduction in the first-harmonic amplitude of the

unsteady forces. In these cases the rotor blades experience only portions of the effect of the wake-fluid "jet" as one of the two unsteady flow vortices is not acting in the passages. This explains the drop in the first-harmonic amplitudes of the unsteady forces for large values of R , for low α_N , and for combinations of the two. As R increases the viscous wakes do not act for large portions of the stator period on the rotor blades. The forces as a function of stator period show a sinusoidal variation near the beginning of the period due to the action of the wake. For the rest of the period (until close to the end of it) the forces become almost constant because there is no disturbance from the wake for these portions of the period (see Fig. 7). Near the end of the period the next incoming wake starts to affect the passages by beginning to form the downstream (positive) unsteady flow vortex. The number of rotor passages affected by the next wake in these large values of R depends on α_N and on the width of the wake (which is a function of R). As R increases further, higher harmonics become more important in order to recapture the spatial shape of these unsteady forces. This explains the trends of the second-harmonic amplitudes of the unsteady forces as R increases.

Potential-Flow-Interaction Effects

The sinusoidal potential-flow-interaction model was considered adequate for the purposes of this study, which did not consider a specific stator geometry.

The results of a series of computational tests for the isolated potential-flow interaction on the cascade of Fig. 2 for high and low α_N are shown on the right (part (c)) of Fig. 3. These results show similar trends with the results of the cases in which the isolated wake interaction is acting on the blades and with the results of the combined interaction of both disturbances. However, the amplitudes of the harmonics of the unsteady forces are different in two important ways: the magnitudes of the first-harmonic amplitudes of the unsteady forces for the isolated potential-flow interaction are much larger than the corresponding magnitudes for the isolated wake interaction; and the fundamental (average) harmonics of unsteady forces and moment for the isolated potential-flow interaction are equal to the steady-flow forces and moment (because the isolated potential-flow interaction does not constitute a loss of momentum). Thus in the results of unsteady-flow computations for the combined interaction (part (a) of Fig. 3) the changes of the average unsteady forces and moment from the steady-flow forces and moment are due to the effects of the wake interaction. These trends are general and they are true for wide ranges of amplitudes for both disturbances to the flow (Korakianitis, 1987). These observations lead to the following conclusion: The assumption by many researchers (before the present work) that the potential-flow interaction is negligible compared to the viscous-wake interaction is erroneous. In the following it will actually be shown that as the stator-to-rotor-pitch ratio R increases the effect of the potential-flow interaction on the rotor unsteadiness also increases.

The potential-flow interaction was prescribed by the use of isentropic relationships (Korakianitis, 1987, 1992). Thus the unsteadiness imposed by the potential-flow interaction cannot be seen clearly in any of the conventional contour plots (entropy, pressure, total pressure, Mach number, density, enthalpy, stagnation enthalpy, entropy, etc.). The unsteady flow vectors for potential-flow interaction decrease very rapidly downstream and they do not contribute to the understanding of how the instantaneous pressure minima and maxima are generated, or how they affect the blade passages downstream. The best way to show the potential-flow interaction is to plot the unsteady pressure contours. Figure 8 shows unsteady-pressure-contour plots for $R = 1.0$ and $R = 3.0$. The unsteady-pressure maxima are centered around the stator trailing edges, and the unsteady-pressure minima are centered around the middle of the line joining the trailing edges. These unsteady-

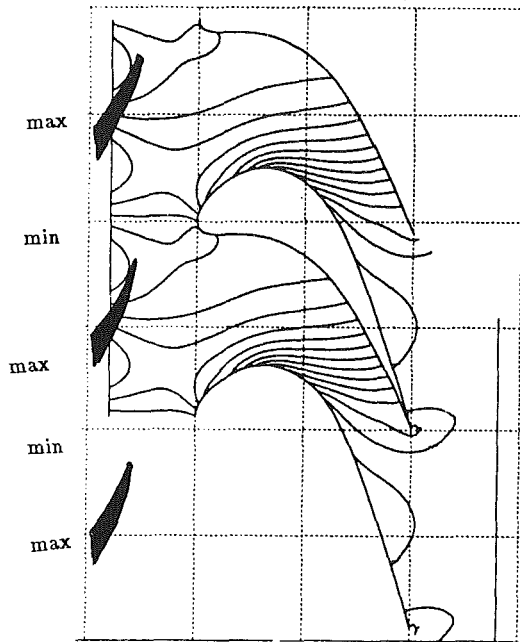


Fig. 8(a) For $R = 1.0$ and for low α_N (increment 0.010)

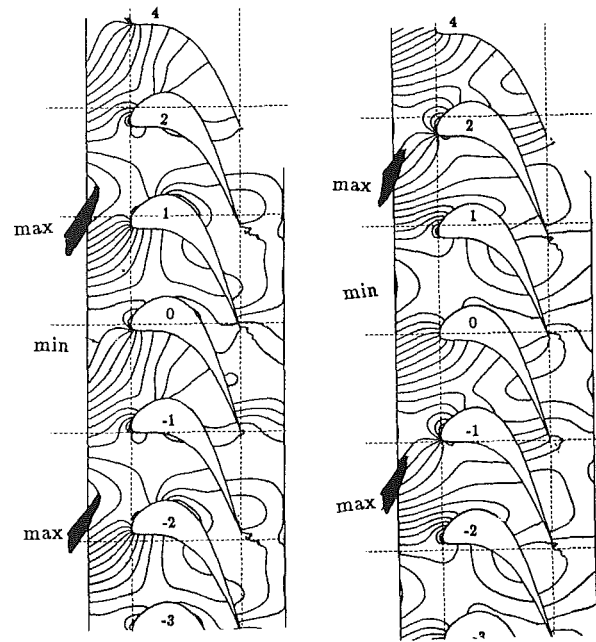


Fig. 8(b) For $R = 3.0$, for high (left) and for low (right) α_N (increment 0.005)

Fig. 8 Unsteady pressure contours for isolated potential-flow interaction

pressure variations generate the unsteady forces. Figure 8 shows that the unsteadiness is much larger at the rotor-inlet boundary and near the leading edge of the rotor cascade than at any other location in the passage, and that it decays exponentially downstream. It also shows how the rotor cascade cuts into the prescribed pressure disturbances due to the potential-flow interaction between the stator and the rotor. For $R = 1.0$ the unsteadiness acts over approximately 30 percent of the rotor axial chord. This explains the conclusions of Fleeter et al. (1978, 1980), Capece et al. (1985), and Capece and Fleeter (1986), who for small values of R observed that the unsteady-pressure disturbances in multi-stage compressor cascades dominate in the front part of the cascades. Figure 8 shows that for $R = 3.0$ the unsteadiness affects the rotor cascade from the leading edge to the trailing edge. In the region near the rotor blades and inside the rotor passages the prescribed potential-flow interaction from the stator trailing edge and the potential flow field of the rotor itself influence each other. Therefore the first-harmonic amplitudes of the unsteady forces increase with R , because R affects the rate of decay of the potential-flow disturbance. For low values of R the potential-flow interaction affects only the leading edge region of the rotor blades, while for higher values of R the potential-flow interaction affects the whole of the rotor cascade.

The effects of α_N are much harder to visualize and they are explained more easily by considering that higher α_N corresponds to a higher rotor tangential velocity V_{rb} . The angle along which the pressure maxima due to the potential-flow interaction lie in the absolute frame is a weak function of α_N . For the sample blade this angle (in the stator frame) is equal to -9.7 deg for the high α_N and -7.2 deg for the low α_N . For the hypothetical case of a rotor cascade that moves with almost zero tangential velocity, the α_N is 40 deg and the line along which the local pressure maxima due to the potential-flow interaction extend from the stator trailing edges is -1.6 deg. Although the pressure variation due to the potential-flow interaction is a pressure disturbance entering the rotor passages, this pressure disturbance does not “propagate” downstream into the rotor passages at the sonic or at any other velocity. The potential-flow disturbance is a pressure field that is located in the traverse of the rotor cascade; it is affected by the potential-flow interaction of the rotor itself, but it does

not “propagate.” The pressure disturbances due to the potential-flow interaction are a function of the local static density in steady flow conditions; the local velocities u and v in steady flow conditions; and the local unsteady velocities due to the potential-flow interaction δu and δv . The rate at which these pressure disturbances are collected in successive rotor passages depends on the rotor velocity. This can be seen by considering two limiting cases for values of R that are large enough for the potential-flow effects from the stator to affect the whole rotor passage (for example, consider $R \geq 3.0$).

For the first limiting case consider the rotor moving with infinitely low tangential speed. Then the collection of the pressure disturbances due to the potential-flow interaction at the rotor inlet can be visualized by a quasi-steady approximation. This will result in an unsteady-pressure maximum or an unsteady-pressure minimum dominating each one of the rotor passages at each instant. For the second limiting case consider the rotor moving with high enough tangential velocity to result in absolute flow at the rotor inlet that is just subsonic. In this case one can visualize the inlet of each rotor passage traversing through a succession of unsteady-pressure maxima and minima such that a few of these unsteady-pressure maxima and minima act in each passage at once. Some of these layers can be seen in the passages of Fig. 8. The location of these unsteady-pressure maxima and minima in each passage is affected by the potential flow field of the rotor itself, and it may act to increase or decrease the first-harmonic amplitude of the unsteady forces and moment. These arguments are complicated by the decay rate of the unsteady-pressure maxima and minima, which is a function of R . If the relative positions of rotors and pressure disturbances are such as to generate increases in unsteady pressure in consecutive passages or decreases in unsteady pressure in consecutive passages (which tend to cancel unsteady forces) then the resulting amplitudes of the harmonics of the unsteady forces are relatively smaller. If the relative positions of rotors and pressure disturbances are such as to generate increases in unsteady pressure in one passage and decreases in unsteady pressure in the next passage (which tend to increase unsteady forces) then the resulting amplitudes of the harmonics of the unsteady forces are relatively larger. Better explanations of the potential-flow interaction have been published recently (Korakianitis, 1991).

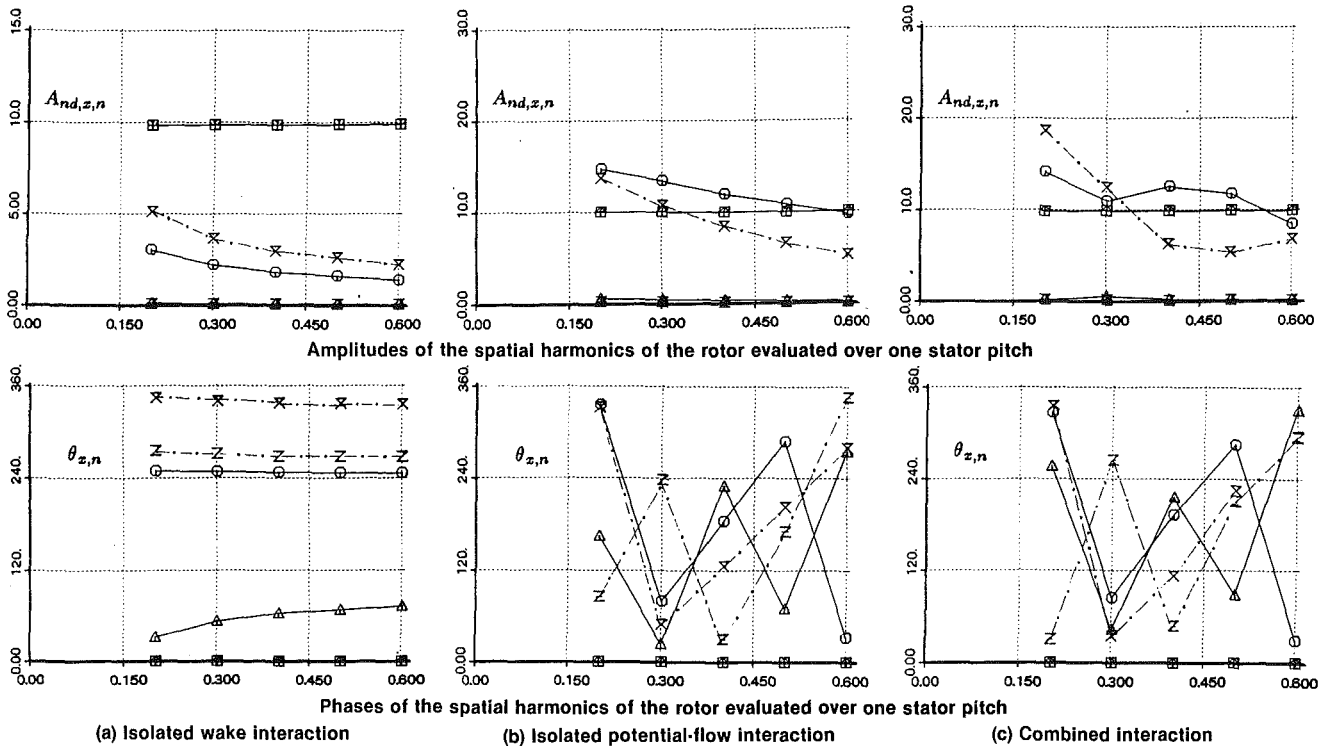


Fig. 9 Amplitudes and phases of the harmonics of $F_x(y)$ for $R = 2.0$ as a function of axial gap d (the abscissae) and α_N . Table 1 includes a legend for the figure.

Axial-Gap Effects

The wake-interaction and the potential-flow interaction effects discussed above do not have equal phase with respect to one stator period. Gallus et al. (1982) showed experimentally that large changes in the axial gap between compressor blade rows result in small changes in the unsteady forces due to wakes, and that small changes in the axial gap result in large changes in the unsteady forces due to potential-flow interaction (see Fig. 14 of that reference). Experimental evidence that decreasing the axial gap between blade rows may actually reduce the losses was provided by Smith (1970), Kramer et al. (1972), and Mikolajczak (1976). Wittig et al. (1987) also showed that the turbulence levels change considerably by changing the axial gap. Dring et al. (1982), by reviewing the results of Smith (1970), Mikolajczak (1976), Hetherington and Moritz (1976), Kosyak et al. (1973), Messegee (1967), Due et al. (1975), and Okapuu (1974), arrived at the following conclusions: There is an optimum axial gap between rotors and stators; the value of this optimum axial gap is hard to generalize; and for changes in axial gap over the ranges found in current engines the change in overall turbine or compressor efficiency could be as much as 2 percent.

As the axial gap between rotor and stator increases the amplitude of the velocity defect of the wake decreases, the wake width increases and the amplitude of the potential-flow interaction at a line joining the leading edges of the rotor cascade decreases. The phases of the unsteadiness due to the wake interaction do not change (since the beginning of the period is defined by the wake centerline), but the phases of the unsteadiness due to the potential-flow interaction change considerably. Therefore the designer could try to arrange so that the maximum of the velocity-wake interaction unsteadiness coincides with the minimum of the potential-flow-interaction unsteadiness by varying the axial gap between the rotor and the stator. (Other factors such as cost and weight will also influence these considerations.)

In order to illustrate these effects we ran tests with the high and low α_N for $R = 2.0$. In the first test we obtained results

for the isolated wake-interaction while varying the axial gap d and the corresponding wake specification for five values of the axial gap: 0.20, 0.30, 0.40, 0.50, and 0.60. The corresponding wake amplitudes were 0.15, 0.10, 0.08, 0.07, and 0.06 (because wake diffusion in UNSFLO is only due to numerical diffusion). The suction-side characteristic widths were 0.15, 0.18, 0.20, 0.21, and 0.22. The pressure-side characteristic widths were 0.10, 0.13, 0.15, 0.16, and 0.17. The results of these tests are shown on the left (part (a)) of Fig. 9. They show that the amplitudes $A_{nd,x,1}$ of the first harmonics of the unsteady forces decrease monotonically as the axial gap increases, while the phases $\theta_{x,1}$ remain reasonably constant (as expected). The second-harmonic amplitudes of the unsteady forces are insignificant for this low value of R . In the second test we obtained results for the isolated potential-flow interaction while varying the axial gap. The five values of the axial gap were: 0.20, 0.30, 0.40, 0.50, and 0.60. The amplitude of the velocity disturbance due to the potential-flow interaction was kept constant, since the potential-flow interaction models the decay from the stator trailing edge (Korakianitis, 1987, 1992). The results of these tests for the force in the axial direction, shown in the middle (part (b)) of Fig. 9, indicate that the amplitudes of the first harmonics $A_{nd,x,1}$ of the unsteady forces for the isolated potential-flow interaction decrease faster than the amplitudes of the first harmonics of the unsteady forces for the isolated wake interaction as the axial gap increases, while the phases $\theta_{x,n}$ of the harmonics of the isolated potential-flow interaction change considerably (as expected).

The phase angles $\theta_{x,1}$ of the first harmonics of the unsteady forces in the x direction due to the isolated wake interaction are about 245 deg for the high α_N and about 340 deg for the low α_N . The phase angles $\theta_{x,1}$ of the first harmonics of the unsteady forces in the x direction due to the isolated potential-flow interaction are about 65 deg for the high α_N , and about 160 deg for the low α_N (corresponding to 180 deg out of phase with the phases of the harmonics due to the isolated wake interaction), for axial gaps of 0.30 and 0.58 for the high α_N and for axial gap of 0.45 for the low α_N . Of course the resulting

unsteady forces depend mainly on the amplitudes of the harmonics, but any counteracting of these unsteady forces is expected at these axial gaps.

These expectations were confirmed by running a third test case for the combined interaction. This test was run with the combined effects of the wake interaction and the potential-flow interaction while varying the axial gap. The results of the third test are shown on the right (part (c)) of Fig. 9 and they confirm the predicted results. The amplitudes of the first harmonics indeed show the expected local minima at the corresponding axial locations.

Conclusions and Recommendations

The unsteady forces on two-dimensional gas-turbine rotors due to potential-flow interaction and viscous-wake interaction from upstream blade rows were computed using a two-dimensional, compressible, inviscid rotor/stator-disturbance interaction program. Unsteady (local instantaneous minus local steady) pressure contours were particularly useful in explaining the interaction mechanisms. It was found that the potential-flow interaction is the dominant cause of unsteady loading over the wake interaction for stator-to-rotor-pitch ratios of design interest. Depending on the stator-to-rotor-pitch ratio and the nozzle angle, the wake interaction causes unsteady loads of the order of 0.5 to 8 percent of the steady load, while the potential-flow interaction causes unsteady loads of the order of 2 to 25 percent of the steady load (in some cases not shown here the higher number approached 40 percent). For flows that are just subsonic and in all geometric cases examined the dominant harmonic of the spatially (or temporally) analyzed unsteady force is the first. The magnitude of higher harmonics increases with increasing stator-to-rotor-pitch ratio. It was shown that variations in the axial gap between rotor and stator can be used to control the amplitude and the phase of the unsteadiness.

It is recommended that the results of this work be tested against experimental data. Further investigation is recommended to study the effects of the following: cooling flows, different potential-flow interaction models, two-dimensional and three-dimensional vortex disturbances, supersonic stator exits, blade erosion, dihedral, circumferential, and axial location of blade rows in multistage components, blade vibration, flutter, and acoustic resonance. It is also recommended that the effects of the wake interaction and the effects of the potential-flow interaction be separated by computing experiments using a viscous code for stator-rotor interactions.

Acknowledgments

The author thanks Professors David Gordon Wilson, A. D. Carmichael, Michael B. Giles, and Anthony T. Patera of MIT, and Mr. Dennis C. Evans of GE (Lynn, MA) for their advice, support, encouragement and constructive suggestions. The material presented in this paper was part of a larger research program funded by GE.

References

Adachi, T., and Murakami, Y., 1979, "Three-Dimensional Velocity Distribution Between Stator Blades and Unsteady Force on a Blade Due to Passing Wakes," *Bulletin of the JSME*, Vol. 22, pp. 1074-1082.

Binder, A., and Romey, R., 1983, "Secondary Flow Effects and Mixing of the Wake Behind a Turbine Stator," *ASME Journal of Engineering for Power*, Vol. 105, pp. 40-46.

Binder, A., Förster, W., Kruse, H., and Rogge, H., 1985, "An Experimental Investigation Into the Effects of Wakes on the Unsteady Turbine Rotor Flow," *ASME Journal of Engineering for Gas Turbines and Power*, Vol. 107, pp. 458-466.

Binder, A., 1985, "Turbulence Production Due to Secondary Vortex Cutting in a Turbine Rotor," *ASME Journal of Engineering for Gas Turbines and Power*, Vol. 107, pp. 1039-1046.

Capece, V. R., Manwaring, S. R., and Fleeter, S., 1985, "Unsteady Blade Row Interactions in a Multi-stage Compressor," AIAA Paper No. 85-1135.

Capece, V. R., and Fleeter, S., 1986, "Wake Induced Unsteady Aerodynamic Interactions in a Multi-stage Compressor," AIAA Paper No. 86-1455.

Dring, R. P., Joslyn, H. D., Hardin, L. W., and Wagner, J. H., 1982, "Turbine Rotor-Stator Interaction," *ASME Journal of Engineering for Power*, Vol. 104, pp. 729-742.

Dring, R. P., and Heiser, W. H., 1985, "Turbine Aerodynamics," G. C. Oates, ed., *Aerothermodynamics of Gas Turbine and Rocket Propulsion*, Chap. 4, AIAA Education Series.

Due, H. F., Easterling, A. E., and Rogo, C., 1975, "Cascade Research on Small, Axial High-Work, Cooled Turbine," ASME Paper No. 75-GT-62.

Fleeter, S., Jay, R. L., and Bennett, W. A., 1978, "Rotor Wake Generated Unsteady Aerodynamic Response of a Compressor Stator," *ASME Journal of Engineering for Power*, Vol. 100, pp. 664-675.

Fleeter, S., Bennett, W. A., and Jay, R. L., 1980, "The Time-Variant Aerodynamic Response of a Stator Row Including the Effects of Airfoil Camber," *ASME Journal of Engineering for Power*, Vol. 102, pp. 334-343.

Gallus, H. E., Grollius, H., and Lambert, J., 1982, "The Influence of Blade Number Ratio and Blade Row Spacing on Axial-Flow Compressor Stator Blade Dynamic Load and Stage Sound Pressure Level," *ASME Journal of Engineering for Power*, Vol. 104, pp. 633-641.

Giles, M. B., 1988, "Calculation of Unsteady Wake/Rotor Interactions," *AIAA Journal of Propulsion and Power*, Vol. 4, pp. 356-362.

Hetherington, R., and Moritz, R. R., 1976, "Influence of Unsteady Flow Phenomena on the Design and Operation of Aero Engines," AGARD Conference Proceedings No. 177, 46th propulsion and Energetics Panel Meeting, Sept. 22-26, 1975; published Apr. 1976.

Hodson, H. P., 1983, "Unsteady Boundary-Layers on Axial-Flow Turbine Rotor Blades," Ph.D. thesis, University of Cambridge, United Kingdom.

Hodson, H. P., 1985, "An Inviscid Blade-to-Blade Prediction of a Wake-Generated Unsteady Flow," *ASME Journal of Engineering for Gas Turbines and Power*, Vol. 107, pp. 337-344.

Korakianitis, T., 1987, "A Design Method for the Prediction of Unsteady Forces on Subsonic, Axial Gas-Turbine Blades," Doctoral thesis (Sc.D.) in Mechanical Engineering, Massachusetts Institute of Technology, Cambridge, MA.

Korakianitis, T., 1988a, "On the Prediction of Unsteady Forces on Gas-Turbine Blades. Part 1: Typical Results and Potential-Flow-Interaction Effects," ASME Paper No. 88-GT-89.

Korakianitis, T., 1988b, "On the Prediction of Unsteady Forces on Gas-Turbine Blades. Part 2: Viscous-Wake-Interaction and Axial-Gap Effects," ASME Paper No. 88-GT-90.

Korakianitis, T., 1989, "Design of Airfoils and Cascades of Airfoils," *AIAA Journal*, Vol. 27, pp. 455-461.

Korakianitis, T., 1991, "On the Propagation of Viscous Wakes and Potential Flow in Axial-Turbine Cascades," *ASME JOURNAL OF TURBOMACHINERY*, in press.

Korakianitis, T., 1992, "On the Prediction of Unsteady Forces on Gas Turbine Blades: Part 1—Description of the Approach," *ASME JOURNAL OF TURBOMACHINERY*, Vol. 114, this issue, pp. 114-122.

Kosyak, Y. F., Sobolev, S. P., Yushkovich, Y. E., Golamn, V. I., and Petrusenko, P. S., 1973, "Selecting the Axial Clearances Between the Stages of a Turbine," *Tepolenergetika*, Vol. 20, pp. 17-18.

Kramer, J. J., Hartman, M. J., Leonard, B. R., Klapproth, J. F., and Sofrin, T. G., 1972, "Fan Noise and Performance," *Aircraft Engine Noise Reduction*, NASA SP-311.

Lefcort, M. D., 1965, "An Investigation of Unsteady Blade Forces in Turbomachines," *ASME Journal of Engineering for Power*, Vol. 87, pp. 345-354.

Messege, J., 1967, "Influence of Axial and Radial Clearances on the Performance of a Turbine Stage With Blunt Edge Non-twisted Blades," Master's thesis, U.S. Naval Postgraduate School, Monterey, CA.

Meyer, R. X., 1958, "The Effect of Wakes on the Transient Pressure and Velocity Distributions in Turbomachines," *Transactions of the ASME*, Vol. 80, pp. 1544-1552.

Mikolajczak, A. A., 1976, "The Practical Importance of Unsteady Flow," AGARD Conference Proceedings No. 177, 46th Propulsion and Energetics Panel Meeting, Sept. 22-26, 1975; published Apr. 1976.

Okapuu, U., 1974, "Some Results From Tests on a High Work Axial Gas Generator Turbine," ASME Paper No. 74-GT-81.

Smith, L. H., 1966, "Wake Dispersion in Turbomachines," *ASME Journal of Basic Engineering*, Vol. 88, pp. 688-690.

Smith, L. H., 1970, "Casing Boundary Layers in Multistage Compressor," L. S. Dzung, ed., *Flow Research on Blading*, Elsevier Publishing Company, New York.

Wittig, S., Dullenkopf, K., Schulz, A., and Hestermann, R., 1987, "Laser-Doppler Studies of the Wake-Effectuated Flow Field in a Turbine Cascade," *ASME JOURNAL OF TURBOMACHINERY*, Vol. 109, pp. 170-176.

The Aerodynamic and Mechanical Performance of a High-Pressure Turbine Stage in a Transient Wind Tunnel

A. G. Sheard¹

Rotadata Ltd.,
Derby, United Kingdom

R. W. Ainsworth

University of Oxford,
Department of Engineering Science,
Oxford, United Kingdom

A new transient facility for the study of time mean and unsteady aerodynamics and heat transfer in a high-pressure turbine has been commissioned and results are available. A detailed study has been made of aspects of the performance and behavior relevant to turbine mechanical design, and an understanding of the variation of the turbine operating point during the test, crucial to the process of valid data acquisition, has been obtained. In this paper the outline concept and mode of operation of the turbine test facility are given, and the key aerodynamic and mechanical aspects of the facility's performance are presented in detail. The variations of the those parameters used to define the turbine operating point during facility operation are examined, and the accuracy with which the turbine's design point was achieved calculated. Aspects of the mechanical performance presented include the results of a finite element stress analysis of the loads in the turbine under operating conditions, and the performance of the rotor bearing system under these arduous load conditions. Both of these aspects present more information than has been available hitherto. Finally, the future work program and possible plans for further facility improvement are given.

1 Introduction

In order to obtain useful heat transfer and pressure field information in rotating turbines at engine representative conditions, globally there is much current activity in the use of short-duration facilities to provide the necessary fluid flow conditions. Three separate concepts may be identified: rotating turbine stages mounted (i) on shock tunnels with a run time of order 10–20 ms (Dunn and Hause, 1982); (ii) on Isentropic Light Piston Tunnels with a run time of order 200 ms (Ainsworth et al., 1988); (iii) on blowdown facilities with run times of the order of 1 s (Epstein et al., 1984). This paper is concerned with the second of these developments. The I.L.P.T. concept is of a free piston compressor, in which the working fluid is compressed isentropically over a period of approximately 1 s to the required temperature and pressure, then passed through a working section under steady state conditions for a period of 0.25 s. This is achieved using gas from a high-pressure reservoir to drive a light piston down a pump tube, isentropically compressing the gas in front of it (Fig. 1). A fast-acting valve (the Annular Gate Valve) separates the pump tube from the working section, and is rapidly opened (30 ms) when the required pressure and temperature have been reached at the end of compression. Further details of the principles of these tunnels are given by Jones et al. (1970) and Schultz et al. (1977).

¹Formerly at Oxford University.

Contributed by the International Gas Turbine Institute and presented at the 35th International Gas Turbine and Aeroengine Congress and Exposition, Brussels, Belgium, June 11–14, 1990. Manuscript received by the International Gas Turbine Institute January 18, 1990. Paper No. 90-GT-353.

The I.L.P.T. has been used at Oxford by Doorly (1983), Doorly and Oldfield (1985), Doorly et al. (1985), Ashworth et al. (1985), Schultz et al. (1987), Johnson et al. (1989, 1990) and Rigby et al. (1989, 1990) with a rotating bar placed upstream of a stationary two-dimensional cascade of rotor blades to simulate the unsteady effects of the nozzle guide vane wake and shock system on the heat transfer and flow field of a moving downstream rotor. This work has culminated in the postulation of at least five mechanisms of unsteady interaction. In addition to wake and shock propagation effects there are many other aspects of the engine thermofluids that are known to be of importance. These include potential flow interactions (vane upstream and rotor downstream), secondary flows, blade overtip flows and centrifugal forces. Dring et al. (1982) and later Blair et al. (1989) made detailed measurements of the surface pressures and heat transfer on both stator and rotor

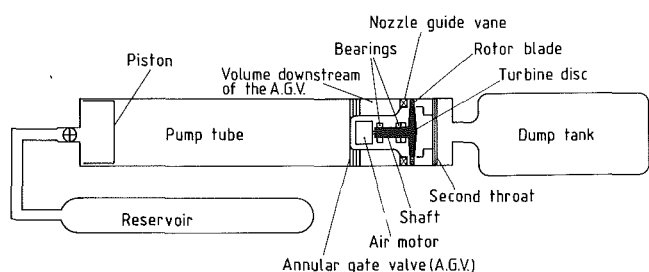


Fig. 1 Layout of the O.U.E.L. transient turbine test facility

at midspan. The upstream potential influence of the rotor on the stator was clearly seen together with the downstream potential flow and wake influence of the stator. Hodson (1984) performed a detailed experimental analysis of the boundary layer state on a low-speed, single-stage, rotor blade. He conducted a similar experiment at the same Reynolds number in a two-dimensional cascade, and found that the rotor midspan profile loss was approximately 50 percent higher than that in the rectilinear cascade. Shear stress measurements indicated that the laminar boundary layers underwent transition as the stator wake was convected through the rotor passage. The increase in loss was due to the time-dependent transitional nature of the boundary layers. Further flow visualization work (Hodson, 1985) related wake-generated unsteadiness to inviscid theories of wake chopping, migration, bowing, and shearing.

A detailed study of the flow in the region of a turbine rotor was carried out by Binder et al. (1985) using an L2F velocimeter, used to measure velocity, yaw angle, and turbulence intensity. The cutting of the stator wakes by the rotor was clearly demonstrated and a marked increase of velocity within the intersected wake was seen. In the rotor passage two counter-rotating circulation regions could be seen at both sides of the stator wake, resulting from the difference in velocities within and outside the wake. This fluctuating flow led to very high levels of turbulence intensity, significantly affecting the boundary layer behavior and the heat transfer. Binder's work clearly illustrated the three dimensionality of the flow.

Dring and Joslyn (1981) have also been using a large-scale rotating rig to investigate the three-dimensional flow over a rotor blade. They demonstrated that the spanwise migration of high loss fluid in a turbine rotor field can be considerably different from that which would be expected from a cascade flow, concluding that unsteadiness and three dimensionality had significant effects on the level and spanwise distribution of loss and heat load.

As the physical understanding of these individual effects has increased, there has been an increasing pressure to provide an experiment that combines both the rotating and three-dimensional nature of the flow with a simulation of high-pressure turbine parameters. In Oxford, this pressure has resulted in the design of a fully three-dimensional rotating turbine stage working section fitted to the I.L.P.T. This work and the associated instrumentation developments, which mirror the earlier two-dimensional cascade technology, are described by Ainsworth et al. (1988, 1989).

By choosing to continue with the Rolls-Royce "B22" turbine profile in its three-dimensional version, an evaluation of the earlier two-dimensional rotating bar simulations of Doorly would be possible, and the essential differences introduced by three-dimensional geometry and rotation could be examined. The mechanical and aerodynamic performance of the "B22" turbine stage is the subject of this paper.

2 Design Concepts and Facility Descriptions

In moving from a stationary two-dimensional cascade mounted on a transient facility to a fully three-dimensional rotating turbine stage, it was felt that facility operation, which was already complex, could become prohibitively difficult if the rotating stage itself required sophisticated operation. Consequently a principle design constraint was one of simplicity, and adherence to previous practice where possible. These themes can be seen in the realized design (Fig. 2), particularly in the absence of a brake and in the use of explosive actuators assisting the opening of the annular gate valve.

The possible design of the facility, with no brake incorporated, was carefully considered at the design concept stage. It was recognized that this would mean that the scope for aerodynamic traversing during a run would be very limited but the proposed data acquisition method for blade surface heat trans-

fer and pressure field information would enable a plentiful supply of data at engine representative conditions. The data acquisition system will be outlined later, but basically by sampling at 500 kHz, given the rotational inertia of the shaft/disk system, at the design operating point some 7 ms (3.5 kbytes) of information would be stored for each measurement point with a change of incidence due to speed change of ± 0.3 deg. The effects of this on Mach number are considered by Ainsworth et al. (1988), and are essentially negligible. During this time of essentially local equilibrium one rotor blade would be influenced by 35 nozzle guide vane wakes at design speed. While ensemble averaging over a number of revolutions on one run would not be possible, the concentration on amplifying signals in the rotating frame (Ainsworth et al., 1989) meant that the expected signal-to-noise ratios were high. In practice signal-to-noise ratios of up to 50 have been achieved, and the effects of rotor/stator interaction are clearly seen both on mean and unsteady heat transfer (Hilditch and Ainsworth, 1990), and on mean and unsteady pressure measurement (Ainsworth et al. (1990).

Other design choices lay in the bearing configuration. The choices lay between a mechanically stiff system, with a high first-mode natural frequency, or an overhung system (which was the chosen route) with a lower first mode natural frequency but permitting much easier removal of the disk from the shaft and easier access to instrumentation wiring routes. Further discussion of the dynamics of the rotating system will be outlined later.

A full description of the working section (Fig. 2) is given by Sheard (1989) and is briefly described here.

The working section, or "turbine module," consists primarily of an Annular Gate Valve (A.G.V.) used to isolate the tunnel pump tube from the working section, a shaft and bearing system on which the turbine was mounted and, an air motor to drive the turbine to its prerun speed prior to facility operation.

This gate valve (Fig. 3) was comprised of 32 radial spokes in three parts. The first and third parts remain stationary at all times, while the center portion may be rotated to block the gaps between spokes. The movement of the center portion was effected using the 37-mm stroke of two 150-mm-dia actuators.

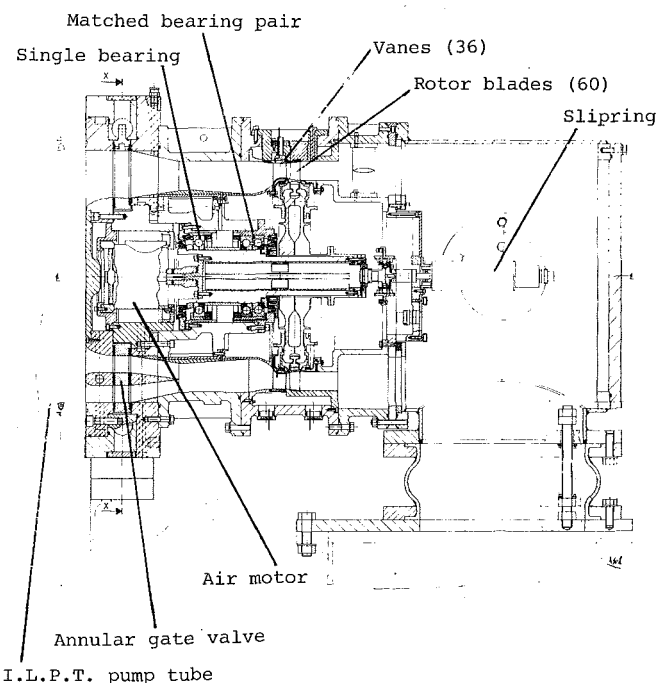


Fig. 2 General arrangement of the turbine module; the O.U.E.L. transient turbine test facility working section

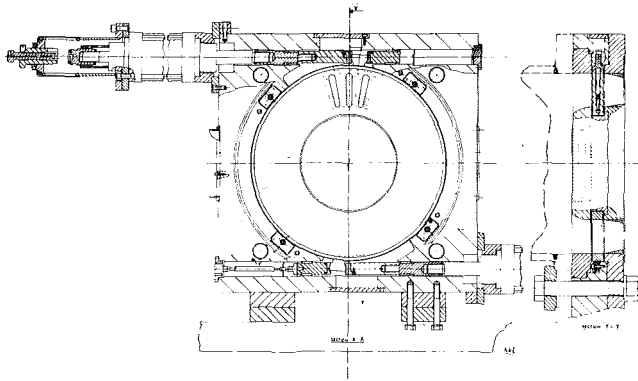


Fig. 3 General arrangement of the annular gate valve

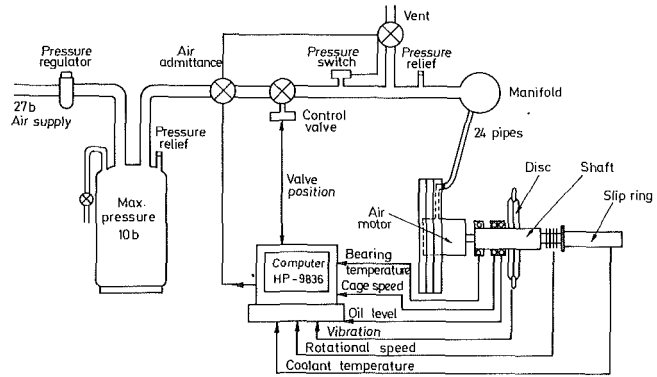


Fig. 5 Air supply and control system for the air motor and the turbine module

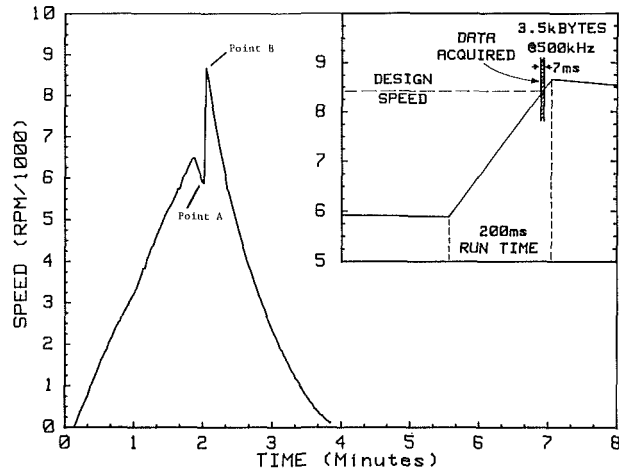


Fig. 4 Operating sequence of the O.U.E.L. transient turbine test facility

With a differential pressure of 4 bar across the actuators, initial movement was restrained by two perspex cylinder, which at the appropriate moment were removed explosively. Opening characteristics of the gate valve were tailored to achieve a total opening time of 40 ms, an acceptably small proportion of the total facility run time. The turbine shaft housed circuit boards, used to condition and amplify signals from rotor-mounted instrumentation.

2.1 Mode of Operation. An air motor was used to spin the turbine to its prerun speed of approximately 6500 rpm. During tunnel operation the turbine speed increased by between 2000 and 4000 rpm, depending on the required turbine temperature ratio. The turbine prerun speed (point A, Fig. 4) was picked to ensure that the turbine passed through its design speed during the run time. The inset on Fig. 4 shows the triggering point of the high-speed data acquisition system, with a data gathering time of 7 ms. The air motor air supply was routed to it through the downstream sections of the A.G.V., and exhausted through the upstream sections. The turbine speed was controlled using a computer based monitoring and control system (Fig. 5). Control of the turbine speed was achieved by changing the position of a control valve, admitting more or less air to the air motor as required. Bearing system parameters (vibration, oil temperature, flow rate, and cage/shaft speed ratio) were constantly monitored and recorded along with the slip ring coolant temperature and turbine speed. If preset values of any critical parameters were exceeded, the control system would shut the rig down.

2.2 The Turbine Design Point. The turbine design point is given in Table 1, with turbine and tunnel geometry given in Table 2. The tunnel total pressure was set by the required Reynolds number and Mach numbers, with total temperature

Table 1 The B22 turbine operating point

Reynolds number (Based on vane exit conditions and mid-height axial chord)	$Re = 2.7 \times 10^6$
Gas to wall temperature ratio	$T_r = 1.3$
Turbine specific speed	$\frac{N}{\sqrt{T}} = 436 \text{ r.p.m./K}^{1/2}$
Turbine pressure ratio	$P_r = 2.872$

Table 2 Turbine and I.L.P.T. geometry

Vane mid-height exit angle	70°
Blade mid-height exit angle	-63.13°
Vane mid-height axial chord	0.0312 m
Number of nozzle guide vanes	36
Number of turbine blades	60
Nozzle guide vane hub/tip ratio	0.846
Turbine blade hub/tip ratio	0.846
Nozzle guide vane aspect ratio	1.348
Turbine blade aspect ratio	1.741
I.L.P.T. tube volume	1.604 m^3

following from the temperature ratio. Since the compression process was isentropic, the initial pressure required was then only dependent on the initial temperature.

Jones et al. (1973) have derived the government equations for I.L.P.T. operation, and using these the available run time could be predicted. This was dependent on the temperature ratio required and varied between order 100 ms to 400 ms. Again a matching of the specific speed to the design point yielded design rotational speeds between 7397 rpm and 9060 rpm, varying with chosen temperature ratio.

3 Rotating System Mechanical Performance

Little published information on the detailed mechanical design was available from the other two groups with transient rotating turbine facilities (Dunn and Hause, 1982; Epstein et al. 1984). Nevertheless both Dr. Mike Dunn and Professor Alan Epstein have been generous with their advice. Because of the novelty of the mode of operation from the conventional turbine design viewpoint, much work was conducted on the bearing system design and the expected stress levels and de-

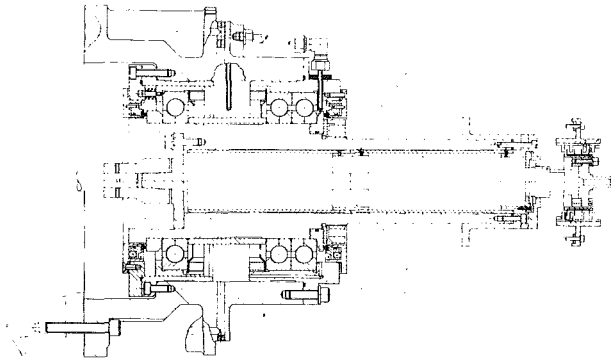


Fig. 6 General arrangement of the turbine module bearing system

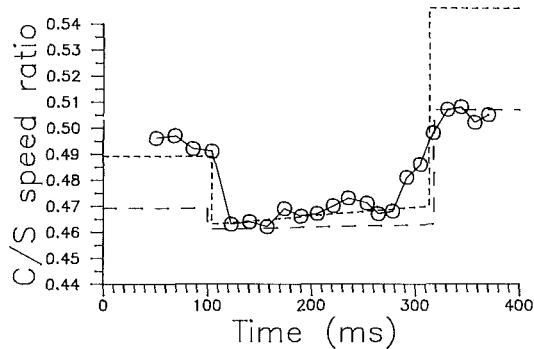


Fig. 7 Cage/shaft speed ratio measured for the upstream bearing of the tandem set during I.L.P.T. Run 6446 and comparison with predictions

Table 3 Bearing loads during I.L.P.T. operation

I.L.P.T. run state	Single floating bearing		Bearing from the Tandem set	
	Bearing load	Turbine speed	Bearing load	Turbine speed
Pre-run	10 KN	6,500 r.p.m.	5 KN	6,500 r.p.m.
Run start	10 KN	6,500 r.p.m.	23 KN	6,500 r.p.m.
Run end	10 KN	9,800 r.p.m.	23 KN	9,800 r.p.m.
Post run	10 KN	9,800 r.p.m.	5 KN	9,800 r.p.m.

--- Combination race control prediction
 Outer race control prediction
 ○○○○○ Run 6446 (tandem pair)

flections of the blade during tunnel operation. These were important in considering the operation of the instrumentation (Ainsworth et al., 1989).

3.1 The Bearing System and Rotating Dynamics

The bearing system had to be designed to operate satisfactorily with the extraordinary load conditions imposed on it. During a typical run, the rotating system accelerated at a rate of 1600 rad/s² for 0.2 s, with an axial gas force on the turbine producing an axial gas load on the bearings. At the end of the run, this load was suddenly removed, leaving a high rotational speed (9800 rpm) with only the preload on the bearings. The two main causes for concern were the possible onset of "skidding" (deviation from pure rolling, leading to severe frictional heating of the bearings, and their subsequent rapid failure) and the occurrence of "truncation" (where the ball overrides the bearing inner raceway shoulder, again causing rapid wear).

To avoid truncation at the high speed-low load condition, a high preload (10 kN) was selected for the chosen bearing configuration (Fig. 6). This and other conditions are given in Table 3. Using a standard technique (Stimpson, 1989), predictions of the bearing cage/shaft speed ratio and inner race

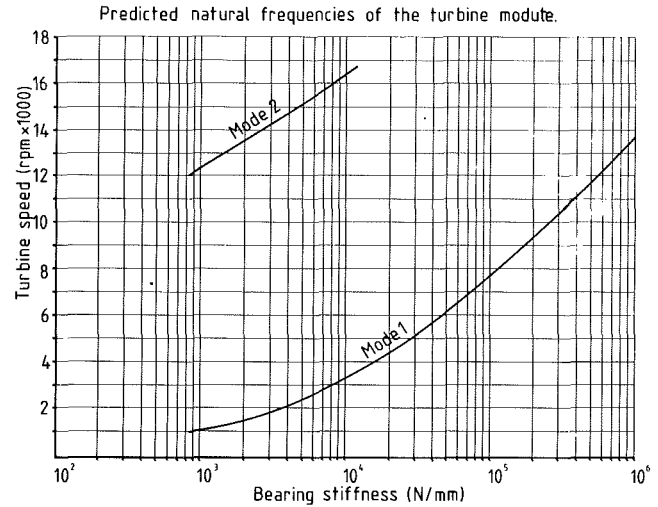


Fig. 8 Predicted first and second natural frequencies of the turbine disk/shaft assembly as a function of bearing stiffness

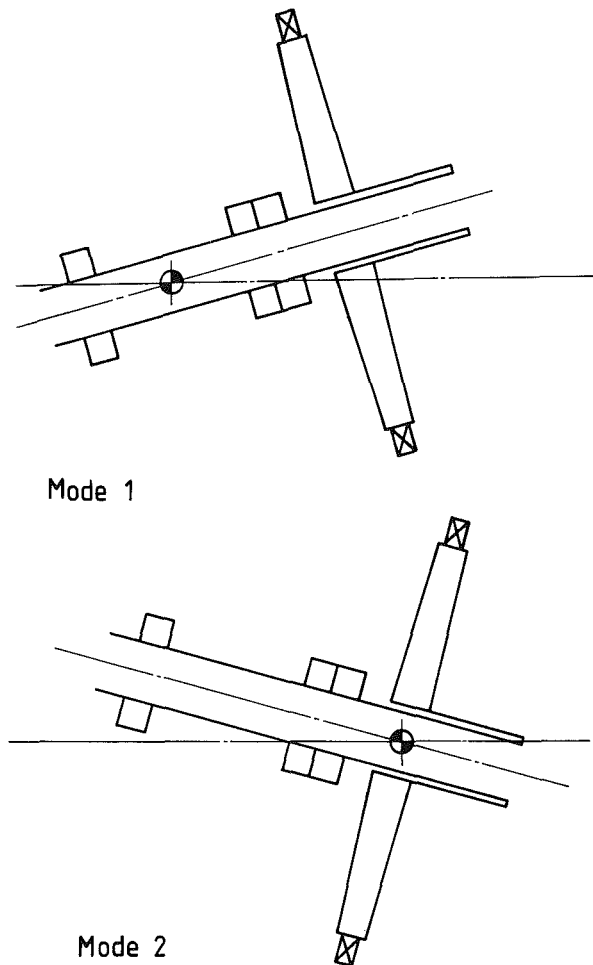


Fig. 9 Mode shapes of the first and second natural frequencies of the turbine disk/shaft assembly

contact angle were made over the operating envelope. These are compared with measurements made on one of the bearings from the matched pair of bearings in Fig. 7, and indicated that the actual bearing cage/shaft speed ratio remained close to its predicted (no skid/no truncation) values.

A single-sided bearing design had been chosen to allow easy removal of the turbine disk, and to permit good access to instrumentation runs. A more straightforward design from the rotating dynamic viewpoint would have had bearings either

Table 4 Turbine module modes of vibration, reproduced from Dietz (1988)

Vibrating component	Frequency	
	Hz	r.p.m.
Bearing housing	29	1750
Facility support structure	33	2000
Dump tank	40	2400
Disc/shaft assembly	66	4000
Facility support structure	75	4500
Facility support structure	110	6600

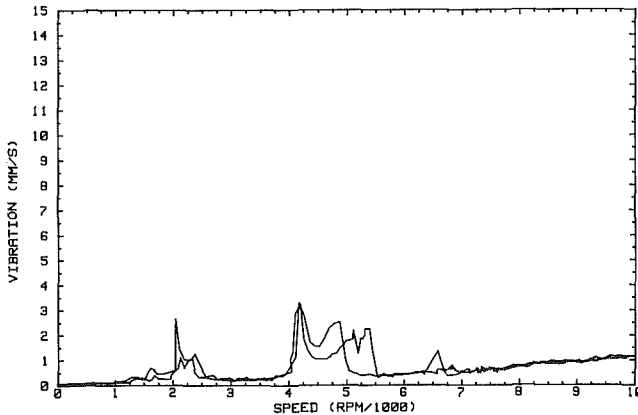


Fig. 10 Turbine vibration/speed history during commissioning Run 64 when the blade turbine disk was spun to 10,000 rpm

side of the disk, rather than an overhung arrangement. Consequently, considerable effort went into an analysis of the vibration modes and frequencies. A dynamic analysis of the working section rotating system was performed by Beynon (1988) who predicted two vibration modes as a function of bearing stiffness (Fig. 8). Both modes were "bearing bounce" modes, the entire rotating assembly vibrating as a rigid body in the bearings (Fig. 9a), while the second mode had a node in the plane of the turbine disk (Fig. 9b).

It was expected that the bearing stiffness would be of the order of 1.4×10^4 N/mm, and efforts were concentrated on keeping the first mode away from the design speed, accepting that the rotating system would pass through the first natural frequency as it was sped up prior to a run. This in turn called for careful attention to balancing to ensure that out of balance forces exciting the natural frequency were minimized. The second critical frequency was outside the facility speed range and therefore was not considered.

After the final build of the working section, resonant frequencies were investigated by striking different parts and analyzing the resulting vibration measurements on a spectrum analyzer (Dietz, 1988). In all, six vibration modes were identified (Table 4), with the disk/shaft assembly critical frequency being equivalent to a speed of 4000 rpm. During commissioning of the working section, the turbine was spun to 10,000 rpm with a vibration transducer mounted over the matched bearing pair. The output of the vibration transducer as a function of rpm (Fig. 10) clearly showed the critical frequencies identified in Table 4. Vibration levels below 4.5 mm/s are deemed acceptable by the international standard ISO 2372 (1974) for rotating machinery similar to this turbine module. Vibration levels of less than 4.5 mm/s were readily attainable over the majority of the turbine speed ranges after trim balancing, and in fact were generally not reached even at the resonant fre-

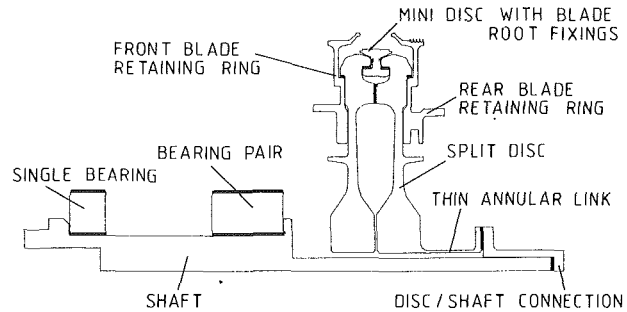


Fig. 11 The nine-component axisymmetric finite element models, using eight noded elements, utilized in the axisymmetric disk/shaft model

quencies providing the residual out of balance force was less than 350 g·mm. After some practice this level of residual out of balance force was routinely achieved after trim balancing of the rotating system.

3.2 Stress Analysis of the Turbine Disk and Blade. In order to understand the behavior of the heat transfer and pressure instrumentation mounted on the turbine (Hilditch and Ainsworth, 1990, Ainsworth et al., 1989), and to have a knowledge of the variation of running clearances during the run (tip clearance for example), it was found necessary to carry out a detailed stress analysis of the turbine blade and its supporting disk system.

The finite element analysis package FESDEC and solid modeling package MODEL described by Moir 1987, were used to perform the stress analysis. The software was run on a Hewlett-Packard 9836 minicomputer.

First, in considering the disk/shaft model, this was built from nine separate models (Fig. 11), where each model was an individual part of the rotating system. The nine sections of the disk/shaft model were restrained as realistically as possible, to simulate the presence of bolted flanges and interfaces between adjacent pieces. The restraints around the blade root have to take into account the absence of the turbine blade. Motion of the front and rear blade retaining ring would be limited by the presence of the blade platform. By assuming the blade to be infinitely stiff, radial motion of the front and rear blade retaining rings must equal radial motion of the root fixing, and therefore they were restrained in this way. The radial force of the blades and their fixings was applied as a distributed load.

The axisymmetric disk/shaft model was loaded in three ways to provide information about its behavior under load. Firstly, the model was loaded centrifugally only, then centrifugally with radial blade load, and finally with centrifugal, radial blade, and axial gas loads. In this way the effect of the radial blade and axial load on disk stress and deflection could be assessed.

Using FESDEC, the disk/shaft model was loaded centrifugally at design speed. The results showed a peak stress on the disk inner bore of 180 MN/m², compared with a value of 266 MN/m² for a simple disk following the hand calculation method of Baumeister et al. (1987). This result was plausible as the turbine disk was not, in fact, a simple disk but heavily cut away, thus reducing the load on the inner bore. The disk/shaft model was then modified by the addition of the centrifugal radial load imposed on the disk by the blades and their root fixings. A new prediction showed stress levels generally increasing, with peak stresses of 240 to 260 MN/m² in the fillet radii around the minidisk/main disk, and 220 MN/m² on the disk inner bore. Addition of the axial gas load had the effect of slightly increasing stress levels in the downstream half of the split disk (Fig. 12), so that peak stress in the disk inner bore was increased to 240 MN/m². The radial growth of the turbine blade root fixing was 137×10^{-6} m (0.0054 in.) with an axial movement of 130×10^{-6} m (0.0051 in.).

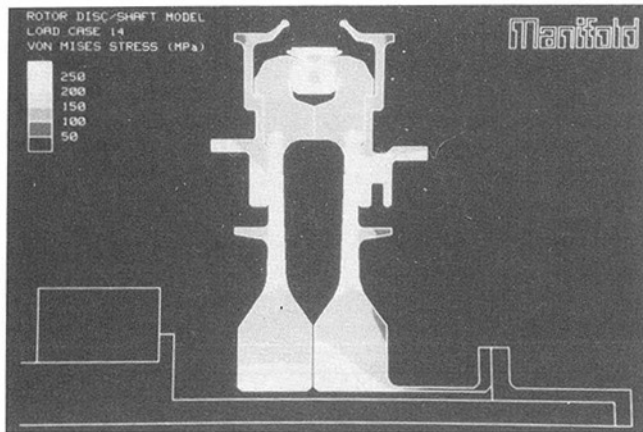


Fig. 12 Stress distribution through the axisymmetric disk/shaft model at 8434 rpm, with a radially distributed load along the blade root fixing, simulating the blade load, and an axial load simulating the gas load

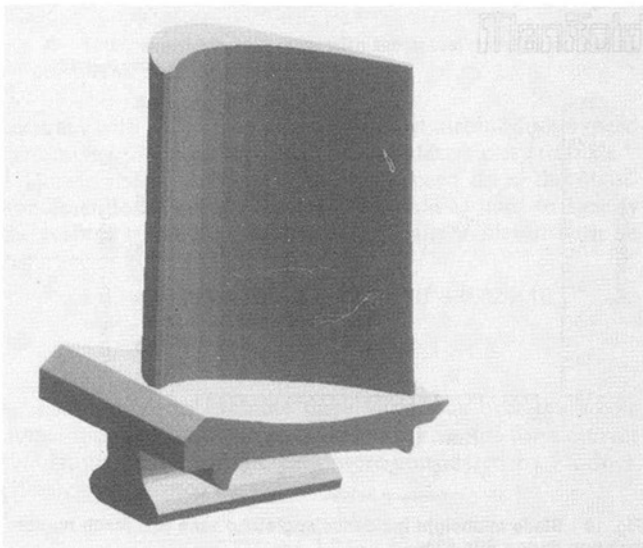


Fig. 13 Solid model of the final turbine blade finite element model, using eight-noded "brick" elements

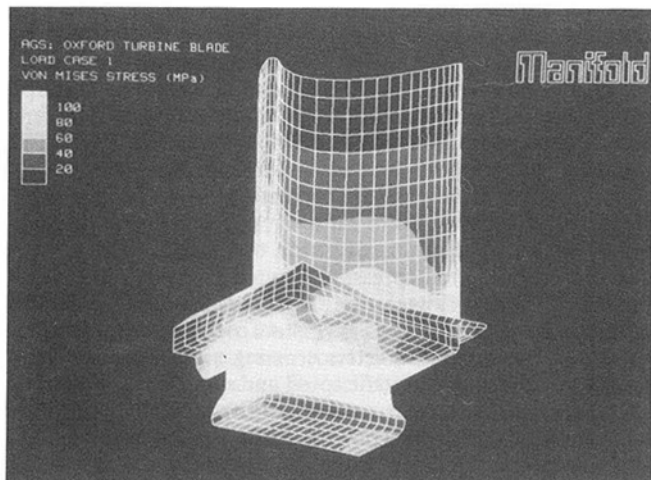


Fig. 14 Stress distribution over the blade due to rotation at 8434 rpm; view of the blade root, underside of the platform, and aerofoil

As far as stressing the blade itself, the model (Fig. 13) was geometrically accurate, though the relatively coarse grid required the omission of fillet radii. Sharp corners in a finite element model can lead to high stress concentration factors and results of the blade stress analysis must be viewed with

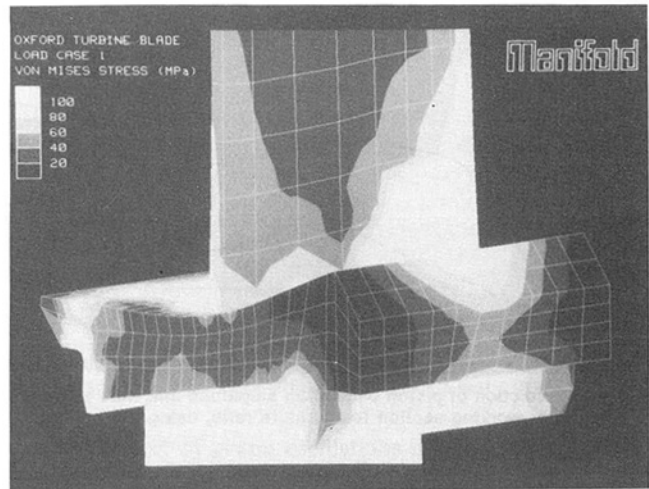


Fig. 15 Stress distribution over the blade due to rotation at 8434 rpm; view of the aerofoil, top side of the platform

caution in the region of sharp corners. Spurious stresses in these regions will however, remain local, and will not, therefore, affect the overall result.

The blade stress analysis results predicted by FESDEC are for a blade rotating at a constant speed of 8434 rpm. The blade stress distribution is best viewed as a set of contours (Fig. 14). Peak stresses occur around the root region and also appear on the blade platform (Fig. 15). The blade root area was larger than that of the 0 percent height aerofoil section, resulting in similar stress levels in the two, despite the root having to carry the additional load imposed by the platform.

The predicted blade stresses of 100–110 MN/m² in the root region compare well with hand-calculated stress levels of 105 MN/m². Stress levels of 40 MN/m² at the aerofoil midheight section also compare well with hand-calculated values of 36 MN/m². Most of the B22 turbine blades in this experiment were manufactured from Jethete with the instrumentation blades being manufactured from Inco-718. Both of these materials have a yield stress in excess of 1000 MN/m² at ambient temperature and consequently the blade material stress remained well below the ultimate tensile stress.

The predicted aerofoil stress levels were essentially one-dimensional at the blade midheight section, but were more complex around the aerofoil/platform interface. The aerofoil and platform were joined at the interface by constraining coincident nodes on both surfaces to move together. No attempt was made to model fillet radii. The consequence of the modeling method around the aerofoil/platform interface is that results there must be viewed with caution. While results around the aerofoil/platform interface are error prone, they are consistent with hand-calculated stress levels of 105 MN/m² in this region.

The essentially one-dimensional stress distribution around the aerofoil midheight section will result in a uniform strain distribution at this location. The Young's Modulus of Inco-718 at 25°C is 205×10^9 N/m², and assuming a stress level of 40 MN/m² this implies instrumentation mounted at the blade mid-height section will experience a strain, ϵ , of 195×10^{-6} . A knowledge of this value was of importance to the design and testing of the instrumentation subsequently mounted on the rotor.

4 Aerodynamic Performance

The aerodynamic performance of the turbine during tunnel operation was complicated due to the transient nature of the experiment. During a tunnel run the stagnation pressure and temperature oscillated about design values due to the finite mass of the piston used in the I.L.P.T. and the volume between

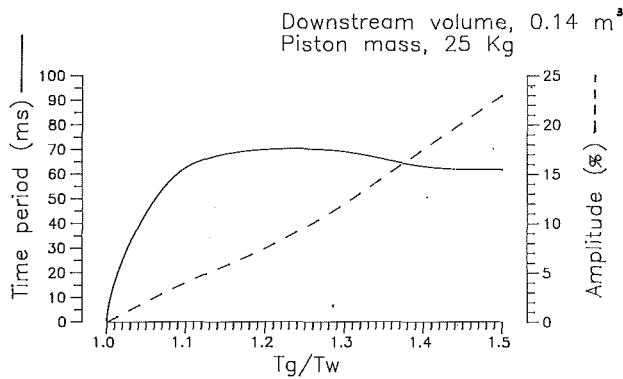


Fig. 16 Prediction of piston oscillation amplitude and time period as a function of working section temperature ratio, using the method of Brooks and Jones (1989)

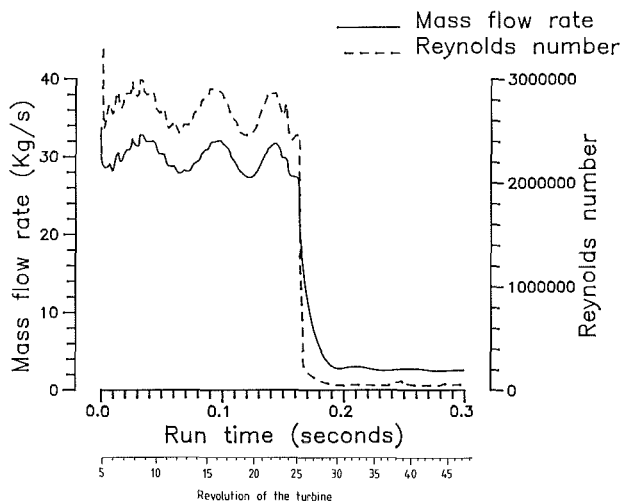


Fig. 17 Mass flow rate and Reynolds number variation during Run 6384

the A.G.V. and the nozzle guide vane ring throat point, as described by Brooks and Jones (1989). Using the method of Brooks and Jones the time period and amplitude of (peak-to-peak) pressure oscillations was calculated (Fig. 16). The turbine speed also rose constantly during one run. The consequence of these changes was that the nondimensional and quasi-nondimensional groups either oscillated about design values, or rose constantly during the run depending on whether they were functions of inlet total pressure and temperature, or turbine speed. In order to ensure that design condition values of all nondimensional and quasi-nondimensional groups were achieved during a run, it was considered desirable to calculate them as functions of time.

Before discussing further the variation of aerodynamic conditions during one run, it is necessary to be clear about the data acquisition system and what measurements were required. In the case of both blade surface heat transfer measurements and surface pressure measurements, the concept of the experiment required the taking of high speed data (500 kHz sampling interval) at the design point. This derived from a wake-passing frequency of 5 kHz at design speed and instrumentation and amplification capabilities up to a bandwidth of 100 kHz. At these speeds of data acquisition, and a data capacity of 3.5 kbytes per channel, some 7 ms or 35 nozzle guide vane-rotor blade interactions could be sampled (0.98 of a disk revolution). As indicated earlier, incidence changes about the design value in this time had a negligible impact on blade surface heat transfer or pressure field. A second data acquisition system, based on a PDP11/34, sampled data at a much slower rate throughout the run (28.8 rotor revolutions) taking data at 430 Hz. This permitted monitoring of the gross operating condi-

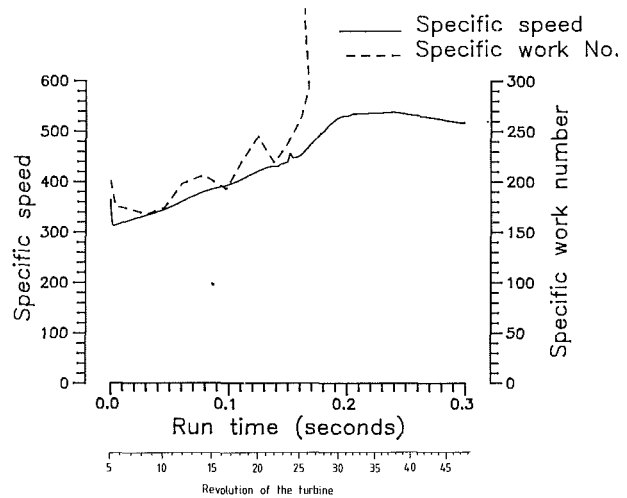


Fig. 18 Turbine specific speed and specific work number variation during Run 6384

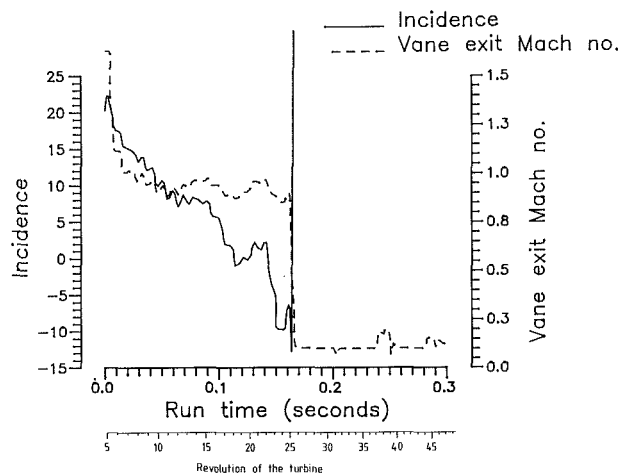


Fig. 19 Blade midheight incidence angle and vane exit Mach number variation during Run 6384

tions throughout the run, but of course, because of the rotor acceleration, data outside the 7 ms data "window" would be off of the design operating point.

For each slow-speed data acquisition measurement point, the turbine nondimensional and quasi-nondimensional groups were derived in terms of working section inlet total pressure and temperature, vane exit static pressure, rotor exit static pressure, turbine speed, and acceleration using the method of Sheard (1989). Total pressure oscillations of 12 percent were predicted at a temperature ratio of 1.3, which was in close agreement with the measured piston oscillations. The 12 percent oscillations in total pressure resulted in a similar predicted oscillation of mass flow rate and Reynolds number, which was observed in practice (Fig. 17). Piston oscillations resulted in the actual value of parameters crossing and recrossing their design value. Turbine specific speed and specific work number were functions of turbine speed, and therefore rose continuously throughout one run (Fig. 18). Since turbine specific speed was defined as N/\sqrt{T} , the effect of taking the square root of temperature was to reduce piston oscillations to the root of their value, with the consequence that the rising turbine specific speed trace incorporated only slight oscillations, passing through its design value once. Turbine specific work number had the full piston oscillations imposed on its rising trajectory, with the consequence that it passed through its design value three times.

The blade midheight incidence angle and turbine vane exit Mach number (Fig. 19) were significant parameters since the

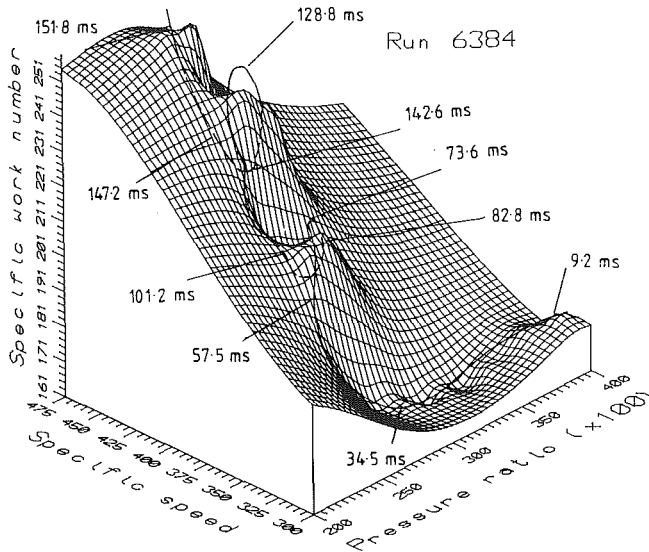


Fig. 20 Turbine performance map, with the actual path traced out by the turbine during Run 6384 overlaid

accuracy with which they were achieved at turbine design speed determined the accuracy of the blade inlet velocity triangle.

During the acquisition of the high-speed data, the quasi-nondimensional groups (defined in Table 1) used to specify the turbine operating point were typically achieved with an accuracy as follows (Sheard, 1989):

$$M_{ex} = 0.946 \pm 0.009; \text{Re} = 2.7 \times 10^6 \pm 0.02 \times 10^6;$$

$$\frac{N}{\sqrt{T}} = 436 \pm 1; \frac{C_p \Delta T}{T} = 216.3 \pm 1.5$$

It is interesting to examine these variations over the whole tunnel run. The dynamic similarity requirements for a correct simulation of the turbine flow were considered by Horlock (1966), who showed that

$$\frac{\dot{m}\sqrt{T}}{P}, \frac{C_p \Delta T}{T} = f \left\{ \frac{N}{\sqrt{T}}, P_r, \text{Re}, \gamma \right\} \quad (1)$$

For performance considerations Reynolds number was found by Horlock to be unimportant, if it was large enough. Over the temperature range encountered in the working section, γ may be regarded as constant, therefore Eq. (1) reduces to two possible equations, giving $\dot{m}\sqrt{T}/P$ and $C_p \Delta T/T$ as functions of N/\sqrt{T} and P_r . The independent and nonconstant variables relevant to turbine performance are, therefore, $C_p \Delta T/T$, N/\sqrt{T} and P_r (pressure ratio). Equation (1) may, therefore, be reduced to

$$\frac{C_p \Delta T}{T} = f \left\{ \frac{N}{\sqrt{T}}, P_r \right\} \quad (2)$$

Speed rose continuously, and consequently $C_p \Delta T/T$ and N/\sqrt{T} rose continuously. Piston oscillations resulted in oscillations of the vane upstream total pressure and temperature, and these in turn resulted in oscillations in turbine pressure ratio. Since N/\sqrt{T} continually rose (due to the speed increase) while $C_p \Delta T/T$ and P_r oscillated about their design values, the achieved turbine operating conditions could be represented as a path across its performance "map" (Fig. 20). From the measured values of $C_p \Delta T/T$, N/\sqrt{T} , and P_r the turbine's performance map may be inferred using a surface fitting routine. The surface in Fig. 20 is the function in Eq. (2), and characterizes the performance of the B22 turbine about its design point. The actual path of the B22 turbine over its performance map during I.L.P.T. Run 6384 is drawn (Fig. 20) to illustrate the range of conditions covered by the turbine during one run. The actual trajectory of the turbine is a helix, due to the

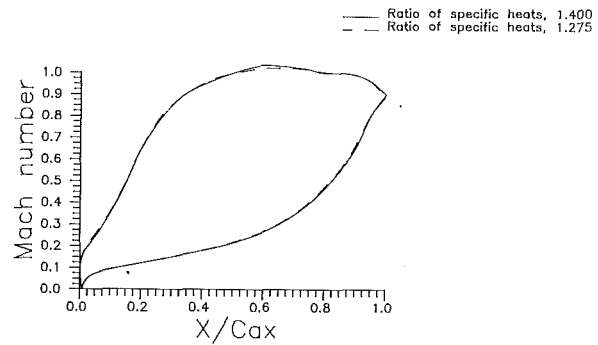


Fig. 21 Vane midheight Mach number distributions at turbine design conditions, with a ratio of specific heats, γ , of 1.4 and 1.275

combined effect of piston oscillations in both pressure ratio and specific work number. This may be seen as "mountains" and "valleys" in the performance map, the trajectory progressing up the first mountain (at time step 57.5 ms), over the peak, into the valley, and up the following peak. The sparsity of data used to create the surface in Fig. 20 is reflected in the lack of surface detail away from the turbine's path, where the surface was interpolated from relatively distant data. The ability of the turbine module to cover a range of conditions during a single I.L.P.T. run was, interestingly, not inconvenient. Future experimental programs will utilize the turbine's ability to cover a range of conditions during a single I.L.P.T. run, enabling the turbine flow field to be studied at design and off-design conditions.

Finally, it should be noted that piston oscillations could be reduced to zero by running at the temperature ratio of 1. All nondimensional and quasi-nondimensional groups used to define the turbine design point can be achieved using the I.L.P.T. as a short-duration air supply for a working section containing the B22 turbine. The I.L.P.T. provided the turbine module with compressed air (γ of 1.4) but for the combustion products entering a high-pressure turbine in the engine γ environment would typically be 1.275.

The error in flow field simulation incurred as a consequence of using a working fluid with a γ of 1.4, rather than 1.275, will be quantified. Using a blade-to-blade prediction code (a finite element potential flow solver with a coupled boundary layer model) the vane midheight flow field was predicted at B22 turbine design conditions using the rig and engine γ (Fig. 21). The two predictions were virtually indistinguishable, with only the slightest variation on the crown of the suction surface. It may be shown that the effect of changing γ from 1.4 to 1.275 (while keeping all other design point nondimensional groups constant) was to reduce, slightly, turbine mass flow rate. As the vanes were not quite choked, a slight reduction in mass flow rate will result in a slight reduction in Mach number at the throat. This observation is consistent with the observed trend (Fig. 21), but has so small a magnitude that it may reasonably be ignored.

5 Summary and Conclusion

A large number of experimental facilities able to test two-dimensional cascades of aerofoils have been used for many years to provide information relevant to turbine aerodynamics and heat transfer, but they inevitably fail to model three-dimensional and rotational effects. A facility has been constructed and described in this paper that goes further toward the goal of an accurate simulation of the turbine stage flow, by including the effects of rotation and three-dimensional geometry, maintaining engine Reynolds and Mach number, together with temperature ratios.

The choice of the B22 turbine profile as the vehicle for the test turbine, typical of modern high bypass ratio engines, has

been especially convenient in allowing the potential for comparison with the extensive database already available in Oxford on the two-dimensional stationary performance of this profile.

In this project, the I.L.P.T. was used as the short-duration air supply for a full B22 turbine stage, and was capable of supplying it with air for 213 ms at the appropriate temperature and pressure for correct simulation of the turbine flow field. When those parameters relevant to a simulation of the turbine flow field were considered, it proved practical to model them all, with the exception of the ratio of specific heats, γ . The error incurred as a consequence of this was shown to be small, leading to the conclusion that the simulation of the turbine flow field was accurate.

The conceptual choices in designing this facility have been discussed, and full details of the aerodynamic and mechanical design given.

Commissioning trials of the turbine module culminated with the turbine achieving design conditions during tunnel operation. A program was written to calculate the time varying turbine nondimensional and quasi-nondimensional groups during a tunnel run. The accuracy with which turbine design conditions were achieved was established, and confirmed that turbine design conditions were reached during the experiment, within a close tolerance.

The first results from the new I.L.P.T. working section have illustrated the viability of achieving the required values of all parameters necessary for a rigorous simulation of the turbine flow field. The next phase in the project will be to make detailed measurements of both pressure and heat transfer rate on the turbine blade, contributing to a better understanding of the mechanisms responsible for unsteady and three-dimensional flow phenomena in the rotating frame of reference. Further investigation of the turbine performance at off-design conditions is recommended, which could be extended to include a study of the effects of varying blade tip clearance on turbine performance.

Acknowledgments

The authors gratefully acknowledge the support of K. J. Grindrod, S. J. Hughes, and others of the Oxford Turbo-machinery Group, together with the expertise of the Osney workshop. The assistance of N. Stimpson of SKF plc., M. G. Rose of Rolls-Royce plc (Derby), and P. J. Moir of ETA was also much appreciated.

The authors gratefully acknowledge the support of Rolls-Royce plc and the Science and Engineering Research Council who jointly funded the work reported in this paper under grants GR/D 21189 and GR/E 28062. Lastly the authors would like to thank Rolls-Royce plc for permission to publish this work.

References

Ainsworth, R. W., Schultz, D. L., Davies, M. R. D., Forth, C. J. P., Hilditch, M. A., Oldfield, M. L. G., and Sheard, A. G., 1988, "A Transient Flow Facility for the Study of the Thermofluid-Dynamics of a Full Stage Turbine Under Engine Representative Conditions," ASME Paper No. 88-GT-144.

Ainsworth, R. W., Allen, J. L., Davies, M. R. D., Doorly, J. E., Forth, C. J. P., Hilditch, M. A., Oldfield, M. L. G., and Sheard, A. G., 1989, "Developments in Instrumentation and Processing for Transient Heat Transfer Measurement in a Full Stage Model Turbine," ASME JOURNAL OF TURBOMACHINERY, Vol. 111, pp. 20-27.

Ainsworth, R. W., Dietz, A. J., and Nunn, T. A., 1991, "The Use of Semiconductor Sensors for Blade Surface Pressure Measurement in a Model Turbine Stage," ASME JOURNAL OF ENGINEERING FOR GAS TURBINES AND POWER, Vol. 113, pp. 261-268.

Ashworth, D. A., LaGraff, J. E., Schultz, D. L., and Grindrod, K. J., 1985, "Unsteady Aerodynamic and Heat Transfer Processes in a Transonic Turbine Stage," ASME JOURNAL OF ENGINEERING FOR GAS TURBINES AND POWER, Vol. 107, pp. 1022-1031.

Baumeister, T., Avallone, E. A., and Baumeister, T., 1987, *Mark's Standard Handbook for Mechanical Engineers*, 8th ed., McGraw-Hill, New York.

Beynon, P., 1988, Dynamics Specialist, Rolls-Royce, Bristol, Private Communication.

Binder, A., Forster, W., Kruss, H., and Rogge, H., 1985, "An Experimental Investigation Into the Effect of Wake on the Unsteady Turbine Rotor Flow," ASME JOURNAL OF ENGINEERING FOR GAS TURBINES AND POWER, Vol. 107, pp. 458-466.

Blair, M. F., Dring, R. P., and Joslyn, H. D., 1989, "The Effects of Turbulence and Stator/Rotor Interaction on Turbine Heat Transfer: Part I—Design Operating Conditions," ASME JOURNAL OF TURBOMACHINERY, Vol. 111, pp. 87-96.

Brooks, A. J., and Jones, T. V., 1989, "The Use of Short Duration Facilities for Testing Gas Turbine Blading," *Proceedings of the Joint European Propulsion Forum on Modern Techniques and Developments in Engine and Component Testing*.

Dietz, A. J., 1988, "Unsteady Aerodynamic Studies on a Three Dimensional Rotating Turbine Stage in a Transient Facility," First Year Report, University of Oxford, United Kingdom.

Doorly, D. J., 1983, "A Study of the Effect of Wake Passing on Turbine Blades," D.Phil. Thesis, University of Oxford, United Kingdom.

Doorly, D. J., and Oldfield, M. L. G., 1985, "Simulation of the Effects of Shock Wave Passing on a Turbine Rotor Blade," ASME JOURNAL OF ENGINEERING FOR GAS TURBINES AND POWER, Vol. 107, pp. 998-1006.

Doorly, D. J., Oldfield, M. L. G., and Scrivener, C. T. J., 1985, "Wake-Passing in a Turbine Rotor Cascade," *Proceedings of Symposium*, AGARD-CP390.

Dring, R. P., and Joslyn, H. D., 1981, "Measurement of Turbine Rotor Blade Flows," ASME JOURNAL OF ENGINEERING FOR POWER, Vol. 103, pp. 400-405.

Dring, R. P., Joslyn, H. D., Hardin, L. W., and Wagner, J. H., 1982, "Turbine Rotor-Stator Interaction," ASME JOURNAL OF ENGINEERING FOR POWER, Vol. 104, pp. 729-742.

Dunn, M. G., and Hause, A., 1982, "Measurement of Heat Flux and Pressure in a Turbine Stage," ASME JOURNAL OF ENGINEERING FOR POWER, Vol. 104, pp. 215-223.

Epstein, A. H., Guenette, G. R., and Norton, R. J. G., 1984, "The M.I.T. Blowdown Turbine Facility," ASME Paper No. 84-GT-116.

Hilditch, M. A., 1989, "Unsteady Heat Transfer Measurements in a Rotating Gas Turbine Stage," D.Phil. Thesis, University of Oxford, United Kingdom.

Hilditch, M. A., and Ainsworth, R. W., 1990, "Unsteady Heat Transfer Measurements in a Rotating Gas Turbine Stage," ASME Paper No. 90-GT-175.

Hodson, H. P., 1984, "Boundary Layer and Loss Measurements on the Rotor of an Axial-Flow Turbine," ASME JOURNAL OF ENGINEERING FOR GAS TURBINES AND POWER, Vol. 106, pp. 391-399.

Hodson, H. P., 1985, "Measurement of Wake Generated Unsteadiness in the Rotor Passages of Axial-Flow Turbines," ASME JOURNAL OF ENGINEERING FOR GAS TURBINES AND POWER, Vol. 107, pp. 458-466.

Horlock, J. H., 1966, *Axial Flow Turbines: Fluid Mechanics and Thermodynamics*, 1st ed., Krieger, United Kingdom.

International Standard, 1974, "Mechanical Vibration of Machines With Operating Speeds From 10 to 200 revs/s—Basis for Specifying Evaluation Standards," ISO 2372, Switzerland.

Jones, T. V., and Schultz, D. L., 1970, "A Study of Film Cooling Related to Gas Turbines Using Transient Techniques," Aero. Res. Council, Report No. A.R.C. 32420.

Jones, T. V., Schultz, D. L., and Henley, A. D., 1973, "On the Flow in an Isentropic Light Piston Tunnel," Aero. Res. Council, R. and M. No. 3731.

Johnson, A. B., Rigby, M. J., Oldfield, M. L. G., Ainsworth, R. W., and Oliver, M. J., 1989, "Surface Heat Transfer Fluctuations on a Turbine Rotor Blade due to Upstream Shock Wave Passing," ASME JOURNAL OF TURBOMACHINERY, Vol. 111, pp. 105-115.

Johnson, A. B., Rigby, M. J., Oldfield, M. L. G., and Giles, M. B., 1990, "Nozzle Guide Vane Shock Wave Propagation and Bifurcation in a Transonic Turbine Rotor Passage," ASME Paper No. 90-GT-310.

Moir, P. J., 1987, "Manifold—Design Analysis of Software on Desk Top Computers," E.T.A. Engineering Consultants Ltd., Hinkley, Leicestershire, United Kingdom.

Rigby, M. J., Johnson, A. B., Oldfield, M. L. G., and Jones, T. V., 1989, "Temperature Scaling of Turbine Blade Heat Transfer With and Without Shock Wave Passing," presented at the 9th International Symposium on Air Breathing Engines, Athens, Sept.

Rigby, M. J., Johnson, A. B., and Oldfield, M. L. G., 1990, "Gas Turbine Rotor Blade Cooling With and Without Simulated NGV Shock Waves and Wakes," ASME Paper No. 90-GT-78.

Schultz, D. L., Jones, T. V., Oldfield, M. L. G., and Daniels, L. C., 1977, "A New Transient Cascade Facility for the Measurement of Heat Transfer Rates," AGARD CP No. 229, *High Temperature Problems in Gas Turbine Engines*.

Schultz, D. L., Johnson, A. B., Ashworth, D. A., Rigby, M. J., and LaGraff, J. E., 1987, "Wake and Shock Interactions in a Transonic Turbine Stage," AGARD CP-401, Munich, Sept.

Sheard, A. G., 1989, "The Aerodynamic and Mechanical Performance of a High Pressure Turbine Stage in a Transient Wind Tunnel," D.Phil Thesis, University of Oxford, United Kingdom.

Stimpson, N., 1989, SKF plc. Bearing Specialist, Private Communication.

Design of Turbomachinery Blading in Transonic Flows by the Circulation Method

T. Q. Dang

Assistant Professor,
Department of Mechanical/Aerospace
Engineering,
Syracuse University,
Syracuse, NY 13244

The newly developed three-dimensional design technique for turbomachinery blading based on the circulation method has been successfully extended into the transonic flow regime. The main task involves replacing the classical Fourier series expansion technique by a finite-volume method. Calculations were carried out for the design of infinitely thin cascaded blades in transonic flows, including shocked and shock-free cascaded blades.

Introduction

Improvements of the aerodynamic performance of turbomachine blades require a correct tailoring of the three-dimensional blade geometry. There are two approaches to the design of turbomachine blades (Meauzé, 1989). In the first instance, the blade profile is optimized through the use of an analysis method via an iterative process; the blade geometry is "modified" by the user based on his past experience until a desired flow field is achieved. In the second way of treating the problem, called the inverse method, the user prescribes certain conditions for the flow field that reflect the desired aerodynamic behavior, and the method provides the resulting blade profile.

The use of inverse methods can be of great help in finding the required blade shape for a given task. They allow a designer to concentrate on the flow behavior rather than on the geometric shape. Although inverse techniques for turbomachinery blading are widely used in industry, they are mostly based on the concept of combined throughflow/blade-to-blade calculations developed in the 1960s (Wu, 1951; Katsanis and McNally, 1973; Novak, 1967). Hence, these design tools possess at least one of the following drawbacks. The existing methods are at most quasi-three-dimensional and/or are limited to shock-free flows (Dulikravich and Sobieczky, 1982; Meauzé, 1982; Ribaut and Martin, 1985; Sanz, 1984; Tong and Thompkins, 1983).

Recently, a fully three-dimensional inverse technique for turbomachinery blading was proposed (Hawthorne et al., 1984). In this method, called the circulation method, the pitch-averaged tangential velocity (or swirl schedule) is prescribed at every point in the bladed region, the flow field is described by the Clebsch formulation of the Euler equations, and the three-dimensional blade profile is determined iteratively using the blade boundary conditions. Successful calculations were carried out for the design of annular rows of thin blades of the free-vortex type (Tan et al., 1984) and of the forced-vortex

type in the presence of an incoming shear flow (Dang and McCune, 1984a) in incompressible flow. The same approach was also applied to the design of radial inflow turbine blades in the subcritical flow regime, including a successful experimental verification of this three-dimensional inverse technique (Ghaly, 1989; Borges, 1989). In these studies, the blockage effect due to the finite thickness of the blade is partially accounted for through the use of a mean stream surface thickness parameter. The general design philosophy of the circulation method is similar to that used by Novak and Haymann-Haber (1983) in their two-dimensional inverse method.

Conventionally, the optimum choice of the prescribed conditions in an inverse method is the imposition of the pressure distributions along the blade pressure and suction surfaces so as to avoid flow separation problems. However, strictly speaking, this design philosophy only applies to the two-dimensional case where the streamlines along the blade pressure and suction surfaces are known a priori; namely they lie on the (x, y) plane. In the general three-dimensional case, the potential presence of large radial velocities and secondary flows can render the estimations of the locations of these streamlines a difficult task. Hence, it is not clear whether there is an advantage in specifying blade surface pressure distributions in a fully three-dimensional inverse method.

As mentioned earlier, the primary input quantity in the present inverse method is the pitch-averaged tangential velocity distribution. Conceptually, there are several advantages in choosing this quantity as the prescribed flow field. Turbomachine devices supply work to or extract work from a flowing fluid by imposing a change in its angular momentum across the rotors. In a design process, the power requirement is known to the designer, and the prescribed overall change in the pitch-averaged tangential velocity across the rotor can be estimated using the Euler turbine equation. Furthermore, the local rate of change of the pitch-averaged tangential velocity along the blade surface in the "streamwise" direction gives the local pressure jump across the blade (Novak and Haymann-Haber, 1983; Tan et al., 1984). Finally, as the quasi-three-dimensional design technique currently used by nearly everyone usually

Contributed by the International Gas Turbine Division for publication in the JOURNAL OF TURBOMACHINERY. Manuscript received by the International Gas Turbine Institute August 1990.

starts with a meridional-plane streamline curvature solution in which an intrablade angular momentum addition rate is a prescribed quantity, the present three-dimensional design philosophy can be used to develop the unique blade profile implied by these meridional-plane input specifications. Currently, strip theories based on two-dimensional blade-to-blade inverse methods are used to design blade profiles along these meridional streamtubes.

Clearly, there exist many distributions of pitch-averaged tangential velocity that one could prescribe to achieve the same amount of work done across the blade row, and it is the designer's job to learn how to specify an optimum distribution. The pitch-averaged tangential velocity distribution should be tailored to control the pressure distributions along the individual blade surfaces and, at the same time, keep the blade warp at an acceptable level (Ghaly, 1989).

The purpose of the present study is to investigate the feasibility of extending the circulation method into the transonic flow regime. For this reason, the simple case of infinitely thin cascade blades in irrotational flow is considered, but the problem is formulated so that it can easily be extended to the three-dimensional case.

Theoretical Background

The classical aerodynamic approach of representing the blades as surfaces of singularities is adopted. However, in the circulation method, the Clebsch transformation of the equations of motion is employed instead of the classical Biot-Savart law. This approach is better suited for internal flows and for mixed-flow conditions.

When the approaching flow is assumed to be irrotational, the absolute vorticity bound to the blades can be expressed as (Hawthorne et al., 1984)

$$\Omega = \delta_p(\alpha) \nabla \bar{V}_y \times \nabla \alpha \quad (1)$$

where $\delta_p(\alpha)$ is the periodic delta function. Note that the inclusion of other physical effects such as flow nonuniformities and vorticity generation behind shocks can readily be incorporated into Eq. (1) (Dang and McCune, 1984a; Hawthorne and Tan, 1987; Dang and Chen, 1989). In Eq. (1), the blade surfaces α are given by (Fig. 1):

$$\alpha = y - f(x) = ns \quad (2)$$

where s is the spacing-to-chord ratio and n is an integer. Using the notations of Fig. 1, the pitch-averaged tangential velocity \bar{V}_y is defined as

$$\bar{V}_y(x) = \frac{1}{s} \int_f^{f+s} V_y(x, y) dy \quad (3)$$

Given the expression for the vorticity vector, a Clebsch representation for the velocity vector is

$$\mathbf{V} = \nabla \phi + \bar{V}_y \nabla \alpha - S(\alpha) \nabla \bar{V}_y \quad (4)$$

where $S(\alpha)$ is the periodic sawtooth function. Note that the curl of Eq. (4) gives Eq. (1) as required. In the present design technique, the swirl schedule \bar{V}_y is prescribed, the potential function ϕ is computed from the continuity equation, and the blade shape described by the function α is determined using the blade boundary conditions. The swirl schedule must be

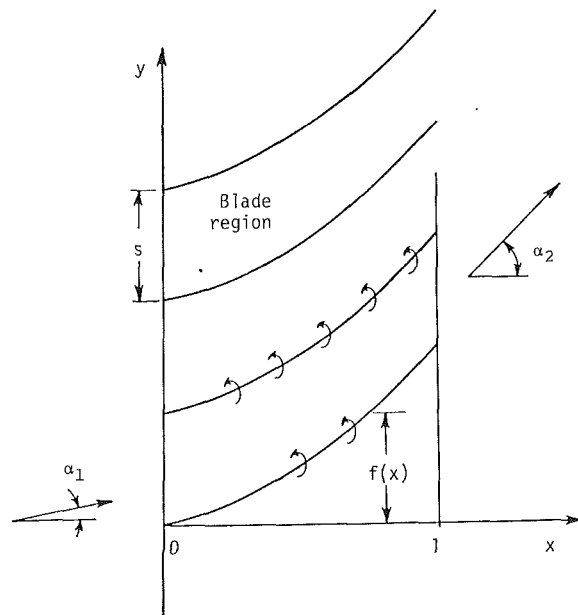


Fig. 1 Cascade notation

chosen to satisfy the Kutta condition at the blade trailing edge. This condition requires that $d\bar{V}_y/dx$ vanishes at the blade trailing edge (Hawthorne et al., 1984). In addition, the same condition is imposed at the blade leading edge to give zero incidence.

As the pitch-averaged tangential velocity is prescribed, it is convenient to divide the flow field into pitch-averaged and periodic terms:

$$\mathbf{V}(x, y) = \bar{\mathbf{V}}(x) + \tilde{\mathbf{v}}(x, y) \quad (5)$$

where the periodic velocity is defined as

$$\tilde{\mathbf{v}} = \nabla \tilde{\phi} - S(\alpha) \nabla \bar{V}_y \quad (6)$$

Hence, the pitch-averaged velocity must satisfy the condition

$$\nabla \times \bar{\mathbf{V}} = \nabla \bar{V}_y \times \nabla \alpha \quad (7)$$

so that the curl of Eq. (5) gives back Eq. (1). The division of the velocity field as described by Eq. (5) is equivalent to the familiar definition of the reduced potential in potential flow calculation. Here, the reference velocity is taken to be the pitch-averaged velocity instead of the usual free-stream velocity. In the two-dimensional case, Eq. (7) is identically satisfied with any expression for the pitch-averaged axial velocity. In the present study, the technique suggested by Ghaly (1989) is used to determine the pitch-averaged axial velocity; it requires the pitch-averaged velocity to satisfy the pitch-averaged form of the continuity equation.

Numerical Technique

Previously, to take advantage of the periodic condition in the pitchwise direction, the classical Fourier (Hawthorne et al., 1984; Tan et al., 1984) and asymptotic (Dang and McCune, 1984a) expansion techniques were employed to solve the continuity equation for the reduced potential function $\tilde{\phi}$. This

Nomenclature

f = blade camber line y coordinate	$\tilde{\mathbf{v}}$ = periodic velocity vector	$\tilde{\phi}$ = reduced potential function
$S(\alpha)$ = sawtooth function	(x, y) = rectangular coordinates	Ω = vorticity vector
s = blade spacing	α = blade camber surface	
\mathbf{V} = total velocity vector	$\delta_p(\alpha)$ = periodic delta function	
$\bar{\mathbf{V}}$ = pitch-averaged velocity vector	(ξ, η) = computational coordinates	Subscripts
	ρ = density	bl = at the blade
	ϕ = potential function	x, y = x and y components

technique is numerically efficient because it reduces the three-dimensional problem to solving a set of two-dimensional Helmholtz equations. However, in the transonic flow regime, in order to have a shock-capturing capability, this simplification no longer exists as the continuity equation must be cast in the conservative form. In the present study, the finite-volume rotated scheme of Jameson and Caughey (1977) is used to solve the continuity equation for the reduced potential function. This type of embedding rotational effects into existing potential flow solvers via the Clebsch transformation has been successfully employed to model the vorticity field generated behind shocks (Dang and Chen, 1989) and to simulate propfan/airframe interference effects (Dang, 1990) in transonic flows.

In the finite-volume rotated scheme of Jameson and Caughey, the discretized quasi-linear form of the potential equation utilized for formulating the iterative scheme is:

$$L^n \{ \tilde{\phi}_{i,j}^{n+1} - \tilde{\phi}_{i,j}^n \} = -\text{Res}_{i,j}^n \quad (8)$$

where n is the iterative level. In Eq. (8), the operator L on the correction is derived from the potential equation, and Res is the residual of the continuity equation during the calculation. When the present Clebsch representation of the velocity vector is employed, the general form of the operator L remains unchanged while the residual Res is computed using the appropriate form of the velocity vector given by Eqs. (5) and (6).

The present inverse technique for cascaded blades has been implemented into a multigrid version of the Jameson and Caughey finite-volume full-potential code (FLO-44). One of the primary tasks involves generating the computational grid. Here, there is an inherent disadvantage in using discretized methods as opposed to series solution techniques. In the inverse mode, as the camber line is continuously updated during the calculation, the discretized methods require a new computational grid in the blade-to-blade plane at every iteration. Clearly, in the three-dimensional case, this step can be computationally intensive. On the other hand, the series-solution methods do not require a grid in the blade-to-blade plane.

To alleviate the task of generating a new grid at every iteration, the following strategy is adopted. First, the H-grid topology is employed. Second, the grid is generated in the (x, α) plane instead of the (x, y) plane. From the definition of the function α in Eq. (2), it can be seen that α satisfies $0 \leq \alpha \leq s$ for a periodic computational domain. As the blade solidity is a prescribed quantity, the computational grid needs to be generated only once on a simple rectangular domain.

In the finite-volume method of Jameson and Caughey, another task involved in solving Eq. (8) is to compute the first-order transformation derivatives between the physical plane (x, y) and the computational plane (ξ, η) . Using the definition of α in Eq. (2), along with the choice of the H-grid topology described above, the first-order transformation derivatives of y are computed as follow:

$$y_\xi = f_\xi \quad (9)$$

$$y_\eta = \alpha_\eta \quad (10)$$

where α_η is fixed during the calculation. Consequently, the transformation derivative y_ξ must be updated continuously as the camber line defined by f changes during the calculation. From the computational point of view, because the original flow solver computes the first-order transformation derivatives as they are needed during the calculation rather than storing them, this step requires no additional computing time.

In solving Eq. (8) for the reduced potential function, the following boundary conditions are employed. Along the upstream boundary, the reduced potential function is set to zero. Along the downstream boundary, the nondimensionalized mass flow rate is enforced by setting $\rho \bar{V}_x = \cos \alpha_1$ where α_1 is the air inlet angle. Finally, along the entire periodic boundaries, including the bladed region, the periodic condition is enforced. Numerically, this is accomplished by setting $\tilde{\phi}$ to be single-

valued along these boundaries and to enforce periodicity in the fluxes when forming the residuals at points along the periodic boundaries.

There are two major differences in the way the boundary conditions are implemented along the periodic boundaries between the present inverse formulation and an analysis method. First, unlike the full-potential formulation, which requires multivalued potential functions along the branch cut behind the blade trailing edge, the present Clebsch formulation does not have this requirement as the circulation is accounted for by the rotational term in Eq. (4). Second, in the present inverse method, the zero-flux condition across the blade surfaces is not enforced in solving Eq. (8) as these periodic boundaries are adjusted during the calculation through the blade function α . The blade function α is updated using the blade boundary condition in the form

$$\langle \mathbf{V} \rangle_{bl} \cdot \nabla \alpha = 0 \quad (11)$$

where $\langle \mathbf{V} \rangle_{bl}$ is defined as the averaged velocity on the blade pressure and suction surfaces. In the two-dimensional case, Eq. (11) simplifies to

$$\langle V_x \rangle_{bl} \frac{df}{dx} = \langle V_y \rangle_{bl} \quad (12)$$

Given the velocity field from the previous iteration step, Eq. (12) can be integrated to update the blade shape. The overall iterative scheme consists of solving Eq. (8) for the potential function $\tilde{\phi}$ and Eq. (12) for the blade camber line f .

Results

Test runs were carried out for the design of an inlet guide vane, an impulse turbine blade, and compressor blades operating in the flow regime ranging from subsonic to transonic, including supersonic inflow conditions. In the following calculations, four levels of mesh refinements are employed with the finest mesh containing 128×32 cells and four multigrid levels. In the practical range of turning angle and solidity, approximately 60 work units are required to drive the residual of the continuity equation and the error in the camber line between successive iterations to 10^{-6} . The CPU time required is 150 seconds on the Apollo 3500 work station.

Table 1 shows the tabulated values of the blade camber line y coordinate and the blade angle for a two-dimensional cascade. The blade solidity employed is 1.0, the free-stream Mach number is 0.01, and the input swirl is of the form $\bar{V}_y(x) = (3 - 2x)x^2$ representing a row of inlet guide vanes of the parabolic type loading with air inlet angle $\alpha_1 = 0$ deg and air outlet angle $\alpha_2 = 45$ deg. Recall that the blade loading is proportional to $d\bar{V}_y/dx$. Also tabulated in Table 1 are the results obtained using the classical Biot-Savart law (Hawthorne

Table 1 Comparison of results between present method and Biot-Savart law

x	PRESENT METHOD		BIOT-SAVART LAW	
	f(x)	Blade angle (degree)	f(x)	Blade angle (degree)
0.00000	0.00000	-10.19260	0.00000	-10.49768
0.05000	-0.01114	-13.68083	-0.01174	-14.23379
0.10000	-0.02320	-12.98779	-0.02438	-13.51160
0.15000	-0.03363	-10.24701	-0.03535	-10.76986
0.20000	-0.04090	-6.04068	-0.04312	-6.52426
0.25000	-0.04394	-0.72826	-0.04658	-1.10216
0.30000	-0.04198	5.33851	-0.04491	5.14522
0.35000	-0.03446	11.77912	-0.03749	11.79599
0.40000	-0.02104	18.20912	-0.02399	18.40724
0.45000	-0.00152	24.28090	-0.00424	24.58522
0.50000	0.02409	29.77476	0.02170	30.08641
0.55000	0.05564	34.52691	0.05360	34.80161
0.60000	0.09281	38.51900	0.09109	38.73239
0.65000	0.13512	41.79486	0.13369	41.95433
0.70000	0.18205	44.43581	0.18087	44.55325
0.75000	0.23301	46.52363	0.23204	46.61130
0.80000	0.28733	48.12100	0.28656	48.18797
0.85000	0.34431	49.25273	0.34374	49.30482
0.90000	0.40310	49.87806	0.40270	49.92021
0.95000	0.46253	49.79928	0.46230	49.84225
1.00000	0.52039	47.90441	0.52039	47.93311

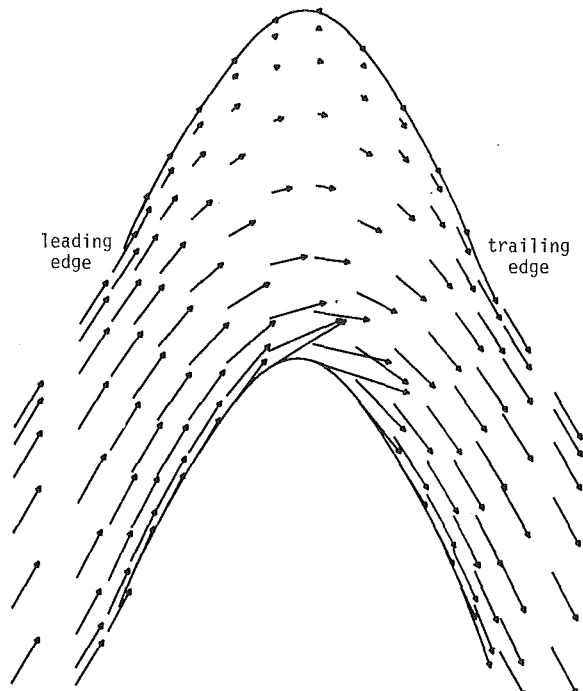


Fig. 2 Velocity vector plot about impulse turbine blade

et al., 1984), which can be considered to be "exact." These comparisons show that the error in the blade camber line y coordinate is no more than 0.3 percent chord and the error in the blade angle is less than 0.5 deg.

More stringent tests of the iteration procedure were carried out, including the design of a subsonic impulse turbine blade of the parabolic loading type with 120 deg deflection and at a solidity of 1.0. In this example, the bound-vorticity at mid-chord is very strong and induces a reverse flow region on the blade pressure surface (Fig. 2).

The next test case illustrates the design of two transonic compressor blades with a free-stream Mach number of 0.90, a solidity of 1.0, and air inlet and outlet angles of 30 deg and 0 deg, respectively. These two blades are designed to perform the same overall work, but with different loading shapes as shown in Fig. 3. Compressor A is designed to have a loading that contains a large negative gradient at the 30 percent chord station while compressor B is designed to have a smooth loading. Figure 4 illustrates comparisons of the Mach number contours between the designed compressors A and B. This figure clearly shows the appearance of a shock in compressor A. On the other hand, compressor B is a shock-free design. The maximum Mach numbers along the blade suction surfaces for compressors A and B are 1.35 and 1.10, respectively.

When strong shocks appear in the blade passage, such as the case of compressor A, the vorticity field generated behind these shocks can significantly alter the flow field predicted by the present isentropic-flow model. In particular, the predictions of shock locations and shock strengths are expected to be inaccurate. This deficiency of the present idealized model can be fixed through the use of an Euler correction method (Dang and Chen, 1989). The boundary layers on the blade surfaces can also alter the flow field significantly in the presence of strong shocks. In this case, a boundary-layer correction must be incorporated into the full thickness problem and is outside the scope of the present study (Dang and McCune, 1984b).

A closer look at the blade camber angle distribution of compressor A reveals a wavy characteristic in the blade camber line around the axial station where there exists a large gradient in the prescribed swirl schedule (Fig. 5). As the camber line is

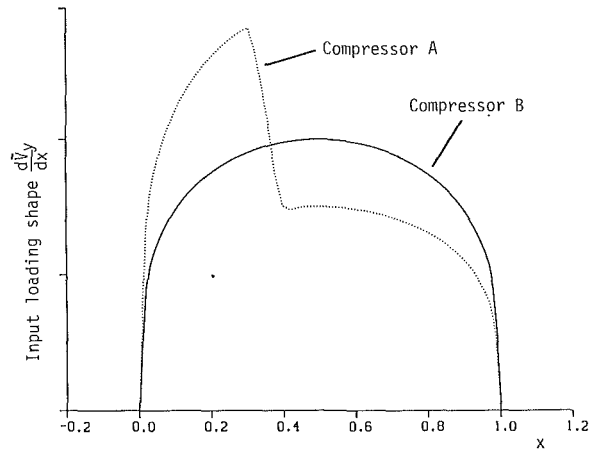


Fig. 3 Comparison of prescribed loading shape

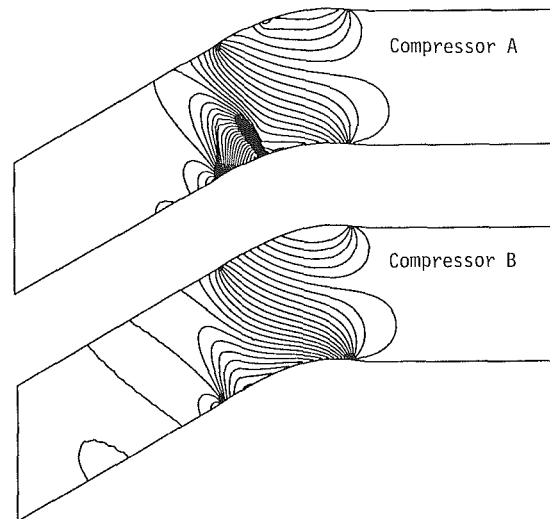


Fig. 4 Comparison of Mach number contour about transonic compressors

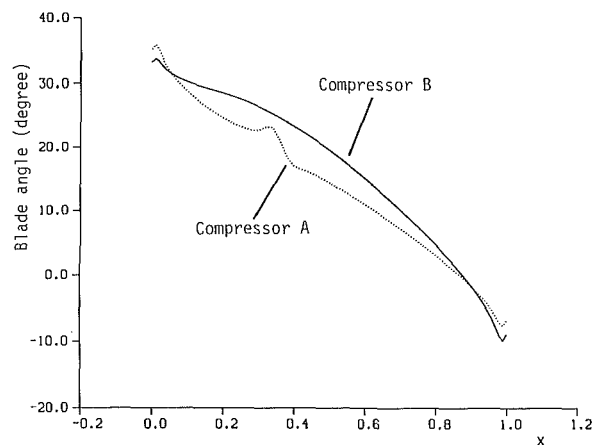


Fig. 5 Comparison of blade angle

generated using the blade boundary condition, namely Eq. (11), this wavy characteristic will appear in the presence of a shock unless the prescribed swirl schedule produces a shock that is locally normal to the blade surface. In general, an arbitrary swirl schedule can produce a normal shock corresponding to a smooth blade profile or an oblique shock corresponding to a kinky (or sharp concave bend) blade profile. Clearly, for the latter case, the discretized equations cannot

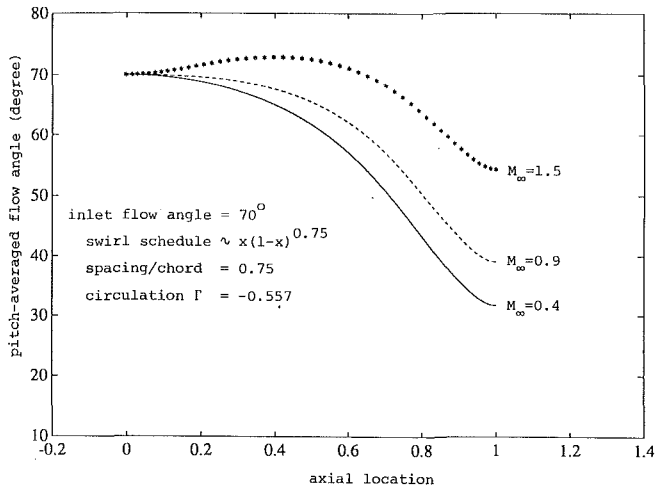


Fig. 6 Comparison of pitch-averaged flow angle

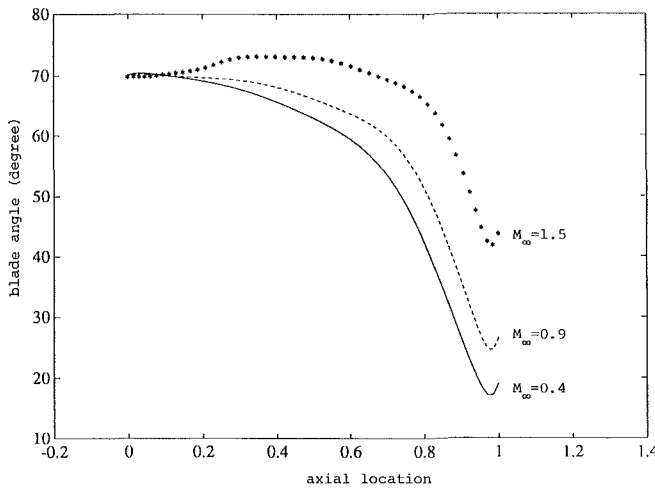


Fig. 7 Comparison of blade angle

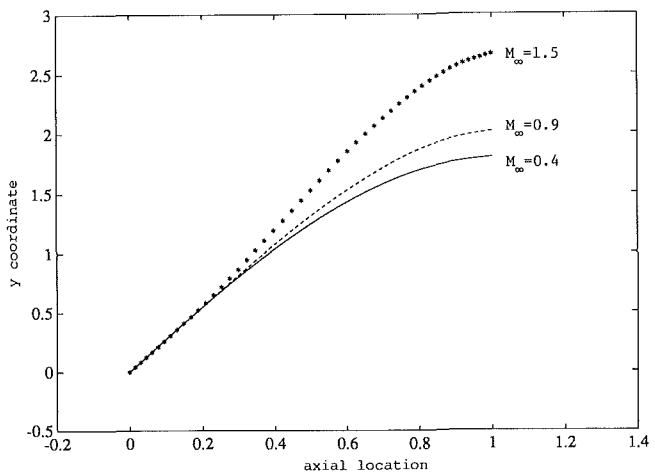


Fig. 8 Comparison of blade camber line

capture this sharp discontinuity in the blade camber line, but instead produce a wavy characteristic. In the transonic flow regime, numerical experiments with various prescribed swirl schedules have shown that both type A and type B swirl schedules can generate shocks in the blade passage and possibly wavy characteristic in the blade camber line. Consequently, in the transonic flow regime, the designer needs to learn how to

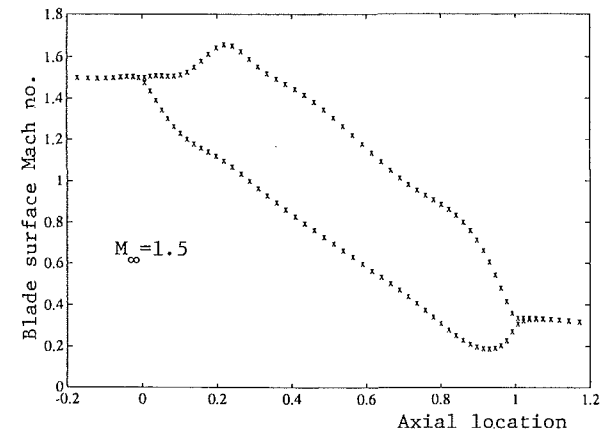
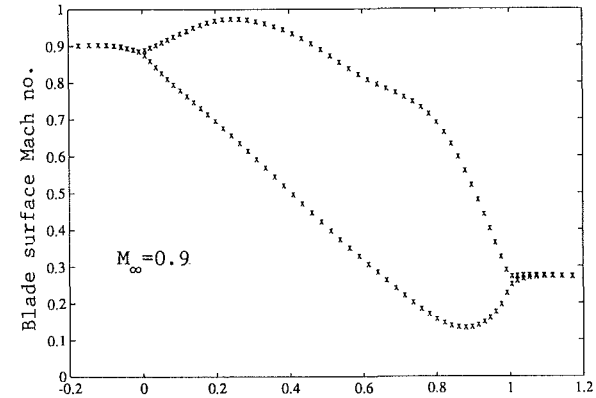
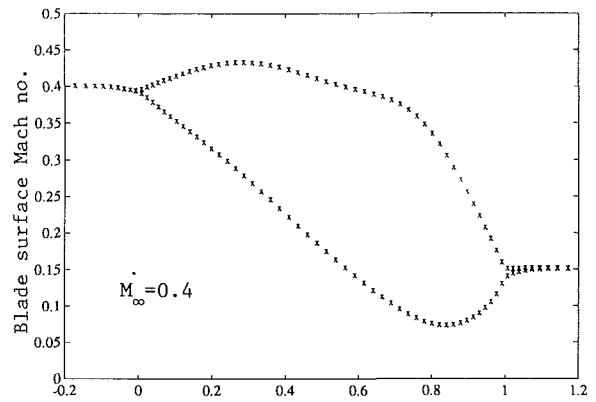


Fig. 9 Comparison of blade surface Mach number distribution

tailor the swirl schedule to produce a smooth blade profile for a desired shocked or shock-free flow conditions.

Figures 6–9 illustrate the design of three compressor blades having the same prescribed pitch-averaged tangential velocity distribution and blade solidity, but with different free-stream Mach number ranging from 0.4 to 1.5. Figures 6 and 7 show comparisons of the pitch-averaged flow angle and blade angle distributions, respectively. Figure 8 shows a comparison of the blade camber line distributions. These results are in agreement with the work of Ghaly (1989) in the subcritical flow regime in that for a given overall blade circulation, compressibility effects reduce the required overall blade turning angle. For the supersonic free-stream case, Fig. 7 shows that a large portion of the blade profile has blade angle greater than the inlet flow angle, even though the prescribed pitch-averaged tangential velocity decreases monotonically from the blade leading edge to the blade trailing edge. Also, note the reverse curvature of the blade near the trailing edge, which is in agreement with

the work reported by Hawthorne et al. (1984). Finally, Fig. 9 shows a comparison of the blade surface Mach number distributions for these three cases. Note that the prescribed swirl schedule of the form $x(1-x)^{0.75}$ produces blades that are slightly aft-loaded and shock-free.

Conclusions

The three-dimensional inverse technique for turbomachinery blading based on the circulation method has been successfully extended into the transonic flow regime. To handle the mixed-flow condition, the previous series expansion techniques in the pitchwise direction are replaced by the Jameson and Caughey finite-volume technique. Numerical results for the design of two-dimensional, infinitely thin cascaded blades in irrotational flow indicate that the proposed numerical technique is accurate and efficient. Calculations were successfully carried out for the design of compressor blades with inlet Mach number varying from the nearly incompressible flow limit to 2.0, excluding choked-flow conditions. The extension of the present method to the three-dimensional case should provide a useful tool for the design of compressor blades in many applications. Finally, the present study indicates that in the transonic flow regime in addition to controlling the pressure distributions along the blade surfaces and minimizing blade warp, the prescribed swirl schedule should be tailored to avoid possible kinky blade profiles arising due to the presence of shocks that are not locally normal to the blade surfaces.

Acknowledgments

This work was partially performed at the Rocketdyne Division of the Rockwell International Corporation under the sponsorship of the Internal Research and Development program.

References

Borges, J. E., 1989, "A Three-Dimensional Inverse Method in Turbomachinery: Part II—Experimental Verification," *ASME JOURNAL OF TURBOMACHINERY*, Vol. 111, No. 3, pp. 355–361.

Dang, T. Q., and McCune, J. E., 1984a, "A 3-D Blade Design Method in Rotational Flow," *Proceedings Int. Conf. on Inverse Design Concepts in Engineering Sciences*, G. S. Dulikravich, ed., University of Texas, Austin, pp. 397–417.

Dang, T. Q., and McCune, J. E., 1984b, "Design Method for Highly-Loaded Blades With Blockage in Cascade," *Proc. ASME Conference on Computation of Internal Flows*, P. M. Sockel and K. N. Ghia, eds., New Orleans, pp. 129–136.

Dang, T. Q., and Chen, L. T., 1989, "Euler Correction Method for Two- and Three-Dimensional Transonic Flows," *AIAA J.*, Vol. 27, No. 10, pp. 1377–1385.

Dang, T. Q., 1990, "Calculations of Propeller/Airframe Interference Effects Using the Potential/Multienergy Flow Method," *AIAA J.*, Vol. 28, No. 5, pp. 771–777.

Dulikravich, G. S., and Sobieczky, H., 1982, "Shockless Design and Analysis of Transonic Cascade Shapes," *AIAA J.*, Vol. 20, No. 11, pp. 1582–1578.

Ghaly, W. S. S., 1989, "A Parametric Study of Radial Turbomachinery Blade Design in Three-Dimensional Subsonic Flow," *ASME JOURNAL OF TURBOMACHINERY*, Vol. 111, No. 3, pp. 338–345.

Hawthorne, W. R., et al., 1984, "Theory of Blade Design for Large Deflections: Part I—2D Cascade," *ASME Journal of Engineering for Gas Turbines and Power*, Vol. 106, No. 2, pp. 346–353.

Hawthorne, W. R., and Tan, C. S., 1987, "Design of Turbomachinery Blading in Three-Dimensional Flow by the Circulation Method: A Progress Report," *Proceedings Int. Conf. on Inverse Design Concepts in Engineering Sciences*, G. S. Dulikravich, ed., Pennsylvania State University.

Jameson, A., and Caughey, D. A., 1977, "A Finite-Volume Method for Transonic Potential-Flow Calculations," *Proceedings of the AIAA 3rd Computational Fluid Dynamics Conf.*, Albuquerque, NM, pp. 35–54.

Katsanis, T., and McNally, W. D., 1973, "Fortran Program for Calculating Velocities and Streamlines on the Hub-Shroud Mid-channel Flow Surface of an Axial- or Mixed-Flow Turbomachine; I—User's Manual," NASA TN D-7343.

Meauzé, G., 1982, "An Inverse Time Marching Method for the Definition of Cascade Geometry," *ASME Journal of Engineering for Power*, Vol. 104, pp. 650–656.

Meauzé, G., 1989, "Overview on Blading Design Methods," AGARD Lecture Series No. 167.

Novak, R. A., 1967, "Streamline Curvature Computing Procedures for Fluid-Flow Problems," *ASME Journal of Engineering for Power*, Vol. 89, pp. 478–490.

Novak, R. A., and Haymann-Haber, G., 1983, "A Mixed-Flow Cascade Passage Design Procedure Based on a Power Series Expansion," *ASME Journal of Engineering for Power*, Vol. 105, pp. 231–242.

Ribaut, M., and Martin, D., 1984, "A Quasi 3-D Inverse Design Method Using Source and Vortex Integral Equations," *Proceedings Int. Conf. on Inverse Design Concepts in Engineering Sciences*, G. S. Dulikravich, ed., University of Texas, Austin, pp. 419–431.

Sanz, J. M., 1984, "Improved Design of Subcritical and Supercritical Cascades Using Complex Characteristics and Boundary-Layer Correction," *AIAA J.*, Vol. 22, No. 7, pp. 950–956.

Tan, C. S., et al., 1984, "Theory of Blade Design for Large Deflections: Part II—Annular Cascade," *ASME Journal of Engineering for Gas Turbines and Power*, Vol. 106, No. 2, pp. 354–365.

Tong, S. S., and Thompkins, W. T., Jr., 1983, "A Design Calculation Procedure for Shock-Free or Strong Passage Shock Turbomachinery Cascades," *ASME Journal of Engineering for Power*, Vol. 105, pp. 369–376.

Wu, C. H., 1951, "A General Through-Flow Theory of Fluid Flow With Subsonic or Supersonic Velocity in Turbomachines of Arbitrary Hub and Casing Shapes," NACA TN 2303.

Aero-Thermal Performance of a Two-Dimensional Highly Loaded Transonic Turbine Nozzle Guide Vane: A Test Case for Inviscid and Viscous Flow Computations

T. Arts

M. Lambert de Rouvroit

von Karman Institute for Fluid Dynamics,
B-1640 Rhode Saint Genèse, Belgium

This contribution deals with an experimental aero-thermal investigation around a highly loaded transonic turbine nozzle guide vane mounted in a linear cascade arrangement. The measurements were performed in the von Karman Institute short duration Isentropic Light Piston Compression Tube facility allowing a correct simulation of Mach and Reynolds numbers as well as of the gas to wall temperature ratio compared to the values currently observed in modern aero engines. The experimental program consisted of flow periodicity checks by means of wall static pressure measurements and Schlieren flow visualizations, blade velocity distribution measurements by means of static pressure tapings, blade convective heat transfer measurements by means of platinum thin films, downstream loss coefficient and exit flow angle determinations by using a new fast traversing mechanism, and free-stream turbulence intensity and spectrum measurements. These different measurements were performed for several combinations of the free-stream flow parameters looking at the relative effects on the aerodynamic blade performance and blade convective heat transfer of Mach number, Reynolds number, and free-stream turbulence intensity.

Introduction

The description of the present test case is a follow-up of similar events, which were presented at the occasion of Lecture Series held at the von Karman Institute for Fluid Dynamics in May, 1973, on "Transonic Flow in Turbomachinery" (Sieverding, 1973) and in April, 1982, on "Numerical Methods for Flows in Turbomachinery Bladings" (Sieverding, 1982). At these occasions, several two and three-dimensional cascade configurations were designed and their aerodynamic performances were experimentally determined as completely and accurately as possible. These measurements mostly served for comparisons with results obtained from inviscid flow calculation methods and presented by different Lecture Series participants. Ever since many other researchers have used the VKI subsonic and transonic turbine cascade test cases to evaluate the accuracy of their two and three-dimensional Euler codes.

A general view on "Test Cases for Computation of Internal Flows in Aero-Engine Components" by AGARD Working Group 18, headed by Prof. Fottner, led to the conclusions that further cascade test cases should provide more information on

boundary layer characteristics including heat transfer and turbulence data (Fottner, 1989) for comparison with the numerous Navier-Stokes numerical codes developed over the last years.

Based on these recommendations, the guidelines for the present experiment were established as follows:

- The experimental data should be as reliable as possible and lend themselves to as little criticism as possible. The choice was therefore limited to axial turbine bladings.
- The experimental data should be used for validation of both inviscid and viscous calculation methods. They should provide information on blade velocity distributions, blade convective heat transfer distributions, and downstream loss and flow angle evolutions.

The present experimental program consists of flow periodicity checks by means of wall static pressure measurements and Schlieren flow visualizations, blade velocity distribution measurements by means of static pressure tapings, blade convective heat transfer measurements by means of platinum thin films, downstream loss coefficient and exit flow angle determinations by using a new fast traversing mechanism, and free-stream turbulence intensity and spectrum measurements. These different measurements have been performed for different combinations of the free-stream flow parameters looking at the relative effects of Mach number, Reynolds number, and

Contributed by the International Gas Turbine Institute and presented at the 35th International Gas Turbine and Aeroengine Congress and Exposition, Brussels, Belgium, June 11-14, 1990. Manuscript received by the International Gas Turbine Institute January 26, 1990. Paper No. 90-GT-358.

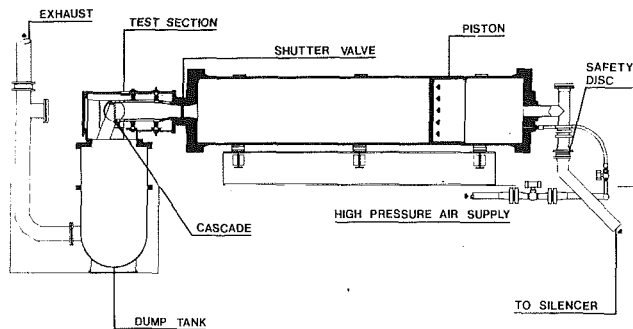


Fig. 1 VKI CT-2 facility

free-stream turbulence intensity on the aerodynamic blade performance and blade convective heat transfer.

A preliminary set of results was presented during the Lecture Series on "Numerical Methods for Flows in Turbomachinery" (Arts et al., 1989) held at the VKI in May 1989, and compared to the numerical predictions provided by a number of participants. The complete, detailed measurement results are available upon request.

Experimental Apparatus

Description of the Facility. The present experimental investigation was carried out in the von Karman Institute Isentropic Light Piston Compression Tube facility CT-2 (Fig. 1). The operating principles of this type of wind tunnel were developed by Jones et al. (1973) and Schultz et al. (1978) about 15 years ago. The VKI CT-2 facility, constructed in 1978, is basically made of three main parts: a 5-m-long and 1-m-dia cylinder, the test section, and a downstream dump tank. The cylinder contains a lightweight piston driven by the air from a high pressure reservoir (...150...250 bar). The cylinder is isolated from the test section by a fast-opening "shutter" or slide valve. As the piston is pushed forward, the gas located in front of it is almost isentropically compressed until it reaches the requested pressure, and hence temperature, levels. The valve is then opened, allowing the pressurized and heated gas to flow through the test section, providing constant free-stream conditions, i. e., total temperature, pressure, and mass flow, until the piston completes its stroke. The free-stream gas total conditions can be varied between 300 and 600 K and 0.5 and 7 bar. The 15-m³ downstream dump tank allows exit static pressure adjustments between 0.15 and 3 bar. This provides an independent selection of both Mach and Reynolds numbers. The typical test duration is about 400 ms. Air is used as working fluid. Further details about the VKI CT-2 facility have been given by Richards (1980) and Consigny and Richards (1982).

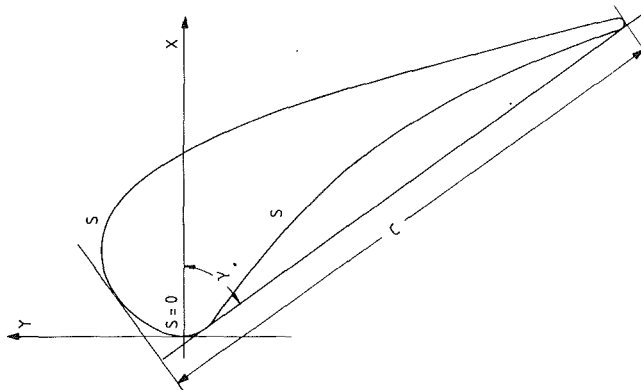


Fig. 2 Geometry of the tested profile

Description of the Model. The different measurements described in the present contribution were carried out on a high-pressure turbine nozzle guide vane profile especially designed for this purpose at the von Karman Institute. The blade shape was optimized for a downstream isentropic Mach number equal to 0.9 by means of an inverse method, developed at VKI by Van den Braembussche et al. (1989). The blade profile is plotted in Fig. 2, whereas its coordinates are listed in Table 1. The blade was mounted in a linear cascade made of five profiles, i.e., four passages. The central blade was instrumented either for static pressure measurements (blade velocity distributions) or for heat flux measurements (blade convective heat transfer distributions). The inlet flow angle to the cascade is 0 deg. The most important geometric characteristics of the cascade are summarized as follows:

c	: 67.647 mm
g/c	: 0.850
γ	: 55.0 deg (from axial direction)
o/g	: 0.2597
$r_{LE/c}$: 0.061 (evaluated around stagnation point)
$r_{TE/c}$: 0.0105

Measurement Techniques. Free-stream total pressure and temperature, static pressure, and turbulence intensity were measured 55 mm ($x/c_{ax} = -1.487$) upstream of the leading edge plane, respectively, by means of a Pitot probe, connected to a variable reluctance Valydine differential pressure transducer, a small type K thermocouple probe, wall static pressure tappings connected to National Semi-Conductor differential pressure transducers, and a constant-temperature hot-wire probe. Wall static pressure tappings were also installed downstream of the cascade, in a plane parallel to the trailing edge

Nomenclature

c = chord	Re = Reynolds number	y = coordinate in tangential direction
d = diameter of bars in turbulence grid	s = coordinate along blade surface	γ = stagger angle
f = frequency	s = pitch of bars in turbulence grid	ρ = density
g = pitch	SPS = pressure side length	Subscripts
h = heat transfer coefficient	SSS = suction side length	0 = total condition
k = isentropic exponent (= 1.4)	T = temperature	1 = upstream condition
M = Mach number	Tu = free-stream turbulence	2 = downstream condition
o = throat	u = velocity	ax = along the axial chord
p = pressure	u' = fluctuating component of velocity	is = isentropic condition
\dot{q}_w = wall heat flux	V = velocity	w = condition at the wall
r_{LE} = leading edge radius	x = coordinate along axial chord	∞ = free-stream condition
r_{TE} = trailing edge radius		

Table 1 Manufacturing coordinates

SUCTION SIDE					PRESSURE SIDE				
X [mm]	Y [mm]	S [mm]	S/SSS [-]	S/C [-]	X [mm]	Y [mm]	S [mm]	S/SPS [-]	S/C [-]
0.000	0.000	0.000	0.000	0.000	0.000	0.000	0.000	0.000	0.000
0.185	1.554	1.565	0.018	0.023	0.185	-0.913	0.932	0.014	0.014
0.742	3.298	3.401	0.039	0.050	0.927	-2.278	2.512	0.038	0.037
1.484	4.548	4.856	0.056	0.072	1.669	-2.963	3.523	0.054	0.052
2.411	5.859	6.462	0.076	0.096	2.782	-3.852	4.947	0.076	0.073
3.895	7.524	8.695	0.101	0.129	4.081	-4.895	6.613	0.101	0.098
11.871	9.783	17.280	0.200	0.255	9.089	-9.023	13.103	0.201	0.194
18.734	4.705	26.013	0.301	0.385	13.540	-13.062	19.115	0.293	0.283
23.000	-2.663	34.541	0.399	0.511	18.363	-18.038	26.047	0.399	0.385
26.338	-10.988	43.515	0.503	0.643	22.444	-23.229	32.653	0.500	0.483
28.750	-18.713	51.608	0.597	0.763	25.967	-28.850	39.290	0.601	0.581
31.161	-27.615	60.831	0.704	0.899	28.935	-34.724	45.873	0.702	0.678
33.201	-35.897	69.361	0.802	1.025	31.347	-40.456	52.092	0.797	0.770
35.241	-44.337	78.044	0.903	1.154	33.757	-46.920	58.991	0.903	0.872
36.355	-48.941	82.781	0.957	1.224	34.870	-49.950	62.220	0.952	0.920
36.726	-50.476	84.360	0.976	1.247	35.427	-51.465	63.834	0.977	0.944
36.814	-52.087	86.041	0.995	1.272	36.075	-52.312	64.956	0.994	0.960
36.461	-52.305	86.463	1.000	1.278	36.461	-52.305	65.348	1.000	0.966

plane and located 16.0 mm ($x/c_{ax} = 1.433$) (measured along the axial chord direction) downstream of the latter. They covered a distance of 130 mm, i.e., a little more than two pitches to verify the downstream periodicity of the flow and to determine the exit Mach number to the cascade. Blade velocity distributions were obtained from 27 static pressure measurements performed along the central blade profile and referred to the upstream total pressure. The downstream loss coefficient evolution as well as the exit flow angle were obtained by means of a fast traversing mechanism, transporting a Pitot probe over two pitches.

Local wall convective heat fluxes were obtained from the corresponding time-dependent surface temperature evolutions, provided by platinum thin-film gages painted onto the central blade, made of machinable glass ceramic. The wall temperature/wall heat flux conversion was obtained from an electrical analogy, simulating a one-dimensional semi-infinite body configuration. A detailed description of this transient measurement technique has been presented by Schultz and Jones (1973). The convective heat transfer coefficient h used in this contribution is defined as the ratio of the measured wall heat flux and the difference between the total free-stream and the local wall temperatures. It is also worth mentioning that the heat transfer measurements discussed in the present paper describe a spanwise averaged behavior as the different thin films were about 20 mm long, but nevertheless situated only in the clean flow region.

Free-Stream Turbulence Generation. One of the important parameters considered in this investigation is the free-stream turbulence. The complete definition of this parameter involves not only its intensity but also its spectrum. These measurements were rather difficult to perform in the CT-2 facility because of the nature of the flow, i.e., an abrupt establishment of a high-speed hot stream, leading to some difficulties in the calibration procedure of the hot-wire probe. The free-stream turbulence was generated by a grid of spanwise oriented parallel bars ($d = 3\text{mm}$; $s/d = 4$). The turbulence intensity was varied by displacing the grid upstream of the model: a maximum of 6 percent could be obtained. The natural turbulence of the facility is about 1 percent. The turbulence intensity quoted in this contribution is defined as:

$$Tu_{\infty} = \sqrt{\frac{u'^2}{\bar{u}^2}}$$

and was measured using a VKI manufactured constant temperature hot-wire probe. The frequency response of this part

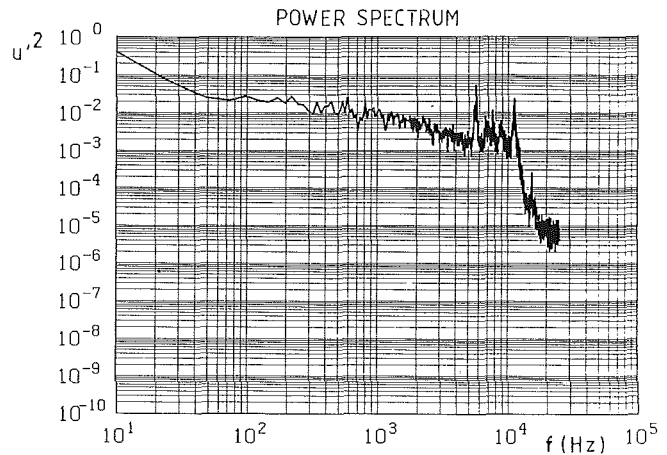


Fig. 3 Free-stream turbulence spectrum analysis

of the measurement chain was observed to be of the order of 10 kHz.

In order to measure the free-stream turbulence spectrum, the raw signal of the hot-wire probe was processed by means of a Fast Fourier analysis. A typical example is shown in Fig. 3. This result is representative of a 4 percent turbulence intensity. Discrete peaks are observed at 5.5 and 11 kHz. In order to investigate the nature of this phenomenon and to determine whether it could have any influence on the boundary layer development, a microphone was mounted inside the test section. The fluctuating component of the output signal was also processed by a Fast Fourier Transform. This analysis revealed the existence of peaks similar to those from the hot-wire signal. Therefore they are obviously of acoustic nature. The information accumulated on this subject up to now seems to indicate that no effect on the boundary layer development is expected from those frequencies. Further investigations on this subject are currently underway at the VKI for high-speed as well as low-speed flows.

Data Acquisition System. All pressure, temperature, and heat flux measurements were directly acquired by a VAX 11/780 computer by means of a VKI manufactured 48 channel data acquisition system through a direct memory access principle. The analog (± 5.0 V) signals were digitized using 12 bit words. For the present measurements, the sampling rate was selected to be 1 kHz for pressure, temperature, and heat flux measurements and 25 or 50 kHz for turbulence intensity and spectrum measurements.

Measurement Uncertainty. The uncertainty on the various measured quantities was carefully evaluated and led to the following error bars, based on a 20:1 confidence interval. The uncertainty on pressure measurements was of the order of ± 0.5 percent, on temperature measurements of the order of ± 1.5 K, on the heat transfer coefficient of the order of ± 5 percent, on the integrated loss coefficient of the order of ± 0.2 points, and on the exit flow angle of the order of ± 0.5 deg.

Test Conditions

The test program was built up by varying the free-stream conditions according to the following limits:

- T_{01} : 420 K
- $M_{2,is}$: 0.70...1.10
- $Re_{2,is}$: $0.5 \cdot 10^5 \dots 2.0 \cdot 10^6$
- Tu_{∞} : 1.0...6.0%

The different flow conditions were defined by all possible combinations of these parameters. All the tests were conducted at least twice to verify the repeatability of the results.

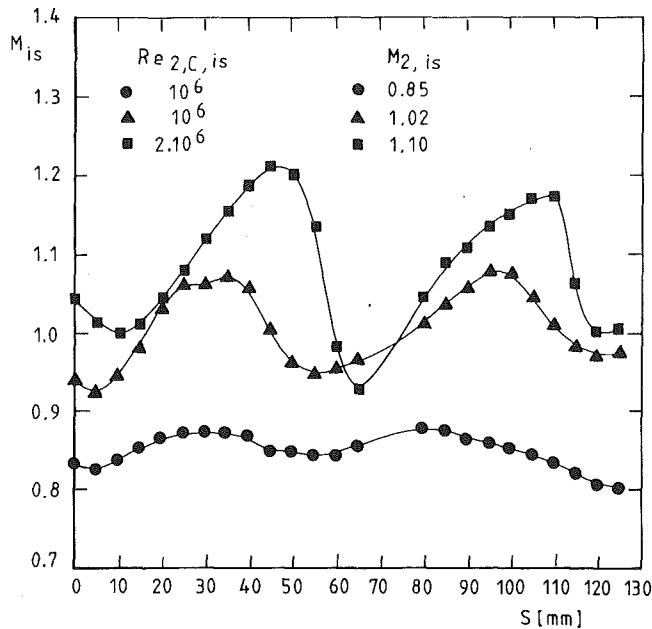


Fig. 4 Downstream static pressure measurements

Periodicity of the Flow

In order to model the flow in a cascade correctly, one must ensure periodic inlet and outlet conditions. The higher the number of blades, the easier it is to establish periodic flow conditions, but for aerodynamic measurements one generally considers eight to ten blades to be a minimum. In the present experiment, however, the scale of the blade has been chosen as large as possible to allow a dense instrumentation, required by the particular goal of this investigation. As a result, only five profiles, i.e., four passages, were used. A careful verification of the flow periodicity was therefore absolutely necessary. Distributions of the downstream wall static pressure were measured and Schlieren flow visualizations were performed for different exit Mach and Reynolds number values. The effect of turbulence intensity was not considered; the measurements were conducted without turbulence grid ($Tu_\infty = 1$ percent).

The downstream static pressure measurements were performed in a plane parallel to the trailing edge plane, located at $x/c_{ax} = 1.433$. The different pressure tappings, located 5 mm from each other, covered 130 mm, i.e., a little more than two pitches. Each tapping was connected to a National Semi-Conductor differential pressure transducer; the low-pressure port of the latter was connected to a vacuum pump to allow a continuous calibration of the system. In order to calculate the downstream flow Mach and Reynolds numbers correctly, the upstream total pressure and temperature were also measured (see section 2.3). The frequency response of the pressure instrumentation was of the order of 150 Hz; the sampling rate was set at 1 kHz. All tests were performed for an upstream total temperature of about 420 K. The useful testing time was of the order of 450 ms. The results are presented as isentropic downstream Mach number distributions versus a coordinate measured along the pitch, toward the lowest profile of the cascade and basically capturing the wakes of blades 3 (the central profile of the cascade) and 4. From these results the averaged exit isentropic Mach number of the cascade was calculated. Based on these measurements, the flow proved to be reasonably periodic for $M_{2,is}$ up to 1.15, as can be seen, e.g., from Fig. 4. Similar measurements were repeated for different downstream Reynolds numbers ranging from 5.0×10^5 to 2.0×10^6 ; they provided the same conclusions.

Flow visualizations were obtained in the transonic regime

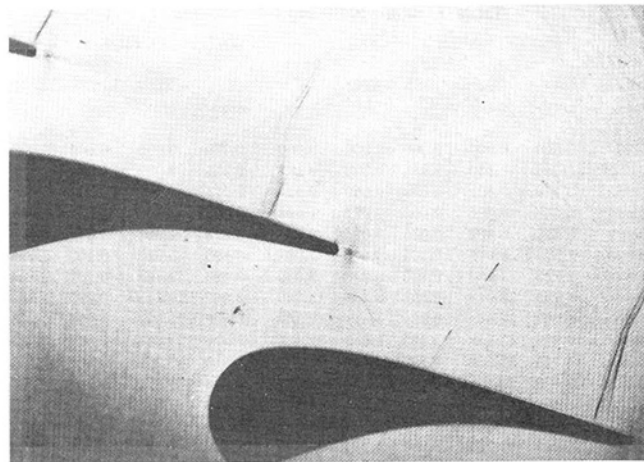


Fig. 5 Schlieren visualization: $M_{2,is} = 1.03$, $Re_{2,is} = 10^6$

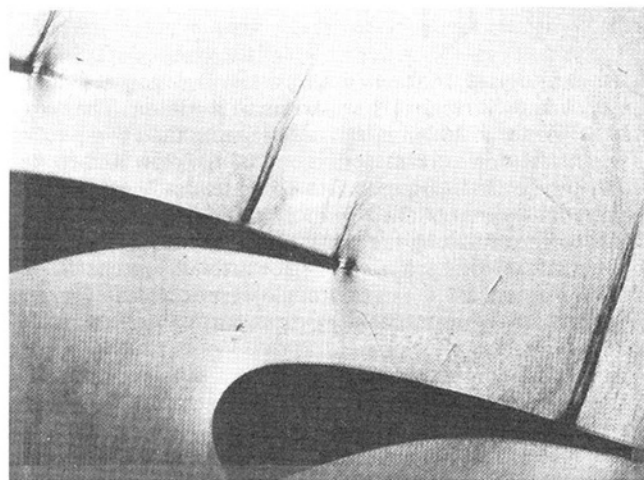


Fig. 6 Schlieren visualization: $M_{2,is} = 1.03$, $Re_{2,is} = 2.0 \times 10^6$

from a single-pass Schlieren system. Figures 5 and 6 present typical results obtained for $M_{2,is} = 1.03$ and $Re_{2,is} = 10^6$ and 2.0×10^6 , respectively. Profiles 3 (the central profile of the cascade) and 4 are shown on these pictures. The spark was initiated about 150 ms after the beginning of the test, to be sure that the flow was correctly established in the cascade. A normal shock is observed on the rear part of the suction side; no definite separated flow regions can clearly be identified for any value of the Reynolds number. These visualizations confirm the periodic character of the downstream flow. For values of $M_{2,is}$ in excess of 1.2, however, the flow periodicity deteriorates very quickly. Additional measurements are presently underway to overcome this difficulty by modifying the downstream tailboard arrangement.

Blade Velocity Distributions

Blade isentropic Mach number distributions were obtained for different loadings from local static pressure measurements, referred to the upstream total pressure. The central blade of the cascade was therefore replaced by a similar profile equipped with 27 static pressure tappings, each of them connected to a National Semi-Conductor differential pressure transducer; the low-pressure ports were again connected to a vacuum pump to allow a regular verification of the calibration characteristics. The uncertainty on the measurements, the frequency response of the measurement chain, and the sampling rate have been quoted in sections 2.6 and 4. The repeatability of results was verified and proved to remain within 0.5 percent. The influence of free-stream turbulence intensity and Reynolds number on

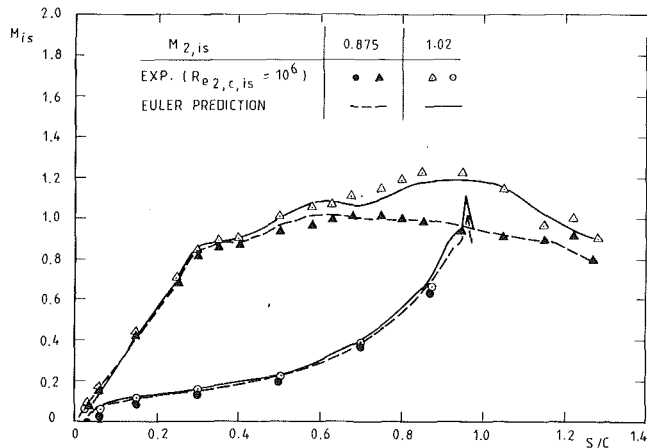


Fig. 7 Blade velocity distributions

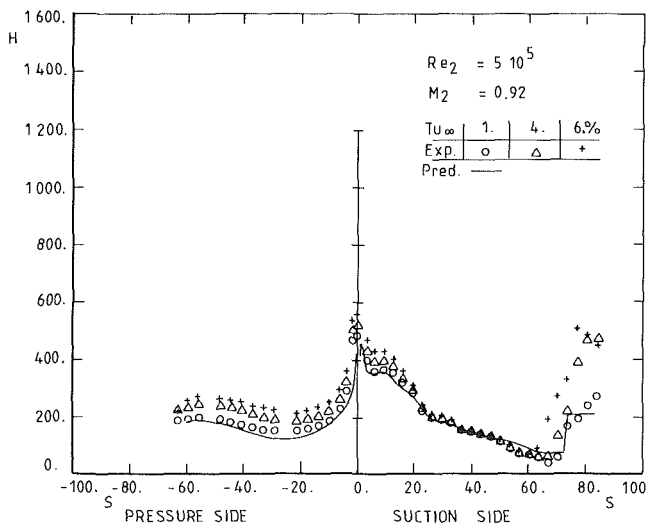


Fig. 8 Blade heat transfer distributions: $M_{2,is} = 0.92$, $Re_{2,is} = 5.0 \times 10^5$

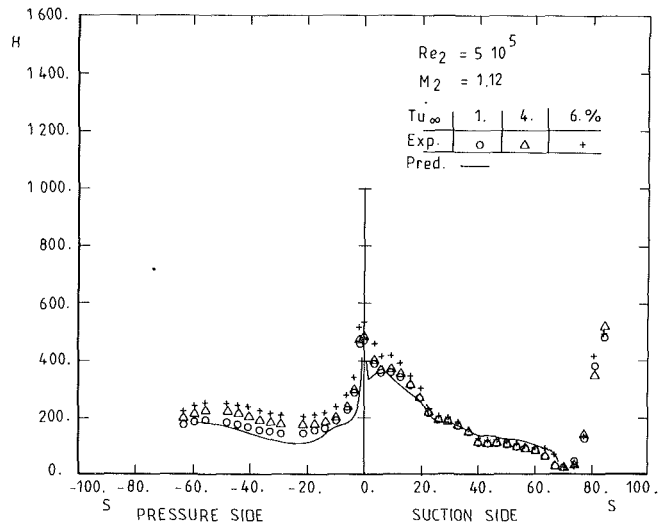


Fig. 9 Blade heat transfer distributions: $M_{2,is} = 1.12$, $Re_{2,is} = 5.0 \times 10^5$

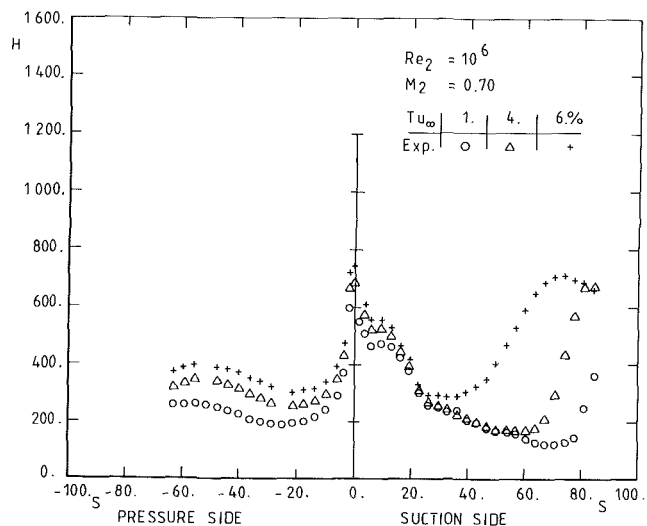


Fig. 10 Blade heat transfer distributions: $M_{2,is} = 0.70$, $Re_{2,is} = 10^6$

the blade velocity distributions were not considered at this stage. All tests were performed for an upstream total temperature of about 420 K. The useful testing time was of the order of 450 ms.

Typical measurement results are presented in Fig. 7. They are plotted as an isentropic Mach number evolution in function of a reduced coordinate (s/c) measured along the profile surface, starting from $x/c_{ax} = 0$. Starting from this theoretical stagnation point, the flow accelerates steeply along the suction side up to $s/c = 0.3$. A small plateau ($s/c = 0.35 \dots 0.40$) is followed by a reacceleration. For the lowest exit Mach number ($M_{2,is} = 0.875$), the velocity distribution is then rather flat with a weak adverse pressure gradient starting from $s/c \approx 0.75$. Let us remember that the blade was initially designed and optimized for about this value of the exit Mach number. For the higher exit Mach number ($M_{2,is} = 1.02$), the flow accelerates up to $s/c \approx 0.85 \dots 0.95$. A shock is then observed ($s/c = \dots 1.05 \dots$); this position is consistent with the one deduced from the Schlieren pictures. The velocity distribution along the pressure side varies smoothly, with no evidence of a velocity peak downstream of the leading edge.

The measurements were compared to the results obtained from a two-dimensional inviscid prediction code (Arts, 1982), based on a time-marching integration technique and a finite volume discretization method. For a subsonic exit Mach number, the calculated results nearly match the measured data (Fig. 7). For transonic exit Mach numbers, only small differences are observed.

Blade Heat Transfer Distributions

Blade convective heat transfer distributions were obtained for different Mach and Reynolds numbers and free-stream turbulence intensities by means of 45 platinum thin films, painted on a machinable glass ceramic blade replacing the central profile of the cascade. The frequency response of the measurement chain associated with the thin films (gages, analogs, amplifiers) is far above 1 kHz. The sampling rate was selected to be 1 kHz, and the signals were filtered at 800 Hz. The useful testing time was of the order of 300 ms. The repeatability of the results was verified and proven to remain within 1 percent. All tests were performed for an upstream total temperature of about 420 K. The different results are presented on Figs. 8 to 14 under the form of a heat transfer coefficient distribution ($W/m^2/K$; see section 2.3) versus a length (mm) measured along the suction and pressure sides of the blade, starting from the theoretical stagnation point ($x/c_{ax} = 0$).

Influence of Free-Stream Turbulence. The influence of free-stream turbulence is presented in Figs. 8 to 14 for three different Mach and Reynolds numbers. The turbulence intensity was varied between 1.0 and 6.0 percent. At low Reynolds numbers (Figs. 8 and 9), Tu_{∞} mainly affects the laminar part of the boundary layer. After having reached relatively high

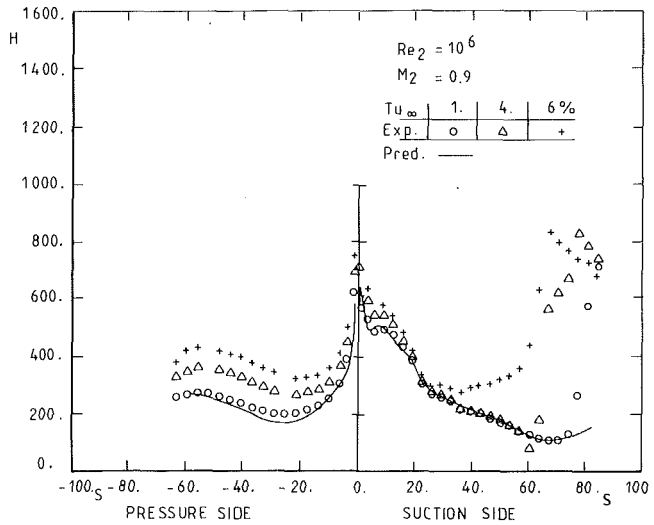


Fig. 11 Blade heat transfer distributions: $M_{2,is} = 0.90$, $Re_{2,is} = 10^6$

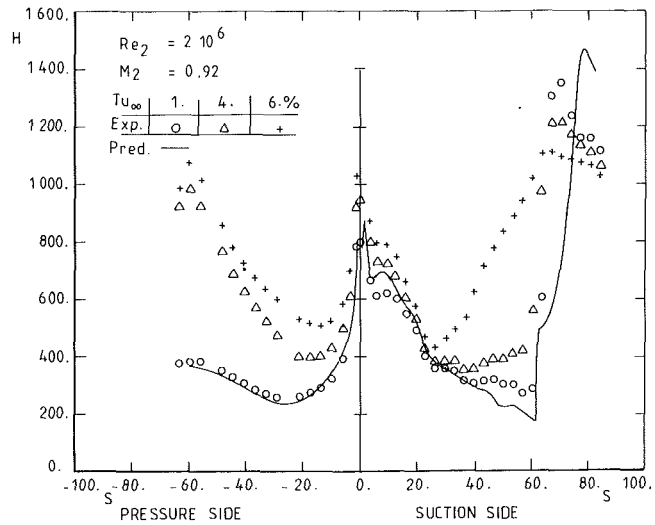


Fig. 13 Blade heat transfer distributions: $M_{2,is} = 0.92$, $Re_{2,is} = 2.0 \times 10^6$

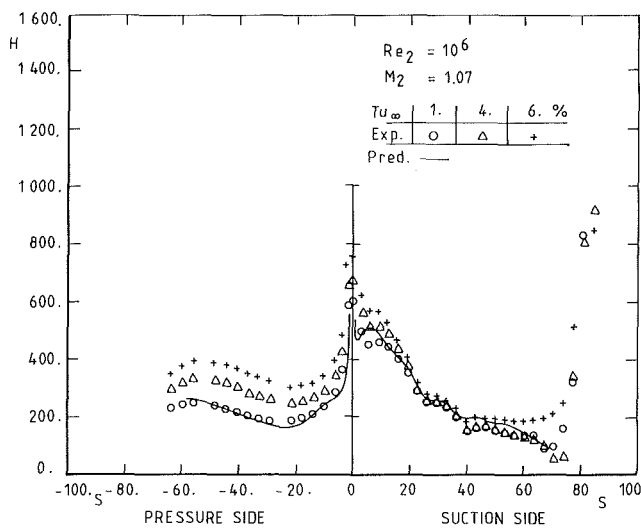


Fig. 12 Blade heat transfer distributions: $M_{2,is} = 1.07$, $Re_{2,is} = 10^6$

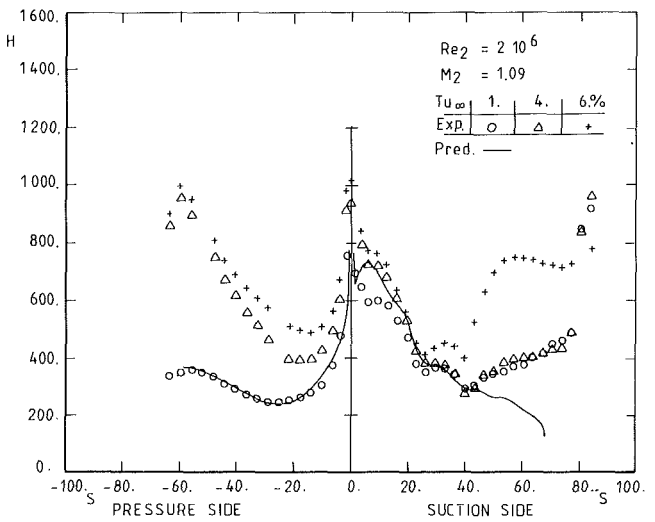


Fig. 14 Blade heat transfer distributions: $M_{2,is} = 1.09$, $Re_{2,is} = 2.0 \times 10^6$

values in the region of the leading edge, the heat transfer falls quite rapidly on either side of the blades; this behavior corresponds to the development of a laminar boundary layer. The level of heating is slightly but distinctly increased by increasing Tu_{∞} ; this effect is, however, less important than at the stagnation point. Similar results were obtained for constant pressure and accelerating laminar boundary layers developing on a flat plate (Smith and Kuethe, 1966). For the lowest Mach number ($M_{2,is} = 0.92$) (Fig. 8), the position of the transition onset ($s = 62 \dots 68$ mm) on the suction side does not seem to be greatly affected by Tu_{∞} . For the highest Mach number ($M_{2,is} = 1.12$) (Fig. 9), the boundary layer transition starts at the shock position ($s = 71.0$ mm). These measurements confirm the shock location observed from the Schlieren pictures and the velocity distributions. Along the pressure side, the boundary layer is most probably in a laminar state.

Similar conclusions are drawn for the intermediate Reynolds number value (Figs. 10, 11, 12), and for the two lowest values of Tu_{∞} ($Tu_{\infty} = 1$ and 4 percent). For the highest value ($Tu_{\infty} = 6$ percent), however, the onset of transition is observed earlier along the suction side. This position corresponds to the small plateau observed on Fig. 7 along the suction side ($s/c = 0.36$; $s = 24.0$ mm). This phenomenon is not marked for the highest exit Mach number where the acceleration rate is high enough to prevent the onset of transition. The behavior along the

pressure side is rather similar to what has been observed for $Re_{2,is} = 5.0 \times 10^5$

The behavior of the boundary layer seems to be quite different for the highest value of the Reynolds number (Figs. 13 and 14). Along the suction side, it appears that the transition onset is very much influenced by the velocity distribution (Fig. 7). It appears in the present case that this transition is triggered by the first important decrease in velocity gradient. Along the pressure side the boundary layer is much more sensitive to free-stream turbulence. It appears that a fully turbulent state is obtained for the highest value of Tu_{∞} .

Influence of Free-Stream Reynolds Number. The influence of free-stream Reynolds number is deduced by comparing Figs. 8 to 14. Different Mach numbers and free-stream turbulence intensities were considered. The Reynolds number was varied between 5.0×10^5 and 2.0×10^6 . The first effect of Reynolds number is, as expected, to increase the overall level of heat flux. This seems to be the only significant effect at low turbulence intensity ($Tu_{\infty} = 1$ percent). For $M_{2,is} = 0.92$, the suction side boundary layer transition onset seems to depend only on the velocity distribution, whereas for $M_{2,is} = 1.10$, the start of transition moves toward the leading edge for the highest value of the Reynolds number. The boundary layer is more sensitive to the acceleration changes along this surface. Along the pressure side the boundary layer remains in a laminar/transitional state.

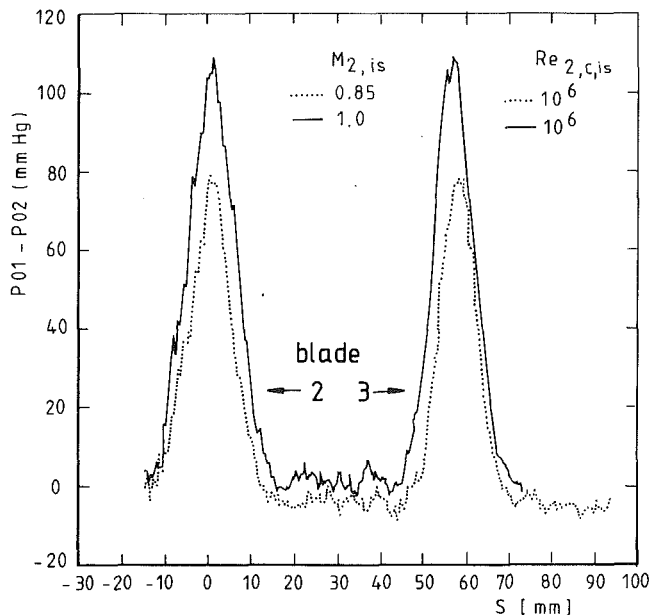


Fig. 15 Measured downstream wakes

For the intermediate turbulence intensity ($Tu_\infty = 4$ percent), similar conclusions can be drawn along the suction side. Along the pressure side, however, the increase in heat transfer is much more important for the highest value of $Re_{2, is}$. For the highest value of turbulence intensity ($Tu_\infty = 6$ percent), the transition of the suction side boundary layer moves gradually upstream with increasing Reynolds number for the two values of the Mach number. For $M_{2, is} = 1.1$ and $Re_{2, is} = 2.0 \times 10^6$, the stabilizing effect of the favorable pressure gradient is clearly observed between $s = 25$ mm (onset of transition) and $s = 40$ mm.

Influence of Free-Stream Mach Number. The influence of free-stream Mach number is deduced by comparing Figs. 8 to 14. Along the pressure side, the velocity distributions are almost similar. As a result, no significant differences appear in the heat transfer coefficient distributions for a given value of the Reynolds number. The behavior of the suction side boundary layer is basically a function of the different acceleration rates observed in Fig. 7.

Numerical Predictions. An attempt was made to predict these heat transfer measurements numerically. A two-dimensional boundary layer code "TEXSTAN" (Crawford, 1988) was used for this purpose. This program is based on the classical Spalding-Patankar approach (1967) to compute boundary layer or pipe flows. It uses a finite difference technique to solve, through a streamwise space marching procedure, the simplified two-dimensional boundary layer equations as applied to flows developing along, e.g., a flat wall or in an axisymmetric tube. In the present paper, the modeling of the turbulent quantities was provided through a Prandtl mixing length approach. The initial velocity and enthalpy profiles were determined 0.5 mm downstream of the theoretical stagnation point by means of the analytical solution of laminar flow around a cylinder (Schlichting, 1968). The predictions (full line) are compared with the measurements (open symbols) on Figs. 8 to 14. This boundary layer code performs rather well as far as laminar boundary layers are concerned, both on the suction side and on the pressure side. The weak point remains the prediction of the suction side transition onset. Attempts were made to use more sophisticated two-equation turbulence models provided into the program (Crawford, 1985). This led to rather disappointing comparisons. More work should be performed in this area from a transition modeling point of view.

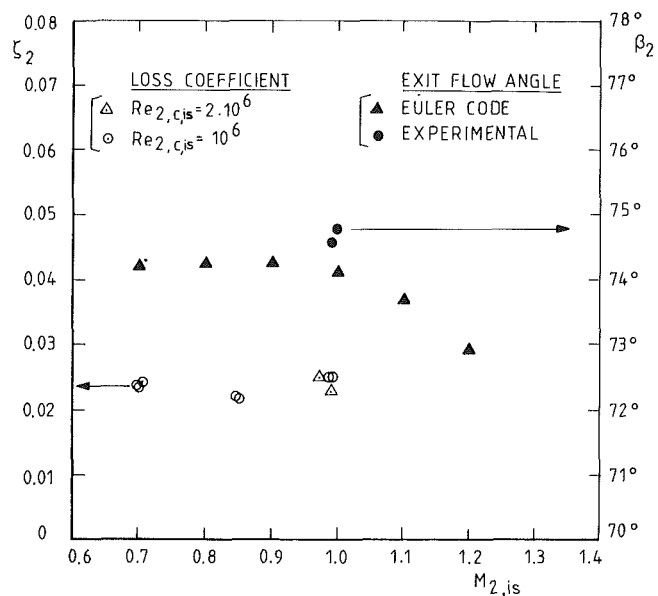


Fig. 16 Downstream loss coefficient and flow angle

Downstream Loss Coefficient and Angle Distributions

Although the VKI CT-2 facility was originally designed for convective heat transfer measurements only, it is evident that it would also be extremely attractive for aerodynamic performance measurements, if the problems related to the short running time ... 400 ... ms and the relatively high air temperature of 400 ... 450 K could be overcome. The first problem was solved by designing a fast traversing mechanism, transporting a Pitot probe at a maximum speed to 800 mm/s over at least two pitches in a plane parallel to the trailing edge plane. The probe carriage is driven by a pneumatic piston. The traversing speed is controlled by the air supply pressure and choked air bleeds. The position of the probe is measured by a linear variable differential transducer. The frequency response of the complete system was evaluated to be 150 Hz. The second problem was solved by locating the transducer outside of the wind tunnel, taking advantage of the conduction effect in the pneumatic pipe between the head of the probe and the transducer. The probe used with this carriage is a classical total, left/right pressure probe except for the absence of the cone head for the static pressure, which was taken instead from the side wall pressure tapings. The performance and accuracy of the complete system were demonstrated in an earlier paper (Sieverding et al., 1988).

Rigorously constant downstream conditions, imperative for this type of measurement, were ensured downstream of the cascade (even with a closed dump tank) by means of a second sonic throat. The total pressure heads of the upstream and downstream Pitot probes were connected respectively to the high and low-pressure ports of a National Semi-Conductor differential pressure transducer, providing a direct measurement of Δp_{01-02} . The left and right heads of the downstream probe were connected to the two ports of a variable reluctance Valydine differential pressure transducer, providing a measure of $\Delta p_{L,R}$, proportional to the exit flow angle. The downstream probe was inclined in such a way to have its head located in the same axial plane ($x/c_{ax} = 1.433$) as the wall static pressure tapings already described in section 4. The sampling rate was set at 4 kHz to have a sufficient number of points to resolve the wake. The influence of free-stream turbulence has not been considered up to now. All tests were performed for an upstream total temperature of about 415 K. The useful testing time was of the order of 250 ms.

Typical examples of measured wakes are shown in Fig. 15

($M_{2,is}=0.85, 1.0$). They correspond from left to right to the wakes of blades 2 and 3 (central blade). The resolution of the deepest point of the wake was confirmed by running different tests with the probe blocked at different positions in this wake, i.e., without being influenced by the frequency response of the system. The loss coefficient was defined as follows:

$$\zeta_2 = 1 - \frac{V_2^2}{V_{2,is}^2}$$

$$1 - \left(\frac{p_2}{p_{02}} \right) \frac{k-1}{k}$$

$$\zeta_2 = 1 - \frac{1 - \left(\frac{p_2}{p_{02}} \right) \frac{k-1}{k}}{1 - \left(\frac{p_2}{p_{01}} \right) \frac{k-1}{k}}$$

The downstream integrated loss coefficient distribution of Fig. 16 was finally obtained as a function of the isentropic exit Mach number. The uncertainty on this loss coefficient was estimated to be 0.2 points. No significant effects of downstream Reynolds number were observed. The general level of the losses, measured for 1 percent free-stream turbulence, is quite low. This is explained by the late transition observed for all Mach and Reynolds number configurations at low turbulence intensity during the heat transfer measurements. Some more confidence in these results was found when comparing them with a classical boundary layer calculation performed by Happel and Ramm (1989) at MTU, Germany for $M_{2,is} = 1.0$. This boundary layer program, based on an integral method, predicts boundary layer losses of the order of 1 percent. To this number one should add trailing edge losses, evaluated at 0.75 percent, base pressure losses, almost zero in this particular situation and shock losses, estimated at 0.5 percent. This reasonable overall estimation is consistent with the measured value.

Because of the lack of a detailed angular calibration of the probe at different Mach numbers, only one result will be presented here (Fig. 16) and compared with the calculated values obtained from the two dimensional inviscid predictions. The uncertainty associated with this angle measurement is most probably of the order of ± 0.5 deg. More detailed work on this subject is presently under way.

Summary—Conclusion

Detailed aerodynamic and convective heat transfer measurements have been obtained on a high-pressure turbine nozzle guide vane, looking at the effect of free-stream Mach and Reynolds numbers as well as turbulence intensity. The measurements were taken using the VKI short duration compression tube facility and were compared to some extent to the results obtained from in-house available two-dimensional inviscid and boundary layer programs.

The aim of this investigation is to provide detailed information about the flow field in this cascade for operating conditions similar to those observed in real engines in order to allow the evaluation of both advanced inviscid and viscous turbomachinery calculation methods. A complete, tabulated description of the aerodynamic and heat transfer experimental results is available from the authors upon request.

References

- Arts, T., 1982, "Cascade Flow Calculations Using a Finite Volume Method," in: *Numerical Methods for Flows in Turbomachinery Bladings*, V.K.I. Lecture Series 1982-07.
- Arts, T., Lambert de Rouvroit, M., and Sieverding, C. H., 1989, "Contribution to the Workshop on Two Dimensional Inviscid and Viscous Turbomachinery Flow Calculations," in: *Numerical Methods for Flows in Turbomachinery*, V.K.I. Lecture Series 1989-06.
- Consigny, H., and Richards, B. E., 1982, "Short Duration Measurements of Heat Transfer Rate to a Gas Turbine Rotor Blade," *ASME Journal of Engineering for Power*, Vol. 104, No. 3, pp. 542-551.
- Crawford, M. E., 1986, "Simulation Codes for Calculation of Heat Transfer to Convectively-Cooled Turbine Blades," in: *Convective Heat Transfer and Film Cooling in Turbomachinery*, V.K.I. Lecture Series 1986-06.
- Crawford, M. E., 1988, Private Communication.
- Happel, H. W., and Ramm, G., 1989, "Contribution to the Workshop on Two Dimensional Inviscid and Viscous Turbomachinery Flow Calculations," in: *Numerical Methods for Flows in Turbomachinery*, V.K.I. Lecture Series 1989-06.
- Jones, T. V., Schultz, D. L., and Hendley, A. D., 1973, "On the Flow in an Isentropic Free Piston Tunnel," ARC R&M 3731.
- Patankar, S. V., and Spalding, D. B., 1967, *Heat and Mass Transfer in Boundary Layers*, 1st ed., Morgan-Grampian, London.
- Richards, B. E., 1980, "Heat Transfer Measurements Related to Hot Turbine Components in the von Karman Institute Hot Cascade Tunnel," in: *Testing and Measurement Techniques in Heat Transfer and Combustion*, AGARD CP 281, Paper 6.
- Schlichting, H., 1968, *Boundary Layer Theory*, 6th ed., McGraw-Hill, New York.
- Schultz, D. L., and Jones, T. V., 1973, "Heat Transfer Measurements in Short Duration Hypersonic Facilities," AGARDograph 165.
- Schultz, D. L., Jones, T. V., Oldfield, M. L. G., and Daniels, L. C., 1978, "A New Transient Facility for the Measurement of Heat Transfer Rates," in: *High Temperature Problems in Gas Turbine Engines*, AGARD CP 229.
- Sieverding, C. H., 1973, "Sample Calculations—Turbine Tests," in: *Transonic Flows in Turbomachinery*, V. K. I. Lecture Series 59.
- Sieverding, C. H., 1982, "Workshop on Two Dimensional and Three Dimensional Flow Calculations in Turbine Bladings," in: *Numerical Methods for Flows in Turbomachinery Bladings*, V. K. I. Lecture Series 1982-07.
- Sieverding, C. H., Arts, T., Pasteels, M.-H., and Klinger, P., 1988, "Transonic Cascade Performance Measurements Using a High Speed Probe Traversing Mechanism in a Short Duration Wind Tunnel," presented at the 9th Symposium on Measuring Techniques for Transonic and Supersonic Flow in Cascades and Turbomachines, Oxford, United Kingdom.
- Smith, M. C., and Kuethe, A. M., 1966, "Effects of Turbulence on Laminar Skin Friction and Heat Transfers," *Physics of Fluids*, Vol. 9, No. 12, p. 2337.
- Van den Braembussche, R. A., Leonard, O., and Nekomouche, L., 1989, "Subsonic and Transonic Blade Design by Means of Analysis Codes," presented at the 64th FDP specialists' meeting on "Computational Methods for Aerodynamic Design (Inverse) and Optimization," Loen, Norway.

D. J. Mee

Department of Engineering Science,
University of Oxford,
Oxford, United Kingdom

N. C. Baines

Department of Mechanical Engineering,
Imperial College,
London, United Kingdom

M. L. G. Oldfield

T. E. Dickens

Department of Engineering Science,
University of Oxford,
Oxford, United Kingdom

An Examination of the Contributions to Loss on a Transonic Turbine Blade in Cascade

Experiments to measure losses of a linear cascade of transonic turbine blades are reported. Detailed measurements of the boundary layer at the rear of the suction surface of a blade and examination of wake traverse data enable the individual components of boundary layer, shock and mixing loss to be determined. Results indicate that each component contributes significantly to the overall loss in different Mach number regimes. Traverses in the near wake of the blade indicate the way in which the wake develops and facilitate examination of the development of the mixing loss.

1 Introduction

An improved understanding of the underlying loss generation mechanisms in transonic turbomachinery blading should lead to better blade design procedures and thus higher engine efficiencies. The desire to gain such an understanding has resulted in a number of detailed experimental studies in recent years. For example, Hoheisel et al. (1987) examined the influence of different free-stream turbulence levels on the loss of three turbine profiles with different pressure gradient levels but the same total loading. The investigation concentrated on the development of blade boundary layers and their contribution to the overall blade loss. For supersonic compressor cascades, where direct and indirect shock losses constitute a major component of the overall loss, Schreiber (1987) has used cascade results to study the individual contributions of viscous and shock losses. Xu and Denton (1988) have studied the mixing losses of transonic turbine blades for different blade trailing edge thicknesses. This included consideration of the effects of blade boundary layers on the subsequent mixing downstream of the blade. Denton and Cumpsty (1987) have given a good summary of the physical processes leading to loss generation in turbomachines.

It is useful to separate the overall loss into components that can be attributed to different loss generation mechanisms. Such a procedure can be used to identify the relative magnitudes of contributions and this may point to where efficiency improvements can be made. A linear cascade of blades of large aspect ratio eliminates certain loss generation mechanisms that occur in gas turbines (such as tip leakage and endwall losses) but simplifies the techniques required to quantify the loss generated

by other mechanisms. At the center span of a two-dimensional transonic cascade we will consider loss as being the sum of three components. These are the loss in the boundary layers formed on the blade surfaces, loss due to shock waves, and the loss that occurs downstream of the blades when the flows from each side of a blade merge and mix to a uniform downstream flow. This last component is referred to as the mixing loss. It is noted that even though there will be increases in loss downstream of the exit plane of the cascade as the wakes mix with the free stream, the overall loss is completely determined by the conditions at the exit plane.

It has been suggested that the loss in the wakes could be separated from mixing losses. However, because the wake mixes rapidly just downstream of the blades, a *wake loss* component would vary strongly with the traverse location. For this reason we have included this wake loss component in the mixing loss term.

The overall loss can be found by traversing downstream of the blades across a full pitch, measuring total and static pressures and flow angle. Assuming mixing downstream occurs at constant area (axially), the well-established method of Amecke (1970) can be used to determine homogeneous or *mixed-out* quantities from which loss coefficients can be found. The boundary layer loss can be estimated by measuring the boundary layer profile at the rear of the suction surface as described in section 3.3.2. Shock losses, up to the plane at which downstream traverses are performed, can be estimated by examining the total pressure drop in the regions outside of the blades' wakes (section 3.3.3). Finally mixing losses can be found by subtracting the boundary layer and shock loss components from the overall loss. This method for differentiating between shock and mixing losses is only valid provided that all the shock loss occurs upstream of the traverse plane. This will be reasonable at low supersonic exit Mach numbers, but for higher exit Mach numbers, where shock loss occurs farther down-

Contributed by the International Gas Turbine Institute and presented at the 35th International Gas Turbine and Aeroengine Congress and Exposition, Brussels, Belgium, June 11-14, 1990. Manuscript received by the International Gas Turbine Institute January 15, 1990. Paper No. 90-GT-264.

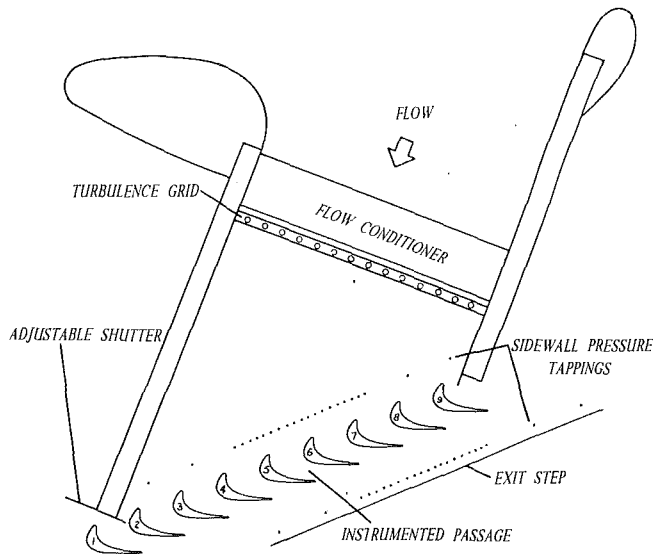


Fig. 1 Cascade arrangement

stream, some of the shock loss may be included in the mixing loss term.

The aim of the present study is to investigate in detail the individual contributions of blade boundary layers, passage, and recompression shocks and downstream mixing to the overall loss of a transonic high-pressure turbine cascade. Part of the experimental program to examine the mixing loss involved detailed examination of the development of the wake just downstream of the blade. Results from these tests are also presented.

2 Experiments

All experiments reported in this paper were performed recently in the Oxford University Engineering Laboratory Transonic Blowdown wind tunnel. This facility, described in detail by Baines et al. (1982), is a short duration tunnel, capable of three or more seconds of steady flow, that was designed for aerodynamic studies of gas turbine blading. The tunnel can be used to test cascades with independent Mach number and Reynolds number variation over a wide operating range. Cascade flow periodicity is maintained by a free-jet exit and adjustable shutters bleeding air past the end blades (see Fig. 1).

A cascade of nine blades of 100 mm true chord and 300 mm span was tested for exit Mach numbers in the range $0.5 \leq M_{ex} \leq 1.15$ and exit Reynolds numbers in the range $450,000 \leq Re_{ex} \leq 2,000,000$. The exit Mach number was based on a single measurement of the total pressure $0.62C_{ax}$ axially upstream of the instrumented passage and an arithmetic average of meas-

Table 1 Details of cascade

Inlet Angle	42.8°	Design Re_{ex}	1,000,000
Inlet Mach Number	0.31	Chord - Axial	76.9 mm
Inlet Total Temperature	285K	- True	100.0 mm
Inlet Turbulence Intensity	4.1%	Span	300 mm
Nom. Exit Flow Angle	68°	Pitch	84.0 mm
Design M_{ex}	0.92	Trailing-edge diameter	2.0 mm

urements from six static pressure tappings equally spaced across the instrumented passage $0.65C_{ax}$ axially downstream of the cascade. (C_{ax} is the axial chord length.) The exit Reynolds number is based on the same total and static pressures, the inlet total temperature, and the true chord of the blades.

The turbine blade profile tested in the present study has been used in previous studies at Oxford University. For example, experiments have been performed to examine its heat transfer performance (Nicholson, 1981), the influences of shock and wake passing (Doorly and Oldfield, 1985), and shock and wake passing in the presence of film cooling (Ashworth, 1987).

The two blades encompassing the central passage were instrumented for static pressure measurement. The pressure surface of blade 5 had 15 tappings and the suction surface of blade 6, 26 tappings. Further details of the cascade and flow conditions are given in Table 1.

Various techniques for transition detection on the suction surface were attempted, the most successful being a hot-wire drag (Hodson, 1983). A Dantec 55M series anemometer was used in conjunction with a type P11 probe held 0.5 mm from the blade surface at different chordwise positions. Qualitatively, the form of the signal was used to identify the start and end of turbulent burst activity.

The overall loss of the profile was determined from traverses made with a trident probe (measuring total and static pressure and flow angle) in a plane parallel to and approximately $0.5C_{ax}$ axially downstream of the trailing edges of the blades. The probe was supported in a microprocessor and stepper-motor controlled traversing mechanism, which is capable of moving the probe in three orthogonal directions. Losses were determined using the method of Amecke (1970) to determine mixed-out quantities, assuming mixing at constant area (axially). Losses are presented in terms of the primary loss coefficient, $1 - \eta$, where η is the primary efficiency defined as the ratio of the actual kinetic energy of the flow at the mixed-out plane to that which would be present if the flow expanded isentropically from the inlet conditions to the measured mixed-out static pressure. This can be written in terms of enthalpy as

$$\eta = \frac{h_{02} - h_2}{h_{01} - h_{2s}} \quad (1)$$

The same trident probe was used in an examination of the development of the wake immediately downstream of the blade.

Nomenclature

C_{ax} = axial chord length
 c_p = specific heat at constant pressure
 \dot{e} = kinetic energy flux
 h = specific enthalpy
 l_t = distance from center of trailing edge circle in nominal exit flow direction
 \dot{m} = mass flow rate
 M_{ex} = exit Mach number
 P = pressure
 Re_{ex} = exit Reynolds number
 s = span of blades
 T = temperature

u = flow speed
 X = axial distance from blade leading edge
 y = distance normal to blade
 z_t = distance normal to l_t
 γ = ratio of specific heats
 δ_{99} = 99 percent boundary layer thickness
 δ^* = displacement thickness
 δ_e = energy defect thickness
 η = primary efficiency (Eq. (1))
 ϑ = momentum thickness
 ξ = primary loss coefficient = $(1 - \eta)$

ρ = density
 φ_{te} = diameter of blade trailing edge

Subscripts

bl = due to boundary layers
 e = at edge of boundary layer
 m = due to mixing
 ref = reference value (at $M_{ex} = 0.92$, $Re_{ex} = 10^6$)
 s = isentropic value
 $shock$ = due to shock waves
 0 = stagnation conditions
 1 = at inlet to cascade
 2 = downstream of cascade

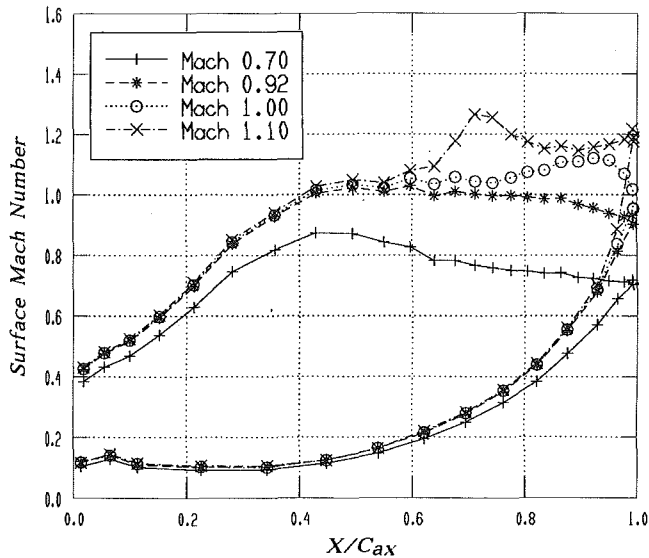


Fig. 2 Blade surface Mach number distributions

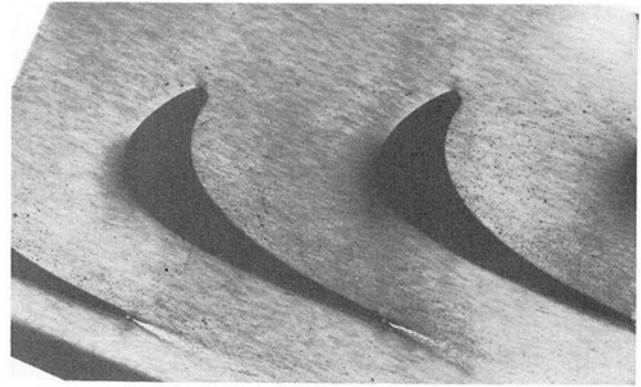
Traverses were made through the wake, perpendicular to the nominal flow exit angle, for three exit Mach numbers, 0.70, 0.92, and 1.00, all at $Re_{ex} = 1,000,000$. Data were recorded for seven locations downstream of the center of the trailing-edge circle at distances 2.2, 3.7, 5.2, 6.7, 8.7, 12.7, and 25.2 times the diameter of the trailing-edge circle (2.0 mm). The traverse planes are designated planes 1 to 7, respectively. Due to the extreme flow angles very close to the trailing edge, the calibration range of the trident probe was exceeded at certain points for the closest two traverse planes. This led to the rejection of results for plane 1 but, for plane 2, the calibration of the probe was estimated from tests at low speeds (Mach 0.3) on probes of similar geometry.

Boundary layer profiles at the rear of the suction surface ($X/C_{ax} = 0.99$) were measured by traversing a flattened Pitot tube (0.13 mm opening, overall height of 0.30 mm, and width of 2.0 mm) through the boundary layer. Up to 1000 points were recorded during the 1.5 to 4.0 s of steady flow. The downstream traverse gear was used to support the probe and drive it toward the surface during the run at constant speed. An electrical potential difference established between the probe and the blade was used to determine the time at which the probe came in contact with the blade. From this and the speed of traverse the distance of the probe from the surface at all prior times could be established. Traverses were made for $0.66 \leq M_{ex} \leq 1.15$ at $Re_{ex} = 1,000,000$.

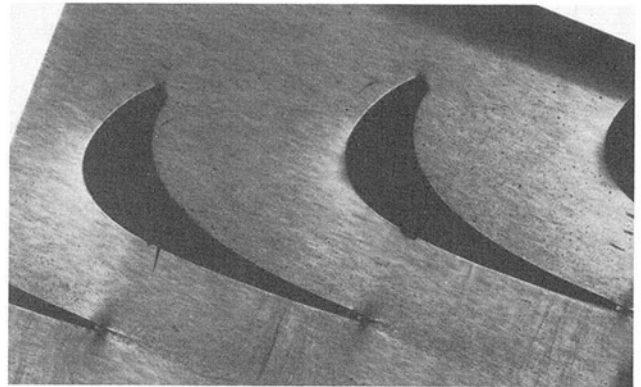
3 Results and Discussion

3.1 Cascade Flow. Typical measured surface Mach number distributions at the design Reynolds number (1,000,000) for $M_{ex} = 0.70, 0.92, 1.00,$ and 1.10 are shown in Fig. 2. Schlieren photographs at these conditions are given in Fig. 3. References to the results presented in these figures will be made in discussion of further results.

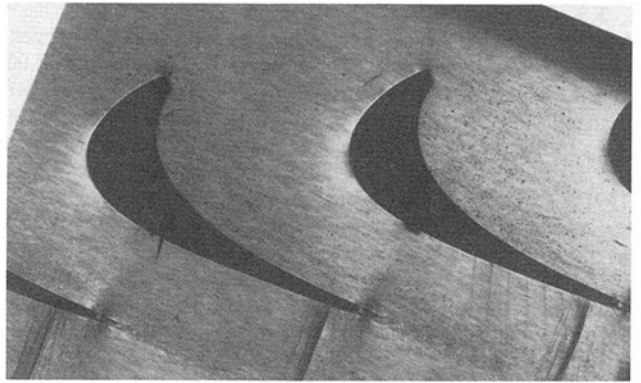
3.2 Transition. Tests with a hot-wire probe to detect transition on the suction surface were performed at the design condition. The results indicated that transition starts at $X/C_{ax} = 0.6$ and is complete at $X/C_{ax} = 0.95$. (Transition length is 46 percent of suction surface length.) This result is in agreement with results of experiments by Nicholson (1981), which involved heat transfer measurements in an isentropic light-piston tunnel at $M_{ex} = 0.96$ for the same exit Reynolds number on the same profile using thin-film gages. Nicholson's results at $M_{ex} = 0.96$ and $Re_{ex} = 2,000,000$ indicated that transition starts earlier ($X/C_{ax} = 0.11$) at the higher Reynolds number and that the length of the transition region is markedly reduced



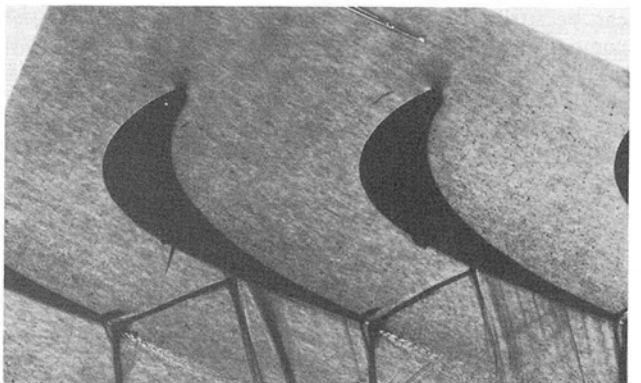
(a) $M_{ex} = 0.70$



(b) $M_{ex} = 0.92$



(c) $M_{ex} = 1.00$



(d) $M_{ex} = 1.10$

Fig. 3 Schlieren photographs

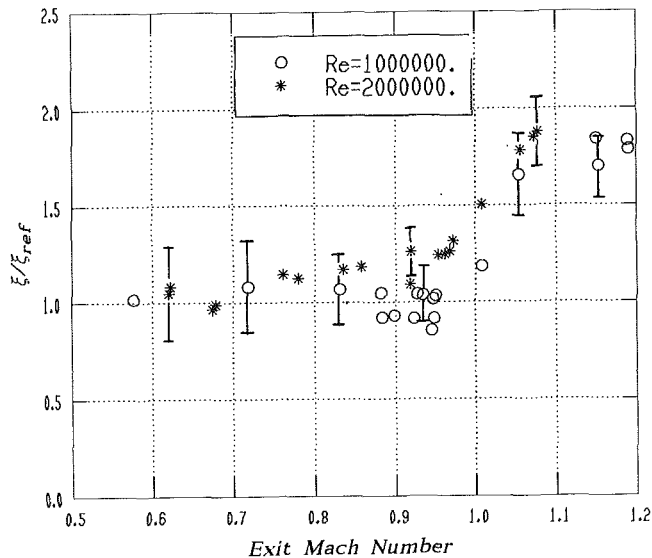


Fig. 4 Variation of loss with exit Mach number

(complete by $X/C_{ax} = 0.55$; transition length is 29 percent of suction surface length). There are a number of effects that the location of transition on the suction surface of the blade can have on the efficiency of the stage. First, the boundary layer loss of the blade can be minimized if a laminar boundary layer can be maintained over as much of the blade as possible. However, at transonic exit Mach numbers where a passage shock or a recompression shock interferes with the boundary layer, a turbulent layer will have less tendency to separate and thus may be preferable in terms of loss. Xu and Denton (1987) have argued that the boundary layer shape factor at the trailing edge of the blade has a direct influence on the mixing loss—a lower shape factor associated with a higher mixing loss.

3.3 Loss

3.3.1 Overall Loss. Overall losses were measured over a range of transonic exit Mach numbers for $Re_{ex} = 1,000,000$ and $2,000,000$. Results are shown in Fig. 4. Losses are normalized with ξ_{ref} , the loss measured at the design condition. Also indicated in the figure are typical uncertainty limits for the measurements (as calculated according to Baines et al., 1991). The overall level of loss is relatively low, which is associated with the fact that there are no large regions of boundary layer separation at either Reynolds number (as evidenced in schlieren photographs and also in the detailed boundary layer traversing of Mee et al., 1991) and that the blade has a relatively thin trailing edge. The differences in level of loss between results at the two Reynolds numbers are within the uncertainty bands, but there is a consistent trend of higher loss at the higher Reynolds number for $M_{ex} > 0.8$. At least part of the increased loss at the higher Reynolds number condition can be attributed to an increase in the boundary layer loss component. Calculations from boundary layer measurements taken at the rear of the suction surface at $M_{ex} = 0.92$ indicate that the boundary layer loss component is 8 percent higher for the higher Reynolds number condition. This, however, is insufficient to account for the magnitude of the difference observed.

At an exit Mach number of 0.92, losses were determined for exit Reynolds numbers ranging from 450,000 to 2,000,000. Results are presented in Fig. 5. The accuracy of loss measurement decreases as the Reynolds number decreases, leading to large uncertainty estimates at the lowest Reynolds numbers. The trend in the measurements is for an approximately constant loss up to $Re_{ex} = 1,200,000$, followed by an increase in loss at the higher Reynolds number.

3.3.2 Boundary Layer Loss. The boundary layer profiles at the trailing edge of the suction surface ($X/C_{ax} = 0.99$) were

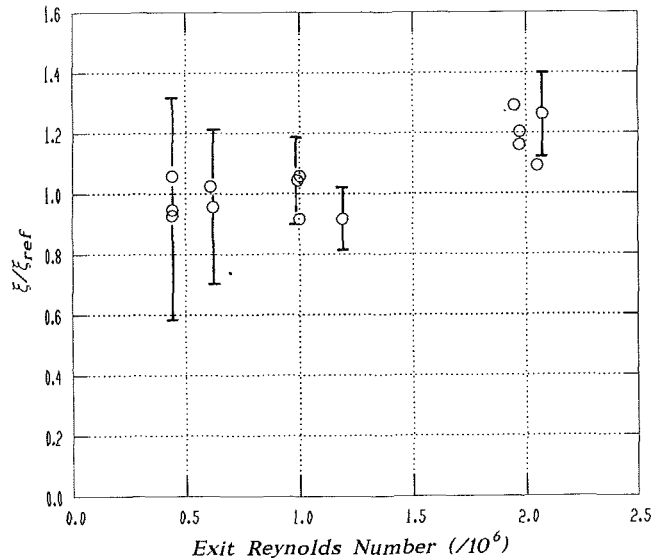


Fig. 5 Variation of loss with exit Reynolds number at $M_{ex} = 0.92$

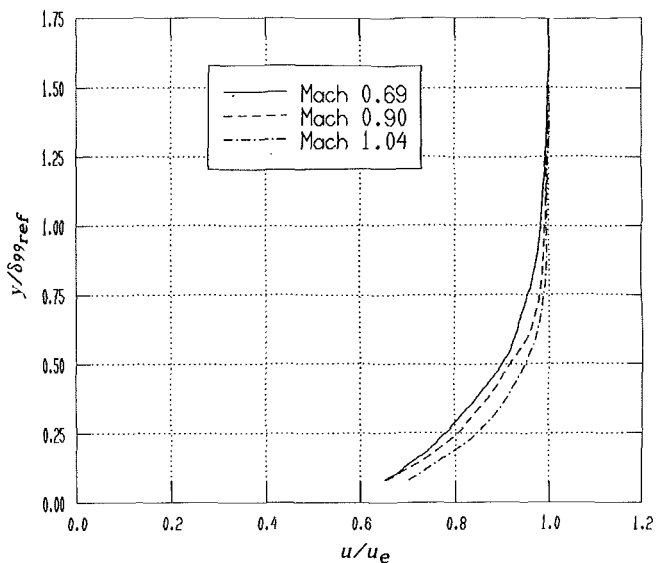


Fig. 6 Smoothed boundary layer velocity profiles at $X/C_{ax} = 0.99$, $Re_{ex} = 1,000,000$

obtained from the blade static pressure, inlet total pressure, and inlet total temperature and instantaneous measurements of the total pressure through the layer. The static pressure across the layer was assumed to be constant. The blade temperature was taken to be the air temperature measured in the test section prior to a run and was assumed to be constant during the short tunnel run time (although the recovery temperature was slightly lower than the blade temperature during a run). The static temperature through the layer was determined from the velocity profile using Eq. (2.5.37b) of Fernholz and Finley (1980) with a turbulent recovery factor of 0.89. A correction was made for wall interference when the flattened Pitot tube was within 0.4 mm of the blade surface based on measurements with geometrically similar probes in a turbulent boundary layer at transonic speeds in the same tunnel. The unmeasured portion of the profile between the blade surface and the first measurement point was filled with a polynomial that was a least-squares fit to the lower 20 percent of the layer and passed through the value at the surface.

Typical boundary layer velocity profiles are given in Fig. 6. Each has been smoothed by passing the profile (as determined from instantaneous pressures and temperatures) through a Hamming filter. The layer thickness decreases as M_{ex} increases and the profile becomes slightly less full. This can be seen in

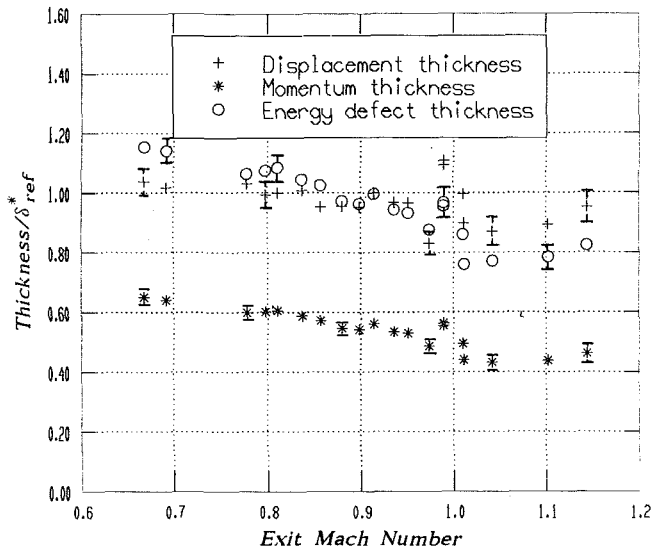


Fig. 7 Variation of boundary layer thicknesses with exit Mach number, $X/C_{ax} = 0.99$, $Re_{ex} = 1,000,000$

the variation with M_{ex} of the boundary layer displacement, momentum, and energy defect thicknesses, plotted in Fig. 7. These show a steady decrease with M_{ex} to a sonic exit Mach number and then a slow increase as M_{ex} increases further. This trend can be explained with reference to the measured surface Mach number distributions plotted in Fig. 2. At low M_{ex} there exists an adverse pressure gradient downstream of the throat. This will lead to an increased boundary layer thickness and a possible reduction in transition length (Walker, 1987) compared with that which would be obtained in a zero pressure gradient flow.¹ As M_{ex} increases, the length of adverse pressure gradient decreases until at $M_{ex} = 1.0$ the passage shock stands at the very rear of the suction surface (Fig. 3) and there is a favorable pressure gradient up to the 95 percent axial chord position. It was at this condition that a minimum suction surface boundary layer thickness was detected. At higher M_{ex} a recompression shock strikes the suction surface, interacting with the boundary layer and leading to a small region of adverse pressure gradient followed by another length of either constant or slightly favorable pressure gradient. These conditions lead to a slight increase in thickness but, as shown in the schlieren photographs, no significant regions of shock-induced boundary layer separation are present.

Noting that the definition of loss being used involves the ratio of actual kinetic energy to ideal kinetic energy at the mixed-out plane, the boundary layer loss can be related to the kinetic energy dissipated in the boundary layer. An estimate can be made of the loss of kinetic energy at a point on the blade by subtracting the actual kinetic energy of the layer from that which would be present if the boundary layer gas was at free-stream conditions,

$$\Delta \dot{e} \approx 0.5 u_e^2 \int_0^\delta \rho u dy - \int_0^\delta 0.5 u^2 \rho u dy = 0.5 \int_0^\delta \rho u (u_e^2 - u^2) dy. \quad (2)$$

But the energy dissipation thickness of the boundary layer is (Schlichting, 1979)

$$\delta_e = \int_0^\delta \frac{\rho u}{\rho_e u_e^2} (u_e^2 - u^2) dy \quad (3)$$

¹There is evidence in the variation of the boundary layer shape factor with M_{ex} (Fig. 8) that the length of transition on the suction surface increases as the length of adverse gradient is reduced and eventually replaced as a favourable gradient. (A higher shape factor is consistent with a transitional boundary layer.) The shape factor slowly increases with M_{ex} up to $M_{ex} = 1.0$ and then remains essentially constant.

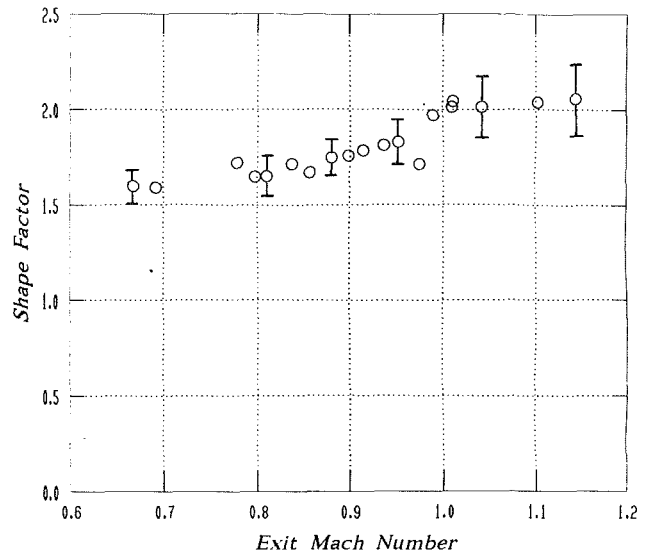


Fig. 8 Variation of boundary layer shape factor with exit Mach number, $X/C_{ax} = 0.99$, $Re_{ex} = 1,000,000$

Therefore Eq. (2) can be written as

$$\Delta \dot{e} \approx 0.5 \rho_e u_e^3 \delta_e. \quad (4)$$

The present analysis deals only with the loss associated with the suction surface boundary layer, with that due to the pressure surface boundary layer being neglected. Measurements (Mee et al., 1992) indicate that the pressure surface layer is an order of magnitude thinner than that on the suction surface and thus does not contribute significantly to the total boundary layer loss.

If the flow expanded isentropically from the inlet conditions to the measured mixed-out conditions, the kinetic energy flux at the mixed-out plane would be

$$\dot{e}_s = \dot{m} (h_{01} - h_{2s}). \quad (5)$$

Noting that $h = c_p T$ and assuming adiabatic flow, this can be written as

$$\dot{e}_s = \dot{m} c_p T_{01} \left\{ 1 - \left(1 + \frac{\gamma-1}{2} M_{2s}^2 \right)^{-1} \right\}. \quad (6)$$

Then, from Eqs. (4) and (6), the component of primary loss coefficient due to viscous dissipation in the boundary layers can be estimated as

$$\xi_{bl} \approx \frac{0.5 \rho_e u_e^3 \delta_e}{\dot{m} c_p T_{01} \left\{ 1 - \left(1 + \frac{\gamma-1}{2} M_{2s}^2 \right)^{-1} \right\}}. \quad (7)$$

The kinetic energy deficit, $\Delta \dot{e}$, will, however, be different from that given by Eq. (4) at the mixed-out static pressure if the static pressure at the boundary layer traverse point is different from that at the mixed-out plane. Since the boundary layer profiles were measured at the rear of the blade and the static pressure at this location is typically very close to the mixed-out value, the difference in kinetic energy deficit will be small and Eq. (7) will give a good estimate of the boundary layer loss.

From the present boundary layer measurements, the boundary layer loss component has been plotted as a function of M_{ex} in Fig. 9. This loss decreases monotonically with Mach number. It continues to decrease for Mach numbers at which a recompression shock strikes the layer.

3.3.3 Shock Loss. When the flow passes through a shock wave, its total pressure decreases and the kinetic energy that is obtained if this flow is expanded to a given static pressure is also decreased. An estimate of the magnitude of the shock loss component of the primary loss coefficient can be obtained

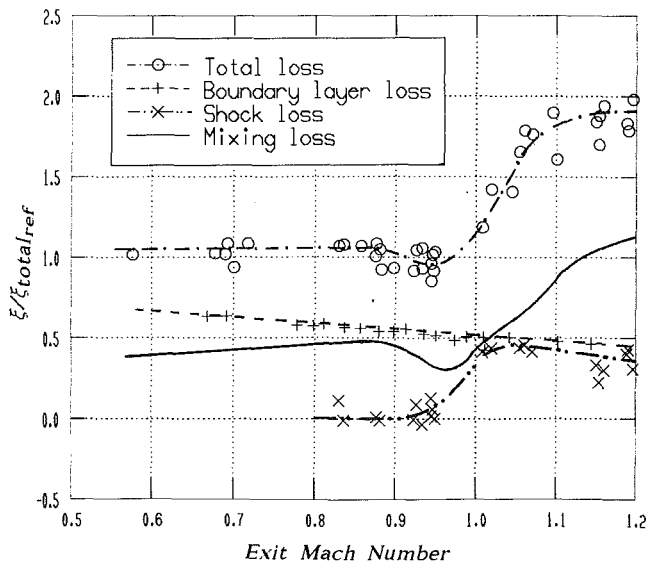


Fig. 9 Individual components of loss, $Re_{ex} = 1,000,000$

by examining the decrement of total pressure in the wake-free regions of the downstream traverse compared with the upstream total pressure. If, in the wake-free regions, the total pressure decrement at each point is approximately equal, then an arithmetic average of this decrement outside the wakes will give an estimate of the total pressure loss due to the presence of shock waves. Using the definition given in Eq. (1), it can be shown that (Oldfield et al., 1981)

$$\xi_{\text{shock}} = 1 - \frac{1 - \left\{ \frac{\bar{P}_2}{\bar{P}_{02}} \right\}^{\frac{\gamma-1}{\gamma}}}{1 - \left\{ \frac{\bar{P}_2}{\bar{P}_{01}} \right\}^{\frac{\gamma-1}{\gamma}}} \quad (8)$$

where the overbar indicates an averaged value.

An average \bar{P}_{02} at the traverse plane has been calculated for the wake-free regions. (Such a procedure has been employed by Schreiber, 1987.) This has been used with Eq. (8) to estimate the shock loss component of the primary loss coefficient. Results for an exit Reynolds number of 1,000,000 over a range of exit Mach numbers are presented in Fig. 9. There is no loss for $M_{ex} < 0.95$. The schlieren photographs indicate at $M_{ex} \approx 0.88$ the first appearance of many weak normal shocks standing downstream of the throat. These do not contribute to the overall loss. It is between $M_{ex} = 0.95$ and 1.00 that these shocks merge to form a stronger single normal shock near the rear of the suction surface. Figure 9 indicates that this shock does contribute significantly to the overall loss. The results indicate that the shock loss levels off and possibly drops at higher values of M_{ex} . This trend is more a result of the way in which the shock loss is calculated than a physical feature of the flow: At higher values of M_{ex} , where the shocks are inclined at higher angles, more of the shock loss will occur downstream of the traverse plane. The present method for dividing the loss into components attributes the shock loss occurring downstream of the traverse plane to mixing losses. An alternative approach to dividing loss into components would be to define the shock loss as only that occurring due to shock waves upstream of the exit plane of the cascade. Then mixing losses would include the increases in entropy due to all processes occurring downstream of the exit plane. This would include some loss due to the presence of shock waves.

3.3.4 Mixing Loss. Given the overall loss, boundary layer loss, and shock loss, the mixing loss component can be estimated using the relation

$$\xi_m = \xi_{\text{total}} - \xi_{bl} - \xi_{\text{shock}} \quad (9)$$

Each component on the right-hand side of Eq. (9) has been measured or estimated so that the variation of the mixing loss component with M_{ex} can be estimated. The three loss components and the overall loss at $Re_{ex} = 1,000,000$ are plotted in Fig. 9.

The mixing loss is of similar magnitude to the boundary layer loss but remains less than it up to $M_{ex} \approx 1.02$. At higher M_{ex} the mixing loss becomes the largest single component of loss; however, as discussed in section 3.3.3, the mixing loss will include some of the loss due to shock waves downstream of the traverse plane. Over most of the Mach number range examined the mixing loss accounts for approximately half the total loss. Each of the three components of loss contributes a significant amount to the total loss in different Mach number regions and thus cannot be neglected in loss considerations or loss correlations.

The experiments to track the development of the wake of the blade can be used to gage where downstream of the blades most of the mixing loss occurs. (Xu and Denton, 1988, have performed similar calculations.) The traverses were performed perpendicular to the wake and did not span the complete passage. A mass-averaged total pressure drop for each of the traverse planes has been calculated, assuming that there is no loss of total pressure outside of the wake regions, in the form

$$\frac{\left(\frac{P_{0x}}{P_{01}} \right)_{av}}{\frac{\dot{m}}{s}} = \frac{\int_{z_{t1}}^{z_{t2}} \rho(z_t) u(z_t) \frac{P_{0x}(z_t)}{P_{01}} dz_t + \left(\frac{\dot{m}}{s} - \int_{z_{t1}}^{z_{t2}} \rho(z_t) u(z_t) dz_t \right)}{\dot{m}} \quad (10)$$

where P_{0x} is the total pressure at plane x and z_{t1} to z_{t2} are the z_t values over which the traverse was performed (z_t being the coordinate normal to the nominal flow exit angle).

The primary loss coefficient is calculated from the mass-averaged total pressure assuming no further loss of total pressure for expansion to the mixed-out static pressure determined from the loss traverses. The loss calculated at each plane is then presented as a percentage of that determined for plane 7. Results are presented in Fig. 10. For $M_{ex} = 1.00$ (where shock losses contribute to the overall loss) it is noted that this method of calculating loss development will include some of the influences of the shocks. However, for $M_{ex} = 0.70$ and 0.92 shock losses are absent or negligible and the results should give a good indication of the development of the mixing loss.

As suggested by the results in Fig. 9 a larger proportion of the overall loss can be attributed to mixing loss at $M_{ex} = 0.92$ than at $M_{ex} = 0.70$. The results indicate that much of the entropy increase takes place close to the trailing edges of the blades where gradients in properties across the wake are largest. This is in agreement with the findings of Xu and Denton (1988). At $M_{ex} = 0.70$ and 0.92 the slopes of the curves in Fig. 10 toward traverse plane 7 suggest that while further mixing loss may occur downstream of this plane, it will be a small fraction of the overall loss. By the same token, the result at $M_{ex} = 1.00$ suggests that there may be further shock and mixing loss generation downstream of plane 7.

3.4 Near Wake Measurements. There is little reported in the literature on the development of the wake of a transonic turbine blade in cascade. Experiments of a similar nature have been performed in incompressible flows (e.g., Raj and Lakshminarayana, 1973) and on isolated aerofoils at transonic flow speeds (e.g., Viswanath and Brown, 1983). Experiments have also been performed using flat plates to simulate compressor wakes at low speed (Patterson and Weingold, 1985) and turbine wakes at transonic speeds (Xu and Denton, 1987). Kiock (1976) presented some measurements in the near wake of a turbine

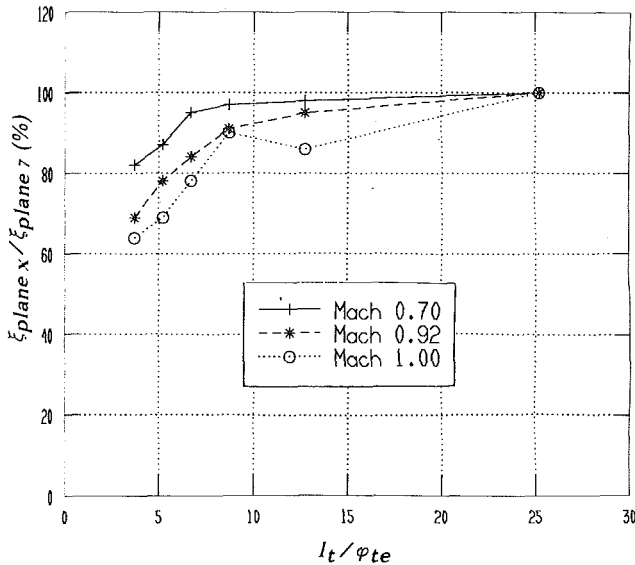


Fig. 10 Development of mixing loss in the wake, $Re_{ex} = 1,000,000$

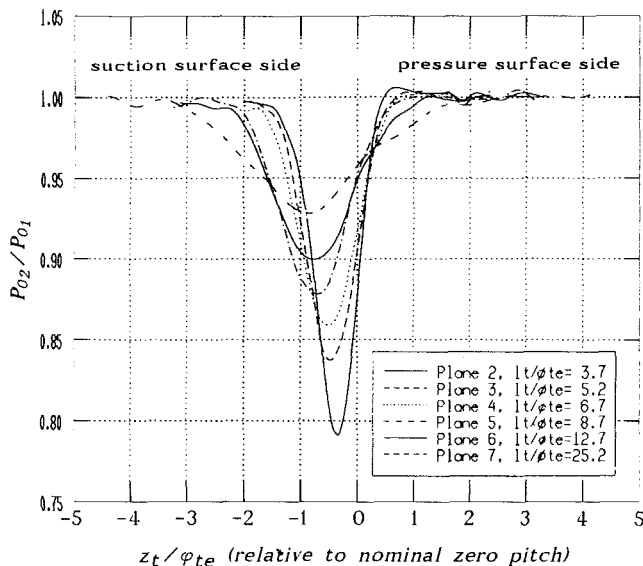


Fig. 11 Total pressure profiles in the wake, $M_{ex} = 0.92$, $Re_{ex} = 1,000,000$

cascade at transonic speeds, noting in particular that not only does the total pressure vary through the wake and across a pitch but nonnegligible variations in static pressure and flow angle may exist. The relatively large chord of blades that can be tested in the present facility and the flexibility of the traversing system reduce the difficulties involved in performing such experiments.

The smoothed total pressure distributions for traverse planes 2 to 7 at $M_{ex} = 0.92$ are presented in Fig. 11. Close to trailing edge the wake is asymmetric, which is a result of the thicker boundary layer separating from the suction surface of the blade. By plane 7, however, the wake is nearly symmetric. The center of the wake curves away from the pressure surface side of the blade. This is associated with a static pressure gradient across the wake just downstream of the blade. For the same condition the variation in flow angle through the wake is presented in Fig. 12. There is initially a large difference in flow angle on either side of the wake and the flow from each side converges. This effect is reduced as the mixing continues and at plane 7 there is little variation in flow angle through the wake.

Contours of total pressure determined from the traverses are superimposed on a schlieren photograph in Fig. 13. This

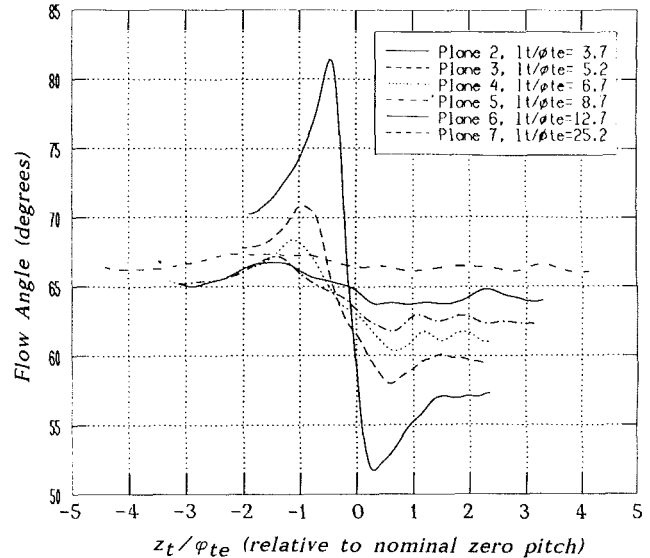


Fig. 12 Variation of flow angle in the wake, $M_{ex} = 0.92$, $Re_{ex} = 1,000,000$

shows more clearly the wake trajectory and gives an indication of the rate at which the wake spreads.

A parameter that is used to gage the rate of spreading of the wake is the semi-wake width (e.g., Raj and Lakshminarayana, 1973). This is the distance between points on either side of the wake at which the speed reaches half the free-stream speed. The measured increase of semi-wake width with distance downstream of the blades is shown in Fig. 14. The accuracy of the width at plane 7 is reduced by the fact that the flow speed through the wake drops by less than 10 percent. The x axis of this graph is $(l_t/\phi_{te})^{0.5}$ where l_t is the distance of the trailing edge circle. It can be seen that the scaling of wake width growth (width $\sim \sqrt{l_t}$), used for isolated two-dimensional wakes in incompressible flows (Schlichting, 1979) but found not to be appropriate for cascade wakes in low-speed flows (Raj and Lakshminarayana, 1973) gives a reasonable representation of the wake development for this transonic cascade wake, at least to within the accuracy of the present measurements.

4 Conclusions

The present study has enabled the overall loss of a transonic turbine cascade to be divided into individual contributions of boundary layer loss, shock loss, and mixing loss. In different Mach number regimes each of the components contributes significantly to the overall loss and thus loss correlations and design procedures should include considerations of each component. While boundary layer loss dominates at low Mach numbers, it is a smaller component at high Mach numbers. In these experiments the recompression shock striking the suction surface boundary layer does not lead to a sharp increase in the boundary layer loss.

Most of the mixing loss is generated immediately downstream of the trailing edge of the blade where the gradients in properties across the wake are largest. The wake starts with an asymmetric form but symmetry is attained as mixing continues. The wake width increases with the square root of distance downstream of the aerofoil as occurs in low-speed flows for isolated aerofoils.

Acknowledgments

The authors wish to thank the Ministry of Defence (Procurement Executive) and Rolls Royce plc. for their support, advice, and assistance for this research and for permission to publish the paper. Thanks also to Mr. S. Harding who performed some of the high Reynolds number tests.

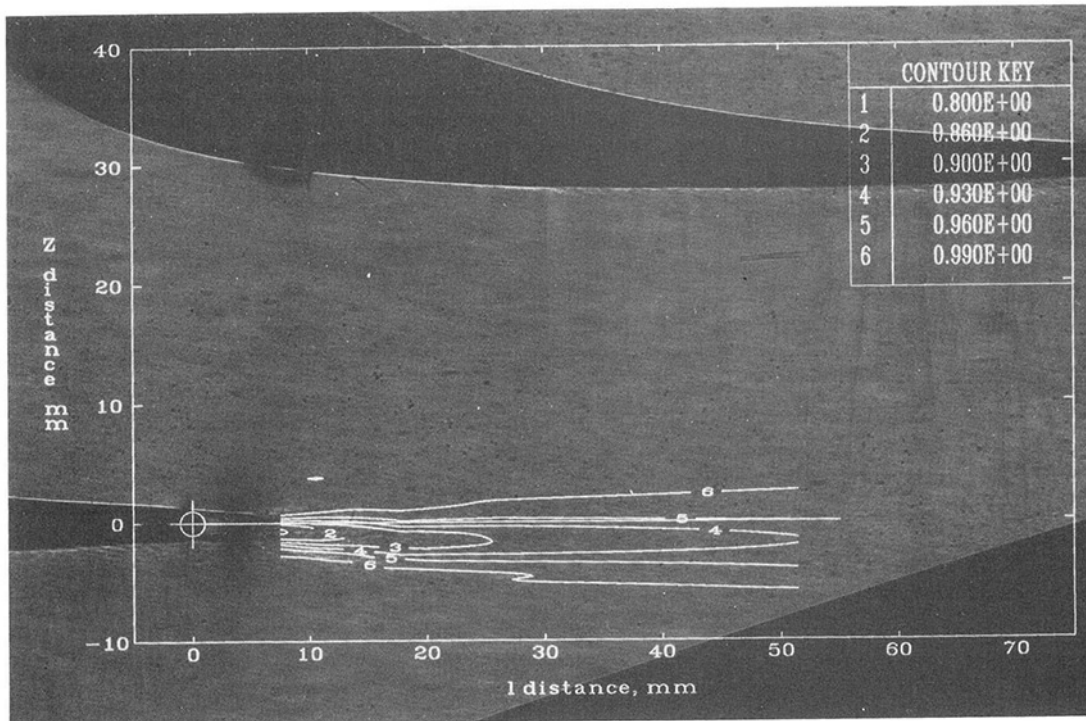


Fig. 13 Contours of P_{02}/P_{01} on schlieren photograph, $M_{ex} = 0.92$, $Re_{ex} = 1,000,000$

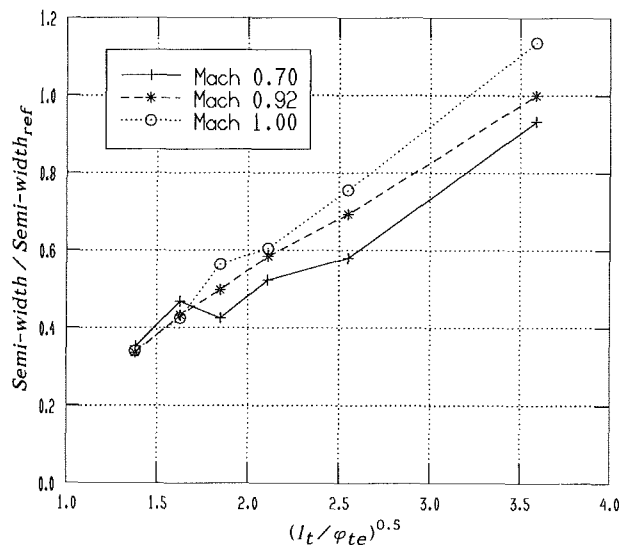


Fig. 14 Wake width growth downstream of a blade, $Re_{ex} = 1,000,000$

References

- Amecke, J., 1970, "Anwendung der transsonischen Ähnlichkeitsregel auf die Stromung durch ebene Schaufelgitter," VDI-Forschungsheft 540, pp. 16-28.
- Ashworth, D. A., 1987, "Unsteady Aerodynamics and Heat Transfer in a Transonic Turbine Stage," D. Phil. Thesis, University of Oxford, United Kingdom.
- Baines, N. C., Oldfield, M. L. G., Jones, T. V., Schultz, D. L., King, P. I., and Daniels, L. C., 1982, "A Short Duration Blowdown Tunnel for Aerodynamic Studies of Gas Turbine Blading," ASME Paper No. 82-GT-312.
- Baines, N. C., Mee, D. J., and Oldfield, M. L. G., 1991, "Uncertainty Analysis in Turbomachine and Cascade Testing," *Int. J. Eng. Fluid Mech.*, Vol. 4, No. 4.
- Denton, J. D., and Cumpsty, N. A., 1987, "Loss Mechanisms in Turbomachines," *I. Mech. E. Paper No. C260/87*.
- Doorly, D. J., and Oldfield, M. L. G., 1985, "Simulation of the Effects of Shock Wave Passing on a Turbine Rotor Blade," *ASME Journal of Engineering for Gas Turbine and Power*, Vol. 107, No. 4, pp. 998-1006.
- Fernholz, H. H., and Finley, P. J., 1980, "A Critical Commentary on Mean Flow Data for Two-Dimensional Compressible Turbulent Boundary Layers," AGARDograph No. 253.
- Hodson, H. P., 1983, "The Detection of Boundary Layer Transition and Separation in High Speed Turbine Cascades," presented at the 8th Int. Symp. on Measurement Techniques in Transonic and Supersonic Flow, Aachen, Sept.
- Hoheisel, H., Kiock, R., Lichtfuß, H. J., and Fottnner, L., 1987, "Influence of Free Stream Turbulence and Blade Pressure Gradient on Boundary Layer and Loss Behavior of Turbine Cascades," *ASME JOURNAL OF TURBOMACHINERY*, Vol. 109, pp. 210-219.
- Kiock, R., 1976, "Experimental Investigation of the Flow Field Downstream of a Plane Turbine Cascade in Transonic Flow," *Proceedings of Symposium on Measuring Techniques in Transonic and Supersonic Cascades and Turbomachines*, Lausanne, Switzerland, Nov.
- Mee, D. J., Baines, N. C., and Oldfield, M. L. G., 1992, "Detailed Boundary Layer Measurements on a Transonic Turbine Cascade," *ASME JOURNAL OF TURBOMACHINERY*, Vol. 114, this issue, pp. 163-172.
- Nicholson, J. H., 1981, "Experimental and Theoretical Studies of the Aerodynamic and Thermal Performance of Modern Gas Turbine Blades," D.Phil. Thesis, University of Oxford, United Kingdom.
- Oldfield, M. L. G., Schultz, D. L., and Nicholson, J. N., 1981, "Loss Measurements Using a Fast Traverse in an ILPT Transient Cascade," presented at Symposium on Measuring Techniques for Transonic and Supersonic Flows in Cascades and Turbomachines, Lyon, Oct.
- Patterson, R. W., and Weingold, H. G., 1985, "Experimental Investigation of a Simulated Compressor Aerofoil Trailing Edge Flow Field," *AIAA J.*, Vol. 23, No. 5, pp. 768-775.
- Raj, R., and Lakshminarayana, B., 1973, "Characteristics of the Wake Behind a Cascade of Airfoils," *J. Fluid Mech.*, Vol. 61, Pt. 4, pp. 707-730.
- Schlichting, H., 1979, *Boundary Layer Theory*, 7th ed., McGraw-Hill, New York.
- Schreiber, H. A., 1987, "Experimental Investigations on Shock Losses of Transonic and Supersonic Compressor Cascades," AGARD-CP-401.
- Viswanath, P. R., and Brown, J. L., 1983, "Separated Trailing-Edge Flow at a Transonic Mach Number," *AIAA J.*, Vol. 21, No. 6, pp. 801-807.
- Walker, G. J., 1987, "Transition Flow on Axial Turbomachine Blading," AIAA Paper No. 87-0010.
- Xu, L., and Denton, J. D., 1987, "Base Pressure Measurements on a Model of a Turbine Blade Trailing Edge," *I. Mech. E. Paper No. C283/87*.
- Xu, L., and Denton, J. D., 1988, "The Base Pressure and Loss of a Family of Four Turbine Blades," *ASME JOURNAL OF TURBOMACHINERY*, Vol. 110, pp. 9-17.

D. J. Mee

Department of Engineering Science,
University of Oxford,
Oxford, United Kingdom

N. C. Baines

Department of Mechanical Engineering,
Imperial College,
London, United Kingdom

M. L. G. Oldfield

Department of Engineering Science,
University of Oxford,
Oxford, United Kingdom

Detailed Boundary Layer Measurements on a Transonic Turbine Cascade

The boundary layers of a transonic turbine blade have been measured in detail. The full velocity profiles have been measured at a number of stations on both the suction and pressure surfaces, at conditions representative of engine operation, using a Pitot traverse technique and a large-scale (300 mm chord) linear cascade. This information has made it possible to follow the development of the boundary layers, initially laminar, through a region of natural transition to a fully developed turbulent layer. Comparisons with other, less detailed, measurements on the same profile using Pitot traverse and surface-mounted thin films confirm the essential features of the boundary layers.

1 Introduction

The boundary layers on the surfaces of a high-temperature, high-pressure gas turbine blade are important to both the aerodynamic and thermal performance of the blade, since they control such parameters as the throat area blockage, the profile loss, and the heat transfer from gas to metal. An understanding of the boundary layer development is essential to the design of highly efficient blades, and increasingly design methods look to controlling this development. For example, this may be used to delay natural transition to maximize the length of the laminar layer, or encourage an early transition to prevent separation in a later adverse pressure gradient or a shock-boundary layer interaction. Current methods require not only a knowledge of overall parameters such as the transition Reynolds number, but also details of boundary layer thickness and shape factor, and the development of the velocity profile normal to the surface as a function of distance along the blade.

Measurements of this type pose considerable difficulties. The flow in a turbine is predominantly accelerating, and this tends to keep the boundary layers thin. This then implies that large-scale models of the turbine blade are required. Gas turbine blades today operate in high subsonic or transonic flow regimes, and this introduces the added complexities of compressibility and shock wave interaction. Very few measurements are available both from a test section that is large enough to give good spatial resolution and from high-speed mainstream flow conditions. Typically the maximum size of high-speed turbine cascades is in the region of 100 mm chord, while larger cascades (up to 1 m chord) run with flow that is entirely incompressible. The present work is based on a transonic, 300 mm chord blade.

Boundary layer profiles are most commonly measured by

means of a traversing Pitot probe. Surface measurements, such as hot films, and flow visualization techniques using oil, paint, or liquid crystals can be used to distinguish laminar, transitional, and turbulent flows, but do not provide any normal profile information. Optical methods such as laser-Doppler or laser-2-focus have the advantage of being nonintrusive but may require the boundary layers to be seeded and may suffer problems of flare from the solid surfaces. Hot-wire anemometers are valuable, particularly for measuring turbulence in low-speed flows, but become very insensitive to velocity near the sonic speed. Pitot probes are generally robust and reliable, but are intrusive so that attention must be paid to blockage and wall interference effects. In many cases, however, these can be corrected for.

There have been a number of experimental investigations over the past few decades directed toward the measurement of boundary layer development in linear cascades of turbine and compressor blades. A recent review of such experiments, given by Deutsch and Zierke (1987), discusses tests in both low and high-speed flows. Since the present paper deals specifically with boundary layer measurements in transonic flows, a brief summary of studies of particular relevance to compressible flows is given below.

Meauze (1979) presented the first boundary layer measurements on a transonic cascade of blades. He measured the total pressure variation through the turbulent boundary layer on the suction surface of a compressor cascade at five locations for various inlet angles and Mach numbers. Comparisons of predicted boundary layer parameters with measurements show reasonable agreement for certain Mach number regimes.

Over the past decade a group at DFVLR Braunschweig has measured boundary layer profiles on the suction surfaces of transonic turbine blades in linear cascade. Their experiments have been performed with flattened Pitot probes (Hoheisel et al., 1987) and, in some cases, with two-finger probes, one finger of which measures the static pressure variation through the

Contributed by the International Gas Turbine Institute and presented at the 35th International Gas Turbine and Aeroengine Congress and Exposition, Brussels, Belgium, June 11-14, 1990. Manuscript received by the International Gas Turbine Institute January 15, 1990. Paper No. 90-GT-263.

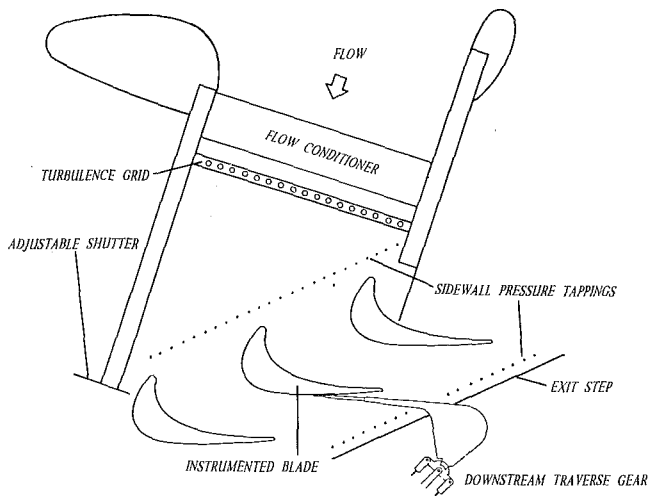


Fig. 1 Cascade arrangement

layer (Hoeger and Hoheisel, 1983). Thorough tests to validate the experimental techniques have been performed (e.g., Hoheisel et al., 1984) and experiments have included such effects as the influence of simulated film cooling on the development of the layers (Kiock et al., 1985).

Chew and Birch (1987) compare numerical predictions of boundary layer profiles and parameters with measurements taken by Hodson at the Whittle Laboratory of Cambridge University. The experimental results at a number of locations on the latter half of the suction surface at low transonic speeds are predicted reasonably well but it is noted that the accuracy of the predictions is limited by transition modeling.

King (1986) measured boundary layer profiles on a transonic turbine blade in cascade in the same facility as that used in the present study. He attempted the first measurements of boundary layer profiles on the pressure surface of a transonic turbine blade in cascade but experienced difficulties in the accuracy to which the probe location must be known for such experiments.

2 Experiments

2.1 Apparatus. The experiments were performed in the Oxford University Engineering Laboratory Transonic Blow-down wind tunnel. This is a short duration facility capable of three or more seconds of steady flow, which was designed for aerodynamic studies of gas turbine blading (Baines et al., 1982).

Table 1 Details of cascade

Inlet angle	42.8°
Inlet Mach number	0.31
Inlet total temperature	280–290K
Inlet turbulence intensity	4.3%
Nominal exit flow angle	68°
Exit Mach number	0.92
Exit Reynolds Number, Re^{des}	1,000,000
Re^+	2,000,000
Chord - axial	230.7 mm
true	300.0 mm
Span	300.0 mm
Pitch	252.1 mm

The use of tandem air ejector pumps downstream of the cascade of blades facilitates independent variation of Mach and Reynolds numbers over a wide range.

A cascade of three blades of 300 mm true chord and 300 mm span (Fig. 1) has been tested at an exit Mach number of 0.92 for exit Reynolds numbers of 1,000,000 (Re^{des}) and 2,000,000 (Re^+). Further details of the cascade are given in Table 1. The Reynolds number (calculated assuming isentropic flow) is based on measurements of the sidewall exit static pressure, the inlet total pressure and temperature, and the true chord of the blade. The cascade flow exits as a free jet and the flow is adjusted by moving the shutters to vary the bleed of air past the end blades. A row of parallel rods was used to generate turbulence in the free stream. At the leading edge of the instrumented blade the turbulence level was measured using a single hot-wire probe at 4.3 percent in the frequency range 300 Hz to 50 kHz.

The profile chosen for the present study is one that has been studied extensively at Oxford (e.g., Nicholson, 1981; Doorly and Oldfield, 1985; Mee et al., 1992). Previous testing indicated no appreciable regions of boundary layer separation on either surface and that both the location and length of transition on the suction surface change over the range of Reynolds number conditions considered.

Care must be taken with cascades of few blades to ensure that the flow field obtained is representative of a periodic cascade flow. The technique used to achieve this in the present study (Mee, 1991) involved first testing a cascade of nine blades of the same profile but smaller chord at the same Mach and Reynolds numbers. The pressure distribution in the central passage of such a cascade was measured once a periodic flow

Nomenclature

C_{ax} = axial chord	u_τ = friction velocity = $(\tau_w/\rho_w)^{0.5}$	
H = external height of probe tip	X = axial distance	
I = intermittency of turbulence	y = distance from blade surface	ex = based on exit sidewall static pressure
M = Mach number	γ = ratio of specific heats	r = recovery factor
p, P = pressure	δ_{99} = 99 percent boundary layer thickness	ref = reference value (at rearmost measurement point on suction surface)
q = dynamic pressure (see Eq. (5))	δ^* = displacement thickness	t = at start of transition
r = recovery factor	ϑ = momentum thickness	w = value at blade surface
Re = Reynolds number	λ = distance between 25 and 75 percent intermittency points	0 = stagnation value
S = surface length from axial leading edge point	ν = kinematic viscosity	1 = upstream of cascade
S_0 = total surface length	ρ = density	
T = temperature	τ = shear stress	
u = flow speed		
Δu = defined in Eqs. (11.23) and (11.24) of Cebeci and Bradshaw (1984)	Subscripts	Superscripts
	e = value at edge of boundary layer	des = design condition
		$+$ = high Reynolds number condition

was established. The large-chord cascade was then “tuned” to give a pressure distribution around the central blade as close as possible to that of the smaller chord cascade. A comparison of the isentropic surface Mach number distributions measured for each of the cascades at the Re^+ condition is given in Fig. 2. The agreement between the results is very good over all but the last 10 percent of the suction surface.

The boundary layer on the central blade of the cascade was studied. Two central blades of the same profile were used during the experiments. One has 73 static pressure tappings distributed around the profile, 47 on the suction surface and 26 on the pressure surface. This blade was used in examining the boundary layer toward the rear of the blade and in setting up the cascade flow. The other blade had ten static pressure tappings around the profile, seven on the suction surface and three on the pressure surface. This blade was used to study the boundary layer toward the leading edge of the blade. The techniques used to measure the boundary layers on each of the central blades are described below.

2.2 Procedure. Boundary layer profiles toward the rear of the blade were determined from measurements made with a flattened Pitot tube supported by a downstream traverse

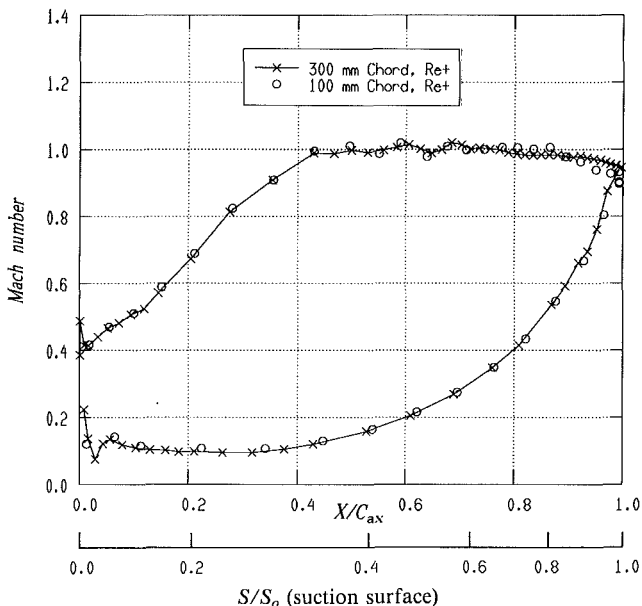


Fig. 2 Measured surface Mach number distributions: comparison of results for 300 mm and 100 mm chord blade cascades, Re^+

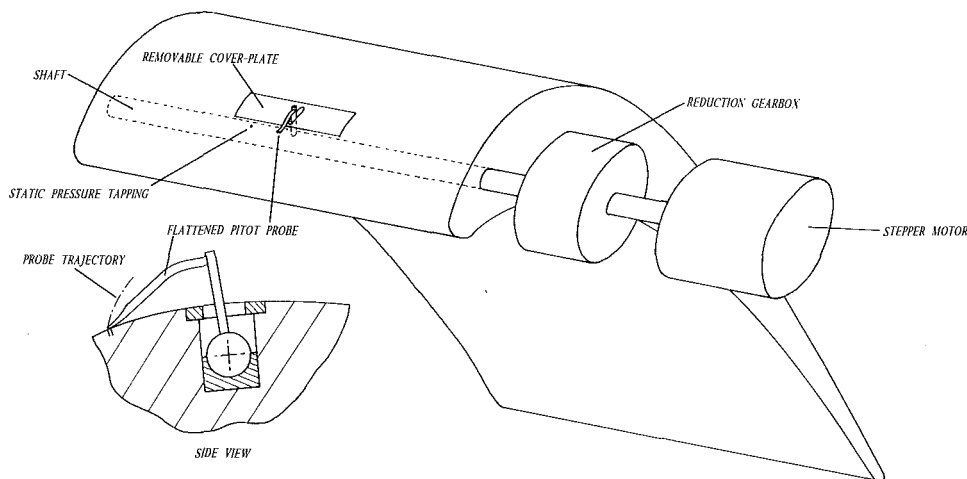


Fig. 3 Shaft-in-blade traversing mechanism

arrangement (Fig. 1) driven by microprocessor-controlled stepper motors. The probe was driven toward the blade at constant speed. An electrical potential difference established between the probe tip and the blade was used to determine the time at which the tip came into contact with the blade. By knowing the contact time and the probe speed and trajectory, its height above the surface at all prior times could be established. The traverse was stopped a short time after contact. Each traverse was performed at the same chordwise location as a static pressure tapping but at a different spanwise location from the tapping. Profiles were obtained at nine locations on the suction surface and three on the pressure surface using this technique. Two flattened Pitot tubes were used. One had tip dimensions $0.21 \text{ mm} \times 2.25 \text{ mm}$, with an opening of 0.10 mm , and the other a $0.16 \text{ mm} \times 1.70 \text{ mm}$ tip, with an opening of 0.07 mm .

Due to slight, unavoidable vibration of the probe during the traverse, contact was made and broken over a finite period of time when the probe tip was close to the surface. Assuming that the probe vibrates with simple harmonic motion and that the probe touching the surface does not interfere with this motion, the center of the contact changing period will give a good estimate of the time of contact. This is the time used in analyzing the results. Examination of the contact trace indicates that the peak-to-peak magnitude of vibration was 0.1 mm .

As is typical of high-pressure turbine blades, the test profile turns the flow through a large angle, in this case 111 deg . The blade geometry makes it very difficult to use the downstream traverse gear to obtain profiles toward the front of the blade. In order to obtain such profiles a new traversing technique has been devised (Fig. 3), referred to as the *shaft-in-blade* technique. A shaft was set in bearings through the body of the blade. A stem, attached to the shaft, protruded through a slot in the blade surface. A goose-necked Pitot tube with a flattened end was connected to the stem and touched the surface ahead of the slot. The slot was set in a removable cover plate. Two cover plates were manufactured for each location and when traversing at one location blank plates were installed at all other locations. A stepper motor was used to rotate the shaft through a high-reduction gearbox, which had negligible backlash. A miniature pressure transducer (Kulite type XCQ-063) located in the shaft was used to measure the Pitot pressure.

The rotation of the shaft caused the tip of the Pitot probe to move in a circular arc. This arrangement was very rigid and the difficulties with the contact signal experienced with the downstream traverse arrangement were not encountered. The use of the reduction gearbox resulted in approximately 300 motor steps per mm. This enabled profiles to be obtained in regions where the boundary layer was less than 1 mm thick.

Profiles were obtained at seven locations on the suction surface and attempts were made to obtain profiles at three locations on the pressure surface using this technique. The flattened Pitot tube used for these tests had tip dimensions of 0.15 mm × 1.68 mm, with an opening of 0.07 mm.

Since the tip of the Pitot travels through a circular arc for the shaft-in-blade experiments, the definition of the distance from the surface needs qualification. This distance has been taken as the shortest distance from the tip of the probe to a line tangential to the point at which the probe contacts the blade.

Another consequence of the circular locus of the probe tip is that the tip travels through a nonzero distance in the chordwise direction. If there is a large chordwise pressure gradient this could result in a change in the static pressure at the tip of the probe during the traverse. (As discussed below the static pressure is taken to be constant across the layer in the analysis of the results.) This effect should be quite small in the present tests because of the large physical scale of the blades and the fact that the boundary layer is thin where pressure gradients are largest. No correction for this has been made in processing the results.

The rotation of the shaft will also cause the angle of attack of the Pitot tube to change as it traverses through the layer. It is known that Pitot tube readings are insensitive to flow angle for low angles of attack (e.g., Gracey, 1956), typically in the range ±10 deg. Care was taken to avoid large angles of attack.

Most traverses were performed at center span but a number with the downstream gear were performed off-center in order to avoid epoxy-filled grooves leading to the static pressure tappings. All traverses with the shaft-in-blade gear were performed at center span. In order to test the validity of off-center traverses and to check the two-dimensionality of the boundary layers, three traverses were performed at the same chordwise position but at 35, 43, and 50 percent span. These results were taken at the rear of the suction surface where spanwise influence of secondary flows may be expected to be greatest. While there was an indication that the layer became thicker away from center span, the profiles and derived parameters agreed to within experimental uncertainty.

3 Data Reduction

For the determination of the velocity and density profiles needed to evaluate boundary layer thicknesses and parameters, measurements were made of the inlet total temperature and pressure, the blade static pressure, and the variation of total pressure through the layer. The static pressure was assumed to be constant across the layer, equal to the value measured at the surface. Isentropic relations were used to determine the variation of Mach number across the layer. In regions of local supersonic flow, a correction was made to the measured probe total pressure using normal shock relations.

The temperature distribution in the boundary layer was related to the velocity profile using Eq. (2.5.37b) of Fernholz and Finley (1980):

$$\frac{T}{T_e} = \frac{T_w}{T_e} + \frac{T_r - T_w}{T_e} \left(\frac{u}{u_e}\right) - r \frac{\gamma - 1}{2} M_e^2 \left(\frac{u}{u_e}\right)^2 \quad (1)$$

The wall temperature, T_w , was taken to be equal to the air temperature measured in the test section prior to a run and was assumed to be constant during the short tunnel run time (although the recovery temperature was slightly lower than the blade temperature during a run). Fernholz and Finley suggest that Eq. (1) strictly applies to compressible turbulent boundary layers on isothermal surfaces with moderate and high cooling rates but no pressure gradient. Given the lack of a relation for the mean temperature profile for compressible flows with pressure gradients, Eq. (1) has been used for all locations.

The temperature distribution of Eq. (1) requires knowledge of the boundary layer recovery factor. Typical values are 0.89 for a turbulent layer and 0.85 for a laminar layer (Schlichting, 1979). The transitional region of the boundary layer on the suction surface of the present profile is not small and a number of profiles are taken through regions of transition. The variation of the recovery factor through transition has been based on the universal intermittency distribution of Narasimha (1985). The intermittency distribution, written as

$$I = 1 - e^{-0.412\xi^2}, \quad (2)$$

has been shown to represent experimental results well even in flows with streamwise pressure gradients (Gostelow and Blunden, 1989). The variation in recovery factor has been taken as an average of the laminar and turbulent values, weighted by the periods of time for which the layer displays a laminar or turbulent nature. The form is

$$r = 0.85 + I(0.89 - 0.85). \quad (3)$$

In applying this relation, the start and end of transition have been taken from experiments by Nicholson (1981) on the same profile.

There are a number of factors that can influence the reading of a Pitot tube immersed in a boundary layer flow. Such factors, which could be of relevance to the present experiments, include an interference of the probe with the flow when the probe is close to the surface, a displacement effect when a velocity gradient exists across the tube, the effect of blockage of the probe, and an incorrect reading in regions of high turbulence intensities. At present no measurements have been made of the turbulence intensity through the layer (although preparations for such experiments are underway), so no correction for this has been made to the measured Pitot pressure.

Displacement effects for Pitot tubes in shear flows have been measured by various researchers in various flow fields, but none have been measured at transonic flow speeds. The corrections are usually presented as a displacement of the nominal probe location in the direction of increased flow speed, measured in terms of a percentage of the external dimension of the tip of the probe. Values range from no correction (Johannesen and Mair, 1952) to 40 percent (Allen, 1972) with typical values in the range 15 to 20 percent (e.g., MacMillan, 1956; Tavoularis and Szymczak, 1989). In view of the small probe size of the present tests and the lack of data for transonic flows, no shear correction to probe location has been made.

Wall interference effects have also been studied widely but again no data are available for transonic flows. There is one correction published in the literature that was determined for subsonic compressible flows by Hoeger and Hoheisel (1983) who examined wall interference effects of flattened Pitot tubes and two finger probes in flat-plate boundary layers for free-stream Mach numbers in the range $0.3 < M < 0.7$. Their correction was determined from deviations of the measured data from law-of-the-wall profiles. This correction was tested for the present results but was not suitable. A series of experiments was performed as part of the present test program in order to quantify the wall interference effect. Five geometrically similar flattened Pitot tubes of tip heights, H , ranging from 0.16 mm to 0.37 mm, were used to measure the profile at the rear of the suction surface at the Re^+ condition. The correction determined has the form

$$\frac{\Delta u}{u_e} = 0.55 \frac{y}{H} e^{-3.85 \left(\frac{y}{H}\right)} \quad (4)$$

This correction has been applied to profiles measured downstream of the transition region. Because no experiments have been performed in transitional or laminar compressible layers, no corrections have been applied to profiles measured in such regions.

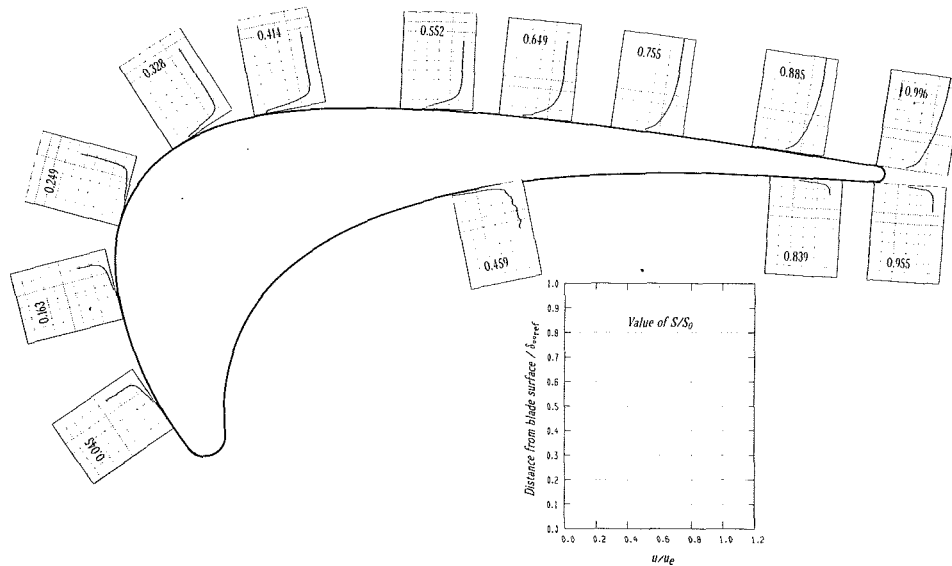


Fig. 4(a) Boundary layer development, Re^{des} ; y axes normalized with δ_{99ref} (blade and y axes of plots not to same scale)

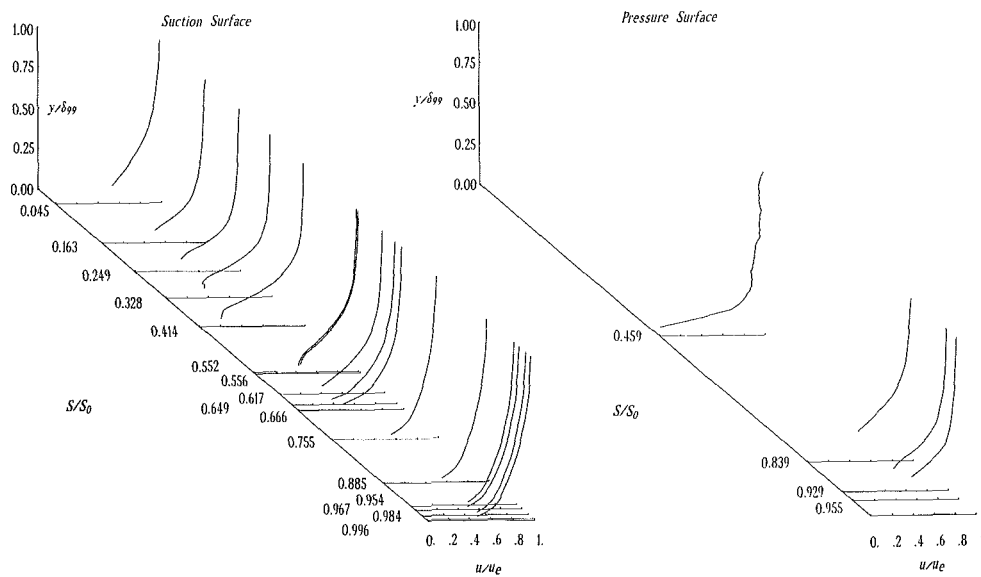


Fig. 4(b) Boundary layer development, Re^{des} ; y axes normalized with local δ_{99}

The effect of probe blockage on the bulk of the flow was considered to be negligible and no correction was made. This was because:

(a) No significant change in static pressure in the region of the probe was observed when the probe was introduced.

(b) The probe head area is a very small fraction of the cascade throat area (<0.01 percent).

(c) In regions where the downstream traverse and shaft-in-blade techniques could be compared directly, no significant differences in the probe measurements were observed (section 4.1).

In order to avoid errors being introduced into the results through insufficient Pitot tube response time, two traverses were performed at each location. A fast traverse was used for profile details far from the surface (where gradients in properties are relatively small) and a slow traverse was used to give details close to the surface of the blade.

A thorough analysis of uncertainties in the derived results was performed for each traverse. This included the uncertainty in the probe location, velocity ratio, density ratio, boundary layer thickness, and shape factor.

4 Results

The basic results from the experiments for both surfaces at the two test conditions, including velocity profile development, boundary layer thicknesses and shape factors, are presented in Figs. 4 to 9. The boundary layer development around the blade surface is presented in two forms. The growth of the layer is indicated in Figs. 4(a) and 7(a), where each plot has the same scale normal to the blade surface. The origin of each plot is the surface location of the traverse plane. Thicknesses are normalized with δ_{99ref} , the value measured at the *reference* location (the rearmost measurement station on the suction surface). However, for clarity the normal axes in these figures are *not* drawn to the same scale as the profile size so that the layer appears artificially thick relative to the blade size. In the second representation of the boundary layer development, the velocity profiles are plotted normalized with the *local* 99 percent boundary layer thickness (Figs. 4(b) and 7(b)). This indicates the change in profile shape as the layers develop. Boundary layer thicknesses in Figs. 5 and 8 are normalized with δ_{ref}^* , the displacement thickness measured at the reference location.

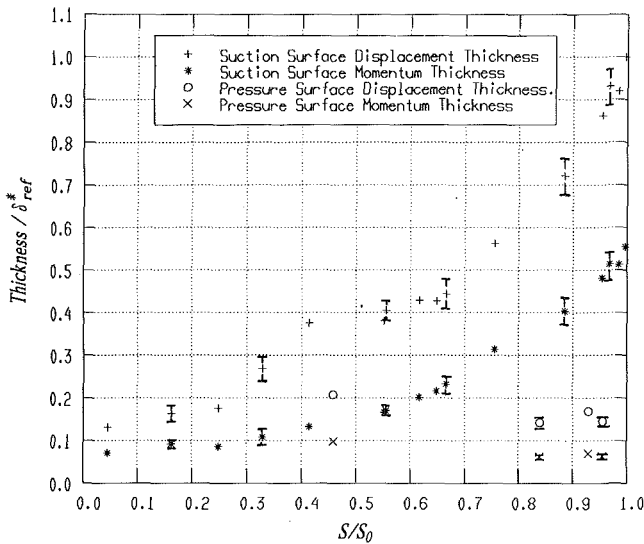


Fig. 5 Boundary layer thickness normalized with δ_{ref}^* , Re^{des}

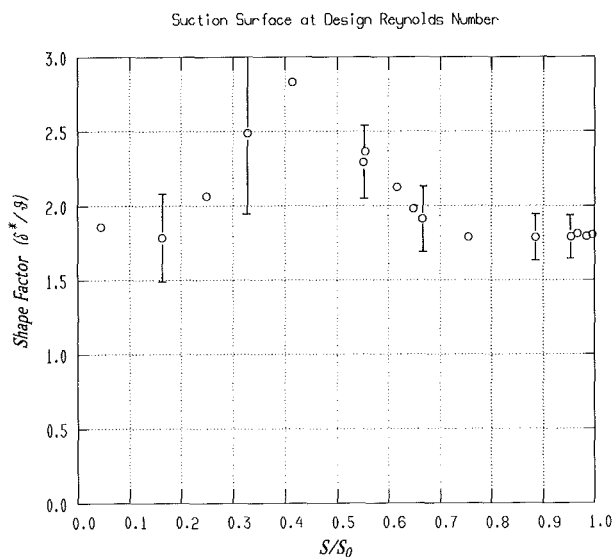


Fig. 6(a) Suction surface shape factors, Re^{des}

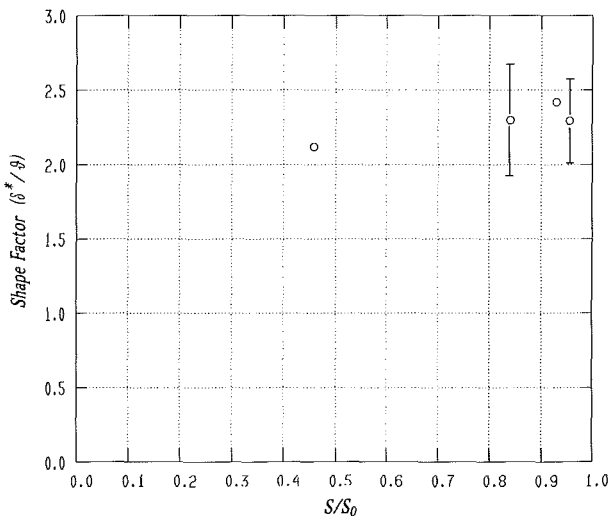


Fig. 6(b) Pressure surface shape factors, Re^{des}

A full set of data is included in this paper, but the restrictions of publication mean that these are rather small. The authors are prepared to supply larger copies on request.

4.1 Suction Surface. The accuracy of the measurements is presented first. Results for typical uncertainties in the velocity and density profiles and in probe position are given in Fig. 10. The step change in position uncertainty is associated with the change from results for the fast traverse to those for the slow traverse. In general the accuracy of the results decreases as the free-stream speed at the traverse location decreases. The uncertainty limits on a velocity profile are indicated in Fig. 11. The corresponding density profile, derived from Eq. (1), is also shown. The uncertainties in position and in the density profile are small at this scale and are not indicated.

The regions on the suction surface over which traverses were performed with each of the traversing systems (downstream gear and shaft-in-blade gear) overlapped. Two locations were chosen to be very close so that a direct comparison between results for the two techniques could be made: $S/S_0 = 0.556$ for the downstream gear and $S/S_0 = 0.552$ for the shaft-in-blade gear. As can be seen from Figs. 4(b) and 7(b), the velocity profiles measured with the two arrangements are in good agreement, within experimental uncertainty. The thicknesses and shape factors also agree well (Figs. 5, 6, 8, and 9). This agreement also gives confidence in the method used to determine the time of contact for a vibrating probe (section 2.2). The probe tip, when supported by the downstream gear, vibrated over a distance of 0.1 mm and, if the interpretation of time of contact had been incorrect, the profile determined for this system would not have been in agreement with that obtained with the more rigid shaft-in-blade system, which had negligible vibration and, typically, a single step from contact off to on.

Nicholson (1981) performed experiments on a cascade of the same profile to measure surface heat transfer distributions using thin-film gages. Tests were conducted at the same exit Reynolds number as the present experiments but at a slightly higher exit Mach number ($M_{ex} = 0.96$). Results from those tests indicate that transition on the suction surface takes place from $S/S_0 = 0.5$ to 0.9 at Re^{des} and from $S/S_0 = 0.1$ to 0.4 at Re^+ . The profile results can be used to gage where transition occurs in the present tests by examining the Pitot pressure measured near the surface (the traversing Pitot technique discussed by Oldfield et al., 1981). The measurement from the Pitot tube at a fixed height from the surface is used to determine the ratio of the local dynamic pressure, q , to that in the free stream above the measurement point, q_e , in the form

$$\frac{q}{q_e}(S/S_0, y) = \frac{P_0(S/S_0, y) - p_w(S/S_0)}{P_{01} - p_w(S/S_0)} \quad (5)$$

where $P_0(S/S_0, y)$ is the measured total pressure at the stream-wise location S/S_0 at a distance y from the blade surface and $p_w(S/S_0)$ is the static pressure at S/S_0 at the surface. The basic change in the shape of the profile indicates where transition takes place. The parameter decreases for a growing laminar or turbulent layer but increases through a region of transition. Separation bubbles give values approaching zero.

Plots of q/q_e around the suction surface for the two test conditions are given in Fig. 12. The actual start and end points of transition are not clearly defined because of the limited number of traverse planes. The results suggest that transition at Re^{des} takes place from $S/S_0 = 0.4$ to 0.8 , slightly earlier than indicated in Nicholson's results. The Re^+ results suggest that transition starts later than indicated by Nicholson's tests ($S/S_0 = 0.3$ to 0.5). Both sets of results indicate that the transition length is much reduced at Re^+ . The end of transition is also indicated by the leveling of the shape factor along the rear of the suction surface (Figs. 6 and 9), which confirms the location determined from the traversing Pitot technique.

The measured boundary layer profile on the suction surface

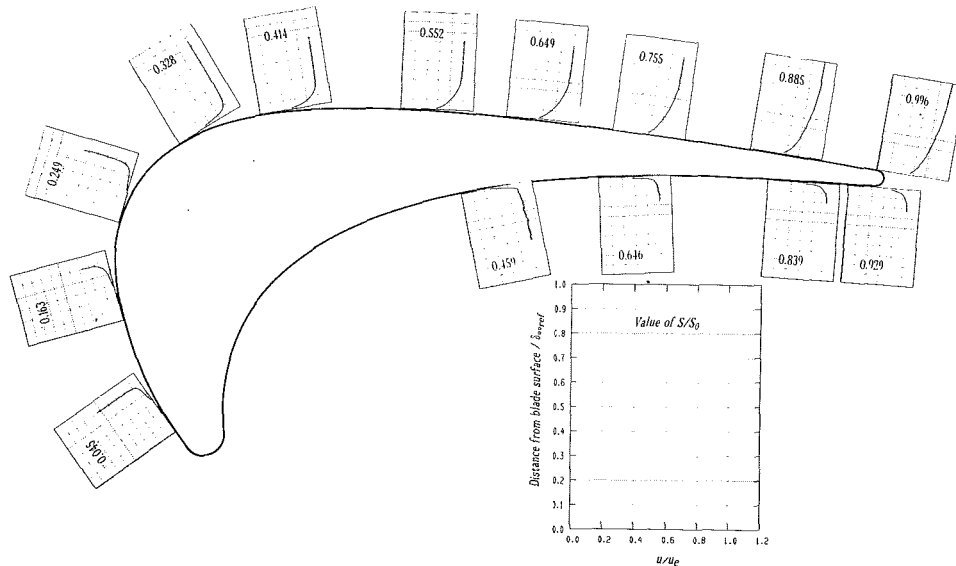


Fig. 7(a) Boundary layer development, Re^+ ; y axes normalized with $\delta_{99,ref}$ (blade and y axes of plots not to same scale)

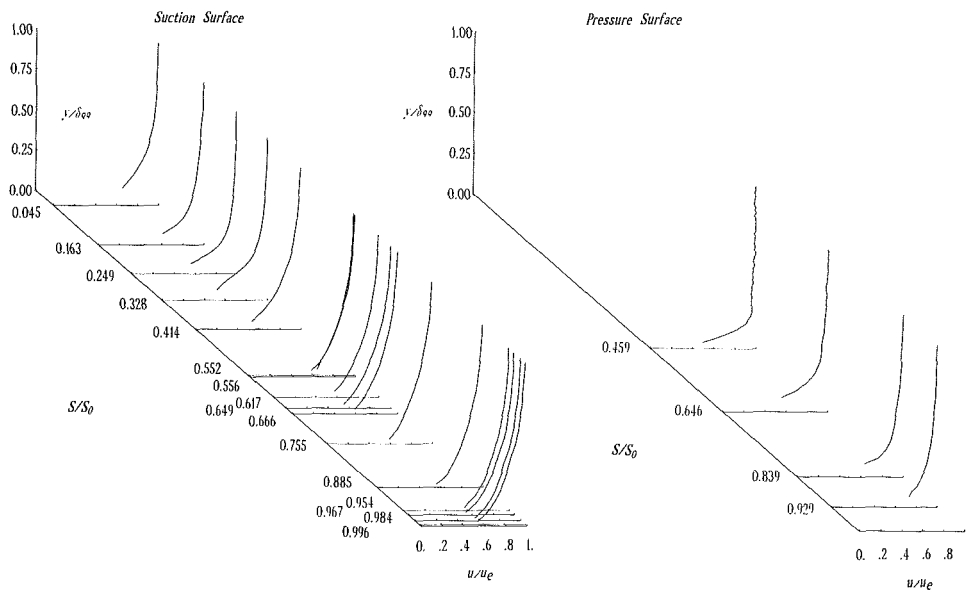


Fig. 7(b) Boundary layer development, Re^+ ; y axes normalized with local δ_{99}

at the Re^{des} condition indicates that there may be a thin separation bubble near the start of the transition region. The velocity profiles (Fig. 4b) show first an inflection near the surface ($S/S_0=0.249$) then, further downstream, a region of almost constant indicated flow speed near the surface ($S/S_0=0.328$ and 0.414). At the measurement stations at $S/S_0=0.552$ and 0.556 the profiles once again show an inflection near the surface. The feature is absent farther downstream.

A series of tests was performed at location $S/S_0=0.414$ where this effect was largest. The first measurement point of the traverse was at 0.08 mm from the surface (half the probe tip height) and the total pressure remained essentially constant up to a distance of approximately 0.15 mm from the surface. The level of this pressure was approximately 2 percent higher than the blade static pressure at this location—a difference within the accuracy to which the pressures can be measured. This feature was the same for repeat runs and was also repeated in a test in which the probe was traversed away from the blade (as opposed to the usual traverse toward the blade). Surface streamline flow visualization proved inconclusive as it did not

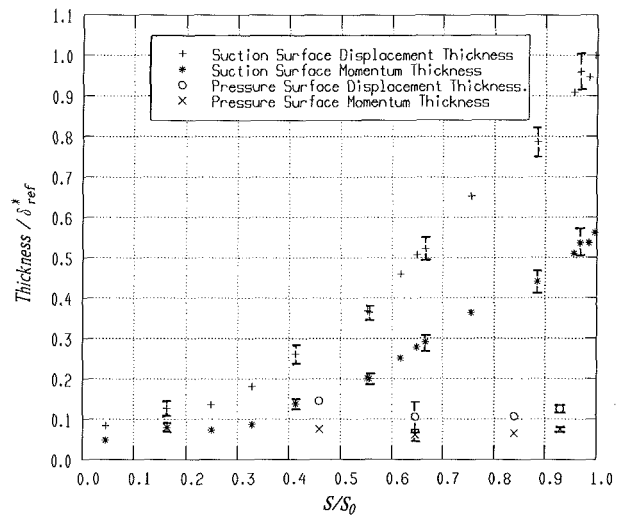


Fig. 8 Boundary layer thicknesses normalized with $\delta_{99,ref}^+$, Re^+

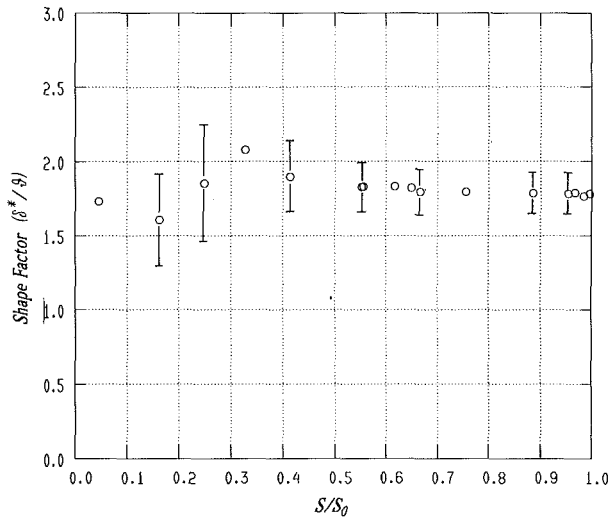


Fig. 9(a) Suction surface shape factors, Re^+

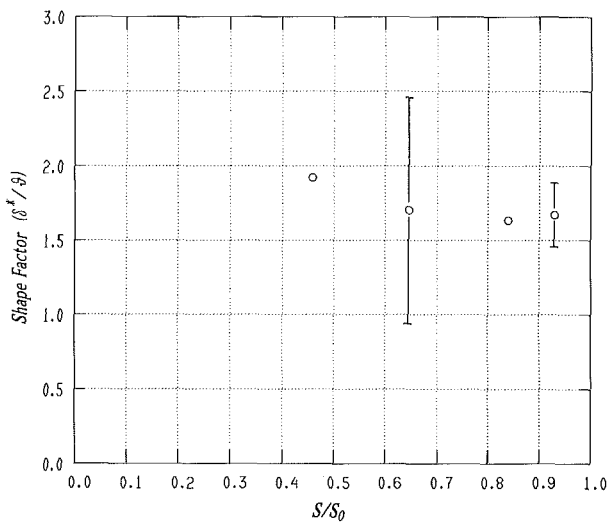


Fig. 9(b) Pressure surface shape factors, Re^+

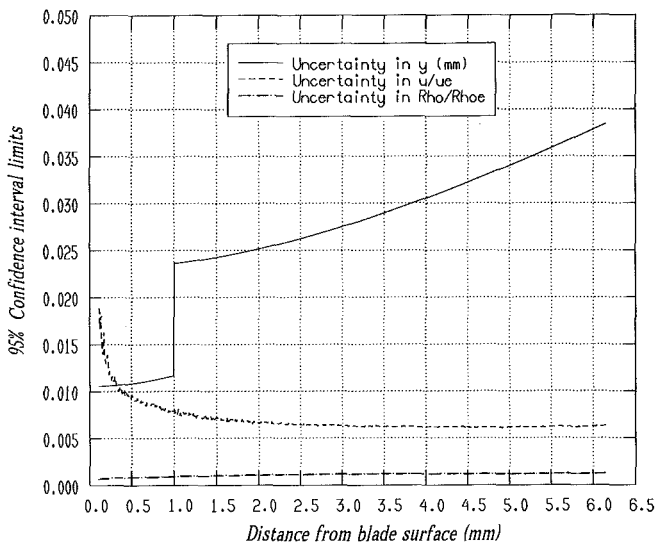


Fig. 10 Typical absolute uncertainties in a suction surface profile, Re^{des}

clearly indicate the presence of separation in this region but could not be used to rule it out.

It is possible that this feature is a result of probe-surface

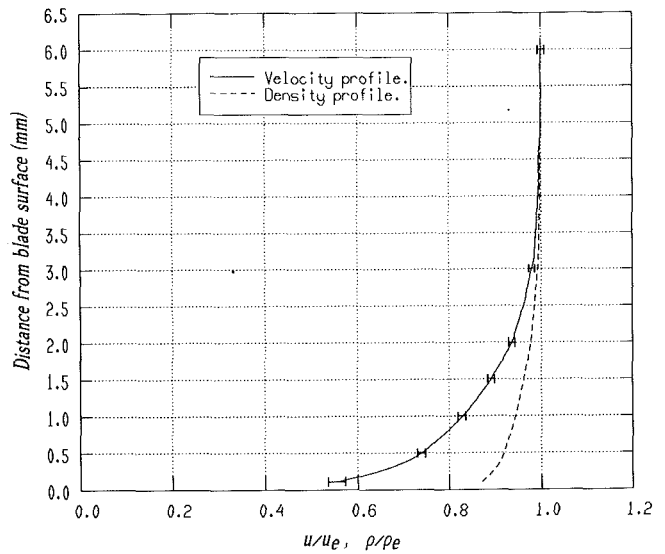


Fig. 11 Uncertainty limits of Fig. 10 on the suction surface velocity profile, Re^{des}

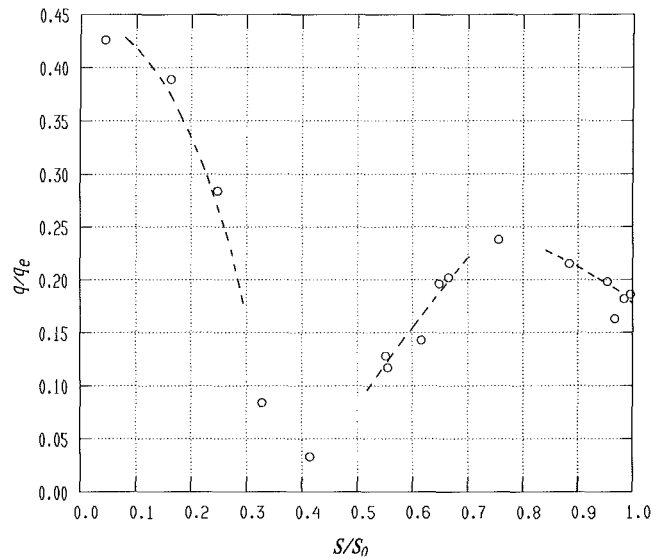


Fig. 12(a) Results from traversing Pitot tests to detect transition, Re^{des} , $y=0.12$ mm

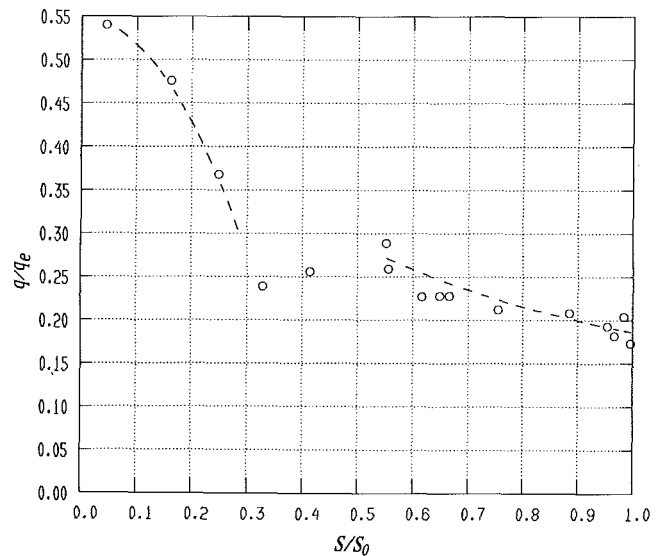


Fig. 12(b) Results from traversing Pitot tests to detect transition, Re^+ , $y=0.15$ mm

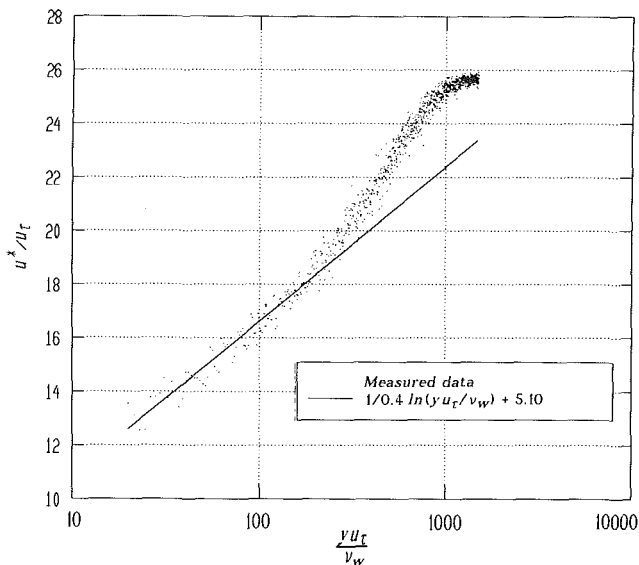


Fig. 13 Velocity profile in law-of-the-wall coordinates

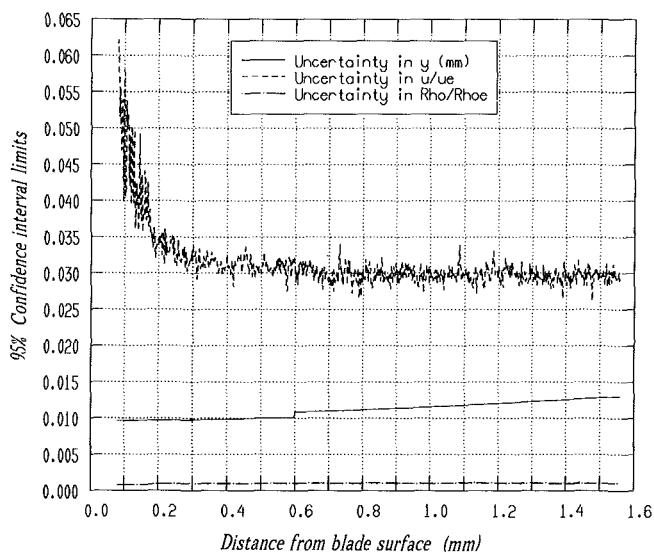


Fig. 14 Typical absolute uncertainties in a pressure surface profile, Re^+

interference in the transitional boundary layer. However, the current interpretation is that it is a thin, unsteady separation bubble in the region where the favorable free-stream pressure gradient ceases ($S/S_0 = 0.3$; see Fig. 2). The fact that the probe total pressure does not equal the blade static pressure, as would be expected in a separation bubble, can be explained by unsteadiness in the separation. Similar results with flattened Pitot tubes in regions of separation in which the probe indicates a pressure higher than the static pressure have been obtained previously (Oldfield et al., 1981).

The same feature is observed, but not as dramatically, at the Re^+ condition. The velocity profile shows an inflection at $S/S_0 = 0.328$ (Fig. 7b), again occurring at the point where a favorable pressure gradient ends, indicating that the layer may be near incipient separation. Investigation into the suction surface boundary layers near the start of transition is continuing.

The results for the suction surface indicate that the boundary layer toward the rear of the blade is fully turbulent at both test conditions. The velocity profiles at these locations can be plotted in the form of a Clauser plot by fitting the lower 20 percent of the layer to a law-of-the-wall profile (e.g., Fig. 13).

The variable u^* is as given by Cebeci and Bradshaw (1984) in Eqs. (11.22) and (11.23). From this fitting procedure an estimate can be made of the friction velocity and thus the surface shear stress.

4.2 Pressure Surface. As can be seen from Figs. 5 and 8, the thickness of the pressure surface boundary layer at the rear of the blade is almost an order of magnitude less than that at the rear of the suction surface. This led to greater uncertainties in profile measurement with the downstream gear because of probe vibration and the related uncertainty in the time of contact. The results with the downstream gear were not as repeatable as those on the suction surface but did agree to within experimental uncertainties. Typical uncertainties in the profiles measured at the rear of the pressure surface are given in Fig. 14 and uncertainties in thickness and shape factor are indicated in Figs. 5, 6, 8, and 9.

Attempts were made to measure profiles with the shaft-in-blade gear at three locations on the pressure surface. However, because of the very low Mach numbers along most of the pressure surface, the present instrumentation was not adequate to determine detail in profiles where the edge Mach number was of order 0.1. Results are presented for the profiles measured with the shaft-in-blade gear at $S/S_0 = 0.459$ (Figs. 4 to 9) but the uncertainties in the measured quantities were large.

The pressure surface velocity profiles are very different for the two test conditions. The results for the Re^+ condition at the rear of the blade have a turbulent form: a full profile (Fig. 7b) and shape factor of approximately 1.6 (Fig. 9). At the Re^{des} condition, however, the profiles are much less full (Fig. 4b) and the shape factor is higher at approximately 2.4 (Fig. 6).

5 Conclusions

Detailed measurements of boundary layer velocity profiles, thicknesses, and shape factors have been made at a number of positions on both the suction and pressure surfaces of a large, high-speed turbine blade in a linear cascade at transonic free-stream flow representative of engine conditions. Measurements were made with a traversing Pitot probe, with corrections for wall interference effects. A full uncertainty estimate of the results was made. These measured profiles will be compared with CFD predictions in a future paper.

Regions of laminar, transitional, and turbulent flow were observed, and these were in generally good agreement with measurements of the onset of these regions made elsewhere on the same blade profile. A significant feature is that there is a thin, unsteady separation bubble on the suction surface of the blade at the design Reynolds number, which initiates transition. This occurs near the point at which a favorable pressure gradient ends.

Acknowledgments

The authors wish to thank the Ministry of Defence (Procurement Executive) and Rolls Royce plc. for their support, advice, and assistance and for permission to publish the paper.

References

- Allen, J. M., 1972, "Impact Probe Displacement in a Supersonic Turbulent Boundary Layer," *AIAA J.*, Vol. 10, pp. 555-557.
- Baines, N. C., Oldfield, M. L. G., Jones, T. V., Schultz, D. L., King, P. I., and Daniels, L. C., 1982, "A Short Duration Blowdown Tunnel for Aerodynamic Studies on Gas Turbine Blading," ASME Paper No. 82-GT-312.
- Cebeci, T., and Bradshaw, P., 1984, *Physical and Computational Aspects of Convective Heat Transfer*, Springer-Verlag, New York.
- Chew, J. W., and Birch, N. T., 1987, "Comparison Between Numerical Solutions and Measurements for a High-Speed Turbine Blade," IMechE Conference Paper No. C268/87.
- Deutsch, S., and Zierke, W. C., 1987, "The Measurement of Boundary Layers on a Compressor Blade in Cascade: Part 1—A Unique Experimental Facility," ASME JOURNAL OF TURBOMACHINERY, Vol. 109, pp. 520-526.

- Doorly, D. J., and Oldfield, M. L. G., 1985, "Simulation of the Effects of Shock Wave Passing on a Turbine Rotor Blade," *ASME Journal of Engineering for Gas Turbines and Power*, Vol. 107, pp. 998-1006.
- Fernholz, H. H., and Finley, P. J., 1980, "A Critical Commentary on Mean Flow Data for Two-Dimensional Compressible Turbulent Boundary Layers," AGARDograph No. 253.
- Gostelow, J. P., and Blunden, A. R., 1989, "Investigations of Boundary Layer Transition in an Adverse Pressure Gradient," *ASME JOURNAL OF TURBOMACHINERY*, Vol. 111, pp. 366-375.
- Gracey, W., 1956, "Wind-Tunnel Investigation of a Number of Total-Pressure Tubes at High Angles of Attack; Subsonic, Transonic and Supersonic Speeds," NACA-TN-3641.
- Hoeger, M., and Hoheisel, H., 1983, "On the Accuracy of Boundary Layer Measurements in Cascades at High Subsonic Speeds," *Proceedings, 7th Symp. on Measuring Techniques for Transonic and Supersonic Flow in Cascades and Turbomachines*, Aachen, Sept.
- Hoheisel, H., Hoeger, M., Meyer, P., and Koerber, G., 1984, "A Comparison of Laser-Doppler Anemometry and Probe Measurement Within the Boundary Layer of an Airfoil at Subsonic Flow," *Proceedings, 2nd Int. Symp. on Applications of Laser Anemometry to Fluid Mechanics*, Lisbon, Portugal.
- Hoheisel, H., Kiock, R., Lichtfuss, H. J., and Fottner, L., 1987, "Influence of Free-Stream Turbulence and Blade Pressure Gradient on Boundary Layer and Loss Behavior of Turbine Cascades," *ASME JOURNAL OF TURBOMACHINERY*, Vol. 109, pp. 210-219.
- Johannesen, N. H., and Mair, W. A., 1952, "Experiments With Large Pitot Tubes in a Narrow Supersonic Wake," *J. Aero. Sci.*, Vol. 19, pp. 785-787.
- King, P. I., 1986, "Aerodynamics of High Performance Turbine Blading," D. Phil. Thesis, University of Oxford, United Kingdom.
- Kiock, R., Hoheisel, H., Dietrichs, H. J., and Holmes, A. T., 1985, "The Boundary Layer Behaviour of an Advanced Gas Turbine Rotor Blade Under the Influence of Simulated Film Cooling," AGARD-CP-390, Paper No. 42.
- MacMillan, F. A., 1956, "Experiments on Pitot Tubes in Shear Flow," *ARC R&M No. 3028*.
- Meauze, G., 1979, "Transonic Boundary Layer on Compressor Stator Blades as Calculated and Measured in Wind Tunnel," presented at the 4th ISABE, *FL*, AIAA Paper No. 79-7025.
- Mee, D. J., 1991, "Large Chord Turbine Cascade Testing of Engine Mach and Reynolds Numbers," *Exp. Fluids*, in press.
- Mee, D. J., Baines, N. C., Oldfield, M. L. G., and Dickens, T. E., 1992, "An Examination of the Contributions to Loss on a Transonic Turbine Blade in Cascade," *ASME JOURNAL OF TURBOMACHINERY*, Vol. 114, this issue, pp. 155-162.
- Narasimha, R., 1985, "The Laminar-Turbulent Transition Zone in the Boundary Layer," *Prog. Aero. Sci.*, Vol. 22, pp. 29-80.
- Nicholson, J. H., 1981, "Experimental and Theoretical Studies of the Aerodynamic and Thermal Performance of Modern Gas Turbine Blades," D.Phil. Thesis, University of Oxford, United Kingdom.
- Oldfield, M. L. G., Kiock, R., Holmes, A. T., and Graham, C. G., 1981, "Boundary Layer Studies on Highly Loaded Cascades Using Heated Thin Films and a Traversing Probe," *ASME Journal of Engineering for Power*, Vol. 103, pp. 237-246.
- Schlichting, H., 1979, *Boundary Layer Theory*, 7th ed., McGraw-Hill, New York.
- Tavoularis, S., and Szymczak, M., 1989, "Displacement Effect of Square-Ended Pitot Tubes in Shear Flows," *Exp. Fluids*, Vol. 7, pp. 33-37.

Secondary Flow Measurements in a Turbine Cascade With High Inlet Turbulence

D. G. Gregory-Smith

J. G. E. Cleak

School of Engineering & Applied Science,
University of Durham,
Science Laboratories,
Durham, DH1 3LE, United Kingdom

Measurements of the mean and turbulent flow field have been made in a cascade of high turning turbine rotor blades. The inlet turbulence was raised to 5 percent by a grid placed upstream of the cascade, and the secondary flow region was traversed within and downstream of the blades using a five-hole probe and crossed hot wires. Flow very close to the end wall was measured using a single wire placed at several orientations. Some frequency spectra of the turbulence were also obtained. The results show that the mean flow field is not affected greatly by the high inlet turbulence. The Reynolds stresses were found to be very high, particularly in the loss core. Assessment of the contributions to production of turbulence by the Reynolds stresses shows that the normal stresses have significant effects, as do the shear stresses. The calculation of eddy viscosity from two independent shear stresses shows it to be fairly isotropic in the loss core. Within the blade passage, the flow close to the end wall is highly skewed and exhibits generally high turbulence. The frequency spectra show no significant resonant peaks, except for one at very low frequency, attributable to an acoustic resonance.

1 Introduction

Secondary flows in axial flow turbine blading have attracted a lot of interest because of the losses and changes in outlet flow angle they produce. In rotor blade passages, the secondary flows are very high due to the high turning, and the resulting losses for low-aspect-ratio blading may account for half the total loss. A comprehensive review of the structure of secondary flows in turbines has been given by Sieverding (1985), but he concluded that not much was known about turbulence in the secondary flow region. Some information was available, e.g., Senoo (1958), Langston et al. (1977), and Bailey (1980), but it was incomplete and no exhaustive measurements had been published.

Moore et al. (1987) studied the flow downstream of a large-scale, low-speed cascade. They recorded a peak level of turbulence of 25 percent of inlet velocity and showed that the turbulence was of major significance in the loss generation process downstream of the cascade. A detailed study of the turbulence within a rotor blade passage was presented by Zunino et al. (1987). They found high turbulence levels of up to 12 percent associated with the loss core near the throat, with peak values of 15 percent of inlet velocity downstream of the cascade. In another detailed investigation, Gregory-Smith et al. (1988b) found rather higher values of turbulence, 29 percent of upstream velocity in the vortex core, and regions of high turbulence associated with high loss. However, only 17 percent of the loss could be accounted for as turbulent kinetic energy. Downstream of the cascade, the wake turbulence dissipated rapidly, but the overall turbulent kinetic energy continued to

rise. A spectral analysis of the turbulence showed a dominant low-frequency peak, indicating gross unsteadiness of the flow. A recent paper by Hebert and Tiederman (1990) also shows high turbulence associated with the passage vortex. Thus it may be concluded that the action of the secondary flow in rolling up the endwall boundary layer, and its interaction with blade boundary layers, results in significant turbulence generation. Although this process accounts for a large portion of the secondary loss, the loss is not manifested as an equal rise in turbulent kinetic energy, because the rate of dissipation of turbulence almost matches the rate of generation.

The understanding of the turbulent structure in the secondary flow region is very important in developing models of turbulence for Navier-Stokes solvers. As shown by Cleak et al. (1989), very different predictions for the secondary velocities may be obtained depending on how the turbulence is specified within the flow regime. Most Navier-Stokes solvers for turbomachinery flows use the Boussinesq eddy viscosity concept, whereby the Reynolds shear stresses are related to local velocity gradients by an isotropic eddy viscosity. It may be expected that for a blade passage, the complex flow results in a nonisotropic eddy viscosity, and that the action of normal Reynolds stresses is important (Moore et al., 1987, give some evidence for the latter).

One area that remains somewhat uncertain is the state of the endwall boundary layer. Senoo (1958) found that the boundary layer near the throat of a nozzle cascade was laminar, and he suggested that the inlet boundary layer was relaminarized by the strong favorable pressure gradient. Langston et al. (1977) and many other workers since then have found that the inlet boundary layer is rolled up into the loss core, and a new, highly skewed boundary layer forms on the endwall.

Contributed by the International Gas Turbine Institute and presented at the 35th International Gas Turbine and Aeroengine Congress and Exposition, Brussels, Belgium, June 11-14, 1990. Manuscript received by the International Gas Turbine Institute January 12, 1990. Paper No. 90-GT-20.

Table 1 Cascade design data

Flow Inlet Angle	42.75°
Blade Exit Angle	-68.60°
Blade Chord	224 mm
Blade Axial Chord	181 mm
Blade Span	400 mm
Blade Pitch	191 mm
Reynolds Number (chord and exit velocity)	4×10^5

Thus Senoo probably observed the new boundary layer, rather than the relaminarized inlet boundary layer. Belik (1972) measured endwall shear stresses with film gages along the centerline of two nozzle cascades, and found a maximum near the point of greatest streamwise pressure gradient. Measurements of boundary layer noise showed this position to be close to the start of a laminar boundary layer. Harrison (1990) has made extensive measurements of endwall shear stresses using film gages and an oil drop method. He found a laminar boundary layer over a large part of the endwall. Intermittency and transition to a turbulent layer were observed near the trailing edge plane. However, a region close to the suction surface corner contained a turbulent boundary layer from inlet to outlet. The state of the endwall boundary layer is very important in flow modelling. Cleak et al. (1991) obtained significant differences in predicted flow patterns depending on whether the endwall flow was specified as turbulent or laminar.

In investigating the turbulent flow in a turbine rotor cascade, there were two main objectives for this work. The first was to obtain a better understanding of the turbulent structure of the flow, including the contribution of the Reynolds stresses to the loss generation. The second was to obtain data for comparison with and development of turbulence models used in Navier-Stokes solvers. An important feature of this work was the use of a turbulence grid upstream of the cascade, giving high inlet turbulence, more representative of that in a real machine, rather than the low inlet turbulence obtained in most wind tunnels.

2 Apparatus

2.1 Cascade and Turbulence Grid. The work reported in this paper forms part of a program of work on secondary flows in turbine cascades at Durham University. The cascade differed from that used for the previous paper by Gregory-Smith et al. (1989b) in that the blade was designed to minimize suction surface diffusion at the low speed of operation. The mean flow field has been reported by Walsh and Gregory-Smith (1987, 1990). The design data for the cascade are given in Table 1.

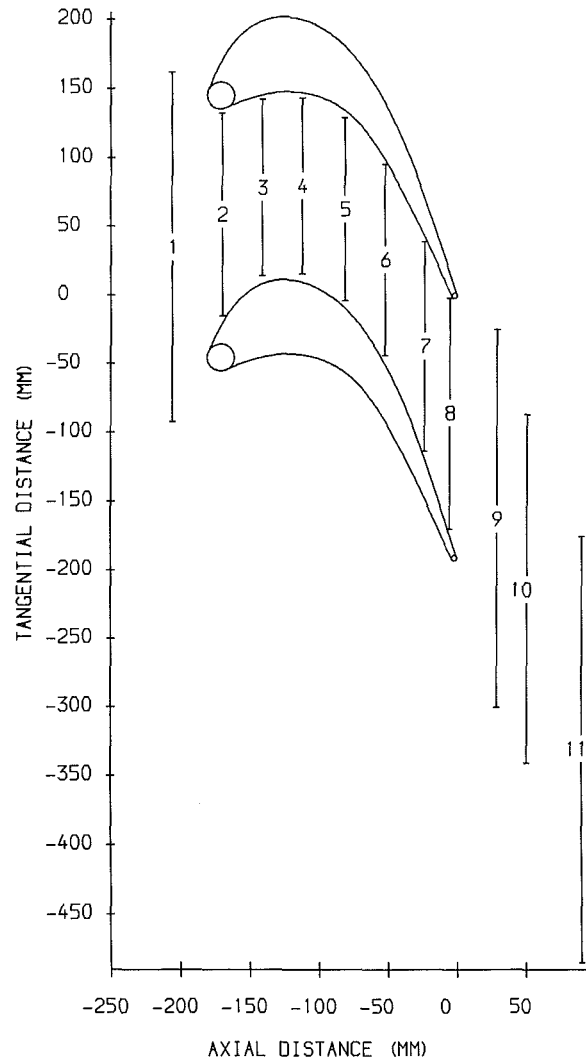
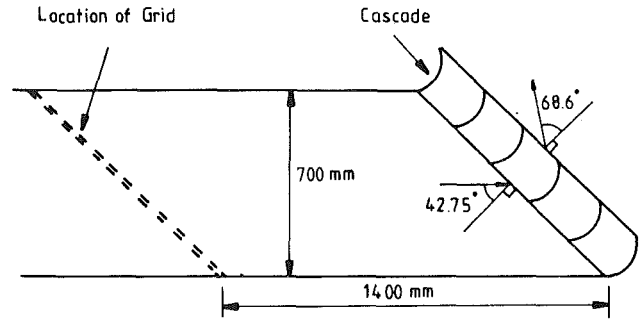


Fig. 1 Cascade and traverse slots

The blade profile and the position of the slots for traversing are shown in Fig. 1.

Nomenclature

b = axial chord
 H = boundary layer shape factor
 U, V, W = mean velocity components in x, y, z directions
 u', v', w' = fluctuating velocity components

V_o = upstream velocity
 V_x = upstream axial velocity
 x, y, z = coordinates in streamwise, cross-passage, and spanwise directions
 δ = boundary layer nominal thickness

δ^* = boundary layer displacement thickness
 ϵ = eddy viscosity
 θ = boundary layer momentum thickness
 μ = dynamic viscosity
 ρ = density

Table 2 Inlet boundary layer

	No grid	Turbulence grid
99% Thickness, δ	39.6mm	37.4mm
Displacement Thickness, δ^*	6.0mm	4.2mm
Momentum Thickness, θ	3.6mm	2.2mm
Shape Factor, $H = \delta^*/\theta$	1.7	1.9
Loss Coefficient	0.041	0.025

The grid for generating the turbulence was made up of 25-mm-dia bars set on a pitch of 80 mm. The grid was placed 1400 mm upstream of the cascade and parallel to the cascade as shown in Fig. 1. Being inclined to the inlet flow, the grid produced a deflection of the flow, but it was felt that this would be preferable to having the grid normal to the flow, and thus at a different distance from each blade. The predicted inlet turbulence intensity using the method of Roach (1987) was 4.6 percent in the streamwise direction and 4.1 percent in the orthogonal directions. The values measured at Slot 1 were 4.1 percent in the streamwise direction, 4.7 percent in the spanwise direction, and 3.9 percent in the cross-passage direction.

The effect of the grid on the inlet flow angle was very small, less than 0.5 deg in the free stream. The endwall boundary layer at inlet was made a little thinner as shown in Table 2.

2.2 Instrumentation. The flow was traversed at Slots 1 and 10 with a five-hole cobra-type probe, to obtain velocity and total pressure data. This was done to compare with the flow measured by Walsh and Gregory-Smith (1987) before the grid was inserted. The instrumentation and computerized data acquisition system were the same as theirs.

Turbulence data was obtained by traversing Slots 1, 5, 8, and 10 with hot-wire probes. Away from the endwall, a double traverse was made with two x -wire probes (DANTEC 55P53 and 55P54), using a technique similar to that described by Gregory-Smith et al. (1988b). However, improvements were made to the electronic components measuring the mean and rms of the signals to increase the accuracy of the results. Improved amplification of the signals was also provided. A further difference was in the alignment of the probes. A given slot area was traversed by placing the probe at a given tangential (or pitchwise) position and moving the probe in the spanwise direction. Gregory-Smith et al. aligned the probes with the local mean flow direction at each spanwise position. In this work, however, the probe was aligned with the flow direction at midspan (i.e., the primary flow direction) and kept at the same angle for all spanwise positions. The double x -probe technique gives the three mean components of velocity, the three Reynolds normal stresses, but only two of the Reynolds shear stresses, $u'v'$ and $u'w'$. The fluctuating components of velocity u' , v' and w' are in the "streamwise," cross-passage, and spanwise directions, as defined by the probe alignment. Thus the streamwise direction was kept as the primary flow direction, rather than varying with spanwise position. This change was made so that the results could be compared more easily with those from computer calculations.

Due to their size, measurements closer to the endwall than about 5 mm could not be obtained using the x -probes. Thus a different technique using a single wire (DANTEC 55PO4)

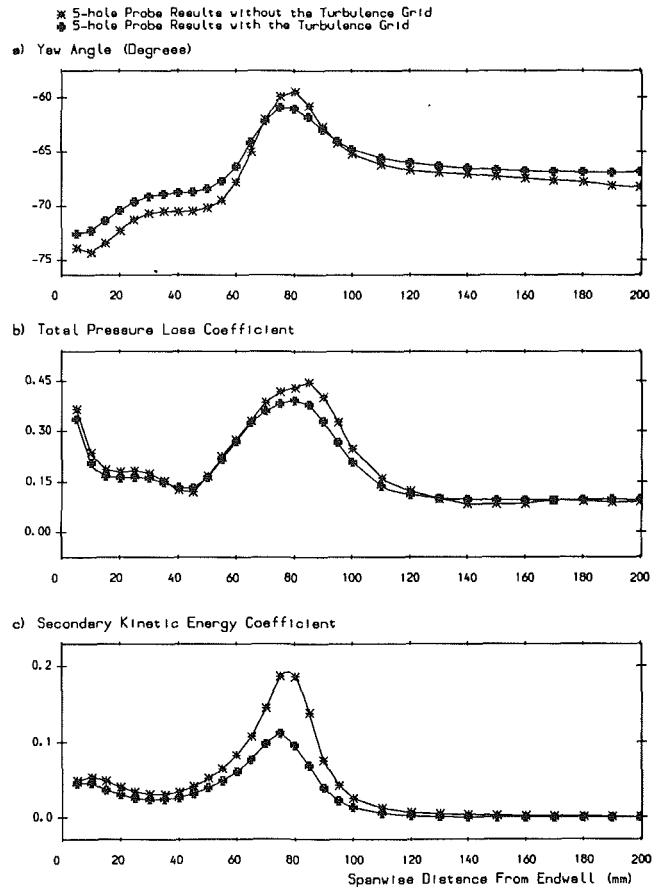


Fig. 2 Pitch-averaged results for Slot 10

was developed to obtain information about the endwall boundary layer. At any position, the wire was rotated about an axis in the spanwise direction, so that the normal to the wire was set at five angles to the streamwise direction, viz., 0, ± 20 , ± 40 deg.

By measuring mean and rms signals, the mean velocity components, U , V , W and the Reynolds stresses, u'^2 , v'^2 and $u'v'$ could be obtained. A least-squares fitting method was used, and this allowed a confidence interval to be estimated for each solution. The choice of five orientations was chosen as a compromise between traversing time and accuracy of solution.

A short spectral survey of the flow field was undertaken to determine whether or not there were any dominant frequencies present, as observed by Gregory-Smith et al. (1988b). For this a Le Croy 9400 digital oscilloscope was used that could perform fast Fourier transforms on signals over a wide range of frequencies. The width of the individual "frequency bins" for which a power was calculated was typically 1 Hz for a low range spectrum (0 to 200 Hz) and 200 Hz for a wider range (0 to 20 kHz). A single-wire probe was used for this survey, with its output being linearized to give a voltage proportional to velocity.

3 Results

For the results presented here, the secondary velocities at any point are obtained from the radial component W of velocity and the component in the cross-stream direction, as defined by the midspan direction for the same tangential position. Total pressure loss coefficient is referenced to free-stream conditions upstream of the cascade. The coefficient may be mass meaned over the pitch of the blades to give the spanwise variation in loss at a given plane, or over the whole area of the plane. Thus the inlet loss coefficient is for the inlet

Table 3 Mixed-out values for Slot 10

	No grid	Turbulence grid
Total Loss Coefficient	0.239	0.211
- Inlet Loss Coefficient	0.041	0.025
= Cascade Loss Coefficient	0.198	0.186
- Midspan Loss Coefficient	0.095	0.102
= Net Secondary Loss Coefficient	0.103	0.084
Midspan Angle	-67.5°	-66.7°

plane, the cascade loss coefficient is the growth in loss across the cascade, and the net secondary loss coefficient is cascade loss less midspan loss. The coefficients for secondary kinetic energy and turbulent kinetic energy are also referenced to upstream velocity, V_0 .

3.1 Effect of Turbulence Grid. The effect of the grid on the inlet flow at Slot 1 was mainly to thin the endwall boundary layer, as mentioned earlier. Walsh and Gregory-Smith (1987) reported a laminar separation bubble near midspan on the suction surface at about 80 percent axial chord. In designing the grid, the inlet turbulence level was chosen so that the separation bubble was predicted to be removed. So surface flow visualization (as described by Walsh and Gregory-Smith) was used to confirm the absence of the separation bubble. Apart from this, the flow looked very similar.

At Slot 10, the traverses with and without the grid gave very similar patterns for loss, secondary velocities, and streamwise vorticity. Figure 2 shows the pitch-averaged results for loss, yaw angle, and secondary kinetic energy. It can be seen that at midspan there is a slight difference in yaw angle, about 0.8 deg, and a slight increase in loss. However, in the loss core the loss is reduced, and the peak in secondary kinetic energy

Hot-Wire Anemometry Secondary Velocities and Turbulence Measurements

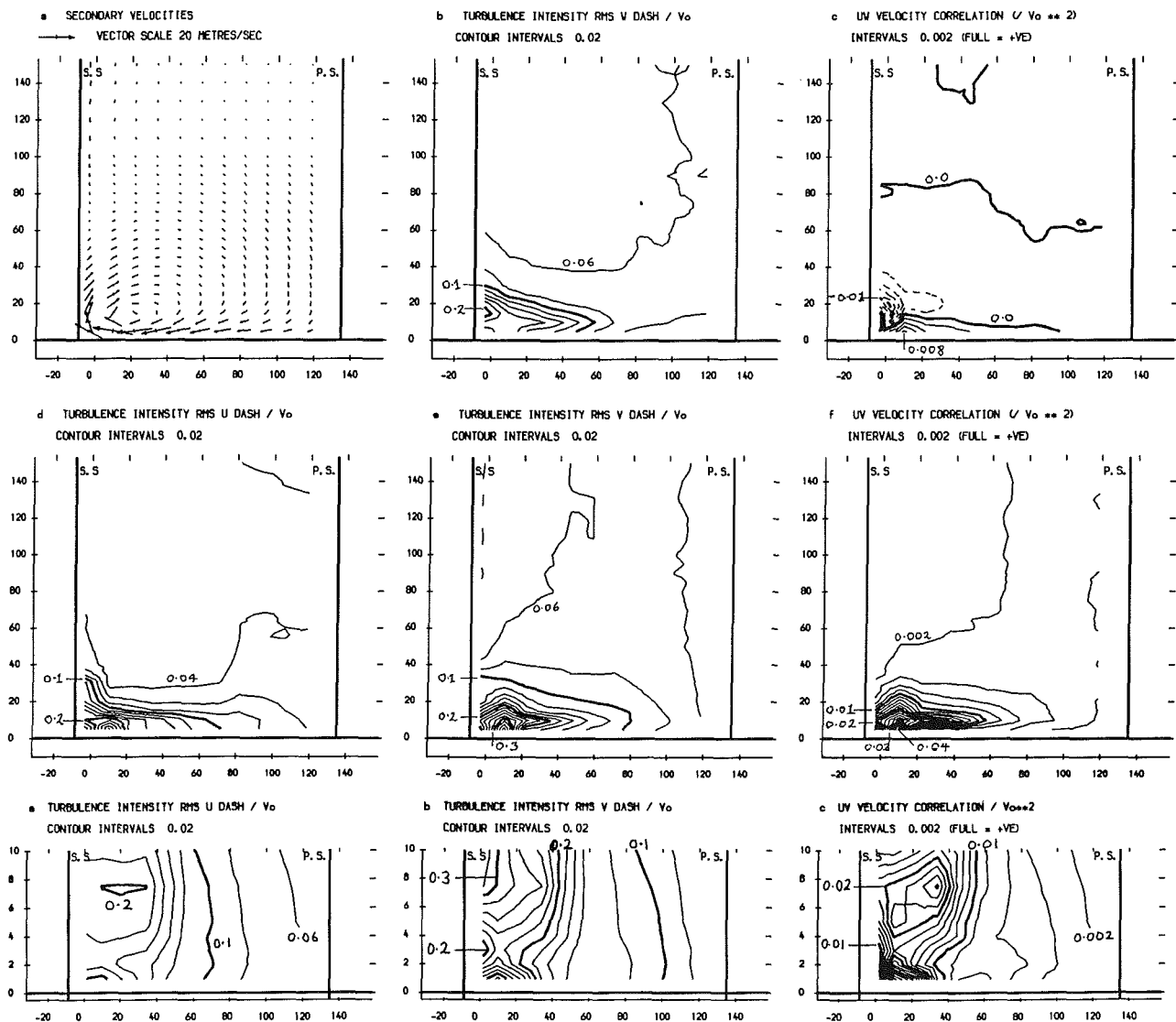


Fig. 3 Area plots for Slot 5

Hot-Wire Anemometry Secondary Velocities and Turbulence Measurements

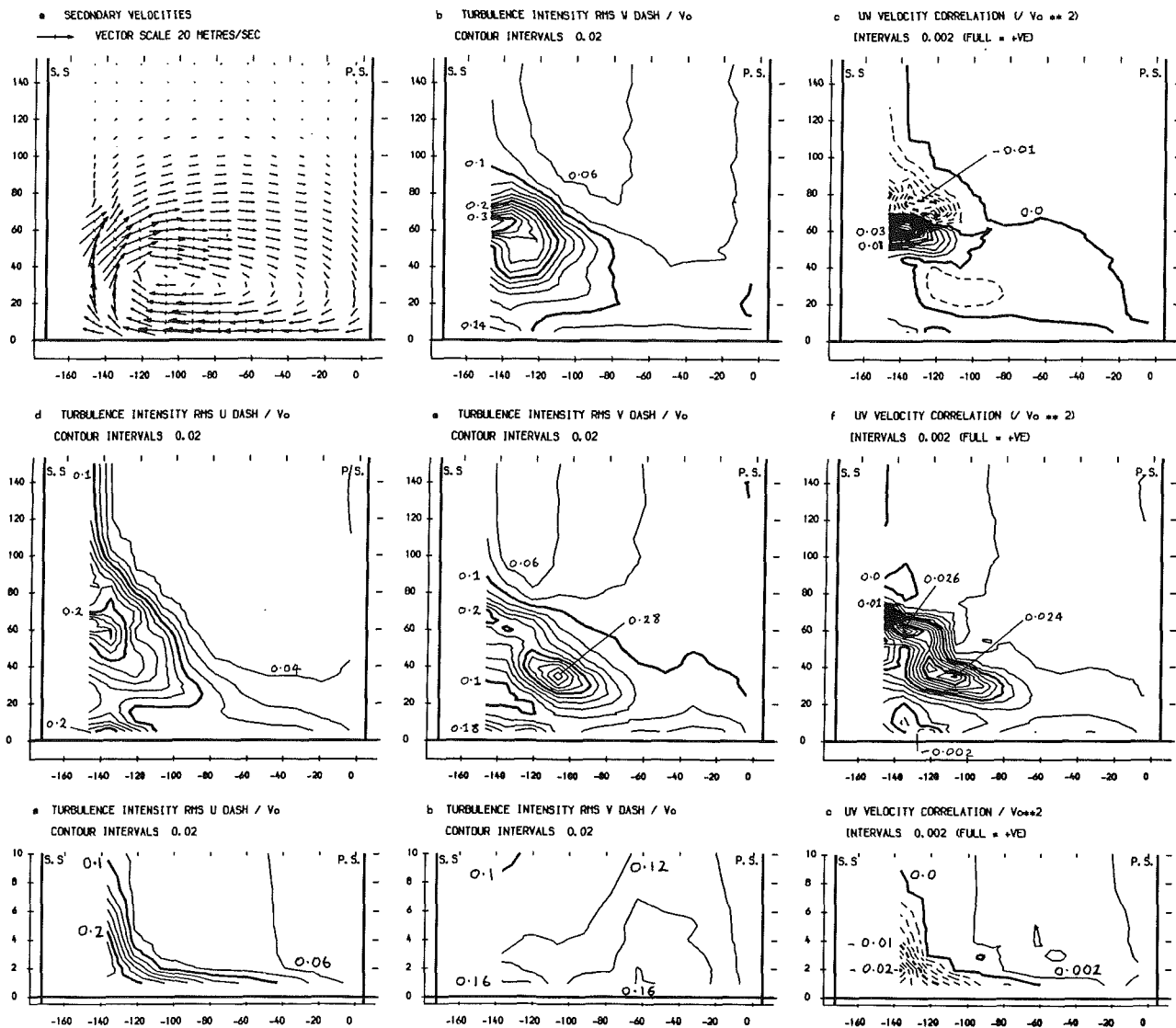


Fig. 4 Area plots for Slot 8

caused by the underturning is considerably reduced. Mixed-out values for Slot 10 are given in Table 3.

It can be seen that the effect of the grid is to reduce the cascade mixed-out loss slightly, and with the higher midspan loss, this results in a reduced secondary loss. The accuracy of the loss measurements is estimated at ± 0.005 , and so the reduction in secondary loss is only marginally significant. However, as can be seen on the later Fig. 8, the rise in actual loss from Slots 1 to 10 (i.e., not mixed-out) is nearly the same, being 0.155 without the grid and 0.157 with the grid. The difference in the mixed-out loss values arises mainly because the secondary kinetic energy of the vortex is less with the grid due to the thinner inlet boundary layer.

3.2 Turbulence Data. At Slot 1, as mentioned above, the free-stream turbulence intensities were around 4 percent. Although not presented here, the pitch-averaged results showed a rise within the boundary layer for the u'^2 intensity to 8 percent and for the v'^2 to 6 percent a 5 mm from the endwall. The w'^2 component was nearly constant, rising only to 5 percent. The turbulence intensities are all expressed as rms values relative to inlet free-stream velocity.

By Slot 5 which is at 55 percent axial chord, the secondary

velocity vectors in Fig. 3 show that the passage vortex is well developed, with its center fairly close to the endwall and suction surface corner. It is about 15 mm closer to the endwall than without the turbulence grid, which may be due to the thinner inlet boundary layer. Next to the velocity vectors, on the top row are shown the spanwise (w') turbulence intensity and the $u'w'$ correlation. On the middle row are shown the other two intensities, u' and v' and the $u'v'$ correlation. Beneath them are shown the same quantities obtained close to the endwall by the rotated single-wire technique. The vertical scale is extended to show the detail near the endwall. It can be seen that the turbulence activity is concentrated in the region near the vortex center, and that on the endwall near the pressure surface the turbulence levels are low. The $u'w'$ (streamwise-spanwise) correlation shows fairly low values, with a sign change across the vortex center. The $u'v'$ correlation (streamwise/cross passage) is positive everywhere, resulting in negative values of shear stress. Within the mainstream this is to be expected, since the cross-passage pressure gradient results in a strong negative gradient of velocity from suction pressure to pressure surface. Of course, very close to the suction surface, the shear stress must be positive in the boundary layer, but the traversing could not go close enough to the surface to show this. Near the

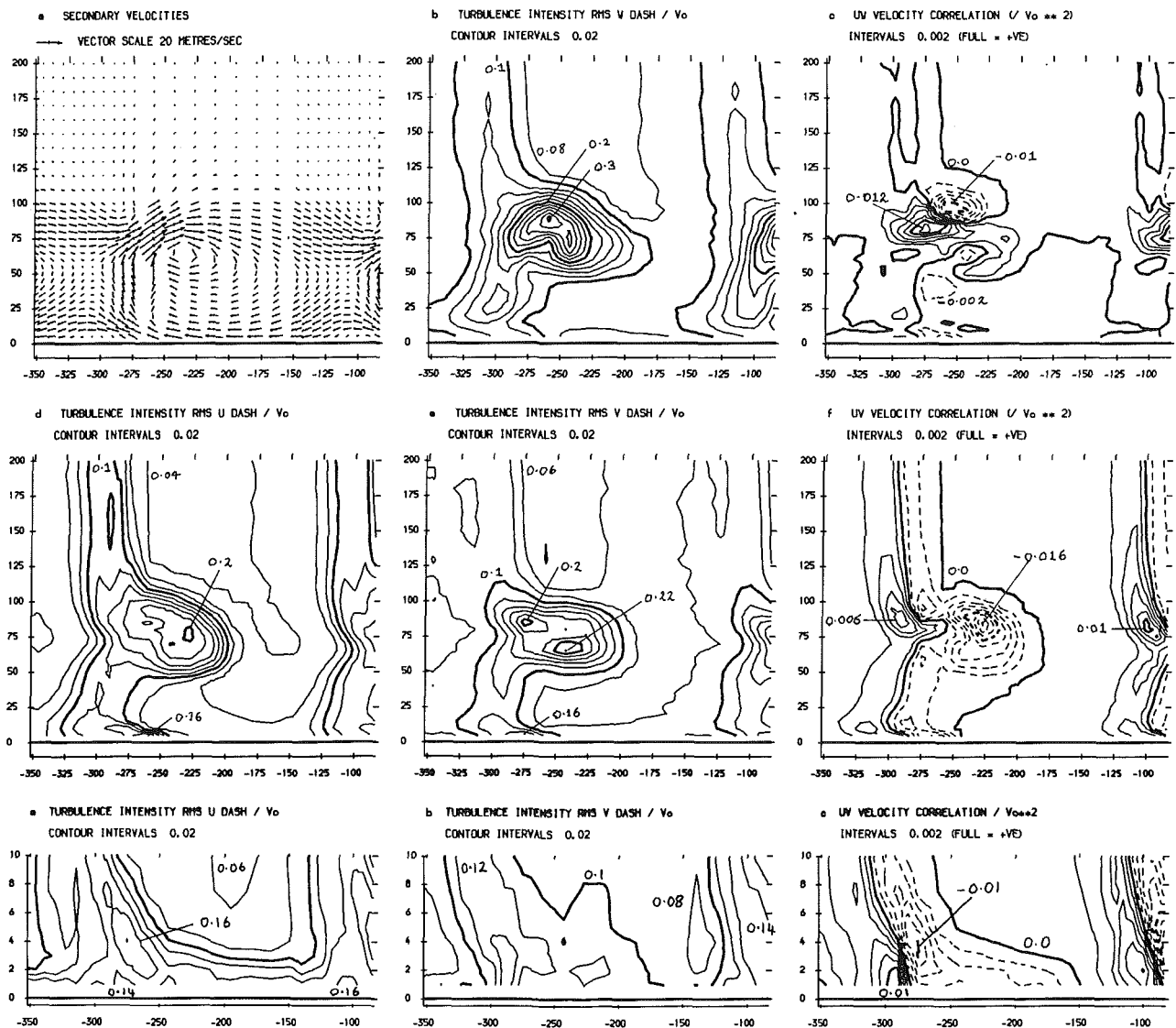


Fig. 5 Area plots for Slot 10

endwall, very high turbulent intensities and shear stress are seen close to the suction surface corner, peaking at about 15 mm from the suction surface. This corresponds to the endwall separation line, which originated from the pressure side leg of the horseshoe vortex, and which runs parallel to the suction surface in the latter half of the passage.

Figure 4 shows the results for Slot 8 (just before the exit) in the same format as Fig. 3. The center of the vortex has moved up and away from the suction surface compared to Slot 5, but is still about 15 mm closer to the endwall than before the turbulence grid was inserted. There are generally high levels of turbulence in the vortex, with high values also at about 65 mm from the endwall on the suction surface. This corresponds closely to the position of the separation line that runs up the suction surface, shown by surface flow visualization. At that point there is also a rapid sign change in the $u'w'$ correlation. Near the endwall, the turbulence is again high near the suction surface corner as at Slot 5, but here the high values spread over toward the pressure surface. Negative values of $u'v'$ are seen in the corner associated with the countervortex there. It may also be noted that the streamwise turbulence intensity has risen considerably all over the suction surface. This may be linked with deceleration in this area, i.e., $u'^2 (\partial u / \partial x)$ is acting

to produce turbulence close to the suction surface. This could be a significant factor in the rapid rise in loss production that is usually observed in the latter half of rotor cascades.

At Slot 10 (Fig. 5), which is 28 percent of an axial chord downstream, the blade/wakes can be seen in the contours of the streamwise (u') and spanwise (w') intensities. However the values are generally much higher in the passage vortex, which has moved farther from the endwall compared to Slot 8, with, in the case of the v' intensity, a second peak close to the center of a countervortex situated above and to the left of the main vortex. This countervortex is associated with the shed vorticity in the blade wake, as described by Walsh and Gregory-Smith (1989), and shown in Fig. 6. Also shown are the total pressure loss contours, which can be compared with the turbulence contours. The $u'w'$ correlation shows a sign change as at Slot 8, but now the $u'w'$ correlation also shows a large area of negative value. In the midspan wake, the signs are as expected, being opposite to those of the velocity gradients in the cross-passage direction. This sign difference persists right through the vortex and loss core, so that compared to Slot 8, there has been a sign change in the vortex region. This somewhat surprising result is discussed below. Near the endwall,

Five-Hole Probe Traverses

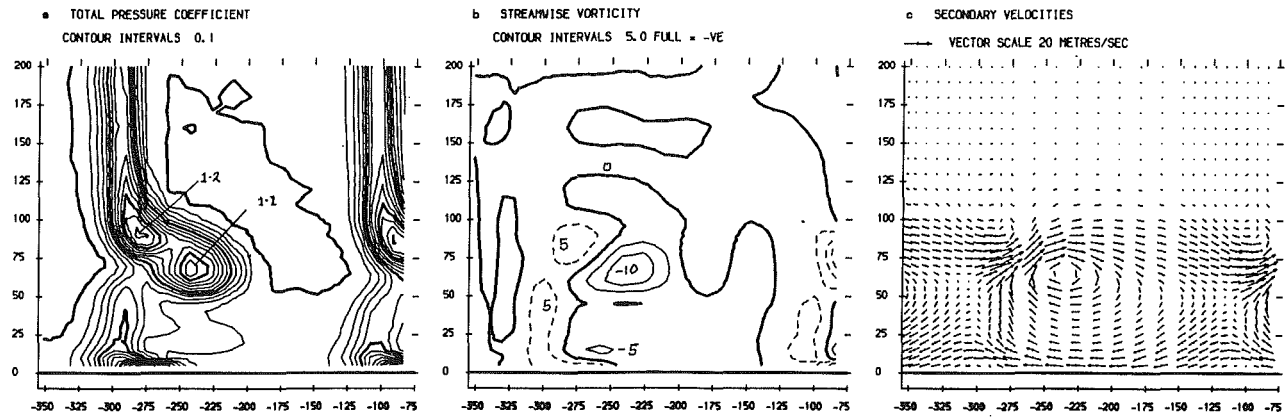


Fig. 6 Area plots for Slot 10

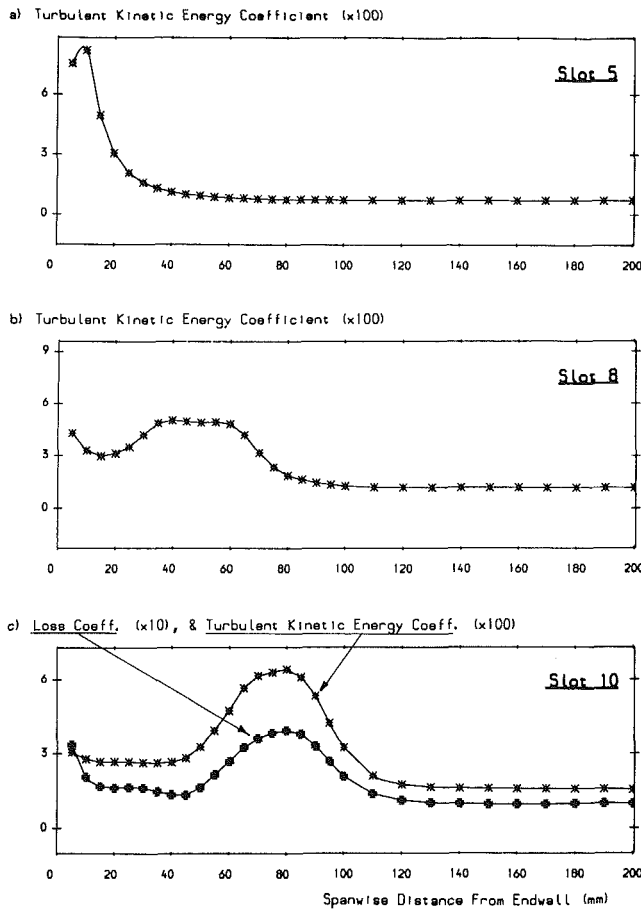


Fig. 7 Pitch-averaged results

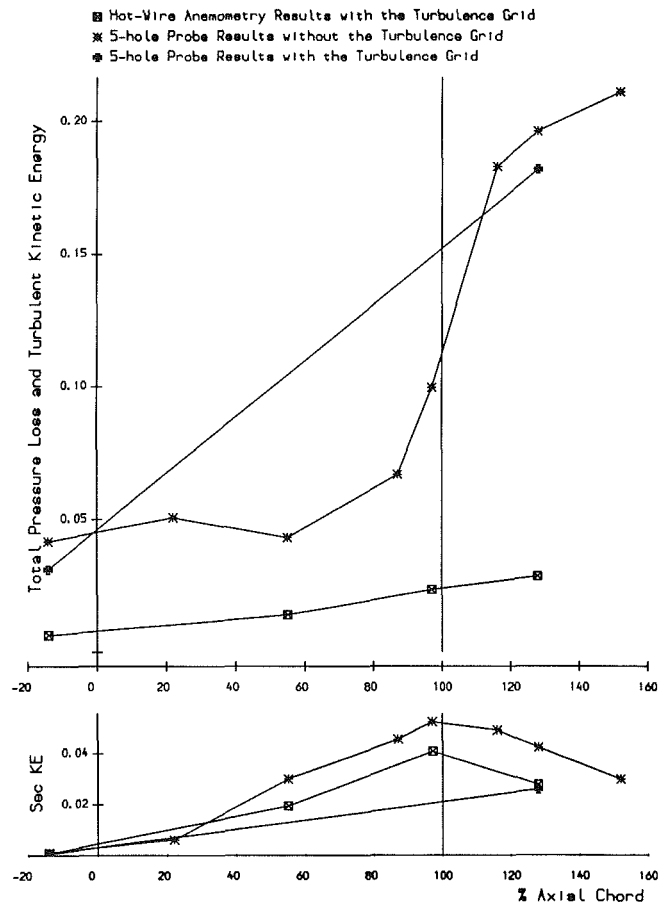


Fig. 8 Mass-averaged loss and secondary KE

high turbulence values are seen everywhere, but particularly in the loss region associated with the countervortex, which was in the suction surface corner. The $u'v'$ correlation shows a corresponding rapid sign change.

3.3 Mass-Averaged Data. At each slot position, the turbulent kinetic energy coefficient ($=u'^2 + v'^2 + w'^2/V_0^2$) was mass averaged across the pitch of the blades. Figure 7 shows the results for Slots 5, 8, and 10, and at Slot 10 the total pressure loss coefficient is also shown. It should be noted that there is a factor of 10 difference in the scales for turbulent kinetic energy and loss. At Slot 5, there is an intense peak close

to the wall, reflecting the proximity of the passage vortex to the endwall. By Slot 8, the peak has moved with the passage vortex away from the endwall; the level is somewhat less but the peak is much broader. There is also a rise near the endwall due to the turbulence caused by the counter vortex in the suction surface corner. At Slot 10 the peak in the loss core region has increased, and a small rise near the endwall is still apparent. The peak follows closely the pattern of the loss peak, although at a much lower level.

The values, mass averaged over the whole slot planes, are shown in Fig. 8. As well as the results with the turbulence grid, those from the traverses with the five-hole probe before the grid was inserted are shown. The upper graphs show the loss

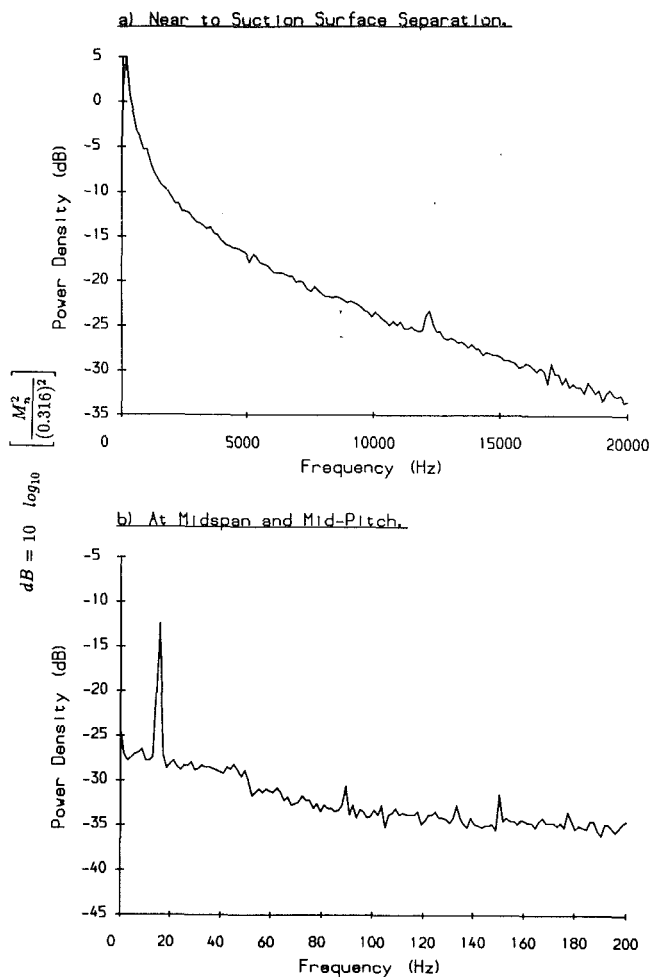


Fig. 9 Turbulence spectra at Slot 8

and turbulent kinetic energy coefficients. With the grid there are only the two points upstream and downstream of the cascade. Although the two points are joined by a straight line, the loss growth is more likely to follow the curve obtained before the grid was inserted, with a rapid rise in loss towards the trailing edge, and a jump across it as the blade wakes are included. It can be seen that the turbulence grows steadily through the cascade, but at a much lower rate than the loss. The lower graphs show the secondary kinetic energy coefficient. The results with the five-hole probe at Slots 1 and 10 agree very closely with those from the hot wires. Without the grid, the secondary kinetic energy is higher, but follows the same pattern, with peak values at Slot 8 and decaying downstream of the cascade.

3.4 Frequency Spectra. Frequency spectra were obtained at a number of positions through the cascade. Two typical results are shown in Fig. 9 at Slot 8. The first is in the high turbulence region near the suction surface separation line at coordinate $(-140, 65)$ (see Fig. 4). There is a steady decay in power density through the frequency range to 20,000 Hz, with no dominant frequencies. The second is out at midspan and midpitch, showing the spectrum over a much reduced frequency range of 200 Hz. The levels are very much lower, but there is a clear peak at 15 Hz. This peak was observed throughout the cascade where the turbulence was low. At positions where the turbulence was high, the peak was not visible, being swamped by the high turbulence. It is thought that the peak is due to an acoustic "organ pipe" resonance, the quarter wavelength of 5.5 m corresponding closely to the total length of the tunnel plus the settling chamber.

Table 4 Mass averaged dissipation of mean kinetic energy

	$\frac{1}{2} \rho V_o^2 \cdot V_x/b$
Rate of Viscous Dissipation	0.02
Rate of Turbulence Production (less $v'w'$ term)	1.92
Rate of Turbulence Production by u'^2	0.13
Rate of Turbulence Production by v'^2	-0.06
Rate of Turbulence Production by w'^2	0.67
Rate of Turbulence Production by $u'v'$	1.05
Rate of Turbulence Production by $u'w'$	0.13

4 Eddy Viscosities and Dissipation Rates

In order to provide a comparison with turbulence models used by computer calculation codes, it was decided to calculate eddy viscosities, ϵ_{ij} , from the relevant shear stresses, as defined by

$$\epsilon_{ij} = \frac{-\rho \overline{u'_i u'_j}}{\frac{\partial u_i}{\partial x_j} + \frac{\partial u_j}{\partial x_i}}$$

The calculation of the velocity gradients was based on the method described by Gregory-Smith et al. (1988a) for obtaining vorticity from experimental data. They used bi-cubic spline fits to obtain gradients of velocity and stagnation pressure in the radial and tangential directions, and then the axial gradients were calculated using the incompressible Helmholtz equation. Using the continuity equation, all nine components of partial velocity derivatives can be determined, and these can then be rotated to the hot-wire coordinates in which the Reynolds stresses were measured. (Since the $\overline{v'w'}$ component was not measured, rotation of the Reynolds stresses to cascade coordinates was not possible.) Over parts of the flow field the denominator in the eddy viscosity definition will tend to zero. Thus the calculation method was forced to give a zero value for viscosity when the denominator fell below a cutoff value and the shear stress was also small. If the shear stress was significant (for instance in the loss core), extrapolation from neighboring points was performed. The final results have to be treated, therefore, with some caution.

The first two contour plots in Fig. 10 show the two eddy viscosities calculated at Slot 10. The values are divided by laminar viscosity, and show maximum levels of around 2000. The contours are fairly similar in the loss core/vortex region, although no values are seen in the wake region for $u'w'$, as are shown by $\overline{u'v'}$. Unfortunately, since the above method requires a total pressure traverse for use in the Helmholtz equation, similar calculations could not be made for Slots 5 and 8.

The partial velocity derivatives can also be used to calculate the dissipation rates of the mean flow. There are two contributions to the dissipation of mean kinetic energy, one by viscous action to molecular motion, the other by Reynolds stresses to turbulent kinetic energy

Eddy Viscosities and Dissipation Rates Calculated from Experimental Data

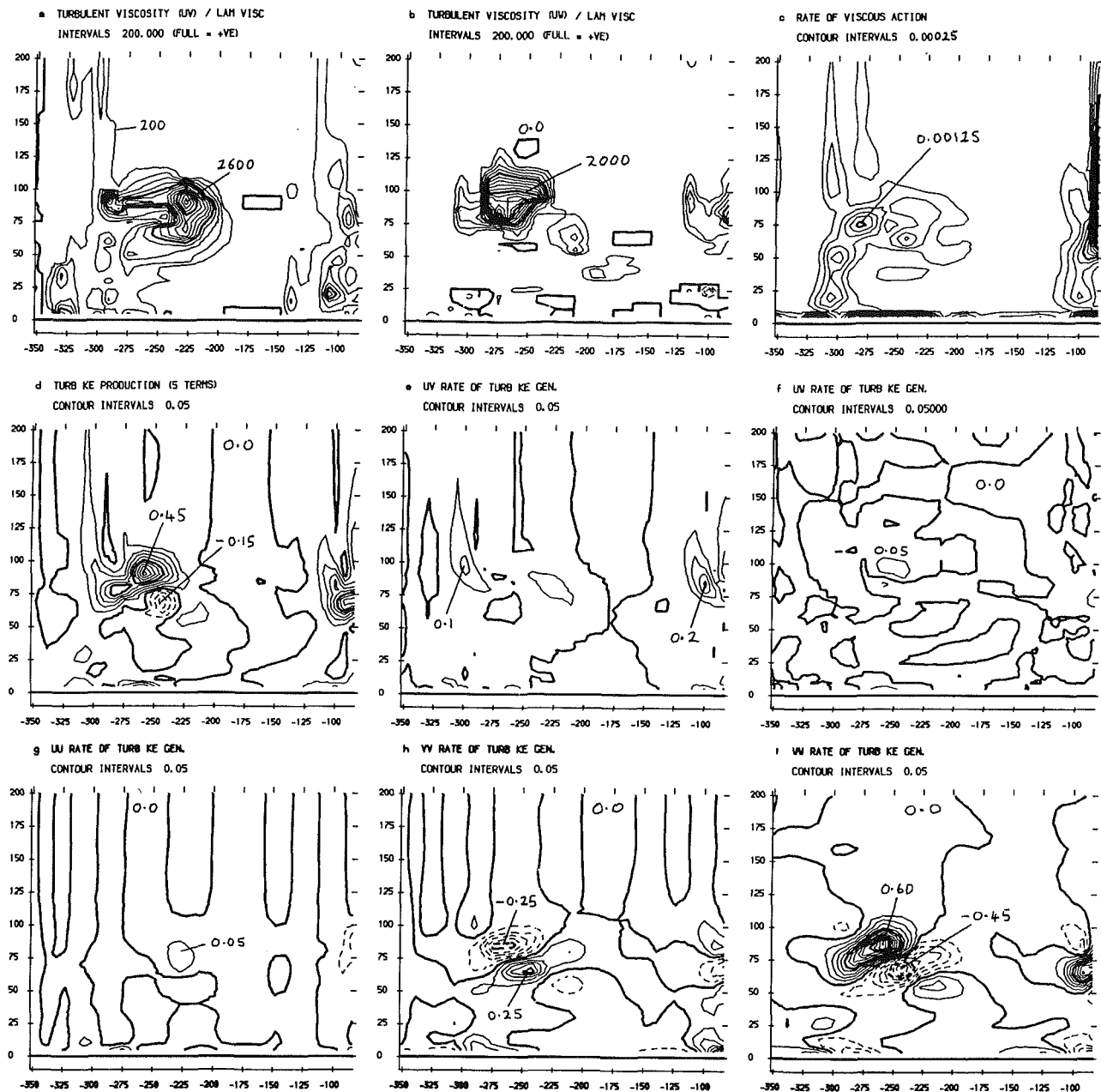


Fig. 10 Area plots for Slot 10

$$\mu \left[\frac{\partial u_i}{\partial x_j} + \frac{\partial u_j}{\partial x_i} \right] \frac{\partial u_i}{\partial x_j} \text{ and } -\rho \overline{u_i' u_j'} \left[\frac{\partial u_i}{\partial x_j} \right]$$

The third plot on the top row of Fig. 10 gives the dissipation by viscous action. The second and third rows show the contributions by the individual Reynolds stresses and their total (excluding the $\overline{v'w'}$ contribution).

It can be seen that generally the dissipation by turbulent actions is two orders of magnitude larger than that by viscous action. By far the largest rates are produced by the normal stresses, particularly in the spanwise direction peaking at 0.57. The values are made dimensionless with respect to inlet dynamic pressure, axial velocity, and axial chord. The action of the normal stresses can be either to extract energy from the mean flow or to return it to the mean flow from the turbulent

energy. The streamwise normal stress has only a small effect, because the streamwise velocity gradient downstream of the cascade is low. This is probably not the case within the passage, where there is strong acceleration of the flow. The $\overline{u'v'}$ shear stress produces some dissipation within the loss core and blade wake regions, while the $\overline{u'w'}$ only has a small effect. The shear stresses are generally dissipative, producing turbulent kinetic energy, since they usually change sign with velocity gradient.

Further information is given in Table 4, which shows the mass-averaged rates over the area of Slot 10. It can be seen that the viscous dissipation is much smaller than the turbulent energy production. The net rate of production due to the $\overline{v'^2}$ component is small and negative, in spite of the high local values seen in Fig. 10. However, the net production due to the $\overline{w'^2}$ component is large, but smaller than that due to the $\overline{u'v'}$ shear stress, which is the most significant.

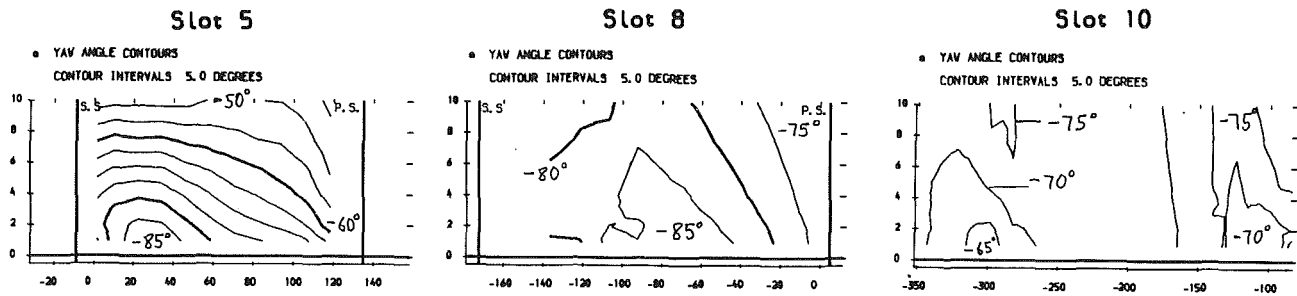


Fig. 11 Skew produced in endwall flow

5 Discussion

5.1 Effect of High Inlet Turbulence. The effect of the turbulence grid on the inlet flow is not only to increase the level of turbulence but also to reduce the inlet boundary layer thickness (Table 2). Thus it is a little difficult to distinguish between the two effects. However, it is clear that away from the secondary flow region, the boundary layer on the suction surface is forced into transition earlier by the high free-stream turbulence. This is seen in the suppression of the laminar separation bubble and the slight increase in profile loss.

Figures 2 and 8 and Table 3 indicate that the loss gain through the cascade is little changed by the presence of the grid. The published literature (e.g., Atkins, 1987; Gregory-Smith and Graves, 1983) indicates that the effect of inlet boundary layer thickness is small on the net secondary loss. Thus the evidence is that high turbulence alone has little effect on secondary loss. It seems likely that a reduction in mixed-out loss is due to reduced secondary kinetic energy resulting from a thinned inlet boundary layer. A significant difference with the grid is noticeable in the secondary kinetic energy. However this is probably a direct effect of the thinner inlet boundary layer producing a smaller vortex closer to the endwall, rather than the turbulence causing more rapid dissipation of the secondary flows. A reduction in secondary kinetic energy with boundary layer thickness decreasing would be expected from "classical" secondary flow theory.

5.2 Distribution of Turbulence. In general, Figs. 3, 4, and 5 show the turbulence to be high in the regions of the passage vortex, and also where the separation lines on the endwall and suction surface feed loss into the flow from close to the surfaces. The flow near the endwall at Slot 5 shows a large area of low turbulence except for a region close to the suction surface, indicating the likelihood of a laminar boundary layer. This would agree with the measurements of Harrison (1990). Proceeding downstream, the endwall becomes more turbulent, until by Slot 10, a turbulent boundary layer across the whole blade pitch is likely. As seen in Fig. 11, the rotated hot-wire measurements show the endwall flow to be highly skewed at Slot 5, varying by 5 deg per mm. By Slot 8, the skew is much less, about 1 deg per mm. Any calculation method may well have difficulty in predicting such a boundary layer flow.

There are significant turbulent shear stresses in the secondary flow region. The streamwise/spanwise ($u'w'$) component changes sign across the position where the separation line is seen on the suction surface, or its continuation to the downstream plane at Slot 10. This is reasonable, since it gives a negative shear stress (positive $u'w'$) where the velocity gradient in the spanwise direction is falling, and vice versa. The streamwise/cross-passage stress ($u'v'$) is generally negative upstream of the trailing edge, consistent with the cross-passage velocity gradient. At Slot 10, the expected sign change across the blade wake is seen. However, from Slot 8 to 10, there is a sign change in the values in the loss core, which was not anticipated.

In an attempt to explain this sign change, the value of terms

in the shear stress convection equation were investigated. Details are given in the appendix, but it was found that for a point in the loss core at Slot 8 (-120, 40) the change in the $u'v'$ coefficient to Slot 10 was of the order of -0.10, compared with an observed change of -0.04 (i.e., 0.024 to -0.016). A second point in the suction surface separation region, (-140, 70), gave a similar change of -0.10. Although this is a fairly rough assessment, it does appear that the observed sign change can be explained in this way. What evidence there is in the published literature seems to support the observation of a sign change in $u'v'$ from inside the blade passage to downstream. Moore et al. (1987), who traversed at a plane 10 percent of axial chord downstream, show negative values in the loss core region. Zunino et al. (1987) show positive values in the loss core with negative values in the suction surface corner for their "normal 5," which is a plane across the throat, roughly normal to the flow. They show no values of shear stress downstream.

5.3 Generation of Turbulence and Loss. A detailed comparison of the effects of the various Reynolds stresses, shown in Fig. 10, with the results of Moore et al. (1987) show general agreement, except for the $u'^2 (\partial u / \partial x)$ term, which they found to be significant. However, their closer measuring plane to the trailing edge (10 percent axial chord, compared to 28 percent for Slot 10), may mean that their streamwise gradients were larger due to the flow being less mixed.

A comparison with the dissipation rates given in Table 4 with the rate of the loss production can be made if it is assumed that in Fig. 8, the gradient of the loss curve downstream of the cascade is the same with and without the turbulence grid. The loss coefficient growth rate is 7.9 percent per axial chord, whereas the total rate of turbulence production in Table 4 is 1.92 percent per axial chord. However Table 4 excludes two components that Moore et al. (1987) found to be significant. Firstly, there is no contribution from $v'w'$, which they found contributed 31 percent to the total, and secondly, no estimate has been included of the effect of $u'w'$ in the near-wall region, which they estimated to be 30 percent of the total. Thus, although these contributions may be less for this work due to the higher aspect ratio and traverse plane position, the value in Table 4 seems reasonable. The fact that the turbulent kinetic energy is not growing rapidly implies strong dissipation of turbulence by viscous action.

These results give some indication of the complexity of the task facing modelers of turbulence for this sort of flow. Although Fig. 10 shows that an isotropic eddy viscosity may cope with the shear stresses (or at least $u'v'$ and $u'w'$) downstream of the cascade, the rapid sign change in $u'v'$ from Slot 8 implies its application within the blade passage may be much less realistic. Furthermore, a Boussinesq eddy viscosity model says nothing about the effect of normal stresses on the flow. These make some overall contribution to the loss, and locally their effects are very large. It would not be surprising if normal stresses were even more significant within the blade passage where the normal rates of strain are large. The streamwise normal stress (u'^2) may be most important, tending to keep losses low at first where the suction surface flow accelerates,

and then producing rapid increases in loss as the flow decelerates.

5.4 Spectrum of Turbulence. The only dominant frequency in the turbulence spectrum was seen at low levels of turbulence, and can be satisfactorily explained as an acoustic resonance. It seems unlikely that it has any significant effect on the mean or turbulent flow characteristics. This contrasts with the results of Gregory-Smith et al. (1988b), who found a dominant low frequency in regions of high turbulence. Their blade had very similar inlet and outlet angles to this one, and similar overall dimensions. As indicated above, there were two major differences: First their blade had large suction surface diffusion from about 50 percent axial chord, and an associated laminar separation bubble, and second the inlet turbulence was low. It seems possible that an instability in the flow due to the large diffusion or the separation bubble may have been affecting their flow. However, generally their levels of turbulence were similar to those observed in this work.

6 Conclusions

Turbulent flow details through a high turning cascade of axial flow turbine blades have been obtained. Special features are the high inlet turbulence level from an upstream grid, and measurement very close to the endwall using hot-wire anemometry. With respect to the general features of the flow, the following conclusions may be drawn:

(a) The high inlet turbulence has little effect on the secondary loss or kinetic energy of secondary flow.

(b) High values of turbulent Reynolds stresses are seen in the loss core and vortex region, and also where separation lines on the endwall and suction surface feed loss into the main flow.

(c) The streamwise/radial shear stress ($\overline{u'w'}$) shows a sign change across the position of the suction surface separation line.

(d) Within the passage the streamwise/cross passage shear stress ($\overline{u'v'}$) shows negative values in the loss core, but this changes to positive values downstream of the cascade. This sign change can be accounted for by the magnitude of terms in the stress transport equation.

(e) The frequency spectrum of the turbulence shows no dominant frequencies where the turbulence is high.

Of particular significance for the modeling of turbulence in Navier-Stokes solvers are the following:

(f) Downstream of the cascade, a fairly isotropic eddy viscosity is seen in the loss core.

(g) There are significant contributions to the loss process by the Reynolds normal stresses, and these will not be allowed for by a Boussinesq eddy viscosity model.

Acknowledgments

The authors gratefully acknowledge the support of Rolls-Royce plc for this work and their permission to publish this paper. The authors are also grateful for additional support from the Science and Engineering Research Council.

References

- Atkins, M. J., 1987, "Secondary Losses and Endwall Profiling in a Turbine Cascade," *Proc. I. Mech. E. Turbomachinery—Efficiency Prediction and Improvement*, Paper No. C255/87, pp. 29–42.
- Bailey, D. A., 1980, "Study of Mean and Turbulent Velocity Fields in a Large-Scale Turbine Vane Passage," *ASME Journal of Engineering for Power*, Vol. 102, pp. 88–95.
- Belik, L., 1972, "Secondary Flow in Blade Cascades of Axial Turbomachines and the Possibility of Reducing Its Unfavourable Effects," *Proc. 2nd Int. JSME Symposium on Fluid Mechanics and Fluidics*, Tokyo, pp. 41–49.
- Cleak, J. G. E., Gregory-Smith, D. G., and Birch, N. T., 1991, "Experimental Verification of a 3D Turbulent Flow Calculation in an Axial Turbine Cascade," *CFD Techniques for Propulsion Applications*, AGARD CP 510, Paper No. 8.
- Gregory-Smith, D. G., and Graves, C. P., 1983, "Secondary Flows and Losses

in a Turbine Cascade," *Viscous Effects in Turbomachines*, AGARD CP351, Paper No. 17.

Gregory-Smith, D. G., Graves, C. P., and Walsh, J. A., 1988a, "Growth of Secondary Losses and Vorticity in an Axial Turbine Cascade," *ASME JOURNAL OF TURBOMACHINERY*, Vol. 110, pp. 1–8.

Gregory-Smith, D. G., Walsh, J. A., Graves, C. P., and Fulton, K. P., 1988b, "Turbulence Measurements and Secondary Flows in a Turbine Rotor Cascade," *ASME JOURNAL OF TURBOMACHINERY*, Vol. 110, pp. 479–485.

Harrison, S., 1990, "Secondary Loss Generation in a Linear Cascade of High-Turning Turbine Blades," *ASME JOURNAL OF TURBOMACHINERY*, Vol. 112, pp. 618–624.

Hebert, G. J., and Tiederman, W. G., 1990, "Comparison of Steady and Unsteady Secondary Flows in a Turbine Stator Cascade," *ASME JOURNAL OF TURBOMACHINERY*, Vol. 112, pp. 625–632.

Langston, L. S., Nice, M. L., and Hooper, R. M., 1977, "Three-Dimensional Flow Within a Turbine Cascade Passage," *ASME Journal of Engineering for Power*, Vol. 99, pp. 21–28.

Moore, J., Shaffer, D. M., and Moore, J. G., 1987, "Reynolds Stresses and Dissipation Mechanisms Downstream of a Turbine Cascade," *ASME JOURNAL OF TURBOMACHINERY*, Vol. 109, pp. 258–267.

Roach, P. E., 1987, "The Generation of Nearly Isotropic Turbulence by Means of Grids," *Int. J. Heat Fluid Flow*, Vol. 8, pp. 82–91.

Senoo, Y., 1958, "The Boundary Layer on the Endwall of a Turbine Nozzle Cascade," *Trans. ASME*, Vol. 80, pp. 1711–1720.

Sieverding, C. H., 1985, "Recent Progress in the Understanding of Basic Aspects of Secondary Flow in Turbine Blade Passage," *ASME Journal of Engineering for Gas Turbines and Power*, Vol. 107, pp. 248–257.

Walsh, J. A., and Gregory-Smith, D. G., 1987, "The Effect of Inlet Skew on the Secondary Flows in a Turbine Cascade," *Proc. I. Mech. E., Turbomachinery—Efficiency Prediction and Improvement*, Paper No. C275/87, pp. 15–28.

Walsh, J. A., and Gregory-Smith, D. G., 1990, "Inlet Skew and the Growth of Secondary Losses in a Turbine Cascade," *ASME JOURNAL OF TURBOMACHINERY*, Vol. 112, pp. 633–642.

Zunino, P., Ubaldi, M., and Satta, A., 1987, "Measurements of Secondary Flows and Turbulence in a Turbine Cascade Passage," *ASME Paper No. 87-GT-132*.

APPENDIX

Estimation of Change in $\overline{u'v'}$ From Slot 8 to Slot 10

Neglecting the redistribution, diffusion, and dissipation terms, the stress transport equation gives:

$$-\frac{D}{Dt} (\overline{u'v'}) \approx \overline{u'v'} \frac{\partial u}{\partial x} + \overline{v'^2} \frac{\partial u}{\partial y} + \overline{v'w'} \frac{\partial u}{\partial z} + \overline{u'^2} \frac{\partial v}{\partial x} + \overline{u'v'} \frac{\partial v}{\partial y} + \overline{u'w'} \frac{\partial v}{\partial z}$$

The substantive derivative on the left-hand side can be approximated to

$$\frac{D}{Dt} (\overline{u'v'}) \approx u \frac{\partial \overline{u'v'}}{\partial x} \approx \frac{u}{\Delta x} \Delta (\overline{u'v'})$$

assuming the $v\partial/\partial y$ and $w\partial/\partial z$ terms are small, and that the values remain constant over the streamwise distance, Δx , from Slot 8 to Slot 10. Inserting values from the experimental data evaluates all terms apart from the third one on the right-hand side involving $\overline{v'w'}$. Neglecting this, and using dimensionless values with respect to upstream velocity gives for the point (–120, 40) in the loss core:

$$\frac{\Delta(\overline{u'v'})}{V_o^2} = -0.096$$

The dominant term is $\overline{v'^2} \frac{\partial u}{\partial y}$.

At the point (–140, 70) near the suction surface separation line, the change is

$$\frac{\Delta(\overline{u'v'})}{V_o^2} = -0.100$$

At this position, the dominant term is $\overline{u'v'} \frac{\partial v}{\partial y}$.

Clearly the above analysis is very approximate, but serves to show that the observed changes of about –0.04 can be accounted for.

The Influence of Blade Lean on Turbine Losses

S. Harrison¹

Whittle Laboratory,
University of Cambridge,
Cambridge, United Kingdom

Three linear cascades of highly loaded, low-aspect-ratio turbine blades have been tested in order to investigate the mechanisms by which blade lean (dihedral) influences loss generation. The blades in all three cascades have the same section but they are stacked perpendicular to the endwall in the first cascade, on a straight line inclined at 20 deg from perpendicular in the second, and on a circular arc inclined at 30 deg from perpendicular at each end in the third cascade. Lean has a marked effect upon blade loading, on the distribution of loss generation, and on the state of boundary layers on the blade suction surfaces and the endwalls, but its effect upon overall loss coefficient was found to be minimal. It was found, however, that compound lean reduced the downstream mixing losses, and reasons for this are proposed. Compound lean also has the beneficial effect of substantially reducing spanwise variations of mean exit flow angle. In a turbine this would be likely to reduce losses in the downstream blade row as well as making matching easier and improving off-design performance.

Introduction

In recent years lean has become a commonly used tool for controlling three-dimensional flows in turbines. In high-aspect-ratio, low hub/tip ratio machines, it can be used to control the spanwise variation of stage reaction (e.g., Deych and Troyanovskiy, 1975; Grant and Borthwick, 1987). In contrast high-pressure turbines, with which the present paper is concerned, tend to have low aspect ratios and high hub/tip ratios and the flow through them is dominated more by secondary flows than by meridional streamline curvature. In these stages nozzle lean may be used to reduce secondary losses and to improve rotor inlet flow.

Liu et al. (1979) have reported improvement in stage efficiency resulting from a package of design changes including lean. However, since a number of design changes were made at once it is impossible to determine the contribution of lean toward these improvements. Studies on the effect of lean alone, notably those of Wang et al. (1981, 1987) have shown that the dominant effect of lean is a radial component of blade force giving rise to a radial pressure gradient. In an annular nozzle with unleaned blades swirl causes a radial pressure gradient, which drives low-momentum fluid, particularly in the latter part of the suction surface boundary layer and the early part of the wake, toward the hub. This leads to radial secondary velocities, which contribute to downstream mixing loss, and the accumulation of low-momentum fluid may lead to boundary layer separation in the hub/suction surface corner. If the blades are leaned so as to increase the pressure at the hub this opposes the radial secondary flow and so may reduce losses.

In a linear cascade there is no such radial secondary flow so this mechanism for loss reduction is not available. Hence Han et al. (1988) found that 20 deg of lean reduced the losses from an annular cascade but Wang et al. (1988) found that it increased the losses from a geometrically similar linear cascade.

This paper examines the other mechanisms by which blade lean can influence losses, principally by changes in flow velocities, boundary layer state and mixing losses.

Experimental Details

Measurements on a linear cascade of unleaned turbine blades have been presented by Harrison (1990). The present paper compares that cascade with two further sets of blades with the

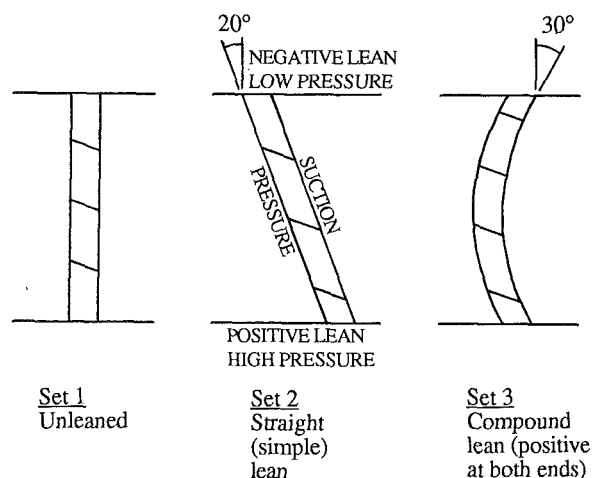


Fig. 1 Blade stacking

¹Now at Frazer-Nash Consultancy Limited, Quay Head House, Colston Avenue, Bristol, United Kingdom.

Contributed by the International Gas Turbine Institute and presented at the 35th International Gas Turbine and Aeroengine Congress and Exposition, Brussels, Belgium, June 11-14, 1990. Manuscript received by the International Gas Turbine Institute January 9, 1990. Paper No. 90-GT-55.

Table 1 Cascade parameters

True chord	278.0 mm
Axial chord	222.0 mm
Pitch	230.0 mm
Span	300.0 mm
Trailing edge thickness	2.2 mm
Trailing edge included angle	5.8°
Inlet blade/flow angle (from axial)	40.0°
Exit blade angle (from axial)	-66.8°
Inlet free stream turbulence	0.4% rms
Exit Mach number	0.14
Blade chord Reynolds' number (based on true chord and exit flow)	8.7×10^5
Zweifel coefficient (midspan, unleaned blades)	1.10
Inlet boundary layer ($x/C_x = -0.56$):	
Displacement thickness	2.6 mm
Momentum thickness	1.9 mm
Kinetic energy thickness	3.3 mm

same profile but stacked as shown in Fig. 1. Blade sections were kept constant and parallel to the endwalls, i.e., the blades were sheared rather than tilted, in order to keep blade angles and blockage unchanged. The stacking lines were leaned in the "circumferential" direction. Brief details are given in Table 1. Full experimental results are presented by Harrison (1989).

Each cascade comprised four blades with two adjustable aluminum endplates to achieve periodic flow. Periodicity was checked using oil surface flow visualization, surface static tapings on the blades and endwalls, cotton streamers on the blade trailing edges, and five-hole probe traverses. Measurements included surface static tapings on blade and endwall surfaces and traverses within and downstream of the blade rows with five-hole probes (3.2-mm tip diameter) in the main stream, a three-hole "cobra" probe (tip dimensions 0.6 mm \times 1.8 mm) in the endwall boundary layer and a flattened Pitot probe (overall tip dimensions 0.4 mm \times 2.3 mm) in the blade boundary layers.

The design of the rig did not permit any measurements in the boundary layer on the low-pressure endwall of set 2. Once it had been confirmed that the flow through blade sets 1 and 3 was symmetric about midspan, measurements were confined to one half span and, where appropriate, data have been reflected to fill a full span.

The oil-dot shear stress measurements described by Harrison (1990) were not repeated on the leaned blade rows. Wall shear stresses were measured using a hot-film gage (Dantec 55R47) stuck to a sliding section of the endwall. A rough calibration was performed assuming $\tau_w^{1/3} \propto E^2 - E_0^2$ and comparing with upstream "Clauser" plots but absolute shear stresses obtained

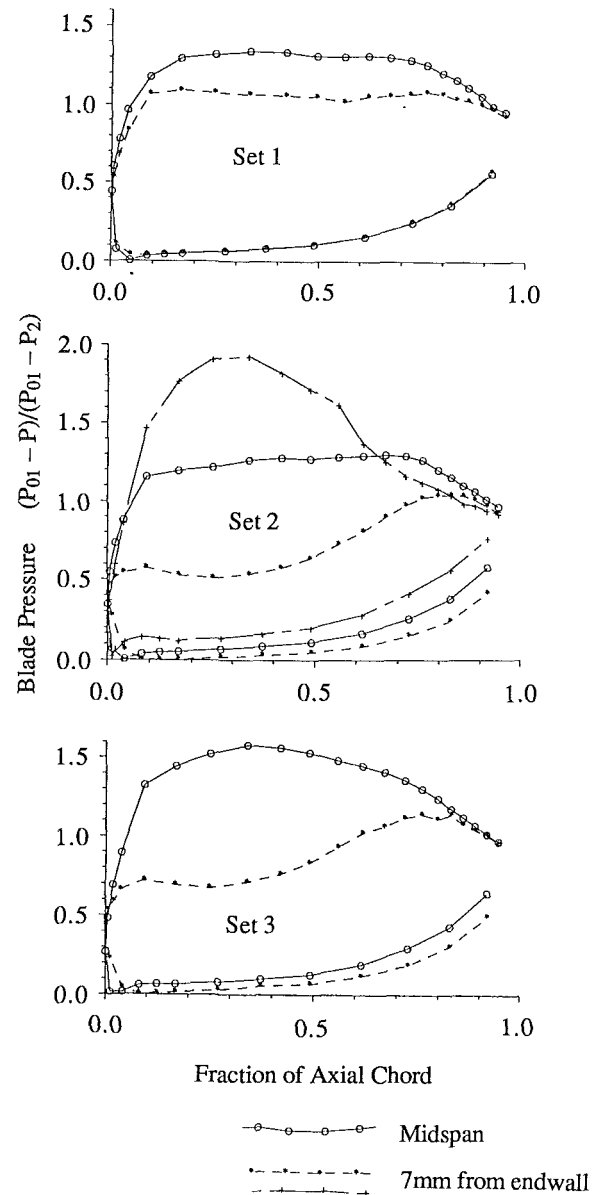


Fig. 2 Blade surface static pressures

using this type of gage are inaccurate and will not be discussed in the present paper. Instead, raw output signals were used to determine the boundary layer state.

Flow Structure

Figure 2 demonstrates the powerful effect of lean on static pressures, particularly near midchord. This has the effect on

Nomenclature

A = area	T = temperature	ρ = density
C_x = blade axial chord	U = free-stream velocity	τ_w = endwall boundary layer shear stress
C_D = boundary layer dissipation integral = $T\xi/\rho U^3$	x = axial coordinate, measured from leading edge	
E = hot film anemometer output voltage	Y = loss coefficient = $(P_{01} - P_0)/(P_{01} - P_2)$	
E_0 = E with no flow	θ = boundary layer momentum thickness	Subscripts
P = pressure	ξ = boundary layer entropy generation rate per unit area	0 = stagnation
Re = Reynolds number		1 = cascade inlet (free stream)
		2 = cascade exit (free stream)

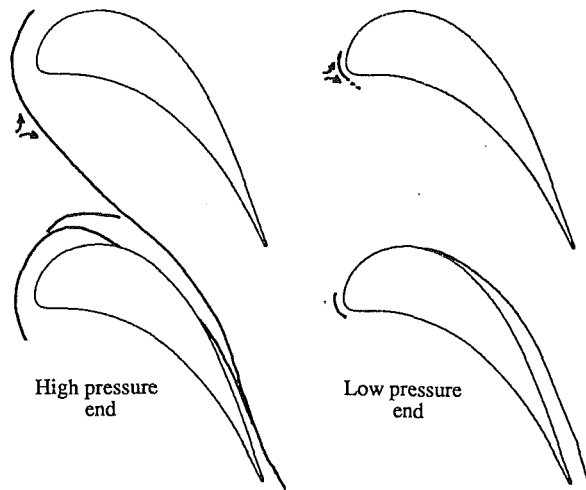


Fig. 3 Vortex lift-off lines on endwalls (set 2)

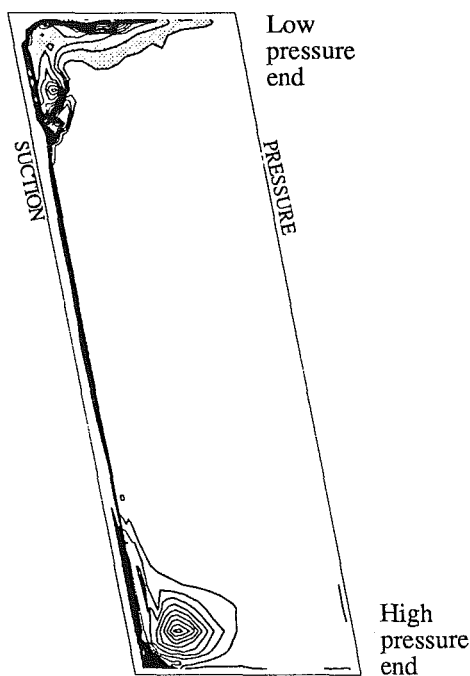


Fig. 4 Streamwise vorticity (set 2, $x/C_x = 0.83$)

set 2 of accelerating and thinning the incoming boundary layer on one wall and decelerating and thickening the one on the opposite wall. Since the inlet flow direction is not axial, it also skews the boundary layers so that blade incidence is increased within the boundary layer, which is decelerated and vice versa. This changes the endwall lift-off lines (see Fig. 3, traced from photographs of oil flow visualization). On the high pressure endwall the lift-off line is distinct and well upstream of the blades and the saddle point is near midpassage. On the opposite endwall the thinner boundary layer and decreased incidence cause the lift-off line and saddle point to be nearer to the blade leading edge. Although the oil shows that there is crossflow at this endwall, and the corner vortex lift-off line is clearly visible, there is no lift-off line associated with the horseshoe or passage vortex except at the leading edge.

This pattern suggests that at the high-pressure end most of the incoming boundary layer fluid leaves the wall along a single line and therefore that downstream of this line the new endwall boundary layer is very thin. The absence of a lift-off line on the low-pressure wall suggests that much of the incoming low-

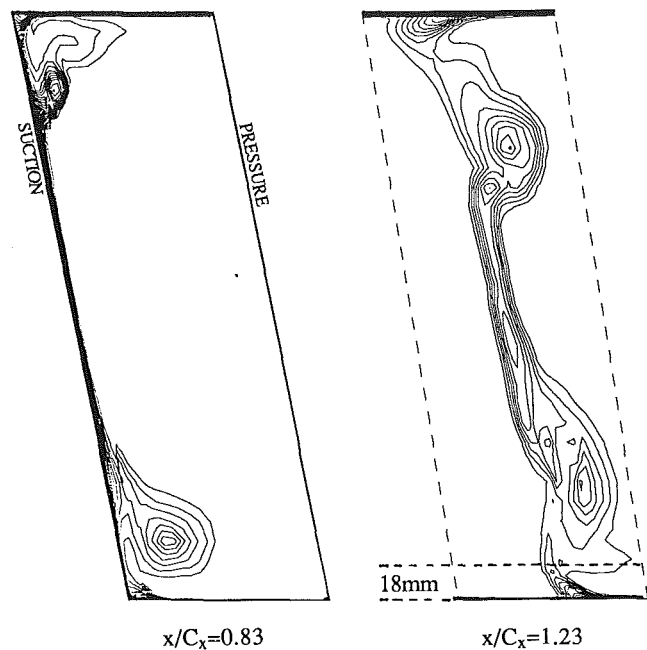


Fig. 5 Stagnation pressure loss (set 2)

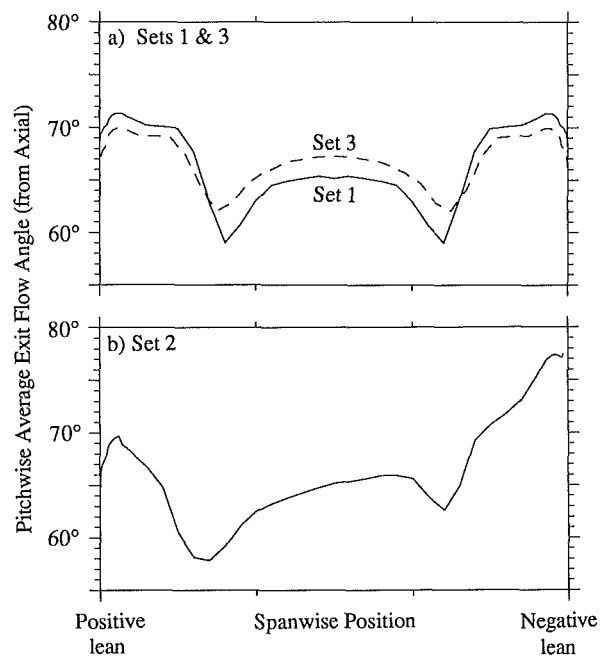
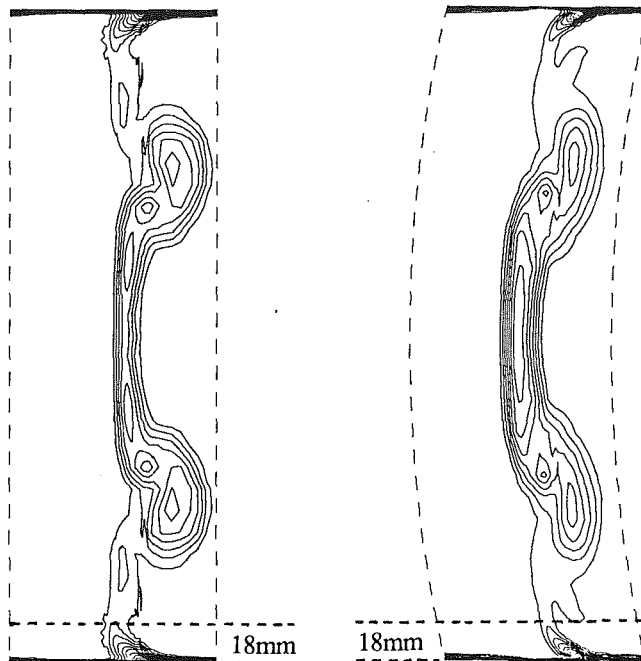


Fig. 6 Pitchwise average exit flow angle

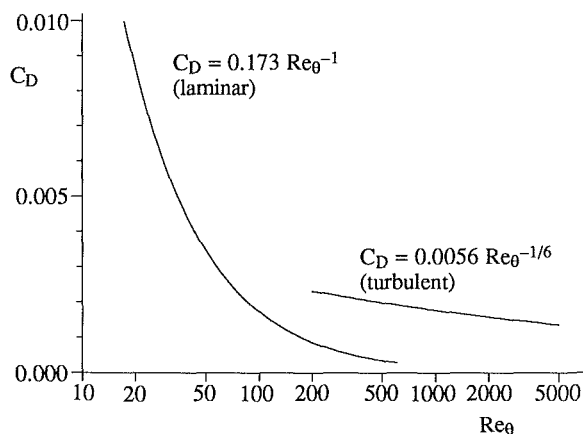
momentum fluid at this end remains attached to the wall, keeping the boundary layer relatively thick. Unfortunately, since the rig design did not permit measurements very close to the low-pressure wall, this could not be confirmed.

The oil flow patterns also suggest that at the high-pressure end, the passage vortex and the pressure side leg of the horseshoe vortex develop as a single vortex along the lift-off line, whereas at the opposite wall they may develop separately. This was checked using a wool tuft, which rotates vigorously in a vortex. The tuft showed a single horseshoe/passage vortex at the high-pressure end but *appeared* to show two distinct vortices rotating in the same direction as one another at the low-pressure end. The wool tuft was held at the end of a very



Set 1

Set 3

Contour interval $0.05 \times (P_{01} - P_2)$ Fig. 7 Stagnation pressure loss ($x/C_x = 1.23$)Fig. 8 Variation of dissipation integral with Re_0 for collateral boundary layers (formulae from Schlichting, 1968)

fine probe and it rotated so vigorously that the rotation could not have resulted merely from the presence of the probe. However, contours of streamwise vorticity (Fig. 4) indicate that the second of these "vortices" is in fact probably heavy skew in most of the endwall boundary layer rather than a discrete vortex. (Streamwise vorticity is defined as the component of vorticity in the local flow direction and its derivation is discussed by Harrison, 1990.) The vortices could not be traced much farther upstream than $x/C_x = 0.83$ using either the wool tuft or the vorticity contours because they were too small and too close to the surface boundary layers.

The pressure difference due to lean makes the loss cores at each end of blade set 2 appear very different within the blade row (Fig. 5) but downstream of the trailing edge, when this pressure difference has been removed, the pattern of loss becomes remarkably symmetric. The maximum loss coefficients in the two cores at $x/C_x = 1.23$ are different but the overall

Table 2 Overall cascade performance

Set number	1	2	3
Exit flow angle (from axial)	65.5°	64.8°	66.3°
Mass average loss coefficient	0.048	0.050	0.048
Mixing loss coefficient	0.0132	0.0207 (0.0187)	0.0116

Unleaned	15.7	15.7	54.6	63.1
Simple lean	11.1	20.2	6.2	63.6
Compound lean	14.0	14.0	6.1	65.9
	Endwalls		Pressure surface	Suction surface

Fig. 9 $\int U^3 dA$ (set 1 total = 100 percent)

loss carried by each is similar. The high pressure half span carries 54.6 percent of the total mass flux and 49.8 percent of the total entropy flux. However, because the spanwise pressure gradient moves suction surface boundary layer fluid toward the low-pressure half it is not possible to draw conclusions regarding rates of entropy generation within the blade row from spanwise variations of mean loss.

The pitchwise average exit flow angle (Fig. 6) shows clearly the over- and underturning due to the passage vortex. The effect of lean, which arises from the variation of blade loading (Fig. 2), is superimposed onto this. It leads to an overall spanwise flow angle variation downstream of set 2 of several degrees. Compound lean (set 3) does not have such a striking effect on blade pressures as simple lean (Fig. 2) but overturning at midspan and underturning near the endwalls oppose the passage vortices so that the spanwise variation of pitchwise average exit flow angle is 30 percent less than on set 1 (Fig. 6a).

The only other major difference between the flow from the unleaned and curved blade rows is that downstream of set 3 the wake is much thicker at midspan (Fig. 7). This is because the high blade loading there leads to higher loss generation and because the spanwise pressure gradient along the suction surface causes a greater accumulation of low-energy fluid at midspan.

Loss Generation

Overall cascade performance is presented in Table 2. Note that the profile loss is low for such a highly loaded blade, partly because the trailing edge is unusually thin. The maximum error in overall mass-averaged loss coefficient is estimated to be ± 0.003 , so the difference in overall loss between set 2 and the other two sets is not significant. The mixing loss presented in Table 2 will be discussed below.

Various ways in which lean affects loss generation will now be discussed.

(a) Flow Velocities. It has been suggested that positive blade lean can reduce losses by reducing velocities near the endwall, where the wetted area is large. A simple loss model will now be used to quantify the effect of velocity changes.

Schlichting (1968) shows that for a turbulent boundary layer the dissipation integral C_D (defined under "Nomenclature")

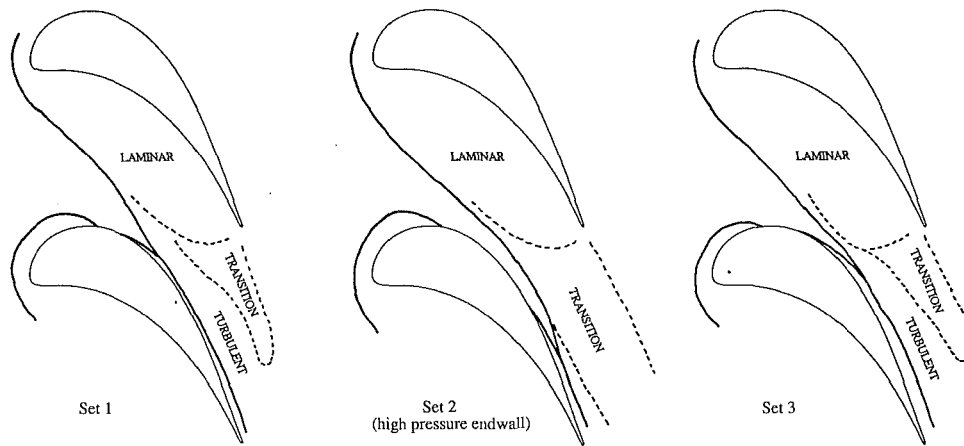


Fig. 10 Endwall boundary layer state

is virtually independent of shape factor and only a weak function of Re_θ . The same is not true of a laminar boundary layer (Fig. 8), but Moore and Moore (1983) and Denton and Cumpsty (1987) suggest that as a rough approximation a constant C_D can be assumed, equivalent to a "typical" turbulent boundary layer. If this is so, then the blade row loss is proportional to $\int U^3 dA$, where U is the local free-stream velocity and the integral is evaluated over all solid surfaces. Harrison (1990) has shown that this approximation can be reasonably accurate.

Here the constant C_D assumption will be used to quantify the influence of lean on boundary layer losses via velocity changes, as distinct from the influence via changes in boundary layer state. The integral $\int U^3 dA$ evaluated from experimental data is presented in Fig. 9. "Free-stream" velocities are derived from inlet free-stream stagnation pressure and local surface static pressure. Static pressures on the low-pressure wall of set 2 were not measured directly so they were extrapolated from five-hole probe data. Figure 9 shows that lean has a greater proportional effect on $\int U^3 dA$ on the endwalls than on the blade surfaces but the suction surface accounts for nearly 2/3 of the overall $\int U^3 dA$, so the net effect of lean is negligible. For these cascades, then, the lean does not affect overall loss by changing free-stream velocity levels. If there is an effect on boundary layer loss it must be through a change of boundary layer state.

(b) Blade Surface Boundary Layer Transition. Pressure surface boundary layers were laminar throughout. On set 1, transition on the suction surface (detected using a flattened Pitot probe and stethoscope) occurs around 65–75 percent surface distance at midspan and progressively earlier nearer the endwalls. Transition on the straight leaned blades was less distinct, possibly because of spanwise flow in the boundary layer. It occurred much earlier, around 45–55 percent surface distance. Midspan transition on the curved blades was also earlier than on set 1, around 50–60 percent.

It is hard to quantify experimentally the effect on loss of movement of the transition line because transition could not be brought forward substantially without using such a large trip that it would itself influence the loss. A two-dimensional boundary layer calculation was performed based on measured surface pressures at midspan on set 1. The calculation (Herbert and Calvert, 1982) used Thwaites' method for the laminar part and Green's lag entrainment method for the turbulent part. It predicted that if transition is brought forward by 20 percent surface distance then the midspan loss coefficient would rise by about 0.004. The increase away from midspan would be less than this, since transition occurs earlier there in any case, so the effect on overall loss would be very small. In an engine environment, high free-stream turbulence would force earlier

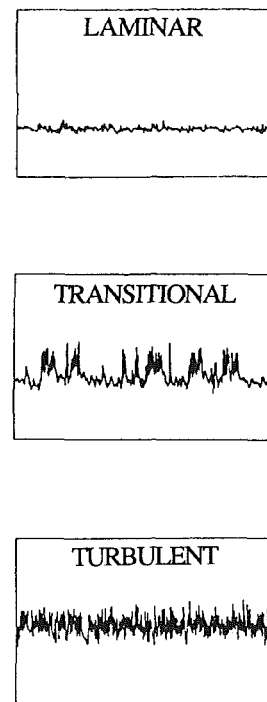


Fig. 11 Typical hot film traces

transition irrespective of lean, so the influence of lean would be less still.

(c) Endwall Boundary Layer Transition. The state of the endwall boundary layer was determined using hot-film output traces over the entire endwall (over 130 positions on each cascade). Low turbulence, intermittent bursts of turbulence, and uniform high turbulence clearly identified the laminar, transitional, and turbulent areas marked on Fig. 10. There is insufficient space to show all the traces here but typically examples are given in Fig. 11 and more are presented by Harrison (1989, 1990).

A "scalar" momentum thickness can be derived from a boundary layer traverse using only the magnitudes of velocity. Reynolds numbers based on this thickness are presented in Fig. 12, which is based on boundary layer traverses at $x/C_x = 0.03, 0.22, 0.45, 0.67, 0.83, 1.03, \text{ and } 1.23$ on set 1 and $x/C_x = 0.22, 0.67, 0.83, \text{ and } 1.23$ on set 2. No boundary layer measurements were made on set 3 except at the exit plane ($x/C_x = 1.23$).

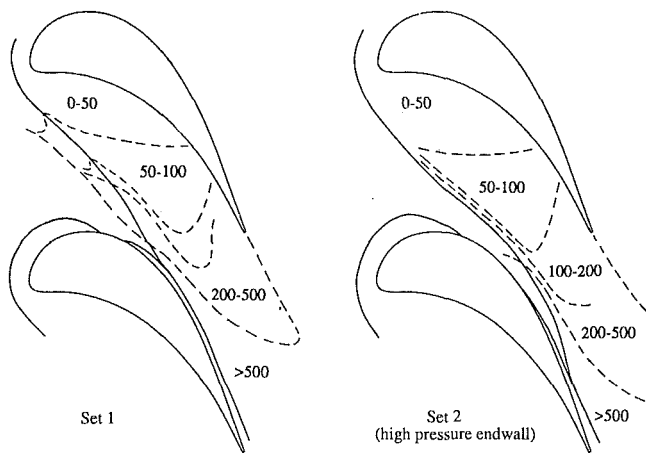


Fig. 12 Endwall boundary layer Re_θ (upstream value 3000)

Comparing Fig. 10 with Fig. 12 transition is seen to begin as soon as Re_θ reaches about 200. It is almost impossible for a collateral boundary layer with Re_θ less than about 160 to be turbulent (Schlichting, 1968). Although the boundary layer in question is skewed, this still implies that the endwall boundary layer states might be as shown in Fig. 10 even with the high free-stream turbulence levels found in an engine.

There is virtually no difference in boundary layer state between sets 1 and 3 except the slightly different wake angle due to the reduced overturning near the endwall with compound lean. A thinner boundary layer on the high-pressure wall of set 2, though, causes transition to end considerably later. Indeed, the boundary layer is not even fully turbulent at the downstream plane. However, an increased area of laminar boundary layer does not necessarily imply a reduction in loss generation beyond that which is attributable to the reduced $\int U^3 dA$. This is because the area covered by an extremely thin boundary layer ($Re_\theta < 50$) is also increased. The dissipation rate of this part of the boundary layer will be very high (Fig. 8).

The loss fluxes within 18 mm of the endwall at $x/C_x = 1.23$ (Fig. 5b and 7) contribute 0.0031, 0.0025, and 0.0029, respectively, to the overall loss coefficient of sets 1, 2 and 3. As expected, lean is seen to have reduced loss generation on the high-pressure endwall. For an approximation it seems reasonable to assume that all this loss originated in the "new" endwall boundary layer downstream of the main lift-off line. By evaluating $\int U^3 dA$ over this part of the endwall and assuming (arbitrarily) a value of $C_D = 0.0014$, loss coefficients of 0.0031, 0.0022, and 0.0027, respectively, are predicted. At best, therefore, the reduction in endwall loss is no more than might be expected from consideration of velocity changes alone. Even though positive lean delays endwall boundary layer transition, any benefit that might arise from this is canceled by the overall reduction of the endwall boundary layer Re_θ within the passage.

(d) Mixing Loss. Downstream mixing loss can be a significant proportion of the total loss of a blade row. The values presented in Table 2 have been calculated from measurements at $x/C_x = 1.23$ by assuming that the flow mixes at constant flow area with no external forces to uniform conditions downstream. The exit flow from set 2 has a net spanwise variation of mean flow angle (Fig. 6b), which in practice need not contribute to mixing loss since the following rotor could be designed to accept this variation. The figure in brackets in Table 2 therefore represents the mixing loss assuming that the downstream flow is not uniform but has a linear spanwise variation of pitch angle of ± 4.5 deg, and this value is considered to be more appropriate. Nevertheless the mixing loss is still much higher than for the unleaned or compound leaned blade rows,

due to spanwise flows resulting from the net component of blade force perpendicular to the endwalls.

The mixing loss from the compound leaned blade row is 12 percent less than that from the unleaned blade row. A reason for this will now be proposed:

A nonuniform flow will generally contain primary velocity deficits (in wakes and boundary layers) and secondary velocities (e.g., in vortices or skewed boundary layers). Both will contribute to mixing loss, but for a given total pressure deficit, the latter tends to be much more serious, since it is reasonable to assume that all the secondary kinetic energy is lost (Moore and Adhye, 1985). In a linear cascade that is symmetric about midspan, the boundary layers at midspan will give rise only to a primary velocity deficit, so will not lead to as much mixing loss as boundary layers on or near the endwall, which reinforce the secondary flow.

The compound leaned blade row therefore gives less mixing loss than the unleaned blade row because more of the loss just downstream of the blade row is concentrated near midspan (Fig. 7). There are two reasons for this:

- Velocities are higher near midspan and lower near the endwalls (Fig. 9), so a greater proportion of the overall loss is generated near midspan;
- The spanwise pressure gradients within the curved blade row tend to move suction surface boundary layer fluid toward midspan early in the blade row rather than allowing it to accumulate in the suction surface/endwall corner and therefore to reinforce the passage vortex.

(e) Other Effects. It has previously been shown (Harrison, 1990) that boundary layer skew probably has relatively little effect on loss generation.

Some workers (e.g., Marchal and Sieverding, 1977; Yamamoto, 1987) suggest that corner stall is the greatest cause of secondary loss. There was no corner stall in any of these cascades, even at the highly loaded end of the straight leaned blades. A true flow reversal would only occur in extreme cases. More usually, accumulation of low-momentum fluid in the blade/endwall corner would lead to strong secondary flows which increase the downstream mixing loss. This effect has been discussed above.

The reduced over- and underturning due to compound lean does not directly influence loss but it would reduce incidence variations onto a following rotor. This would make matching easier and may reduce rotor losses, particularly away from the design point.

Conclusions

Simple lean reduces velocities and hence loss generation substantially at one endwall and increases them at the opposite wall. Compound lean reduces endwall losses but at the expense of midspan loss.

Simple lean causes boundary layer transition on the lightly loaded endwall to occur later but also increases the area covered by a very thin (i.e., high rate of entropy generation) laminar boundary layer. On the endwalls of both the simple and compound leaned blade rows the reduction in loss generation is no more than can be expected simply by taking account of the decrease in free-stream velocities.

On the blades tested simple lean marginally increased the loss coefficient and compound lean had no overall effect on loss. However, compound lean increased flow turning, reduced downstream mixing losses, and substantially reduced spanwise variations in mean flow angle. This would lead to an improvement in turbine efficiency, particular if the blade profiles were adapted to take account of the altered blade loading.

Acknowledgments

The work described in this paper formed part of a PhD

project at the Whittle Laboratory, University of Cambridge, United Kingdom. The author wishes to thank the teaching and workshop staff of the laboratory and is particularly grateful to his supervisor, Dr. J. D. Denton. The work was carried out with the support of the Procurement Executive, Ministry of Defence and the Science and Engineering Research Council.

References

- Denton, J. D., and Cumptsy, N. A., 1987, "Loss Mechanisms in Turbomachines," *Turbomachinery—Efficiency Prediction and Improvement*, Institution of Mechanical Engineers International Conference No. 1987-6, Paper No. C260/87.
- Deych, M. Ye., and Troyanovskiy, B. M., 1975, "Investigation and Calculation of Axial-Turbine Stages," CIRC Translation MT6500409.
- Grant, J., and Borthwick, D., 1987, "Fully 3D Inviscid Flow Calculations for the Final Stage of a Large, Low-Pressure Steam Turbine," *Turbomachinery—Efficiency Prediction and Improvement*, Institution of Mechanical Engineers International Conference No. 1987-6, Paper No. C281/87.
- Han Wan-Jin, Wang Zhong-Qi, and Xu Wen-Yuan, 1988, "An Experimental Investigation Into the Influence of Blade Leaning on the Losses Downstream of Annular Cascades With a Small Diameter-Height Ratio," ASME Paper No. 88-GT-19.
- Harrison, S., 1989, "The Influence of Blade Stacking on Turbine Losses," PhD dissertation, Cambridge University Engineering Department.
- Harrison, S., 1990, "Secondary Loss Generation in a Linear Cascade of High-Turning Turbine Blades," ASME JOURNAL OF TURBOMACHINERY, Vol. 112, pp. 618-624.
- Herbert, M. V., and Calvert, W. J., 1982, "Description of an Integral Method for Boundary Layer Calculation in Use at NGTE, With Special Reference to Compressor Blades," NGTE Memorandum M82019.
- Liu, H. C., Booth, T. C., and Tall, W. A., 1979, "An Application of 3D Viscous Flow Analysis to the Design of a Low Aspect Ratio Turbine," ASME Paper No. 79-GT-53.
- Marchal, P., and Sieverding, C. H., 1977, "Secondary Flows in Turbomachinery Bladings," *Secondary Flows in Turbomachines*, AGARD CP-214.
- Moore, J., and Moore, J. G., 1983, "Entropy Production Rates From Viscous Flow Calculations: Part 1—A Turbulent Boundary Layer Flow," ASME Paper No. 83-GT-70.
- Moore, J., and Adhyc, R. Y., 1985, "Secondary Flows and Losses Downstream of a Turbine Cascade," ASME *Journal of Engineering for Gas Turbines and Power*, Vol. 107, pp. 961-968.
- Schlichting, H., 1968, *Boundary Layer Theory*, 6th ed., McGraw-Hill, New York.
- Wang Zhong-Chi, Lai Sheng-Kai, and Shu Wen-Yuan, 1981, "Aerodynamic Calculation of Turbine Stator Cascades With Curvilinear Leaned Blades and Some Experimental Results," presented at the 5th International Symposium on Airbreathing Engines.
- Wang Zhong-Qi, Han Wan-Jin, and Xu Wen-Yuan, 1987, "An Experimental Investigation Into the Influence of Diameter-Blade Height Ratios of Secondary Flow Losses in Annular Cascades With Leaned Blades," ASME Paper No. 87-GT-131.
- Wang Zhong-Qi, Xu Wen-Yuan, Han Wan-Jin, and Bai Jie, 1988, "An Experimental Investigation Into the Reasons of Reducing Secondary Flow Losses by Using Leaned Blades in Rectangular Turbine Cascades With Incidence Angle," ASME Paper No. 88-GT-4.
- Yamamoto, A., 1987, "Production and Development of Secondary Flows and Losses Within Two Types of Straight Turbine Cascades: Part 1—Stator Case," ASME JOURNAL OF TURBOMACHINERY, Vol. 109, pp. 186-193.

Endwall Losses and Flow Unsteadiness in a Turbine Blade Cascade

L. Adjlout

S. L. Dixon

Department of Mechanical Engineering,
The University of Liverpool,
Liverpool, United Kingdom

The purpose of this paper is to describe an investigation of the flow within and downstream of a turbine blade cascade of high aspect ratio. A detailed experimental investigation into the changes in the endwall boundary layer in the cascade (100 deg camber angle) and total pressure loss downstream of the cascade was carried out. Flow visualization was used in order to obtain detailed photographs of the flow patterns on the endwall and for exhibiting the trailing edge vortices. Pressure measurements were carried out using a miniature cranked Kiel probe for three planes downstream of the cascade, with two levels of turbulence intensity of the free stream. Pressure distributions on the blade were measured at three spanwise locations, namely 4, 12, and 50 percent of the full span from the wall. Hot-wire anemometry combined with a spectrum analyzer program was used to determine the frequencies of the flow oscillations. The change in turbulence level of the free stream has a significant influence on all three pressure distributions. The striking difference between two of the pressure distributions is in the aft half of the suction side where the distribution with the lower turbulence intensity has the larger lift. The oil flow visualization reveals what appear to be two separation lines within the passage and are believed to originate from the horseshoe vortex. The pitchwise-averaged total pressure loss coefficient increases with the distance of the measurement plane downstream of the cascade blades. A substantial part of this loss increase close to the wall is caused by the high rate of shear of the new boundary layer on the endwall.

Introduction

In recent years the phenomenon of the secondary flow in turbine blade cascade has been the focus of many investigators; Hawthorne (1955), Langston et al. (1977), Moore (1983), Marchal and Sieverding (1977), Gregory-Smith and Graves (1983), Yamamoto (1988), Chen and Dixon (1985), and others.

The behavior of the three-dimensional flow in turbomachinery passages is now well understood but the variation of the losses with some important parameters is less so. Correlations of the measurements made by different investigators on different tunnels and cascade geometries can only be undertaken when a better understanding of spatial variations of total pressure losses has been achieved.

The recent developments over the last decade on the experimental investigations of secondary flows in turbine cascades have been comprehensively reviewed by Sieverding (1985). This review provided an important contribution in understanding many basic aspects of the phenomenon.

Gregory-Smith et al. (1988) and Zunino et al. (1987) have recently performed experimental investigations into the turbulence related to secondary flows within turbine cascades. As

pointed out by Gregory-Smith et al. (1988) in their recommendations, some work needs to be done to investigate the effects of the free-stream turbulence since the role of turbulence in the loss generation process is not fully understood.

In the present paper, a detailed experimental investigation of the changes in the endwall boundary layer in the cascade (100 deg camber angle) and the total pressure loss downstream of the cascade was carried out at three levels of free-stream turbulence. The main geometric parameters for the cascade are given in Table 1.

Measuring Technique

A miniature cranked Kiel probe of 3 mm o.d. was used for the measurement of the downstream total pressure traverse. The Kiel probe (or shrouded total pressure probe) has the important characteristic of being insensitive to large changes in flow direction (i.e., ± 40 deg approximately). As shown in Fig. 1, the point of measurement is moved forward by 3.2 cm of the probe stem with a view of reducing possible flow interface effects caused by the stem. These characteristics were exploited in this investigation by simply setting the probe against the average flow direction. A fast response was achieved by connecting the probe close to a small sensitive pressure transducer (Gaelttec type 8T) by a short length of plastic tube, which gave passages of low volumes and minimum resistance. The

Contributed by the International Gas Turbine Institute and presented at the 35th International Gas Turbine and Aeroengine Congress and Exposition, Brussels, Belgium, June 11-14, 1990. Manuscript received by the International Gas Turbine Institute January 26, 1990. Paper No. 90-GT-355.

Table 1 Cascade design data

Blade chord	275mm
Blade aspect ratio	2.36
Pitch/chord ratio	.635
Maximum thickness/chord	.272
Blade inlet angle	34.8deg.
Blade outlet angle	-66.05deg.
Blade chord Reynold number	3.65×10^6
Mach number at blade exit	0.06

Table 2 Coordinate of the blade design (in CMS)

Suction surface		Pressure surface	
X	Y	X	Y
0.8494	0.1673	1.908	0.0345
0.1673	0.9954	2.447	0.1592
0.0159	1.5581	3.277	0.5098
0.0000	2.563	4.613	1.276
0.4512	4.402	6.810	2.641
2.556	7.659	8.769	3.540
5.932	10.11	10.73	4.132
10.07	11.07	13.09	4.636
14.01	10.31	15.84	4.528
17.37	8.817	18.73	3.888
20.28	6.945	21.66	2.914
22.84	4.801	24.46	1.520
25.29	2.657	26.78	0.095
27.32	0.775		
27.39	0.167		

Gaeltec transducer is a differential pressure transducer for measuring small pressure differences such as those required in low-speed flow traverses. The full-scale pressure range was 10 cm of water, a natural frequency of 400 Hz, and a nominal internal volume of 150 mm³/diaphragm side. The small size (27, 27, 15 mm) and light weight allowed the transducer to be secured. Good results were obtained with the Kiel probe and Gaeltec transducer as described by Dixon and Chen (1985).

Turbulence Production

Varying intensities of turbulence were produced by a square-mesh grid of square bars situated respectively at 150 and 200 cm upstream and parallel to the leading edge plane, of the blade cascade. Turbulence levels of 3.79 and 2.22 percent, respectively, were produced.

Nomenclature

C = blade chord
 d = typical dimension
 f = frequency
 h = blade span
 l = distance from the leading edge plane
 P = pressure
 Re = Reynolds number
 s = blade pitch

S = Strouhal number
 Tu = turbulence intensity
 V = exit velocity
 x, y, z = streamwise, pitchwise, and spanwise coordinate directions
 X = distance from the leading edge plane
 Y = pitchwise mass-averaged total pressure loss coefficient

$Y1$ = spanwise mass-averaged total pressure loss coefficient

Subscripts

0 = total
 1 = cascade inlet measuring plane
 a = atmosphere
 S = static

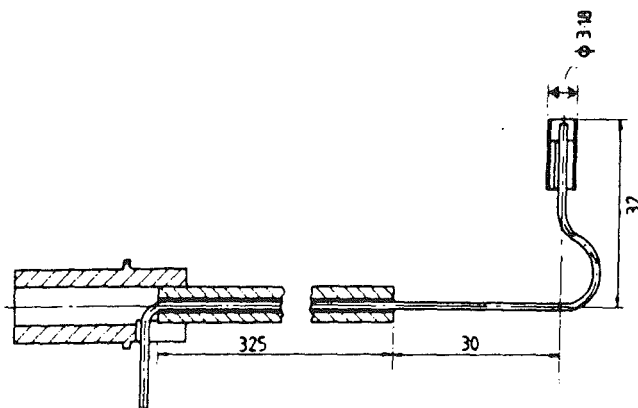


Fig. 1 Kiel probe (sizes in mm)

Area Traversing Procedure

Area traversing had been performed over a constant mesh grid system using an L.C. Smith traverse gear, which provided the necessary vertical and horizontal motions. The traverse unit was remotely controlled; a horizontal motion of 35.5 cm, a vertical motion of 40.5 cm, and 180 deg of rotation about the vertical axis were assured by an electrically driven unit.

Presentation of Data

The measurements were performed at three locations downstream of the cascade with three levels of turbulence intensity, Tu . The measuring planes were $X/C = 1.14, 1.36, \text{ and } 1.58$, X being the distance from the leading edge plane.

The data recorded were transferred to the IBM CMS main-frame computer where a Fortran program converted the data from voltages to pressures using the calibration factor and then calculated the total pressure loss coefficient at each mesh grid point. Using the spatial coordinate, contours of total pressure loss coefficient were plotted using a Ginosurf computer program.

Pressure distributions on the blade were measured at three spanwise locations, namely 4, 12, and 50 percent of the full span from the wall.

Experimental Results

Figures 2, 3, and 4 represent the contour plots of the total pressure loss coefficient for the three planes downstream of the cascade for turbulence intensity of the free stream equal to 0.9 percent. These plots show an island of high loss, which is believed to be associated with the passage vortex. For the planes $X/C = 1.36 \text{ and } 1.58$, there is an increase in the total pressure loss coefficient near the endwall and a hint of a counter-vortex is observed. However, the position of the high loss region does not change with distance downstream. Similar results have been reported by many investigators, e.g., Gregory-Smith et al. (1988).

Contour plots of total pressure loss coefficient for the 3.79

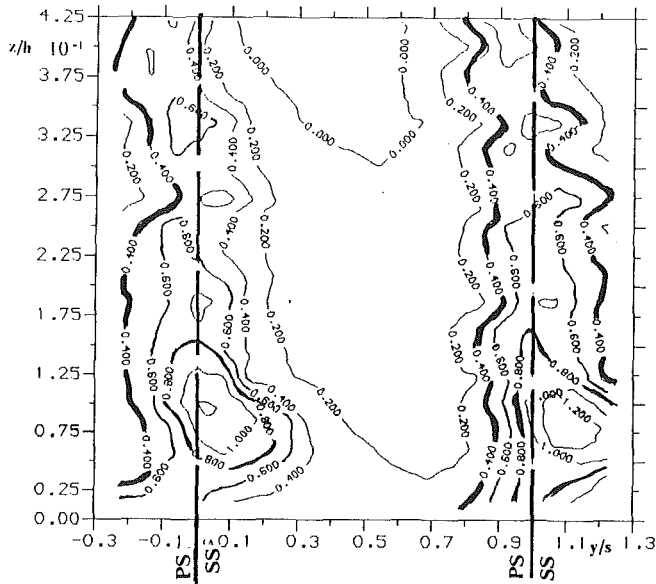


Fig. 2 Total pressure loss coefficient at $x/c = 1.14$ for $Tu = 0.9$ percent

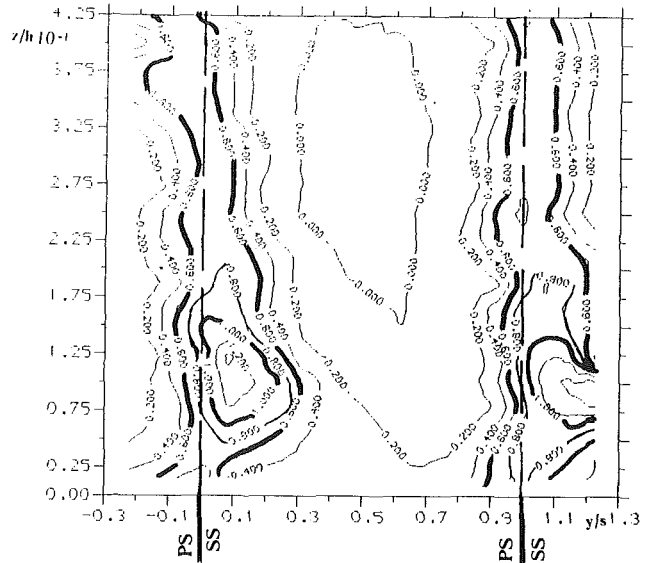


Fig. 5 Total pressure loss coefficient at $X/C = 1.14$ for $Tu = 3.79$ percent

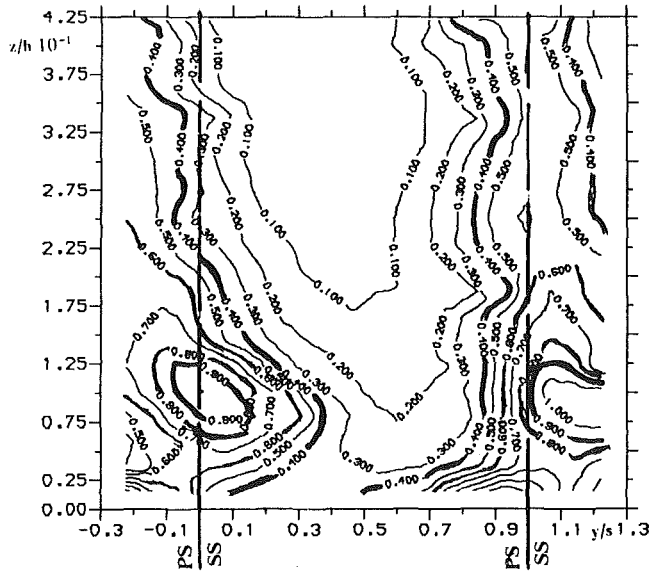


Fig. 3 Total pressure loss coefficient at $x/c = 1.36$ for $Tu = 0.9$ percent

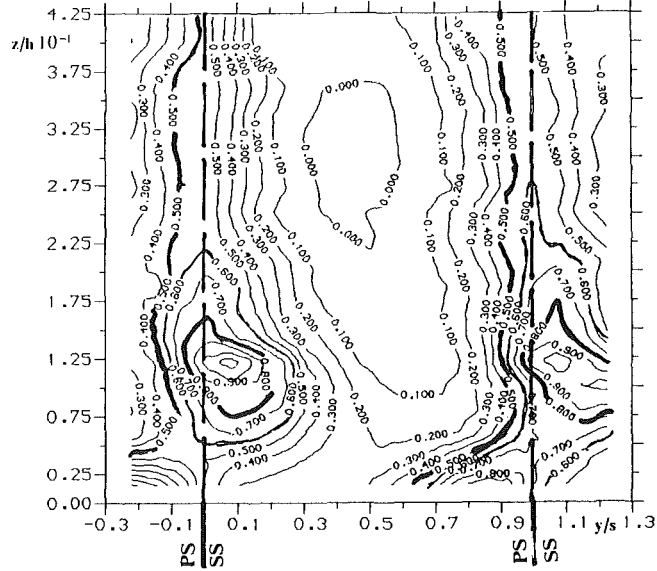


Fig. 6 Total pressure loss coefficient at $X/C = 1.36$ for $Tu = 3.79$ percent

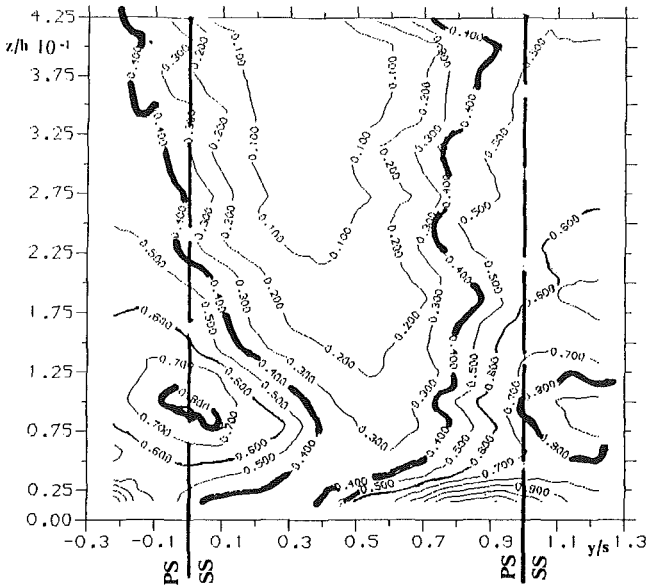


Fig. 4 Total pressure loss coefficient at $x/c = 1.58$ for $Tu = 0.9$ percent

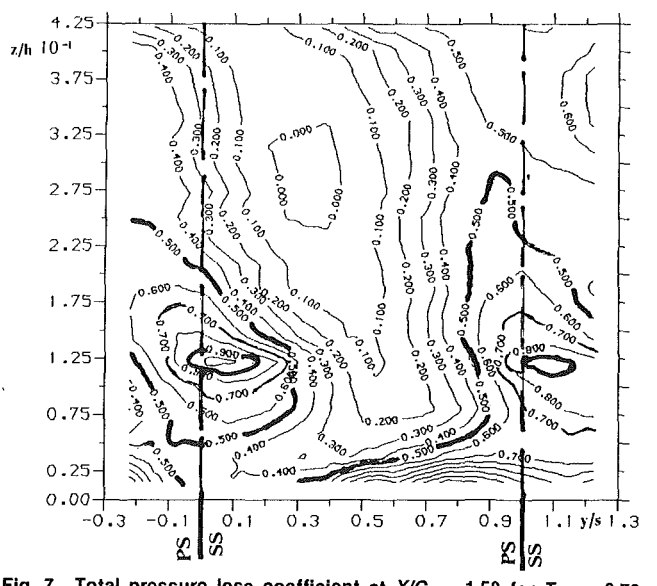


Fig. 7 Total pressure loss coefficient at $X/C = 1.58$ for $Tu = 3.79$ percent

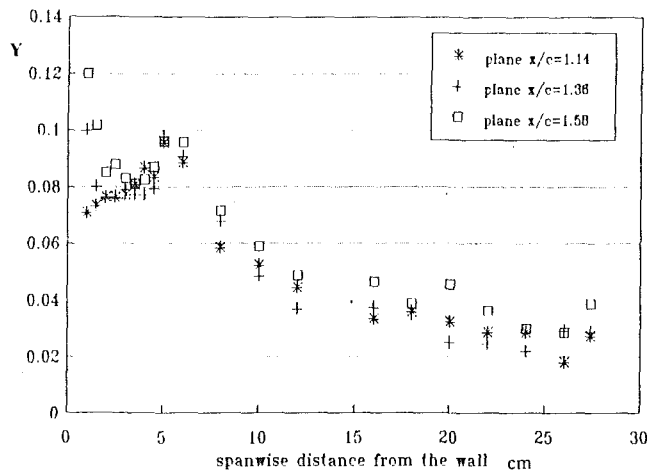


Fig. 8 Variation of the pitchwise mass-averaged total pressure loss coefficient with distance along the span for three distances downstream for $Tu = 0.9$ percent

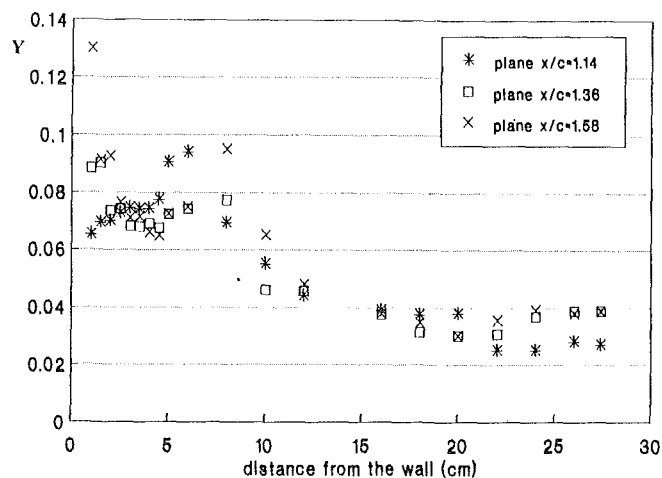


Fig. 10 Variation of the pitchwise mass-averaged total loss pressure coefficient at the plane $X/C = 1.14$

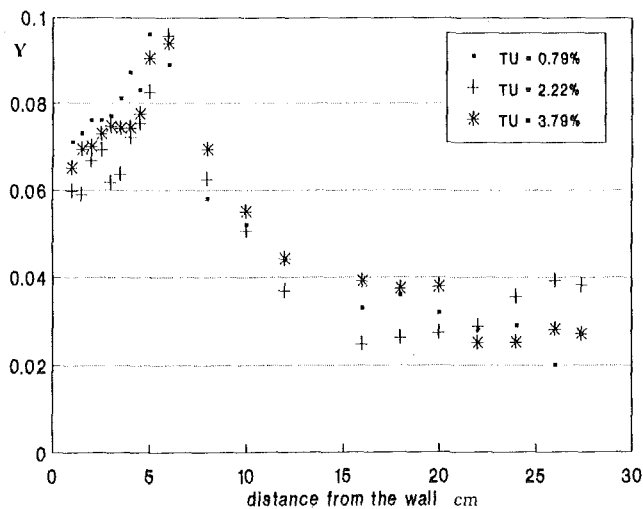


Fig. 9 Variation of the pitchwise mass-averaged total loss pressure coefficient with three distances downstream for $Tu = 3.79$

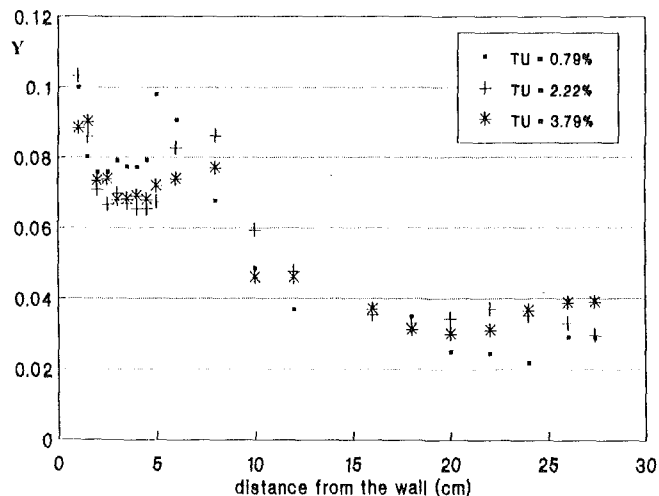


Fig. 11 Variation of the pitchwise mass-averaged total loss pressure coefficient at the plane $X/C = 1.36$ for different turbulence levels

percent intensity of the free-stream turbulence are presented in Figs. 5, 6, and 7. The same conclusions for the turbulence level of 0.9 percent apply for the turbulence level of 3.79 percent as well as 2.22 percent (not presented here).

Figure 8 shows the increase in the pitchwise-averaged total pressure loss coefficient with the increased distance downstream of the cascade for the turbulence level of 0.9 percent. A peak of total pressure loss coefficient is present for the three planes. The distance of the peak total pressure loss coefficient from the wall does not change with distance downstream from the trailing edge plane.

As shown in Fig. 9, the same features found in the case of 0.9 percent of turbulence level are also found for the 3.79 percent of turbulence level.

Figures 10 and 11 show the variation of the pitchwise mass-averaged total pressure loss coefficient at two planes downstream for three different turbulence levels of the free stream. These figures show no trend of the pitchwise mass-averaged total pressure loss coefficient with inlet turbulence level of the free-stream. The net secondary loss coefficient does not change significantly with turbulence level.

Within the experimental uncertainties the pressure distributions on the blade for the three locations were approximately the same. As shown in Fig. 12, the change in turbulence level of the free stream has a significant influence on the midspan pressure distribution. The striking difference between the two

pressure distributions is in the aft half of the suction side of the blade where the distribution with the lower turbulence intensity has the larger lift. It is believed that increasing the turbulence level of the free stream also promotes transition. From flow visualization tests on the suction surface of the blade (not reported here) it was found that a region of flow separation followed by reattachment was apparent. With an increase in the intensity of the free-stream turbulence the length of this region decreased. This feature of flow could be an important factor influencing the pressure distribution.

Flow Visualization

A surface-oil technique described by Maltby and Keating (1962) was used in the present tests. A special drawing paper 0.5 mm thick was sprayed with a matte black paint used for painting vehicle exteriors and allowed to dry. The paper was carefully fixed to the bottom endwall. A mixture of 10.7 g of titanium dioxide powder (which had been filtered through 0.25 mm screen), 40 ml of diesel oil paraffin, and a couple of drops of oleic acid was painted on the surface. The speed of the tunnel was set at 35m/s and left running for 15 min, then photographs were taken.

The tests were performed with and without the turbulence grid. For the latter, the paper was fixed on the bottom endwall

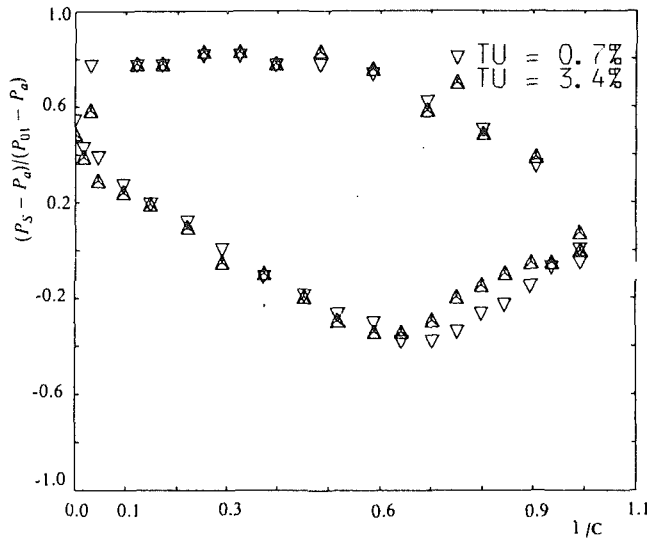


Fig. 12 Pressure distribution on the blade at 50 percent of the span for two turbulence intensities

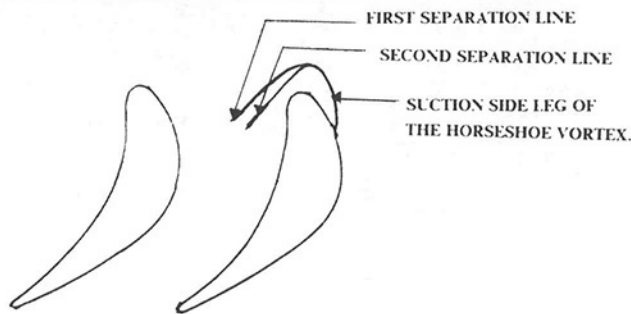
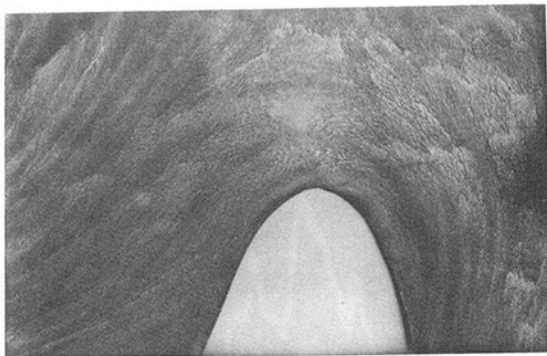


Fig. 13 Photograph of the horseshoe vortex for $Tu = 0.7$ percent

just around the leading edge of the blade and was not extended over the whole passage.

Figure 13 shows clearly the suction side of the horseshoe vortex curling around and onto the suction surface of the blade. The pressure side of the horseshoe vortex appears weak. This pressure side vortex leg appears to cross the passage to meet the suction surface of the adjacent blade. However, there is a small hint of another pressure side vortex leg, which appears to converge with the same suction side leg of the previous horseshoe vortex. These observations are for the case without grid. A photograph of the oil flow patterns on the endwall for the test made with the grid is shown in Fig. 14. This shows two lines along the passage believed to be two separation lines, one of which seems to cross from the pressure side to the suction side of the passage and the other one appears to follow a totally different pattern. This could be explained by the attempt made by Sieverding (1985) to explain the endwall lim-

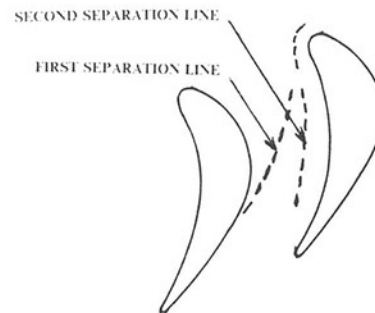
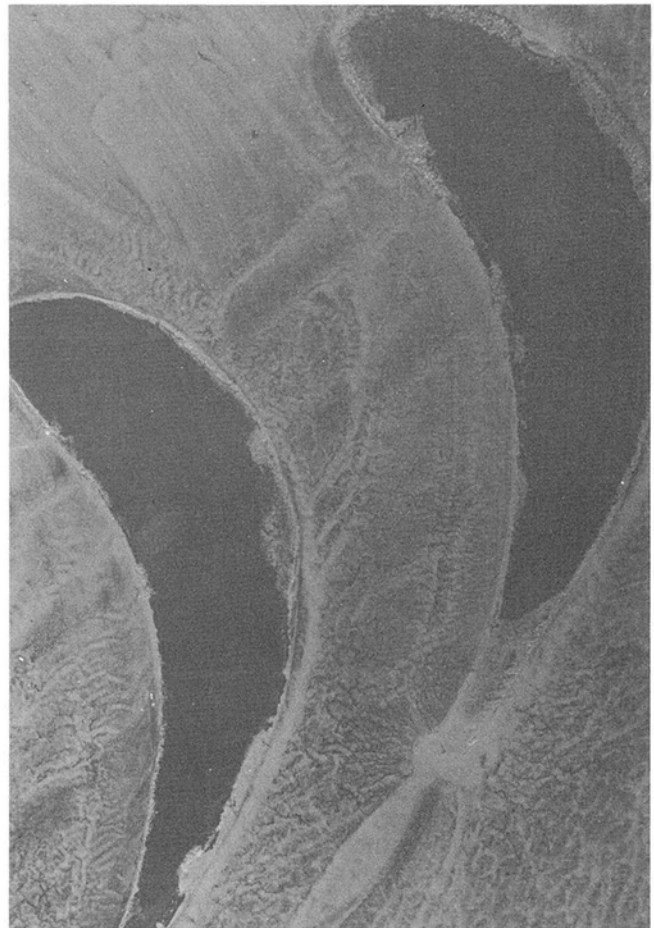


Fig. 14 Photograph of the separation lines for $Tu = 3.4$ percent

iting streamline patterns in which he stated that they could be two separation lines. The first separation line is due to the boundary layer separation ahead of the horseshoe vortex; however, the second separation line corresponds to the "lift off" of the horseshoe vortex. The conclusion to be drawn is that the phenomenon of the endwall flow is much more complicated than it at first seemed. It was noticed that with this technique, the quality of the oil flow patterns improves with increasing flow speed.

A laser light sheet was used next to reveal details of the vortex flow field downstream of the trailing edge plane. With this technique, first described by Marchal and Sieverding (1977), a laser light beam is shone onto a round, clear glass rod with its axis normal to the beam, producing a plane sheet of light by internal reflection. In use the light sheet enables a series of downstream planes to be viewed in turn. Oil smoke introduced upstream of the blades was used to get sufficient reflecting particles in the test planes. Contrary to the surface oil flow

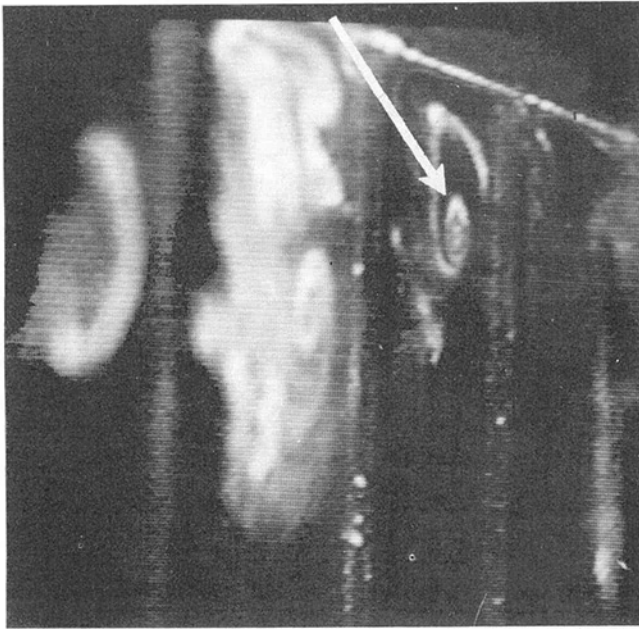


Fig. 15 Photograph of the trailing edge vortices at $X/C = 1.1$

visualization technique, which produces better results at high flow speeds, the light sheet technique must be used with rather lower speeds to allow sufficient smoke density to occur. It is possible that the phenomena observed in these tests were subject to some form of Reynolds number dependence and thus not completely representative of normal test conditions.

The smoke was introduced into the flow from the top wall in the boundary layer at 2.5 m upstream of the inlet cascade. The tests were performed at low velocity (estimated at 5m/s).

A 75 mW helium-neon laser was used for the illumination. Figure 15 was photographed in a plane just downstream of the trailing edge and shows clearly the presence of the large vortex often named "the passage vortex." There is a hint of a small vortex at the midspan side of this passage vortex.

The photograph shown in Fig. 15 was taken from a video tape. First an attempt was made to get a photograph with a camera, which proved to be unsatisfactory due to the unsteadiness of the flow. Then, a videotape was made to facilitate the work. An improved video recording, which gave a clear still picture, was used to illustrate the photograph of the trailing edge vortices.

This was caused by the observed unsteadiness in the position of the vortex cores, which helps in understanding why sampling measurements and pressure probe measurements are always varying. It is the nature of the flow within the cascade over a wide range of Reynolds number that causes such unsteadiness to arise.

Spectral Analysis

For the reason cited above, a spectral analysis study of the flow was needed. This was performed using a hot-wire anemometry technique and a spectrum analyzer program. The latter was an alternative method of signal processing using an analogue-to-digital converter and a microcomputer running on a machine code. This analogue system works well but it can be restrictive, and for this reason in the present work the signal from the hot-wire anemometer is digitized and stored in the memory of a microcomputer.

In the current application, an Apple 2e microcomputer and interactive structure A113 12 bit a-d converter are used.

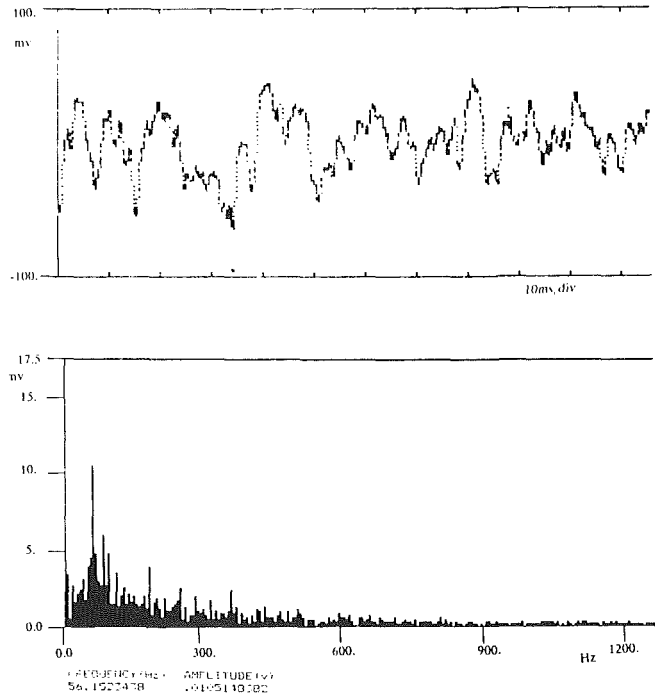


Fig. 16 Hot-wire signal and frequency spectrum

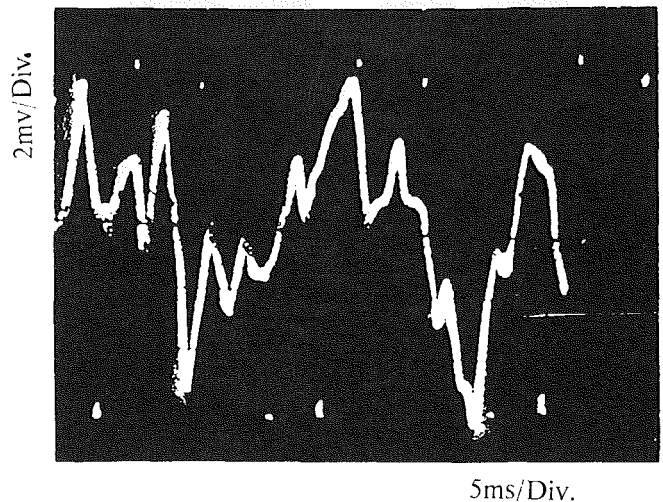


Fig. 17 Oscilloscope waveform

The Apple 2e is a 64k machine, and in this application 16 k is used for data storage, 8k for graphic display, and 8k for basic and machine code programs. The data are collected at a constant sample rate of 20 kHz using a method similar to that of Shaw et al. (1985); 8192 data points are stored in memory with each 12 bit number stored in 2 consecutive 8 bit memory locations.

The spectrum analyzer program uses fast Fourier transforms to obtain the amplitude of various frequencies within the hot-wire signal. 512 frequency bands could be identified within 40 s. The maximum frequency that can be identified after discretization is one half of the sampling frequency, i.e., 10 kHz in the current case.

This study was concentrated in the plane $X/C = 1.58$. Three traverses were made resulting in 24 positions and hence 24 data files had to be analyzed. It was found that there is a dominant band of frequency of around 50 Hz in that plane as shown in Figs. 16 and 17. Photographs of the waves were taken from the oscilloscope and the dominant frequencies could

be deduced. Within the experimental uncertainties the same frequencies were found while using the spectral program, which gave both the wave plot and the histogram showing the frequency with the highest amplitude was about 50 Hz. This frequency was found in both the corner vortices where the total pressure loss coefficient was the highest.

As concluded by Gregory-Smith et al. (1988), who determined that the dominant frequency was around 30 Hz in their case, this was not due to the shedding vortex in the trailing edge. The dominant frequency here, which is around 50 Hz, cannot be due to the shedding vortex of the trailing edge, which has a thickness of 5 mm. For that thickness a frequency of 800 Hz would be expected so this dominant frequency must be caused by something else. A frequency of around 10 Hz will result from replacing the trailing edge thickness by the blade chord for an exit velocity of 20 m/s and a Strouhal number $S = fd/V$ of 0.2. So, by taking d as a fifth of the blade chord, a frequency of 50 Hz is obtained.

Conclusions

An experimental investigation of the flow field downstream of a low speed linear cascade of turbine blades using a Kiel probe transducer, hot wire, and flow visualization has shown that:

- The total pressure loss coefficient has no trend with turbulence level of the free stream.
- The pressure distribution on the blade with the lower turbulence intensity of the free stream has the larger lift in the aft half of the suction side of the blade.
- An observed unsteadiness in the position of the vortex was revealed by the flow visualization.

- A discrete dominant frequency of the flow unsteadiness appears downstream of the trailing edge plane.

References

- Chen, L. D., and Dixon, S. L., 1985, "Growth of Secondary Flow Losses Downstream of a Turbine Blade Cascade," *ASME Journal of Engineering for Gas Turbines and Power*, Vol. 108, pp. 270-276.
- Dixon, S. L., and Chen, L. D., 1985, "Computer-Controlled Flow Traversing of Blade Cascade Using Fast-Response Pressure Probe," *Developments in Measurements and Instrumentation in Engineering*, Conference Organized by the Mech./Aero. Eng. Div., Hatfield Polytechnique, Sept. 11-13, pp. 119-125.
- Gregory-Smith, D. G., and Graves, C. P., 1983, "Secondary Flows and Losses in a Turbine Cascade," in: *Viscous Effects in Turbomachines*, AGARD CP-351, pp. 17.1-17.24.
- Gregory-Smith, D. G., Walsh, J. A., Graves, C. P., and Fulton, K. P., 1988, "Turbulence Measurements and Secondary Flows in a Turbine Rotor Cascade," *ASME JOURNAL OF TURBOMACHINERY*, Vol. 110, pp. 479-485.
- Hawthorne, W. R., 1955, "Rotational Flow Through Cascades," *Journal of Mechanics and Applied Mathematics*, Vol. 8, Pt. 3.
- Langston, L. S., Nice, M. L., and Hooper, R. M., 1977, "Three-Dimensional Flow Within a Turbine Cascade Passage," *ASME Journal of Engineering for Gas Turbines and Power*, Vol. 99, pp. 21-28.
- Maltby, R. L., and Keating, R. F. A., 1962, "The Surface Oil Flow Technique for Use in Low Speed Wind Tunnels," AGARDograph No. 70.
- Marchal, Ph., and Sieverding, C. H., 1977, "Secondary Flows Within Turbine Turbomachinery Bladings," AGARD CP-214, pp. 11.1-11.8.
- Moore, J., 1983, "Flow Trajectories, Mixing and Entropy Fluxes in a Turbine Cascade," AGARD CP-351, pp. 5.1-5.14.
- Shaw, R., Hardcastle, J. A., Riley, S., and Roberts, C. C., 1985, "Recording and Analysis of Fluctuating Signals Using a Microcomputer," *Measurement*, Vol. 3, No. 1.
- Sieverding, C. H., 1985, "Recent Progress in the Understanding of Basic Aspects of Secondary Flows in Turbine Blade Passages," *ASME Journal of Engineering for Gas Turbines and Power*, Vol. 107, No. 2, pp. 248-257.
- Yamamoto, A., 1988, "Endwall Flow/Loss Mechanisms in a Linear Turbine Cascade With Blade Tip Clearance," ASME Paper No. 88-GT-231.
- Zunino, P., Utaldi, M., and Satta, A., 1987, "Measurements of Secondary Flows and Turbulence in a Turbine Cascade Passage," ASME Paper No. 87-GT-132.

The Development of Axial Turbine Leakage Loss for Two Profiled Tip Geometries Using Linear Cascade Data

J. P. Bindon

G. Morphis

University of Natal,
Durban, South Africa

To assess the possibility of tip clearance loss reduction and to explore the nature and origin of tip clearance loss, blade tip geometries that reduce the roughly 40 percent of total loss occurring within the gap were studied. The shapes investigated aimed at reducing or avoiding the gap separation bubble thought to contribute significantly to both internal gap loss and to the endwall mixing loss. It was found that radiusing and contouring the blade at gap inlet eliminated the separation bubble and reduced the internal gap loss but created a higher mixing loss to give almost unchanged overall loss coefficients when compared with the simple sharp-edged flat-tipped blade. The separation bubble does not therefore appear to influence the mixing loss. Using a method of assessing linear cascade experimental data as though it were a rotor with work transfer, one radiused geometry, contoured to shed radial flow into the gap and reduce the leakage mass flow, was found to have a significantly higher efficiency. This demonstrates the effectiveness of the data analysis method and that cascade loss coefficient alone or gap discharge coefficient cannot be used to evaluate tip clearance performance accurately. Contouring may ultimately lead to better rotor blade performances.

1 Introduction

In this paper the tip clearance loss is measured in a linear cascade for three different gap geometries with the threefold objective of improving the understanding of the flow phenomena giving rise to rotor loss, of developing an experimental procedure to assess rotor efficiency based on detailed stationary cascade anemometry, and of identifying tip shapes for improved performance.

With respect to the flow phenomena responsible for tip clearance loss, Bindon (1989) showed that for a simple sharp-edged flat-tipped blade, the loss generated internally within the gap was 40 percent of the overall tip region loss while 50 percent was due to the mixing of leakage vortex over the final half of the cascade flow. It appeared that chordwise flow inside the gap separation bubble caused not only the high internal gap loss but was also the reason for a low discharge coefficient. Over the forward half of the blade, leakage flow reattaches behind the bubble with a relatively low loss and high discharge coefficient.

At midchord, however, where the gap pressure is the lowest, well below that at gap exit on the suction side, the flow inside the bubble accumulates and is ejected from the gap by mixing with the high-velocity inlet jet induced by the low pressure at that point. Thus high internal gap loss and low discharge coef-

ficient develop at midchord and a concentration of low-momentum fluid is fed into the suction corner flow at this point. Since this flow encounters the diffusing gradient of the suction corner, it was suggested that it may "separate" to form the high mixing loss seen to develop after midchord. No mixing loss was seen on the endwall prior to the 50 percent chord position despite significant leakage occurring over the forward half of the blade.

Thus the formation of both the internal gap loss and the mixing loss is thought to be related to the separation bubble.

In order to improve the understanding of the loss phenomena as well as to address the objective of developing improved gap shapes, it was considered profitable to examine tip geometries that avoid the formation of the bubble. In a preliminary study, Morphis and Bindon (1988) showed that a radiused edge eliminated the separation bubble and the associated very low gap inlet static pressures. The first tip geometry chosen was therefore the simple flat tip with radiused edge. The second shape was a contoured tip intended to avoid the separation bubble and to shed radial flow into the gap so as to reduce the leakage mass flow.

An experimental technique is required to compare the performance of the different gap geometries. While the ultimate test is that on an actual rotor, as done for example by Offenburg et al. (1987) and Booth et al. (1982), such a test does not normally provide any flow detail since rotor flow anemometry is costly. Booth et al. (1982) approached the problem by measuring the overall gap discharge coefficient in gap simulation

Contributed by the International Gas Turbine Institute and presented at the 35th International Gas Turbine and Aeroengine Congress and Exposition, Brussels, Belgium, June 11-14, 1990. Manuscript received by the International Gas Turbine Institute February 7, 1990. Paper No. 90-GT-152.

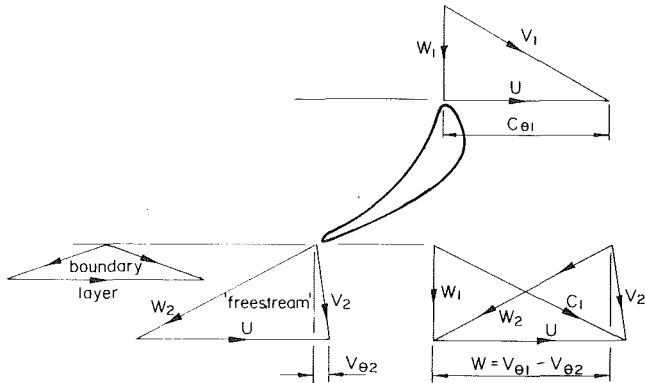


Fig. 1 By adding blade speed U to inlet velocity W and outlet velocity W a stationary cascade flow field is converted to a simulated rotor with absolute velocities V_1 and V_2

rigs. This method provides no flow detail and is based on the assumption that discharge coefficient is the dominant factor. Bindon (1987, 1988) used the total pressure loss coefficient obtained in a linear cascade with tip clearance. While this provides flow detail, in reality rotor performance depends on the Euler work obtained by flow deflection. Total pressure loss, while having an important effect, is not the only factor involved in determining rotor work transfer. As shown in Fig. 1, loss will reduce the velocity but ultimately it is the change in angular momentum that creates rotor output. This paper therefore presents and uses an analysis of experimental cascade data whereby the stationary velocity vectors are converted to the rotating frame by the addition of a hypothetical blade speed to evaluate a hypothetical rotor work and efficiency.

2 Rotor Performance Simulation

The performance of a stationary cascade may be gaged by determining the loss in total pressure. Such a loss (or entropy increase) should be used with caution as a performance indicator for a rotor where the work output is created by the change in swirl velocity. Thus the effect of both flow deflection and pressure loss in the presence of tip clearance needs to be included in a comparative performance assessment. Since flow field measurements are easier to make in stationary cascades than in moving rotors, cascade flow field data are not only more accessible but also provide more intricate flow detail, which enhances the understanding of the flow physics.

If therefore stationary flow field data could be adapted to simulate a rotor flow, a tool for the evaluation of secondary flow phenomena in rotors would become available that is both inexpensive and highly informative. The proposed adaptation of linear cascade data is shown in Fig. 1 where the blade speed U is added to the measured cascade velocities W_1 and W_2 at inlet and outlet to create a simulated rotor with absolute ve-

locities V_1 and V_2 and work transfer w . The intention of this section is to obtain the mean work transfer \bar{w} for the whole measured flow field and use it to deduce a simulated rotor efficiency.

The incompressible energy equation for a rotor with work transfer is

$$p_{01} = p_2 + \frac{1}{2} \rho \bar{V}_2^2 + \Delta \bar{p} + \rho \bar{w} \quad (1)$$

The terms are all mass-averaged quantities, which are determined by integration of the whole flow field.

In an incompressible rotor the pressure difference represents the isentropic change. Therefore rotor efficiencies may be defined in various ways following the normal concept of real and ideal work. Thus

$$\eta = w/w_{is} = \rho \bar{w} / \Delta p \quad (2)$$

where Δp is the driving pressure difference.

For the "total-to-total" case

$$\eta_{tt} = \frac{\rho \bar{w}}{p_{01} - p_{02}} = \frac{\rho \bar{w}}{\rho \bar{w} + \Delta \bar{p}_0} \quad (3)$$

The "total-to-static" case is

$$\eta_{ts} = \frac{\rho \bar{w}}{p_{01} - p_2} = \frac{\rho \bar{w}}{\rho \bar{w} + \Delta \bar{p}_0 + \frac{1}{2} \rho \bar{V}_2^2} \quad (4)$$

When applied to the simulated "rotor" some explanations and assumptions are needed. The kinetic energy is simply the mass-averaged integration of V_2 . The work term is the Euler work $U(V_{\theta 1} - V_{\theta 2})$ mass averaged over the inlet and outlet flows. The total pressure loss term, because it primarily involves fluid friction generated in the flow over the blade and endwall surfaces and that generated by secondary flows, is assumed to be the same for the stationary cascade and for the "rotor." The main factor that would make the two losses different in reality would relate to the different outer endwall motion (for unshrouded blades), which affects the shear forces and the leakage flow quantity and sets up the "scraping vortex."

Nondimensionalizing each term with the cascade inlet freestream velocity head $\frac{1}{2} \rho W^2$

$$\eta_{tt} = C_w / (C_w + \bar{C}_L) = 1 / (1 + \bar{C}_L / C_w) \quad (5)$$

$$\eta_{ts} = C_w / (C_w + \bar{C}_L + C_{v2}^2) = 1 / (1 + \bar{C}_L / C_w + C_{v2}^2 / C_w) \quad (6)$$

The integration for the rotor work transfer coefficient C_w would normally span the whole of the rotor passage between hub and tip. Since the resulting efficiency would then be somewhat insensitive to changes in tip clearance performance because of the large loss free zones at midheight, only the endwall zone affected by leakage is integrated. In Bindon (1989) the reference mass flow was that of free inlet fluid through an area 1 pitch \times a spanwise distance of $\frac{1}{4}$ chord, a figure selected as pro-

Nomenclature

C_v = velocity ratio = V/W
 \bar{C}_L = loss coefficient
 C_m = mixing loss coefficient
 C_g = internal gap loss coefficient
 C_w = work coefficient = $\rho \bar{w} / \frac{1}{2} \rho W^2$
 C_D = gap discharge coefficient = \dot{m} / \dot{m}_{is}
 C_f = gap mass flow coefficient
 = gap mass flow/inlet flow through 1 pitch \times blade length of $\frac{1}{4}$ chord
 C'_L = one-dimensional gap loss coefficient at given chord position

\dot{m} = mass flow
 p = pressure
 S = pitch
 s = pitchwise distance
 U = hypothetical rotor velocity
 V = absolute velocity
 V_{2id} = mass-averaged velocity above vortex at height Z_2
 V_θ = swirl velocity
 W = relative velocity
 w = specific work
 Z = spanwise flow integration height

z = spanwise distance
 β = relative flow angle
 η = efficiency
 ρ = density

Subscripts

o = total quantity
 1 = cascade inlet
 2 = cascade exit
 is = isentropic or loss free
 ts = total to static
 tt = total to total
 x = axial

viding a height greater than the affected zone at cascade exit. This reference mass flow is retained here.

At cascade exit, the integration is taken up to a height Z_2 just sufficient for the mass flow through the exit plane to match the mass flow through the inlet plane. The exit plane height will depend on the extent and intensity of the secondary flow and also of the flow direction and is found by iteration, for each tip clearance shape and associated flow field, from

$$\dot{m} = \rho W S Z_1 = \int_0^S \int_0^{Z_2} \rho W_2 \cos \beta_2 dz ds$$

For convenience, this can be nondimensionalized with the mass flow \dot{m}

$$1 = \int_0^S \int_0^{Z_2} \frac{W_2}{W} \cos \beta_2 \frac{dz ds}{Z_1 S} \quad (7)$$

The work term $\rho \bar{w}$, and later the work coefficient C_w , can be found by mass averaging the Euler work $U(V_{\theta 1} - V_{\theta 2})$ for the inlet and outlet flow fields:

$$\bar{w} = \frac{\int \dot{m} UV_{\theta 1} d\dot{m}}{\dot{m}} - \frac{\int \dot{m} UV_{\theta 2} d\dot{m}}{\dot{m}} \quad (8)$$

As shown in Fig. 1 for this hypothetical rotor analysis of flow in the leakage-affected zone near the tip, the linear cascade had an "axial" inlet and thus the simulated swirl velocity $V_{\theta 1}$ is constant even within the inlet boundary layer.

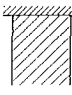
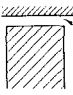
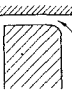

$$C_w = \frac{\rho \bar{w}}{\frac{1}{2} \rho W^2} = \frac{\rho}{\frac{1}{2} \rho W^2} \left(\frac{\int \dot{m} UV_{\theta 1} d\dot{m}}{\dot{m}} - \frac{\int \dot{m} UV_{\theta 2} d\dot{m}}{\dot{m}} \right) \\ = \frac{2}{W^2} \left(\frac{U^2 \int \dot{m} d\dot{m}}{\dot{m}} - \frac{U_o \int_0^S \int_0^{Z_2} V_{\theta 2} \rho W_2 \cos \beta_2 dz ds}{\rho W S Z_1} \right) \\ = \frac{2U^2}{W^2} - \frac{U}{W} \int_0^S \int_0^{Z_2} \frac{V_{\theta 2}}{W} \frac{W^2}{W} \cos \beta_2 \frac{dz ds}{Z_1 S} \quad (9)$$

3 Cascade Geometry and Apparatus

A linear cascade of seven 186 mm span, 186 mm chord blades with the same profile and spacing as used by Bindon (1989) was used. As shown in Fig. 2, three tip shapes were used, a flat sharp-edged reference blade that corresponded with the previous study and two rounded tip designs to minimize the size and formation of the separation bubble in the gap. The first rounded tip has a rounded pressure side edge with a radius of 2.5 gap widths as found by Morphis and Bindon (1988) to avoid bubble formation. The second tip is intended to deflect flow radially into the gap so as to reduce the gapwise component and hence the leakage mass flow. The contours used to turn the flow radially are generously curved to control the bubble formation. All results are for a gap size of 2.5 percent chord. In all the results the cascade exit Reynolds number was 470,000.

A five-hole probe survey was done in the cascade exit plane using a combination of two separate traverses. The first traverse was done with a 1.5 mm × 0.5 mm three-hole cobra probe with the stem shaped in a tight gooseneck. This allowed access to the flow through holes in the tunnel wall and allowed the main pitchwise flow direction to be determined by null yawing without probe tip movement. The second traverse was done with a 1.8 mm × 0.9 mm two-hole probe that was manually yawed in the main pitchwise flow direction as determined by the first traverse. The two holes were oriented in the radial direction to provide the radial flow components.

Table 1 Tip region performance criteria for various tip clearance geometries (clearance = 2.5 percent chord)

Schematic of Geometry					
Rotor eff ts	η_{ts}	97.70	76.90	74.09	80.68
Rotor eff tt	η_{tt}	98.38	87.81	86.56	88.82
Loss coefficient	C_L	0.152	0.874	0.964	0.843
Internal gap loss	C_g	-	0.270	0.061	0.062
Mixing loss	C_m	0.152	0.452	0.751	0.629
Gap exit normal ke		-	0.684	0.926	0.869
Work Coef	C_w	9.225	7.869	6.212	6.700
Exit Height	Z_2	1.046	1.123	1.112	1.179
Gap Mass Flow Coef	C_F	-	0.240	0.287	0.256
Gap discharge Coef	C_D	-	0.824	0.926	0.920
Vel Coef	$(\bar{V}_2/W)^2$	1.194	1.862	1.994	1.600

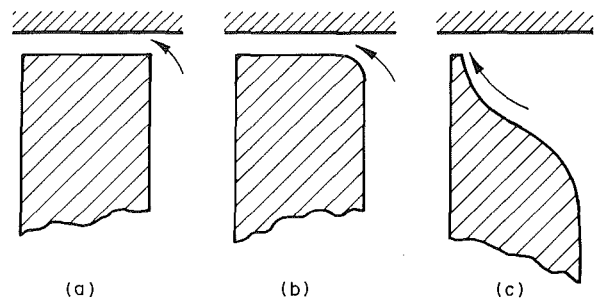


Fig. 2 Schematic of the three blade tip shapes tested: (a) square tip with sharp pressure edge; (b) flat tip with radiused pressure edge; (c) contoured tip radiused to create radial leakage flow

As described by Bindon (1989), the total secondary flow and leakage mixing loss is found by subtracting the loss occurring within the clearance gap from the total loss measured in the cascade exit plane. The internal gap loss was found from 10 endwall traverses of the gap exit flow with the gooseneck probe located exactly in line with the suction surface. For the two flat-tipped gap geometries there will be no radial components. For the contoured tip specifically chosen to create radial flow, the regime was too narrow to use the second probe. Fortunately the resulting inaccuracy is not serious since the cobra probe alone would tend to overestimate the total pressure loss and, as will be discussed later, the loss was found to be relatively low.

4 Experimental Results

Table 1 presents the experimental results for the three tip geometries as well as for the zero clearance case necessary for comparison and to provide some data to determine the mixing loss. Some quantities in the table are defined in Section 2. All the results were computed for an inlet to blade speed ratio W/U of 1/2.

5 Internal Gap Loss and Leakage Mixing Loss

The losses formed within the gap have been shown to be an important part of the overall loss in a cascade with tip clearance. As with any other loss measurement, the gap loss should be determined from traverses at inlet and outlet. However, the flow at the gap inlet has intense directional changes within the space of a few millimeters and is difficult to traverse.

Since the inlet loss is largely contained in the boundary layer against the endwall, the contoured blade tip geometry presents the possibility of determining both the gap inlet and gap exit loss from a single traverse at gap exit. All of these traverses showed a virtually loss-free core flow, which separates the inlet loss against the endwall and the loss in the boundary layer against the blade. The loss on the endwall does not have a

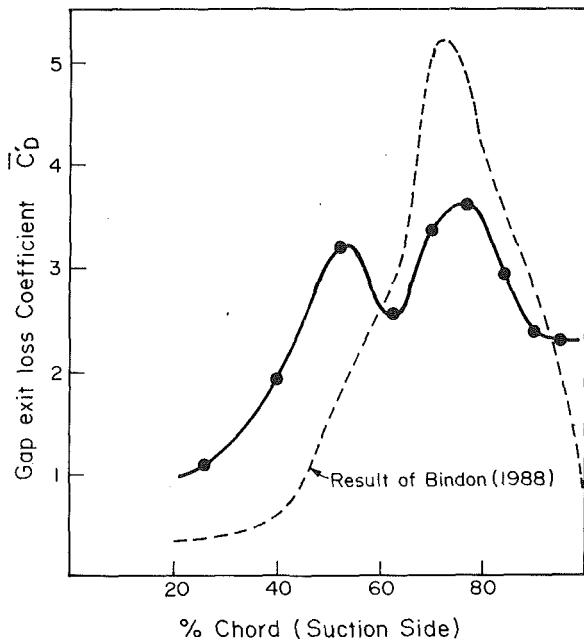


Fig. 3 Distribution of internal clearance gap loss with chord; square sharp-edged blade with clearance of 2.5 percent chord

chance to grow because the flow path length is short and the pressure gradient accelerating. Since the gap inlet loss is due to the cascade inlet boundary layer and endwall shear flow being drawn into the gap, the variation of this ingested loss quantity between the three tip geometries should not be large and the value measured for the contoured blade (0.037) was assumed to apply to the other two tip shapes.

The internal gap loss coefficients are also presented in Table 1 above and figures for the radiused blade and for the contoured tip are only 22 percent of that for the sharp-edged square tip, thus confirming that the separation bubble is largely responsible for the formation of internal gap loss and can be significantly reduced by suitable contouring.

Figure 3 shows the variation of gap loss with chord for the sharp-edged blade. The shape of the curve is very different from that presented by Bindon (1989) for the same blade profile and tip region geometry. A peak had previously been seen at midchord. The total integrated loss for the gap flow is lower at 31 percent of total as compared to the previously measured 38 percent. This difference in the distribution of loss between the leading and trailing edges for the same blade shape but made in different laboratories and tested in different wind tunnels would indicate that the microflow phenomena measured in tip gaps are highly sensitive and not easily reproduced, and the applicability to completely different profiles is doubtful.

The sharp peak previously seen in the gap loss distribution had been linked with the flow within the bubble accumulating near midchord where the static pressure was a minimum. The loss peak was thought to result from the high-velocity leakage jet mixing with the bubble fluid. The absence of such a peak in the present study suggests that there is a more even mixing of the bubble fluid across the length of the blade chord. Despite the lower internal gap loss measured in the present study, the overall cascade loss was the same as that previously measured.

As in Bindon (1989), the mixing loss is calculated by subtracting the internal gap loss and the endwall shear flow and secondary loss from the overall cascade loss. It is assumed that the normal secondary flow loss is that found for the zero clearance case. The results appear in Table 1. The figure of 0.451 for the flat sharp-edged reference blade compares favorably with that of 0.4 measured previously.

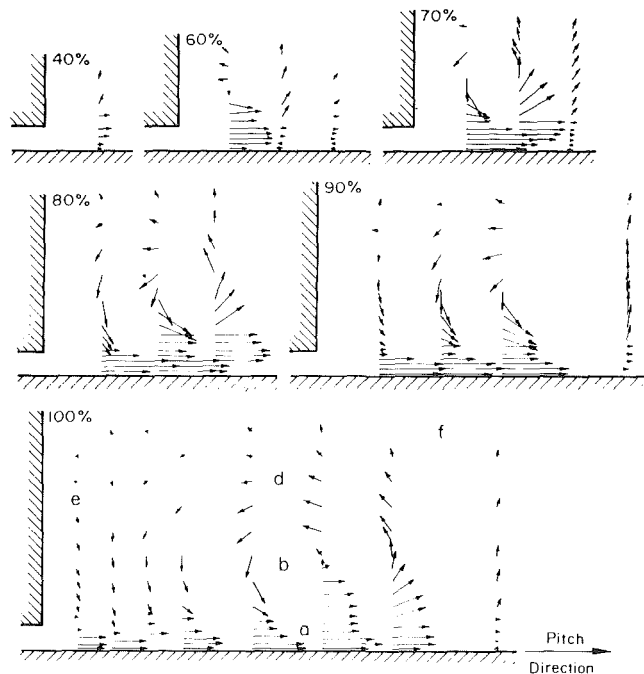


Fig. 4 The development of the leakage vortex at various axial chord positions for square sharp-edged tip

The highest value is for the radiused edge and the lowest for the square tip. The hypothesis suggested by Bindon (1989) that the mixing loss could possibly be due to the separation of the high loss wake within the leakage flow leaving the gap is not corroborated because in both cases where the separation bubble has been eliminated, the mixing loss is significantly higher. The fact that the peak in the gap exit flow for the flat-tipped blade is no longer present cannot explain the failure to validate the hypothesis. The flat-tipped blade still has the lowest mixing loss and is virtually the same as when the peak was present.

It had been hoped to extend the measurements to cover the detailed flow on the endwall for each tip geometry before attempting to review the hypothesis or to attempt an explanation of why it was not validated. In the absence of these results it would appear that the interaction of the leakage jet with the main flow is much more complex than originally suggested and clearly a great deal more research is required in order to arrive at the reasons for any performance changes realized. The rapid growth of mixing loss over the last 20 percent of chord needs urgent explanation.

The mixing loss is also not simply a function of the leakage mass flow or of the gap discharge coefficient. Dishart and Moore (1990) found that the mixing loss was almost identical to the difference between the normal kinetic energy leaving the clearance gap and the secondary kinetic energy at cascade exit for a sharp-edged square-tipped blade. In each of the present cases the mixing loss was slightly lower than this kinetic energy difference, 78 percent for the square blade, 97 percent for the radiused blade, and 80 percent for the contoured blade.

6 Exit Plane and Endwall Traverses

The gradual development of the leakage vortex on the endwall from the 40 percent axial station where it is very small and close to the suction surface to the exit plane (100 percent axial) is shown in Fig. 4 for the square tip. At all stations the leakage jet clings to the endwall and lifts off suddenly to roll into the vortex. Between the 80 and 90 percent stations, the distance of the center of the vortex from the suction surface almost doubles.

The vortex pattern in the exit plane for the contoured clear-

ance gap shape is presented in Fig. 5. The vortex center is farther away from the blade and the secondary kinetic energy is the lowest of all three tip shapes, which could partly contribute to the improved performance.

7 Simulated Rotor Performance

When the total to static performances of the two new radiused tip shapes are compared with the original datum flat-tipped sharp-edged blade, the efficiency resulting from the simulated rotor analysis is 4.9 percent higher for the contoured tip and 3.7 percent lower for the blade with the simply radiused edge. Since the improvement with the contoured tip relates to the flow through a blade height of 1/4 chord, the improvement for a short blade of aspect ratio 1 would be approximately 1.2 percent and for a long blade with an aspect ratio of 2 it would be in the region of 0.6 percent.

The total-to-total efficiency is surprisingly different. The contoured tip has only a 1.2 percent improvement while the radiused edge is only 1.4 percent down. The reason for this is the significant difference in leaving kinetic energy (\bar{V}_2) for the two shapes, a factor that does not affect the total-to-total result.

While these results may be of some importance to designers of small machines, which tend to have low-aspect-ratio blades ground sharply square at the tip for minimum clearance, of greater importance is that cascade data have been used to compare one rotor tip gap geometry with another. A wide range of geometries pertinent to the type of turbine built can thus be compared before final testing and selection.

The relative rank in performance is also shown by the total pressure loss coefficient. Although it is logical, it is difficult to prove that the simulated rotor efficiency analysis method is a more reliable quantity. Rotor flows may well exist where pressure loss and efficiency show a contradictory performance rank of one geometry with respect to another.

Another significant result is that all three leakage flows have a much higher absolute outlet velocity than does the zero clear-

ance case. To show this and to highlight the distortion caused to the exit velocity triangles by leakage and total pressure loss, Fig. 6 presents diagrams at various points in the flow field for the square-tipped blade and Fig. 7 the averaged or mean result for each tip shape. The mean flow field diagrams show that tip clearance increases the axial velocity and decreases the deflection when compared to the zero clearance case, which adversely affects work transfer and leaving loss. The most interesting vector plots are those in the vortex region. In the center of the vortex where there is high loss, Fig. 6(b) shows that despite the high loss the "relative" velocity W_2 is as high as in the free stream due to the low static pressure in the middle of the rotating flow field. The work transfer is still good, as reflected by the small exit swirl. At the top of the vortex (Fig. 6d) there is an even better work transfer and swirl. At the bottom of the vortex (Fig. 6a), which is in reality the low loss leakage jet flowing near the endwall, the swirl velocity is very large, as is the axial velocity, both factors contributing to this segment of the flow field having a poor performance. Near the trailing edge wake (Fig. 6e), the total pressure loss has reduced the "relative" velocity W_2 and the swirl is therefore high with a low work content.

The results in Table 1 are for W/U ratio of 0.5. Figure 8 shows the results over a range of blade speed ratios. The effect upon the total-to-static efficiency is minimal but the total-to-total efficiency increases with increasing blade speed. It would seem that at the higher blade speed, more work is extracted from the flow but at the penalty of an increased leaving loss, the latter fact not being reflected in the total-to-total concept.

8 Conclusions

It was shown that radiusing and contouring the leakage gap geometry to prevent the formation of the separation bubble significantly reduced the internal gap loss, which had been shown to form from 35 to 38 percent of the overall cascade total pressure deficit.

The relationship between the bubble and the leakage mixing loss was not established. The two geometries that avoided bubble formation both showed a higher mixing loss. However, the leakage jet entering the flow did not show the high loss concentration that had previously been associated with the separation bubble.

A method whereby detailed stationary cascade flow field data can be converted into a simulated rotor flow to calculate work transfer and efficiency was presented and its use demonstrated by comparing the endwall region performance of the tip clearance geometries tested. The contoured tip with a loss-free gap flow and reduced leakage rate by radial deflection of the jet showed a better performance than the datum sharp-

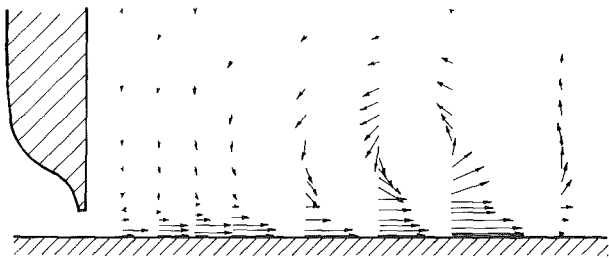


Fig. 5 The exit plane (100 percent chord) leakage vortex for the contoured clearance gap

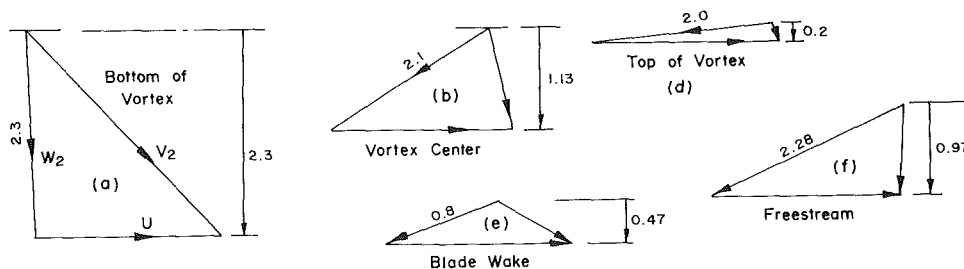


Fig. 6 Velocity triangles at various points marked in the exit plane flow field in Fig. 4 of the square sharp-edged blade showing the influence of flow phenomena on exit swirl and local work transfer

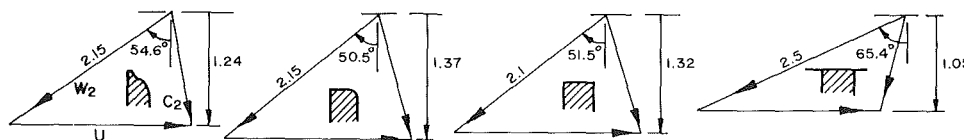


Fig. 7 Mean flow field outlet velocity triangles for zero clearance and for the three tip gap shapes

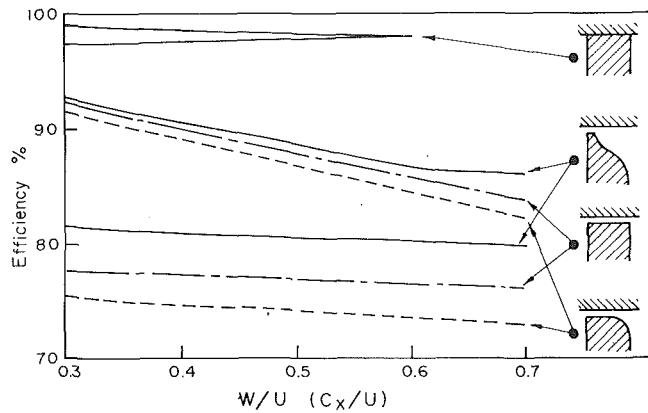


Fig. 8 Total-to-total efficiency (upper curves); total-to-static efficiency (lower curves); over a range of blade speed W/U (C_x/U) ratios

edged square tip despite having almost the same overall loss coefficient. These results show the usefulness of the method and point the way toward using stationary cascades to develop tip geometries for better performance.

The improved tip geometry realized in this paper was primarily studied in order to reveal fundamental flow phenomena changes. In practice the increase in efficiency would be applicable only to sharply ground flat-tipped blades and would depend on the length of the blade and on what type of efficiency

is quoted. Nevertheless, the fact that the internal gap loss has been greatly reduced and the fact an improved performance was achieved is regarded as encouraging.

The results of this paper seem to indicate that tip clearance flow and loss are very sensitive to geometry and flow conditions. The internal gap loss measured for the square-edged blade was not the same as previously measured and the high loss wake in the gap exit flow was not reproduced. Further study is warranted to test new shapes for loss reduction and for the purpose of understanding the factors involved in determining rotor efficiency.

References

- Bindon, J. P., 1987, "The Measurement of Tip Clearance Flow Structure on the Endwall and Within the Clearance Gap of an Axial Turbine Cascade," *Proc. I. Mech. E. Int. Conference Turbomachinery—Efficiency Prediction and Improvement*, Cambridge, Paper No. C273/87.
- Bindon, J. P., 1989, "The Measurement and Formation of Tip Clearance Loss," *ASME JOURNAL OF TURBOMACHINERY*, Vol. 111, p. 257.
- Booth, T. C., Dodge, P. R., and Hepworth, H. K., 1982, "Rotor Tip Leakage: Part 1—Basic Methodology," *ASME Journal of Engineering for Power*, Vol. 104, p. 154.
- Dishart, P. T., and Moore, J., 1990, "Tip Leakage Losses in a Linear Turbine Cascade" *ASME JOURNAL OF TURBOMACHINERY*, Vol. 112, pp. 599–608.
- Morphis, G., and Bindon, J. P., 1988, "The Effects of Relative Motion, Blade Edge Radius and Gap Size on the Blade Tip Pressure Distribution in an Annular Turbine With Tip Clearance," *ASME Paper No. 88-GT-256*.
- Offenberg, L., Fischer, J., and Vander Hoek, T., 1987, "An Experimental Investigation of Turbine Case Treatments," presented at the 23rd AIAA/SAE/ASME/ASEE Joint Propulsion Conference, San Diego, CA, June 29.

M. I. Yaras
Graduate Research Assistant.

S. A. Sjolander
Associate Professor.
Assoc. Mem. ASME

Department of Mechanical and Aerospace
Engineering,
Carleton University,
Ottawa, Ontario, Canada K1S 5B6

Prediction of Tip-Leakage Losses in Axial Turbines

Existing methods for predicting the tip-leakage losses in turbomachinery are based on a variety of assumptions, many of which have not been fully verified experimentally. Recently, several detailed experimental studies in turbine cascades have helped to clarify the physics of the flow and provide data on the evolution of the losses. The paper examines the assumptions underlying the prediction methods in the light of these data. An improved model for the losses is developed, using one of the existing models as the starting point.

Introduction

Beginning with the work of Betz (1926), various correlations and models have been suggested for predicting the effects of tip leakage on the performance of axial turbomachinery. However, until recently detailed data for the tip leakage flow were not available and the physics of the flow was not fully understood. As a result, the prediction methods were often based on assumptions that had not been verified experimentally. Recently, several detailed studies in turbine cascades have provided a much better understanding of this complex flow. These studies included measurements inside the tip gap as well as downstream of the trailing edge, thus allowing the development of the losses to be traced in some detail. Not all aspects of the flow have been clarified. For example, the effect of the inlet boundary layer thickness needs further investigation. Nevertheless, a critical assessment is now possible of a number of major assumptions used in the prediction methods.

In most earlier experimental studies, the tip leakage losses were estimated from measurements made downstream of the trailing edge only. For example, the flow downstream of compressor rotors has been studied extensively by Inoue and his co-workers (e.g., Inoue and Kuroamaru, 1984, 1989; Inoue et al., 1986) and by Lakshminarayana and his co-workers (e.g., Lakshminarayana et al., 1987). Schmidt et al. (1987a, 1987b) investigated the effect of leakage on the spanwise loss distribution in an isolated compressor rotor and similar measurements were made by Patel (1980) for an axial-turbine rotor. Patel also examined the effects of blade tip treatment. More recently, Yamamoto (1988, 1989) has investigated the tip leakage flow downstream of a linear turbine cascade. While such studies provide useful data and insights into some of the effects that influence the tip-leakage losses, they give a somewhat incomplete picture.

The three recent studies in, turbine cascades by Bindon (1989), Dishart and Moore (1990), and Yaras and Sjolander (1989) provide a considerably more detailed picture. Bindon examined three clearances in a linear cascade of turbine blades, although detailed data were obtained only for a clearance of

2.5 percent of the blade chord. Measurements were made in the tip gap and at the trailing edge plane. Bindon concluded that of the tip leakage losses generated up to the trailing edge, about 40 percent occurred within the gap, due mainly to the separation bubbles formed on the blade tip. In addition, he indicates that the fluid of low total pressure, which is discharged into the passage from the separation bubbles, contributes significantly to the mixing losses after the flow leaves the gap. He thus attaches great importance to the separation bubbles on the blade tip. Dishart and Moore (1990) investigated the tip-leakage losses in a linear turbine cascade with a clearance of 2.1 percent of axial chord. They measured the flow at the gap outlet and at 40 percent axial chord downstream of the trailing edge. The authors also calculated the fully mixed-out losses. They found that the losses measured at the gap exit represented only about 17 percent of the total mixed-out losses. They also found that nearly 90 percent of the final losses had occurred by the downstream measurement plane. Thus Dishart and Moore's results imply that the losses inside the gap play a smaller role in the overall losses than was concluded by Bindon. The most detailed data currently available were presented recently by Yaras and Sjolander (1989). The authors examined four clearances from 1.5 to 5.5 percent of the blade chord. Very detailed results were obtained for clearances of 2.0 and 5.5 percent: inside the clearance gap, at the trailing-edge plane, and at one axial chord length downstream. The tip-leakage loss models are evaluated primarily on the basis of these data. Therefore, the main results and conclusions are summarized in a later section.

It thus appears that, based on the available experimental studies, it should now be possible to develop a tip-leakage loss model that is reasonably consistent with the physics of the flow. The present paper reviews the commonly used tip-leakage loss models and examines the validity of the physical assumptions that underlie them. The examination is confined to models that produce total pressure loss coefficients. A number of methods have also been developed for predicting the change in stage efficiency with tip clearance. Some of these are primarily correlations of available data, with some physical reasoning being applied to choose the correlating parameters (e.g., Hesselgreaves, 1969; Amann et al., 1963; Moyle, 1990). Others incorporate some degree of flow modeling (e.g., Senoo and

Contributed by the International Gas Turbine Institute and presented at the 35th International Gas Turbine and Aeroengine Congress and Exposition, Brussels, Belgium, June 11-14, 1990. Manuscript received by the International Gas Turbine Institute February 7, 1990. Paper No. 90-GT-154.

Ishida, 1986; Farokhi, 1988). However, models that predict the total pressure losses seem preferable since they deal with flow quantities that are directly measurable. They are thus inherently more closely linked to the physics of the flow. They also have the advantage of direct compatibility with the form in which the other losses through the blade row, such as profile and secondary losses, are usually handled.

An improved model for the tip-leakage losses is developed using one of the existing models as the starting point.

Review of Existing Tip-Leakage Loss Models

Experimental Background. The loss models will be evaluated primarily by comparison with the present authors' own data for the tip-leakage flow field in a planar cascade of turbine blades (Yaras and Sjolander, 1989, 1990; Yaras et al., 1989). This flow is idealized in a number of respects. The results were obtained at realistic Reynolds numbers but under essentially incompressible conditions and for a free stream with a low level of turbulence intensity. There was also no relative motion between the tip wall and the tip of the blade. Nevertheless, the cascade flow has many of the essential features of the tip leakage flow in the actual machine. In any case, there is a long-standing and successful tradition of using turbomachinery performance correlations and models which are based at least partly on cascade results. For reference, the main results obtained from the Yaras-Sjolander measurements are summarized here.

It is conventional to divide the losses in turbomachinery blade rows into several components. It is usually assumed that these can be evaluated independently and then combined linearly to obtain the total loss. Thus, for a blade row with clearance the overall loss coefficient might be written:

$$Y = Y_p + Y_{sec} + Y_{tip}, \quad (1)$$

where Y_p is the blade profile loss, Y_{sec} is the loss due to the secondary or endwall boundary layer flow, and Y_{tip} is the tip-leakage loss. The secondary loss is obtained at zero clearance and the value is generally assumed to remain unchanged as the clearance gap is opened. The tip clearance loss is then taken as the loss that must be added to the secondary loss to obtain the total observed loss in the blade end region. This simple, pragmatic decomposition is widely recognized as rather unsatisfactory physically (e.g., Vavra, 1960; Dunham and Came, 1970).

For the Yaras-Sjolander cascade, the blade wake was identifiable over the entire span. Thus, it was relatively easy to distinguish and separate the profile losses from the other components of the loss. On the other hand, it was clear that there was a strong interaction between the tip-leakage and endwall boundary layer aspects of the flow. It was evident that a substantial fraction of the original endwall boundary layer fluid passed through the tip gap and became an indistinguishable part of the tip-leakage flow. The remaining endwall boundary layer fluid was swept across the passage and rolled up into a passage vortex in the usual way. However, the vortex was far smaller than the secondary vortex that formed at zero clearance. Likewise, the losses associated with this identifiable "secondary flow" were much smaller.

The alternative breakdown of the losses that emerges from the Yaras-Sjolander study is shown schematically in Fig. 1. The pattern corresponds roughly to the fully mixed-out losses. It was found that the losses increased substantially downstream of the trailing edge but that most of the additional loss production occurred over about the first axial chord length.

The losses inside the gap itself were found to be a relatively small fraction of the total losses. The secondary loss is now taken as the loss that can be clearly assigned to a secondary flow structure, namely the passage vortex. As shown in Fig. 1, this component of the loss fell off very quickly with clearance; even at 2 percent clearance, it accounted for an insignificant fraction compared with the loss in the tip-leakage flow. However, this may not be a general result. The Yaras-Sjolander cascade had a thin endwall boundary layer at the inlet and a relatively low turning of about 45 deg. The secondary flow is therefore comparatively weak. More data are needed on the effects of inlet boundary thickness. Rotation may also have some influence since, in a turbine blade row, the scraping effect would tend to enhance the passage vortex.

The remaining loss, which is identifiably associated with the tip-leakage flow, was referred to as "end loss" by Yaras and Sjolander (1989b). This was to avoid confusion with the common usage of the term "tip-leakage loss." However, as indicated in Fig. 1, the latter term is being readopted since it is more descriptive. The end loss is then taken as the total loss that occurs in the endwall region, apart from the profile loss. In the Yaras-Sjolander experiment, the non-gap end loss (that is, the loss in the endwall region apart from the loss inside the gap itself) was made up almost entirely of tip-leakage loss.

Nomenclature

c = blade chord length	h = blade span	
C = empirical constant relating local gap loss coefficient to clearance size (see Eq. (19))	k_s = fraction of zero-clearance secondary loss still present with clearance (Eq. (16))	x' = coordinate in chordwise direction
C_D = discharge coefficient for tip gap	K = retained lift coefficient (Eq. (4))	Y = mass-averaged total pressure loss coefficient based on outlet dynamic pressure
C_L = lift coefficient	K_E, K_G = constants related to the blade loading distribution (Eqs. (12), (18))	Y' = loss coefficient averaged over local mass flow rate (e.g., in the gap)
$C_p = (P - P_1) / \frac{1}{2} \rho V_1^2$ = static pressure coefficient	\dot{m}_g = mass flow rate through tip gap	α = flow angle, relative to axial direction
C_{p_o}'' = mass-averaged total pressure loss coefficient based on inlet dynamic pressure	\dot{m}_p = mass flow rate for the blade passage	δ = boundary layer thickness
C_{q_s}'' = mass-averaged coefficient of secondary kinetic energy for downstream flow	P = static pressure	ρ = density
C_{q_n}'' = mass-averaged coefficient of gap kinetic energy normal to chord line	P_{PS} = blade pressure-side pressure	σ = blade row solidity = c/S
d = diameter of tip leakage vortex	P_{SS} = blade suction-side pressure	τ = tip gap height
E = kinetic energy	S = blade spacing	
	t_{MAX} = blade maximum thickness	Subscripts
	V = velocity	1, 2 = inlet, outlet
	V_N = component of gap velocity normal to chord line	m = mean value through blade row
		p = profile or passage

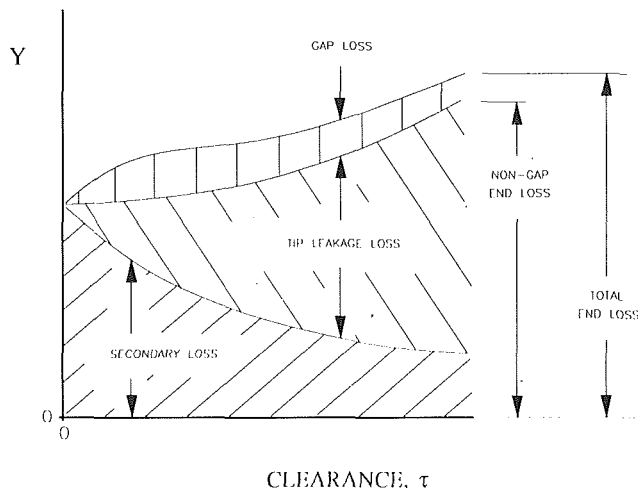


Fig. 1 Schematic breakdown of the losses in the end region (excluding profile losses)

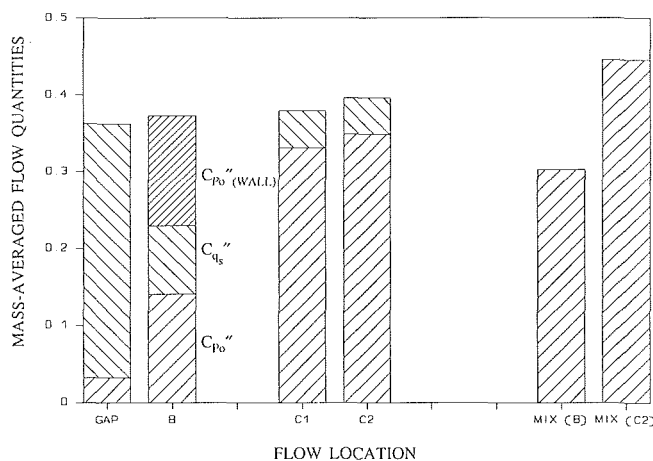


Fig. 2 Downstream development of losses and secondary kinetic energies for $\tau/c = 0.055$ (from Yaras and Sjolander, 1989)

The loss processes contributing to the tip-leakage loss can be summarized in terms of Fig. 2 (taken from Yaras and Sjolander, 1989b). The stacked bars show the total pressure losses and secondary kinetic energies measured at several locations for a clearance of 5.5 percent of the blade chord. Plane B is at the trailing edge and planes C1 and C2 are two closely spaced planes one axial chord length downstream. The fully mixed-out losses calculated from the data at planes B and C2 are also shown. For the gap flow, the "secondary" kinetic energy is in fact that corresponding to the component of gap velocity normal to the blade chord. For the downstream locations it is that associated with the components of velocity in the plane normal to the downstream mean velocity. All quantities are averaged over the mass flow rate through one passage and over half the blade span.

The clearance flow was discharged from the gap with a large amount of kinetic energy normal to the gap exit. Much of this gap kinetic energy was found to have been recovered by the time the flow reached the trailing edge. Evidently, the gap discharge did not act as a simple sudden expansion. Instead, the relatively orderly roll-up of the tip leakage vortex apparently allows a significant recovery of static pressure. The losses then increased substantially over the first axial chord downstream of the trailing edge. At that point the loss generation seemed to be largely complete. Interestingly, it was found that the end loss observed at the downstream plane agreed well with the sum of the losses within the gap itself together with a loss equal to the kinetic energy in the flow at the gap outlet.

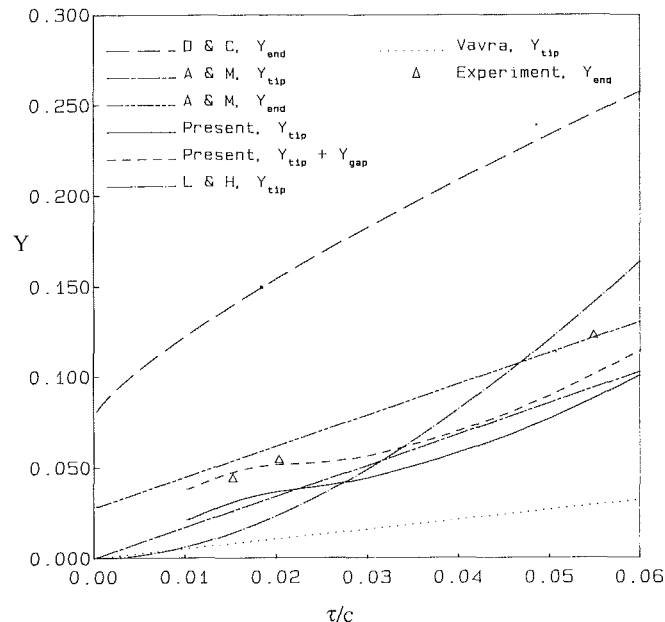


Fig. 3 Comparison between tip-leakage loss models and measurements (D & C: Dunham and Came, 1970; A&M: Ainley and Mathieson, 1951; L & H: Lakshminarayana and Horlock, 1965)

This was true at both the clearances for which detailed data were obtained. The gap energy, which was initially recovered, was thus ultimately lost. The loss appeared to occur through two main mechanisms. The energy was partly recovered as secondary kinetic energy of the tip-leakage vortex. This energy was eventually lost as the vortex mixed with the surrounding free-stream fluid. Secondly, the presence of the tip-leakage vortex seemed to lead to higher shear stresses at the endwall and therefore to higher entropy production there. It was tentatively concluded that the loss production at the endwall, over the axial chord length of downstream distance, was in fact substantial. This conclusion was based on the indirect evidence of the very different values of mixed-out loss obtained at planes B and C, as shown at the right of the bar chart. The most obvious loss mechanism not taken into account by the mixing calculations is the viscous loss production on the endwall. It is seen that when the difference in the mixed-out losses (marked $C_{p0}''(WALL)$ on the figure) is added to the loss observed at B, the trailing edge plane, it agrees well with the final loss obtained at plane C, one chord length downstream.

Finally, the nature of the tip-leakage vorticity field needs to be mentioned. A number of loss models calculate the tip leakage losses in terms of the "induced drag" of the blade. They therefore make assumptions about the strength of the trailing vortex system. The vorticity aspects of the present flow were examined by Yaras and Sjolander (1990). It was found that, unlike the case of a finite wing, the circulation of the tip leakage vortex is considerably less than the bound circulation of the blade, and varies with clearance. The physics of this odd result is not fully understood. However, a number of other researchers have come to the same conclusion: for example, Lakshminarayana and Horlock (1965), Lewis and Yeung (1977) and Inoue et al., (1986). The data of Inoue et al. show the value of the shed circulation also depends on the relative wall speed.

The tip-leakage loss models are then examined in the light of these experimental observations. The losses predicted by most of the models are compared with the results of the Yaras-Sjolander experiment in Fig. 3.

The models can be divided into two broad categories: those that arrive at the losses indirectly as a result of a momentum balance, and those that consider energy directly.

Models Based on Momentum Considerations. This group

of models determines the effect of the tip-leakage flow initially in the form of a drag force on the blade. The drag force is generally seen as the equivalent of the induced drag of a finite wing. To convert the resulting momentum deficiency into a total pressure loss, it is necessary to assume that the loss is distributed uniformly over the mass flow. Thus, these models implicitly predict the fully mixed-out value of the losses. This is something of a practical disadvantage. The measurements show that fully mixed-out conditions are approached about one axial chord length or further downstream. The momentum-based models will therefore overestimate the losses at the inlet to a downstream blade row that is closely spaced.

Betz (1926) appears to have been the first to model some aspects of the tip-leakage flow. The author calculated the induced drag due to the vortices shed at the trailing edge of the blade. The strength of the shed vorticity was obtained from the gradient of the bound circulation distribution, with the assumption that the bound circulation went to zero at the blade tip. However, as noted earlier, there is considerable experimental evidence that the circulation in the tip-leakage vortex is less than the bound circulation and varies with both clearance and rotation.

The well-known and widely used Ainley and Mathieson (1951) model takes much the same approach. Their tip-leakage model was in fact adapted from an earlier theory for secondary flows developed by Carter (1948). Carter had determined the incidence induced by the secondary flow based on conventional theory for the downwash at a finite wing. Both Carter and Ainley and Mathieson again assumed that the full bound circulation would appear in the trailing vortex system. The resultant expression given by Ainley and Mathieson is as follows:

$$Y_{\text{tip}} = \frac{\cos^2(\alpha_2)}{\cos^3(\alpha_m)} \frac{1}{s/c} 0.5 \left(\frac{\tau}{s}\right) \frac{c_L^2}{h/c} \quad (2)$$

Figure 3 shows the loss variation predicted by this model for the Yaras-Sjolander cascade geometry. The figure also shows that when Ainley and Mathieson's secondary loss is added to their tip-leakage loss, the agreement with the measured end loss is quite reasonable. However, this agreement is probably fortuitous since the simple decomposition of the losses, which is assumed by the Ainley and Mathieson approach, is not supported by the Yaras-Sjolander measurements.

Dunham and Came (1970) modified Ainley and Mathieson's model in the light of some later cascade data, which suggested a nonlinear variation of the tip-leakage losses with clearance size. The resultant expression is as follows:

$$Y_{\text{tip}} = \frac{\cos^2(\alpha_2)}{\cos^3(\alpha_m)} \frac{1}{(s/c)^2} 0.47 \left(\frac{\tau}{c}\right)^{0.78} \frac{c_L^2}{(h/c)} \quad (3)$$

However, as seen from Fig. 3, this model substantially overestimates the losses. This behavior was also noted by Kacker and Okapuu (1982).

In their scheme for predicting the tip-leakage losses in compressors, Lakshminarayana and Horlock (1965) followed a procedure somewhat similar to that of Ainley and Mathieson. They simulated the tip leakage vortex with a Rankine vortex and determined the drag induced on the blade by this vortex. The vortex was modeled in considerable detail, taking into account its location and alignment relative to the blade, its initiation point, and the estimated radius of the core. Furthermore, the authors had noted the lower value of the circulation for the tip-leakage vortex compared with the bound circulation and therefore took this into account. The expression for the tip-leakage loss is then:

$$Y_{\text{tip}} = \frac{\cos^2(\alpha_2)}{\cos^3(\alpha_m)} \frac{1}{(s/c)} \frac{c_L^2(1-K)}{8\pi(h/c)} (A-B), \quad (4)$$

where

$$A = \ln \left(\frac{e^{2\pi h/s} - 1}{\left(1 + \coth\left(\frac{2\pi\tau}{s}\right)\right) (e^{2\pi h/s} - 1) + 2} \right),$$

$$B = \ln \left(\frac{e^{\pi d/s} - 1}{\left(1 + \coth\left(\frac{2\pi\tau}{s}\right)\right) (e^{\pi d/s} - 1) + 2} \right),$$

and $(1-K)$ is the fraction of the bound circulation shed in the tip-leakage vortex. The model was found to be quite sensitive to the assumed diameter, d , of the vortex. Figure 3 shows that the trend in the losses predicted by the model is not in good agreement with the turbine cascade measurements. Quantitative comparison requires that a secondary loss component be added to the prediction. If, for example, the Ainley and Mathieson secondary loss were used, the predicted end loss would clearly be much higher than the measured. In a modified version of the model (Lakshminarayana, 1970), the losses associated with the spanwise flow in the blade surface boundary layer were taken into account; the change in the predicted loss was quite small.

Models that predict the losses based on an induced drag are essentially inviscid models. The viscous losses in the blade boundary layers are of course accounted for by the profile loss component, although as noted by Lakshminarayana (1970) the profile losses near the tip may be increased somewhat by the tip-leakage vortex. It could also be argued that the viscous losses on the endwall will be taken into account by the separate secondary loss model. However, the Yaras-Sjolander experiment suggested that there was enhanced viscous loss production on the endwall, downstream of the trailing edge, which was directly attributable to the leakage flow. This is thought to be due to the higher wall shear stresses that occur beneath the vigorous tip-leakage vortex. This indicates that an additional loss ought to be added to the purely inviscid loss component, which is derived from the induced drag analysis. However, Fig. 3 shows that most of the models already tend to overpredict the end losses. Therefore, addition of a viscous loss component, as suggested by the physics, would only make the agreement poorer.

Models Based on Energy Considerations. The alternative to the momentum-based models is to consider the mechanical energy changes directly.

In his influential study on the tip-leakage problem, Rains (1954) adopted this approach. Rains suggested that the tip-leakage fluid rolls up into a vortex whose energy cannot be recovered. In other words, the kinetic energy in the gap flow normal to the blade chord is assumed to be lost eventually and that this loss accounts for the whole of the tip-leakage loss. As discussed earlier, this simple idea is in fact supported by the Yaras-Sjolander cascade experiment. The key to the application of this idea is then a prediction of the mass flow rate through the gap and of the magnitude of the velocity component normal to the gap. Rains himself developed a somewhat involved analysis for the resulting efficiency drop in the stage. Subsequently, Vavra (1960) used the idea with some simplifications to arrive at the following loss coefficient:

$$Y_{\text{tip}} = \frac{\cos^2(\alpha_1)}{\cos^3(\alpha_m)} \frac{1}{s/c} \frac{4(2)^{0.5}}{5} k\omega^3 \frac{\tau}{h} c_L^{1.5}, \quad (5)$$

where ω accounts for the flow resistance in the gap and k is the contraction factor for the flow through the gap. It will be noticed that the energy approach leads to a weaker dependence on the blade loading than the momentum approach (Eqs. (2)-(4)). Hesselgreaves (1969) and Lewis and Yeung (1977) followed Vavra's approach but set ω and k to 1.0. As shown in Fig. 3,

Vavra's model would predict a much lower loss than was measured in the turbine cascade even if a plausible value of secondary loss were added to it. This would be the case particularly at higher clearances.

Since the underlying idea is physically sound, the problem with Vavra's model must lie in the prediction of the gap kinetic energy. In an earlier paper (Yaras et al., 1989), the present authors examined the gap flow in detail and devised a simple model that appears to predict the flow, including its kinetic energy, with good accuracy. These results are combined with some of the ideas from Vavra's model to arrive at an improved tip-leakage loss model.

Improved Tip-Leakage Loss Model

The kinetic energy associated with the component of the gap velocity normal to the blade chord can be written:

$$\Delta E = \int_{\dot{m}_g} 0.5 V_N^2 d\dot{m}_g \quad (6)$$

Yaras et al. (1989) showed that the leakage flow passed through the gap with little change in chordwise momentum. Therefore, the driving pressure difference experienced by the fluid went entirely to accelerate it normal to the chord line. Furthermore, most of the fluid experienced no loss as it passed through the gap. Thus, Bernoulli's equation can be applied to the acceleration process:

$$V_N = [2(P_{PS} - P_{SS})/\rho]^{(1/2)} \quad (7)$$

It is well known that the blade loading near the tip is highly distorted by the presence of the leakage flow (e.g., see Sjolander and Amrud, 1987). However, Yaras et al. found that this distorted pressure field did not extend very far into the tip gap. Toward the endwall, where most of the leakage mass flow occurs, the fluid experiences essentially the undistorted blade pressure difference; that is, the pressure difference that would occur on the blade tip profile in the absence of clearance. Thus, the chordwise distribution of pressure difference used in Eq. (7) is the blade loading at the tip, neglecting the effects of the clearance. This is comparatively easy to calculate. In Vavra's model the velocity given by Eq. (7) is multiplied by a flow resistance factor. This implies a loss of kinetic energy inside the gap, which is not supported by the measurements.

The mass flow rate through the gap can be expressed as

$$d\dot{m}_g = C_D \rho V_N \tau dx' \quad (8)$$

where C_D is a discharge coefficient. Vavra used a constant value of 0.5 for the discharge coefficient. The measurements of Yaras et al. (1989) gave somewhat larger values and indicated that C_D varied with the aspect ratio of the gap. The measured variation is shown in Fig. 4. The values shown on the figure are somewhat larger than those quoted by Yaras et al. The discharge coefficients in the earlier paper apply to mass flow rates calculated from the component of velocity normal to the blade mean line. The C_D was therefore recalculated to be consistent with the velocity component normal to the chord line, as used in the model. The variation in C_D with clearance shown in Fig. 4 reflects the observed size of the separation bubble, relative to the gap height, on the tip of the blade. The trend may be somewhat different for a different blade design. Therefore, it is probably more reasonable to use a mean value, of about 0.7 to 0.8, for the discharge coefficient. Dishart and Moore (1989) found an average value of about 0.7 for their experiment.

The expression for the gap kinetic energy then becomes

$$\Delta E = \left(\frac{2}{\rho}\right)^{0.5} C_D \tau \int_0^c (P_{PS} - P_{SS})^{1.5} dx' \quad (9)$$

For a design that is well advanced, so that the blade loading is known, Eq. (9) could be used to investigate the effect on

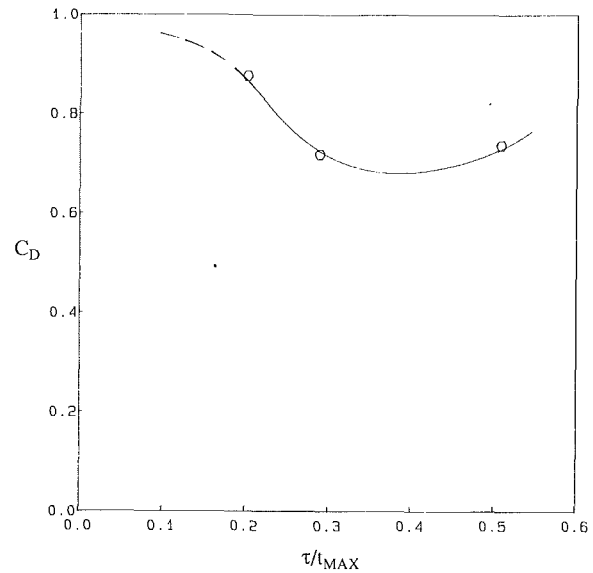


Fig. 4 Variation of gap discharge coefficient with clearance for Yaras-Sjolander Cascade

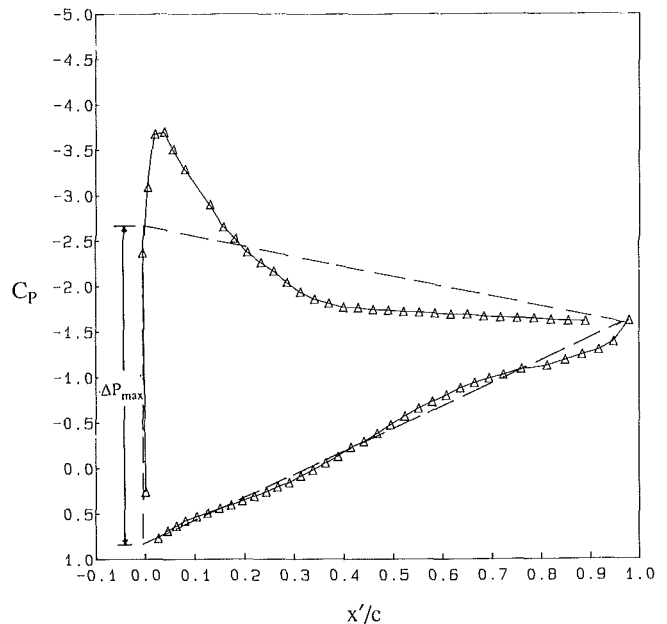


Fig. 5 Measured blade loading distribution and triangular approximation (Yaras-Sjolander cascade)

the tip-leakage losses of changes in the loading, such as at off-design conditions.

For use in the early stages of a design, an approximate loading distribution can be assumed. This was also done by Hesselgreaves (1969) in his version of the Vavra model. The simplest choice is a linear variation. The assumed variation can then reflect in broad terms the intended design philosophy for the blade; that is, whether it is expected to be front-, mid-, or aft-loaded. As shown in Fig. 5, a front-loaded, triangular distribution is a reasonable approximation for the Yaras-Sjolander blade:

$$P_{PS} - P_{SS} = \Delta P_{\max} \left(1 - \frac{x'}{c}\right) \quad (10)$$

The integral in Eq. (9) can then be evaluated for the assumed loading distribution. If it is also assumed that the lift force is roughly normal to the chord line, then

$$C_L = \frac{\int_0^c (P_{PS} - P_{SS}) dx'}{\frac{1}{2} \rho V_m^2 c}, \quad (11)$$

where V_m is the mean velocity through the blade row. Evaluating Eq. (11) with the assumed loading, the expression for the kinetic energy loss becomes

$$\Delta E = K_E \rho c C_D \tau V_m^3 C_L^{1.5}, \quad (12)$$

where $K_E = 0.566$ for a front- or aft-loaded blade,
 $= 0.5$ for a mid-loaded blade.

The loss is seen to be relatively insensitive to the loading distribution.

The loss coefficient Y , for a cascade flow where absolute and relative frame of references are the same, is defined as follows:

$$Y = \frac{\Delta E}{E} = \frac{\Delta E}{\dot{m}_p V_m^2 / 2}. \quad (13)$$

The passage kinetic energy, E , can also be written in terms of the mean velocity:

$$E = \frac{\rho h s}{2} \frac{V_m^3 \cos^3(\alpha_m)}{\cos^2(\alpha_2)}. \quad (14)$$

The tip-clearance loss coefficient then becomes,

$$Y_{\text{tip}} = 2K_E \sigma \frac{\tau}{h} C_D \frac{\cos^2(\alpha_2)}{\cos^3(\alpha_m)} C_L^{1.5}, \quad (15)$$

where $\sigma (= c/S)$ is the solidity of the blade row. Since for given flow turning C_L varies inversely with σ , Eq. (15) indicates that the tip-leakage loss will vary as $\sigma^{-0.5}$.

It is envisaged that Eq. (15) would be used in a loss system in which the total loss through the blade row is calculated from

$$Y = Y_p + (Y_{\text{sec}})_{\text{HUB}} + (Y_{\text{end}})_{\text{TIP}}, \quad (16)$$

where $(Y_{\text{end}})_{\text{TIP}} = Y_{\text{gap}} + k_s Y_{s,0} + Y_{\text{tip}}$ and $Y_{s,0}$ is the secondary loss coefficient at the tip for zero clearance. The factor k_s is the fraction of the secondary loss that remains identifiably associated with a secondary flow structure, principally the passage vortex. In loss systems such as that of Ainley and Mathieson, k_s is implicitly taken to be 1.0. However, as described earlier, k_s appeared to be much less than 1.0 for the Yaras-Sjolander cascade. In general, k_s might be expected to be a function of the inlet boundary layer thickness, perhaps as δ/τ , and also of the rotation. With the enhancement of the passage vortex by the scraping effect, it is conceivable that k_s could become larger than 1.0. More data are needed on these aspects.

The tip-leakage losses calculated from Eq. (15), using the measured values of C_D , are compared with the measured $(Y_{\text{end}})_{\text{TIP}}$ in Fig. 3. They are somewhat lower than the measured values, as would be expected since Y_{gap} and $Y_{s,0}$ are not included in the predictions.

As noted earlier, the gap loss contributes a relatively small amount to the overall end loss. Dishart and Moore (1990) came to the same conclusion. Nevertheless, it is not negligible and it is desirable to include it in the model for completeness. For the Yaras-Sjolander experiment, Y_{gap} was reasonably constant for clearances of 2.0 to 5.5 percent, the range for which gap measurements were made. The loss coefficient averaged over the gap mass flow rate, Y'_{gap} , decreased roughly in proportion to the increase in flow rate as the gap size increased. The relationship between the two loss coefficients is:

$$Y_{\text{gap}} = Y'_{\text{gap}} \frac{\dot{m}_g}{\dot{m}_p}. \quad (17)$$

Calculating the gap flow rate from Eq. (8) with the assumed

loading distributions and writing the passage mass flow rate as $\rho V_m \cos \alpha_m h S$, Eq. (17) becomes,

$$Y_{\text{gap}} = Y'_{\text{gap}} K_G \frac{\sigma C_D C_L^{1/2}}{\cos \alpha_m} \left(\frac{\tau}{h} \right), \quad (18)$$

where $K_G = 0.943$ for front- or aft-loaded blades,
 $= 1.0$ for mid-loaded blades.

The gap loss is seen to be even less sensitive than the tip-leakage loss to the distribution of the blade loading.

To a good approximation, the local gap loss coefficient varied as $C/(\tau/c)$, with $C \cong 0.007$. Equation (17) can then be written:

$$Y_{\text{gap}} = CK_G \frac{\sigma C_D C_L^{1/2}}{\cos \alpha_m} \left(\frac{c}{h} \right). \quad (19)$$

It should be noted that there is considerable uncertainty in the local gap loss coefficient, Y'_{gap} , since some of the loss detected in the gap originated in the upstream boundary layer. It was assumed that about one quarter of the inlet boundary layer passed through the gap and the corresponding loss was subtracted from the measured gap loss. However, the assumed fraction could not be verified experimentally. In view of this, the value of C should be treated as very approximate. Figure 3 shows the sum of the losses calculated from Eqs. (15) and (19). It is seen that inclusion of the gap loss improves the agreement with the measurements.

Conclusions

Existing methods for predicting the tip-leakage loss coefficient were reviewed in the light of several detailed studies conducted recently in turbine cascades. It was found that methods that assume the loss is primarily due to an induced drag, resulting from the trailing vortex system, did not give very satisfactory results. These methods neglect the additional viscous loss production on the endwall that results from the presence of the tip-leakage vortex. Some of the recent data suggest that this loss production may be significant. However, if the momentum-based methods were modified to include the viscous loss production, they would produce even poorer results.

Recent experiments suggest that the kinetic energy carried by the normal component of the gap velocity is ultimately lost. Furthermore, this appears to account for essentially all the tip-leakage loss downstream of the gap. This confirms a hypothesis originally advanced by Rains and subsequently used by Vavra as a basis for a tip-leakage loss model. However, Vavra made several other assumptions that are not supported by the recent data and that led to poor predictions for the gap kinetic energy.

Vavra's model was used as the starting point to derive an improved tip-leakage loss model that is consistent with the recent experimental observations. The model gave very satisfactory agreement with the limited available data. More data are needed to clarify the interaction between the tip-leakage and secondary flows and the influence of the scraping effect that occurs with relative wall motion.

Acknowledgments

Financial support for this study provided by the Natural Sciences and Engineering Research Council of Canada under Grant A1671 and by Pratt & Whitney Canada Inc. is gratefully acknowledged.

References

- Ainley, D. G., and Mathieson, G. C. R., 1951, "A Method of Performance Estimation for Axial-Flow Turbines," ARC R&M 2974.
- Amann, C. A., Dawson, D. W., and Yu Manson, K., 1963, "Consideration in the Design Development of Turbines for Automotive Gas Turbine Engines," SAE Paper 653, Jan.

- Betz, A., 1926, "Vorgaenge an den Schaufelenden von Kaplan-turbinen," in: *Hydraulische Probleme*, VDI Verlag, Berlin.
- Bindon, J. P., 1989, "The Measurement and Formation of Tip Clearance Loss," *ASME JOURNAL OF TURBOMACHINERY*, Vol. 111, No. 3, pp. 257-263.
- Carter, A. D. S., 1948, "Three-Dimensional Flow Theories for Axial Compressors and Turbines," *Proc. Inst. Mech. Engrs.*, Vol. 159, p. 41.
- Dishart, P. T., and Moore, J., 1990, "Tip Leakage Losses in a Linear Turbine Cascade," *ASME JOURNAL OF TURBOMACHINERY*, Vol. 112, pp. 599-608.
- Dunham, J., and Came, P. M., 1970, "Improvements to the Ainley & Mathieson Method of Turbine Performance Prediction," *ASME Journal of Engineering for Power*, Vol. 92, No. 3, pp. 252-256.
- Farokhi, S., 1988, "Analysis of Rotor Tip Clearance Loss in Axial-Flow Turbines," *AIAA Journal of Propulsion and Power*, Vol. 4, No. 5, pp. 452-457.
- Hesselgreaves, J. E., 1969, "A Correlation of Tip-Clearance/Efficiency Measurements on Mixed-Flow and Axial-Flow Turbomachines," National Engineering Laboratory, U.K., Report No. 423, Sept.
- Inoue, M., and Kuroumaru, M., 1984, "Three-Dimensional Structure and Decay of Vortices Behind an Axial Flow Rotating Blade Row," *ASME Journal of Engineering for Gas Turbines and Power*, Vol. 106, No. 3, pp. 561-569.
- Inoue, M., Kuroumaru, M., and Fukuhara, M., 1986, "Behavior of Tip Leakage Flow Behind an Axial Compressor Rotor," *ASME Journal of Engineering for Gas Turbines and Power*, Vol. 108, No. 1, pp. 7-14.
- Inoue, M., and Kuroumaru, M., 1989, "Structure of Tip Clearance Flow in an Isolated Axial Compressor Rotor," *ASME JOURNAL OF TURBOMACHINERY*, Vol. 111, No. 3, pp. 250-256.
- Kacker, S. C., and Okapuu, U., 1982, "A Mean Line Prediction Method for Axial Flow Turbine Efficiency," *ASME Journal of Engineering for Power*, Vol. 104, No. 1, pp. 111-119.
- Lakshminarayana, B., and Horlock, J. H., 1962, "Tip-Clearance Flow and Losses for an Isolated Compressor Blade," *ARC R&M* 3316.
- Lakshminarayana, B., and Horlock, J. H., 1965, "Leakage and Secondary Flows in Compressor Cascades," *ARC R&M* 3483.
- Lakshminarayana, B., 1970, "Methods of Predicting the Tip Clearance Effects in Axial Flow Turbomachinery," *ASME Journal of Basic Engineering*, Vol. 92, pp. 467-480.
- Lakshminarayana, B., Zhang, J., and Murthy, K. N. S., 1987, "An Experimental Study on the Effects of Tip Clearance on Flow Field and Losses in an Axial Flow Compressor Rotor," *ISABE Paper No. 87-7045*.
- Lewis, R. I., and Yeung, E. H. C., 1977, "Vortex Shedding Mechanisms In Relation to Tip Clearance Flows and Losses in Axial Fans," *ARC R&M* 3829, May.
- Moyle, I. N., 1990, "A Note of Efficiency Sensitivity to Tip Clearance Changes in Axial Flow Compressors," *ASME JOURNAL OF TURBOMACHINERY*, Vol. 112, pp. 795-796.
- Patel, K. V., 1980, "Research on a High Work Axial Gas Generator Turbine," *SAE Paper No. 800618*.
- Rains, D. A., 1954, "Tip Clearance Flows in Axial Flow Compressors and Pumps," California Institute of Technology, Hydrodynamics and Mechanical Engineering Laboratories, Report No. 5, June.
- Schmidt, M. J. P., Agnew, B., and Elder, R. L., 1987a, "Tip Clearance Flows—Part 1: Experimental Investigation of an Isolated Rotor," *ISABE Paper No. 87-7034*.
- Schmidt, M. J. P., Agnew, B., and Elder, R. L., 1987b, "Tip Clearance Flows—Part 2: Study of Various Models and Comparison With Test Results," *ISABE Paper No. 87-7035*.
- Senoo, Y., and Ishida, M., 1986, "Pressure Loss Due to the Tip Clearance of Impeller Blades in Centrifugal and Axial Blowers," *ASME Journal of Engineering for Gas Turbines and Power*, Vol. 108, No. 1, pp. 32-37.
- Sjolander, S. A., and Amrud, K. K., 1987, "Effects of Tip Clearance on Blade Loading in a Planar Cascade of Turbine Blades," *ASME JOURNAL OF TURBOMACHINERY*, Vol. 109, No. 2, pp. 237-245.
- Vavra, M. H., 1960, *Aero-Thermodynamics and Flow in Turbomachines*, Wiley, New York.
- Yamamoto, A., 1988, "Interaction Mechanisms Between Tip Leakage Flow and the Passage Vortex in a Linear Turbine Rotor Cascade," *ASME JOURNAL OF TURBOMACHINERY*, Vol. 110, No. 3, pp. 329-338.
- Yamamoto, A., 1989, "Endwall Flow/Loss Mechanisms in a Linear Turbine Cascade With Blade Tip Clearance," *ASME JOURNAL OF TURBOMACHINERY*, Vol. 111, No. 3, pp. 264-275.
- Yaras, M. I., and Sjolander, S. A., 1989, "Losses in the Tip-Leakage Flow of a Planar Cascade of Turbine Blades," Paper 20, AGARD Specialists Meeting "Secondary Flows in Turbomachines," Luxembourg, Aug.; to be published, AGARD-CP-469.
- Yaras, M. I., Zhu, Y., and Sjolander, S. A., 1989, "Flow Field in the Tip Gap of a Planar Cascade of Turbine Blades," *ASME JOURNAL OF TURBOMACHINERY*, Vol. 111, No. 3, pp. 276-283.
- Yaras, M. I., and Sjolander, S. A., 1990, "Development of the Tip-Leakage Flow Downstream of a Planar Cascade of Turbine Blades: Vorticity Field," *ASME JOURNAL OF TURBOMACHINERY*, Vol. 112, pp. 609-617.

Local Heat Transfer in Turbine Disk Cavities: Part I—Rotor and Stator Cooling With Hub Injection of Coolant

R. S. Bunker

D. E. Metzger

S. Wittig

Lehrstuhl und Institut für Thermische
Strömungsmaschinen,
Universität Karlsruhe,
Karlsruhe, Federal Republic of
West Germany

Results are presented from an experimental study designed to obtain detailed radial heat transfer coefficient distributions applicable to the cooling of disk-cavity regions of gas turbines. An experimental apparatus has been designed to obtain local heat transfer data on both the rotating and stationary surfaces of a parallel geometry disk-cavity system. The method employed utilizes thin thermochromic liquid crystal coatings together with video system data acquisition and computer-assisted image analysis to extract heat transfer information. The color display of the liquid crystal coatings is detected through the analysis of standard video chrominance signals. The experimental technique used is an aerodynamically steady but thermally transient one, which provides consistent disk-cavity thermal boundary conditions yet is inexpensive and highly versatile. A single circular jet is used to introduce fluid from the stator into the disk cavity by impingement normal to the rotor surface. The present study investigates hub injection of coolant over a wide range of parameters including disk rotational Reynolds numbers of 2 to 5×10^5 , rotor/stator spacing-to-disk radius ratios of 0.025 to 0.15, and jet mass flow rates between 0.10 and 0.40 times the turbulent pumped flow rate of a free disk. The results are presented as radial distributions of local Nusselt numbers. Rotor heat transfer exhibits regions of impingement and rotational domination with a transition region between, while stator heat transfer shows flow reattachment and convection regions with evidence of an inner recirculation zone. The local effects of rotation, spacing, and mass flow rate are all displayed. The significant magnitude of stator heat transfer in many cases indicates the importance of proper stator modeling to rotor and disk-cavity heat transfer results.

Introduction

In high-temperature gas turbine engines, cooling air must be supplied to the various disk-shroud cavities existing radially inboard from the blades and vanes, particularly to those cavities in the high-pressure turbine initial stages. This cooling air is used both to actively cool the disk and to prevent the ingestion of hot turbine passage gases into the cavity region.

Stresses in the rotating disk are often critical to service life. Knowledge of the temperature distribution on turbine disks is necessary to predict stresses and durability. This temperature distribution is a major factor in determining the disk dimensions and radial positioning, and thus in establishing the clearance space between blade tip and stationary outer seal. Without reliable local convection information on the disk face the thermal stress contribution cannot be reliably assessed. In the ab-

sence of such information, a conservative and excessive amount of coolant is often supplied to the disk-shroud cavity, imposing an unnecessary penalty on the engine cycle that must compress and pump the coolant.

On all rotating disks there is an induced pumping of fluid radially outward along the disk surface. If not counteracted by some means, this pumping action of the disk will serve to ingest hot mainstream combustion gases into the disk-shroud cavity to replenish the pumped flow. Such ingestion would cause elevated disk and shroud temperatures and temperature gradients, thereby reducing the disk service life. In addition to cooling the disk, the cooling air acts to seal the wheel-space against the ingress of hot gases. This sealing is generally done in conjunction with some arrangement of disk-cavity rim seals at the outer radial locations. However, the disk windage increases with increasing coolant throughflow, so that excessive cooling also imposes additional rotational drag, which is another cycle penalty. It is therefore desirable to cool the disk with a minimum of coolant while also minimizing any hot gas

Contributed by the International Gas Turbine Institute and presented at the 35th International Gas Turbine and Aeroengine Congress and Exposition, Brussels, Belgium, June 11–14, 1990. Manuscript received by the International Gas Turbine Institute January 13, 1990. Paper No. 90-GT-25.

ingestion. For designers to accomplish this task, a detailed knowledge of the convection heat transfer and flow characteristics in the wheel-space is necessary.

Research dealing with rotating disk and disk cavity heat transfer and fluid flow has been performed by various groups over the past few decades. Even so, knowledge of detailed heat transfer characteristics on rotating surfaces has been acquired slowly starting with, among others, the analysis of von Karman (1921) and the experiments of Cobb and Saunders (1956) and Kreith et al. (1959) dealing with heat and mass transfer from a free disk. These studies acquired disk-average transfer coefficients for the case of freely induced flow onto and from a rotating disk (rotor). A subsequent study by Kreith et al. (1963) dealt with mass transfer from an enclosed rotating disk with a shroud (stator) of variable spacing, and with or without a source flow.

Many of the published works to date have dealt with the fluid flow aspects of enclosed rotating disks, such as Daily and Nece (1960) and Bayley and Owen (1970). The acquisition of heat transfer information has been comparatively slow due to the expense and complexity of making local heat transfer measurements with conventional methods. Most of the studies so far have obtained disk-average heat transfer coefficients without the application of consistent thermal boundary conditions upon all of the cavity walls. Metzger (1970) obtained such information for a parallel rotor-stator system with a shroud rim, for source flows less than the turbulent pumping flow of a free disk (per Schlichting, 1979). Haynes and Owen (1975) presented such results for a similar system using large source flows on the order of or exceeding the turbulent pumping flow. Subsequent experiments of Metzger and Grochowsky (1977) and Metzger et al. (1979) have looked at jet impingement onto a free rotating disk.

Among other conclusions, these prior studies have indicated the effectiveness of a shroud-rim, particularly an overlapping rim, in reducing ingress of gases into the disk-cavity and thereby allowing the disk to be cooled with a source flow of only a fraction of the disk pumping flow. Also, a single jet impinging onto the disk has been found to provide effective heat transfer with little effect of jet size. These conclusions have been born out in more recent studies of Owen and Phadke (1980) and Phadke and Owen (1983) dealing with the reduction of gas ingress through the use of rim geometries, as well as a study of free disk local jet impingement by Popiel and Boguslawski (1986). A comprehensive review of flow and heat transfer in simple basic disk-shroud geometries is presented in a review by Owen (1984). While these researchers all deal with simple geometries, work of Haaser et al. (1988) has also shown the effects of rim sealing upon windage and ingestion for specific gas turbine geometries.

Other factors that may contribute to the effectiveness of

disk heat transfer with a minimum of cooling fluid include inlet jet swirl and cavity geometry. Dibelius et al. (1984) performed experiments obtaining information on disk friction with inlet jet swirl showing that swirl can reduce the disk windage. Uzkan and Lipstein (1986) have shown that a honeycomb stator design reduces the ingress of gases further.

Most recently, Qureshi et al. (1989) have measured local heat transfer coefficients for a specific turbine disk section geometry using the steady-state-isothermal method. Employing multiple section isolation and heating on the rotor only, they obtained radial-segment-averaged coefficients at four or five radial locations. Metzger et al. (1991) have obtained a limited amount of detailed local heat transfer information for a parallel rotor-stator system with shroud-rim. There a transient method was demonstrated using a thin coating of a visually indicating material upon the rotor surface with optical data acquisition of local surface temperatures to obtain radial variations of rotor heat transfer coefficients with consistent thermal boundary conditions over the entire disk cavity.

Experimental Apparatus and Procedures

A schematic of the test apparatus is shown in Fig. 1. The disk is rotated at speeds up to 10,000 rpm by a 400 W motor connected by toothed belt to the shaft-bearings set upon which the disk is attached. The disk is composed of two pieces, as shown in the detailed test section schematic of Fig. 2. The disk test surface is made of black, cell-cast acrylic plastic of 6.5 mm thickness and 10 cm radius. Black acrylic plastic is used to provide improved surface coating visual display. The plastic disk is fit tightly into an aluminum retaining disk, and the two-piece assembly is fastened to the rotating shaft.

The rotating disk is faced by a plane stationary shroud, or stator disk, at a spacing of z . The stator surface is maintained parallel to the disk surface and positioned laterally with a shroud support and precision positioning table. The shroud includes an attached rim at the stator disk edge to discourage entrainment of air into the disk-cavity from the rim region. The shroud rim is positioned so that it overlaps the disk edge and angled to direct jet supplied air out of the disk-cavity and away from the apparatus. The stator disk is made of clear acrylic plastic of 15 mm thickness. A sector of the cavity side of the stator is coated to obtain stator surface heat transfer information. The remainder of the stator disk remains clear to allow viewing of the rotor disk through the stator. The stator disk contains five jet nozzle insert holes at radial locations of $r_j/r_o = 0, 0.2, 0.4, 0.6, \text{ and } 0.8$. The jet nozzle, also made of acrylic plastic, is inserted at the desired radial location while the remaining insert holes are plugged with solid acrylic plastic pieces. The jet nozzle is circular with 0.5 cm i.d.

Nomenclature

A = heat transfer area	r_o = disk radius	z = rotor/stator spacing
C_p = specific heat	Re_m = flow Reynolds number = $Q/2\pi z\nu$	α = thermal diffusivity
f = rotational frequency	Re_{ro} = disk rotational Reynolds number = $\omega r_o^2/\nu$	θ = time
G = dimensionless rotor/stator spacing = z/r_o	R_T = turbulent pumping ratio = Q/Q_p	ν = kinematic viscosity = μ/ρ
h = heat transfer coefficient	T = temperature	μ = fluid dynamic viscosity
k = thermal conductivity	T_i = initial temperature	ρ = fluid density
\dot{m} = jet mass flow rate	T_r = reference temperature	τ = time step
Nu_{r0} = Nusselt number = hr_o/k_{air}	T_m = local mean fluid temperature	ω = angular speed = $2\pi f$
\dot{q}_w = wall heat flux	T_w = wall temperature	
Q = jet volumetric flow rate	U, V = chrominance signals	
Q_p = turbulent pumped flow of a free disk = $0.219r_o^3\omega Re_{ro}^{-0.2}$	V = jet velocity	
r = radial location		

Subscripts

i = i th element subscript
 j = jet inlet quantity subscript

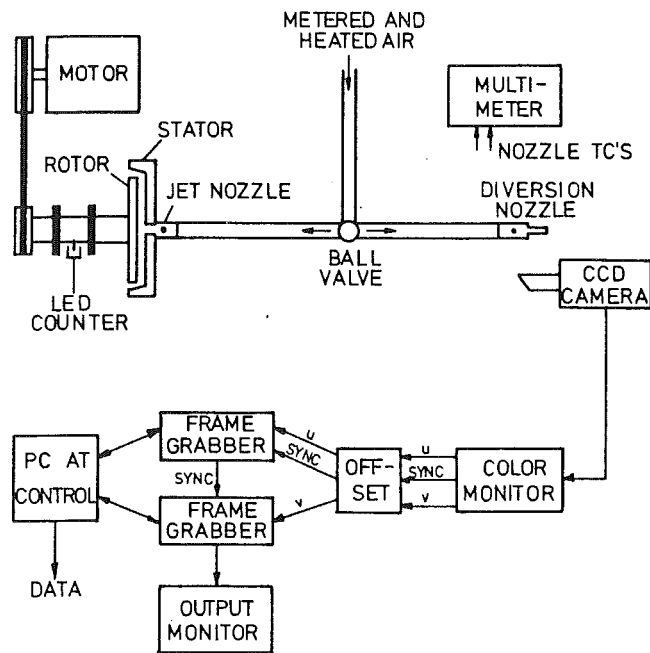


Fig. 1 Schematic of test apparatus and data acquisition system

and is fitted with a thermocouple to indicate the jet transient temperature.

The rotating shaft is affixed with a small, lightweight finger for the purpose of breaking the circuit of a light emitting diode (LED), which is affixed between the bearing housings. The output from the LED is then sent to an electronic counter to monitor the rotational speed of the shaft, and so also the disk. Laboratory compressed air is supplied to the apparatus through a filtering pressure regulating valve, followed by a flow regulating needle valve. The air is metered through an orifice, which has been accurately calibrated using a gas counter. After metering, the air flow is heated and hence proceeds to the ball diverter valve.

A test begins with heated air first diverted away from the test section so that the test section and jet nozzle remain uniformly at the laboratory ambient temperature. The diversion channel is composed of a length of flexible hose and jet nozzle identical to those of the test section. The nozzle is also fitted with a thermocouple to monitor the fluid temperature prior to the test. The diverter valve remains in the diverted position until steady flow and a steady-state temperature have been achieved in the diversion channel. At that time the valve is used to route the heated air flow suddenly through the test section. The data acquisition program is initiated simultaneously with the change of valve position.

The surface coating used in this study is a Thermochromic Liquid Crystal (TLC), which is painted on the entire rotor surface as well as on a sector of the stator surface. The color responses of the thin TLC coatings (less than 5×10^{-3} cm) in the presence of a heated air stream are used to determine the local surface heat transfer rates. Metzger et al. (1991) present a more detailed discussion of the use of TLC, so only a few brief notes will be mentioned here with regard to the specific TLC used. The material used in the present tests is a commercially available, chiral nematic TLC (BHD Thermochromics, Type TCA262; R38C1W; Poole, United Kingdom). For this TLC, the nominal temperatures for the initiation of red, green, and blue under room lighting conditions are 37°C , 37.5°C , and 38°C , respectively. In the current usage, both the application of a uniform intensity studio light and the use of black acrylic plastic serve to improve the TLC color display.

As a test proceeds, the TLC at various radial locations changes color and is detected by the data acquisition system

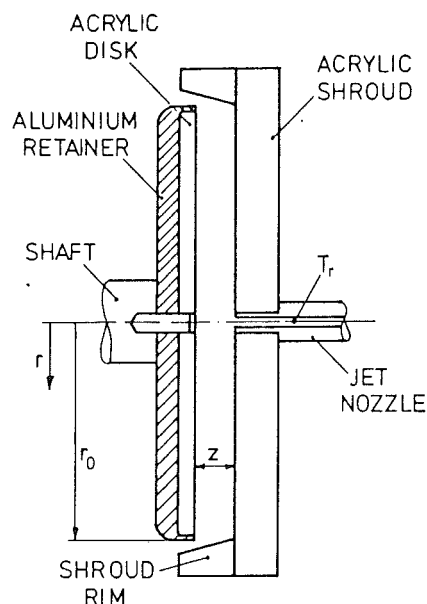


Fig. 2 Disk-cavity test section

shown in Fig. 1. A particular surface temperature is determined by detecting a desired color. The system utilizes a color CCD camera whose signal is sent to a color monitor, from which signals are sent to two frame grabbers for processing of the image. When a small region of the surface covered by a single pixel has been determined to satisfy preset conditions, the surface temperature at this point is known. The desired color and preset conditions are determined through calibration of the system using a TLC-coated aluminum bar.

The method of color detection known here as the chrominance method was developed in the work of Hirsch (1987) and Platzer et al. (1991) and is more fully explained in those references. Simply put, the color CCD camera sends a standard video signal to the color monitor. Any particular color in three-dimensional color space is represented by a vector of hue, saturation, and luminance. The video signal represents color in the two-dimensional plane of a constant luminance or "whiteness." In such a plane, a color signal Y is a combination of the primary colors red, green, and blue (R, G, B) as

$$Y = \alpha R + \beta B + \gamma G; \quad \alpha + \beta + \gamma = 1$$

The monitor utilizes this signal, in which wavelength gives hue and white reference comparison gives saturation, to derive the R, G, B color signals as well as difference signals

$$U = \delta(R - Y); \quad V = \sigma(B - Y); \quad \delta, \sigma, > 0$$

known as chrominance values (explanations of color and chrominance may be found in any good text on color television). Figure 3 shows the relationship between colors and chrominance, where the "color circle" represents a particular color intensity level of the more general color cylinder. The center of this circle represents white, an equal combination of the primary colors. By offsetting this circle into the positive quadrant, a new chrominance system is obtained as

$$U^* = U + U_c; \quad V^* = V + V_c$$

where U_c, V_c represents white again. Through system calibration using the white mask feature of the CCD camera, the values of U_c and V_c are determined. Then, by calibration with TLC display, the chrominance values U_o and V_o of a desired color are determined. It is then possible to detect this color by computing the nearness of a displayed color to the desired value. This computation is done by computer algorithm using tolerance measures, which correspond to the allowable error in color vector magnitude (saturation) and direction (hue).

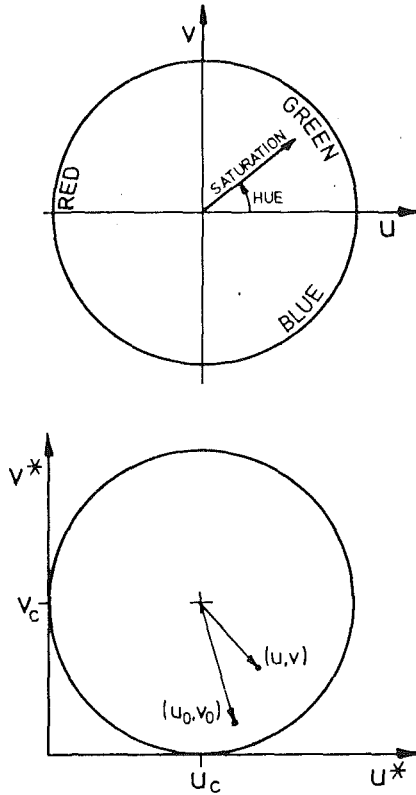


Fig. 3 Color circle and chrominance detection

When a displayed color's vector comes within these tolerance limits, the surface location that it represents is considered to have the desired color and therefore temperature at that time.

In the current application, this detection method is used to detect a light blue TLC color with corresponding surface temperature of 38.4°C. The tolerance limits are kept constant at ± 2 deg hue variation and 85 percent saturation. It is important to emphasize here that the detection of color on the rotor and stator surfaces is achieved simultaneously in these experiments.

A brief description of the experimental technique employed in this study is given here. Details of this technique as used with melting point surface coatings may be found from Metzger and Larson (1986). A test is started by the sudden diversion of a heated flow, of some desired steady-state mass flow rate and temperature, into the disk cavity. For the acrylic plastic test surfaces, the depth of heating into the walls over the time duration of the test is less than the wall thickness, 6.5 mm minimum for the present rotor. In addition, lateral conduction in the walls has been shown by Metzger and Larson (1986) and in more detail by Vedula et al. (1988) to have a negligible effect upon the local surface temperature response. At any surface point, the wall (rotor or stator) temperature is thus represented by the classical one-dimensional response of a semi-infinite medium to the sudden step application of a convecting fluid at temperature T_r ,

$$\frac{T - T_i}{T_r - T_i} = 1 - \exp\left(\frac{h^2}{k^2\alpha\theta}\right) \operatorname{erfc}\left(\frac{h}{k}\sqrt{\alpha\theta}\right) \quad (1)$$

If each surface point were subjected to a true step increase in T_r , then measurement of the required times to reach a predetermined TLC color, and therefore temperature, allows solution of equation (1) for the heat transfer coefficients. This is the essence of the model, with the thin layer of TLC providing a means of acquiring an array of temperature-time pairs over the surfaces.

However, in actual practice, the wall surfaces will not ex-

perience a pure step change in air temperature because of the transient heating of upstream regions. Nevertheless, equation (1) is a fundamental solution that can be used to represent the response to a superposed set of elemental steps in T_r arranged to represent the actual air temperature rise,

$$T - T_i = \sum_{i=1}^N U(\theta - \tau_i) \Delta T_i \quad (2)$$

where

$$U(\theta - \tau_i) = 1 - \exp\left(\frac{h^2}{k^2\alpha}(\theta - \tau_i)\right) \operatorname{erfc}\left(\frac{h}{k}\sqrt{\alpha(\theta - \tau_i)}\right) \quad (3)$$

By recording the T_r variation with time, and approximating it by steps, the resulting superposed solution given by equations (2) and (3) is solved for the local surface heat transfer coefficients using observed local color response times.

In the present research, a digital multimeter is used to observe the response of T_r during each test. By recording the value of T_r at the midtime of a test transient, equation (1) is solved for the heat transfer coefficients by using this T_r as a single-step approximation to the actual variation. This study utilizes the injection jet temperature as the reference temperature. Because of the small jet diameter, 5 mm, the actual response of T_r with time very nearly approximates a true step change response. Thus, the use of a single-step solution does, in this instance, give an acceptable accuracy without an undue increase in experimental uncertainty. Using the single-sample experimental methods of Kline and McClintock (1953), the estimated uncertainty in the present experiments is ± 10 percent.

While the present work generally obtains local heat transfer coefficients based upon the jet temperature to surface temperature difference (i.e., jet temperature potential), certain cases do allow an approximate analysis to be performed to obtain coefficients based upon a local mean temperature within the disk-cavity. In the special case of injection on the center of the rotor, the flow field is predominantly radially outward on both the rotor and the stator, although a recirculation zone does appear to exist near the stator just downstream of the injection jet. In this circumstance the mass flow rate can be approximated at each radial location as a constant, equal to that of the jet flow rate, and to be directed radially outward. A heat balance may then be used to calculate downstream local mean temperature T_m by accounting for the heat transferred to the rotor and stator at upstream locations. The solution of equation (1) gives a set of coefficients h_{ji} based upon jet temperature T_j . These coefficients are related to the heat flux into the walls by

$$\dot{q}_w = \sum_{i=1}^M h_{ji} A_i (T_j - T_w) \quad (4)$$

where i represents the data location radially and $h_{ji} A_i$ may be divided into contributions from the rotor and stator. If the local mean temperatures and coefficients were known, then the heat flux would also be

$$\dot{q}_w = \sum_{i=1}^M h_i A_i (T_{mi} - T_w) \quad (5)$$

Since the mass flow rate is considered to be constant and essentially unidirectional, the heat flux is related to the fluid exchange by

$$\dot{q}_w = \sum_{i=1}^M \dot{m} C_{pi} (T_j - T_{mi}) \quad (6)$$

Equating equations (4) and (6) yields the local mean temperature as

$$T_{mi=k} = T_j - \sum_{j=1}^k \frac{h_{ji} A_i (T_j - T_w)}{\dot{m} C_{pi}} \quad (7)$$

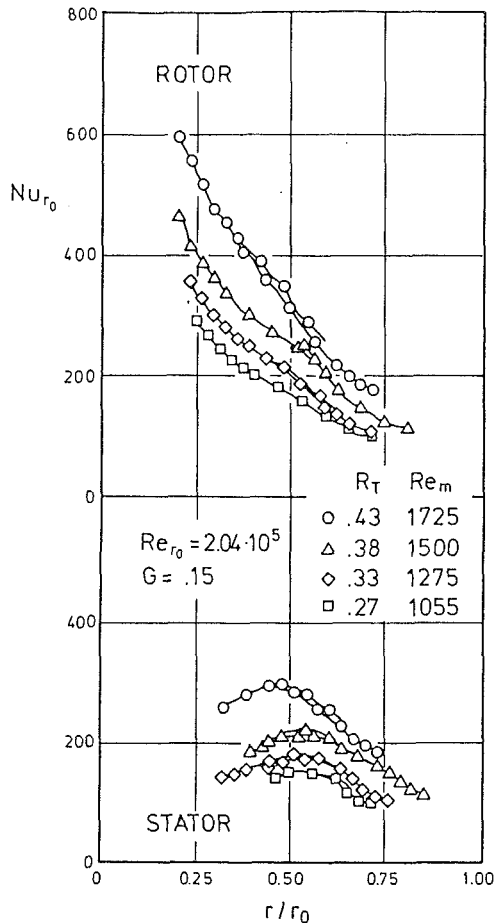


Fig. 4 Jet inlet temperature based Nu_{r_0} for $Re_{r_0} = 2.04 \times 10^5$; $G = 0.15$

The effect of windage upon local mean fluid temperature is implicit in this formulation due to the use of jet inlet temperature based heat transfer coefficients, which include windage phenomena. Then, equating equations (4) and (5) gives the heat transfer coefficient based upon local mean temperature

$$h_i = h_{ji} \left(\frac{T_j - T_w}{T_{mi} - T_w} \right) \quad (8)$$

where T_{mi} is given by equation (7). In this manner an approximate correction for heat transfer into the disk-cavity walls may be made. Since this approximate computation of the local fluid mean temperature does not account for recirculating flows or rotating core flow, the actual local mean temperature may differ to some extent depending upon the particular experimental configuration in question. The present calculation was judged appropriate for the close rotor-stator spacings involved with the addition of a shroud-rim. It should be noted that the performance of such a computation also increases the uncertainty in the resulting values of local heat transfer coefficients; in fact this uncertainty rises with increasing radial position in the disk-cavity.

Two additional notes are necessary at this point. First, because of the small jet diameter used and the very large expansion that the fluid undergoes upon entering the cavity, a reference temperature correction of the form

$$T_r = T_j + \frac{\Delta V^2}{2C_p} \quad (9)$$

must be made to account for the large decrease in fluid velocity, and thus the associated increase in fluid temperature. This correction must be made prior to performing a heat balance

computation when more than one test is used to obtain data at various cavity radial locations. To ensure a proper basis for computation of the heat balance, the heat transfer coefficients of equation (1) must be based upon this corrected jet reference temperature. Second, the color display of TLC has been noted in the present study to undergo a compression for conditions of high surface temperature radial gradient. In extreme cases, the strength of the desired color for detection may not be sufficient, thereby necessitating the recalibration and detection of a darker blue TLC color. A darker blue color results in a less accurate temperature indication and so also a higher uncertainty. These conditions did occur in a very few of the experiments, and were confined to a limited radial extent.

Results and Discussion

Verification of Methodology. For the purpose of method, system, and apparatus verification, a series of tests were performed using hub injection with a rotor-stator spacing ratio of $G = 0.15$. Tests covered a range of jet injection flow Reynolds numbers Re_m , and two disk rotational Reynolds numbers Re_{r_0} . For the Re_{r_0} used, Owen (1984) indicates that this spacing results in essentially separate rotor and stator boundary layers in a disk-cavity without a shroud-rim. The effect of the shroud-rim, however, is to discourage the ingress of noninjection air, as shown by Metzger (1970). For this rotor-stator spacing Kreith et al. (1963) and also Metzger (1970) have shown that the effect of the shroud (i.e., its physical proximity, not its heat transfer character) upon rotor heat transfer is small. However, Kreith et al. (1963) have indicated that the presence of the shroud tends to hasten transition of the rotor boundary layer to turbulent flow. Furthermore, Metzger (1970) has indicated that for turbulent forced jet flow, even at these low Re_m values (i.e., those of the present study), the rotor boundary layer is apparently turbulent.

Figure 4 shows a composite of the Nusselt number results based upon jet inlet temperature for rotor and stator surfaces at $Re_{r_0} = 2.04 \times 10^5$. Each group of curves on this plot (four groups on each portion) represents data at a particular Re_m , with Re_m decreasing with Nu level. A single group of curves may consist of one or more test runs performed at various jet temperature potentials. The fact that these various tests overlap so well indicates good repeatability of the test method. Furthermore, all the data shown have excellent consistency, therefore increasing confidence in the method and the system. The limited and somewhat variable radial extent of data shown here and in subsequent figures is a consequence of the experimental method as noted by Metzger et al. (1991). Figure 5 shows the Nu_{r_0} results for both rotor and stator surfaces, based upon a computed local radial mixed mean fluid temperature using equations (7), (8), and (9). It is interesting to note the considerable differences in these heat transfer coefficient radial distributions, over those of Fig. 4, due to the influence of rotor and stator heat transfer upon the local mean fluid temperature. This aspect shall be discussed in more detail later. (Note that the present experiments each obtained 128 data points for the full disk radius of 10 cm, but that relatively few data points are given symbols in these figures.)

The only data of prior studies that cover the present parameter ranges are those of Metzger (1970). These data, however, present only rotor average Nu , obtained by a different method under differing boundary conditions. For the purpose of comparison, the present local heat transfer data must be averaged and modified to account for the major testing differences. The average Nu obtained by Metzger used a heated aluminum disk cooled by an air supply at the hub. The stator and shroud-rim were made of acrylic plastic and initially at ambient temperature. The air was at ambient temperature and supplied through a hub plenum and annular jet. The only active heat transfer

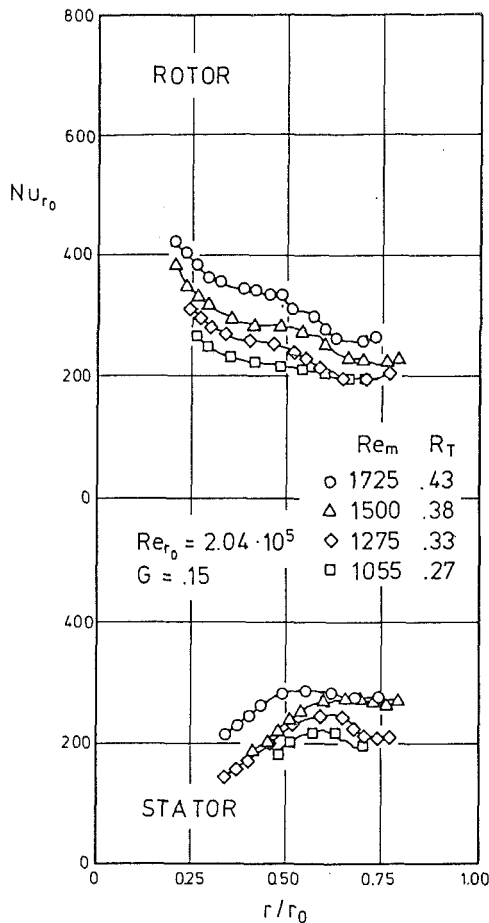


Fig. 5 Local mean temperature based Nu_{r_0} for $Re_{r_0} = 2.04 \times 10^5$; $G = 0.15$

surface in these tests was the rotor. The reference temperature was that of the hub plenum, with a low fluid velocity.

In the present test, two major differences are apparent. First, the rotor and stator are both active heat transfer surfaces. Second, the jet velocity at the point of reference temperature measurement is very high, on the order of 100 to 150 m/s. To facilitate comparison of data, the local Nu of Fig. 4 are first averaged to obtain a radially area-averaged Nu for the rotor and also for the stator. The data are projected along the lines of existing gradients, to provide estimated local Nu for small and large radii where no data were obtained. The reference temperature used to compute these Nu was then corrected to account for the heat transferred into the stator, using the stator average heat transfer coefficient over the entire stator surface. In addition, the reference temperature was further corrected to account for the high jet velocity of the present tests. The new reference temperature was then used to obtain a new rotor average Nu for comparison to the data of Metzger. Figure 6 shows this comparison. The lines represent curve fits to the data of Metzger, while the symbols refer to the present averaged and modified data. The agreement is seen to be excellent, considering the approximate manner of the data averaging performed. This comparison in particular verifies the current methodology and data acquisition.

Typical Parametric Effects Upon Heat Transfer Coefficient Distributions. In the review article of Owen (1984), maximum and minimum values of G are given that estimate the spacings for fully separate rotor and stator boundary layers and fully merged boundary layers, respectively,

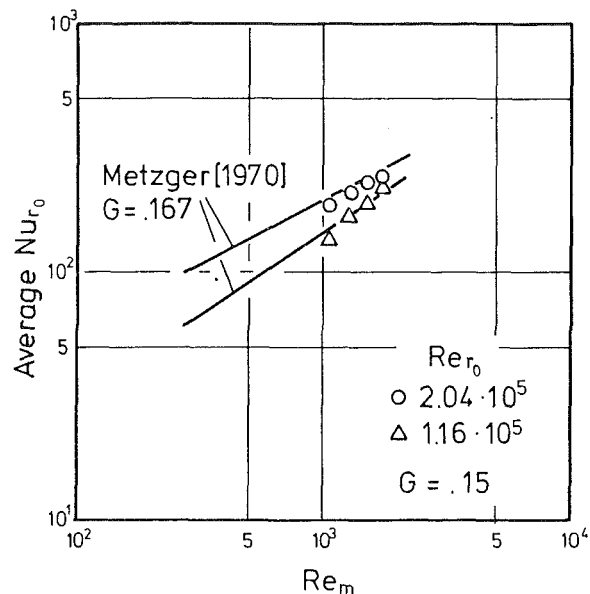


Fig. 6 Comparison of rotor-averaged Nu with data of Metzger (1970)

$$G_{max} = 1.05Re_{r_0}^{-0.2}; \quad G_{min} = 0.23Re_{r_0}^{-0.2}$$

These spacing values correspond well with the available data for disk-cavity heat transfer in an open system (i.e., without a shroud-rim). For $G > G_{max}$, the rotor acts hydrodynamically essentially as a free disk; for $G < G_{min}$, a Couette-type flow exists in the disk-cavity. While the present tests employ a shroud-rim and thereby restrict entrainment of ambient air, these limiting estimates of G should still hold approximately true. For the present range of Re_{r_0} , G_{max} is about 0.08 while G_{min} is about 0.02. Hence, the present results dealing with $G = 0.10$ and 0.15 should both show essentially free disk rotor characteristics; results with $G = 0.05$ should show some divergence from these free disk traits; and results with $G = 0.025$ should approach Couette-type behavior. All results shown in this section are based upon a computed local mean fluid temperature.

Typical results showing the effects of Re_m variation are depicted in Figs. 7 and 8 for rotor-stator spacing of $G = 0.10$ and 0.05 with rotational Reynolds number of $Re_{r_0} = 3.5 \times 10^5$ (the characteristics discussed here apply to all rotational speeds of the present study). In general, there appear definite regions of impingement and rotationally dominated heat transfer on the rotor, separated by a region of low heat transfer coefficient. Impingement is dominant in the region of high Nu gradient at smaller radii, while rotational dominance is seen in the larger radii locations where the Nu gradient becomes increasingly positive after passing through zero. The specific radial coverage of these regions in the radial distribution of rotor heat transfer coefficient shifts with varying parameters. The impingement region on the rotor moves inboard radially as spacing G is decreased. Noting this region as extending to the location where Nu gradient begins to decrease or level off, impingement influence is then present to $r/r_0 = 0.70$ at $G = 0.15$, to $r/r_0 = 0.50$ at $G = 0.10$, and to $r/r_0 = 0.30$ at $G = 0.05$. At radii inboard of these locations the impingement character of the rotor heat transfer is quite evident. For spacings of $G > G_{max}$, the rotor Nu is proportional to Re_m^n with n of about 0.6. The Nu gradient and distribution broadness also are affected by changes in Re_m . For spacings of $G < G_{max}$, the effect of Re_m in the impingement region is essentially lost. Results obtained with $G = 0.025$ showed virtually no change from those at $G = 0.05$ in this area, indicating the approach to an optimal spacing for impingement heat transfer. The Nu magnitude and gradient are however greater for these closer

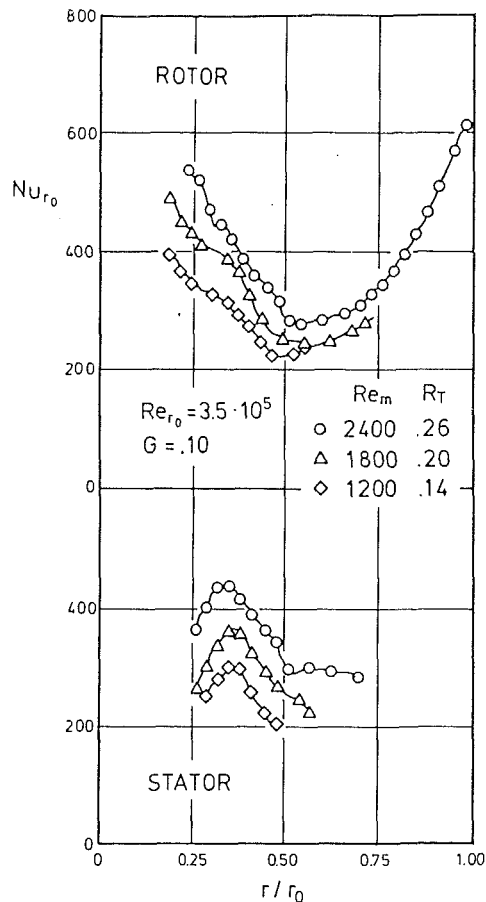


Fig. 7 Effect of Re_m on Nu_{r_0} ; $Re_{r_0} = 3.5 \times 10^5$; $G = 0.10$ (local mean temperature based Nu_{r_0})

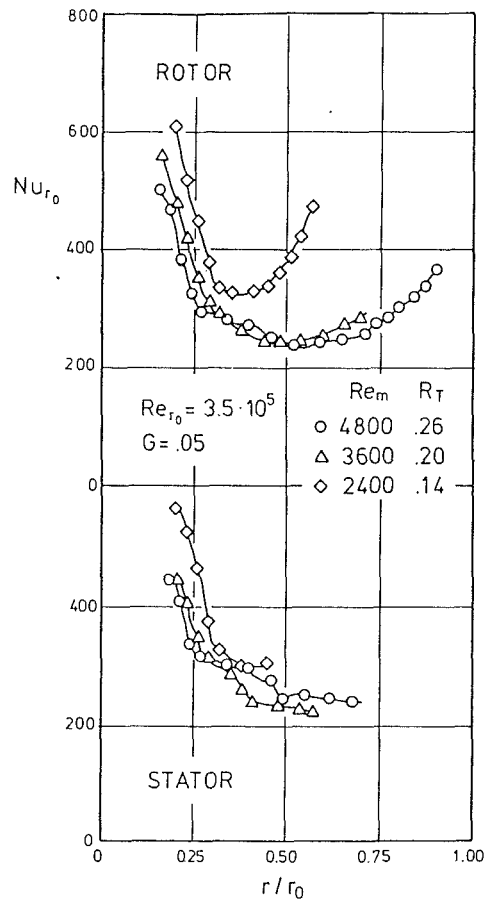


Fig. 8 Effect of Re_m on Nu_{r_0} ; $Re_{r_0} = 3.5 \times 10^5$; $G = 0.05$ (local mean temperature based Nu_{r_0})

spacings than for larger spacings. These characteristics are all typical of impingement heat transfer as previously noted in the research of Gardon and Cobonpue (1962) and Gardon and Akfirat (1965) for heat transfer from an axisymmetric jet to a flat plate, as well as in more current impingement studies for airfoil leading edge regions by Bunker and Metzger (1988).

The radial Nu variations shown for the stator surface show the primary influence of flow reattachment on the stator. The radial location of reattachment, as noted by the peak in Nu magnitude, also moves inboard with decreasing rotor-stator spacing as noted by comparing Figs. 4, 7, and 8. At $G = 0.15$ flow reattachment occurs at about $r/r_0 = 0.55$, for $G = 0.10$ at $r/r_0 = 0.35$, and for $G = 0.05$ at $r/r_0 = 0.20$. At $G = 0.025$, no stator flow reattachment was observed, indicating an essentially Couette-type flow field. Inboard of the reattachment location, Nu decreases monotonically. This evidence supports the existence of a recirculation zone of fluid between the injection jet and the reattachment position on the stator. Outboard of stator reattachment, the stator heat transfer coefficient is consistently a bit greater than that of the rotor for larger spacings, $G = 0.10$ and 0.15 . This quality of stator heat transfer is apparently due to a higher velocity present on the stator downstream of its reattachment position. As spacing is decreased to $G = 0.05$, the reattachment position moves closer to the rotor impingement location, and the stator Nu variation becomes more like that of the rotor in the impingement-dominated region. At $G = 0.25$, rotor and stator Nu distributions were observed to be essentially identical to each other at all but large radii. The flow reattachment region on the stator exhibits stator Nu variations very like impingement. In fact, the aspects of Re_m dependence and changes with spacing G , which have been noted for rotor impingement region Nu , are

all present for the stator heat transfer in the reattachment area. Additionally, the stator heat transfer coefficient is observed to fall off at larger radii, which decline is located essentially where the influence of rotation is first seen for the rotor heat transfer coefficient. This may indicate that the rotor pumping action at large radii, away from impingement, is actually drawing fluid down from the stator.

The typical effects of rotational speed variation upon rotor and stator heat transfer coefficient are shown in Figs. 9 and 10 for $G = 0.10$ with $Re_m = 2400$ and $G = 0.05$ with $Re_m = 4800$ (these configurations have the same jet mass flow rate). Again, the characteristics discussed here apply as well to other mass flow rates in the range investigated. The effect of rotation upon the rotor heat transfer coefficient is very evident, serving to increase Nu with rotational speed in the rotationally dominated region. This increase is due to the fluid acceleration from centrifugal forces, over and above the decelerating effect of the increasing radius and area. Equally evident is that Re_{r_0} has no apparent effect upon rotor heat transfer coefficient in the impingement-dominated region, due to the relatively low local rotational rates at small radii combined with the effects of impingement. The intermediate region of low rotor heat transfer coefficient is observed to be of varying extent depending upon Re_m and G , not just Re_{r_0} . A comparison of Figs. 9 and 10 shows this low heat transfer coefficient region to be of greater extent at $G = 0.05$, delaying the onset of rotational influence as well as diminishing this influence. This delay effect is observed to extend to even larger radii for $G = 0.025$. The extent of this region is further increased due to the shortened rotor impingement region as spacing is decreased. These effects are due to the decrease in spacing and indicate an interaction of rotor and stator boundary layers,

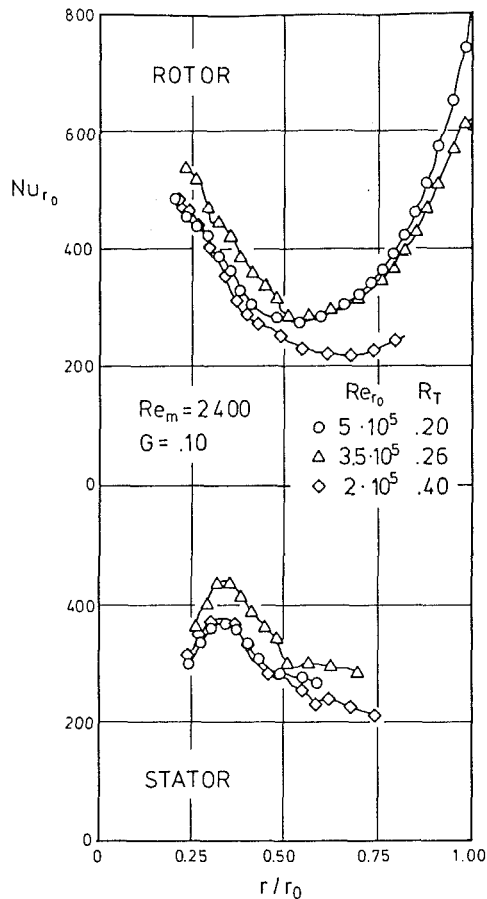


Fig. 9 Effect of Re_{r_0} on Nu_{r_0} ; $Re_m = 2400$; $G = 0.10$ (local mean temperature based Nu_{r_0})

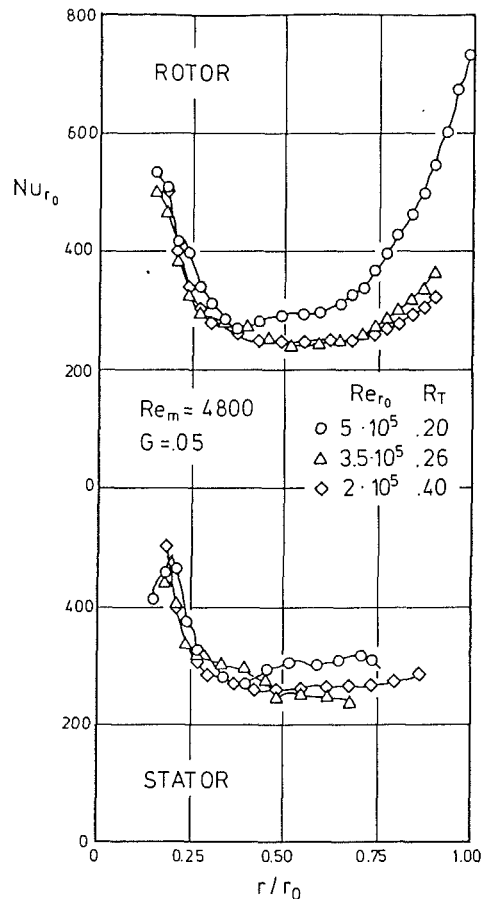


Fig. 10 Effect of Re_{r_0} on Nu_{r_0} ; $Re_m = 4800$; $G = 0.05$ (local mean temperature based Nu_{r_0})

which serves to disrupt the growth of the rotor boundary layer. Also commensurate with the decreased spacing is the increase in velocity for stator convective heat transfer: roughly twice as large at $g = 0.05$ as at $G = 0.10$ due to the halved disk-cavity volume. Thus, the stator heat transfer coefficient is seen to maintain the same level as that of the rotor until the delayed effect of rotation begins. Because these factors delay the increase in local rotor heat transfer coefficient to larger radii, the overall rotor heat transfer coefficient for $G = 0.05$ is less than that for $G = 0.10$. The decrease in overall rotor heat transfer as G is decreased from 0.10 to 0.05, as manifested by the jet temperature based heat transfer coefficients, is small (estimate 10 percent or less). However, in decreasing the spacing further to $G = 0.025$, there was observed a small but consistent increase in overall rotor heat transfer from that at $G = 0.05$. The behavior of decreasing overall rotor heat transfer with spacing until a Couette-type flow is obtained has been observed in prior research, as noted by Owen (1984).

The stator heat transfer coefficients shown in Figs. 9 and 10 indicate that the effect of Re_{r_0} upon stator Nu is small. Most apparent is that the stator heat transfer coefficient declines below that of the rotor beginning at the radial location where rotational dominance on the rotor is initiated. As a consequence of the effects of both Re_m and Re_{r_0} , this initiation of rotational dominance moves inboard as mass flow rate is decreased and as rotational speed is increased. The effect of rotation upon a low mass flow rate is most dramatically seen in Fig. 8 with the sharp upswing in rotor heat transfer coefficient at a relatively small radius. As a result of this, a lower mass flow rate may actually provide a higher local rotor heat transfer coefficient at small radii. This may also result in an apparent rotor Nu trend with Re_m as seen by a comparison of

Figs. 7 and 8. This locally larger heat transfer coefficient can however only endure as long as the local fluid temperature remains sufficiently above the surface temperature, which will not be long due to the ever-increasing surface area. At some point this heat transfer coefficient must peak and then fall off.

In the foregoing discussion many of the effects due to the variation in rotor-stator spacing G have been noted. Figures 11 and 12 show direct comparisons of results obtained at three spacings for $Re_{r_0} = 5 \times 10^5$ and ratios of $R_T = 0.15$ and 0.20, respectively. While some of the local effects of spacing upon rotor heat transfer coefficient may be seen here, it is more apparent from these comparisons that spacing changes greatly affect the stator heat transfer coefficient distributions. The location of stator flow reattachment, the magnitude of heat transfer coefficient, and also the form of coefficient radial variation all change significantly with spacing. In these figures this is made even more evident by the inclusion of data at $G = 0.15$. At this large spacing, stator flow reattachment occurs at a large radial location of $r/r_0 = 0.55$, while rotor impingement domination extends all the way out to $r/r_0 = 0.70$. It is this extension to larger radial locations that accounts for the stator heat transfer coefficient maintaining its level or even increasing, rather than declining as is the case at lower spacings. Of primary importance here is the realization that the heat transfer behavior of the stator does impact the resulting rotor heat transfer coefficients. This is particularly apparent from the $G = 0.15$ results presented.

Influence of Stator Heat Transfer. As has been previously noted, the present study differs from most prior studies in that consistent thermal boundary conditions are realized for the entire disk cavity. Because the stator is in the present case an

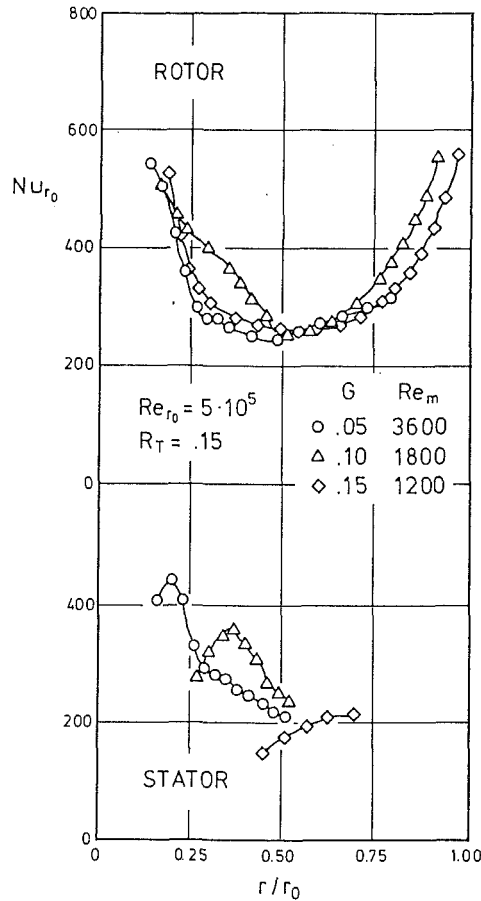


Fig. 11 Effect of G on Nu_{rot} ; $Re_{ro} = 5 \times 10^5$; $R_T = 0.15$ (local mean temperature based Nu_{ro})

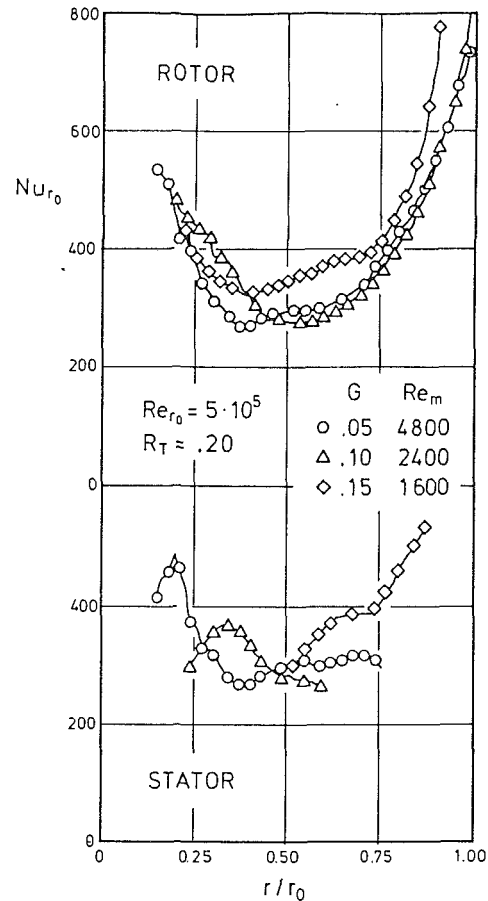


Fig. 12 Effect of G on Nu_{rot} ; $Re_{ro} = 5 \times 10^5$; $R_T = 0.20$ (local mean temperature based Nu_{ro})

active heat transfer surface upon which data are obtained, it has been possible to compute heat transfer coefficients based upon local mixed mean fluid temperatures. To display the importance of local stator heat transfer coefficient knowledge, various computations may be compared with differing stator coefficient variations. Figure 13 shows the results of such computations for three representative cases at differing mass flow rates. In each case the rotor heat transfer coefficients based upon jet inlet temperature are compared with three rotor coefficient variations based upon computed local mixed mean temperatures with stator conditions of (1) adiabatic stator, (2) adiabatic stator only over radii where data were not obtained, otherwise nonadiabatic with use of the test data, and (3) non-adiabatic stator using test data and reasonable projections of these data to radial extremes. The initial difference between coefficient variations based on jet inlet temperature and other variations is due to the inclusion of the dynamic temperature. The use of an adiabatic stator results in rotor heat transfer coefficient variations based upon local total temperature, which are similar in form and magnitude to the jet inlet based variations. The inclusion of a partially nonadiabatic stator to account for actual experimental data results in a significant increase in rotor heat transfer coefficients of as much as 50 percent at larger radii. The further inclusion of projected stator data, such that a fully nonadiabatic stator is used, gives rise to even more dramatic increases in resulting rotor heat transfer coefficients, some of 100 percent or more. In all cases, the use of an adiabatic stator surface—whether experimentally or computationally imposed—results in a severely conservative estimation of local rotor heat transfer coefficients. This does not imply that errors of such magnitude would necessarily be made, as designers could estimate the effect of stator heat transfer

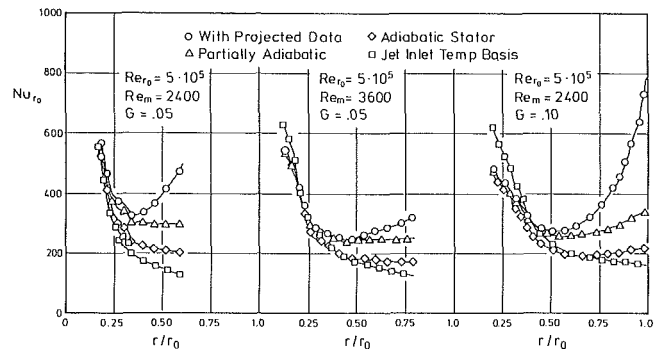


Fig. 13 Computation of the influence of stator heat transfer upon rotor radial variation of Nu_{ro}

upon the local mixed mean temperature. However, this does emphasize that the level of the stator heat transfer is high enough to have a fluid temperature, so that accurate knowledge of the stator heat transfer coefficients is necessary in order to apply the rotor heat transfer coefficients properly.

Summary and Conclusions

The principal conclusions of the present study can be summarized as follows:

- A previously utilized experimental method employing thin coatings of encapsulated liquid crystals has been extended in its usefulness by the application of a chrominance method for detecting color. In conjunction with a color CCD camera and

automated image analysis, this system has been applied to determine local heat transfer coefficients on both the rotating and stationary surfaces of a disk-cavity system for a range of parameters.

- The local variation in rotor heat transfer coefficient exhibits definite regions of impingement and rotational dominance, with a region of low heat transfer coefficient situated between these. The radial extent of these various regions is configuration dependent.
- The same rotor-stator spacing criteria recommended by prior studies on systems without shroud-rims appear to apply to the system with shroud-rim for the present range of parameters.
- Impingement dominance of rotor heat transfer coefficient depends upon both Re_m and G . Typical impingement characteristics with regard to magnitude and extent of influence are observed. Stator flow reattachment location and heat transfer coefficient magnitude are also primarily affected by G and to some extent Re_m .
- The radial location at which the rotor heat transfer coefficient is observed to be influenced by rotation depends upon Re_{ρ} and G . The stator heat transfer coefficient appears to be little affected by rotation.
- The stator heat transfer level is sufficiently high to have a significant effect upon the radially local mixed mean fluid temperature. It is therefore necessary to have knowledge of the stator heat transfer coefficients, and to apply them properly, in order to utilize rotor heat transfer coefficients correctly.

Acknowledgments

The research described in this paper has been supported through a Research Fellowship granted to R. S. Bunker by the Alexander von Humboldt-Stiftung. Thanks are due to K.-H. Platzer for his help in setting up the test facility.

References

- Bayley, F. J., and Owen, J. M., 1970, "The Fluid Dynamics of a Shrouded Disk System With a Radial Outflow of Coolant," *ASME Journal of Engineering for Power*, Vol. 92, pp. 335-341.
- Bunker, R. S., and Metzger, D. E., 1988, "Local Heat Transfer in Internally Cooled Turbine Airfoil Leading Edge Regions—Part I: Impingement Cooling Without Film Coolant Extraction," *Heat Transfer in Gas Turbine Engines and Three-Dimensional Flows*, Elovic, O'Brien, and Pepper, eds., ASME HTD-Vol. 103, pp. 53-63.
- Cobb, E. C., and Saunders, O. A., 1956, "Heat Transfer From a Rotating Disk," *Proceedings of the Royal Society*, Vol. 236A, pp. 343-351.
- Daily, J. W., and Nece, R. E., 1960, "Chamber Dimension Effects on Induced Flow and Frictional Resistance of Enclosed Rotating Disks," *ASME Journal of Basic Engineering*, Vol. 82, pp. 217-232.
- Dibelius, G., Radtke, F., and Ziemann, M., 1984, "Experiments on Friction, Velocity and Pressure Distribution of Rotating Disks," in: *Heat and Mass Transfer in Rotating Machinery*, D. E. Metzger and N. H. Afgan, eds., Hemisphere, Washington, DC, pp. 117-130.
- Gardon, R., and Cobonpue, J., 1962, "Heat Transfer Between a Flat Plate and Jets of Air Impinging on It," *International Developments in Heat Transfer, Proceedings, 2nd International Heat Transfer Conference*, ASME, New York, pp. 454-460.

- Gardon, R., and Akfirat, J. C., 1965, "The Role of Turbulence in Determining the Heat Transfer Characteristics of Impinging Jets," *International Journal of Heat and Mass Transfer*, Vol. 8, pp. 1261-1272.
- Haaser, F., Jack, J., and McGreehan, W., 1988, "Windage Rise and Flowpath Gas Ingestion in Turbine Rim Cavities," *ASME Journal of Engineering for Gas Turbines and Power*, Vol. 110, pp. 78-85.
- Haynes, C. M., and Owen, J. M., 1975, "Heat Transfer From a Shrouded Disk System With a Radial Outflow of Coolant," *ASME Journal of Engineering for Power*, Vol. 97, pp. 28-36.
- Hirsch, C., 1987, "Aufbau und Inbetriebnahme eines Versuchsstandes zur instationären Wärmeübergangsmessung an rotierenden Scheiben bei erzwungener Konvektion und Prallkühlung unter Nutzung thermochromer Flüssigkristalle als Temperaturindikatoren," *Diplomarbeit No. 302*, Institut für Thermische Strömungsmaschinen, Universität Karlsruhe, Federal Republic of Germany.
- Kline, S. J., and McClintock, F. A., 1953, "Describing Uncertainties in Single Sample Experiments," *Mechanical Engineering*, Vol. 75, pp. 3-8.
- Kreith, F., Taylor J. H., and Chong, J. P., 1959, "Heat and Mass Transfer From a Rotating Disk," *ASME Journal of Heat Transfer*, Vol. 81, pp. 95-105.
- Kreith, F., Doughman, E., and Kozlowski, H., 1963, "Mass and Heat Transfer From an Enclosed Rotating Disk With and Without Source Flow," *ASME Journal of Heat Transfer*, Vol. 85, pp. 153-163.
- Metzger, D. E., 1970, "Heat Transfer and Pumping on a Rotating Disk With Freely Induced and Forced Cooling," *ASME Journal of Engineering for Power*, Vol. 92, pp. 342-348.
- Metzger, D. E., and Grochowsky, L. D., 1977, "Heat Transfer Between an Impinging Jet and a Rotating Disk," *ASME Journal of Heat Transfer*, Vol. 99, pp. 663-667.
- Metzger, D. E., Mathis, W. J., and Grochowsky, L. D., 1979, "Jet Cooling at the Rim of a Rotating Disk," *ASME Journal of Engineering for Power*, Vol. 101, pp. 68-72.
- Metzger, D. E., and Larson, D. E., 1986, "Use of Fusion Point Surface Coatings for Local Convection Heat Transfer Measurements in Rectangular Channel Flows With 90-Degree Turns," *ASME Journal of Heat Transfer*, Vol. 108, pp. 48-54.
- Metzger, D. E., Bunker, R. S., and Bosch, G., 1991, "Transient Liquid Crystal Measurement of Local Heat Transfer on a Rotating Disk With Jet Impingement," *ASME JOURNAL OF TURBOMACHINERY*, Vol. 113, pp. 52-59.
- Owen, J. M., and Phadke, U. P., 1980, "An Investigation of Ingress for a Simple Shrouded Rotating Disk System With a Radial Outflow of Coolant," *ASME Paper No. 80-GT-49*.
- Owen, J. M., 1984, "Fluid Flow and Heat Transfer in Rotating Disk Systems," *Heat and Mass Transfer in Rotating Machinery*, D. E. Metzger and N. H. Afgan, eds., Hemisphere, Washington, DC, pp. 81-104.
- Phadke, U. P., and Owen, J. M., 1983, "An Investigation of Ingress for an 'Air-Cooled' Shrouded Rotating Disk System With Radial-Clearance Seals," *ASME Journal of Engineering for Power*, Vol. 105, pp. 178-183.
- Platzer, K.-H., Hirsch, C., Metzger, D. E., and Wittig, S., 1991, "Applications of Thermochromic Liquid Crystals (TCL) for Surface Temperature Measurement and Local Heat Transfer Coefficient Determination Using a Computer Based Color Detection System," *Experiments in Fluids*, in press.
- Popiel, C. O., and Boguslawski, L., 1986, "Local Heat Transfer From a Rotating Disk in an Impinging Round Jet," *ASME Journal of Heat Transfer*, Vol. 108, pp. 357-364.
- Qureshi, G., Nguyen, M. H., Saad, N. R., and Tadros, R. N., 1989, "Heat Transfer Measurements for Rotating Turbine Discs," *ASME Paper No. 89-GT-236*.
- Schlichting, H., 1979, *Boundary-Layer Theory*, 7th ed., McGraw-Hill, New York.
- Uzkan, T., and Lipstein, N. J., 1986, "Effects of Honeycomb-Shaped Walls on the Flow Regime Between a Rotating Disk and a Stationary Wall," *ASME Journal of Engineering for Gas Turbines and Power*, Vol. 108, pp. 553-561.
- Vedula, R. P., Bickford, W., and Metzger, D. E., 1988, "Effects of Lateral and Anisotropic Conduction on Determination of Local Convection Heat Transfer Characteristics With Transient Tests and Surface Coatings," *Collected Papers in Heat Transfer*, ASME HTD-Vol. 14, pp. 21-27.
- von Karman, T., 1921, "Über laminare und turbulente Reibung," *Z. angew. Math. Mech.*, Vol. 1, p. 233.

Local Heat Transfer in Turbine Disk Cavities: Part II—Rotor Cooling With Radial Location Injection of Coolant

R. S. Bunker

D. E. Metzger

S. Wittig

Lehrstuhl und Institut für Thermische
Strömungsmaschinen,
Universität Karlsruhe,
Karlsruhe, Federal Republic of Germany

Detailed radial distributions of rotor heat transfer coefficients are presented for three basic disk-cavity geometries applicable to gas turbines. The experimental apparatus has been designed to obtain local heat transfer data on a number of easily interchangeable rotor surfaces. The method employs thin thermochromic liquid crystal coatings upon the rotor surfaces together with video system data acquisition and computer-assisted image analysis to detect surface color display and to extract heat transfer information. A thermally transient, aerodynamically steady technique is used, which attains consistent thermal boundary conditions over the entire disk cavity. Cooling air is introduced into the disk cavity via a single circular jet mounted perpendicularly into the stator at one of the three radial locations: 0.4, 0.6, or 0.8 times the rotor radius. Rotor heat transfer coefficients have been obtained over a range of parameters including disk rotational Reynolds numbers of 2 to 5×10^5 , rotor/stator hub spacing-to-disk radius ratios of 0.025 to 0.15, and jet mass flow rates between 0.10 and 0.40 times the turbulent pumped flow rate of a free disk. The rotor surfaces include a parallel rotor-stator system, a rotor with 5 percent diverging taper, and a similarly tapered rotor with a rim sealing lip at its extreme radius. Results are presented showing the effects of the parallel rotor, which indicate strong variations in local Nusselt numbers for all but rotational speed. These results are compared to associated hub injection data of Part I of this study, demonstrating that overall rotor heat transfer is optimized by either hub injection or radial location injection of coolant dependent upon the configuration. Results with the use of the tapered rotor show significant variations in local Nusselt number compared with those of the parallel rotor, while the addition of a rim sealing lip appears to increase the Nusselt number level.

Introduction

In the design of high-temperature gas turbine engines, cooling air must be supplied to the various disk-shroud cavities, existing radially inboard from the blades and vanes, particularly to those in high pressure turbine initial stages. The cooling air, drawn from the engine compressor, is used both to actively cool the rotating disk and to discourage the ingestion of hot mainstream gases into the cavity region. For many reasons, designers require a detailed knowledge of convective heat transfer characteristics to provide the most efficient use of cooling air over the applicable range of engine operating conditions. In particular, knowledge of the temperature distribution on turbine disks is necessary to predict stresses and durability. This has direct impact upon the disk dimensions and radial positioning, and so also upon blade tip clearances and leakage

flows. Also, the inherent pumping action of the rotating disk (rotor) serves to ingest hot turbine passage gases into the disk cavity to replenish the pumped flow, thereby elevating cavity temperatures. To accomplish disk cooling with a minimum of supply air, a knowledge of local convective heat transfer information is necessary. In minimizing the coolant air required, designers also minimize wheel space windage, reduce the engine cycle penalty associated with drawing of compressor air, and reduce the thermodynamic penalty associated with mixing of the cooling air into the mainstream. Thus the potential benefits to be drawn from a more precise knowledge of disk-cavity heat transfer are considerable.

Many researchers have been involved in the study of rotating disk and disk-cavity heat transfer and fluid flow over the past several decades. Early works include the analysis of von Karman (1921), the experiments of Cobb and Saunders (1956), Kreith et al. (1959 and 1963), and Daily and Nece (1960). A comprehensive review of flow and heat transfer in simple, basic disk-shroud geometries is presented by Owen (1984). Most of

Contributed by the International Gas Turbine Institute and presented at the 35th International Gas Turbine and Aeroengine Congress and Exposition, Brussels, Belgium, June 11-14, 1990. Manuscript received by the International Gas Turbine Institute January 13, 1990. Paper No. 90-GT-26.

the studies to date have obtained rotor-averaged heat transfer coefficients by the use of conventional heat transfer measurement methods. Many of the works have dealt exclusively with free disk heat transfer, most with hub injection coolant. Of those studies that have sought rotor heat transfer information in basic shrouded disk systems, most have done so without the application of consistent thermal boundary conditions upon all of the cavity walls. Investigations that have obtained more localized rotor heat transfer information include those of Metzger et al. (1979) dealing with jet impingement onto the rim of a free rotating disk, Popiel and Boguslawski (1986) looking at local free disk heat transfer at a particular radial location with jet impingement at the hub or at the radial location of measurement, and Qureshi et al. (1989), which measured local rotor coefficients for a specific turbine disk section geometry. All of these studies obtained radial-section-averaged heat transfer coefficients. Other factors that affect the disk-cavity flow field, and therefore also the heat transfer, include cavity geometry, the use of injection jet swirl, and the employment of various cavity sealing mechanisms. Some research into these areas has been noted in Part I of the present study.

The current study utilizes a transient method demonstrated by Metzger et al. (1989) to obtain detailed radial distributions of both rotor and stator heat transfer coefficients over a range of applicable parameters. The method uses a thin coating of a visually indicating material upon the surfaces of interest, with optical data acquisition of local surface temperatures to obtain heat transfer coefficients with consistent thermal boundary conditions over the entire disk cavity. A single injection jet is employed to deliver cooling air to the cavity by impingement onto the rotor; an overlapping shroud rim is used to reduce outer air ingestion. While Part I of this study investigated the heat transfer associated with hub injection of coolant into a parallel rotor-stator system, the present part deals with the more realistic case of radial location jet injection. Furthermore, the effect of small changes in the rotor geometry is demonstrated through the acquisition of detailed data on a slightly tapered rotor and also on a tapered rotor with a rim-sealing lip. Rotor heat transfer coefficient radial distributions are presented showing the independent effects of variations in jet mass flow rate, rotor-stator spacing, and rotational speed. The distributions at various radial injection locations are compared to associated hub injection distributions to ascertain the effect of injection location upon overall rotor heat transfer. Also, significant changes in local rotor heat transfer due to rotor geometry variations are indicated.

Experimental Apparatus and Procedures

A schematic of the test apparatus is shown in Fig. 1. The disk is rotated at speeds up to 10,000 rpm by a 400 W motor connected by toothed belt to the shaft bearings set upon which the disk is attached. The disk is composed of two pieces, as shown in the detailed test section schematic of Fig. 2. Also shown in Fig. 2 are cross sections of the three disk insert pieces,

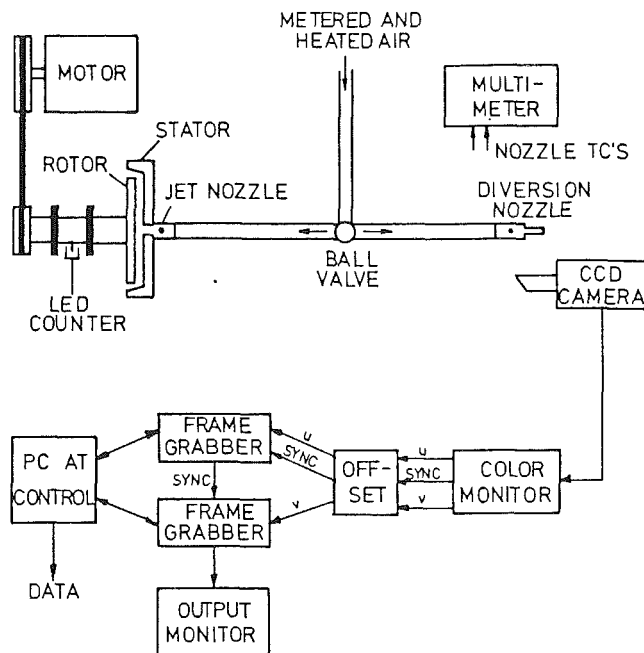


Fig. 1 Schematic of test apparatus

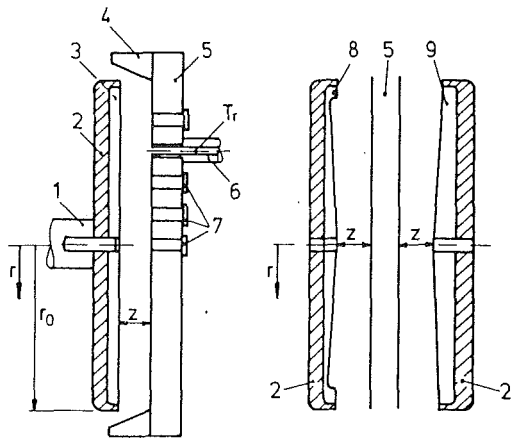
each made of black, cell-cast acrylic plastic of 10 cm radius and 6.5 mm thickness (portions of the tapered rotor are less thick). Black acrylic plastic is used to provide improved surface coating visual display. The plastic disk is fit tightly into an aluminum retaining disk, and the two-piece assembly is fastened to the rotating shaft.

The rotating disk is faced by a plane stationary shroud, or stator disk, at a spacing of z . The stator surface is maintained normal to the axis of rotation and positioned laterally with a shroud support and precision positioning table. The shroud includes an attached rim at the stator disk edge to discourage entrainment of air into the disk cavity from the rim region. The shroud rim is positioned so that it overlaps the disk edge and angled to direct jet supplied air out of the disk cavity and away from the apparatus. The stator disk is made of clear acrylic plastic of 15 mm thickness. The stator disk contains five jet nozzle insert holes at radial locations of $r_j/r_o = R_j = 0, 0.2, 0.4, 0.6, \text{ and } 0.8$. The jet nozzle, also made of acrylic plastic, is insert at the desired radial location while the remaining insert holes are plugged with solid acrylic plastic pieces. The jet nozzle is circular with 0.5 cm i.d. and is fitted with a thermocouple to indicate the jet transient temperature.

The rotating shaft is affixed with a small, lightweight finger for the purpose of breaking the circuit of a light-emitting diode (LED), which is affixed between the bearing housings. The output from the LED is then sent to an electronic counter to monitor the rotational speed of the shaft, and so also the disk.

Nomenclature

f = rotational frequency	r = radial location	T_i = initial temperature
G = dimensionless rotor/stator spacing = z/r_o	r_o = disk radius	T_r = reference temperature
h = convective heat transfer coefficient	$Re_m = \frac{Q}{2\pi z \nu}$ = flow Reynolds number	U, V = chrominance signals
k = thermal conductivity	$Re_{r_o} = \frac{\omega r_o^2}{\nu}$ = disk rotational Reynolds number	z = rotor/stator spacing
$Nu_{r_o} = \frac{hr_o}{k_{air}}$ = Nusselt number	$R_j = \frac{r_j}{r_o}$ = relative jet radial location	α = thermal diffusivity
\dot{Q} = jet volumetric flow rate	$R_T = \frac{Q/Q_p}{Q/Q_p}$ = turbulent pumping ratio	θ = time
Q_p = turbulent pumped flow of a free disk = $0.219r_o^3\omega Re_{r_o}^{-0.2}$ per Schlichting (1979)	T = temperature	μ = fluid dynamic viscosity
		ν = kinematic viscosity = μ/ρ
		ρ = fluid density
		τ = time step
		ω = angular speed = $2\pi f$



- 1 SHAFT
- 2 ALUMINIUM RETAINER
- 3 PLANE ACRYLIC DISK
- 4 SHROUD RIM
- 5 CLEAR ACRYLIC SHROUD
- 6 JET NOZZLE
- 7 INSERT PLUGS
- 8 TAPERED DISK WITH RIM SEALING LIP
- 9 TAPERED DISK

Fig. 2 Details of test section and rotor geometries

Laboratory compressed air is supplied to the apparatus through a filtering pressure regulating valve, followed by a flow regulating needle valve. The air is metered through an orifice, which has been accurately calibrated using a gas counter. After metering, the air flow is heated, and thence proceeds to the ball diverter valve.

A test begins with heated air first diverted away from the test sections so that the test section and jet nozzle remain uniformly at the laboratory ambient temperature. The diversion channel is composed of a length of flexible hose and jet nozzle identical to those of the test section. The nozzle is also fitted with a thermocouple to monitor the fluid temperature prior to the test. The diverter valve remains in the diverted position until steady flow and a steady-state temperature have been achieved in the diversion channel. At that time the valve is used suddenly to route the heated air flow through the test section. The data acquisition program is initiated simultaneously with the change of valve position.

The surface coating used in this study is a Thermochromic Liquid Crystal (TLC) painted on the entire rotor surface. The color responses of the thin TLC coatings (less than 5×10^{-3} cm) in the presence of a heated air stream are used to determine the local surface heat transfer rates. Metzger et al. (1991) present a more detailed discussion of the use of TLC, so only a few brief notes will be mentioned here with regard to the specific TLC used. The material used in the present tests is a commercially available, chiral nematic TLC (BDH Thermochromics, Type TCA262: R38C1W, Poole, England). For this TLC, the nominal temperatures for the initiation of red, green, and blue under room lighting conditions are 37°C , 37.5°C , and 38°C , respectively. In the current usage, both the application of a uniform intensity studio light and the use of black acrylic plastic serve to improve the TLC color display.

As a test proceeds, the TLC at various radial locations changes color and is detected by the data acquisition system shown in Fig. 1. A particular surface temperature is determined by detecting a desired color. The system utilizes a color CCD camera whose signal is sent to a color monitor, from which signals are sent to two frame grabbers for processing of the image. When a small region of the surface covered by a single

pixel has been determined to satisfy preset conditions, the surface temperature at this point is known. The desired color and preset conditions are determined through calibration of the system using a TLC-coated aluminum bar. Part I of the present work contains a concise description of the method of color detection utilized, known as the chrominance method. Briefly stated, chrominance signals are color difference signals, which in a two-dimensional color plane or color circle contain the information necessary to ascertain a particular color. These signals are available from a standard color video system, and are denoted in Fig. 1 as U and V . By comparing the displayed chrominance values of a pixel of TLC-coated surface with desired or calibrated chrominance values, it is possible to determine that this pixel has the desired color to within some tolerance criterion. The computation required to determine color, and so also surface temperature for each pixel, is carried out by computer algorithm for a fine surface mesh of pixels.

A brief description of the experimental technique employed in this study is given here. Details of this technique as used with melting point surface coatings may be found from Metzger and Larson (1986). A test is started by the sudden diversion of a heated flow, of some desired steady-state mass flow rate and temperature, into the disk cavity. For the acrylic plastic test surfaces, the depth of heating into the walls over the time duration of the test is less than the wall thickness. In addition, lateral condition in the walls has been shown by Metzger and Larson (1986) and in more detail by Vedula et al. (1988) to have a negligible effect upon the local surface temperature response. At any surface point, the wall (rotor or stator) temperature is thus represented by the classical one-dimensional response of a semi-infinite medium to the sudden step application of a convecting fluid at temperature T_r ,

$$\frac{T - T_i}{T_r - T_i} = 1 - \exp\left(\frac{h^2}{k^2} \alpha \theta\right) \operatorname{erfc}\left(\frac{h}{k} \sqrt{\alpha \theta}\right) \quad (1)$$

If each surface point were subjected to a true step increase in T_r , then measurement of the required times to reach a pre-determined TLC color, and therefore temperature, allows solution of equation (1) for the heat transfer coefficients. This is the essence of the model, with the thin layer of TLC providing a means of acquiring an array of temperature-time pairs over the surfaces.

However, in actual practice, the wall surfaces will not experience a pure step change in air temperature because of the transient heating of upstream regions. Nevertheless, equation (1) is a fundamental solution that can be used to represent the response to a superposed set of elemental steps in T_r , arranged to represent the actual air temperature rise

$$T - T_i = \sum_{i=1}^N U(\theta - \tau_i) \Delta T_r \quad (2)$$

where

$$U(\theta - \tau_i) = 1 - \exp\left(\frac{h^2}{k^2} \alpha (\theta - \tau_i)\right) \operatorname{erfc}\left(\frac{h}{k} \sqrt{\alpha (\theta - \tau_i)}\right) \quad (3)$$

By recording the T_r variation with time, and approximating it by steps, the resulting superposed solution given by equations (2) and (3) is solved for the local surface heat transfer coefficients using observed local color response times.

In the present research, a digital multimeter is used to observe the response of T_r during each test. By recording the value of T_r at the midtime of a test transient, equation (1) is solved for the heat transfer coefficients by using this T_r as a single-step approximation to the actual variation. This study utilizes the injection jet temperature as the reference temperature. Because of the small jet diameter, 5 mm, the actual response of T_r with time very nearly approximates a true step change response. Thus, the use of a single-step solution does, in this instance,

give an acceptable accuracy without an undue increase in experimental uncertainty. Using the single-sample experimental methods of Kline and McClintock (1953), the estimated uncertainty in the present experiments is ± 10 percent.

While the present work obtains local heat transfer coefficients based upon the jet inlet temperature to surface temperature difference, certain cases do allow an approximate analysis to be performed to obtain coefficients based upon a computed local mixed mean fluid temperature. This was the case in Part I of the present study dealing with hub injection of coolant. For radial location injection, however, the flow field is not known to a degree that would enable the application of an appropriate energy balance. Hence, the results reported herein are all presented on the basis of jet inlet temperature.

Results and Discussion

The changes in heat transfer behavior for radial location injection as compared to hub injection will be seen to be substantial, and are to a large extent due to the considerable alteration of the flow field. In the present study, this flow field change has ramifications upon both the rotor and stator heat transfer. Dealing first with the rotor, hub injection of coolant involved an axisymmetric flow, which was entirely outward on the rotor surface. Consider now the case of some $R_j > 0$ injection, which impinges upon the rotor at a single radial location as the rotor surface is swept beneath the single jet. In the immediate impingement location, the flow will remain axisymmetric about the stagnation point. However, away from the stagnation point the rotor flow will develop asymmetries with respect to the injection axis, which will depend upon radial location, mass flow rate, rotational speed, and spacing. As shown by the study of Metzger and Grochowsky (1977), the flow field may be either impingement dominated or rotationally dominated; there also exists a transition region between these extremes. For the present experiments, the flow field is typically impingement dominated and so tends to a partitioning of the flow about the radius of impingement, with roughly half going inboard and half proceeding outboard. The strength and duration of this partitioning will depend upon radial injection location and all variable parameters to some magnitude. In fact, for the anticipated turbulent flow field of the present study the specifics of the flow remain unknown so that no reasonably accurate heat balance may be performed to determine local fluid mean temperatures. Were the jet to be delivered as an annular jet, axisymmetry would be preserved about the axis of rotation and a reasonable knowledge of the flow field could be assumed. However, for the same mass flow rate supplied, Metzger et al. (1979) have shown that a single jet provides better heat transfer when operating in the impingement dominated regime; hence its use in the present study.

With regard to the rotor heat transfer, this also no longer takes place in an axisymmetric manner. For hub injection of coolant, the heat transfer between jet fluid and rotor surface takes place over the entire disk as the jet fluid spreads out on its outward radial journey. For radial location jet injection, the situation changes to one of a jet spreading inboard and outboard from the impingement location. Here the heat transfer occurs as the rotor sweeps beneath the jet flow. Depending upon the configuration, the jet flow may not spread over the entire disk surface. The jet flow is certainly more of a one-sided flow over the disk, to a lesser or greater extent. While the swept area of the rotor surface increases with r^2 as R_j is increased, the area of the disk surface upon which the jet spreads decreases relative to the total disk surface area. A consequence of this character will be seen later in the rotor heat transfer results.

The flow field on the stator surface for $R_j > 0$ remains basically axisymmetric with respect to the axis of injection. Thus, as with hub injection of coolant, the stator surface

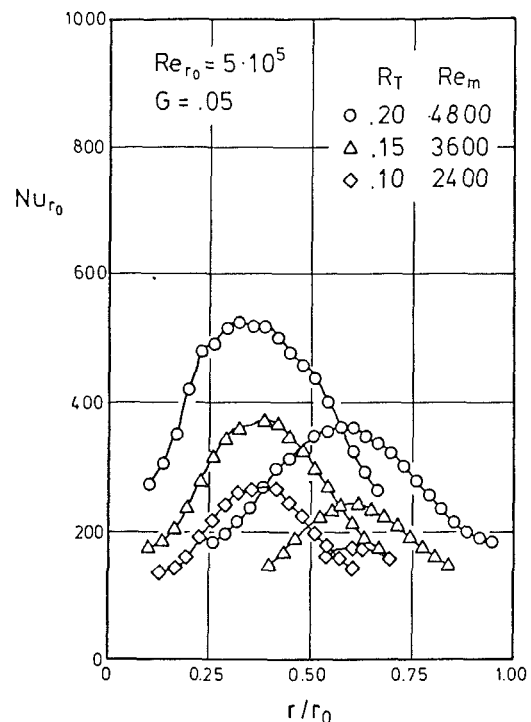


Fig. 3 Effect of Re_m on Nu_{r_0} for $R_j = 0.4$ and 0.6 , parallel rotor with $Re_{r_0} = 5 \times 10^5$ and $G = 0.05$

experiences flow reattachment and outward flow in the sense of the injection location as the origin. As shown with hub injection, the region of the stator surface that experiences significant heat transfer (on the same order as the rotor heat transfer) may increase or decrease depending upon the particular configuration. Due again to the more one-sided nature of the present flow, as R_j increases, the area of stator surface that experiences significant heat transfer is expected to decline. The stator heat transfer then has less influence with respect to the overall disk-cavity heat transfer, although it still has an impact upon the local fluid mean temperature distribution on the side of the disk that contains the jet. Certainly also, the stator heat transfer has its influence upon the rotor heat transfer coefficients, and thus the stator thermal boundary condition must be properly retained.

Parallel Rotor/Stator Geometry. The basic impingement-dominated results with respect to variations in Re_m are shown in Fig. 3 for both $R_j = 0.4$ and 0.6 with $Re_{r_0} = 5 \times 10^5$ and $G = 0.05$. At this rotor-stator spacing as well as others examined, a clear dependence of rotor heat transfer coefficient (or rotor heat transfer) upon mass flow rate is seen. Expressing this dependence as Re_m^n , the exponent n appears to be variable, increasing as mass flow rate is increased. This characteristic of an increasing exponent is consistent with free disk impingement heat transfer data of Metzger and Grochowsky (1977), which showed a similar dependence in the impingement-dominated regime of rotor heat transfer.

For all spacings G , the radial heat transfer coefficient distributions are basically symmetric in the immediate region of the radius of impingement (i.e., like a normal distribution). This symmetry may be noted in Fig. 4 where spacings of $G = 0.05, 0.10,$ and 0.15 are compared for $Re_{r_0} = 5 \times 10^5$ and $R_T = 0.20$, again for both $R_j = 0.4$ and 0.6 . At the more inboard injection location of $R_j = 0.4$ however, asymmetries exist particularly for larger G spacings as the level of rotor heat transfer coefficient remains high inboard of impingement, while that outboard declines more rapidly. This is most apparent for high mass flow rates, whereas low flow rate coefficient dis-

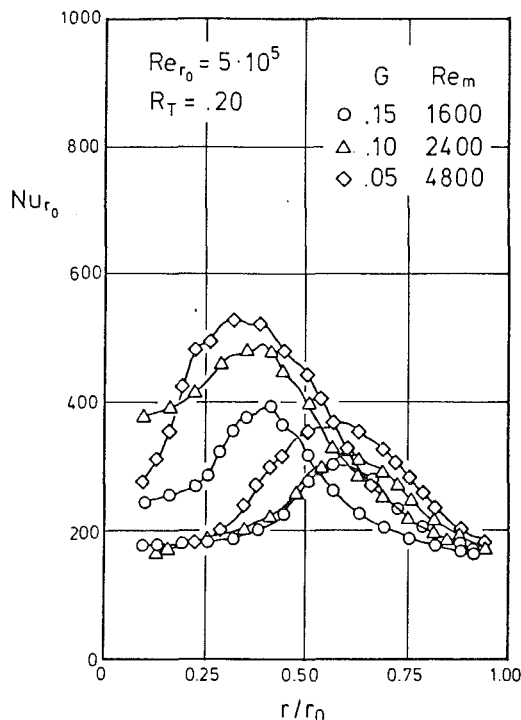


Fig. 4 Effect of G on Nu_{r_0} for $R_j = 0.4$ and 0.6 , parallel rotor with $Re_{r_0} = 5 \times 10^5$ and $R_T = 0.20$

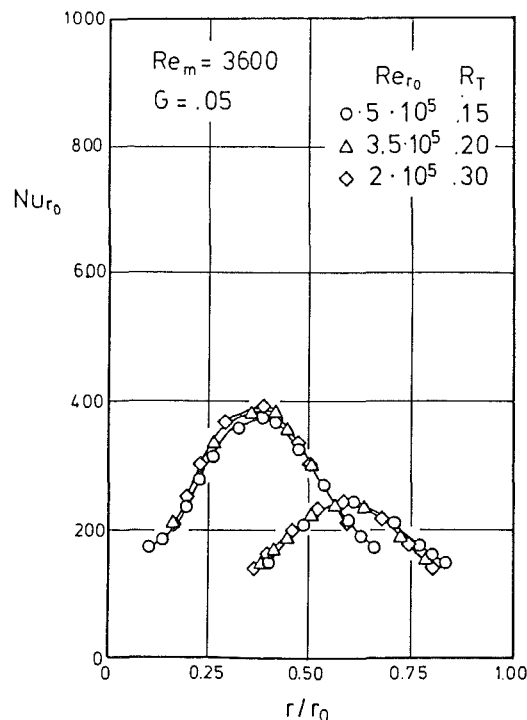


Fig. 5 Effect of Re_{r_0} on Nu_{r_0} for $R_j = 0.4$ and 0.6 , parallel rotor with $Re_m = 3600$ and $G = 0.05$

tributions tend back toward symmetry. At the lower spacing of $G = 0.05$, all mass flow rates result in essentially symmetric coefficient distributions about impingement and over the entire radial extent of the data as shown in Fig. 3. Here though, the distribution is less peaked and the coefficient radial gradients are steeper both inboard and outboard, with some gradient reduction as mass flow is decreased. At $G = 0.025$, the heat transfer coefficient radial distributions are not only similar in nature to those at $G = 0.05$, they are in fact essentially identical in both form and magnitude for all R_j tested. As expected for impingement-dominated heat transfer, the magnitude of rotor heat transfer coefficient at impingement increases as the spacing is decreased until an optimal spacing is reached, below which no further increase in heat transfer occurs. At larger spacings, the spread of the jet prior to impingement is greater and so the result of a lesser inboard radial gradient. The more rapid decline outboard of impingement may be attributed to the increasing heat transfer surface area, in contrast with the decreasing area radially inboard. At lower spacings, the jet spread prior to impingement is less and a more axisymmetric heat transfer is evident about the stagnation point. This results in the retention of a higher magnitude of heat transfer over a larger radial segment about the impingement radius, as well as the higher inboard and outboard radial gradients as the fluid velocity decreases.

With regard to the rotor heat transfer coefficient radial distributions at $R_j = 0.6$, shown in Figs. 3 and 4, and also at $R_j = 0.8$, the features noted for $R_j = 0.4$ are again present but to a much smaller degree. The asymmetries discussed for the larger spacings exist only slightly at these more outboard radial injection locations. In addition, the coefficient magnitude and radial gradient differences between distributions at various spacings are greatly reduced: for example, the close proximity of distributions for $R_j = 0.6$ at $G = 0.10$ and 0.15 shown in Fig. 4. In essence, the distinctions associated with variations in rotor-stator spacing at $R_j = 0.4$ are being merged at the greater R_j locations. These changes may be reasonably associated with the great increase in surface area of the rotor being swept under the impinging jet as R_j is increased. This

increase in area for heat transfer not only reduces the local magnitude of heat transfer as R_j is increased, but also tends to smooth out to some extent local differences arising from a change in spacing.

Figure 5 depicts the effect of rotational speed upon rotor heat transfer coefficient distributions for $R_j = 0.4$ and 0.6 with $Re_m = 3600$ and $G = 0.05$. Both here and at the higher spacing of $G = 0.10$, there are no definite changes to be seen in rotor heat transfer coefficients over the range of rotational speeds tested.

Comparisons to Hub Injection. Part I of the present study dealt exclusively with hub injection of coolant and obtained rotor and stator heat transfer coefficient radial distributions based upon either the jet inlet temperature or upon a computed local mixed mean fluid temperature. At this point, several of the radial location injection distributions for the rotor and the associated hub injection distribution may be brought together to discern the overall character of rotor heat transfer with respect to injection location R_j . Figures 6–8 show three typical composite Nu_{r_0} plots with rotor heat transfer coefficient distributions for $R_j = 0, 0.4, 0.6$, and 0.8 , all based upon jet inlet temperature. Each figure depicts results for $Re_{r_0} = 5 \times 10^5$ and $R_T = 0.20$, for the rotor-stator spacings of $G = 0.15, 0.10$, and 0.05 , respectively. In each composite figure, the heat transfer at and radially outboard of impingement for every $R_j > 0$ exceeds the hub injection heat transfer level at these radial locations. The amount by which these radial location injection coefficients exceed those of hub injection depends upon the nature of the rotor flow field and heat transfer at each spacing G . For instance, the very great differences observed at $G = 0.05$ are due in part to this being the optimal impingement spacing at $R_j > 0$, and in part to the decreased hub injection heat transfer (noted in Part I of this work) as G is decreased toward a Couette-type flow. As noted earlier, the impingement heat transfer level decreases as R_j is increased for a particular configuration; this is clearly seen in each composite figure. However, this decrease is not in strict accord with the increase in surface area available for heat transfer at impingement; it

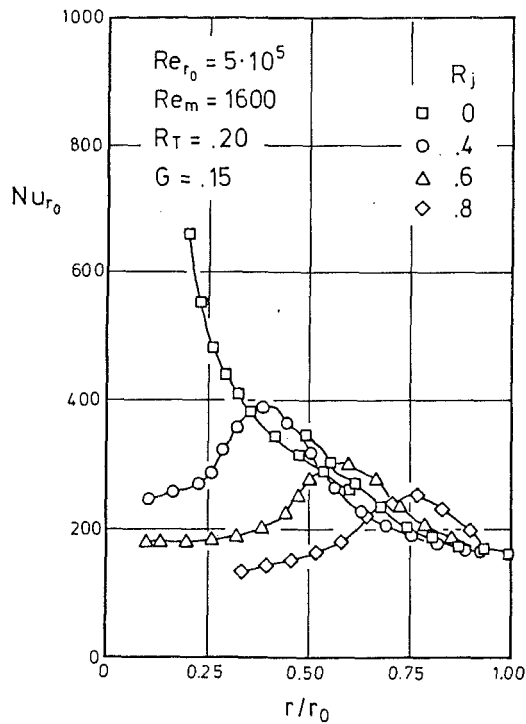


Fig. 6 Radial Nu_{r_0} distributions with varying R_j for parallel rotor with $Re_{r_0} = 5 \times 10^5$, $Re_m = 1600$, $G = 0.15$

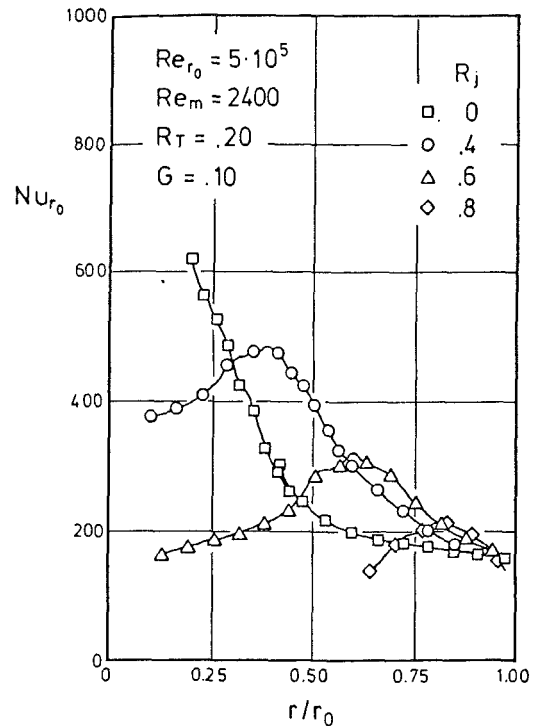


Fig. 7 Radial Nu_{r_0} distributions with varying R_j for parallel rotor with $Re_{r_0} = 5 \times 10^5$, $Re_m = 2400$, $G = 0.10$

is less than a $1/r^2$ decline. Neither is this decrease uniform between configurations, as a comparison of Figs. 6–8 shows it to be changing with spacing G . The explanation lies in the altered flow field for which the jet spreads out over a decreased area of the rotor, relative to that for $R_j = 0$, as R_j is increased. The very substantial result is that for rotor–stator spacings of $G \leq 0.10$ in the present range of experiments, overall rotor heat transfer is greatest for jet injection at some median radial location (e.g., $0.4 < R_j < 0.6$). At the larger spacing of $G = 0.15$, overall rotor heat transfer appears to be greatest with jet injection at the hub. These results with respect to spacing do change however for lower mass flow rates than those shown in Figs. 6–8. Typically, as Re_m is decreased the reduction in local rotor heat transfer coefficients is less for $R_j = 0$ than for $R_j > 0$, resulting in overall rotor heat transfer being greatest for injection at the hub. This was the case for the limited data of Metzger et al. (1991) which utilized a spacing of $G = 0.10$ and a mass flow rate of $Re_m = 1850$ for comparison of R_j cases. The effect of rotational speed upon these results is to strengthen the $R_j > 0$ rotor heat transfer relative to that with $R_j = 0$, since it has been seen that rotational speed changes have little effect upon rotor heat transfer with $R_j > 0$ yet serve to reduce rotor heat transfer with decreasing rotational speed for $R_j = 0$. Finally, one common feature of each composite figure may be discerned, that in all cases the rotor heat transfer coefficients progress to essentially the same level at the disk edge; that level being independent of R_j and also of G . This demonstrates the similarity of the heat transfer and flow field at the disk edge regardless of the upstream conditions associated with varying R_j injection location.

Tapered Rotor Geometries. To discern the effect of small geometry changes upon rotor heat transfer coefficient radial distribution, a new rotor acrylic plastic insert piece was coated with TLC and mounted in the test assembly. As shown in Fig. 2, a more realistic rotor surface was fabricated with a diverging taper of about 5 percent, and a rim sealing lip at the disk edge. The stator in this new disk-cavity geometry is the same plane stator used previously. Figures 9–11 show the rotor heat trans-

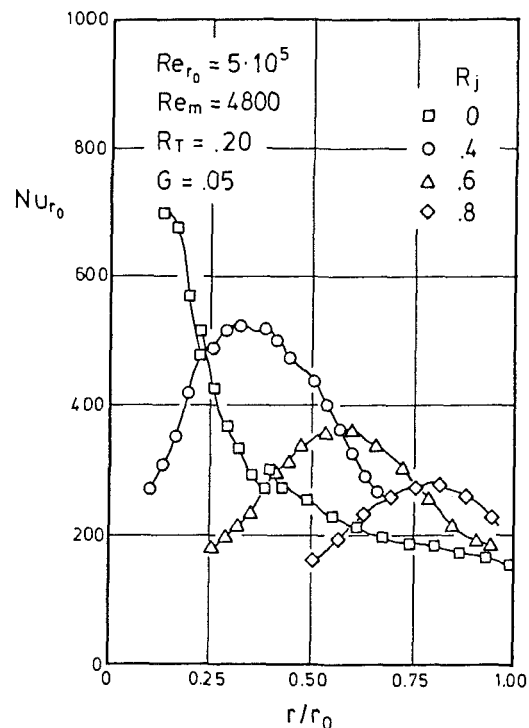


Fig. 8 Radial Nu_{r_0} distributions with varying R_j for parallel rotor with $Re_{r_0} = 5 \times 10^5$, $Re_m = 4800$, $G = 0.05$

fer coefficient distributions for both $R_j = 0.4$ and 0.6 , and for the same conditions as Figs. 3–5 dealing with the parallel rotor/stator geometry. Figure 9 depicts the Re_m effect, Fig. 10 shows the effect of spacing G , and Fig. 11 displays the effect of rotational speed Re_{r_0} . Most of the aspects of these coefficient distributions are similar to those already discussed for the parallel rotor/stator geometry, but with a few notable excep-

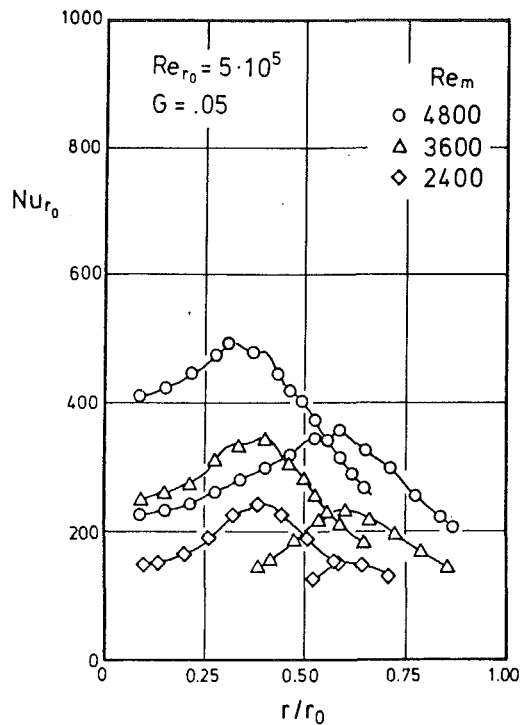


Fig. 9 Effect of Re_m on Nu_{r_0} for $R_j = 0.4$ and 0.6 , tapered rotor with lip, $Re_{r_0} = 5 \times 10^5$, $G = 0.05$

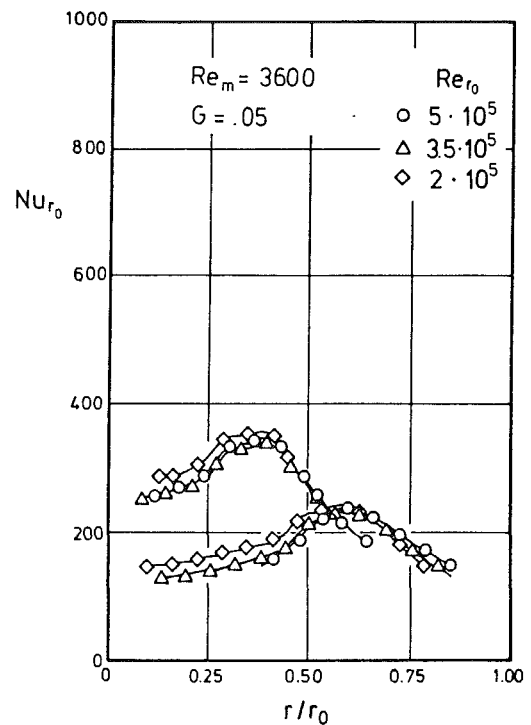


Fig. 11 Effect of Re_{r_0} on Nu_{r_0} for $R_j = 0.4$ and 0.6 , tapered rotor with lip, $Re_m = 3600$, $G = 0.05$

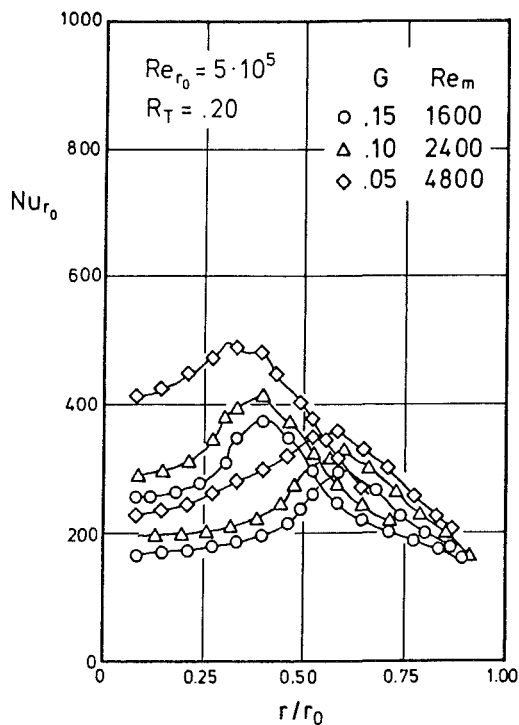


Fig. 10 Effect of G on Nu_{r_0} for $R_j = 0.4$ and 0.6 , tapered rotor with lip, $Re_{r_0} = 5 \times 10^5$, $R_T = 0.20$

tions. First, since the rotor is tapered away (radially outward) from the stator surface, the spacing G measured at the hub is less than the spacing at the radius of injection. For $R_j = 0.4$ this injection location spacing is about 0.02 greater than that at the hub (e.g., $G = 0.07$ rather than 0.05), while for $R_j = 0.6$ this spacing is about 0.03 greater than that at the hub. As a result, a comparison of Figs. 3 and 9 shows rotor heat transfer

to be reduced at the impingement location for the tapered rotor. This reduction corresponds to the increase in local spacing, and is of greater magnitude for $R_j = 0.4$ than for $R_j = 0.6$; this latter fact is associated with the same blending of distributions noted for increasing R_j with the parallel geometry. Second, unlike the parallel geometry, there does appear to be a small influence of rotational speed, particularly radially inboard of injection and more so for the larger R_j . The apparent reason for this effect is tied to the third and major change associated with this new geometry. In all cases, but more noticeably at $R_j = 0.4$ and at higher mass flow rates such as shown in Fig. 10, the level of rotor heat transfer radially inboard of R_j has increased substantially. This occurs to the extent that all radial distributions of a particular R_j now show essentially the same form of variation regardless of spacing, which was not the case for the parallel geometry. The plausible explanation for this change is the inboard acceleration of fluid caused by the converging volume that the radially inboard traveling fluid encounters. This rise in heat transfer level is greater than $R_j = 0.4$ due to the greater relative change in spacing as compared to that at $R_j = 0.6$, given the same mass flow rate and rotational speed. This also explains why the lower rotational speed results in a higher local rotor heat transfer coefficient inboard of injection, as the outward pumping action of the rotor is reduced while the inboard acceleration due to the surface taper remains constant.

Finally, to verify the effect of the tapered rotor positively, and to separate this from and identify the effect of the rim sealing lip, a third rotor insert piece was fabricated. As shown in Fig. 2, this additional rotor has no rim sealing lip but retains the diverging taper. Figure 12 shows a comparison of all three rotor geometries at $R_j = 0.4, 0.6$, and 0.8 for $Re_{r_0} = 5 \times 10^5$, $Re_m = 4800$, and $G = 0.05$. This comparison shows the rotor heat transfer coefficient radial distribution form to be the same for the tapered rotors with and without the rim sealing lip. The apparent effect of the rim sealing lip is to raise the magnitude of the entire radial distribution. This is accomplished as the lip effectively turns the flow up towards the stator,

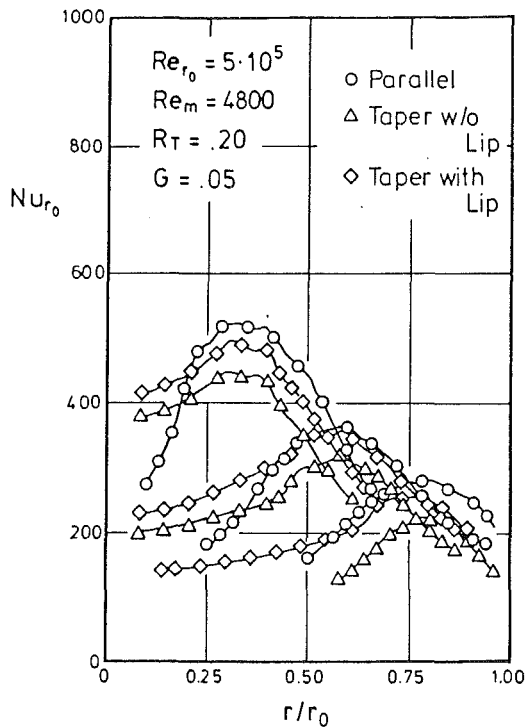


Fig. 12 Comparison of rotor geometry Nu_{r_0} results at $R_j = 0.4, 0.6,$ and 0.8 with $Re_{r_0} = 5 \times 10^5$, $Re_m = 4800$, $G = 0.05$

providing a better cavity seal against the ingestion of ambient air.

Summary and Conclusions

The principal conclusions of the present study can be summarized as follows:

- Detailed radial distributions of rotor heat transfer coefficients have been obtained with radial locations of coolant injection of $R_j = 0.4, 0.6,$ and 0.8 over a range of parameters applicable to the design of turbine disk cavities. The experimental method utilized has allowed the easy and inexpensive exchange of rotor surfaces such that geometry changes may be affected and analyzed with great versatility.

- In the parallel rotor/stator geometry with radial location injection, the radial coefficient distributions all show basically symmetric, normal distributions about the injection radius with some asymmetries noted at the more radially inboard R_j locations. A strong Re_m dependence is observed for all R_j locations; a strong dependence upon spacing G is also apparent, which diminishes as R_j is increased; little dependence upon rotational speed Re_{r_0} is seen.

- Comparisons of various radial location injection radial rotor heat transfer coefficient distributions with hub injection radial distributions obtained under the same conditions show that overall rotor heat transfer is optimized in the present geometry by either a median location of radial injection or by hub injection depending upon the parameters Re_m , Re_{r_0} , and G . Radial location injection typically results in higher overall rotor heat transfer for close spacings, high rotational speeds, and high mass flow rates.

- Significant radial distribution changes in the rotor heat transfer coefficients have been shown to occur for small changes in the rotor geometry.

Acknowledgments

The research described in this paper has been supported through a Research Fellowship granted to R. S. Bunker by the Alexander von Humboldt-Stiftung.

References

- Cobb, E. C., and Saunders, O. A., 1956, "Heat Transfer From a Rotating Disk," *Proceedings of the Royal Society*, Vol. 236A, pp. 343-351.
- Daily, J. W., and Nece, R. E., 1960, "Chamber Dimension Effects on Induced Flow and Frictional Resistance of Enclosed Rotating Disks," *ASME Journal of Basic Engineering*, Vol. 82, pp. 217-232.
- Kline, S. J., and McClintock, F. A., 1953, "Describing Uncertainties in Single Sample Experiments," *Mechanical Engineering*, Vol. 75, pp. 3-8.
- Kreith, F., Taylor, J. H., and Chong, J. P., 1959, "Heat and Mass Transfer From a Rotating Disk," *ASME Journal of Heat Transfer*, Vol. 81, pp. 95-105.
- Kreith, F., Doughman, E., and Kozlowski, H., 1963, "Mass and Heat Transfer From an Enclosed Rotating Disk With and Without Source Flow," *ASME Journal of Heat Transfer*, Vol. 85, pp. 153-163.
- Metzger, D. E., and Grochowsky, L. D., 1977, "Heat Transfer Between an Impinging Jet and a Rotating Disk," *ASME Journal of Heat Transfer*, Vol. 99, pp. 663-667.
- Metzger, D. E., Mathis, W. J., and Grochowsky, L. D., 1979, "Jet Cooling at the Rim of a Rotating Disk," *ASME Journal of Engineering for Power*, Vol. 101, pp. 68-72.
- Metzger, D. E., and Larson, D. E., 1986, "Use of Fusion Point Surface Coatings for Local Convection Heat Transfer Measurements in Rectangular Channel Flows With 90-Degree Turns," *ASME Journal of Heat Transfer*, Vol. 108, pp. 48-54.
- Metzger, D. E., Bunker, R. S., and Bosch, G., 1991, "Transient Liquid Crystal Measurement of Local Heat Transfer on a Rotating Disk With Jet Impingement," *ASME JOURNAL OF TURBOMACHINERY*, Vol. 113, pp. 52-59.
- Owen, J. M., 1984, "Fluid Flow and Heat Transfer in Rotating Disk Systems," *Heat and Mass Transfer in Rotating Machinery*, D. E. Metzger and N. H. Afgan, eds., Hemisphere, Washington, DC, pp. 81-104.
- Popiel, C. O., and Boguslawski, L., 1986, "Local Heat Transfer From a Rotating Disk in an Impinging Round Jet," *ASME Journal of Heat Transfer*, Vol. 108, pp. 357-364.
- Qureshi, G., Nguyen, M. H., Saad, N. R., and Tadros, R. N., 1989, "Heat Transfer Measurements for Rotating Turbine Discs," *ASME Paper No. 89-GT-236*.
- Schlichting, H., 1979, *Boundary-Layer Theory*, 7th ed., McGraw-Hill, New York.
- Vedula, R. P., Bickford, W., and Metzger, D. E., 1988, "Effects of Lateral and Anisotropic Conduction on Determination of Local Convection Heat Transfer Characteristics With Transient Tests and Surface Coatings," *Collected Papers in Heat Transfer*, ASME HTD-Vol. 104, pp. 21-27.
- von Karman, T., 1921, "Über laminare und turbulente Reibung," *Z. angew. Math. Mech.*, Vol. 1, p. 233.

Rotating Cavity With Axial Throughflow of Cooling Air: Heat Transfer

P. R. Farthing¹

C. A. Long

J. M. Owen²

J. R. Pincombe

Thermo-Fluid Mechanics Research Centre,
University of Sussex,
Falmer,
Brighton, BN1 9RH, United Kingdom

Heat transfer measurements were made in two rotating cavity rigs, in which cooling air passed axially through the center of the disks, for a wide range of flow rates, rotational speeds, and temperature distributions. For the case of a symmetrically heated cavity (in which both disks have the same temperature distribution), it was found that the distributions of local Nusselt numbers were similar for both disks and the effects of radiation were negligible. For an asymmetrically heated cavity (in which one disk is hotter than the other), the Nusselt numbers on the hotter disk were similar to those in the symmetrically heated cavity but greater in magnitude than those on the colder disks; for this case, radiation from the hot to the cold disk was the same magnitude as the convective heat transfer. Although the two rigs had different gap ratios ($G = 0.138$ and 0.267), and one rig contained a central drive shaft, there was little difference between the measured Nusselt numbers. For the case of "increasing temperature distribution" (where the temperature of the disks increases radially), the local Nusselt numbers increase radially; for a "decreasing temperature distribution," the Nusselt numbers decrease radially and become negative at the outer radii. For the increasing temperature case, a simple correlation was obtained between the local Nusselt numbers and the local Grashof numbers and the axial Reynolds number.

1 Introduction

The gas turbine designer needs to calculate the stress inside the compressor disks of an aeroengine under steady-state and transient conditions. During takeoff, the compressor blades and disk rim heat up much faster than the "cobs" or hubs of the disks; for landing, the reverse occurs. The resulting temperature gradients, which cause large thermal stresses in the disks, affect significantly the flow and heat transfer between the disks and adjacent air. In modern compressors, it is common practice to cool the high-pressure disks using air extracted from the low-pressure stages, and a schematic diagram of such an arrangement is shown in Fig. 1. The axial throughflow of cooling air sets up secondary flow inside the cavity between adjacent disks, and this flow is affected significantly by the temperature difference between the disks and coolant.

Although the flow and heat transfer inside the cavity will depend on the shape of the disks, insight into the problem can be gained by studying a simple rotating cavity comprising two plane disks and cylindrical shroud, as shown in Fig. 2(a). The cavity has an outer radius b , and the axial distance between the disks is s . Coolant enters the cavity through a hole, of radius a , in the upstream disk and leaves through a similar

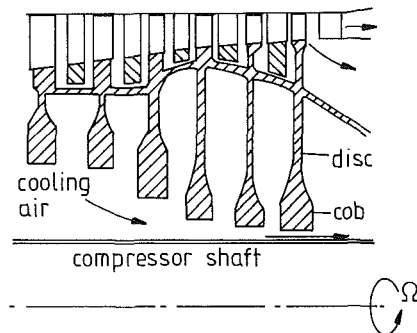


Fig. 1 Simplified arrangement of a high-pressure compressor drum

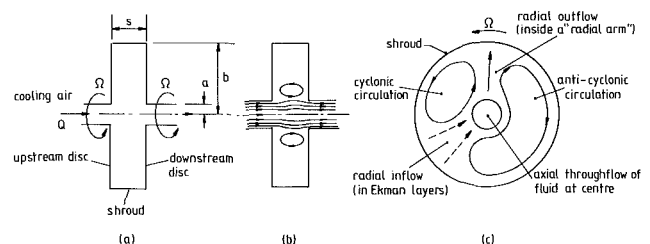


Fig. 2 Rotating cavity with an axial throughflow of cooling air: (a) schematic of geometry; (b) isothermal flow structure ($r-z$ plane); (c) non-isothermal flow structure ($r-\phi$ plane)

¹Present address: Motoren-und Turbinen Union (ETWW), Munich, Germany.

²Present address: School of Mechanical Engineering, University of Bath, Bath, United Kingdom.

Contributed by the International Gas Turbine Institute and presented at the 35th International Gas Turbine and Aeroengine Congress and Exposition, Brussels, Belgium, June 11-14, 1990. Manuscript received by the International Gas Turbine Institute January 13, 1990. Paper No. 90-GT-16.

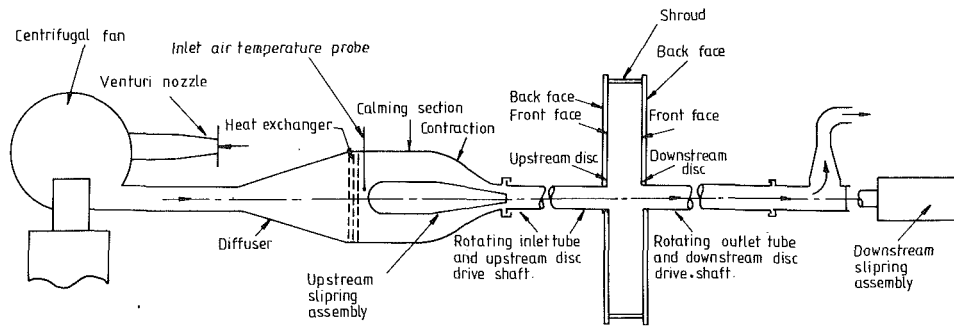


Fig. 3 Schematic of the experimental apparatus

hole in the downstream disk. The volumetric axial flow rate is Q and the angular speed of the cavity Ω . For isothermal flow, the disks are unheated and the disk surface temperature, T_s , is equal to that of the air at inlet to the system, T_i . For nonisothermal flow, where $T_s > T_i$, either the disks have the same radial temperature distribution (symmetric heating), or one disk may be hotter than the other (asymmetric heating). In either case, the surface temperature can be a function of the radius, r .

The companion paper to this one, Farthing et al. (1992), describes the results of flow visualization and velocity measurements in both an isothermal and a heated cavity. The isothermal flow structure, which is illustrated in Fig. 2(b), comprises a central throughflow and an inner toroidal vortex. For cavities with large gap ratios ($G > 0.4$), the superposed axial flow generates a powerful toroidal vortex; for small gap ratios, there are weak counterrotating toroidal vortices. Depending on the gap ratio and Rossby number, ϵ , axisymmetric and nonaxisymmetric vortex breakdown can occur, and circulation inside the cavity itself becomes weaker as ϵ is reduced.

When the disks are heated, the flow structure referred to above changes, and a schematic of the nonisothermal flow structure is shown in Fig. 2(c). Between the disks, the fluid

rotates with almost solid-body rotation, and the ratio of this core rotation to that of the disks depends on the Rossby number. Cold fluid enters the cavity in a "radial arm" which bifurcates at the shroud. With respect to the rotation of the disk, some of the fluid moves tangentially forward and some rearward. These forward and rearward-moving zones do not merge but are separated by a region referred to as the "dead zone." The authors noted a similarity with large-scale meteorological flows: Namely, the "forward zone" is cyclonic and has a lower pressure than the "rearward" zone of anticyclonic flow. The resulting circumferential pressure gradient provides the Coriolis forces necessary for the cold dense air to move radially into the hot cavity. There was also evidence to suggest that the fluid leaves the cavity by flowing radially inward in Ekman layers on the surface of the disks.

Hennecke, et al. (1971) made a numerical study of the heat transfer problem for laminar, axisymmetric nonisothermal flow. They obtained results for $200 \leq Re_z \leq 1000$, $0 \leq Re_\phi \leq 2500$, and, as a result of assuming an axisymmetric flow, found that very little of the axial throughflow penetrated the outer part of the cavity.

Experimental heat transfer measurements were made by Owen and Billimoria (1977) for $G = 0.267$ and 0.4 and by

Nomenclature

a = inner radius of cavity	q = heat flux	Δt = time-step length
A_0, A_1, A_2 = fluxmeter coefficients	Q = volume flow rate	ΔT = temperature difference = $T_s - T_i$
b = outer radius of cavity	r = radial coordinate	ϵ = Rossby number = $W/\Omega a = 1/2 b^2 Re_z / a^2 Re_\phi$
C_0, C_1, C_2, C_3 = regression coefficients	Re_z = axial Reynolds number = $2\rho W a / \mu$	θ = nondimensional surface temperature = $(T_s - T_i) / (T_{s,max} - T_i)$
D = disk diameter	Re_ϕ = rotational Reynolds number = $\rho \Omega b^2 / \mu$	μ = dynamic viscosity
g = acceleration due to gravity	s = axial distance between disks	ρ = density
G = gap ratio = s/b	t = time	Ω = angular speed of cavity
Gr = Grashof number = $\rho^2 \Omega^2 r^4 \beta \Delta T / \mu^2$	T = temperature	
Gr_y = modified Grashof number = $\rho^2 \Omega^2 r y^3 \beta \Delta T / \mu^2$	V = voltage	
k = thermal conductivity	W = bulk-average axial velocity at inlet to cavity	
N = time-step number	x = nondimensional radial coordinate = r/b	Subscripts and Symbols
Nu = local Nusselt number = $q_s r / k (T_s - T_i)$	y = distance from shroud = $b - r$	av = radially weighted average
Nu_{av} = average Nusselt number = $q_{s,av} b / k (T_s - T_i)_{av}$	Y = nondimensional distance from shroud = $1 - x$	i = pertaining to the inlet air
Nu_y = modified Nusselt number = $q_{s,y} / k (T_s - T_i)$	β = coefficient of volumetric expansion = T_i^{-1}	max = maximum value
		R = radiant value
		s = pertaining to the disk surface
		tot = total value
		$\langle \rangle$ = denotes a time average

Owen and Onur (1983) for $G = 0.133, 0.267,$ and 0.4 . Results were obtained for $2.0 \times 10^4 < Re_z \leq 2.0 \times 10^5$, $2.0 \times 10^4 \leq Re_\phi \leq 2.0 \times 10^6$, and for $\beta\Delta T \approx 0.27$. In both cases the tests were conducted for a disk temperature that increased with radius; Owen and Bilimoria's work was conducted on a symmetrically heated cavity and that of Owen and Onur on an asymmetrically heated cavity with only the downstream disk heated. However, the results from these earlier tests were subject to large experimental uncertainties: The data analysis did not take account of radiation from the disks, and thermocouple embedding errors were likely to be significant. It is shown below that even when the temperature of the disks is low (< 400 K) the radiative heat transfer for an asymmetrically heated cavity can be of the same magnitude as the convective heat transfer. The heat transfer measurements in these earlier tests were obtained by solving the steady-state conduction equation using measured temperatures as boundary conditions; Owen (1979) and Long (1985a) have shown that small thermal-disturbance errors (caused, for example, by embedding thermocouples into the surface of a steel disk using epoxy resin adhesive) can lead to large errors in the measured Nusselt numbers.

Heat transfer experiments have also been carried out by Graber et al. (1987), and their measurements were made using RdF thermopile-type fluxmeters in a compressor-drum rig with a nonplane disk geometry. Some Nusselt numbers are presented by the authors, but these are at radial locations where the results are likely to be influenced by the impingement of the axial throughflow of cooling air.

In this paper, results are presented of recent heat transfer experiments in a heated rotating cavity with an axial throughflow of cooling air. The errors associated with radiation and embedded thermocouples, referred to above, are minimized by the use of radiation corrections for the disks and the use of fluxmeters to measure the local heat flux. Section 2 describes the experimental apparatus and data analysis, and the results of this work are presented in Section 3.

2 Experimental Apparatus, Data Acquisition, and Analysis

Most of the heat transfer experiments discussed in this paper were conducted on rig (*d*) of Farthing et al. (1992). A detailed description of this apparatus is given by Northrop (1984), so only the relevant features will be discussed here. The data were analyzed using the transient analysis technique described by Long (1985b), and the salient points are described below.

2.1 The Experimental Apparatus. A schematic diagram of the rotating cavity rig (*d*) is shown in Fig. 3. The cavity has an outer radius of $b = 426$ mm, and is formed from two disks and a peripheral shroud. For the tests discussed here the axial gap $s = 59$ mm, corresponding to a gap ratio of $G = 0.138$. Both disks have a diameter, D , of 950 mm, and there is a central hole, of radius $a = 45$ mm, in each disk.

Cooling air passes through a 27:1 area-ratio contraction and a rotating inlet tube, and then enters the cavity axially through the central hole in the upstream disk. It leaves through a similar hole in the downstream disk where it passes through a rotating outlet tube. For $Re_z \geq 4 \times 10^4$ the cooling air is supplied by an 18.8 kW Alldays and Peacock centrifugal fan, and the flow rate is measured by a calibrated contraction at the entrance to the cavity. For $Re_z < 4 \times 10^4$ the air is supplied by a smaller 0.25 kW Secomak fan and the flowrate measured by an Anubar differential-pressure flowmeter. In both cases the differential pressure is measured (with an accuracy of ± 0.1 mm W. G.) by a T.E.M. manometer, and before entering the cavity the air is cooled to approximately $T_i = 20^\circ\text{C}$ by a heat exchanger.

The disks are driven by a 90 kW thyristor-controlled electric

Table 1 Radial locations of the fluxmeters

Fluxmeter No.	Upstream disc		Downstream disc	
	x	r (mm)	x	r (mm)
1	0.420	178.2	0.418	179.0
2	0.613	259.1	0.608	261.0
3	0.684	292.5	0.687	291.3
4	0.759	320.9	0.753	323.3
5	0.824	348.5	0.818	351.0
6	0.880	373.0	0.876	375.0
7	0.932	397.0	0.932	397.0
8	0.986	418.0	0.981	420.0

motor and the maximum speed of the cavity, which is measured (to an accuracy of ± 1 rpm) by an E.A.L. tacho-ratiometer, is 4000 rpm ($Re_\phi \approx 5 \times 10^6$). The disks themselves are of composite construction. Each disk is internally heated with five separate 4.8 kW annular heaters, and so it is possible to control the radial distribution of temperature. The shroud is also of composite construction, comprising two hiduminium rings (each of 10 mm radial thickness), separated by a layer of "Rohacell" insulation foam ($k \approx 0.04$ W/m K), of 10 mm radial thickness. On the inside of the cavity the shroud is insulated; another layer of Rohacell (17 mm radial thickness) is bonded to the innermost hiduminium ring. The front face of each disk is instrumented with eight RdF fluxmeters located in slots, 10 mm wide and 0.7 mm deep, with epoxy resin adhesive. These are positioned on a radially weighted basis (see Table 1); The disk is divided into a number of equal areas and the fluxmeters are located at the boundaries.

The RdF fluxmeters (10 mm \times 5 mm \times 0.5 mm) comprise five copper-constantan thermopile junctions between layers of Kapton polyimide film. To minimize thermal disturbances, the disks are coated with a surface layer of 1-mm-thick epoxy resin and glass fiber "instrumentation mat" having a similar thermal conductivity to both the adhesive resin and Kapton film. The fluxmeters were calibrated by Long (1986) using a simple theoretical model to predict their output. The total (radiative and convective) heat flux, q_{tot} , is given by

$$q_{tot} = A_0 V [(A_1 + (4A_2 T_s))^{1/2} + A_2 V] \quad \text{W/m}^2 \quad (1)$$

where A_0 , A_1 , and A_2 are coefficients that depend on the physical properties of the fluxmeter, T_s is the temperature in $^\circ\text{C}$, and V is the voltage output in mV. Long used a statistical regression to find values of the three coefficients for each fluxmeter and typical values are: $A_0 = 694$ W/m²K, $A_1 = 24.8$ ($^\circ\text{C}/\text{mV}$)², and $A_2 = -0.016$ $^\circ\text{C}/\text{mV}^2$.

The surface temperatures of the disks are measured by 0.15-mm-diameter copper-constantan thermocouples. An epoxy resin adhesive is used to locate these in slots, 0.2 mm wide by 0.5 mm deep, cut into the instrumentation mat. There are 13 thermocouples on the back face of each disk, 18 on the front face of the downstream disk and 23 on the front face of the upstream disk. The temperature of the air entering the cavity is measured by a stationary thermocouple probe located upstream of the contraction and approximately 1.65 m upstream of the cavity inlet. At the outer radius, the air temperature outside the cavity is measured by another stationary thermocouple probe. The signals from the fluxmeters and thermocouples are measured by a Solartron IMS 3510 data logger controlled by a PDP 11/44 minicomputer. The data logger has a resolution of ± 1 μV , which is approximately equivalent to ± 2 W/m² for the fluxmeters and $\pm 0.025^\circ\text{C}$ for the ther-

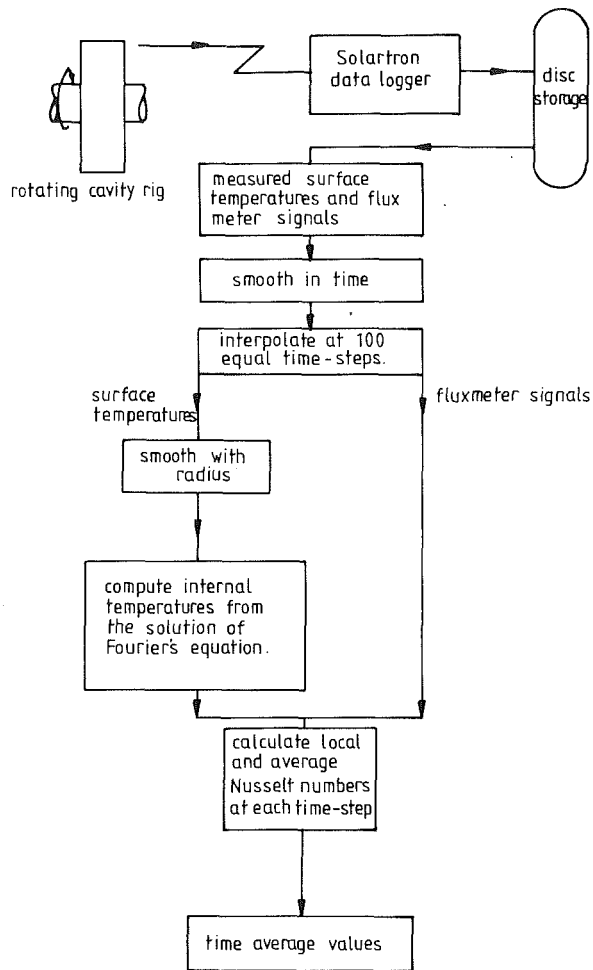


Fig. 4 Flow chart for the data analysis

mocouples. The accuracy of the thermocouple measurements depends mostly on the ratio of the thermal conductivity of the thermocouple, insulation, and adhesive to that of the instrumented surface (see Long, 1985a). Since the instrumentation mat and epoxy resin have similar thermal conductivities, errors in the measured temperatures will be negligible and the accuracy of temperature measurement is estimated to be better than $\pm 0.2^\circ\text{C}$.

Some tests were also conducted on another (smaller) rig, with $a = 38.1$ mm and $b = 381$ mm (rig (c) of Farthing et al., 1992). Unlike the rig described above, the smaller rig has a 25-mm-dia drive shaft in the center of the cavity, the gap ratio is $G = 0.267$, and only the downstream disk can be heated.

2.2 Acquisition and Analysis of Data. A flowchart illustrating how the measured Nusselt numbers are obtained from the thermocouple and fluxmeter signals is given in Fig. 4.

Tests were conducted at a constant flow rate and rotational speed. The disk temperatures were virtually invariant with time and the maximum disk temperature $T_{s,\max}$ was approximately 100°C . A test comprised about 100 consecutive scans, each of which took about 4 s to record the temperatures and fluxmeter signals, and consecutive scans would usually be separated by a 6 s period.

The measured fluxmeter signals and disc temperatures for each test were stored on magnetic tape for processing. A statistical smoothing technique (see Long, 1985b) was used to smooth the fluxmeter signals and temperatures in time, and the surface temperatures and fluxmeter signals were interpolated at 100 time steps from the time-smoothed data. The

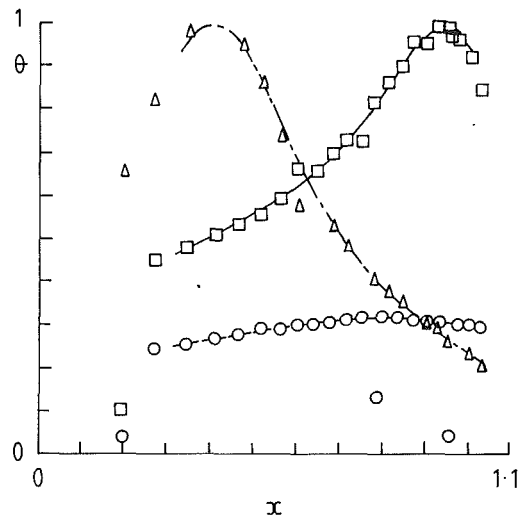


Fig. 5 Surface temperature distributions for $Re_\phi = 3 \times 10^6$ and $Re_z = 1.6 \times 10^5$

Symbol	Temperature distribution	$T_{s,\max}$	T_i
—□—	increasing (heated disk)	108°C	26°C
—○—	increasing (unheated disk)	103°C	25°C
—△—	decreasing (heated disk)	115°C	26°C

surface temperatures of the disks, at each time step, were then obtained by smoothing the interpolated time-smoothed temperatures with radius. These temperatures, which are referred to as “smoothed temperatures,” were used as boundary conditions for the solution of Fourier’s transient conduction equation, from which the “measured” heat fluxes were calculated. The convective heat losses from the outer radius of the disk and from the shroud were estimated by modeling the outer surface as a rotating cylinder; the heat transfer coefficient was obtained from Kays and Bjorklund (1958).

Some numerical tests were conducted to examine the influence of the boundary condition at the outer radius. Either a rotating cylinder boundary condition, as described above, or an adiabatic boundary condition at the outer radius was used; for $x \leq 0.85$ the computed Nusselt numbers were not affected. At the inner radius, a solution to the one-dimensional (in the axial direction) transient heat conduction equation was chosen as the boundary condition. At $t = 0$, the temperatures inside the disk (the initial conditions) were obtained from the steady-state conduction equation, with the same boundary conditions as used in the transient conduction solution.

At each time step, the measured fluxes from the fluxmeters were calculated from equation (1); the measured fluxes from the transient conduction solution were obtained by differentiation of the computed temperature distribution inside the disk. These fluxes, q_{tot} , include both the convective and radiative fluxes, and the convective heat flux at the disk surface, q_s , is given by

$$q_s = q_{\text{tot}} - q_R \quad (2)$$

where the local radiative fluxes, q_R , were calculated using the method described by Long (1985b). The local Nusselt numbers, which are defined in the nomenclature, are based on the convective flux q_s . The average Nusselt numbers, Nu_{av} , were calculated using Simpson’s rule to obtain the radially weighted average values of the convection flux from either the conduction solution or the fluxmeters; for both cases, the average was taken between the radial limits of the innermost and outermost fluxmeters.

Time-averaged values of the local and average Nusselt number, $\langle Nu \rangle$ and $\langle Nu_{av} \rangle$, respectively, were also obtained. These were taken as the arithmetic mean of the instantaneous values from the 10th to the 90th time steps.

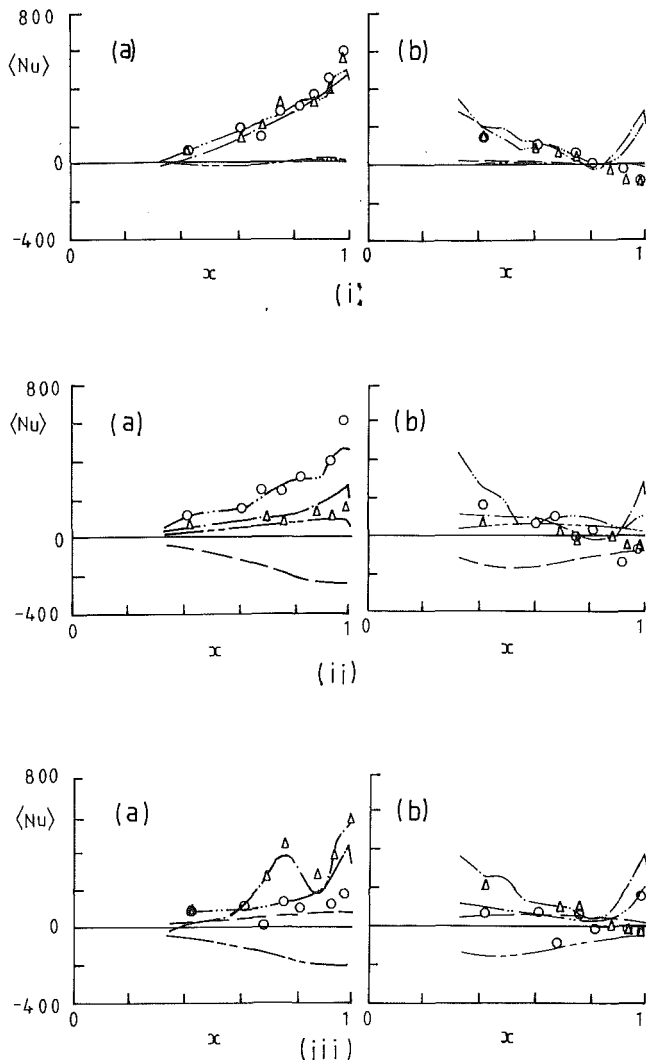


Fig. 6 Local Nusselt numbers for $Re_\phi = 3 \times 10^6$, $Re_z = 1.6 \times 10^5$, $0.26 \leq \beta\Delta T \leq 0.3$ and (a) increasing temperature distribution; (b) decreasing temperature distribution; (i) symmetrically heated cavity; (ii) downstream disk heated; (iii) upstream disk heated

Fluxmeter measurements: Δ , upstream disk
 O, downstream disk
 Conduction solution: \cdots , upstream disk
 \cdots , downstream disk;
 Radiation: $---$, upstream disk
 $---$, downstream disk

3 Experimental Results

3.1 Temperature Distributions. Examples of radial temperature distributions for tests at $Re_\phi = 3.0 \times 10^6$ and $Re_z = 1.6 \times 10^5$ in rig (d) are shown in Fig. 5. The temperatures shown are for: (i) the upstream disk of a symmetrically heated cavity with a temperature distribution that increases with radius; (ii) the upstream disk of an asymmetrically heated cavity, where the downstream disk is heated; and (iii) a symmetrically heated cavity with a temperature distribution that decreases with radius.

This figure shows the variation of nondimensional surface temperature, θ , with nondimensional radial coordinate, x , where $\theta = (T_s - T_i)/(T_{s,max} - T_i)$ and $x = r/b$, and the subscript "max" is used to denote the maximum disk surface temperature for the test. The surface temperatures at the thermocouple locations are shown by the symbols. The curves show the "smoothed temperatures," which are used as boundary conditions for the transient conduction solution.

Although there was some variation of radial temperature distribution with rotational Reynolds number and flow rate, these variations were small in comparison with the differences between the three different distributions. The temperatures illustrated here are typical examples of increasing and decreasing temperature distributions. For the tests with an increasing temperature distribution, the maximum temperature on the heated disk occurs at $x \approx 0.95$; for the decreasing temperature distribution, it occurs at $x \approx 0.4$. Radiation from the heated disk raises the temperature of the unheated one above that of the cooling air at inlet to the cavity. For an increasing temperature distribution, the temperature distribution on the unheated disk shows a small increase with radius, and the maximum surface temperature ($T_s \approx 52^\circ\text{C}$) occurs at $x \approx 0.8$. Although not shown in this figure, for asymmetrically heated disks with a decreasing temperature distribution, the temperature of the unheated disk decreases with radius and has roughly the same maximum value as that for the asymmetrically heated cavity with an increasing temperature distribution.

In the tests discussed here, some thermocouples were not working correctly. For example, thermocouples 1, 13, and 19 at $x = 0.2, 0.78$, and 0.95 on the unheated upstream disk of the asymmetrically heated cavity with an increasing temperature distribution were not working. The measurements from these faulty thermocouples were not used in the analysis, and as seen the smoothing curves give a good fit to the other temperatures.

3.2 Measured Nusselt Numbers. Tests were conducted in rig (d) for two different temperature distributions with symmetrical and asymmetrical heating and for $2 \times 10^4 \leq Re_z \leq 1.6 \times 10^5$, $2 \times 10^5 \leq Re_\phi \leq 5 \times 10^6$ and $0.25 \leq \beta\Delta T \leq 0.3$. Figure 6 shows the radial variation of time-averaged local Nusselt numbers for tests at $Re_\phi = 3.0 \times 10^6$, $Re_z = 1.6 \times 10^5$ and $0.26 \leq \beta\Delta T \leq 0.3$. For reference, the radiative Nusselt numbers, which were calculated using the radiative heat flux, are also shown in the figures.

For symmetrically heated disks and an increasing temperature distribution (Fig. 6(a(i))), the conduction solution and fluxmeter results on each disk are in good agreement. The results for each disk are also similar: $\langle Nu \rangle$ increases with radius from approximately zero at $x = 0.3$ to approximately 500 at $x = 1$. This similarity between the Nusselt numbers for the two disks is consistent with the symmetry of the flow structure about the midaxial plane as observed by Farthing et al. (1992).

The results for an asymmetrically heated cavity with an increasing temperature distribution on the downstream and upstream disks are shown in Fig. 6(a(ii)) and (a(iii)), respectively. In both cases the local Nusselt numbers on the heated disk are broadly similar to those for the symmetrically heated cavity (frame a(i)). The results for the unheated disk, in frames a(ii) and a(iii), are also similar, but the values of $\langle Nu \rangle$ are significantly lower than those on the heated disk.

It can be seen that for the symmetrically heated cavity the radiative Nusselt numbers are small ($\langle Nu_R \rangle \approx 10$). By contrast, $\langle Nu_R \rangle$ is relatively large in the asymmetrically heated cavity: The ratio of the magnitude of the radiative to the convective Nusselt numbers is small for the heated disk and large for the unheated one.

The results for tests at $Re_\phi = 3.0 \times 10^6$ and $Re_z = 1.6 \times 10^5$ and for a temperature distribution that decreases with radius are shown in Fig. 6(b). In these tests, the relatively large differences between the conduction solution and fluxmeter results for $x > 0.85$ are attributed to the boundary condition at the outer radius. For $x \geq 0.85$, where numerical tests have shown that the computed Nusselt numbers were affected by the boundary conditions at the outer radius, it is considered that the fluxmeters provide the more accurate results.

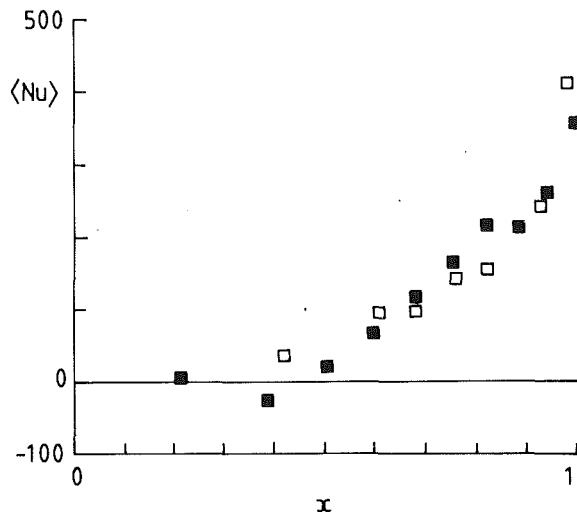


Fig. 7 Comparison between local Nusselt numbers measured by fluxmeters on two different rigs with an increasing temperature distribution on the downstream disk at $Re_\phi = 1.2 \times 10^6$ and $Re_z = 4 \times 10^4$: □ $G = 0.138$ and no central drive shaft; ■ $G = 0.267$ and with a central drive shaft

Comparison between Figs. 6(a) and 6(b) illustrates that the radial temperature distribution has a significant effect on both the magnitude and distribution of the Nusselt numbers. In Fig. 6(b) the local Nusselt numbers on both disks decrease with radius and for $x > 0.7$ they are negative, which implies that the local air temperature (which was not measured) is above that of the disks. As was noted above for the increasing temperature distribution, the local Nusselt numbers for the heated disks of the asymmetrically heated cavity are also similar to those for symmetrically heated disks. The values of $\langle Nu \rangle$ for the unheated disk are smaller than those for the heated one.

It is also of interest to compare the measured Nusselt numbers for rig (d) with those for rig (c). It should be remembered (see Section 2) that for rig (d) the gap ratio was $G = 0.138$ and there was no central shaft; for rig (c), $G = 0.267$ and there was a shaft. Comparisons were carried out for $2 \times 10^4 \leq Re_z \leq 8 \times 10^4$ and $4 \times 10^5 \leq Re_\phi \leq 1.6 \times 10^6$, and the results for tests at $Re_\phi = 1.2 \times 10^6$ and $Re_z = 4 \times 10^4$ are shown in Fig. 7. The results suggest that the effect of gap ratio and the presence of a central shaft have little influence on the Nusselt numbers. Also, tests conducted at the same values of Re_z and Re_ϕ on the two different rigs, and repeat tests on one rig, showed similar variations in the radial distribution of local Nusselt numbers.

The variation of average Nusselt numbers, $\langle Nu_{av} \rangle$, with Re_ϕ for $Re_z = 2, 4, 8,$ and 16×10^4 is shown in Fig. 8. These results are for tests in rig (d) on the symmetrically heated cavity with an increasing temperature distribution. The following observations can be made:

- (i) There is little difference between the average Nusselt numbers on the upstream and downstream disks;
- (ii) at the lower values of Re_ϕ , $\langle Nu_{av} \rangle$ increases with increasing Re_ϕ ($\langle Nu_{av} \rangle \sim Re_\phi^{1/2}$);
- (iii) for $Re_\phi > 3 \times 10^6$, the results for $Re_z = 2 \times 10^4$ show that $\langle Nu_{av} \rangle$ decreases with increasing Re_ϕ ;
- (iv) $\langle Nu_{av} \rangle$ increases with increasing Re_z , but the effect is more significant at the higher values of Re_ϕ .

3.3 Correlation of Measured Local Nusselt Numbers. The above results show that the Nusselt numbers are affected by Re_z and Re_ϕ . Also the flow visualization of Farthing et al. (1992) showed that there is radial inflow inside the boundary layers on the rotating disks. If, as is believed, the heat transfer is governed by buoyancy effects, it would be appropriate to

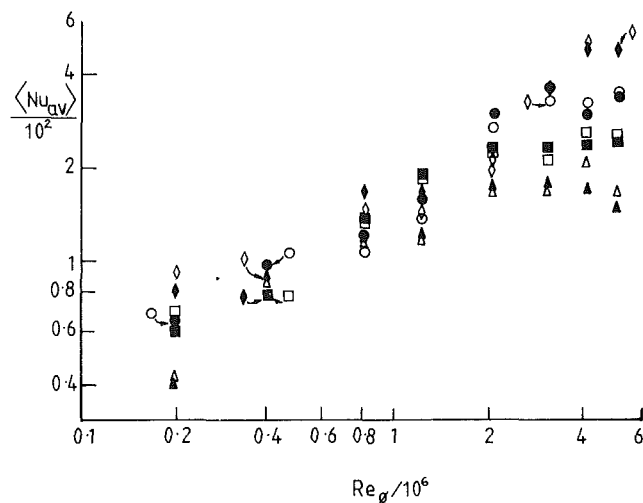


Fig. 8 Variation of average Nusselt number with Re_ϕ and Re_z for a symmetrically heated cavity with an increasing temperature distribution

$Re_z / 10^4$	2	4	8	16
Upstream disk	△	□	○	◇
Downstream disk	▲	■	●	◆

define a Grashof number, Gr_y , based on the local centripetal acceleration, $\Omega^2 r$, the local buoyancy parameter, $\beta \Delta T$, and the radial distance from the shroud, $y = b - r$.

It was therefore assumed that

$$Nu_y = C_0 Re_z C_1 Y C_2 Gr_y C_3 \quad (3)$$

and a multiple regression analysis on all the data for the symmetrically heated cavity with an increasing temperature distribution gave $C_0 = 0.0065$, $C_1 = 0.299$, $C_2 = 0.0377$, and $C_3 = 0.245$; the correlation coefficient was 0.928. The small value for C_2 suggests that the effect of Y ($Y = y/b$) is weak. Also, $C_3 \approx 0.25$, the value associated with laminar free convection from a stationary surface.

A second correlation was considered in which the effect of Y was ignored, and the exponent for Gr_y was assumed to be 0.25. This gave

$$Nu_y = 0.0054 Re_z^{0.30} Gr_y^{0.25} \quad (4)$$

with a correlation coefficient of 0.529.

Equation (4), together with the measured local Nusselt numbers for a symmetrically heated cavity with an increasing temperature distribution and for the tests at $Re_z = 2$ and 16×10^4 , is shown in Fig. 9. Also shown are correlations for natural convection in air from a heated vertical plate with a constant surface temperature (see Jaluria, 1980), given by

$$Nu_y = 0.36 Gr_y^{0.25} \quad (5)$$

for laminar flow, and

$$Nu_y = 0.022 Gr_y^{0.4} \quad (6)$$

for turbulent flow; where y is now the vertical height from the base and the centripetal acceleration, $\Omega^2 r$, is replaced by the acceleration due to gravity, g .

Although there is some scatter, equation (4) provides a reasonable fit to the data. The scatter is worse at the higher value of Re_z and for the innermost fluxmeter (No. 1); this scatter may be caused by the forced convection effect of the central throughflow. As Re_z increases, the measured values of Nu_y approach the laminar free convection correlation. However, there appears to be no sign of transition even at Grashof numbers above that normally associated with transition to turbulent free convection in air ($Gr_y \approx 10^9$). Figures 9(a) and (b) demonstrate that equation (4) provides a reasonable fit over a wide range of the experimental data.

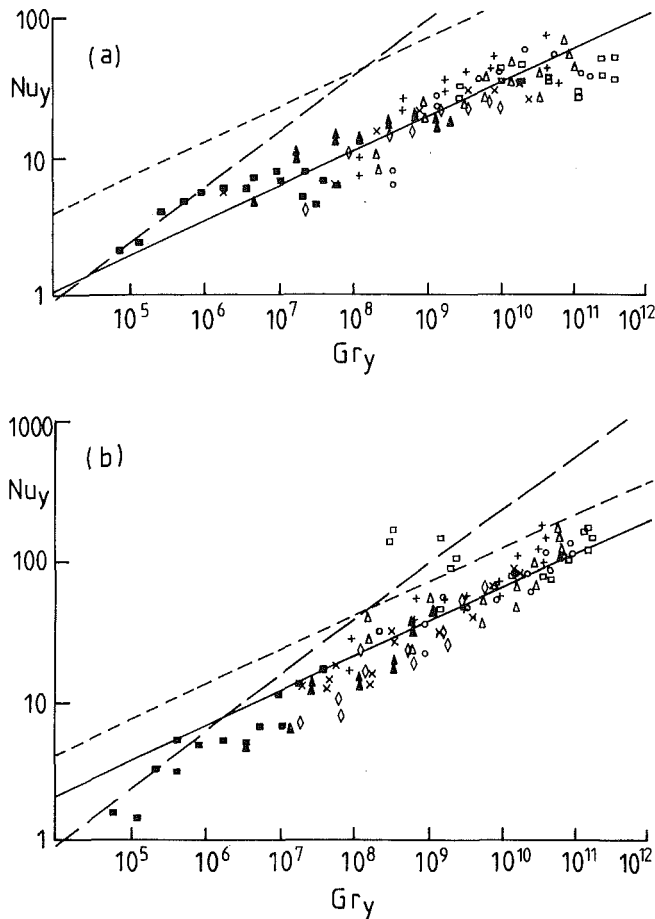


Fig. 9 Variation of local Nusselt numbers with local Grashof number for a symmetrically heated cavity with an increasing temperature distribution: (a) $Re_z = 2 \times 10^4$; (b) $Re_z = 16 \times 10^4$

Fluxmeter No. (see table 1)	Symbol
1	□
2	○
3	△
4	+
5	x
6	◇
7	▲
8	■

— correlation (equation(4))
 - - - laminar vertical plate (equation (5))
 - · - turbulent vertical plate (equation (6))

Equation (4) can be rewritten as:

$$Nu = 0.0054 Re_z^{0.30} Gr^{0.25} (x^{-1} - 1)^{0.25} \quad (7)$$

where the characteristic length used for the Nusselt and Grashof numbers is the radius r , and it is instructive to compare the radial variations of local Nusselt number obtained from equation (7) with those actually measured. This is illustrated in Figs. 10(a) and 10(b), for $Re_z = 2$ and 16×10^4 , respectively, where for each value of Re_z the measured and correlated values are presented for tests at $Re_\phi = 0.4, 2$, and 5×10^6 . At the lower flow rate and for $Re_\phi = 0.4$ and 2×10^6 , the measured and correlated radial variations of $\langle Nu \rangle$ are in good agreement; for $Re_\phi > 2 \times 10^6$, the measured values of $\langle Nu \rangle$ actually decrease with increasing Re_ϕ and the correlation overestimates these measurements. As noted above this also occurs in the average Nusselt numbers; a decrease of $\langle Nu_{av} \rangle$ with increasing Re_ϕ is consistent with all of the superposed axial flow entering the cavity. At the higher flow rate there is good agreement between the measured and correlated Nusselt numbers for Re_ϕ

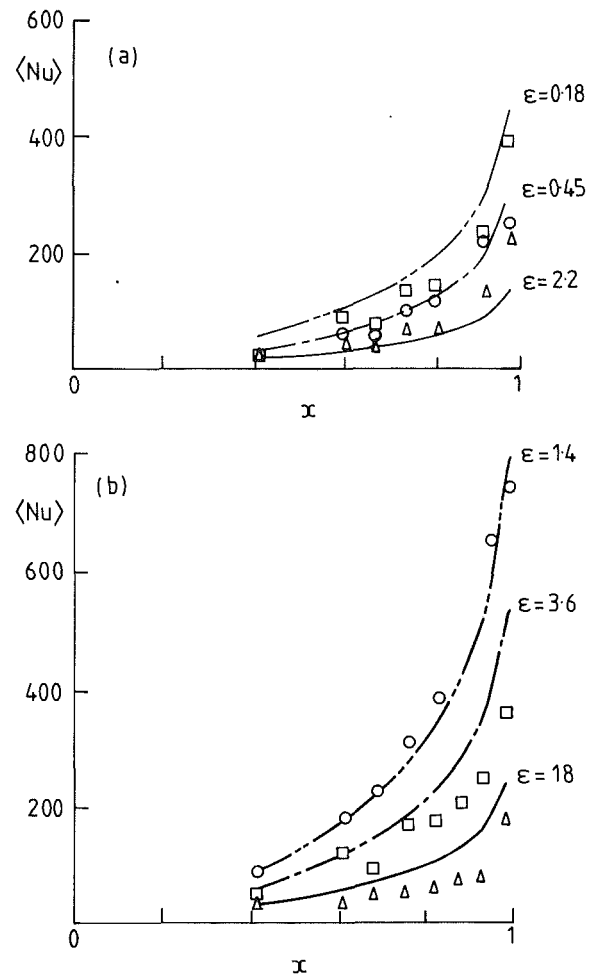


Fig. 10 Radial variation of local Nusselt numbers for the downstream disk of a symmetrically heated cavity with an increasing temperature distribution: (a) $Re_z = 2 \times 10^4$; (b) $Re_z = 16 \times 10^4$

$Re_\phi / 10^6$	Fluxmeter measurements	Correlation (equation (7))
0.4	△	—
2.0	□	- - -
5.0	○	- · -

$= 5 \times 10^6$, but at the lowest rotational Reynolds number the measured values are significantly lower than those obtained from the correlation.

It is also of interest to note that the magnitude of the local Nusselt numbers does not appear to depend on the Rossby number ϵ ($\epsilon = 1/2 b^2 Re_z / a^2 Re_\phi$). For example, the tests conducted at $Re_\phi = 5.0 \times 10^6$ and $Re_z = 16.0 \times 10^4$ ($\epsilon = 1.4$) and $Re_\phi = 0.4 \times 10^6$, $Re_z = 2.0 \times 10^4$ ($\epsilon = 2.2$) have Rossby numbers of similar magnitudes but the magnitude of the local Nusselt numbers is quite different. This suggests that the effects of vortex breakdown and core rotation, which Farthing et al. (1992) showed to be dependent on the Rossby number, do not have a large influence on the heat transfer. It would therefore appear that the flow in the disk boundary layers, which control the heat transfer, is insensitive to vortex breakdown and conditions in the core.

4 Conclusions

Heat transfer experiments have been conducted on two rotating cavity rigs with an axial throughflow of cooling air. The local and average Nusselt numbers were obtained from the

transient conduction solution and from calibrated RdF fluxmeters. Most experiments were conducted on a rig having an inner and outer radius of $a = 45$ mm and $b = 426$ mm, with a gap ratio of $G = 0.138$. These experiments were carried out for the range of rotational Reynolds numbers, $2.0 \times 10^5 \leq Re_\phi \leq 5.0 \times 10^6$, axial Reynolds numbers $2 \times 10^4 \leq Re_z \leq 1.6 \times 10^5$, and buoyancy parameter $0.25 \leq \beta\Delta T \leq 0.3$. Different disk surface temperature distributions were also tested: The temperature of the disks either increased with radius (the increasing temperature distribution) or decreased (the decreasing temperature distribution). Tests were conducted either with both disks at the same temperature (symmetric heating), or with one disk hotter than the other (asymmetric heating). Some tests were also carried out on a smaller rig ($a = 38.1$ mm, $b = 381$ mm) having a gap ratio of $G = 0.267$ and a 25-mm-dia central drive shaft. In this rig, only the downstream disk could be heated, and tests were conducted with an increasing temperature distribution on the downstream disk.

For the symmetrically heated cavity, the disks were found to have the same radial variation of local Nusselt number and the radiative heat transfer was small. For tests with an increasing temperature distribution, the local Nusselt numbers increase with radius and are always positive (that is, heat is convected from the disk to the surrounding air). For tests with a decreasing temperature distribution, the local Nusselt numbers decrease with radius and become negative for $x > 0.7$.

Although the flow structure between the disks is strongly influenced by the Rossby number, there appears to be no consistent effect of this parameter on the magnitude of the local Nusselt numbers. In general, the local and average Nusselt numbers increase with increasing Re_z and Re_ϕ . However, at the lower values of Re_z and the higher values of Re_ϕ , the Nusselt numbers actually decrease with increasing Re_ϕ . It is suggested that this occurs when all the available throughflow penetrates the cavity.

In the asymmetrically heated cavity, the local Nusselt numbers on the heated disk are similar in both magnitude and radial variation to those for the symmetrically heated cavity. For the unheated disk, the radial variation of Nusselt number is similar to that for the symmetrically heated cavity, but the magnitude is reduced. Radiation in the asymmetrically heated cavity is significant and can be as large as the convective heat transfer.

Comparison between the results obtained from the two different rigs suggests that the presence of the central drive shaft and an increase in the gap ratio from $G = 0.138$ to 0.267 have no significant effect on the Nusselt numbers.

A correlation was obtained for the local Nusselt numbers

in a symmetrically heated cavity with an increasing temperature distribution, and it was shown that

$$Nu_y = 0.0054 Re_z^{0.30} Gr_y^{0.25}$$

This correlation, which is similar to that for laminar natural convection from a vertical plate, provided a reasonable fit to most of the data.

Caution is obviously needed in applying these results to gas turbine engines where typical values of the relevant nondimensional groups are:

$$0.1 < G < 0.4, 0.2 < a/b < 0.5, 4 \times 10^6 < Re_\phi \text{ and } 0.01 < \epsilon < 1.$$

Acknowledgments

We wish to thank the Science and Engineering Research Council, Rolls Royce plc, and Ruston Gas Turbines Ltd. for sponsoring the work described in this paper. We are also indebted to Mr. Sri Kantha for obtaining the correlations referred to in Section 3.

References

- Farthing, P. R., 1988, "The Effect of Geometry on Flow and Heat Transfer in a Rotating Cavity," D. Phil. thesis, University of Sussex, United Kingdom.
- Farthing, P. R., Long, C. A., Owen, J. M., and Pincombe, J. R., 1992, "Rotating Cavity With Axial Throughflow of Cooling Air: Flow Structure," ASME JOURNAL OF TURBOMACHINERY, Vol. 114, this issue.
- Graber, D. J., Daniels, W. A., and Johnson, B. V., 1987, "Disk Pumping Test," Air Force Wright Aeronaut. Lab., Report No. AFWAL-TR-87-2050.
- Hennecke, D. K., Sparrow, E. M., and Eckert, E. R. G., 1971, "Flow and Heat Transfer in a Rotating Enclosure With Axial Throughflow," *Wärme- und Stoffübertragung*, Vol. 4, p. 222.
- Jaluria, Y., 1980, *Natural Convection Heat and Mass Transfer*, Pergamon, London, United Kingdom.
- Kays, W. M., and Bjorklund, I. S., 1958, "Heat Transfer From a Rotating Cylinder With and Without Crossflow," *Trans. ASME*, Vol. 80, p. 70.
- Long, C. A., 1985a, "The Effect of Thermocouple Disturbance Errors on the Measurement of Local Heat Transfer Coefficients," *Test and Transducer Conference*, Wembley, United Kingdom, Vol. 3, p. 73.
- Long, C. A., 1985b, "Transient Analysis of Experimental Data From the Mark II Rotating Cavity Rig," Report No. 85/TFMRC/76, School of Engineering and Applied Sciences, University of Sussex, United Kingdom.
- Long, C. A., 1986, "Calibration of the Fluxmeters on the Mark II Rotating Cavity Rig," Report No. 86/TFMRC/88, School of Engineering and Applied Sciences, University of Sussex, United Kingdom.
- Northrop, A., 1984, "Heat Transfer in a Cylindrical Rotating Cavity," D. Phil. thesis, University of Sussex, United Kingdom.
- Owen, J. M., 1979, "On the Computation of Heat Transfer Coefficients From Imperfect Temperature Measurements," *J. Mech. Eng. Sci.*, Vol. 21, p. 323.
- Owen, J. M., and Bilimoria, E. D., 1977, "Heat Transfer in Rotating Cylindrical Cavities," *J. Mech. Eng. Sci.*, Vol. 19, p. 175.
- Owen, J. M., and Onur, H. S., 1983, "Convective Heat Transfer in a Rotating Cylindrical Cavity," *ASME Journal of Engineering for Power*, Vol. 105, p. 265.

Rotating Cavity With Axial Throughflow of Cooling Air: Flow Structure

P. R. Farthing¹

C. A. Long

J. M. Owen²

J. R. Pincombe

Thermo-Fluid Mechanics Research Centre,
University of Sussex,
Falmer,
Brighton, BN1 9RH, United Kingdom

A rotating cavity with an axial throughflow of cooling air is used to provide a simplified model for the flow that occurs between adjacent corotating compressor disks inside a gas turbine engine. Flow visualization and laser-Doppler anemometry are employed to study the flow structure inside isothermal and heated rotating cavities for a wide range of axial-gap ratios, G , rotational Reynolds number, Re_ϕ , axial Reynolds numbers, Re_z , and temperature distributions. For the isothermal case, the superposed axial flow of air generates a powerful toroidal vortex inside cavities with large gap ratios ($G \geq 0.400$) and weak counterrotating toroidal vortices for cavities with small gap ratios. Depending on the gap ratio and the Rossby number, ϵ (where $\epsilon \propto Re_z/Re_\phi$), axisymmetric and nonaxisymmetric vortex breakdown can occur, but circulation inside the cavity becomes weaker as ϵ is reduced. For the case where one or both disks of the cavity are heated, the flow becomes nonaxisymmetric: Cold air enters the cavity in a "radial arm" on either side of which is a vortex. The cyclonic and anticyclonic circulations inside the two vortices are presumed to create the circumferential pressure gradient necessary for the air to enter the cavity (in the radial arm) and to leave (in Ekman layers on the disks). The core of fluid between the Ekman layers precesses with an angular speed close to that of the disks, and vortex breakdown appears to reduce the relative speed of precession.

1 Introduction

In many gas turbine engines, air extracted from the compressor for cooling turbine blades and disks is passed through the center of a stack of compressor disks, as illustrated in Fig. 1. The axial throughflow of cooling air sets up secondary flow inside the cavity between adjacent disks, and this flow is affected significantly by the temperature difference between the disks and the coolant. Although the shape of the disks may be complicated, insight into the basic flow structure can be gained by studying a simple rotating cavity comprising two plane disks and a cylindrical shroud, as shown in Fig. 2.

Heat transfer measurements inside a rotating cavity with an axial throughflow of cooling air were made by Owen and Bilimoria (1977) and Owen and Onur (1983). They observed that, at certain Rossby numbers, nonaxisymmetric vortex breakdown could occur: The axial jet of air at the center of the cavity precessed about the axis of the cavity. Similar vortex breakdown was observed inside a heated rotor-stator system by Yu et al. (1973) and inside an isothermal rotating cavity by Owen and Pincombe (1979). The interested reader is referred to the comprehensive review of Escudier (1988) for more details of vortex breakdown.

Graber et al. (1987) made aerodynamic and heat transfer

measurements inside a six-cavity compressor-drum model operating at conditions representative of those found in gas turbine engines. Three bleed locations were used to introduce the cooling air into the drum, and pressure measurements were used to calculate the tangential component of velocity in the cavities; the radial distribution of pressure was strongly dependent on coolant flow rate and bleed location. During transient heating tests, where the temperatures of the air and disks increased with time, the measured heat fluxes were approximately half the magnitude of those obtained during cooling tests. This was attributed to stabilization of the flow during heating and destabilization during cooling. Heating and cooling the drum did not, however, significantly affect the radial distributions of pressure or velocity inside the cavities.

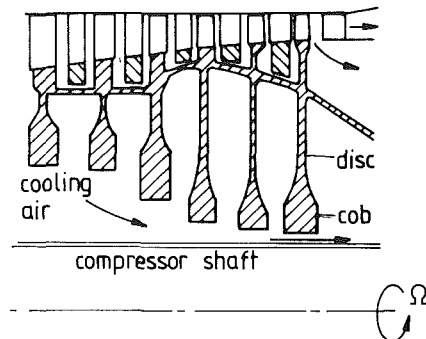


Fig. 1 Simplified arrangement of high-pressure compressor drum

¹Present address: Motoren-und Turbinen Union (ETWW), Munich, Germany.

²Present address: School of Mechanical Engineering, University of Bath, Bath, United Kingdom.

Contributed by the International Gas Turbine Institute and presented at the 35th International Gas Turbine and Aeroengine Congress and Exposition, Brussels, Belgium, June 11-14, 1990. Manuscript received by the International Gas Turbine Institute January 13, 1990. Paper No. 90-GT-17.

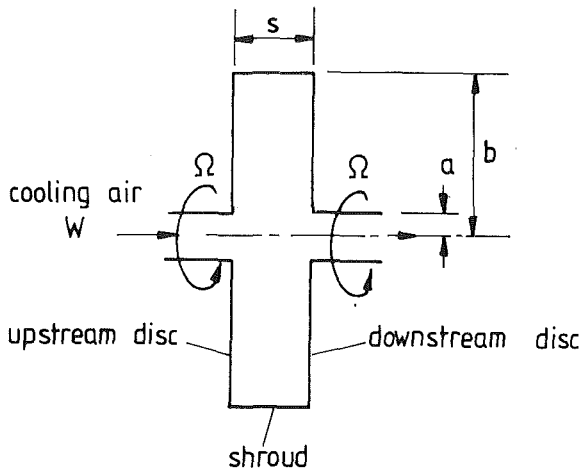


Fig. 2 Rotating cavity with an axial throughflow of cooling air

In the work described below, attention is concentrated on the flow structure. The basic equations for a rotating system are discussed in Section 2, and the experimental apparatus is described in Section 3. Flow visualization and velocity measurements are presented in Sections 4 and 5 for isothermal and heated rotating cavities, respectively, and the conclusions are given in Section 6. The heat transfer problem is considered by Farthing et al. (1992) in a companion paper to this one.

2 Linear Equations for Flow in a Rotating Cavity

It is convenient to separate a rotating flow into an inviscid core surrounded by boundary layers on the solid surfaces. If the core rotates at an angular speed close to that of the disks, which is the case for the flow considered in Section 5 below, the linear equations can be used; the nonlinear inertia terms are negligibly small compared with the linear Coriolis terms. Under these conditions, the boundary layers are often referred to as Ekman layers.

2.1 Incompressible Flow. For a frame of reference rotating with the same angular velocity Ω as the disks, the continuity equation and the linear equations of motion for steady, incompressible inviscid flow are given by Greenspan (1968) as

$$\nabla \cdot \bar{\mathbf{q}} = 0 \quad (1)$$

$$2\Omega \times \bar{\mathbf{q}} + \Omega \times (\Omega \times \mathbf{r}) = -\frac{1}{\rho} \nabla P \quad (2)$$

Here \mathbf{q} is the velocity vector in the rotating frame, P is the static pressure, ρ the density, and \mathbf{r} the position vector; the overbar is used to denote flow in the inviscid core. The three terms in equation (2) relate to the Coriolis acceleration, the centripetal acceleration, and the pressure gradient, respectively.

In cylindrical polar coordinates, where $\Omega = \Omega \mathbf{k}$ (\mathbf{k} being the unit vector in the axial direction at the axis of rotation), equations (1) and (2) become

$$\frac{\partial}{\partial r} (r\bar{u}) + \frac{\partial \bar{v}}{\partial \phi} + \frac{\partial}{\partial z} (r\bar{w}) = 0 \quad (3)$$

$$-2\Omega\bar{v} = -\frac{1}{\rho} \frac{\partial p}{\partial r}, \quad 2\Omega\bar{u} = -\frac{1}{\rho r} \frac{\partial p}{\partial \phi} \quad (4)$$

Here \bar{u} , \bar{v} , \bar{w} are the components of velocity in the r , ϕ , z directions, and p is the reduced pressure defined by

$$p = P - 1/2\rho\Omega^2 r^2 \quad (5)$$

Two important points can be deduced from the above equations. Firstly, manipulation of equations (3) and (4) shows that

$$\frac{\partial \bar{w}}{\partial z} = 0 \quad (6)$$

Secondly, there is no radial component of velocity in the core when the flow is axisymmetric (that is, when $\partial p/\partial \phi = 0$).

Equation (6), which is a simplified form of the Taylor-Proudman theorem, implies that \bar{w} must be invariant with axial location inside the core. For the case where there is symmetry about the midaxial plane of the cavity (as is often the case for the flows considered below), then $\bar{w} = 0$. That is, the Ekman layers on the disks are nonentraining: This holds for both laminar and turbulent incompressible Ekman layers (see Owen et al., 1985).

For axisymmetric flow, the Ekman-layer equations can be expressed as

$$-2\Omega\rho v = -\frac{\partial p}{\partial r} + \frac{\partial \tau_r}{\partial z} \quad (7)$$

$$2\Omega\rho u = \frac{\partial \tau_\phi}{\partial z} \quad (8)$$

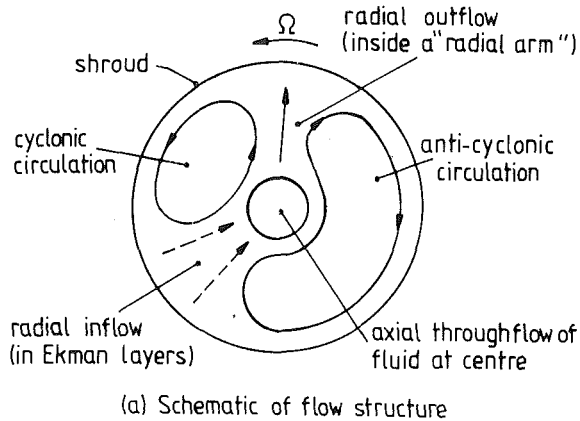
where τ_r and τ_ϕ are the respective radial and tangential components of shear stress. From equation (8), if $\partial \tau_\phi/\partial z > 0$ then $u > 0$ (that is, the flow is radially outward in the Ekman layer), and vice versa. It is also apparent that $\partial \tau_\phi/\partial z > 0$ if $\bar{v} < 0$. Hence, if $\bar{v} < 0$, the flow in the Ekman layer is radially outward;

Nomenclature

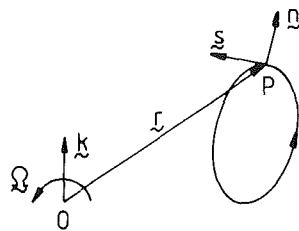
a = inner radius of cavity
 b = outer radius of cavity
 G = gap ratio = s/b
 \mathbf{k} = unit vector in axial direction
 \mathbf{n} = unit vector normal to streamline
 p = reduced pressure = $P - 1/2\rho\Omega^2 r^2$
 P = static pressure
 \mathbf{q} = velocity vector in rotating frame of reference
 r = radial coordinate
 \mathbf{r} = position vector
 Re_z = axial Reynolds number = $2\rho W a/\mu$
 Re_ϕ = rotational Reynolds number = $\rho\Omega b^2/\mu$
 t = time

t_c = period of one revolution of cavity
 T = temperature
 T_s = surface temperature
 s = axial distance between disks
 \mathbf{s} = unit vector tangential to streamline
 u, v, w = radial, tangential, and axial components of velocity in a rotating frame of reference
 V_r, V_ϕ, V_z = radial, tangential, and axial components of velocity in a stationary frame of reference ($V_r = u$, $V_\phi = v + \Omega r$, $V_z = w$)

W = bulk-average axial velocity at inlet to cavity
 z = axial coordinate (measured from upstream disk)
 β = coefficient of volumetric expansion
 ΔT = maximum temperature difference between disk and cooling air
 ϵ = Rossby number = $W/\Omega a = 1/2b^2 Re_z/a^2 Re_\phi$
 μ = dynamic viscosity
 ρ = density
 τ_r, τ_ϕ = radial, tangential components of shear stress
 ϕ = angular coordinate
 ω = angular speed of flow in core
 Ω = angular velocity = $\Omega \mathbf{k}$



(a) Schematic of flow structure



(b) Coordinate system

Fig. 3 Cyclonic and anticyclonic circulation inside a rotating cavity: (a) schematic of flow structure; (b) coordinate system

if $\bar{v} > 0$, the flow is inward. For either case, the radial component of the Coriolis acceleration is produced by the tangential component of the shear stress.

In practice, source-sink flows in which all the fluid enters at the center of the cavity and leaves at the periphery, or vice versa, are often axisymmetric. For radial outflow, the core rotates slower than the disks; for inflow, it rotates faster. In either case, the radial flow is confined to the Ekman layers on the disks.

For axial throughflow in a rotating cavity, where fluid enters and leaves at the center, axisymmetric flows are less common. It is difficult to envisage a practical axisymmetric mechanism that will provide the opposing Coriolis forces necessary to maintain simultaneous radial inflow and outflow inside the cavity. For the buoyancy-induced flows discussed in Section 5, it appears that a system of cyclonic and anticyclonic circulations inside the cavity provides the necessary Coriolis forces.

2.2 Cyclonic and Anticyclonic Flow. Although details of the flow structure inside a heated rotating cavity with axial throughflow are given in Section 5, it is convenient to discuss here the main features of the flow and to outline the relevant properties of cyclonic and anticyclonic flow in a rotating cavity. (The idea of cyclonic and anticyclonic circulations is well known to those who are familiar with the weather maps on television: Cyclonic circulations are usually referred to as “lows” and the anticyclonic ones as “highs.”)

Figure 3(a) provides a schematic of the observed nonaxisymmetric flow structure. In the core, between the Ekman layers on the disks, the cold fluid enters in a radial arm, on either side of which is a vortex; in one vortex, the circulation is cyclonic (that is, the fluid rotates in the same sense as the disk); in the other, the circulation is anticyclonic. Fluid leaves the cavity in Ekman layers (which, as described in Section 5, have only been observed in the so-called “dead zone” between the two vortex systems).

Figure 3(b) shows a coordinate system for steady, incompressible, inviscid flow along a closed streamline. The unit

vectors \mathbf{k} , \mathbf{n} , and \mathbf{s} refer respectively to the axial direction, the normal outward direction to the streamline, and the tangential direction of the streamline; the three vectors form a right-handed orthogonal set.

The system rotates with angular velocity $\Omega = \Omega \mathbf{k}$, and the velocity $\bar{\mathbf{q}}$ relative to the rotating frame is

$$\bar{\mathbf{q}} = \bar{q}_s \mathbf{s} + \bar{w} \mathbf{k} \quad (9)$$

The Coriolis acceleration is given by

$$2\Omega \times \bar{\mathbf{q}} = 2\Omega \mathbf{k} \times (\bar{q}_s \mathbf{s} + \bar{w} \mathbf{k}) \quad (10)$$

$$= -2\Omega \bar{q}_s \mathbf{n} \quad (11)$$

Hence, equation (2) can be written as

$$-2\Omega \bar{q}_s \mathbf{n} = -\frac{1}{\rho} \nabla p \quad (12)$$

where p is the reduced pressure given by equation (5). Hence,

$$2\Omega \bar{q}_s = \frac{1}{\rho} \frac{\partial p}{\partial n} \quad (13)$$

For a cyclone (where $\bar{q}_s > 0$), equation (13) implies that the “pressure” at the center is low compared with that outside; for an anticyclone, there is high “pressure” at the center. (“Pressure” is used here to refer to the reduced pressure p , not the static pressure P .)

Referring to Fig. 3(a), it can be seen that the radial outflow is associated with low “pressure” to the left and high “pressure” to the right. That is, where $\bar{u} > 0$, $\partial p / \partial \phi < 0$: this is consistent with equation (4). Conversely, radial inflow occurs in the Ekman layers in regions where $\partial p / \partial \phi > 0$.

The above model of cyclonic and anticyclonic circulation is qualitatively consistent with the observed flow patterns that are discussed in Section 5. Under some conditions, two or more systems of cyclones and anticyclones were observed to occur inside the heated rotating cavity.

Quantitatively, compressibility will affect the resulting flow, and one effect of variable density is discussed below.

2.3 Compressible Flow. For compressible flow, equations (1) and (2) become

$$\frac{\partial(\bar{\rho} r \bar{u})}{\partial r} + \frac{\partial(\bar{\rho} \bar{v})}{\partial \phi} + \frac{\partial(\bar{\rho} r \bar{w})}{\partial z} = 0 \quad (14)$$

$$2\Omega \bar{v} = 1/\bar{\rho} \frac{\partial P}{\partial r} + \Omega^2 r, \quad 2\Omega \bar{u} = -1/\bar{\rho} r \frac{\partial P}{\partial \phi} \quad (15)$$

Equation (15) can be differentiated to give

$$\frac{\partial}{\partial r} (\bar{\rho} r \bar{u}) + \frac{\partial}{\partial \phi} (\bar{\rho} \bar{v}) = 1/2\Omega r \frac{\partial \bar{\rho}}{\partial \phi} \quad (16)$$

Comparing equations (14) and (16), it can be seen that

$$\frac{\partial(\bar{\rho} \bar{w})}{\partial z} = 1/2\Omega \frac{\partial \bar{\rho}}{\partial \phi} \quad (17)$$

For axisymmetric flow, where $\partial \bar{\rho} / \partial \phi = 0$, equation (17) gives a similar result to the Taylor–Proudman theorem: The mass flux $\bar{\rho} \bar{w}$ is invariant with z . For the case where there is symmetry about the midaxial plane, $\bar{\rho} \bar{w} = 0$; the Ekman layers for axisymmetric compressible flow are nonentraining. This is the same result as for the axisymmetric (and nonaxisymmetric) incompressible flow discussed in Section 2.1.

For the nonaxisymmetric buoyancy-induced flow considered in Section 5 (for which $\partial \bar{\rho} / \partial \phi \neq 0$), equation (17) implies that the Ekman layers can entrain fluid.

3 Experimental Apparatus

3.1 The Rotating-Cavity Rigs. Flow visualization was carried out using four different rigs, which, for convenience, are ranked in order of size and are referred to below as rigs (a), (b), (c), and (d).

Table 1 Salient features of the four rigs

Rig	Outer radius b(mm)	Inner radius a(mm)	Axial gap s(mm)	Diameter of central shaft (mm)	Maximum speed (rev/min)
(a)	108	11	29	-	2000
(b)	190	19	25-101	-	2600
(c)	381	38	102	25	1000
(d)	475	45	59-171	-	1000

Each rig was driven by an electric motor, and the rotational speed was measured to an accuracy of ± 1 rpm by a timing wheel, transducer, and timer-counter. Air was supplied from a centrifugal compressor, and the flow rate was measured to an accuracy of ± 3 percent by means of an orifice plate, a rotameter or an Annubar differential-pressure device in the stationary piping upstream of the rotating cavity. Temperatures were measured by thermocouples embedded in the heated disk, and the signals were brought out via silver slip-rings to a data-logger; the estimated accuracy of the measured temperatures is $\pm 0.25^\circ\text{C}$.

Additional details of each rig are given below, and the salient features are summarized in Table 1. Further information is given by Pincombe (1983) and Farthing (1988).

3.1.1 Rig (a). This was the smallest of the four rigs with inner and outer radii of $a=11$ mm, $b=108$ mm, and $s=29$ mm ($a/b=0.1$, $G=s/b=0.27$), and the length of the rotating upstream and downstream tubes attached to the disks was approximately 300 mm. The disks and shroud were made from transparent polycarbonate, for optical access, and the system was rotated up to 2000 rpm. The disks were heated to a maximum temperature of 70°C by means of hot-air blowers.

3.1.2 Rig (b). For rig (b), $a=19$ mm, $b=190$ mm ($a/b=0.1$), and the axial gap was varied to give $G=0.133$, 0.267 , 0.4 , and 0.533 . The lengths of the rotating upstream and downstream tubes were 610 mm and 150 mm, respectively. The disks and shroud were made from perspex, and the whole system was rotated up to 2600 rpm. Only isothermal tests were conducted with this rig.

3.1.3 Rig (c). For rig (c), $a=38$ mm, $b=381$ mm ($a/b=0.1$); although the axial gap could be varied, the tests discussed below were conducted at $G=0.267$. The other rigs were driven by pulleys on the upstream and downstream rotating tubes attached to the disks, but for rig (c) the upstream disk was connected to the downstream one by a central drive shaft. The upstream tube, which was 200 mm long, contained four rectangular ports that allowed the cooling air to flow from the stationary piping into the rotating cavity; the downstream tube was similarly constructed. The drive shaft, which was 25 mm in diameter, extended through both rotating tubes; the air passed to and from the cavity through the annulus between the shaft and the tubes.

The downstream disk, which was made from steel, could be heated up to 100°C by stationary radiant heaters. The upstream disk and shroud were made from polycarbonate, and this limited the rotational speed to 1000 rpm.

3.1.4 Rig (d). Rig (d) was the largest with $a=45$ mm and $b=475$ mm ($a/b\approx 0.1$); for the tests reported below $G=0.12$, 0.24 , and 0.36 . The upstream and downstream rotating tubes were each 800 mm long. The disks were made from a composite construction, and built-in electric heaters enabled the radial distribution of the disk temperature to be varied. The shroud was made from transparent polycarbonate, which limited the maximum rotational speed to 1000 rpm.

3.2 Optical Instrumentation. For photographic purposes, a 4-W Spectra-Physics argon-ion laser was used to provide slit illumination in either the $r-\phi$ or the $r-z$ plane of the

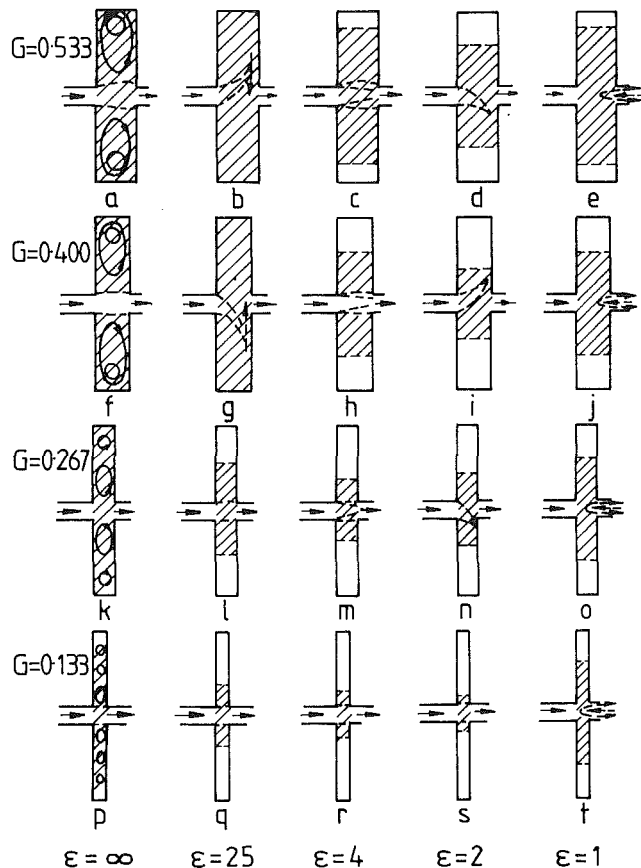


Fig. 4 Visual impressions of smoke patterns in an isothermal rotating cavity: $Re_z=5000$

cavity, and a Concept smoke generator provided "clouds" of micron-size oil particles. Photographs were taken using either an Olympus OM2 or a Canon A1 camera with 400 ASA black and white film. Except for rig (a), video recordings were made with a Sony camera and either a Sanyo or a JVC recorder. For rig (a), a Kodak Ektapro 1000 high-speed video (loaned by the Science and Engineering Research Council) was used to make recordings at up to 500 frames per second. For flow visualization where recordings were not required, a 0.5 mW Spectra-Physics He-Ne laser was used to illuminate rig (b).

For rig (b), where there was optical access through both disks, forward-scatter LDA measurements were made using a 5-mW Spectra-Physics He-Ne laser and a Cambridge Consultants tracking filter. For rigs (c) and (d), where back-scatter was necessary, the argon-ion laser was used, and for most measurements in rig (d) the tracking filter was replaced by a TSI 1990 counter.

Further details of the optical instrumentation and techniques are given by Pincombe (1983) and Farthing (1988).

4 Flow in an Isothermal Rotating Cavity

Unless stated to the contrary, the flow visualization and LDA measurements discussed in this section were made in rig (b).

4.1 Flow Visualization. For isothermal flow, the principal dimensionless groups are the gap ratio G , the rotational Reynolds number Re_ϕ , the axial Reynolds number Re_z , and the Rossby number ϵ , all of which are defined in the nomenclature. It should also be pointed out that, although the experiments were conducted for a wide range of Rossby numbers, in most practical applications inside gas turbines $\epsilon < 1$.

Figure 4 shows the visual impressions obtained from flow

visualization in the r - z plane for $Re_z = 5000$ and $G = 0.133$, 0.267, 0.400, and 0.533; the flow in the upstream tube was "tripped" to ensure turbulent flow for $Re_z \geq 2300$ when the cavity was stationary. For $G = 0.533$, a powerful axisymmetric, toroidal vortex (centered at $r/b \approx 0.8$, $z/s \approx 0.5$) was formed inside the stationary cavity, which quickly filled with oil particles from the smoke generator. Reducing the gap ratio reduced the strength of the recirculation inside the stationary cavity, and for $G \leq 0.267$ there was evidence of more than one toroidal vortex.

For $G = 0.533$, flow visualization in the rotating cavity revealed that both nonaxisymmetric (referred to as mode I) and axisymmetric (mode II) vortex breakdown could occur (see Owen and Pincombe, 1979). For turbulent flow, as the rotational speed was increased from zero, there appeared to be no discernible change in the behavior of the toroidal vortex until $\epsilon \approx 100$, where an occasional precession of the main jet about

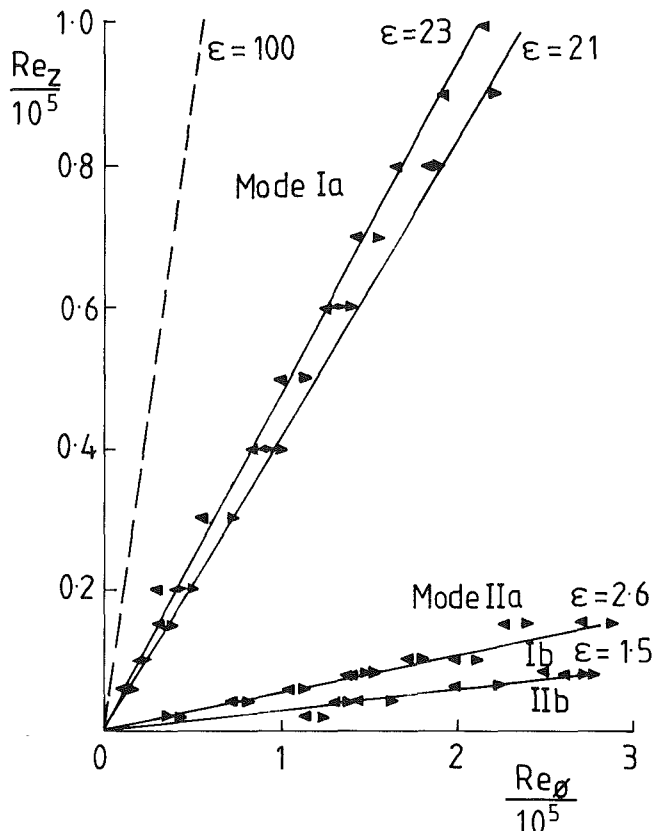


Fig. 5 Regimes of vortex breakdown in an isothermal rotating cavity: $G = 0.533$; \blacktriangleright , Re_θ increasing; \blacktriangleleft , Re_θ decreasing (Modes I and II refer to nonaxisymmetric and symmetric breakdown, respectively)

its central axis was seen. Further increase in rotational speed caused more regular precession of the jet (see Fig. 4b), and the amplitude reached a maximum at $\epsilon \approx 21$; this dramatic nonaxisymmetric breakdown, which was similar to that observed by Yu et al. (1973) and in which most or all of the jet would enter the cavity, was referred to as mode Ia behavior. At higher speeds, the jet would suddenly stop precessing; the boundaries would become axisymmetric again with occasional oscillations (mode IIa behavior), and the smoke-filled region of the cavity would be reduced in size (see Fig. 4c). For $\epsilon < 10$, there would be occasional excursions of the jet into the cavity, and at $\epsilon \approx 2.6$ the jet produced a "flickering flame" effect (see Fig. 4d), which was referred to as Mode Ib behavior. The smoke-filled region continued to shrink until $\epsilon \approx 1.5$, where signs of reverse flow were observed at the downstream edge of the jet (mode IIb); further increase in speed caused the smoke to penetrate farther into the cavity (see Fig. 4e). The four regimes of vortex breakdown for $G = 0.533$ are shown in Fig. 5: The "b" modes were also observed in laminar flow, whereas the "a" modes were not.

Photographic evidence of the flow referred to above for $G = 0.533$ is shown in Fig. 6. The r - z plane of the cavity was illuminated by the laser, and smoke-filled regions appear white in contrast to the black air-filled parts of the cavity. (The white horizontal streaks are caused by flare from the laser.) Figures 6(a, b, and c) show sequential frames for $\epsilon = 29$ (mode Ia); the precessing jet, which enters the center of the cavity from the left, changes from white to black as smoke is convected radially outward. Figure 6(d), for $\epsilon = 5$, illustrates that the smoke-filled jet has become more axisymmetric (mode IIa); the black region near the shroud in Fig. 6(e) reveals that the smoke is confined to the inner part of the cavity. Figures 6(f, g), for $\epsilon = 2$, indicate the "flickering flame" effect (mode Ib). Figure 6(h), for $\epsilon = 1.25$, shows a region of reverse flow at the downstream end of the jet (mode IIb), and it can be seen that smoke has penetrated to a greater radius than for $\epsilon = 2$. (Additional evidence of vortex breakdown at $G = 0.533$ was provided by Owen and Pincombe from the analysis of pressure measurements and velocity spectra.)

The flow structure for $G = 0.4$, shown in Figs. 4(f-j), was similar to that described above for $G = 0.533$. For $G = 0.267$ (Figs. 4k-o), the weak outer toroidal vortex, seen in the stationary cavity, was not visible when the cavity was rotated, and the inner vortex was reduced in strength with increasing rotational speed. There was no evidence of mode Ia breakdown for this gap ratio; however, for $\epsilon = 21$, the smoke-filled region increased in radius and the jet appearance was similar to that described above for the large gap ratios (see Fig. 4m). The jet appeared nonaxisymmetric for $1.5 \leq \epsilon \leq 2.6$, and at $\epsilon \approx 1.5$ the smoke-filled region suddenly increased in size before decreasing again with increasing rotational speed.

For $G = 0.133$ (Figs. 4p-t), the effect of rotation was to suppress the outer vortices and to reduce the strength of the

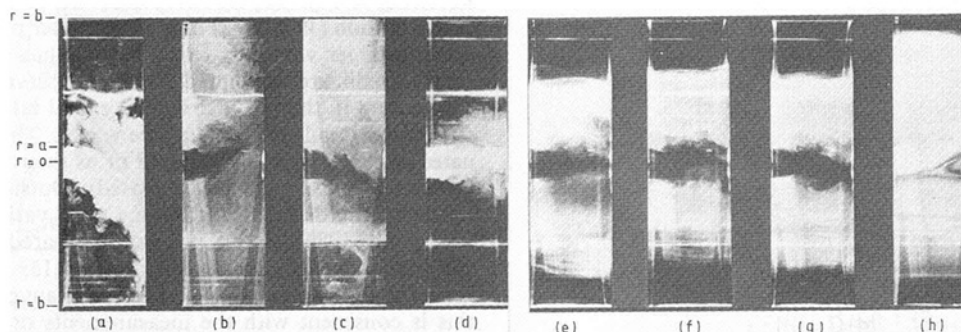


Fig. 6 Photographs of flow structure in an isothermal rotating cavity: $G = 0.533$, $Re_z = 10^4$; (a, b, c) $\epsilon = 29$ (mode Ia); (d, e) $\epsilon = 5$ (mode IIa); (f, g) $\epsilon = 2$ (mode Ib); (h) $\epsilon = 1.25$ (mode IIb)

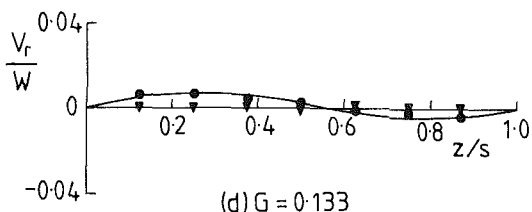
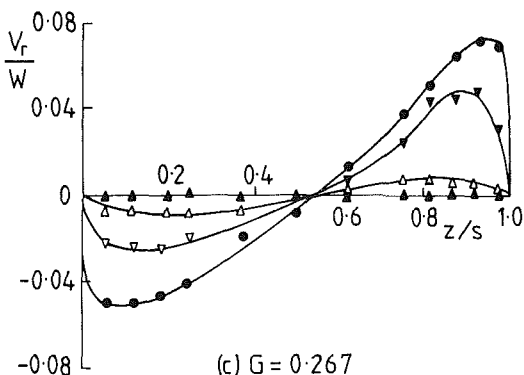
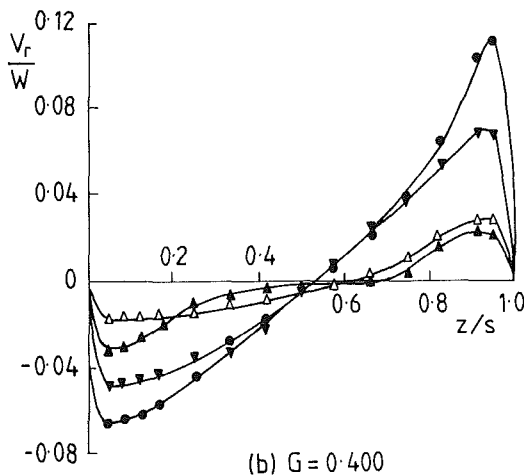
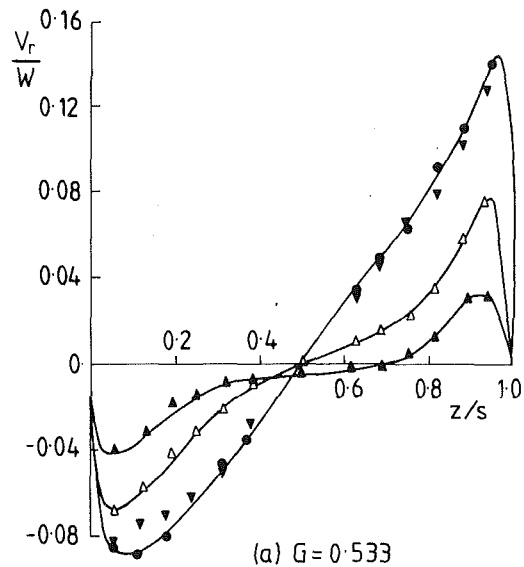


Fig. 7 Axial profile of radial component of velocity in an isothermal rotating cavity: $Re_z = 8 \times 10^4$, $r/b = 0.8$; \bullet , $\epsilon \rightarrow \infty$; ∇ , $\epsilon = 160$; Δ , $\epsilon = 80$; \blacktriangle , $\epsilon = 40$

inner one. The flow inside the smoke-filled region appeared highly turbulent and, as shown in Figs. 4(*g, r, s*), this region decreased in radial extent with increasing rotational speed. For $\epsilon \leq 1.5$, further increase in speed caused the smoke-filled region to increase. At $\epsilon \approx 1$ there was evidence of reverse flow in the jet, and smoke would occasionally penetrate into the cavity in a series of axisymmetric waves.

The above observations were made for isothermal flow in rig (*b*); Onur (1980) carried out tests for $G = 0.400$ in rig (*c*), which has a central drive shaft. He observed the occurrence of mode Ia vortex breakdown, for $23 \leq \epsilon \leq 50$, for isothermal conditions and for the case where the downstream disk was heated to a temperature about 30°C above that of the cooling air. (While Onur found it easy to determine where the breakdown ended, he found it more difficult to find the point at which the jet started to precess. The boundary of $\epsilon \approx 50$ was obtained when a "honeycomb" flow straightener was inserted into the upstream tube: This made the flow visualization easier to interpret.)

4.2 Velocity Measurements. Figure 7 shows the effect of ϵ on the axial variation of the radial component of velocity, V_r , for $r/b = 0.8$ and $Re_z = 8 \times 10^4$; the velocity is normalized with respect to W , the bulk average axial component of velocity in the upstream tube. Referring to Fig. 7(*a*) for $G = 0.533$, the radial outflow near the downstream disk, and inflow near the upstream one, is consistent with the toroidal vortex referred to above. The strength of the vortex reduced with increasing rotational speed (that is, with decreasing ϵ). The area normal to V_r at $r/b = 0.8$ is greater than the area normal to W at the center of the cavity: Thus, although $V_r/W < 1$, the radial flow rate in the toroidal vortex can be greater than that of the superposed axial throughflow.

The flow in the cavity is highly turbulent, and inspection of Fig. 7(*a*) shows that shear occurs across the entire axial gap between the disks. Measurements at other radial locations (see Pincombe, 1983) revealed that the magnitude of V_r increases with increasing radius, reaches a maximum at $r/b \approx 0.8$, and then decays to zero at $r/b = 1$. Unlike the model assumed in Section 2, there is no inviscid core under these conditions, and (as discussed below and as shown in Fig. 8*a*) the flow is not in solid-body rotation except near the outer part of the cavity.

The measured velocities for $G = 0.400$ and 0.267 , shown in Figs. 7(*b, c*), display similar effects to those for $G = 0.533$, although the magnitude of the radial velocity decreases with decreasing gap ratio. In particular, the radial flow at this radius is suppressed for $G = 0.267$ when $\epsilon \leq 40$. The reverse flow shown in Fig. 7(*d*), for $G = 0.133$, is consistent with the counterrotating vortices observed in the stationary cavity; for $\epsilon \leq 160$, this motion is suppressed at $r/b = 0.8$.

Figure 8 shows the effect of ϵ on the radial variation of the tangential component of velocity for $z/s = 0.5$ and $Re_z = 4 \times 10^4$. Referring to Fig. 8(*a*) for $G = 0.533$, the flow is in near solid-body rotation ($V_\phi/\Omega r \approx 1$) only in the outer part of the cavity. For the larger values of ϵ , the large values of $V_\phi/\Omega r$ at the smaller radii are attributed to the conservation of angular momentum in the toroidal vortex; radial inflow near the upstream disk tends to create a free vortex. This effect is attenuated as the gap ratio is reduced or as the rotational speed is increased (that is, as ϵ is decreased). Outside the boundary layers on the disks, there is some axial variation of V_ϕ (see Pincombe, 1983), but it is small compared with the radial variation shown in Fig. 8(*a*). For $G = 0.133$ and 0.267 , there is near solid-body rotation over a significant part of the cavity; this is consistent with the measurements of the radial component of velocity at $r/b = 0.8$ (and, although not shown here, at smaller values of r/b), which indicate reduced circulation at the smaller values of ϵ .

5 Flow in a Heated Rotating Cavity

5.1 Flow Visualization. Initial flow-visualization studies were undertaken in rig (*d*) with $G=0.124$, $1 < Re_z/10^4 < 2$, $0.5 < Re_\theta/10^3 < 8$ ($0.57 < \epsilon < 9.2$). The disks could be heated to produce distributions of temperature that increased, decreased or remained approximately constant with increasing radius. Typical "increasing," "decreasing," and "constant" temperature distributions are shown in Fig. 9. Results were obtained for the case where both disks were heated to the same temperature (the "symmetrically heated" cavity) or where only the downstream disk was heated. For the tests described below for rig (*d*) and other rigs, the shroud was unheated.

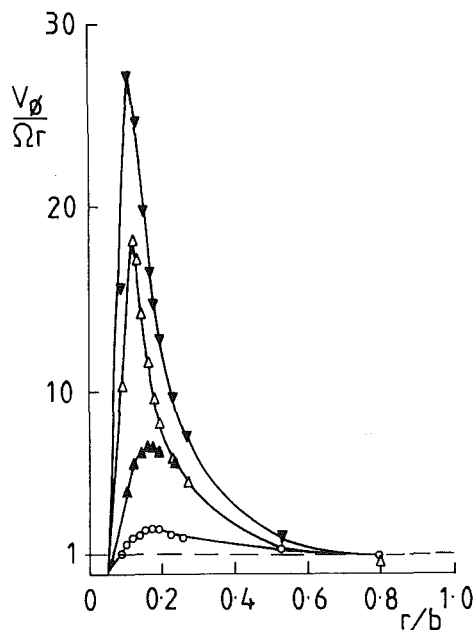
A burst of smoke was injected into the cooling air, upstream of the cavity, and the resulting flow structure was observed through the transparent shroud. For all temperature distributions,

the flow inside the cavity was seen to be nonaxisymmetric. Smoke entered the cavity in a "radial arm," which rotated at an angular speed, ω , close to that of the cavity ($\omega/\Omega \approx 1$). (The motion was similar to that associated with a buoyant plume in which a hot column of air rises through the surrounding colder atmosphere.) From the arm, the smoke was convected in the tangential direction to fill most, but not all, of the cavity; there was always a "dead zone" into which smoke would only penetrate slowly by diffusion rather than rapidly by convection. In addition, for a "decreasing" temperature distribution, there was a stagnant layer adjacent to the shroud into which the smoke was never convected.

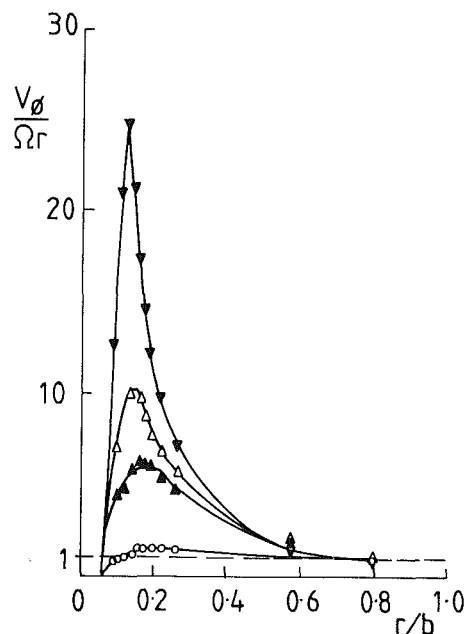
Similar observations were made in rig (*c*), where an "increasing" temperature distribution was generated on the downstream disk for $G=0.267$. Additional tests were carried out on this rig with "cobs" (see Fig. 1) attached to the center of the disks. The cobs were made from a lightweight foam material that not only changed the shape of the disks but also insulated them; it was difficult, therefore, to separate the effects of geometry from those of surface temperature. With the cobs fitted, the cold fluid formed two or three radial arms, and the amount of fluid penetrating the cavity depended on the axial spacing between the cobs and on the temperature difference between the air and the cobs.

Rig (*a*) was used for most of the flow-visualization studies; as the rig was small, and both disks and shroud were transparent, it was easily illuminated. In addition, owing to the relatively high intensity of illumination, the Kodak Ektapro high-speed video system could be used effectively. The results discussed below were obtained in rig (*a*) for $G=0.27$, $2.2 < Re_z/10^3 < 7.7$, and $1.3 < Re_\theta/10^4 < 8.7$ ($1.25 < \epsilon < 30$). The tests were conducted with a "decreasing" temperature distribution (similar to that shown in Fig. 9): This distribution produced a clearly defined flow structure.

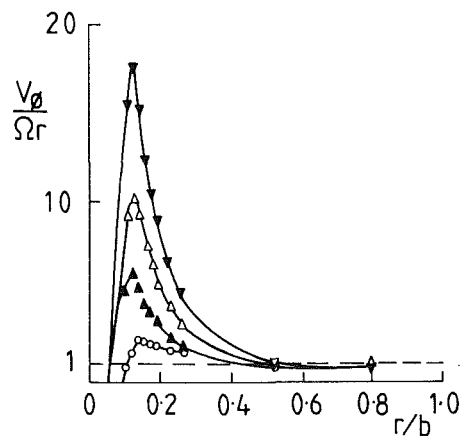
Figure 10 shows a sequence of photographs of the flow



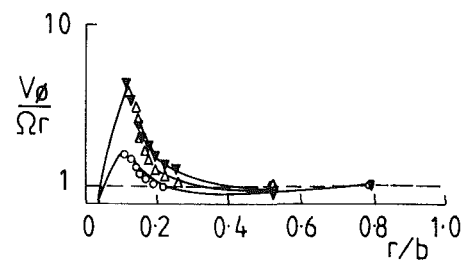
(a) $G = 0.533$



(b) $G = 0.4$



(c) $G = 0.267$



(d) $G = 0.133$

Fig. 8 Radial distribution of tangential component of velocity in an isothermal rotating cavity: $Re_z = 4 \times 10^4$, $z/s = 0.5$; ∇ , $\epsilon = 160$; Δ , $\epsilon = 80$; \blacktriangle , $\epsilon = 40$; \circ , $\epsilon = 10$

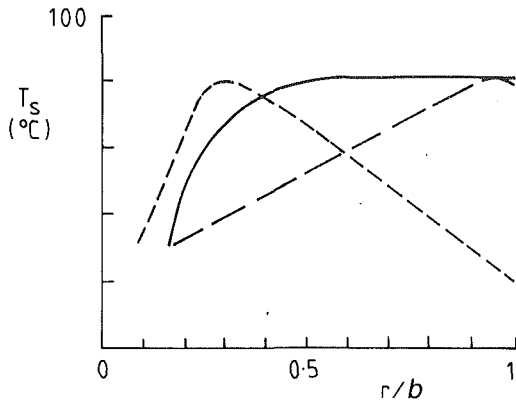


Fig. 9 Typical radial distributions of temperature on the heated disk of a rotating cavity: ——— “constant” distribution; - - - “increasing” distribution; - . - - “decreasing” distribution

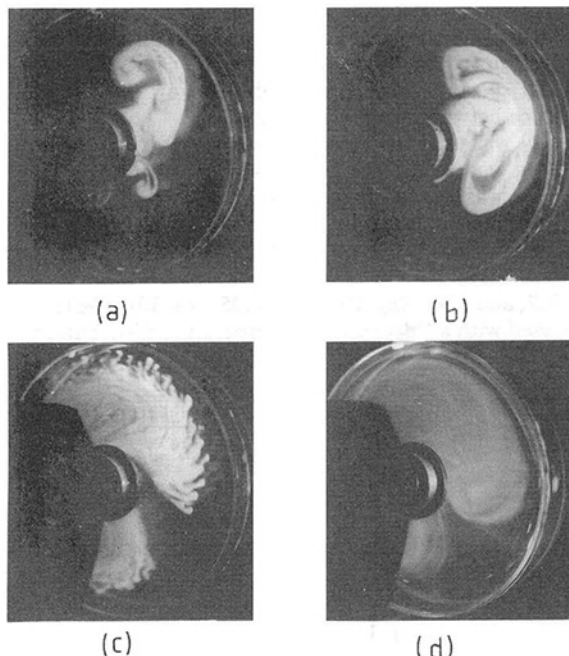


Fig. 10 Photographs of flow structure in a heated rotating cavity: $G = 0.267$, $Re_z = 2180$, $Re_\phi = 1.3 \times 10^4$, $\epsilon = 8.4$, $\Delta T = 55^\circ\text{C}$: (a, b, c): $z/s = 0.5$; (d): $z/s = 0.03$

structure. The photographs were obtained in rig (a) with $Re_z = 2180$, $Re_\phi = 1.3 \times 10^4$ ($\epsilon = 8.4$), and with symmetrically heated disks (both having the same “decreasing” distribution of temperature with $\Delta T \approx 55^\circ\text{C}$, ΔT being the difference between the maximum disk temperature and the air temperature). The photographs in Figs. 10(a, b, c) were taken at sequential times in the midaxial r - ϕ plane ($z/s = 0.5$), and 10(d) was taken in an r - ϕ plane adjacent to the upstream disk. The left-hand side of the cavity is partially obscured by the bearing and slipping assembly on the rig.

Smoke entered the cavity in the “radial arm,” referred to above, and this bifurcated to form a “forward zone” (moving relative to, but in the same direction as, the disks) and a “rearward zone” (moving in the opposite direction). The circulation inside the forward and rearward zones is consistent with the cyclonic and anticyclonic flows discussed in Section 2.2. The two smoke fronts moved around the cavity until they reached the edge of the “dead zone.” The above was termed the primary flow structure; a secondary structure was also observed in which “fingers” of smoke extended radially outward from the rearward zone toward the shroud. Smoke was

observed to move, in an annular layer between the shroud and the rearward zone, toward the dead zone; it was then seen to flow radially inward in boundary layers on the disks. The density of smoke in the remainder of the cavity prevented observation of radial inflow on the disks in regions outside the dead zone.

Although not determined accurately, the flow rate in the radial arm appeared to be significantly greater than that in the “observable boundary layers.” This gives rise to the speculation that inflow must also occur inside boundary layers adjacent to the forward or rearward zones. The speculation was further supported by the observation that smoke was convected out of the forward zone as fast as it was from the rearward zone; as the latter supplied fluid to the “observable boundary layers,” the forward zone presumably supplied fluid to “unobservable boundary layers.” This conjecture is consistent with the argument advanced in Section 2 that radial inflow can occur in Ekman layers on those regions of the disk in which $\partial p / \partial \phi > 0$.

Features of the flow structure described above can also be seen in Fig. 10 where, for $Re_\phi = 1.3 \times 10^4$, the period of one revolution, t_c , is approximately 0.37 s. Figure 10(a) shows the smoke (appearing white) in the midaxial plane approximately two seconds after it was released into the cooling air: The radial arm and the start of the forward zone are both visible. Figure 10(b), photographed one second later, shows a mushroom shape, associated with the forward and rearward zones; the curling smoke patterns provide further evidence of the cyclonic and anticyclonic circulations. Figure 10(c), photographed 9.5 s after 10(b), shows the dead zone and the radial fingers referred to above. Photograph 10(d) was taken in a plane approximately 1 mm from the upstream disk, otherwise the conditions are equivalent to those for Fig. 10(c). The boundary layer on the disk entrains smoke, and this makes the dead zone appear gray in Fig. 10(d). The layer adjacent to the shroud, from which the disk boundary layers are fed, appears as a gray ring around the rearward zone.

From frame-by-frame examination of the high-speed-video recordings, it was possible to determine: The angular-speed ratio (ω/Ω) of the flow structure; the angle ϕ between the radial arm and the dead zone (measured in the direction of rotation); the speed of advance of the two smoke fronts; and the time for each front to reach the dead zone. For the range of conditions specified above ($0.57 < \epsilon < 9.2$), it was found that $0.95 \leq \omega/\Omega \leq 1$, $270 \text{ deg} \geq \phi \geq 90 \text{ deg}$, and the smoke fronts took times between $20 t_c$ and $30 t_c$ to reach the dead zone.

Flow visualization was also carried out in rig (a) for the case where only the downstream disk was heated. Although the flow structure was broadly similar to that described above, there was no longer symmetry about the midaxial plane, and no boundary layer was observed on the unheated disk.

It is also worth noting that the central jet became unstable for $\epsilon \leq 2.5$. The jet appeared to lock onto the radial arm, and both precessed at an angular speed ω slightly less than that of the cavity ($\omega/\Omega \approx 0.95$). This effect, which is similar to the vortex breakdown observed in isothermal flow, is discussed further below.

5.2 Velocity Measurements. LDA measurements were made in rig (d), for $G = 0.12, 0.24$, and 0.36 , $0.5 < Re_z/10^4 < 1$, and $0.5 < Re_\phi/10^5 < 9.5$ ($0.5 \leq \epsilon \leq 7$). Both disks were heated to give a “constant” temperature distribution, similar to that shown in Fig. 9, with a maximum value of $\Delta T \approx 80^\circ\text{C}$.

Optical access was restricted to the shroud, and only the tangential component of velocity, V_ϕ , was measured. As the measurements were time averaged, it was not possible to determine the angular variation of V_ϕ . The LDA system was validated under isothermal conditions, and the measured velocities were always within 1 percent of the value for solid-body rotation.

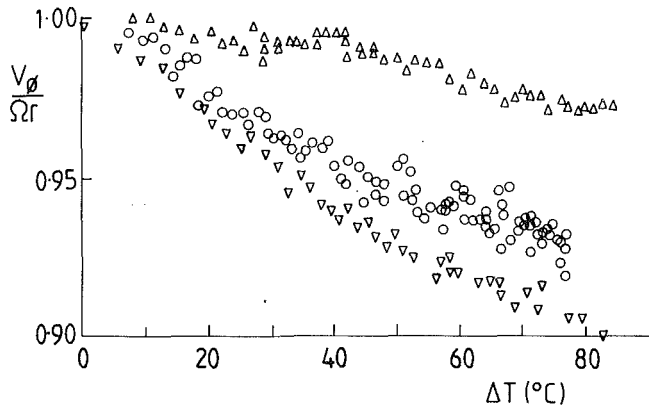


Fig. 11 Variation of $V_\phi/\Omega r$ with ΔT for a heated rotating cavity: $Re_z = 10^4$, $Re_\phi = 4 \times 10^5$, $\epsilon = 1.4$, $z/s = 0.5$, $r/b = 0.63$; Δ , $G = 0.12$; \circ , $G = 0.24$; ∇ , $G = 0.36$

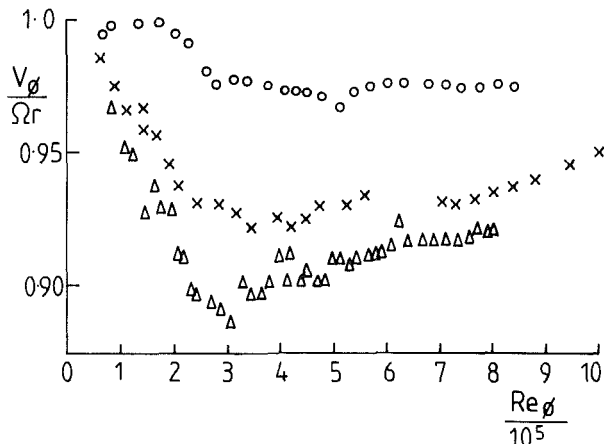


Fig. 12 Variation of $V_\phi/\Omega r$ with Re_ϕ for a heated rotating cavity: $Re_z = 10^4$, $\Delta T = 80^\circ\text{C}$, $z/s = 0.5$, $r/b = 0.63$; \circ , $G = 0.12$; \times , $G = 0.24$; Δ , $G = 0.36$

Figure 11 shows the variation of $V_\phi/\Omega r$ with ΔT for $Re_z = 10^4$ and $Re_\phi = 4 \times 10^5$ ($\epsilon \approx 1.4$), and the measurements were made in the midaxial plane ($z/s = 0.5$) and at $r/b = 0.63$. For each gap ratio, the tests were conducted under transient conditions: The heaters were switched on and the measurements were made as ΔT increased. A set of tests would take approximately one hour.

The scatter of the results in Fig. 11 is exaggerated by the large scale chosen, but it can be seen that the trend is for $V_\phi/\Omega r$ to decrease as ΔT increases. These results are consistent with the flow visualization carried out in rig (a) where the ratio of the angular speed of the smoke core to that of the cavity was in the range $0.95 < \omega/\Omega < 1$. Figure 11 also suggests that ω/Ω decreases as G increases.

Figure 12 shows the variation of $V_\phi/\Omega r$ (measured at the same location as for Fig. 11) with Re_ϕ for $Re_z = 10^4$ and a steady-state value of $\Delta T \approx 80^\circ\text{C}$. It can be seen that the fluid is in near solid-body rotation at the smaller values of Re_ϕ ($Re_\phi < 10^5$). Increasing Re_ϕ past 10^5 for $G = 0.24$ and 0.36 , and past 2×10^5 for $G = 0.12$, causes an initial reduction in $V_\phi/\Omega r$. However, for $Re_\phi \geq 2.5 \times 10^5$ ($\epsilon \leq 2.3$) there is no further reduction and, for the two larger gap ratios, $V_\phi/\Omega r$ returns slowly toward unity as Re_ϕ is increased.

The variation of $V_\phi/\Omega r$ (measured at the same location as above) with ϵ for $G = 0.24$ is shown in Fig. 13. The results were obtained for $\Delta T \approx 80^\circ\text{C}$ and with $Re_\phi/10^5 = 4, 6$, and 8 . The apparent trend is that $V_\phi/\Omega r$ decreases as ϵ is increased from 0.5 to 2 , and then increases as ϵ is further increased.

When the disks of rig (d) were heated, flow visualization

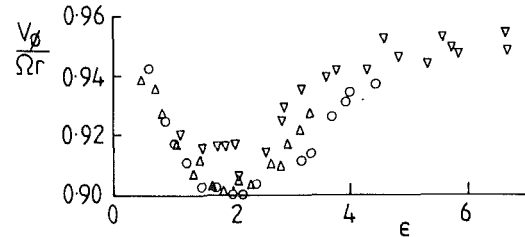


Fig. 13 Variation of $V_\phi/\Omega r$ with ϵ for a heated rotating cavity: $G = 0.24$, $\Delta T = 80^\circ\text{C}$, $z/s = 0.5$, $r/b = 0.63$; ∇ , $Re_\phi = 4 \times 10^5$; \circ , $Re_\phi = 6 \times 10^5$; Δ , $Re_\phi = 8 \times 10^5$

showed that, for all three gap ratios, the central jet was steady but nonaxisymmetric at $\epsilon = 5.8$, and some of the cold air migrated to the shroud. At $\epsilon = 2.9$, the jet was unsteady, and for $0.16 < \epsilon < 1.45$ it was very unstable and cold air was shed into the cavity. In fact, under these conditions, it appeared that for $G = 0.24$ and 0.36 most of the air in the jet was diverted into the cavity. (It should be remembered that jet instability was also observed for $\epsilon \leq 2.5$ in rig (a) with $G = 0.27$.) It seems likely, therefore, that vortex breakdown in the central jet has a strong influence in returning the flow in the core toward solid-body rotation (as seen in Fig. 13 for $\epsilon \leq 2$).

6 Conclusions

Flow visualization and LDA measurements were made in both isothermal and heated rotating cavities with an axial throughflow of air. Tests were conducted in a number of rigs and for a number of gap ratios, and the inner/outer radius ratio was $a/b \approx 0.1$.

Under *isothermal conditions*, the central jet of air passing through the rotating cavity creates a toroidal vortex (or, for $G \leq 0.267$, multiple vortices) around the jet. Although a decrease in either the gap ratio, G , or the Rossby number, ϵ , tends to reduce the strength of the toroidal vortex, axisymmetric or nonaxisymmetric vortex breakdown of the jet can increase the secondary flow inside the cavity. For the larger gap ratios, $G \geq 0.4$, the effects of vortex breakdown can be dramatic: The jet can enter the cavity and create a strong, nonaxisymmetric circulation. For the smaller gap ratios, $G \leq 0.267$, the effects of vortex breakdown are relatively weak, and for $\epsilon < 20$ the fluid in most of the cavity reverts to solid-body rotation.

The flow structure in a *heated* cavity with an axial throughflow of cold air is different from that described above. Flow visualization revealed a core of fluid with a "radial arm," a "forward zone," a "rearward zone," and a "dead zone." Smoke, injected into the cooling air, entered the cavity in the radial arm and was convected into the forward and rearward zones. Smoke in these zones was convected circumferentially until it reached the dead zone, which it permeated slowly by diffusion. The forward and rearward zones are believed to be regions of cyclonic and anticyclonic circulation associated with low and high pressure on either side of the radial arm; the resulting circumferential pressure gradient provides the Coriolis force necessary to enable the "buoyant plume" of cold, dense air to move radially into the hot cavity. There is evidence of radial inflow, in boundary layers on the disks, in regions close to the dead zone.

LDA measurements of the tangential component of velocity in the midaxial plane of the heated cavity confirmed that the angular speed, ω , of the core of fluid is smaller than that of the disk, Ω . For $G = 0.12, 0.24$, and 0.36 , $0.5 < Re_z/10^4 < 1$, and $0.5 < Re_\phi/10^5 < 9.5$ ($0.5 \leq \epsilon \leq 7$), and with both disks heated to produce a near-constant temperature with $\Delta T \leq 80^\circ\text{C}$, it was found that $0.9 \leq \omega/\Omega \leq 1$; ω/Ω decreases with increasing ΔT and with increasing G . The angular-speed ratio also depends on ϵ , and ω/Ω reaches a minimum at $\epsilon \approx 2$; for $\epsilon \leq 2$, ω/Ω tends

toward unity as ϵ is reduced. As jet instability was observed for $\epsilon \leq 2.9$, it is presumed that vortex breakdown of the central jet tends to synchronize the rotation of the core to that of the disks. Caution is obviously needed in applying these results to gas turbine engines where typical values of the relevant non-dimensional groups are: $0.1 < G < 0.4$, $0.2 < a/b < 0.5$, $4 < Re_\phi / 10^6 < 10$, and $0.01 < \epsilon < 1$.

Acknowledgments

We wish to thank the Science and Engineering Research Council, Rolls Royce plc, and Ruston Gas Turbines Ltd. for sponsoring the work presented in this paper. We are also indebted to Dr. R. H. Rogers for drawing our attention to cyclones, anticyclones, and other phenomena more familiar to the meteorologist than to the engineer.

References

Escudier, M. P., 1988, "Vortex Breakdown: Observations and Explanations," *Prog. Aerospace Sci.*, Vol. 25, pp. 189-229.

Farthing, P. R., 1988, "The Effect of Geometry on Flow and Heat Transfer in a Rotating Cavity," D. Phil. thesis, University of Sussex, United Kingdom.

Farthing, P. R., Long, C. A., Owen, J. M., and Pincombe, J. R., 1992, "Rotating Cavity With Axial Throughflow of Cooling Air: Heat Transfer," *ASME JOURNAL OF TURBOMACHINERY*, Vol. 114, this issue.

Graber, D. J., Daniels, W. A., and Johnson, B. V., 1987, "Disk Pumping Test," Air Force Wright Aeronaut. Lab., Report No. AFWAL-TR-87-2050.

Greenspan, H. P., 1968, *The Theory of Rotating Fluids*, Cambridge University Press, London, United Kingdom.

Onur, H. S., 1980, "Convective Heat Transfer in Rotating Cavities," D. Phil. thesis, University of Sussex, United Kingdom.

Owen, J. M., and Bilimoria, E. D., 1977, "Heat Transfer in Rotating Cylindrical Cavities," *J. Mech. Eng. Sci.*, Vol. 19, pp. 175-187.

Owen, J. M., and Onur, H. S., 1983, "Convective Heat Transfer in a Rotating Cylindrical Cavity," *ASME Journal of Engineering for Power*, Vol. 105, pp. 265-271.

Owen, J. M., and Pincombe, J. R., 1979, "Vortex Breakdown in a Rotating Cylindrical Cavity," *J. Fluid Mech.*, Vol. 90, pp. 109-127.

Owen, J. M., Pincombe, J. R., and Rogers, R. H., 1985, "Source-Sink Flow Inside a Rotating Cylindrical Cavity," *J. Fluid Mech.*, Vol. 155, pp. 233-265.

Pincombe, J. R., 1983, "Optical Measurements of the Flow Inside a Rotating Cylinder," D. Phil. thesis, University of Sussex, United Kingdom.

Yu, J. P., Sparrow, E. M., and Eckert, E. R. G., 1973, "Experiments on a Shrouded, Parallel Disk System With Rotation and Coolant Throughflow," *Int. J. Heat Mass Transfer*, Vol. 16, pp. 311-328.

Computation of Heat Transfer in Rotating Cavities Using a Two-Equation Model of Turbulence

A. P. Morse

C. L. Ong

Thermo-Fluid Mechanics Research Centre,
School of Engineering & Applied Sciences,
University of Sussex,
Falmer, Brighton, United Kingdom

The paper presents finite-difference predictions for the convective heat transfer in symmetrically heated rotating cavities subjected to a radial outflow of cooling air. An elliptic calculation procedure has been used, with the turbulent fluxes estimated by means of a low Reynolds number $k-\epsilon$ model and the familiar "turbulence Prandtl number" concept. The predictions extend to rotational Reynolds numbers of 3.7×10^6 and encompass cases where the disk temperatures may be increasing, constant, or decreasing in the radial direction. It is found that the turbulence model leads to predictions of the local and average Nusselt numbers for both disks that are generally within ± 10 percent of the values from published experimental data, although there appear to be larger systematic errors for the upstream disk than for the downstream disk. It is concluded that the calculations are of sufficient accuracy for engineering design purposes, but that improvements could be brought about by further optimization of the turbulence model.

1 Introduction

Current design methodology for obtaining efficient cooling of the disk components of gas turbine engines can be significantly enhanced by knowledge of the flow structure and heat transfer processes occurring in idealized rotating disk systems, as obtained by both experimental and numerical approaches. This paper focuses attention on the radial outflow of cooling air through the annular cavity formed between two heated corotating plane disks and an outer cylindrical shroud (see Fig. 1). In addition to geometric parameters, the rotational Reynolds number, $Re_\theta (= \rho \omega b^2 / \mu)$, and the mass flow rate parameter, $C_w (= \dot{m} / \mu b)$, the convective heat transfer rates from the disks will be dependent on the radial temperature distribution. Whereas an approximately uniform disk temperature is appropriate for a gas turbine in steady-state operation, radially increasing and decreasing temperature profiles have relevance to periods of engine acceleration (e.g., during aircraft takeoff) and deceleration (landing), respectively. For all the cases considered here, the temperature variation on the two disks is closely symmetric and the flow structure is then essentially similar to that found under isothermal conditions. The case of asymmetric heating, where rotationally induced buoyancy effects may dominate the flow, will be dealt with in later work.

The isothermal flow structure in rotating cavities has been investigated, using laser-Doppler anemometry and flow visualization, by Owen et al. (1985), who also employed integral-momentum techniques to predict their data. Subsequent numerical analyses have been based on the solution of the sim-

plifying boundary-layer forms of the governing transport equations (Ong and Owen, 1989) and on the full elliptic equations (Chew 1985; Morse, 1988, 1991b). With the exception of Morse (1991b), each of the authors adopted the assumption of a flow with a uniform radial source instead of the axial inlet used in the experiments. However, notwithstanding this and other simplifying assumptions made, the predictions have generally been in sufficiently good agreement with the experimental data for design purposes. The main justification for the use of elliptic solvers and advanced turbulence models would appear to be the lack of necessity for a priori knowledge of the flow structure, upon which all the simpler techniques to some extent rely.

Heat transfer measurements in rotating-cavity geometries have been published by Long and Owen (1986) and Northrop and Owen (1988b), and corresponding predictions, using momentum-integral and boundary-layer approaches, by Chew and Rogers (1988) and Ong and Owen (1991), respectively. In the latter work, the calculated local Nusselt numbers were generally within ± 10 percent of the experimental values over a fairly wide range of the parameters Re_θ and C_w : surprisingly good agreement in view of the simplifying assumptions made regarding the flow structure. The only significant discrepancies occurred at high flow rates and low rotational speeds, where there is pronounced flow asymmetry due to the wall-jet effect resulting from impingement of the inlet flow on the downstream disk.

Sultanian and Nealy (1987) have used an elliptic solver incorporating the low Reynolds number $k-\epsilon$ turbulence model of Launder and Sharma (1974) for the prediction of the data of Long and Owen (1986), but there were fairly large errors and their model is suspect because of the omission of one of the terms in the ϵ equation. However, it is now believed that

Contributed by the International Gas Turbine Institute and presented at the 35th International Gas Turbine and Aeroengine Congress and Exposition, Brussels, Belgium, June 11-14, 1990. Manuscript received by the International Gas Turbine Institute January 16, 1990. Paper No. 90-GT-135.

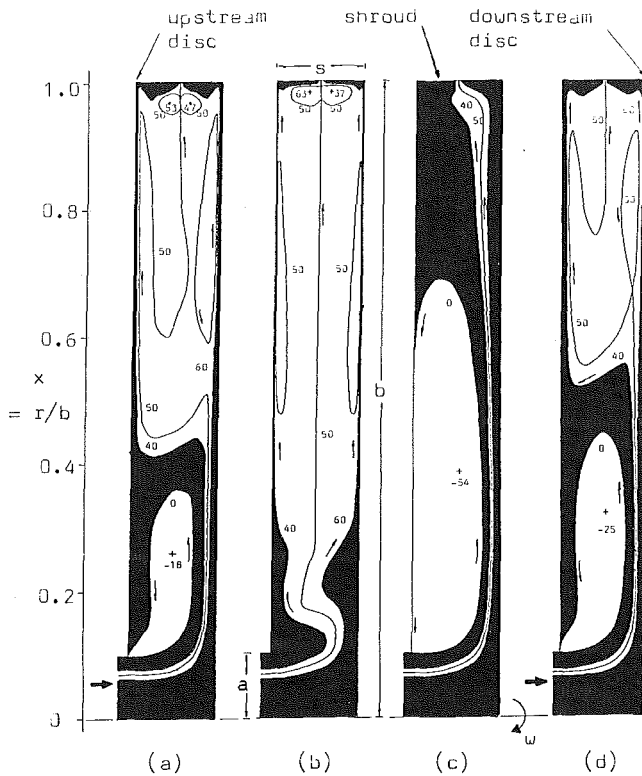


Fig. 1 Predicted flow structures for symmetrically heated rotating cavity; radially increasing disk temperature profiles: (a) $C_w = 1740$, $Re_\theta = 6.62 \times 10^5$, (b) $C_w = 1651$, $Re_\theta = 3.12 \times 10^6$, (c) $C_w = 12850$, $Re_\theta = 6.08 \times 10^5$, (d) $C_w = 12795$, $Re_\theta = 3.18 \times 10^6$

these experimental data, obtained from the solution of Laplace's conduction equation, are less accurate than those obtained by Northrop and Owen (1988b), where an improved conduction solution was supported by measurements using heat fluxmeters.

The sister paper by Northrop and Owen (1988a), concerning convective heat transfer from a free disk, is also of relevance to the present work in the context of validation of the turbulence model used. For this purpose, however, the published data have been reprocessed on the basis of an improved calibration of the heat flux meters by Long (1986). Throughout the paper, allowance has been made for radiative heat fluxes (although these are negligible for the case of a symmetrically heated cavity); the results shown thus indicate the purely convective effect on the local Nusselt numbers.

The present work is the latest in a series of papers (Morse, 1988, 1991a, 1991b) on the numerical prediction of flow and heat transfer in rotating disk systems, using a low-Reynolds-number $k-\epsilon$ turbulence model in conjunction with an elliptic solver. Previous investigations have validated the model for the prediction of isothermal flows in rotating cavities (with superimposed radial inflow or outflow) and in closed rotor-stator, corotating and counterrotating disk systems. However, the present application represents the first use of the model, by the authors, for the calculation of flows where compressibility, buoyancy, fluid property variation, and frictional heating are fully taken into account.

2 Mathematical Solution

2.1 Transport Equations. When the centripetal acceleration $\omega^2 r$ is much greater than the gravitational acceleration g , natural convection can be neglected and, under the assump-

Nomenclature

a = inlet flow radius
 A^+ = coefficient in near-wall damping function
 b = outer radius of cavity
 C_p = specific heat at constant pressure
 C_w = flow rate parameter = $\dot{m}/\mu b$
 $C_\mu, c_{\epsilon 1}, c_{\epsilon 2}$ = coefficients in turbulence model
 D = sink term in k equation
 E = source term in ϵ equation
 $E(\)$ = error in
 F = sink term in ϵ equation
 f_μ = near-wall damping function
 G = production rate of turbulent kinetic energy
 \bar{h} = stagnation enthalpy = $C_p T + 1/2(U^2 + V^2 + W^2) + k$
 h' = static enthalpy fluctuation
 k = turbulent kinetic energy
 k = thermal conductivity
 \dot{m} = mass flow rate through cavity
 Nu = local Nusselt number
 Nu = average Nusselt number for whole disk
 Nu_{av} = average Nusselt number at fluxmeter locations
 q = heat flux
 R = recovery factor
 r = radial coordinate
 r_i = inner disk radius
 Re_T = turbulence Reynolds number = $k^2/\epsilon\nu$
 Re_θ = rotational Reynolds number = $\omega b^2/\nu$
 Re_* = local rotational Reynolds number = $x^2 Re_\theta$
 s = disk spacing
 T = temperature
 U = time-averaged radial velocity
 U_τ = friction velocity = $\sqrt{\tau_s/\rho}$

$\bar{u}_i \bar{u}_j$ = Reynolds stress tensor
 V = time-averaged circumferential velocity
 \mathbf{V} = velocity vector
 \bar{W} = time-averaged axial velocity
 x = dimensionless radius = r/b
 y = generalized wall distance
 y^+ = wall distance Reynolds number = yU_τ/ν
 z = axial coordinate
 β = volumetric expansion coefficient
 Γ = diffusivity
 ΔT = appropriate temperature difference
 ϵ = dissipation rate
 θ = circumferential coordinate
 μ = viscosity
 ν = kinematic viscosity
 ρ = density
 σ = Prandtl number = $\mu C_p/k$
 σ_h = turbulence Prandtl number for enthalpy
 σ_k = turbulence Prandtl number for k
 σ_ϵ = turbulence Prandtl number for ϵ
 τ = total shear stress
 ϕ = generalized transport variable
 ψ = stream function
 ω = angular velocity

Subscripts

ad = adiabatic wall value
 eff = effective (i.e., laminar + turbulent)
 I = inlet value
 i, j, l = Cartesian tensor coordinates
 s = wall value
 T = turbulent
 ∞ = ambient value

Table 1 Transport equations

ϕ	$\Gamma_{\phi,z}$	$\Gamma_{\phi,r}$	S_ϕ
U	μ_{eff}	$2\mu_{eff}$	$-\frac{\partial}{\partial r}(P+2/3\rho k) - \frac{\rho V^2}{r} - 2\mu_{eff} \frac{U}{r^2}$ $+ \frac{\partial}{\partial z}(\mu_{eff} \frac{\partial W}{\partial r}) - \frac{2}{3} \frac{\partial}{\partial r}(\mu_{eff} \nabla \cdot \mathbf{V})$
V	μ_{eff}	μ_{eff}	$-\frac{\rho UV}{r} - \mu_{eff} \frac{V}{r^2} - \frac{V}{r} \frac{\partial \mu_{eff}}{\partial r}$
W	$2\mu_{eff}$	μ_{eff}	$-\frac{\partial}{\partial z}(P+2/3\rho k) + \frac{1}{r} \frac{\partial}{\partial r}(r\mu_{eff} \frac{\partial U}{\partial z})$ $-\frac{2}{3} \frac{\partial}{\partial z}(\mu_{eff} \nabla \cdot \mathbf{V})$
\bar{h}	$\frac{\mu}{\sigma} + \frac{\mu_T}{\sigma_h}$		$\frac{\partial}{\partial z} \left[\mu_{eff} \left(1 - \frac{1}{\sigma_{eff,h}} \right) \frac{\partial}{\partial z} \left(\frac{U^2+V^2+W^2}{2} \right) \right]$ $+ \frac{1}{r} \frac{\partial}{\partial r} \left[r\mu_{eff} \left(1 - \frac{1}{\sigma_{eff,h}} \right) \frac{\partial}{\partial r} \left(\frac{U^2+V^2+W^2}{2} \right) \right]$
k	$\mu + \frac{\mu_T}{\sigma_k}$		$G - \rho\epsilon - D$
ϵ	$\mu + \frac{\mu_T}{\sigma_\epsilon}$		$\frac{\epsilon}{K} (c_{\epsilon 1} G - c_{\epsilon 2} \rho\epsilon) + E - F$
$G = -\frac{\partial U_i}{\partial x_j} \frac{\partial U_j}{\partial x_i}$, $D = 2\mu \left[\frac{\partial k}{\partial x_j} \right]^2$, $E = \frac{2\mu\mu_T}{\rho} \left[\frac{\partial^2 U_i}{\partial x_j \partial x_j} \right]^2$ $F = 2\mu \left[\frac{\partial \epsilon}{\partial x_j} \right]^2$			

Table 2 Constants and functions in transport equations

Coefficient	Value/Function
C_μ	0.09
$A+$	24.5
$c_{\epsilon 1}$	1.44
$c_{\epsilon 2}$	$1.92 - 0.43 \exp(-R_T^2/36)$
σ_k	1.0
σ_ϵ	1.3
σ_h	0.9

tions that the flow is steady and axisymmetric, the governing transport equations for momentum, stagnation enthalpy, and turbulence quantities can be written in the common form

$$\frac{\partial}{\partial z}(\rho W\phi) + \frac{1}{r} \frac{\partial}{\partial r}(\rho r U\phi) = \frac{\partial}{\partial z} \left(\Gamma_{\phi,z} \frac{\partial \phi}{\partial z} \right) + \frac{1}{r} \frac{\partial}{\partial r} \left(r \Gamma_{\phi,r} \frac{\partial \phi}{\partial r} \right) + S_\phi \quad (1)$$

where ϕ denotes the generalized transport variable. The effective diffusivities, $\Gamma_{\phi,z}$ and $\Gamma_{\phi,r}$, and the source terms S_ϕ for each variable are shown in Table 1. The momentum equations embody a representation of the Reynolds stress tensor based upon an isotropic turbulent viscosity, according to

$$\overline{\rho u_i u_j} = \frac{2}{3} \delta_{ij} \rho k - \mu_T \left(\frac{\partial U_i}{\partial x_j} + \frac{\partial U_j}{\partial x_i} - \frac{2}{3} \delta_{ij} \nabla \cdot \mathbf{V} \right), \quad (2)$$

where $\nabla \cdot \mathbf{V}$ is the divergence of the velocity vector, i.e.,

$$\nabla \cdot \mathbf{V} = \frac{\partial w}{\partial z} + \frac{1}{r} \frac{\partial}{\partial r}(rU). \quad (3)$$

The source term for stagnation enthalpy neglects some of the formal terms arising from frictional heating, which have been found to be inconsequential. In this term, $\sigma_{eff,h}$ denotes the effective Prandtl number for enthalpy, which is defined by the relationship

$$\frac{\mu_{eff}}{\sigma_{eff,h}} = \frac{\mu}{\sigma} + \frac{\mu_T}{\sigma_h}. \quad (4)$$

2.2 Turbulence Model. The turbulent viscosity is calculated from the expression

$$\mu_T = C_\mu f_\mu \rho k^2 / \epsilon, \quad (5)$$

which incorporates a near-wall damping function, i.e.,

$$f_\mu = [1 - \exp(-y^+ / A^+)]^2, \quad (6)$$

where y^+ ($= yU_\tau/\nu$) is the Reynolds number based on the normal distance to the nearest wall. (Justification for the use of this particular form of correlation for f_μ is given by Nagano and Hishida, 1987, and Morse, 1991b.) Values of the turbulent kinetic energy k and the dissipation rate ϵ are obtained from transport equations of the same form as equation (1); again, the effective diffusivities and source terms are listed in Table 1. For brevity, the source terms are expressed in Cartesian tensor notation; the full forms of the D , E , F , and G terms appropriate to axisymmetric flow in cylindrical-polar coordinates may be found from Morse (1988). It should be noted that the current form of the turbulence model owes its origins to that first proposed by Jones and Launder (1972): The f_μ correlation has been modified and the F term included to improve the performance of the model in nonrotating wall-bounded shear flows (see Morse, 1991b).

Values of the numerical constants and functions appearing in the stagnation enthalpy and turbulence transport equations are listed in Table 2. Note that the turbulence model is used here in its isotropic form, where μ_T is the same for all six components of the Reynolds stress tensor. This differs from the practice adopted by Morse (1991a), where an anisotropic model was employed in the near-wall region as a simple expedient to improve calculated disk moment coefficients. With the isotropic model, moment coefficients for the *isothermal* free disk are typically 6 percent lower than given by the equation of Dorfman (1963).

Throughout the system of equations shown in Table 1, local fluid properties are used with the thermal conductivity k and the molecular viscosity μ expressed as linear functions of temperature (the specific heat C_p is taken as constant at 1006 J/kg/K). The density ρ is obtained from the perfect gas law, including the pressure effect. The equations take no account of density fluctuations, the effects of which are believed to be minor.

2.3 Computational Procedure. The numerical method was based on a modified version of the TEACH elliptic solver, giving the option of conventional hybrid differencing or the second-order upwind differencing scheme of Castro and Jones (1987) for discretization of the convection terms. A finite-difference mesh of 65×115 (axial-radial) nodes was employed, with a combination of geometrically expanding/contracting and uniform grid spacings to cluster nodes near the disks and outer shroud while avoiding excessively coarse meshes elsewhere in the flow domain. For all the cases considered, the closest off-wall node spacing could be maintained at $y^+ < 0.5$ with geometric expansion factors not exceeding 1.20. This near-wall proximity ensured that the surface fluxes could be calculated accurately using a simple two-point gradient. Comparison of the two discretization schemes revealed only slight differences, mainly confined to the core flow, on the fine mesh

that was employed, with little difference in the CPU times required for convergence. Accordingly, the Castro and Jones scheme was employed, since there was no disadvantage to its use and the global second-order accuracy imparted to the calculation procedure presumably led to some reduction of numerical diffusion. Sensible grid independence of the solutions has been verified by comparison with predictions obtained on a grid with 50 percent more nodes in both the axial and radial directions.

The pressure corrections required to satisfy mass continuity and update the pressure field were obtained using the SIMPLEC algorithm of Van Doormal and Raithby (1984), in conjunction with a block-correction procedure. Two criteria were set for the assessment of convergence: (i) that the residuals of all the dependent variables, normalized with the product of the mass flow rate and the mean value of the variable at the cavity inlet, were less than 10^{-4} , and (ii) that the calculated disk moment coefficients and average Nusselt numbers were constant to within ± 0.01 percent for 25 successive iterations.

CPU times for converged solutions varied between 1.5 h (450 iterations) and 4 h (1200 iterations) on a VAX 8530 computer. Generally speaking, convergence was faster when the values of C_w and Re_θ were such as to promote early establishment of flow symmetry about the midaxial plane (as in Fig. 1b); this was presumably a consequence of the symmetry imposed within the gap at the exit radius (see below).

2.4 Boundary Conditions. Boundary conditions at entry to the cavity were based on a 1/7th power-law profile, a turbulent kinetic energy of 10^{-4} times the square of the mean axial velocity, and a dissipation rate obtained by inversion of the definition of the turbulence Reynolds number $Re_T (= k^2/\epsilon\nu)$, using a value of $Re_T = 250$. As a compromise between the imposition of zero swirl or solid-body rotation at inlet, a swirl fraction that varied linearly from zero at the axis of rotation to unity at the inlet pipe radius was employed. At the cavity exit, the series of holes located centrally in the shroud in the experimental rig was modeled as a gap of equivalent flow area. Within this gap, the local mass flux ρU was taken as uniform at a value determined by the overall mass flow rate, and the radial diffusion was set to zero for all the dependent variables (e.g., zero radial heat flux in the stagnation enthalpy equation). Radial temperature profiles on the disks were obtained from smoothed variations of the raw experimental data (Northrop, 1984). The outer shroud was considered to be adiabatic.

3 Numerical Results

3.1 Validation of Turbulence Model—the Free Disk. Northrop and Owen (1988a) have reported measurements of the heat transfer from a free disk of radius 433 mm rotating at speeds up to 3000 rpm in air, giving rotational Reynolds numbers, based on ambient fluid properties, in excess of 3×10^6 . The heating of the disk was adjusted to give temperature profiles of the form

$$(T_s - T_\infty) \propto r^n, \quad (7)$$

with values of the exponent n approximately equal to -0.2 , 0.1 , 0.4 , and 0.6 . Here, attention is focused on the case $n = 0.1$, which indicates sensibly constant temperature, at least away from the disk edges. Between the individual runs, the average disk temperature varied from roughly 60°C to 80°C above ambient.

Figure 2 shows the predicted variation of the local disk Nusselt numbers for Re_θ in the range 5.5×10^5 – 3.2×10^6 . The Nusselt numbers are evaluated on the basis of the difference between the local disk temperature and the adiabatic wall temperature, i.e.,

$$Nu = r q / k_\infty (T_s - T_{ad}), \quad (8)$$

where

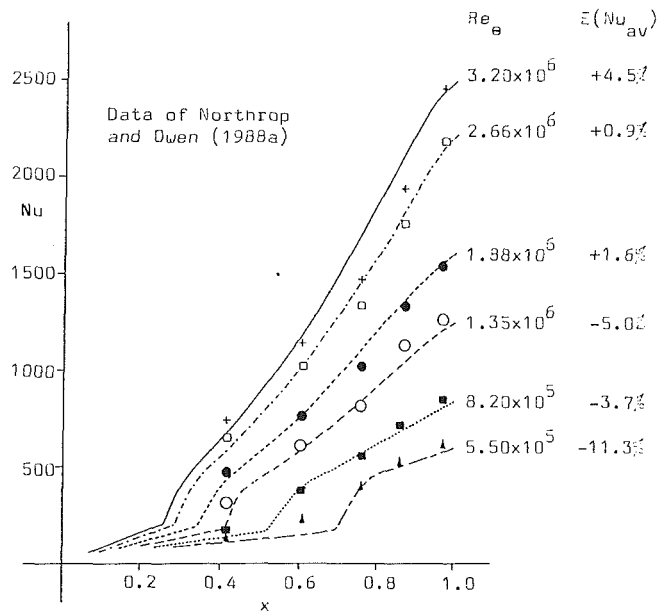


Fig. 2 Predicted local Nusselt numbers for the free disk ($n = 0.1$)

$$T_{ad} = T_\infty + \frac{1}{2} R \omega^2 r^2 / C_p, \quad (9)$$

and the recovery factor R has been taken as $\sigma^{1/3}$. Computations of this flow were made using the parabolic (marching) procedure of Patankar and Spalding (1970); brief details of the adaptation of the procedure are given by Morse (1991a, 1991b).

Agreement with the experimental data is generally good, although there is a tendency to underestimate the Nusselt number at the location of the first heat fluxmeter. As explained by Morse (1991a), the k - ϵ model requires an artificial input of turbulence energy in order to promote the transition from laminar to turbulent flow. This artificial input is provided by modifying the energy production term G to include a small fraction (0.2 percent) of that obtained from a mixing length formulation of the turbulent viscosity. This level was optimized on the basis of transition at a local rotational Reynolds number $Re_\theta (= x^2 Re_\theta)$ of 3×10^5 , in accordance with the experimental data of Theodorsen and Regier (1944) for isothermal flow. It seems clear from Fig. 2 that transition in Northrop and Owen's experiment occurs at a lower value of Re_θ ; hence the underprediction of the heat flux at the first meter location and, for $Re_\theta = 5.5 \times 10^5$, at the second location also. It should also be mentioned that the disk temperature was not measured for $x < 0.319$, which introduces further uncertainty into the predictions for low radii.

Based on the measured and calculated Nusselt numbers, an average Nusselt number, Nu_{av} , can be defined to estimate the error in the aggregate heat flux at the measurement locations, i.e.,

$$Nu_{av} = \frac{\Sigma Nu \Delta T}{\Delta T_{av}}, \quad (10)$$

where ΔT_{av} represents a radially weighted temperature difference. This Nusselt number can be used as a guide in estimating the average Nusselt numbers for the disk as a whole. Values of the errors in Nu_{av} obtained in this way are shown in Fig. 2, and it can be seen that these are less than ± 5 percent for $Re_\theta \geq 8.2 \times 10^5$, although there is a trend to worsening prediction as Re_θ is reduced. Again, this is mainly due to the delayed occurrence of transition in the calculations.

3.2 Rotating Cavities—Flow Structure. Figure 1 shows specimen predicted flow structures for the symmetrically heated

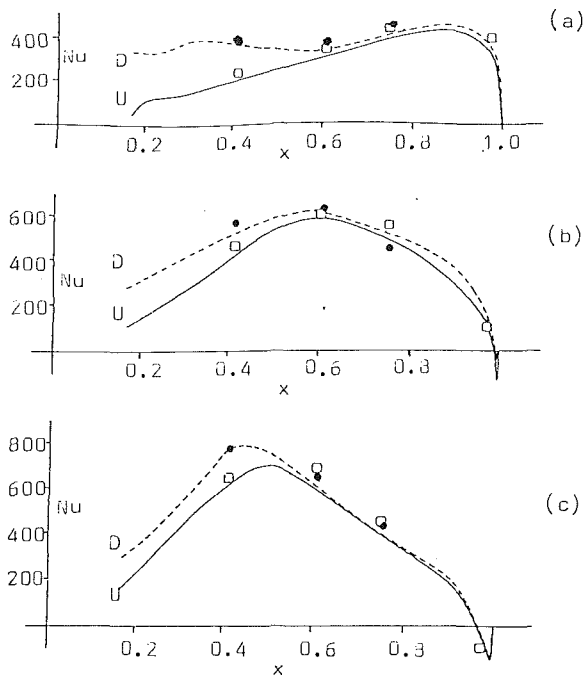


Fig. 3 Predicted local Nusselt numbers for the symmetrically heated rotating cavity: C_w nominally 7000, constant disk temperature profiles; (a) $C_w = 7081$, $Re_\theta = 6.60 \times 10^5$, (b) $C_w = 7081$, $Re_\theta = 1.98 \times 10^6$, (c) $C_w = 6972$, $Re_\theta = 3.26 \times 10^6$; data of Northrop and Owen (1988b): \circ upstream disk, \bullet downstream disk

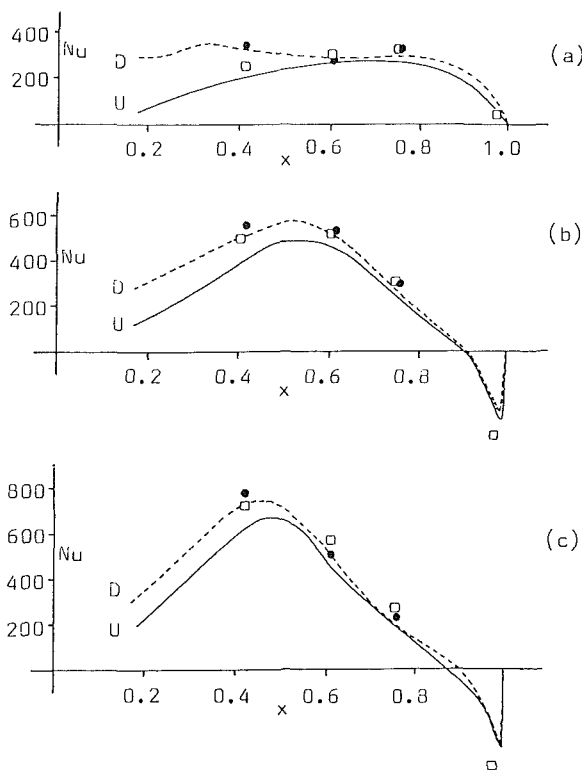


Fig. 4 Predicted local Nusselt numbers for the symmetrically heated rotating cavity: C_w nominally 7000, radially decreasing disk temperature profiles; (a) $C_w = 7081$, $Re_\theta = 6.57 \times 10^5$, (b) $C_w = 7081$, $Re_\theta = 1.97 \times 10^6$, (c) $C_w = 7081$, $Re_\theta = 3.29 \times 10^6$; data of Northrop and Owen (1988b): \circ upstream disk, \bullet downstream disk

pattern as to their dependence on Re_θ . The negative values at the outer radii are much larger than in Fig. 3 and are under-predicted by 35 percent; however, it is not clear whether the fluxmeter calibrations are valid for negative heat transfer rates. Predictions for positive disk temperature profiles are sum-

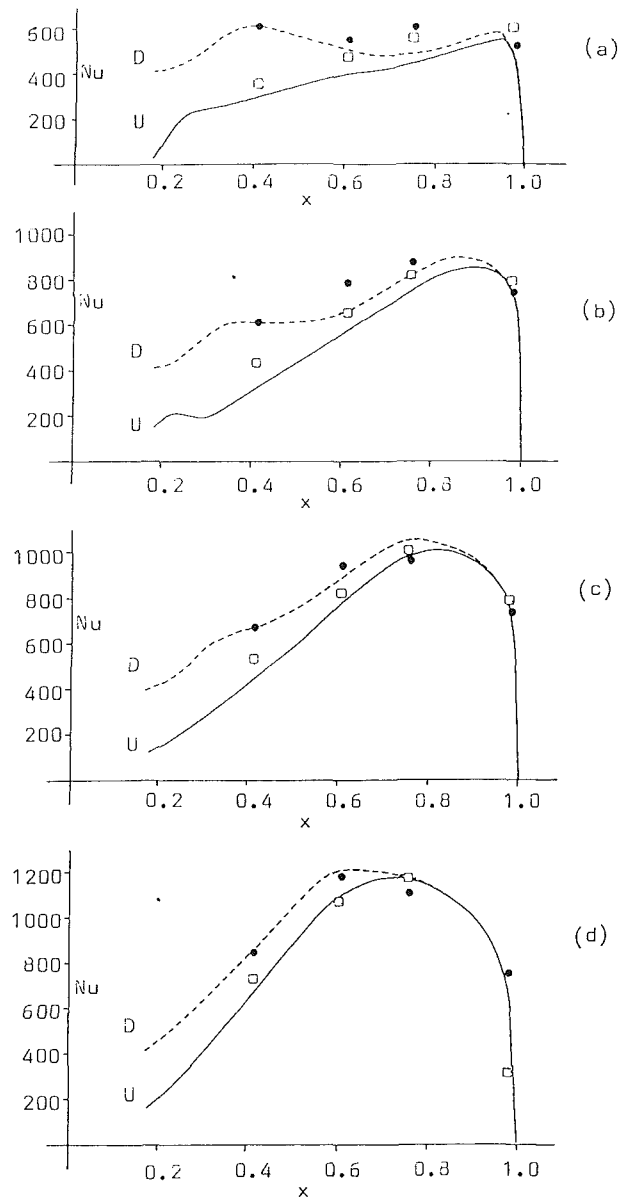


Fig. 5 Predicted local Nusselt numbers for the symmetrically heated rotating cavity: C_w nominally 14,000, radially increasing disk temperature profiles; (a) $C_w = 12,850$, $Re_\theta = 6.08 \times 10^5$, (b) $C_w = 12,905$, $Re_\theta = 1.24 \times 10^6$, (c) $C_w = 12,960$, $Re_\theta = 1.90 \times 10^6$, (d) $C_w = 12,795$, $Re_\theta = 3.18 \times 10^6$; data of Northrop and Owen (1988b): \circ upstream disk, \bullet downstream disk

marized in Table 3 and show errors of similar magnitude to those found for constant and negative profiles; as would be expected, local Nusselt numbers are higher than for the previous cases.

Figure 5 shows results obtained for the case of radially increasing temperature profiles at the highest flow rate measured, corresponding to a nominal value of $C_w = 14,000$. The predictions support the previous conclusions as regards the better accuracy for the downstream disk and the general improvement with increase in rotational Reynolds number. At $Re_\theta = 6.08 \times 10^5$ (see also Fig. 1c), there are errors of order -20 percent for the upstream disk, which seemingly arise from the lack of entrainment due to the large size of the source vortex. Since the disk temperatures increase with radius, the vortex recirculates warmer fluid inward across the upstream disk and into the entrance of the cavity, thereby reducing the heat flux from the downstream disk also. Presumably, this effect occurs in the experiment to some degree, but is exaggerated in the

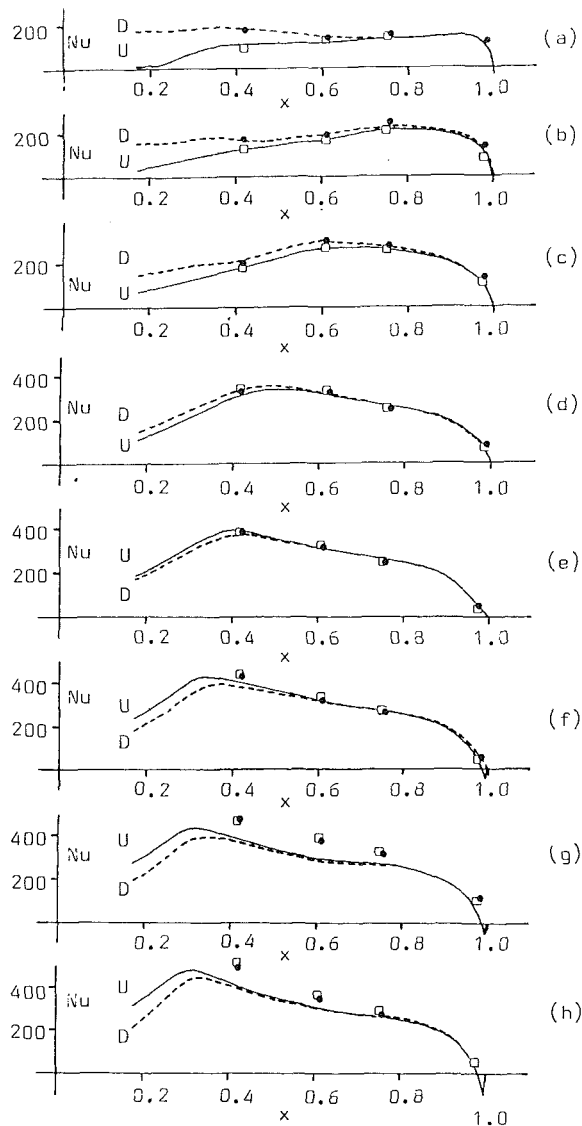


Fig. 6 Predicted local Nusselt numbers for the symmetrically heated rotating cavity: C_w nominally 2800, radially increasing disk temperature profiles; (a) $C_w = 2912$, $Re_\theta = 1.28 \times 10^5$, (b) $C_w = 2806$, $Re_\theta = 3.31 \times 10^5$, (c) $C_w = 2912$, $Re_\theta = 6.58 \times 10^5$, (d) $C_w = 2912$, $Re_\theta = 1.31 \times 10^6$, (e) $C_w = 2912$, $Re_\theta = 1.93 \times 10^6$, (f) $C_w = 2912$, $Re_\theta = 2.57 \times 10^6$, (g) $C_w = 2806$, $Re_\theta = 3.13 \times 10^6$, (h) $C_w = 3014$, $Re_\theta = 3.71 \times 10^6$; data of Northrop and Owen (1988b): \circ upstream disk, \bullet downstream disk

predictions. It is not until $Re_\theta = 1.9 \times 10^6$ that entrainment into the boundary layer on the upstream disk is predicted to begin from the inner flow radius, but there remains a significant underestimate of the Nusselt number at the first fluxmeter location (16 percent at $Re_\theta = 1.9 \times 10^6$ and 9 percent at $Re_\theta = 3.18 \times 10^6$). At the two highest values of the rotational Reynolds number, the local Nusselt numbers are however within ± 6 percent of the measured values at all the remaining fluxmeter locations, while at $Re_\theta = 3.18 \times 10^6$, the average Nusselt numbers are in error by less than 1 percent for both disks. It is also noteworthy that for all four rotational Reynolds numbers, the worst-case error at the first fluxmeter location on the downstream disk is only +1.5 percent. (Predictions for constant and radially decreasing disk temperature profiles are again summarized in Table 3.)

Finally, predictions are shown in Figs. 6 and 7 for nominal values of $C_w = 2800$ and 1400, respectively, the disk temperature profiles being positive in each case. At low values of the rotational Reynolds number, there is excellent agreement with the experimental data; indeed, for $C_w = 2800$, $Re_\theta \leq 2.57 \times 10^6$ and $C_w = 1400$, $Re_\theta \leq 6.62 \times 10^5$, over 50 percent of the

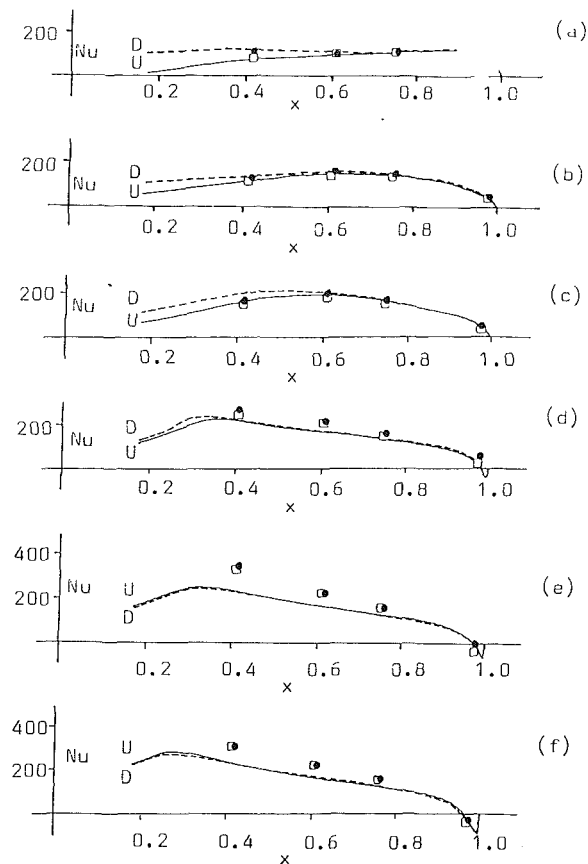


Fig. 7 Predicted local Nusselt numbers for the symmetrically heated rotating cavity: C_w nominally 1400, radially increasing disk temperature profiles; (a) $C_w = 1906$, $Re_\theta = 1.33 \times 10^5$, (b) $C_w = 1556$, $Re_\theta = 3.30 \times 10^5$, (c) $C_w = 1740$, $Re_\theta = 6.62 \times 10^5$, (d) $C_w = 1556$, $Re_\theta = 1.24 \times 10^6$, (e) $C_w = 1556$, $Re_\theta = 1.87 \times 10^6$, (f) $C_w = 1651$, $Re_\theta = 3.12 \times 10^6$; data of Northrop and Owen (1988b): \circ upstream disk, \bullet downstream disk

predicted local Nusselt numbers are, remarkably, within ± 2 percent of the experimental values. However, beyond a critical value of Re_θ , the predictive accuracy worsens abruptly, most dramatically for the lower flow rate, where there is a consistent error of -27 percent in Nu_{av} for the downstream disk for $Re_\theta \geq 1.24 \times 10^6$. For both flow rates, at high rotational Reynolds numbers, the largest errors in Nu are at the first fluxmeter location on each disk, and are of the order 30–35 percent. It is noticeable, however, that the underprediction of the Nusselt numbers in the source region is not counterbalanced by a corresponding overprediction at higher radii.

It is not thought that the above discrepancies between calculations and experiment are the fault of either the numerical scheme or the turbulence model, neither of which could be envisaged as leading to such an abrupt deterioration in predictive accuracy as that found. Rather, it is suspected that some physical change occurs in the experimental flow structure. Certainly, the fact that the critical rotational Reynolds number increases with C_w is consistent with the possible occurrence of the phenomenon of fluid ingress: At sufficiently high values of Re_θ , the pressure inside the cavity may become subatmospheric to the extent that fluid is drawn into the cavity through the holes in the outer shroud (Owen et al., 1985), despite the fact that the net flow is radially outward. Although the ingress layer is probably confined to the outer regions of the cavity, the radial influx of fluid may well give rise to instabilities in the source region, particularly for flow conditions where vortex breakdown may occur in the incoming jet. Oscillatory flow in the source region has been reported by Owen and Onur (1983) and Northrop and Owen (1988b), but only for the case of asymmetric heating (i.e., where the heating was confined to

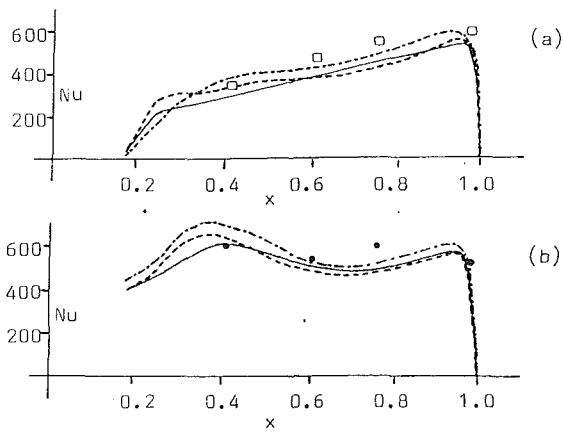


Fig. 8 Predicted local Nusselt numbers for the symmetrically heated rotating cavity: comparison of turbulence models: $C_w = 12,850$, $Re_\theta = 6.08 \times 10^5$, radially increasing disk temperature profiles; data of Northrop and Owen (1988b); — current model; - - - model of Launder and Sharma (1974); - · - model of Lam and Bremhorst (1981); (a) upstream disk, (b) downstream disk

the downstream disk), and has been attributed to the increasing importance of rotationally induced buoyancy effects. Therefore, it must be emphasized that there is no direct evidence to support the contention of oscillatory flow for the particular test cases examined here, but, of course, putative flow behavior of this type (unsteady and possibly three dimensional) cannot be accounted for within the confines of the present calculation procedure. It is also open to question as to whether fluid ingress, vortex breakdown, or buoyancy-induced effects could really bring about the higher convective heat transfer rates observed experimentally.

4 Discussion

In view of the excellent agreement obtained previously (Morse, 1988) for rotating cavities under isothermal conditions and the current predictions for the nonisothermal free disk, the calculations for the symmetrically heated cavity can only be seen as slightly disappointing. Predictive accuracy has consistently been found to be better for the downstream disk than for the upstream disk and, generally, to improve with increase in Re_θ , with its implied earlier establishment of flow symmetry. However, at low flow rates, the predictions worsen abruptly beyond a certain value of Re_θ . Although these latter predictions (shown in Figs. 6 and 7) might be excused on the grounds of the neglect of three-dimensional and unsteady flow effects, the calculated Nusselt numbers under most other flow conditions exhibit only a marginal improvement in accuracy over simpler solutions obtained at a fraction of the cost in computer time (Chew and Rogers, 1988; Ong and Owen, 1989).

The weakest link of the turbulence model is undoubtedly the simple connection between the diffusivities for momentum and enthalpy expressed via the concept of the "turbulence Prandtl number," σ_h . While a value of $\sigma_h = 0.9$ has generally been regarded as the optimum for wall-bounded flows, paradoxically, $\sigma_h = 0.5$ is more appropriate to free shear flows (see, e.g., Launder and Spalding, 1972). However, variation of σ_h between these limits results in no overall improvement as regards the current predictions for the rotating cavity, while values lower than 0.7 lead to considerable overestimates of the heat transfer from the free disk.

The natural tendency when trying to explain away discrepancies of the order found in the current predictions is to examine the modeled transport equations for the Reynolds stresses and the turbulent heat fluxes, which are conveniently presented by Hossain and Rodi (1982). As noted by Ince and Launder (1989), the most notable deficiency of the present turbulence model is its inability to predict correctly the radial turbulent

fluxes of angular momentum and enthalpy (\overline{uv} and $\overline{uh'}$, respectively), which are in reality comparable to (but less than) the corresponding axial fluxes. However, since it is the gradient of these fluxes that enters the governing transport equations, the effect caused by the modeling deficiencies then becomes negligibly small. It is concluded that an isotropic turbulent viscosity formulation, in the manner of equation (2), has at least the potential of predicting this class of flow accurately.

The main difficulty that arises in a turbulent viscosity model is that the Reynolds stresses are assumed to be locally determined and thus no account is taken of historical effects. More specifically, for the near-wall region, equation (6) and its associated numerical coefficient have been developed on the basis of flows in which there is a well-defined boundary layer. There is little doubt that, for such flows, a correlation of f_μ in terms of y^+ rather than the turbulence Reynolds number, Re_T (e.g., Launder and Sharma, 1974), gives better overall agreement with experimental data, particularly for flows in adverse pressure gradients (Nagano and Hishida, 1987). However, a correlation in terms of y^+ is less applicable for the source region and furthermore is susceptible to error in regions of flow separation, where the wall shear stress passes through zero, causing rapid, though temporary, laminarization of the flow. Such an effect may occur in the predictions of the test cases for which the source vortex is large in extent, e.g., for $C_w = 12,850$ and $Re_\theta = 6.08 \times 10^5$ (see Figs. 1c and 5a), where the recirculation brings about a change in the sign of the (dominant) tangential shear stress. Figure 8 shows a comparison of the predictions of this test case with the current turbulence model and that of Launder and Sharma, which is presumably free of this defect. Use of the latter essentially removes the discrepancy in the Nusselt number prediction at the first fluxmeter location on the upstream disk, but leads to a corresponding overprediction for the downstream disk; elsewhere, the errors in prediction are slightly worse than with the current model. Also shown in Fig. 8 are predictions obtained with the $k-\epsilon$ model of Lam and Bremhorst (1981) in which f_μ is correlated in terms of both Re_T and the wall-distance Reynolds number $Re_y (= yk^{1/2}/\nu)$. This performs slightly better than either the current model or that of Launder and Sharma, at least for this test case. As noted by Patel et al. (1985), the correlation adopted for f_μ is crucial to the performance of turbulence models of this type. It seems likely therefore that model performance could be improved by re-optimization of this correlation in terms of the three available near-wall parameters (y^+ , Re_T , and Re_y).

5 Conclusions

A low-Reynolds-number $k-\epsilon$ turbulence model has been applied to the prediction of convective heat transfer in symmetrically heated rotating cavities with a superimposed radial outflow of cooling air. The model has been validated with respect to good predictive accuracy for the heat transfer from the free disk, but systematic errors remain for the symmetrically heated rotating cavity, particularly for the upstream disk. Predictive accuracy does, however, in general, appear to improve as the rotational Reynolds number is increased, apart from test cases where nonasymmetric flow oscillations are postulated to occur. Otherwise, it seems reasonable to estimate the global accuracy of the computational procedure as regards calculation of the local Nusselt numbers as ± 10 percent, with the values tending generally to be on the low side.

As regards the shortcomings of the current predictions, it is concluded that the turbulence model does not truly portray the flow structure in the source region, where streamline curvature and the diminution of the tangential shear stress may be influential factors. Retuning of the correlation for the near-wall damping effect on the turbulent viscosity should lead to some improvement in predictive capabilities. However, within

the requirements of engineering design calculations, the current predictions will probably prove to be sufficiently accurate.

References

- Castro, I. P., and Jones, J. M., 1987, "Studies in Numerical Computations of Recirculating Flows," *Int. J. Num. Methods in Fluids*, Vol. 7, p. 793.
- Chew, J. W., 1985, "Prediction of Flow in a Rotating Cavity With Radial Outflow Using a Mixing Length Turbulence Model," *Proc. 4th International Conference on Numerical Methods in Laminar and Turbulent Flow*, Pineridge Press, Swansea, United Kingdom.
- Chew, J. W., and Rogers, R. H., 1988, "An Integral Method for the Calculation of Turbulent Forced Convection in a Rotating Cavity With Radial Outflow," *Int. J. Heat Fluid Flow*, Vol. 9, p. 37.
- Dorfman, L. A., 1963, *Hydrodynamic Resistance and Heat Loss of Rotating Solids*, Oliver and Boyd, Edinburgh.
- Hossain, M. S., and Rodi, W., 1982, "A Turbulence Model for Buoyant Flows and Its Application to Vertical Buoyant Jets," in: *Turbulent Buoyant Jets and Plumes*, Pergamon Press, New York.
- Ince, N. Z., and Launder, B. E., 1989, "On the Computation of Buoyancy-Driven Turbulent Flows in Rectangular Enclosures," *Int. J. Heat Fluid Flow*, Vol. 10, p. 102.
- Jones, W. P., and Launder, B. E., 1972, "The Prediction of Laminarization With a Two Equation Model of Turbulence," *Int. J. Heat Mass Transfer*, Vol. 15, p. 301.
- Lam, C. K. G., and Bremhorst, K. A., 1981, "Modified Form of the $k-\epsilon$ Model for Predicting Wall Turbulence," *ASME Journal of Fluids Engineering*, Vol. 103, p. 456.
- Launder, B. E., and Spalding, D. B., 1972, *Mathematical Models of Turbulence*, Academic Press, London-New York.
- Launder, B. E., and Sharma, B. I., 1974, "Application of the Energy-Dissipation Model of Turbulence to the Calculation of Flow Near a Spinning Disc," *Letters in Heat and Mass Transfer*, Vol. 1, p. 131.
- Long, C. A., 1986, "Calibration of the Fluxmeters on the Mark II Rotating Cavity Rig," Report No. 86/TFMRC/88, School of Engineering and Applied Sciences, University of Sussex, United Kingdom.
- Long, C. A., and Owen, J. M., 1986, "The Effect of Inlet Conditions on Heat Transfer in a Rotating Cavity With a Radial Outflow of Fluids," *ASME JOURNAL OF TURBOMACHINERY*, Vol. 108, p. 145.
- Morse, A. P., 1988, "Numerical Prediction of Turbulent Flow in Rotating Cavities," *ASME JOURNAL OF TURBOMACHINERY*, Vol. 110, p. 202.
- Morse, A. P., 1991a, "Assessment of Laminar-Turbulent Transition in Closed Disk Geometries," *ASME JOURNAL OF TURBOMACHINERY*, Vol. 113, pp. 131-138.
- Morse, A. P., 1991b, "Application of a Low Reynolds Number $k-\epsilon$ Turbulence Model to High-Speed Rotating Cavity Flows," *ASME JOURNAL OF TURBOMACHINERY*, Vol. 113, pp. 98-105.
- Nagano, Y., and Hishida, M., 1987, "Improved Form of the $k-\epsilon$ Model for Wall Turbulent Shear Flows," *ASME Journal of Fluids Engineering*, Vol. 109, p. 156.
- Northrop, A., 1984, "Heat Transfer in a Cylindrical Rotating Cavity," D.Phil. thesis, University of Sussex, United Kingdom.
- Northrop, A., and Owen, J. M., 1988a, "Heat Transfer Measurements in Rotating-Disc Systems. Part 1: The Free Disc," *Int. J. Heat Fluid Flow*, Vol. 9, p. 19.
- Northrop, A., and Owen, J. M., 1988b, "Heat Transfer Measurements in Rotating-Disc Systems. Part 2: The Rotating Cavity With a Radial Outflow of Cooling Air," *Int. J. Heat Fluid Flow*, Vol. 9, p. 27.
- Ong, C. L., and Owen, J. M., 1989, "Boundary-Layer Flows in Rotating Cavities," *ASME JOURNAL OF TURBOMACHINERY*, Vol. 111, pp. 341-348.
- Ong, C. L., and Owen, J. M., 1991, "Prediction of Heat Transfer in a Rotating Cavity With a Radial Outflow," *ASME JOURNAL OF TURBOMACHINERY*, Vol. 113, pp. 115-123.
- Owen, J. M., and Onur, H. S., 1983, "Convective Heat Transfer in a Rotating Cylindrical Cavity," *ASME Journal of Engineering for Power*, Vol. 105, p. 265.
- Owen, J. M., Pincombe, J. R., and Rogers, R. H., 1985, "Source-Sink Flow Inside a Rotating Cylindrical Cavity," *J. Fluid Mech.*, Vol. 155, p. 233.
- Patankar, S. V., and Spalding, D. B., 1970, *Heat and Mass Transfer in Boundary Layers*, Intertext Books, London.
- Patel, V. C., Rodi, W., and Scheuerer, G., 1985, "Turbulence Models for Near-Wall and Low Reynolds Number Flows: A Review," *AIAA J.*, Vol. 23, p. 1308.
- Sultanian, B. K., and Nealy, D. A., 1987, "Numerical Modeling of Heat Transfer in the Flow Through a Rotor Cavity," *Heat Transfer in Gas Turbine Engines*, Vol. 87, p. 11.
- Theodorsen, T., and Regier, A., 1944, "Experiments on Drag of Revolving Disks, Cylinders and Streamline Rods at High Speeds," NACA Report No. 793.
- Van Doormal, J. P., and Raithby, G. D., 1984, "Enhancements of the SIMPLE Method for Predicting Incompressible Fluid Flows," *Num. Heat Transfer*, Vol. 7, p. 147.

A Numerical Study of the Influence of Disk Geometry on the Flow and Heat Transfer in a Rotating Cavity

B. L. Lapworth

J. W. Chew

Theoretical Science Group,
Rolls-Royce plc,
Derby, United Kingdom

Numerical solutions of the Reynolds-averaged Navier-Stokes equations have been used to model the influence of cobs and a bolt cover on the flow and heat transfer in a rotating cavity with an imposed radial outflow of air. Axisymmetric turbulent flow is assumed using a mixing length turbulence model. Calculations for the non-plane disks are compared with plane disk calculations and also with the available experimental data. The calculated flow structures show good agreement with the experimentally observed trends. For the cobbled and plane disks, Nusselt numbers are calculated for a combination of flow rates and rotational speeds; these show some discrepancies with the experiments, although the calculations exhibit the more consistent trend. Further calculations indicate that differences in thermal boundary conditions have a greater influence on Nusselt number than differences in disk geometry. The influence of the bolt cover on the heat transfer has also been modeled, although comparative measurements are not available.

Introduction

In this paper a theoretical investigation into the effect of disk geometry on flow and heat transfer in the cavity formed between two corotating disks with an imposed radial outflow of air is reported. The mathematical model assumes axisymmetric, steady flow and involves a finite difference solution of the Reynolds-averaged Navier-Stokes equations. A mixing length model of turbulence is employed. Three different geometries are considered: plane disks, disks with cobs, and disks with cobs plus a bolt cover on one disk. The cavities between the disks for these cases are shown in Fig. 1.

The flow structure for the plane disk geometry in isothermal conditions has been established in previous experimental and theoretical studies (see, for example, Owen and Pincombe, 1980, and Chew, 1985). It is shown by the streamline plots in Fig. 2(a). Immediately downstream of the inlet to the cavity a source region is formed in which the air is progressively entrained into the disk boundary layers. Farther downstream, where all the supplied flow has been entrained, a core region develops in which the fluid velocity is purely rotational; the disk boundary layers here are often referred to as Ekman layers. The influence of the outlet, which in this case is a uniform cylindrical sink, is confined to the boundary layer on the outer surface.

For flow in a heated plane disk geometry Pincombe (1983) and Owen and Onur (1983) have observed the development of

unsteady nonaxisymmetric effects. However, comparison of steady, axisymmetric theory with heat transfer measurements suggests that the departure from the isothermal flow structure has a relatively small effect on disk heat transfer. Analysis of flow in rotating cavities using integral methods also suggests that buoyancy effects are relatively weak (Chew, 1983). The most reliable heat transfer measurements available are probably those of Northrop and Owen (1988). These authors found fair agreement of the integral solution of Chew and Rogers (1988) with their data in the parameter range for which the Ekman-type layers are present. Ong and Owen (1991) have found a similar agreement between these data and numerical solutions of the boundary layer equations with a mixing length turbulence model. Long and Owen (1986a, 1986b) have compared the integral solution with heat transfer data from a different rig and claim reasonable agreement. Some discrepancies between theory and experiment are noticeable, however, and it is not clear as to whether these are due to experimental error or shortcomings in the model (see Chew, 1987).

Experimental studies of the effect of disk shape on flow and heat transfer have been reported by Metzger et al. (1979), Farthing and Owen (1988) and Farthing (1988). Metzger et al. found that disk face contour had little effect on heat transfer from a single rotating disk, either with or without jet cooling at the rim. Farthing and Owen presented flow visualization and heat transfer measurements from the corotating disk rig used by Long and Owen. Cobs made from a lightweight foam material were attached to the metal disks. The observed flow structure was similar to that for the plane disk geometry. Reasonable agreement between the data and plane disk integral

Contributed by the International Gas Turbine Institute and presented at the 35th International Gas Turbine and Aeroengine Congress and Exposition, Brussels, Belgium, June 11-14, 1990. Manuscript received by the International Gas Turbine Institute January 16, 1990. Paper No. 90-GT-136.

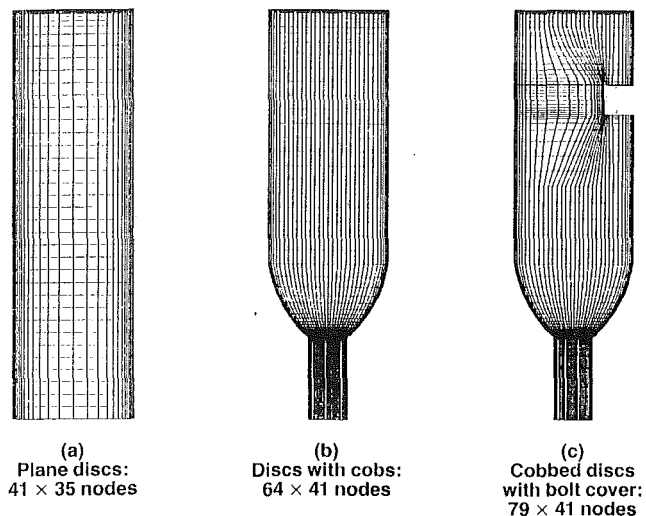


Fig. 1 Calculation grids

method solutions for the heat transfer was claimed, although the measurements suggest some sensitivity to disk shape. Farthing has reported flow visualization results showing the effect of various protrusions on the flow, including the axisymmetric ring considered here.

The mathematical model used in the present study is described in the next section. The influence of disk shape on the flow and convective heat transfer are then discussed in the next two sections. Comparisons with experimental data are also given in these sections. The main conclusions are summarized in the final section.

Mathematical Model

Governing Equations. With the assumption of an isotropic effective viscosity (μ_e), the steady, Reynolds-averaged continuity and Navier-Stokes equations in a coordinate system that rotates at speed Ω with the disks are

$$\nabla \cdot (\rho \mathbf{u}) = 0 \quad (1)$$

$$\rho \mathbf{u} \cdot \nabla \mathbf{u} - \nabla \cdot \mu_e \nabla \mathbf{u} = \nabla \cdot \mu_e \nabla \mathbf{u}^T - \nabla p - 2\rho \Omega \times \mathbf{u} - \rho \Omega \times (\Omega \times \mathbf{r}) \quad (2)$$

where the effects of compressibility in the viscous terms and gravity are neglected. Here ρ and p denote density and pressure, and \mathbf{r} , \mathbf{u} , and Ω are position, velocity, and system rotation vectors, respectively. With the further assumption of incompressible flow, the continuity and momentum equations (together with a turbulence model and boundary conditions) may be solved directly to model the flow field. Once the flow so-

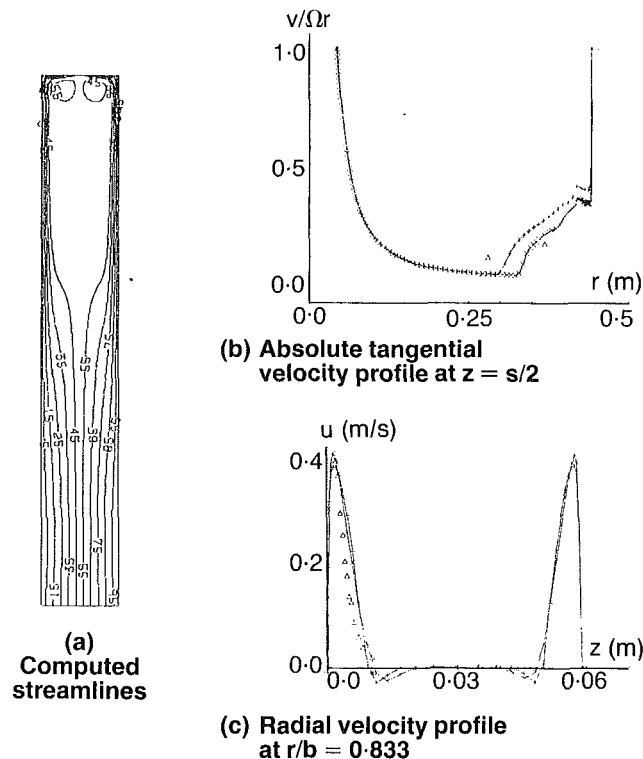


Fig. 2 Plane disk results, $C_w = 1544$, $Re_s = 10^5$

lution has been obtained, the heat transfer parameters may be calculated from a solution of the energy equation. An absolute frame of reference is used for the energy equation, which, neglecting some dissipation terms, may be written as

$$\rho \mathbf{v} \cdot \nabla H - \nabla \cdot (\mu / Pr + \mu_t / Pr_t) \nabla H = 0 \quad (3)$$

where $\mathbf{v} = \mathbf{u} + \Omega \times \mathbf{r}$ is the absolute velocity, Pr is the Prandtl number, (subscript t denotes a turbulent value, and

$$H = C_p T + \frac{1}{2} (\mathbf{v} \cdot \mathbf{v}) \quad (4)$$

is the absolute total enthalpy. In the calculations below the laminar and turbulent Prandtl numbers are taken as 0.7 and 0.9, respectively.

Turbulence Model. The effective viscosity ($\mu_e = \mu + \mu_t$) is calculated using a Prandtl mixing length model with the turbulent viscosity given by

Nomenclature

a, b = inner and outer radii of disk
 C_p = specific heat at constant pressure
 C_w = dimensionless flow rate (equation (8))
 H = stagnation enthalpy
 l = mixing length
 Nu = Nusselt number
 p = static pressure
 Pr = Prandtl number
 Q = volumetric flow rate
 q_s = heat flux from disk to fluid

\mathbf{r} = position vector
 (r, ϑ, z) = cylindrical coordinates
 Re_s = rotational Reynolds number (equation (8))
 r_e = radius at edge of source region
 s = axial disk spacing
 T = temperature
 \mathbf{u} = relative velocity
 (u, v, w) = radial, tangential, axial relative velocity components

\mathbf{v} = absolute velocity
 α = relaxation factor
 ρ = density
 μ = viscosity
 Ω = angular velocity of disks

Subscripts

e = effective value
 i = inlet
 s = disk surface
 t = turbulent value

$$\mu_t = \rho l^2 / \left(\frac{du}{dy} \right) \quad (5)$$

where l is the mixing length and " du/dy " is a velocity gradient across the shear layer. The complete details of this model have been reported by Moore and Moore (1985). Briefly, the model uses nondimensional total pressure gradients to find the edges and hence width (δ) of any boundary or shear layers. The nondimensional gradients are calculated with reference to a specified reference length scale (such as the passage width). The model also accounts for a free-stream mixing length (l_f), which is calculated from a specified free-stream turbulence intensity. In the inner part of a boundary layer, l is set to 0.41 y multiplied by the van Driest damping factor, where y is the normal distance to the nearest wall. Elsewhere, l is set to be the maximum of 0.086 δ and l_f .

Close to the walls the calculation of μ_e is modified so as to improve the model in cases for which the finite difference mesh does not extend into the laminar sublayer. At near-wall control volume faces μ_e is set to $\sqrt{\{\mu(\mu + \mu_e)\}}$. Justification for this approach is given by Moore (1984).

The sensitivity of the turbulence model to the specified values of the reference length scale and the free-stream turbulence intensity has been studied by Lapworth (1989) for the case of a plane disk. If the disks were stationary the axial disk spacing would be the appropriate value for the reference length scale. However, the rotation of the disks reduces the thickness of the disk boundary layers so it is appropriate to use a somewhat smaller reference length scale. Tests showed some sensitivity of the radial velocity profiles to this parameter (of the order of the discrepancies between theory and experiment). For the results presented below a single reference length scale of half the disk spacing was used for all cases; with hindsight a value related to the boundary layer thickness might have been more appropriate. Varying the free-stream turbulence intensity (and hence l_f) was found to have a relatively minor influence on the results; except where otherwise stated a value of 2 percent was used here.

Boundary Conditions. In the calculations, the inner cylindrical surface ($r=a$) was specified as an inlet and the outer cylindrical surface ($r=b$) was specified as an outlet. At the inlet the source flow rate is fixed and the total pressure is uniform. At the outlet a uniform radial velocity is specified. At both the inner and outer radii, the axial and tangential velocity components are set to zero, and at the cavity walls the no-slip condition is used for all velocity components. It is noted that in Farthing and Owen's (1988) experimental work the flow entered the cavity through a central axial inlet in one disk and left through discrete holes in the outer shroud. In this case, at relatively high flow rates, the incoming flow impinges on the downstream disk and flows outward in the source region as a radial wall jet, which is then entrained into symmetric Ekman layers on each disk. Hence, some differences between the numerical and experimental results are to be expected in the source and sink regions. In the Ekman layer region the flow is expected to be largely independent of the inlet and outlet conditions and the calculations may still be compared with the experiments provided the source region does not cover a significant region of the cavity. Even with the different inlet and outlet conditions, the calculations may still be used to investigate the effects of the cobs and bolt cover.

Numerical Solution Algorithm. The numerical solution is obtained using a slightly modified version of the computer program developed by Moore and Moore (1985) and Moore (1985). The governing conservation equations are discretized via a finite volume integration procedure with the primitive variables stored on the same set of discrete grid nodes. The continuity control volumes have the grid nodes at their corners. The momentum (and energy) control volumes are upwinded so as to align themselves approximately with the local flow

direction (this alignment may adjust as the iterations proceed). The advantage of upwinded control volumes is that they remove the need to add either implicit or explicit numerical diffusion in order to stabilize the finite difference representation of the convection terms. In particular, a second-order accurate discretization of the convection terms is obtained for all cell Reynolds numbers. Complete details of the control volume upwinding are described by Moore. The semi-Cartesian formulation is used for the momentum equations, which allows generalized (nonorthogonal) grid systems to be used. An iterative algorithm similar to the SIMPLER scheme of Patankar (1980) is used to solve the discretized equations. The calculation procedure is generally run to a given number of iterations, with convergence determined by examining changes in the flow variables from iteration to iteration. A reduction in rms changes to below 1 percent of their initial values is deemed to give a converged solution. Each solution is stored and may be subsequently continued if convergence has not been achieved.

The very high rates of swirl encountered in disk cavities have a strong destabilizing influence on the numerical solution algorithm. In the core region, where the radial velocity is negligible compared to the tangential velocity, the radial momentum equation is dominated by the radial pressure gradient and the Coriolis and centripetal forces. Slight imbalances between these forces can produce large destabilizing effects. To help preserve stability, the damping term suggested by Gosman et al. (1976):

$$\alpha_G(\Omega r + v)(u^{\text{old}} - u^{\text{new}})\rho/r \quad (6)$$

was added to the source term in the radial momentum equation (α_G is a specified relaxation-type parameter). This term attempts to anticipate the appropriate change in the Coriolis force corresponding to a given change in the radial velocity. Instabilities may also arise in the axial momentum equation since slight imbalances in the radial momentum equations may also produce a destabilizing axial pressure gradient in the core region (where convection and diffusion are negligible and the pressure gradient is the only axial momentum force term). Lapworth (1989) found that stability could be further enhanced if the analogous term to equation (6) was also included in the axial momentum equation, i.e.,

$$\alpha'_G(\Omega r + v)(w^{\text{old}} - w^{\text{new}})\rho/r \quad (7)$$

This term is adopted in the present calculations.

Relative to the specialized, plane disk flow, multigrid code of Vaughan et al. (1989), the present code was very inefficient for this application. Typically, about 400 iterations, using 2.5 h IBM 3090 cpu time on a 35×41 mesh, were needed to reach a converged solution. This compares to a few minutes cpu time for the equivalent solution from the Vaughan et al. code. Note, however, that the present program carries overheads as it is a generalized three-dimensional code used in axisymmetric mode.

Flow Field

The flow is characterized by the nondimensional flow rate C_w and the rotational Reynolds number Re_θ :

$$C_w = \rho Q / \mu b, \quad Re_\theta = \rho \Omega b^2 / \mu \quad (8)$$

where Q is the volumetric source flow rate.

Flow in a Plane Disk Cavity. The turbulent flow between corotating plane disks is considered for a cavity with dimensions $s=0.059$ m, $a=0.4425$ m, and $b=0.4425$ m. Predictions from the present model are compared with Pincombe's (1983) measurements and numerical results from the program described by Vaughan et al. (1989). The Vaughan et al. program uses a different mixing length model of turbulence, which was validated for this problem by Chew (1985). The principal differences between these turbulence models are in the estimation

of the boundary layer thickness and the absence of a free-stream length scale l_f in the Vaughan et al. model. For present purposes it was not considered worthwhile modifying the code to reproduce the Vaughan et al. model exactly.

Flow conditions of $C_w = 1544$, $Re_\theta = 1 \times 10^5$ are considered, for which experimental results are available. For the calculations, 35 grid points are used in the axial direction with a uniform expansion factor of 1.2 to cluster grid points near the disk walls. In the radial direction, 50 points are equally spaced from the source to approximately 95 percent height and a further 17 points are used with a contraction factor of 1.3 to cluster the grid points near the sink. A free-stream turbulence intensity of 1 percent was used for this case.

The calculated streamlines in the r - z plane are illustrated in Fig. 2(a). Figures 2(b) and 2(c) show the absolute tangential velocity at $z=s/2$ and the radial velocity at $r/b=0.833$. The two sets of computed tangential velocities in Fig. 2(b) both show the anticipated free vortex behavior for v in the source region. The two computations differ somewhat on the radial extent of the source region and the velocity distribution in the core, the present model showing the greatest discrepancy from the measurement at $r/b=0.833$. The measurement at $r/b=0.633$ is within the source region and some difference between measurement and theory might be expected due to different inlet conditions. Further computations with the present model (Lapworth, 1989) show that reducing the reference length scale in the turbulence model brings the results very close to the Vaughan et al. model. It is considered that use of a reduced reference length scale would modify slightly the results presented below, but the qualitative trends would not be affected. The extent of the source region may also be estimated from von Karman's (1921) solution for a disk rotating in a quiescent environment, where it is assumed that the source region extends to the point where all the flow is entrained into the disk boundary layers. For the present values of C_w and Re_θ , this method gives $r_e/b=0.67$, agreeing with the present computations.

The present calculations of radial velocity agree well with the Vaughan et al. model and reasonably well with Pincombe's measurements. The differences are attributed mainly to the turbulence models used. Note, however, that numerical and experimental errors may contribute to these small discrepancies between the different sets of results.

Influence of Disk Geometry. The three disk geometries considered, together with the calculation grids, are shown in Fig. 1. The three disks have the same overall dimensions of $s=0.101$ m, $a=0.381$ m and $b=0.381$ m. The cobs extend to a radius $r=0.168$ m and full details of the geometry are reported by

Farthing and Owen (1988). The bolt cover has an annular width 24.5 mm and is positioned at a radial height of 0.305 m on the face of one of the disks. The bolt cover protrudes to a height of 25 mm into the cavity. This geometry matches that studied experimentally by Farthing (1988). Note that the mesh in Fig. 1(c) has redundant points in the area constituting the bolt cover (these are not shown in the figure). Making use of these redundant points, a calculation was performed for the geometry in Fig. 1(b), using the mesh in Fig. 1(c). This calculation indicated that the mesh distortions introduced to accommodate the bolt covers were not unduly affecting the results.

Numerical solutions were obtained for each cavity at the flow condition $C_w = 1760$ and $Re = 1.5 \times 10^5$. Flow streamlines for the three cavities are compared in Fig. 3. When interpreting these plots it should be remembered that the flow spirals outward with the major velocity component being in the θ direction. In the case of the cavity with cobs, Fig. 3(b) illustrates that the region of recirculation downstream of the cob corners that would be expected in a stationary cavity has been suppressed by rotational effects. In comparison with Fig. 3(a), it can be seen that the cobs modify the flow within the source region, but do not significantly influence the size of the source region. This trend was observed experimentally by Farthing and Owen at this C_w and Re_θ , but the source region in the experiments was somewhat larger due to different inlet conditions.

In Fig. 3(c), the existence of the bolt cover introduces an asymmetry into the flow, which influences the flow at the edge of the source region but (in comparison with Fig. 3b) has only a small influence on the flow within the source region. The bolt cover also presents a blockage around which the Ekman layer must pass, and so flow separation might be expected. However, the tendency to separate is suppressed by the high rotation of the fluid, as illustrated in Fig. 3(c), where the streamlines follow very closely the bolt cover geometry. These trends are consistent with the experimental observations reported by Farthing. Also evident in Fig. 3(c) is a small region of recirculation near the lower surface of the bolt cover, which is induced by the change in flow direction caused by the impingement of the Ekman layer on the bolt cover. Farthing's flow visualization showed unsteady flow in the region of the bolt cover. Note, however, that the velocities associated with the predicted recirculation and observed unsteadiness are relatively small, so it may not be necessary to model these effects in detail.

In Fig. 4 contours of tangential velocity for the three cavities

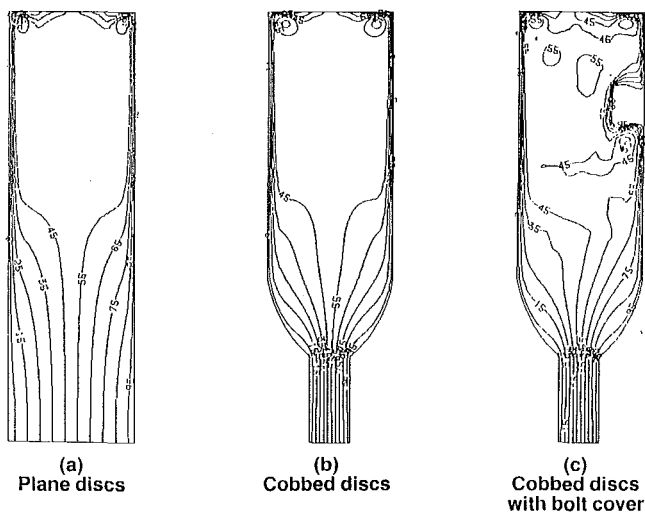


Fig. 3 Computed streamlines, $C_w = 1760$, $Re_\theta = 1.5 \times 10^5$

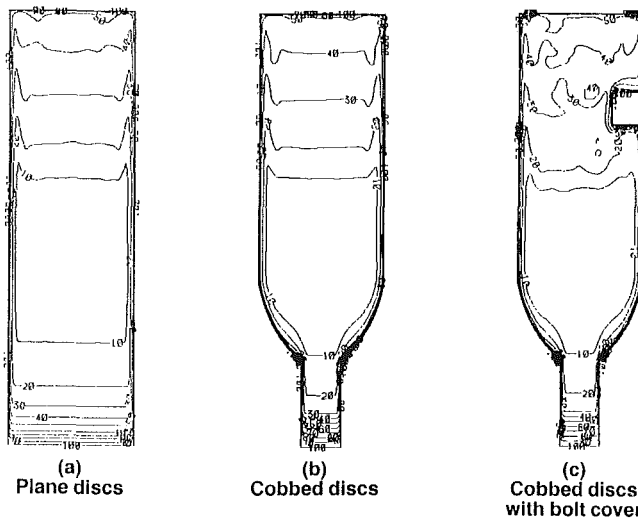


Fig. 4 Computed absolute tangential velocity $v/\Omega r (\times 100)$, $C_w = 1760$, $Re_\theta = 1.5 \times 10^5$

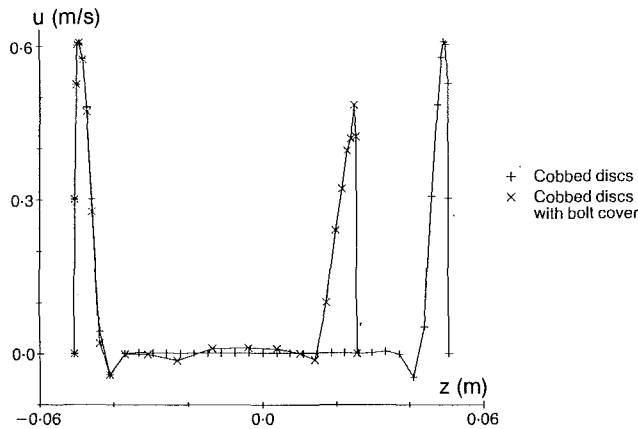


Fig. 5 Comparison of computed radial velocities at $r=0.305$ m, $C_w=1760$, $Re_\theta=1.5 \times 10^5$

are compared. Here it can be seen that the cobs have a negligible influence on the swirl and even the influence of the bolt cover is weak. Note that, in Fig. 4(c), the axial variation of v in the rotating core may be due to slight unsteadiness in the iterative solution.

The influence of the bolt cover is further illustrated in Fig. 5 where profiles of radial velocity along lines of constant radius at $r=0.305$ m (corresponding to the center of the bolt cover) are compared with the results for the cavity with cobs alone. (At this radius fully developed Ekman layers have formed and the velocity profiles for the plane and cobbed disks are indistinguishable.) Figure 5 shows that the boundary layer on the bolt cover surface is somewhat thicker than that on the opposite disk.

Heat Transfer

In the experimental measurements of Farthing and Owen (1988), the disk downstream of the axial inlet was heated and Nusselt numbers along this steel disk were deduced from temperature measurements by solving the conduction equation. The Nusselt number, Nu , is defined by

$$Nu = q_s r / k(T_s - T_i) \quad (9)$$

where q_s is the convective heat flux from the disk to the fluid, k is the thermal conductivity, T_s is the local disk surface temperature, and T_i is the temperature of the air at the inlet to the cavity. The cobs were made from lightweight insulating material attached to the plane disks and were assumed to give adiabatic boundary conditions. Note also that this was a transient experiment and the disk temperature distribution varied during the experiment. No heat transfer measurements for the bolt cover configuration are available.

In the calculations, thermal boundary conditions are specified and the numerical solution of the energy equation (3) gives the temperature field. For surfaces with specified temperature, surface heat fluxes are calculated from energy balances for the otherwise redundant near-wall control volumes; this ensures consistency of accuracy between the energy equation solution and estimation of q_s . A specified fluid temperature provides the inlet boundary condition. At the outlet, diffusive heat flux in the radial direction is assumed to be zero. As will be discussed below, various thermal boundary conditions have been specified for the disks. Where comparisons have been made with measurements these have been chosen approximately to match the experimental conditions.

Influence of Adiabatic Cobs. Nusselt numbers were computed for cavities with and without cobs for $C_w=3500$ and 7000 , with $Re_\theta=2.5 \times 10^5$ and 6×10^6 in both cases. Adiabatic boundary conditions were specified on the cobs and the tem-

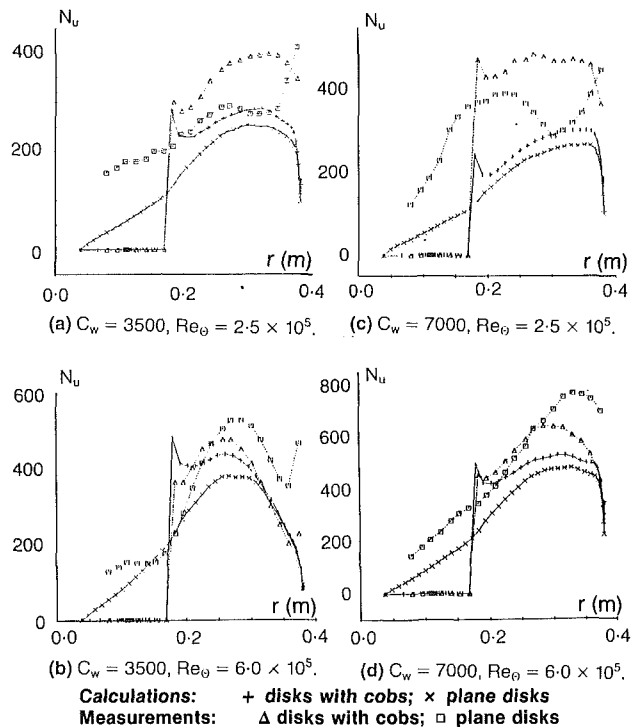
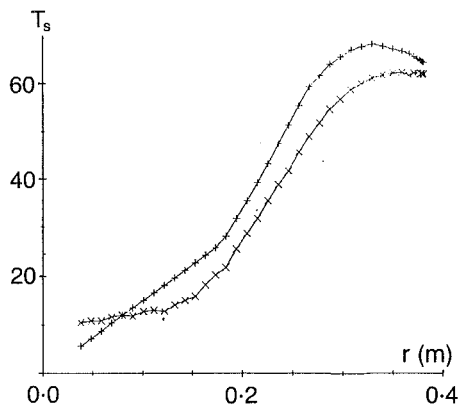


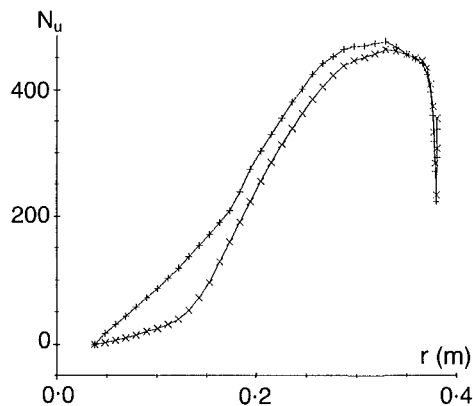
Fig. 6 Comparison of calculated and measured Nusselt numbers along heated disk surface

perature distribution over the remainder of the disks was estimated from the time average of the measurements for $C_w=3500$, $Re_\theta=2.5 \times 10^5$. For the plane disks the temperature distribution was obtained from that for the cobbed disk with extrapolation at lower radii. The calculated radial variations of Nu along the heated disk are compared with the experimental values in Fig. 6. Of these comparisons, the case with the lowest flow rate and highest rotational speed ($C_w=3500$, $Re_\theta=6 \times 10^5$) is least influenced by the different inlet conditions in the calculations and measurements. Considering this case (Fig. 6b), the calculated Nusselt numbers for the disks with cobs are in good agreement with the corresponding measured values. In particular, both results show a peak in Nu at approximately the same radius. However, the measured peak Nusselt numbers are higher in the plane disk cavity than in the cavity with cobs, whereas the calculated Nusselt numbers in the plane disk cavity are consistently lower than in the cavity with cobs (apart from the region $r \leq 0.168$ m in which the adiabatic cobs prevent any heat transfer). In addition, as might be expected from the flow calculation, at the higher radii the calculated values of Nu are similar for both disks. The measured Nu values for the plane disks at higher radii remain consistently higher than those for the disks with cobs.

For $C_w=7000$, $Re_\theta=6.0 \times 10^5$ (Fig. 6d) the calculated trend in Nu between the two cavities is again opposite to the measured trend, as for $C_w=3500$, $Re_\theta=6.0 \times 10^5$; but the level of agreement is less at the higher flow rate. For $Re_\theta=2.5 \times 10^5$ (Figs. 6a and 6c) the calculated and measured Nusselt numbers in the two cavities both show higher Nusselt numbers for the disk with cobs (apart from near the outer radius and on the cobs), with the level of agreement again deteriorating at the higher flow rate. In general, the level of agreement between the calculations and measurements becomes worse as the flow rate is increased and/or the rotational speed is reduced (as illustrated by comparing Figs. 6b and 6c). This may be readily associated with the increases in the size of the source region and hence the increasing importance of the different inlet flows as C_w is increased and/or Re_θ is reduced. Indeed, for $C_w=7000$, $Re_\theta=2.5 \times 10^5$, fully developed Ekman layers do not form and the source region fills the entire cavity.



(a)
Temperature profiles ($T_s - T_i$) along heated disc: + Farthing; x Long & Owen



(b)
Calculated Nusselt numbers corresponding to surface temperature profiles in (a)

Fig. 7 Influence of surface temperature profile on calculated Nusselt numbers; $C_w = 7000$, $Re_\theta = 6 \times 10^5$

The preceding Nusselt numbers are influenced by both differences in geometry and differences in the temperature profile along the heated disk (due to the cobs being adiabatic and variation in experimental conditions). In the following section, numerical results are presented to assess the relative importance of the separate influences of geometry and thermal boundary conditions.

Influence of Temperature Profile. Nusselt numbers are calculated for the plane disk cavity using two different temperature profiles along the heated disk. The first profile is that used in the previous section (i.e., the extrapolation of the profile measured by Farthing and Owen); the second profile is that reported by Long and Owen (1986a) for the measurements in a plane disk cavity. The two temperature profiles are presented in Fig. 7(a), with the maximum difference between the two profiles being no more than 8 K. Nusselt numbers are calculated for the single operating condition $C_w = 7000$, $Re_\theta = 6 \times 10^5$, and are presented in Fig. 7(b), illustrating distinct differences in Nu over most of the heated disk; the differences increase near the inner radius, but decrease near the outer radius. These results indicate the level of disagreement that might be expected due to the discrepancies between the experimental temperature distribution and that specified in the calculations. It should also be noted that the temperature dis-

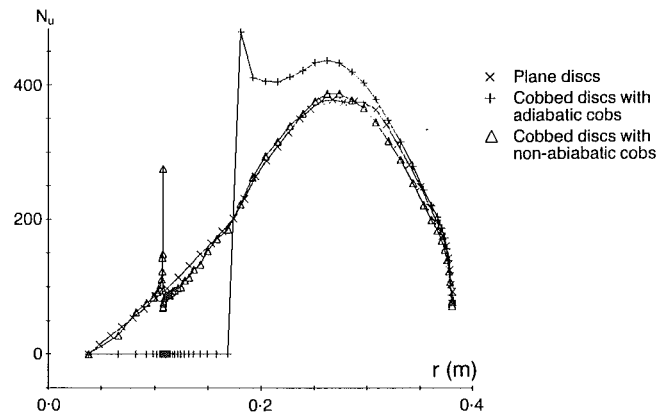


Fig. 8 Influence of adiabatic regions on calculated Nusselt numbers, $C_w = 3500$, $Re_\theta = 6 \times 10^5$

tribution variations during the transient experiment are of comparable magnitude to those in Fig. 7(a).

Influence of Nonadiabatic Cobs. In order to isolate the influence of geometry on the heat transfer, Nusselt numbers are calculated for the cavities with and without cobs using an identical temperature profile in each cavity and assuming the cobs to be made of noninsulating material (i.e., nonadiabatic). In these calculations, the single operating condition $C_w = 3500$, $Re_\theta = 6.0 \times 10^5$ is considered and the temperature profile from Farthing and Owen is used (with extrapolation where required). These Nusselt numbers are presented in Fig. 8; the previously calculated Nusselt numbers for the adiabatic cobs are also included for comparison. In this case, the Nu values for the nonadiabatic cobs are very close to the plane disk values over most of the heated disk, the only significant difference arising near the corners of the cobs. The “spike” at the corner may be a physical feature associated with high accelerations around the cob corners; but truncation errors, which are likely to be locally high in this region, may also contribute. The Nusselt numbers for the adiabatic cobs show much greater differences (apart from at the higher radii) with the plane disk Nusselt numbers than when the two cavities are compared using identical temperature distributions.

Comparing Figs. 7(b) and 8, it is observed that the differences in Nusselt number due to relatively small changes in the temperature profile (i.e., no more than 8 K) are greater than the difference due to changes in the geometry, apart from localized differences such as at the corners of the cobs. In addition, the differences between the cavities are much greater if adiabatic regions are specified in one cavity and not the other. Hence, it may be concluded that the thermal boundary condition has a much greater influence on Nusselt number than the influence of the geometry alone.

Influence of a Bolt Cover. In this section the heat transfer in the cavity with a bolt cover is investigated numerically. The disk with the bolt cover is assumed to be heated and the temperature profile from Farthing and Owen is used as the thermal boundary condition. Both the cobs and the bolt cover are assumed to be nonadiabatic; with the temperature of the bolt cover assumed to vary only with radius.

Nusselt numbers, Nu, are shown for both the cavity with the bolt cover and the cavity with cobs alone at the single flow condition $C_w = 1760$, $Re_\theta = 1.5 \times 10^5$ in Fig. 9. In Fig. 9(a), Nusselt numbers are presented for the heated disk surface and the bolt cover surface parallel to the disk for the cavity with the bolt cover, and for the heated disk surface of the cavity with cobs alone. As illustrated, the Nusselt numbers for the two cavities are virtually identical for radii up to approximately

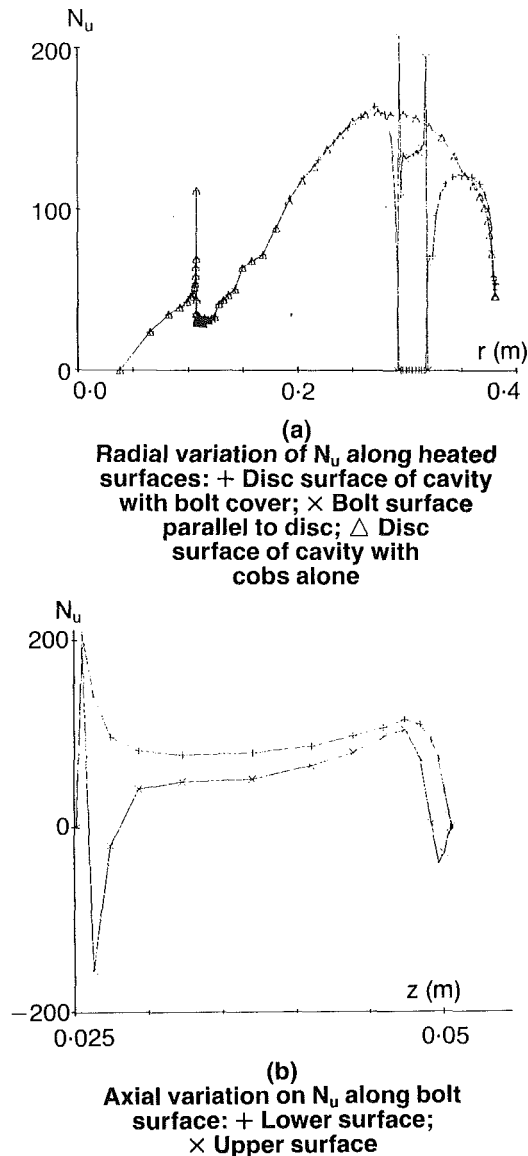


Fig. 9 Calculated Nusselt numbers for cavity with bolt cover and cavity with cobs alone, $C_w = 1760$, $Re_\theta = 1.5 \times 10^5$

$r = 0.25$ m (i.e., slightly greater than one annular bolt cover width below the lower bolt cover surface). The Nusselt numbers show large differences in the vicinity of the bolt but again become similar near the outer radius. For the bolt cover configuration, Nu is low in the vicinity of an enclosed corner (i.e., the junction of the upper and lower surfaces of the cover with the disk surface), but is high at an exposed corner (i.e., the junction of the upper or lower surfaces with the outer surface of the bolt cover). This may be a result of the higher accelerations around the exposed corners, but may also be influenced by locally higher truncation errors in these regions. In Fig. 9(b), Nusselt numbers along the upper and lower surfaces of the bolt cover are presented. In particular, Nu is higher on the lower surface than the upper surface, and is again higher near the exposed corners than the enclosed corners. In addition, there are local regions of negative Nu on the upper surface suggesting that the fluid is heating the bolt cover in these regions. However, negative values of Nu may also be associated with locally high truncation errors in the highly accelerating regions of the flow.

Conclusions

A numerical investigation into the flow and heat transfer

between corotating disks with a net radial outflow of fluid has been reported. It has been found that the present mixing length model of turbulence gives similar agreement with measurements for flow between plane disks to the models used by Chew (1985), although some care is advised in setting the model parameters. Calculations for disks with cobs and a model bolt cover have also been presented and compared with the available experimental data.

The numerical results confirm Farthing and Owen's (1988) and Farthing's (1988) experimental findings that cobs have little effect on the flow structure and the flow remains attached as it passes over the bolt cover. These observations would also seem to be consistent with the measurements of Metzger et al. (1979), which indicate that disk face contour has little effect on heat transfer from a single rotating disk.

Heat transfer calculations for plane and cobbled disks indicate that the disk shape has little effect on heat transfer, but thermal boundary conditions have an important influence. In particular the theoretical results indicate that in Farthing and Owen's experiments the change in thermal boundary conditions by the use of insulating cobs will have had a greater effect on the heat transfer than the change in disk shape. It is difficult to draw firm conclusions regarding the agreement between theory and measurement because of uncertainties regarding inlet conditions and experimental accuracy. The experimental results show some different trends to the calculations and these are difficult to explain. However, the level of agreement of the present theory with measurements is similar to that of the integral solution given by Farthing and Owen and claimed to be a reasonable approximation.

Heat transfer calculations for the cavity with a bolt cover show some local effects of the cover on the level of heat transfer. Generally, the local Nusselt numbers are reduced in this area, compared to a plane disk.

Acknowledgments

The authors would like to thank Dr. John Northall for help in modifying and running the computer program.

References

- Chew, J. W., 1983, "Buoyancy-Affected Turbulent Ekman Layer Flow Between Rotating Disks," Rolls-Royce Report, Derby, United Kingdom.
- Chew, J. W., 1985, "Prediction of Flow in a Rotating Cavity With Radial Outflow Using a Mixing Length Turbulence Model," *Proc. 4th Int. Conf. Num. Meth. Lam. and Turb. Flow*, Pineridge Press, Swansea, United Kingdom, pp. 318-329.
- Chew, J. W., 1987, Discussion of a paper by Long and Owen (1986a), *ASME JOURNAL OF TURBOMACHINERY*, Vol. 109, p. 149.
- Chew, J. W., and Rogers, R. H., 1988, "An Integral Method for the Calculation of Turbulent Forced Convection in a Rotating Cavity With Radial Outflow," *Int. J. Heat Fluid Flow*, Vol. 9, pp. 37-48.
- Farthing, P. R., 1988, "The Effect of Geometry on Flow and Heat Transfer in a Rotating Cavity," D. Phil. thesis, University of Sussex, United Kingdom.
- Farthing, P. R., and Owen, J. M., 1988, "The Effect of Disk Geometry on Heat Transfer in a Rotating Cavity With a Radial Outflow of Fluid," *ASME Journal of Engineering for Gas Turbines and Power*, Vol. 110, pp. 70-77.
- Gosman, A. D., Koosinlin, M. L., Lockwood, F. C., and Spalding, D. B., 1976, "Transfer of Heat in Rotating Systems," ASME Paper No. 76-GT-25.
- Karman, T. von, 1921, "Über laminare und turbulente reibung," *Z. angew. Math. Mech.*, Vol. 1, pp. 233-252.
- Lapworth, B. L., 1989, "Calculation of the Source-Sink Flow in Plane and Non-plane Rotating Cavities Using the Moore Elliptic Flow Program," Rolls-Royce Report, Derby, United Kingdom.
- Long, C. A., and Owen, J. M., 1986a, "The Effect of Inlet Conditions on Heat Transfer in a Rotating Cavity With a Radial Outflow of Fluid," *ASME JOURNAL OF TURBOMACHINERY*, Vol. 108, pp. 145-152.
- Long, C. A., and Owen, J. M., 1986b, "Transient Analysis of Heat Transfer in a Rotating Cavity With a Radial Outflow of Fluid," *Proc. 8th Int. Heat Transfer Conf.*, San Francisco, CA, Hemisphere, Vol. 3, pp. 1257-1263.
- Metzger, D. E., Mathis, W. J., and Grochowsky, L. D., 1979, "Jet Cooling at the Rim of a Rotating Disk," *ASME Journal of Engineering for Power*, Vol. 101, pp. 68-72.
- Moore, J. G., 1984, Comments on Report TSG0095, Virginia Polytechnic Institute and State University, College of Engineering, Report No. JM/84-2.

- Moore, J. G., 1985, "Calculation of 3-D Flow Without Numerical Mixing," *AGARD Lecture Series No. 140* on '3-D Computational Techniques Applied to Internal Flows in Propulsion Systems.'
- Moore, J. G., and Moore, J., 1985, "Calculation of Viscous Flow Using the Moore Elliptic Flow Program," Virginia Polytechnic Institute and State University, College of Engineering, Report No. JM/85-1.
- Northrop, A., and Owen, J. M., 1988, "Heat Transfer Measurements in Rotating-Disk Systems. Part 2: The Rotating Cavity With a Radial Outflow of Cooling Air," *Int. J. Heat Fluid Flow*, Vol. 9, pp. 27-36.
- Ong, C. L., and Owen, J. M., 1991, "Prediction of Heat Transfer in a Rotating Cavity With a Radial Outflow," *ASME JOURNAL OF TURBOMACHINERY*, Vol. 113, pp. 115-122.
- Owen, J. M., and Onur, H. S., 1983, "Convective Heat Transfer in a Rotating Cylindrical Cavity," *ASME Journal of Engineering for Power*, Vol. 105, pp. 265-271.
- Owen, J. M., and Pincombe, J. R., 1980, "Velocity Measurements Inside a Rotating Cylindrical Cavity With a Radial Outflow of Fluid," *J. Fluid Mech.*, Vol. 99, pp. 111-127.
- Patankar, S. V., 1980, *Numerical Heat Transfer and Fluid Flow*, Hemisphere, New York.
- Pincombe, J. R., 1983, "Optical Measurements of the Flow Inside a Rotating Cylinder," D. Phil. thesis, University of Sussex, United Kingdom.
- Vaughan, C. M., Gilham, S., and Chew, J. W., 1989, "Numerical Solutions of Rotating Disk Flows Using a Non-linear Multigrid Algorithm," *Proc. 6th Int. Conf. Num. Meth. Lam. and Turb. Flow*, Pineridge Press, Swansea, United Kingdom, pp. 63-73.

Pressure Losses in Combining Subsonic Flows Through Branched Ducts

N. I. Abou-Haidar

Department of Engineering,
University of Leicester,
Leicester, United Kingdom

S. L. Dixon

Department of Mechanical Engineering,
The University of Liverpool,
Liverpool, United Kingdom

An investigation of the "additional" total pressure losses occurring in combining flow through several sharp-edged three-leg junctions has been made. Experimental results covering a wide speed range up to choking are presented for three flow geometries of a lateral branch off a straight duct using dry air as the working fluid. A new theoretical flow model provided results in fairly good agreement with the experimental data obtained. Flow visualization of the high-speed flow using the Schlieren method revealed the presence of normal shock waves in the combined flow about one duct diameter downstream of the junction. The highest attainable Mach number (M_3) of the averaged downstream (combined) flow was 0.66 for several of the flow geometries. This value of M_3 appears to be the maximum possible and is the result of a combination of flow separation and local flow choking.

Introduction

This investigation of the total pressure losses caused by the flow in branched ducts arose from a suggestion made by Rolls Royce (Bristol) that further data were urgently needed to cover the flow range up to choking. The work reported here is primarily concerned with the additional total pressure losses (i.e., additional to those arising from simple skin friction in a straight duct) of the combining flow in sharp-edged duct junctions. In an earlier report (Abou-Haidar and Dixon, 1988), the results of an experimental and analytical study of the additional total pressure losses in the dividing flow through sharp-edged duct junctions were reported. The results of these investigations are of practical importance in assisting the design and performance of the secondary air systems in gas turbine engines. In aircraft gas turbines as much as 20 percent of the core engine airflow may be diverted to the secondary air systems and accurate data on the total pressure in branches, bends, and area changes are important for the design engineer.

Previous investigations of junction losses have been carried out by Vogel (1928), Kinne (1931), McNown (1954), Gardel (1957), Blaisdell and Manson (1963), and Ito and Imai (1973). Probably the most complete and well-known data are those of Miller (1971) and the compilation of data of ESDU (1973). All of these data relate to incompressible flow losses. No data on total pressure losses could be found for compressible flow.

The present authors have measured the junction losses for a variety of sharp-edged duct intersections over a wide range of subsonic Mach numbers. The free-streamline potential flow theory was incorporated in order to calculate the junction losses (for low-speed flow) and comparison is made with the meas-

ured results and experimental data obtained by earlier researchers. Previous applications of the free-streamline theory have been made by Mathew (1975) on bends and fittings and more recently by Hager (1984) and Abou-Haidar and Dixon (1988) on dividing flows in a straight duct, with a lateral branch (of equal area) inclined at an arbitrary angle to the straight duct. Separate Schlieren tests were carried out in order to render visible any shock waves that might be present and indicate the extent of any separation region, etc. Details of the present work and the mathematical derivation of the loss coefficient equations can be found from Abou-Haidar (1989).

Flow Modeling

A two-dimensional flow model for one type of combining flow geometry in a T-junction is shown in Fig. 1. Upstream of the junction the flow is assumed to be fully developed in both legs but downstream the flow is assumed to contain a

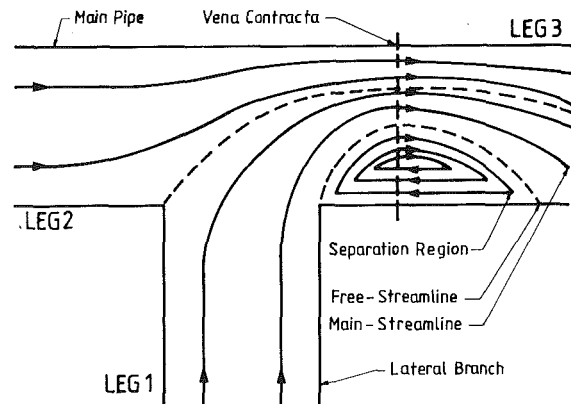


Fig. 1 Flow streamlines in a T-junction with combining flows

Contributed by the International Gas Turbine Institute and presented at the 35th International Gas Turbine and Aeroengine Congress and Exposition, Brussels, Belgium, June 11-14, 1990. Manuscript received by the International Gas Turbine Institute January 16, 1990. Paper No. 90-GT-134.

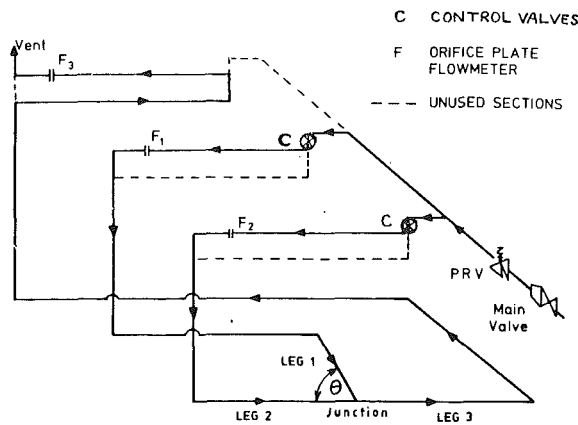


Fig. 2 Layout of ducting for combining flows

large region of separation, the main source of the additional total pressure losses. A free-streamline is assumed for the boundary between the region of separation and the main flow. The momentum of the flow in the lateral branch causes the fluid to separate as it enters the main duct leaving a separation region of lower pressure and possibly recirculating flow within the region. The size of the region is dependent on the geometry of the junction and the sharpness of the duct intersection.

Total pressure losses in the flow through the duct junction are composed of frictional losses and "additional" losses. The former are considered to be evenly distributed along each leg as though the flow was undistributed by the junction and the latter appears as a result of the junction itself causing the flow to become locally disturbed with separation and mixing processes. The friction losses can be easily determined from the pressure gradient in the duct legs well upstream of the junction. The main causes of the additional losses are attributed in this paper to the summation of the losses due to the flow contraction and the assumed sudden enlargement of the flow cross section caused by the presence of the adjacent region of separation. Such losses can be determined from momentum theory considerations as is usually done for abrupt expansions. Other causes of additional losses may arise from the formation of shock waves in high-speed flow, flow entrainment, and expulsion across the boundary of the flow separation region and skin friction stresses due to localized flow disturbances.

Experimental evidence of other earlier researchers has shown that junction losses do not occur so much in the junction itself as in the downstream branch immediately following the junction. This is where flow mixing takes place, giving rise to the production of eddies and loss in total pressure.

Nomenclature

A_R = aspect ratio = d/D

c_3 = contraction coefficient (vena contracta) in leg 3

d = depth of branch

D = pipe diameter or breadth of branch

F = dynamic pressure correction factor

K = additional overall total pressure loss coefficient

K_{13} = additional total pressure loss coefficient between legs 1 and 3

K_{23} = additional total pressure loss coefficient between legs 2 and 3

m = mass flow rate

M = Mach number

P = static pressure

P_t = total pressure

q = mass flow ratio = m_1/m_3 , or Q_1/Q_3 if constant ρ

Q = volume flow rate

Re = Reynolds number

θ = angle between legs 1 and 3

ρ = mass density of the fluid

ϕ = inlet lateral branch flow angle

Subscripts

e = extrapolated value of pressure at the geometric center of the junction

1 = leg carrying the lateral branch flow

2 = leg carrying the upstream duct branch flow

3 = leg carrying the whole flow

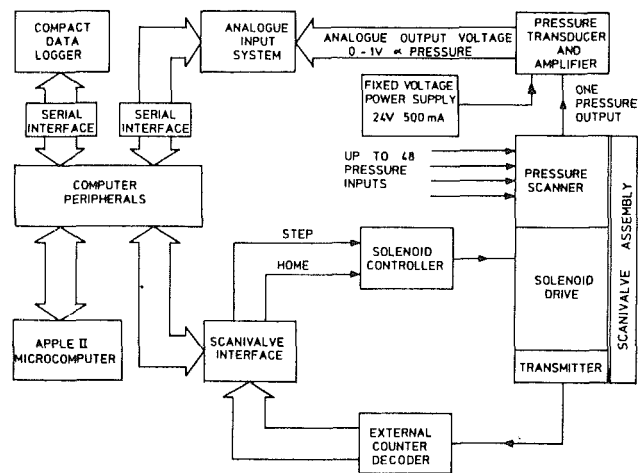


Fig. 3 Instrumentation layout

Equipment and Instrumentation

A simple schematic diagram of the test equipment for the combining flow is shown in Fig. 2. Dried air was supplied via the main and pressure reducing valves (PRV) at about 0.8 MPa. The required test conditions for the combined flow were Mach number $0.2 \leq M \leq 1.0$ and $Re \geq 2 \times 10^5$ based on duct diameter (4.04 cm). Control valves in each line enabled any suitable combination of flow directions and mass flow ratios to be obtained. The mass flow rates in each leg were measured by means of orifice plate flowmeters conforming to British Standard 1042 (1987). Air temperatures within the test sections were measured with calibrated shielded thermocouple probes. Further details of the air supply equipment manufacture, etc., are given by Abou-Haidar (1989).

The pipe network was designed for testing a great variety of flow configurations. Figure 2 shows the junction geometries tested and reported in this paper, i.e., a straight-through duct with a lateral branch at $\theta = 90, 120$, and 150 deg. All the junctions and ducts were of the same diameter. A flow straightener followed by an area reducing duct upstream ensured that the flow entering the test sections was fairly uniform. This was followed by a straight length of $15D$ upstream of the first pressure measurement point on each leg. The pressure variation along each test section was measured at six locations along each leg up to 65 cm from the duct axes intersection. At each location an average static pressure was obtained from a piezometer ring connected to four evenly spaced tappings around the circumference.

The instrumentation system shown schematically in Fig. 3

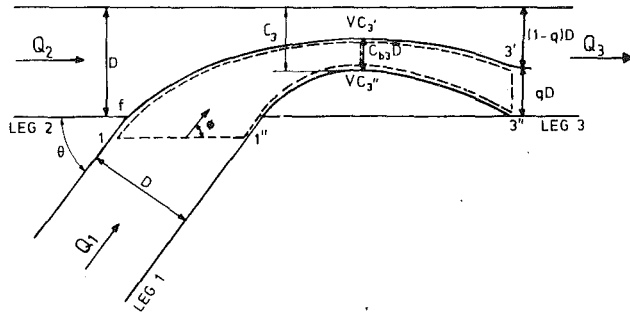


Fig. 4 Control volumes for flow from lateral branch into the main duct

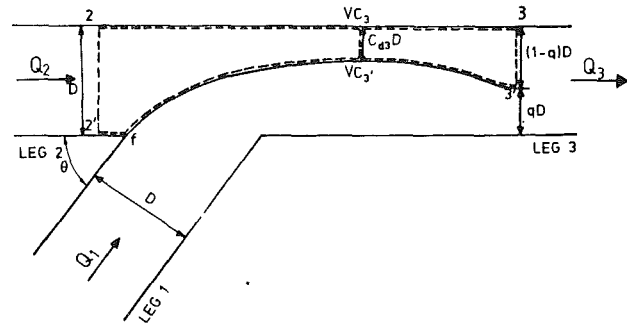


Fig. 5 Control volumes for the straight duct flow

enabled fast and accurate readings of the test section pressures to be made. Each test took about one minute and comprised 30 pressure and temperature readings together with mass flow measurements for each leg. The instrumentation used was comprised of the following: a pressure transmission system including a 48-port scanivalve, a pressure transducer, an AI13 analogue to digital device, a compact data logger (for recording temperature readings) and an Apple II microcomputer. A computer program controlled the necessary calculations to reduce the data to the required form.

Test Results

Although a large amount of experimental data has been obtained for various flow configurations and duct geometries (Abou-Haidar, 1989), only a selection of results is reported in this paper. The geometries are $\theta = 90, 120,$ and 150 deg and the results obtained illustrate important trends. The additional total pressure loss coefficients K_{13} and K_{23} are represented as functions of the Mach number M_3 for $q = 0, 0.25, 0.50, 0.75,$ and 1.0 (Figs. 6–8).

The loss coefficients are defined as:

$$K_{13} = \frac{P_{te1} - P_{te3}}{P_{te3} - P_{e3}} \quad K_{23} = \frac{P_{te2} - P_{te3}}{P_{te3} - P_{e3}}$$

where $P_{te1}, P_{te2},$ and P_{te3} are the total pressures for legs 1, 2, and 3 and P_{e3} is the static pressure for leg 3 all extrapolated to the geometric center of the junction. The overall loss coefficient K is defined by:

$$K = qK_{13} + (1 - q)K_{23}$$

where q is the mass flow ratio m_1/m_3 .

Theoretical Analysis

The analytical treatment developed here for calculating the total pressure losses is based on the innovative use of “free-streamline” potential flow theory. From this theory the shape of the downstream branch flow is determined. Control volumes are then selected to divide the flow into regions with either converging or diverging streamlines, a strategy enabling some simplifications to be made. Application of the momentum and energy equations to the contracting control volumes yields the contraction coefficients c_{b3} and c_{d3} , shown in Figs. 4 and 5, for the branch and main duct flows, respectively. A further application of the momentum equation to the diverging control volume is then sufficient to allow the loss coefficient to be determined.

Some important assumptions made are:

- (i) The flow is two-dimensional, steady, inviscid and incompressible.
- (ii) The boundary of the flow separation region is regarded as a streamline.

- (iii) Average static pressures act along the dividing streamline, free-streamline, and branch sections.
- (iv) The total pressure loss occurring between upstream and downstream branch flows is due to a sudden expansion after the “vena contracta.”

The following empirical rules were derived based on many flow visualization tests (Schlieren) and computational investigations:

(a) In Fig. 4, point f represents the stagnation point on the dividing streamline and the static pressure is assumed to be:

$$P_f = P_{e3} + \frac{F\rho Q_3^2}{2c_3^2 D^2}$$

where F is a dynamic pressure correction factor. The variation of F with respect to q was found to be:

q	0.1	0.2	0.3	0.4	0.5	0.6
F	0.020	0.832	1.200	1.442	1.580	1.673

q	0.7	0.8	0.9	1.0
F	1.730	1.736	1.735	1.717

(b) The contraction coefficient c_3 can be represented by:

$$c_3 = AB^q C^q$$

where A, B, C are given below for the three junctions:

θ, deg	90	120	150
A	0.540	0.502	0.488
B	0.693	0.653	0.609
C	-0.0670	-0.0752	-0.0783

(c) The lateral branch flow enters the main duct at $= 60$ deg (Fig. 4) for all $\theta \geq 90$ deg.

1. Lateral Branch Flow. Applying the momentum equation to the control volume $1 - 1''$ to $vc_3' - vc_3''$ in Fig. 4 in the main duct direction:

$$P_1 - P_{e3} = \frac{2\rho Q_3^2}{(1 - c_3)D^2} \left[\frac{F}{4c_3^2} (1 - c_3 + c_{b3}) + q^2 \cos \phi - \frac{q^2}{c_{b3}} \right] \quad (1)$$

Applying the energy equation to the above control volume:

$$P_1 - P_{e3} = \frac{\rho Q_3^2}{2D^2} \left[\frac{1}{c_{b3}^2} - 1 \right] q^2 \quad (2)$$

Equating Eqs. (1) and (2), a cubic equation for c_{b3} is obtained:

$$\frac{Fc_{b3}^3}{q^2(1 - c_3)c_3^2} + c_{b3}^2 \left[\frac{F}{q^2 c_3^2} + \frac{4 \cos \phi}{1 - c_3} + 1 \right] - \frac{4c_{b3}}{1 - c_3} - 1 = 0 \quad (3)$$

Table 1 Contraction coefficients c_{b3} and c_{d3}

q/θ°	c_{b3} from eqn.(3)			c_{d3} from eqn.(7)		
	90	120	150	90	120	150
0	2.0	2.0	2.0	1.0	1.0	1.0
0.1	0.610	0.576	0.557	0.498	0.498	0.498
0.2	0.159	0.145	0.139	0.400	0.389	0.384
0.3	0.186	0.167	0.159	0.333	0.316	0.309
0.4	0.216	0.192	0.180	0.275	0.256	0.247
0.5	0.246	0.218	0.203	0.222	0.205	0.196
0.6	0.277	0.241	0.220	0.174	0.158	0.148
0.7	0.305	0.264	0.237	0.128	0.115	0.106
0.8	0.334	0.288	0.258	0.084	0.075	0.068
0.9	0.357	0.309	0.277	0.041	0.036	0.033
1.0	0.376	0.327	0.300	0	0	0

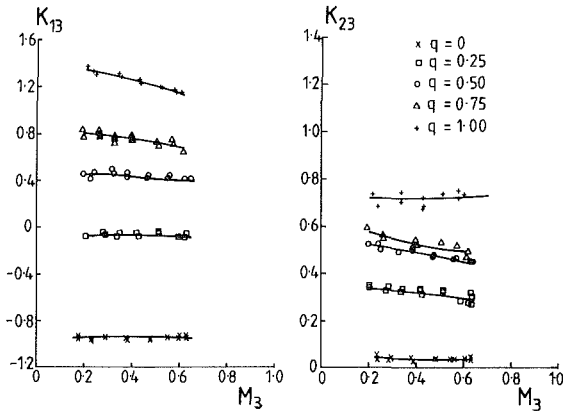


Fig. 6 Compressible flow loss coefficients K_{13} and K_{23} for $\theta = 90$ deg (uncertainty in $K_{13} = \pm 0.064$, in $K_{23} = \pm 0.057$, in $M_3 = \pm 0.012$, in $q = \pm 0.025$)

Values of c_{b3} calculated from Eq. (3) are shown in Table 1.

Again applying the momentum equation to the control volume $vc_3' - vc_3''$ to $3' - 3''$ in Fig. 4 in the main duct direction:

$$P_{c3} - P_3 = \frac{2\rho Q_1^2}{(q + c_{b3})D^2} \left[\frac{1}{q} - \frac{1}{c_{b3}} \right] \quad (4)$$

With the energy equation applied to the above control volume:

$$P_{c3} - P_3 = \frac{\rho Q_1^2}{2D^2} \left[\frac{1}{q^2} + \frac{K_{13}}{q^2} - \frac{1}{c_{b3}^2} \right] \quad (5)$$

Equating Eqs. (4) and (5) the loss coefficient K_{13} is derived:

$$K_{13} = \left\{ \frac{q}{c_{b3}} \right\}^2 + \frac{4q^2}{(c_{b3} + q)} \left(\frac{1}{q} - \frac{1}{c_{b3}} \right) - 1 \quad (6)$$

Main Duct Flow. The same procedure as above is applied to the control volume $cv_3 - vc_3'$ in Fig. 5, yielding a cubic equation for c_{d3} :

$$\frac{Fc_{d3}^3}{4c_3^2(1-q)^2} + c_{d3}^2 \left[0.5 - \frac{F}{4c_3^2(1-q)^2} \right] - c_{d3} + 0.5 = 0 \quad (7)$$

Values of c_{d3} calculated from Eq. (7) are shown in Table 1.

With the momentum and energy equations applied to the control volume $cv_3 - vc_3'$ to $3 - 3'$ in Fig. 5 and after reduction, the loss coefficient K_{23} is derived:

$$K_{23} = \frac{4(1-q)^2}{(1-q + c_{d3})} \left[\frac{1}{1-q} - \frac{1}{c_{d3}} \right] + \frac{(1-q)^2}{c_{d3}^2} - 1 \quad (8)$$

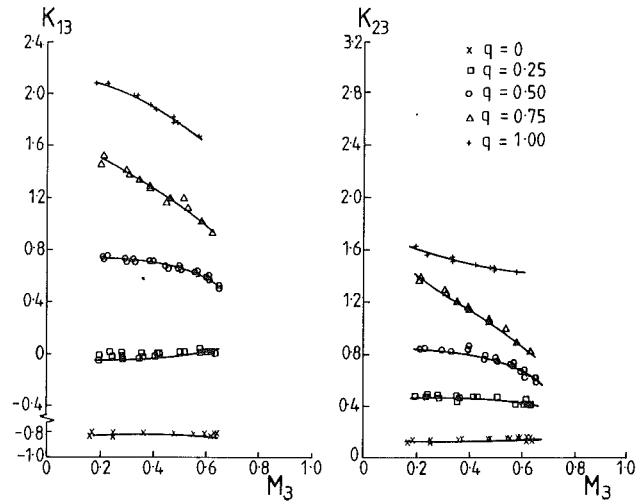


Fig. 7 Compressible flow loss coefficients K_{13} and K_{23} for $\theta = 120$ deg (uncertainty in $K_{13} = \pm 0.064$, in $K_{23} = \pm 0.057$, in $M_3 = \pm 0.012$, in $q = \pm 0.025$)

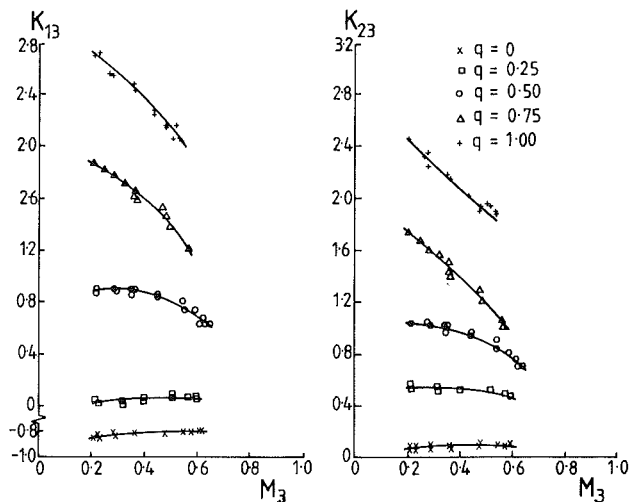


Fig. 8 Compressible flow loss coefficients K_{13} and K_{23} for $\theta = 150$ deg (uncertainty in $K_{13} = \pm 0.064$, in $K_{23} = \pm 0.057$, in $M_3 = \pm 0.012$, in $q = \pm 0.025$)

Discussion of Results

Compressible Flow ($0.2 \leq M_3 \leq 0.66$). Figures 6–8 show the variation of the loss coefficients K_{13} and K_{23} with Mach number M_3 for the 90, 120, and 150 deg junction configurations. The hoped-for full range up to $M_3 = 1$ could not be obtained despite adequate pressure being available upstream. M_3 ranged from 0.2 up to a maximum of about 0.66, which was effectively the choking limit. That sonic conditions had been reached was confirmed by Schlieren tests on a separate two-dimensional T-junction. Figures 9 and 10 show Schlieren pictures of the flow in the downstream branch of the junction for $M_3 = 0.66$, $q = 0.5$ and $M_3 = 0.61$, $q = 1$, respectively. In both photographs the distinct thick dark curve commencing at the duct intersection corresponds with the assumed boundary between the two flow regions. After about one duct width downstream this dark line has broadened into a region of flow mixing. Careful examination of Fig. 9 reveals the presence of successive lines of brightness, believed to be weak normal shock waves, in the upper flow region and over a length of about 1

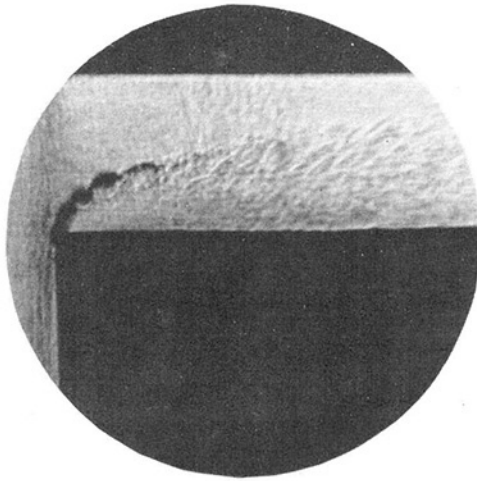


Fig. 9 Schlieren photograph showing successive weak shock waves at about 1 to 1.5 duct widths downstream of the junction: $M_3 = 0.66$, $q = 0.5$, $A_R = 2$, and flow is from the left

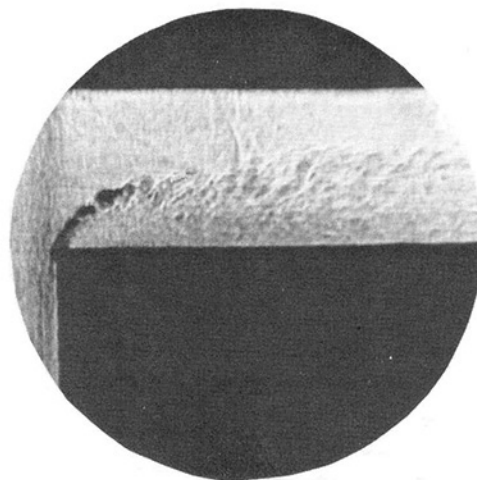


Fig. 10 Schlieren photograph showing a single shock wave at about one duct width downstream of the junction: $M_3 = 0.61$, $q = 1$, $A_R = 2$, and flow is from the left

to 1.5 duct widths from the junction. Also in Fig. 10 a single normal shock is located about one duct width from the junction in the upper flow region. Thus, the evidence for flow choking seems to be clear.

In Fig. 6 the variation in K_{13} and K_{23} with M_3 at $\theta = 90$ deg is fairly small. Other tests for $\theta \leq 60$ deg (not included in this paper) show very little variation of the loss coefficient with M_3 . At $\theta = 120$ and 150 deg (Figs. 7 and 8) K_{13} and K_{23} decrease for $q > 0.5$ as M_3 increases toward choking. The reason for the decrease in the loss coefficients as M_3 increases is that they are defined in terms of the downstream (leg 3) conditions where the difference between P_{t3} and P_{e3} is increasing more rapidly than the total pressure loss. It will also be noticed that negative losses are obtained for K_{13} at low values of q for all values of θ . This effect has been noted by other researchers and is caused by the re-energization of the flow from the lateral branch (leg 1) by the main duct flow. However, the overall total pressure loss coefficient K always has a positive value, so the Second Law of Thermodynamics is not defied!

The ranges of K_{13} and K_{23} are large. For example at $q = 1$ and $M_3 = 0.2$, the values are:

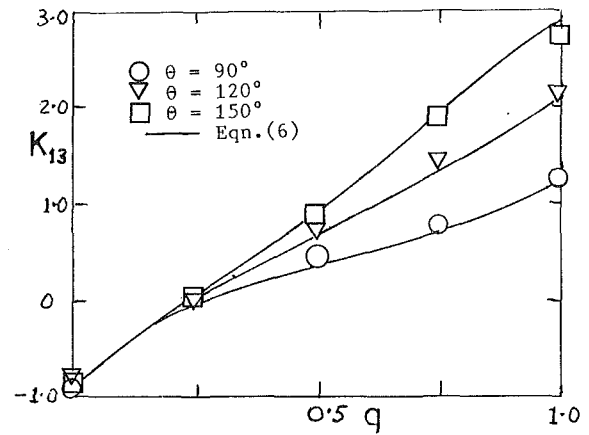


Fig. 11 Comparison between experimental data and calculated values (uncertainty in $K_{13} = \pm 0.064$, in $q = \pm 0.025$)

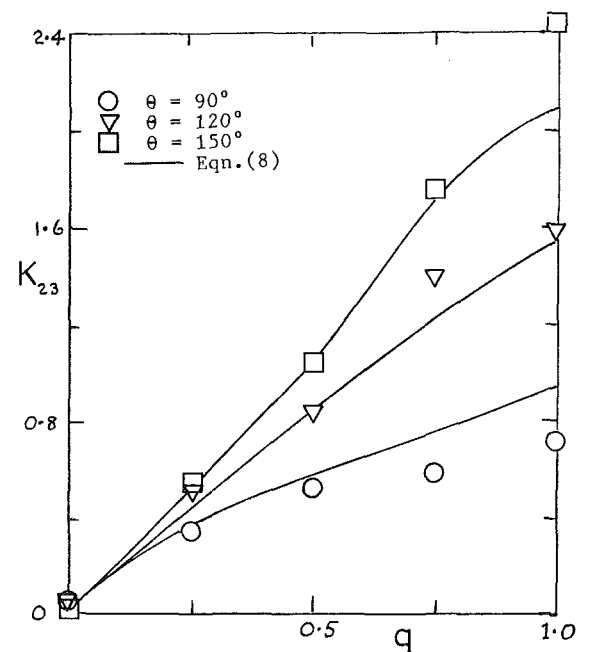


Fig. 12 Comparison between experimental data and calculated values (uncertainty in $K_{23} = \pm 0.057$, in $q = \pm 0.025$)

θ , deg	90	120	150
K_{13}	1.27	2.04	2.75
K_{23}	0.72	1.62	2.46

For $M_3 = 0.2$ the overall loss coefficient K for $\theta = 150$ deg is about 15 times larger than that for $\theta = 30$ deg at $q = 1$.

Incompressible Flow ($M_3 \leq 0.2$) The experimentally derived loss coefficients at $M_3 = 0.2$ are compared with the theoretical results based on Eqs. (6) and (8). In Figs. 11 and 12, experimental values of K_{13} and K_{23} are shown for $\theta = 90$, 120 , and 150 deg together with the theoretical curves over the full range of q . These theoretical results generally match fairly well with the experimental results.

In Figs. 13–15 the present data and theoretical results for K_{13} and K_{23} are compared with data obtained by earlier researchers. At $\theta = 90$ deg (Fig. 13) the present results for K_{13} are in good agreement with data obtained by McNown (1954) and Gardel (1957). Again, for $\theta = 120$ and 150 deg (Figs. 14

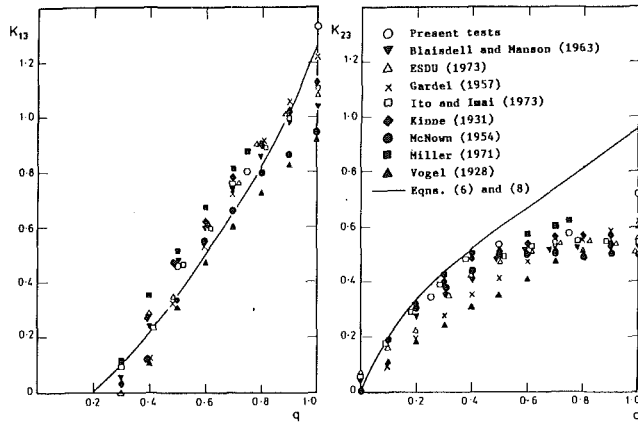


Fig. 13 Calculated values of K_{13} and K_{23} compared with various data: $\theta = 90$ deg

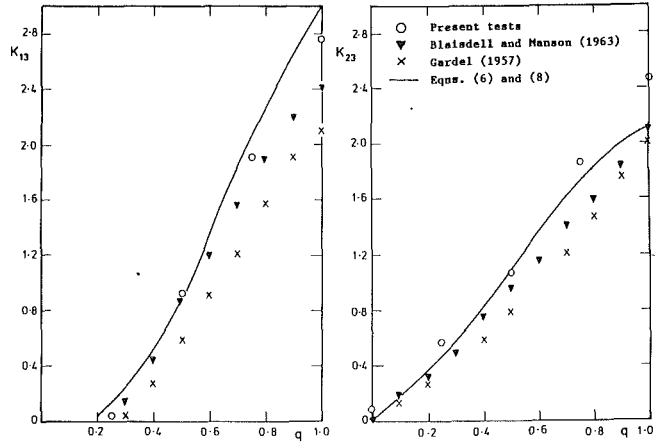


Fig. 15 Calculated values of K_{13} and K_{23} compared with various data: $\theta = 150$ deg

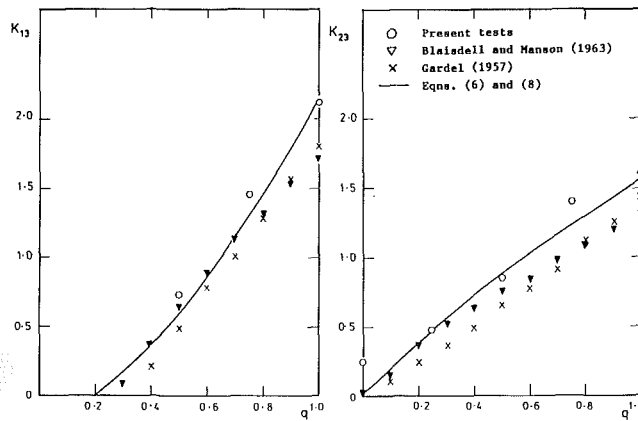


Fig. 14 Calculated values of K_{13} and K_{23} compared with various data: $\theta = 120$ deg

and 15) the data for K_{13} are in accord with those of Blaisdell and Manson (1963) over the ranges $0 \leq q \leq 0.7$. At $q = 1$ for $\theta = 120$ and 150 deg, Eq. (6) gives a value of K_{13} , which is 25 percent greater than the data of Gardel and Blaisdell and Manson.

For K_{23} the theoretical values and data at $\theta = 90, 120,$ and 150 deg are generally larger than the data other researchers obtained at $q \leq 0.5$, $\theta = 90$ deg. For $\theta = 120$ and 150 deg they are in fair agreement with the data of Gardel and Blaisdell and Manson. Overall Eqs. (6) and (8) can be used to give reasonable estimates for the additional total pressure loss coefficients in sharp-edged duct junctions.

A comparison is made between the present theory and the much-quoted theory of Blaisdell and Manson (1963) in connection with research on junction losses. Although based on the same primary set of assumptions, the latter theory does not provide satisfactory results, the values of K_{13} being grossly in error for $q \geq 0.5$. Comparison between the results of the two theories is shown in Fig. 16, where it can be seen that for $\theta = 90$ deg at $q = 0.5$ and 0.75 the Blaisdell and Manson values of K_{13} are about twice those determined by Eq. (6).

Ackeret (1967) showed experimentally derived plots of incompressible flow loss coefficients against Reynolds number for various 90 deg elbow duct configurations, one of which was for an elbow with sharp inner and outer corners. At $Re = 2 \times 10^5$ the loss coefficient he found was 1.278. In the low-speed tests ($M_3 = 0.2$) the present experiments for $\theta = 90$ deg,

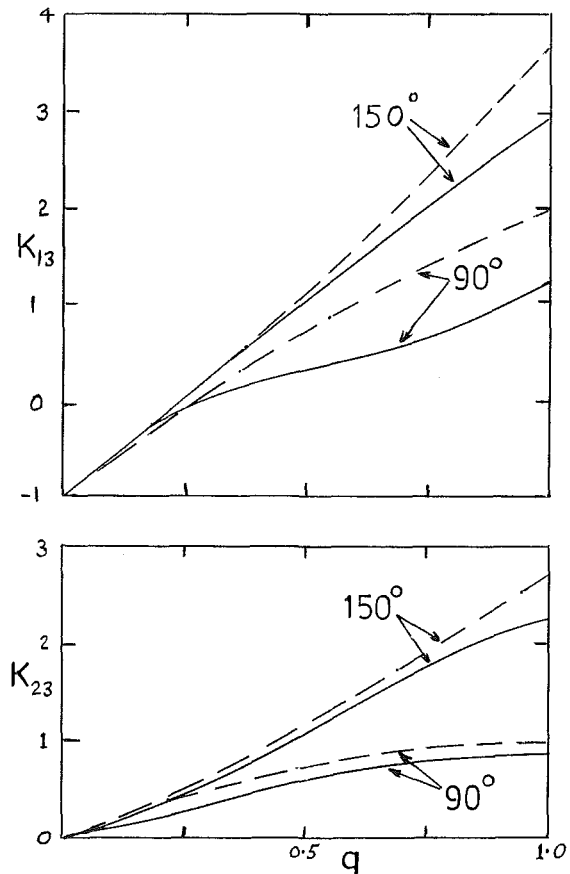


Fig. 16 Comparison of theoretical results: — present theory; --- Blaisdell and Manson (1963)

$q = 1$ gave a loss coefficient (Fig. 16) K_{13} of 1.26. This result is in good agreement with that of Ackeret and not with the Blaisdell and Manson value of about 2.0.

Conclusions

For combining flows through branched ducts with sharp intersections, the main conclusions drawn concerning the additional total pressure loss coefficients and the nature of the flow are:

- 1 The maximum Mach number M_3 of the combined flow

was 0.66, a limit caused by a combination of choking and flow separation in the downstream leg of the junction.

2 Flow visualization revealed the presence of normal shock waves at about 1 to 1.5 duct widths downstream of the junction at the choking limit.

3 The experimental results obtained at low Mach number were in good agreement with the experimental results of other researchers.

4 The measured values of K_{13} and K_{23} (for $\theta \geq 90$ deg) decrease with increase in M_3 over the measurement range. The effect is due to the pressure difference ($P_{te3} - P_{e3}$) increasing more rapidly at higher M_3 than the additional total pressure loss.

5 Comparison of the predicted and experimental data shows good agreement over most of the flow range.

6 The results obtained with Eqs. (6) and (8) show better agreement with experimental data than the values predicted by the theory of Blaisdell and Manson (1963).

7 The theoretical results tend to overestimate the loss coefficient at high Mach number. Therefore, the derived equations give a conservative prediction of the loss coefficients at high values of M_3 .

References

Abou-Haidar, N. I., and Dixon, S. L., 1988, "Compressible Flow Losses in Branched Ducts," *Collected Papers in Heat Transfer*, ASME HTD-Vol. 104, No. 2, pp. 17-23.

Abou-Haidar, N. I., 1989, "Compressible Flow Pressure Losses in Branched Ducts," Ph.D. Thesis, The University of Liverpool, Department of Mechanical Engineering, Liverpool, United Kingdom.

Ackeret, J., 1967, "Aspects of Internal Flow," in: *Fluid Mechanics of Internal Flow*, Gino Sovran, ed., Elsevier Publ. Co., Amsterdam, pp. 1-24.

B. S. 1042, 1987, "Measurement of Fluid Flow in Closed Conduits," British Standards Institution.

Blaisdell, F. W., and Manson, P. W., 1963, "Loss of Energy at Sharp-Edged Pipe Junctions in Water Conveyance Systems," U.S. Department of Agriculture, Technical Bulletin No. 1283.

E.S.D.U., 1973, "Pressure Losses in Three-Leg Pipe Junctions: Combining Flows," Engineering Science Data Unit, No. 73023.

Gardel, A., 1957, "Les Pertes de Charge dans les Ecoulements au Travers de Branchements en Te," *Bulletin Technique de la Suisse Romande*, Vol. 83, No. 9, pp. 123-130; No. 10, pp. 143-148.

Hager, W. H., 1984, "An Approximate Treatment of Flow in Branches and Bends," *Proceedings of the Institution of Mechanical Engineers*, Vol. 198C, No. 4, pp. 63-69.

Ito, H., and Imai, K., 1973, "Energy Losses at 90° Pipe Junctions," *Proceedings of the American Society of Civil Engineers, Journal of the Hydraulics Division*, Vol. 99, No. HY9, pp. 1353-1368.

Kinne, E., 1931, "Contribution to the Knowledge of Hydraulic Losses in Branches," *Mitteilungen, Hydraulischen Institute*, Munchen Technische Hochschule, Munich, No. 4, pp. 70-93.

McNown, J. S., 1954, "Mechanics of Manifold Flow," *Transactions of the American Society of Civil Engineers*, Vol. 119, Paper No. 2714, pp. 1103-1142.

Mathew, G. D., 1975, "Simple Approximate Treatment of Certain Incompressible Duct Flow Problems Involving Separation," *Journal of Mechanical Engineering Science*, Vol. 17, No. 2, pp. 57-64.

Miller, D. S., 1971, "Internal Flow. A Guide to Losses in Pipe and Duct Systems," B.H.R.A.

Vogel, G., 1928, "Investigation of the Loss in Right-Angled Pipe Branches," *Mitteilungen Hydraulischen Institute*, Munchen Technische Hochschule, Munich, No. 2, pp. 61-64.